Le rapport isotopique du bore dans l'océan, un marqueur géodynamique et climatique global : évaporites au Phanérozoïque et mesures miniaturisées de foraminifères à la transition interglaciaire-glaciaire à proximité du volcan Toba

Matthieu Buisson

To cite this version:

Matthieu Buisson. Le rapport isotopique du bore dans l'océan, un marqueur géodynamique et climatique global : évaporites au Phanérozoïque et mesures miniaturisées de foraminifères à la transition interglaciaire-glaciaire à proximité du volcan Toba. Sciences de la Terre. Université Paris Cité, 2021. Français. NNT : 2021UNIP7073 . tel-04010776

HAL Id: tel-04010776
https://theses.hal.science/tel-04010776
Submitted on 2 Mar 2023

Thèse préparée à l'Institut de physique du globe de Paris
Université de Paris

École doctorale Sciences de la Terre et de l'environnement
et physique de l'Univers STEP'UP n°560

Équipes de recherche : Géochimie des Enveloppes Externes - Géomicrobiologie

---

Le rapport isotopique du bore dans l'océan, un marqueur géodynamique et climatique global

Évaporites au Phanérozoïque et mesures miniaturisées de foraminifères à la transition interglaciaire-glaciaire à proximité du volcan Toba

par Matthieu Buisson

Thèse de doctorat de Sciences de la Terre et de l'environnement

---

- dirigée par
  Pascale Louvat
  Claire Rollion-Bard

- présentée et soutenue publiquement le
  29 Mars 2021

- devant un jury composé de
  Éric Douville, Chercheur CEA-HDR, LSCE/IPSL-Université Paris-Saclay, Rapporteur
  Kazuyo Tachikawa, Directrice de recherche, CEREGE-Aix-Marseille Université, Rapportrice
  Magali Ader, Professeure, IPGP-Université de Paris, Présidente du jury et Examinatrice
  Damien Cardinal, Professeur, LOCEAN-Sorbonne Université, Examinateur
  Markus Raitzsch, Chercheur, MARUM-Université de Brême, Invité
  Pascale Louvat, Chercheuse-HDR, IPGP-Université de Paris, Directrice de thèse
  Claire Rollion-Bard, Chercheuse-HDR, IPGP-Université de Paris, Directrice de thèse

Le rapport isotopique du bore dans l'océan, un marqueur géodynamique et climatique global

Evaporites au Phanérozoïque et mesures miniaturisées de foraminifères à la transition interglaciaire-glaciaire à proximité du volcan Toba

par Matthieu Buisson

Résumé

Face au changement climatique de l'Anthropocène, l'étude des paléoclimats et des perturbations associées du cycle du carbone au cours des temps géologiques s'est révélée fondamentale afin de comprendre les réactions du système Terre lors d'épisodes à forte teneur en CO_2 atmosphérique. Depuis les années 1990, la composition isotopique du bore ($\delta^{11}B$) dans les carbonates biogéniques marins est utilisée pour reconstruire le paléo-pH des océans, directement lié à la pCO_2 atmosphérique. Cette relation $\delta^{11}B_{carbonate}$-pH est au cœur de ce travail de thèse, jalonné par ces différentes questions.

A/ Le $\delta^{11}B_{sw}$ de l'océan dans lequel le carbonate s'est formé, est le premier paramètre clé à connaître pour utiliser ce traceur. En raison de son long temps de résidence (14 Ma), la composition isotopique en bore de l'eau de mer est aujourd'hui homogène, mais elle a évolué au cours des temps géologiques. Nous avons dans un premier temps étudié la possibilité que les halites primaires, présentant en leur sein des inclusions fluides qui témoignent de la chimie de l'eau de mer dont elles sont issues. Par notre étude, nous avons écarté la possibilité que ces inclusions puissent enregistrer directement le $\delta^{11}B_{sw}$. Nous avons dans un second temps modélisé la variation séculaire du $\delta^{11}B_{sw}$ en faisant évoluer au cours du Phanérozoïque les sources (érosion continentale) et les puits (adsorption sur les sédiments marins) de bore à l'océan, selon les dernières estimations disponibles pour ces flux.

B/ La mesure du $\delta^{11}B_{carb}$ dans les biocarbonates, présente plusieurs difficultés, notamment liées à sa volatilité en milieu acide et un fort effet mémoire en ICP-MS (entrainant risque de contamination croisée et blanc élevé). La mesure du $\delta^{11}B_{carb}$ de petits échantillons à faible [B] tels que les foraminifères (2-20 ppm de B et $m_{chantillon} \leq 5$ mg), communément utilisés en paléocéanographie, devient alors critique. Afin de maitriser ces obstacles, nous avons développé un protocole combinant 1/ la technique de microsublimation, rapide et peu contaminante, pour extraire le bore de la matrice carbonatée et 2/ un système d'injection directe des échantillons en MC-ICPMS automatisé et miniaturisé pour de faibles volumes et débits, le µ-dDIHEN. Celui-ci a permis d'atteindre des précisions inégalées pour des biocarbonates permettant d'analyser en triplicat seulement 1-2 ng de bore dans un volume de 300 µL.

C/ Ce nouveau protocole a ainsi permis d'effectuer à l'IPGP les premières mesures de $\delta^{11}B_{carb}$ dans des foraminifères planctoniques *(Globigerina bulloides)*, sur trois fractions granulométriques (250-315, 315-400 et > 400 µm) issues d'un même sommet de carotte sédimentaire. Pour ces échantillons nous avons également validé une méthode d'analyse de $\delta^{11}B$ utilisant un volume encore plus réduit d'échantillon (seulement 100 µL) nécessitant la mesure de signaux transitoires, et permettant d'analyser moins d'un ng de bore. Ces mesures de foraminifères planctoniques de différentes tailles visaient à mieux appréhender l'impact de la biominéralisation sur la relation $\delta^{11}B_{carbonate}$-pH. Pour *G. bulloides*, la variation ontogénétique du $\delta^{11}B_{carb}$ est peu significative, s'expliquant par l'absence de symbiontes et dont la densité peut impacter le microenvironnement de calcification.

D/ Ces développements analytiques ont abouti sur le quatrième volet de mon travail, la reconstruction paléocéanographique. Afin d'estimer les effets de la super-éruption du Toba (Île de Sumatra, Indonésie) sur le pH océanique au niveau de la thermocline, nous avons étudié des échantillons de foraminifères planctoniques (*Pulleniatina obliquiloculata*), issus de la carotte BAR94-25 prélevée en mer d'Andaman à proximité du volcan. Cette éruption s'est déroulée il y a environ 74 000 ans en concomitance avec la dernière transition interglaciaire-glaciaire. Considérée, par son ampleur, comme étant la plus grande catastrophe volcanique du Quaternaire, son impact sur le climat et surtout son implication dans l'entrée en glaciation restent encore controversés, tandis que ses conséquences sur la chimie de l'océan demeurent inconnues. Nous mettons ainsi en évidence un probable épisode d'acidification synchrone à des niveaux de pyroclastes volcaniques et à des phases de dissolution de $CaCO_3$ dans le sédiment.

Mots-clés

Isotopes du Bore, Paléo-pH, Paléocéanographie, Phanérozoïque, Halite, Modélisation, Microsublimation, Injection Directe, µ-dDIHEN, MC-ICP-MS, Signaux Transitoires, Carbonates, Foraminifères, Biominéralisation, Volcan Toba, Pléistocène, Interglaciaire-Glaciaire

---

The isotopic ratio of boron in the ocean, a global geodynamic and climatic marker

Phanerozoic evaporites and miniaturised measurements of foraminifera at the interglacial-glacial transition near the Toba volcano

by Matthieu Buisson

Abstract

In the light of Anthropocene climate change, studying paleoclimates and the associated carbon cycle perturbations over geological time has proved to be fundamental to understand the reactions of System Earth to episodes of high atmospheric CO_2 levels. Since the 1990s, the isotopic composition of boron (δ^{11}B) in marine biogenic carbonates is used to reconstruct the oceanic paleo-pH, directly related to the atmospheric pCO_2. This $\delta^{11}B_{carbonate}$-pH relationship is the core of this thesis work, and was considered under different approaches.

A/ The $\delta^{11}B_{sw}$ of the ocean in which the carbonate was formed, is the first key parameter to know in order to use this proxy. Due to its long residence time (14 Myr), the boron isotopic composition of seawater is nowadays homogeneous, but it has evolved over geological time. We first studied (and then ruled out) the possibility that primary halites, that contain fluid inclusions witnessing the seawater chemistry from which they precipitated, could directly record $\delta^{11}B_{sw}$. We then modelled the secular variation of $\delta^{11}B_{sw}$ by varying the sources (continental weathering) and sinks (reverse weathering) of boron in the ocean during the Phanerozoic, considering the up to date variations that are reported for these fluxes.

B/ The measurement of $\delta^{11}B_{carb}$ in biocarbonates presents several difficulties mainly due to its volatility in acidic medium and strong memory effect in ICP-MS (hence the risk of cross-contamination and high blank). On small samples with low [B] such as foraminifera (2-20 ppm B and $m_{sample} \leq 5$ mg) commonly used in paleoceanography, $\delta^{11}B_{carb}$ determination then becomes critical. These obstacles have been overcome by the development of a protocol combining 1/ the fast-handling and low blanks microsublimation technique to extract boron from the carbonate matrix and 2/ an automated and miniaturised direct injection system for sample introduction to ICP-MS, the µ-dDIHEN, that allows small volumes and low uptake rates. Our system achieved unprecedented precisions for triplicate analyses of carbonate samples containing down to 1-2 ng of boron in only 300 µL.

C/ The implementation of this protocol thus led the IPGP to the first measurements of $\delta^{11}B_{carb}$ in planktonic foraminifera *(Globigerina bulloides)* on three size fractions (250-315, 315-400 and > 400 µm) from the same sediment coretop. For these samples we also validated another method requiring even lower sample volume (only 100 µL) that necessitates the measurement of transient signals and allows decreasing the required B amount below one ng. These measurements of planktonic foraminifera aimed at better understanding the impact of biomineralisation on the $\delta^{11}B_{carbonate}$-pH relationship. For *G. bulloides*, the ontogenetic variation of $\delta^{11}B_{carb}$ is not very significant, due to the absence of symbionts whose density can impact the calcification microenvironment.

D/ These analytical developments led to the fourth aspect of my work : paleoceanographic reconstruction. In order to estimate the effects of the Toba super-eruption (Sumatra Island, Indonesia) on the oceanic pH of the thermocline, we studied the planktonic foraminifera *Pulleniatina obliquiloculata*, sampled from the BAR94-25 core taken in the Andaman Sea near the volcano. This eruption took place approximately 74,000 years ago in conjunction with the last interglacial-glacial transition. Considered by its global scale, to be the greatest volcanic disaster of the Quaternary, its impact on the climate and especially its involvement in the onset of glaciation are still controversial, while its consequences on ocean chemistry remain unknown. We thus highlight a probable acidification episode, synchronous to volcanic pyroclasts and $CaCO_3$ dissolution phases in the sediment layers.

Keywords

Boron Isotopes, Paleo-pH, Paleoceanography, Phanerozoic, Halite, Modelling, Microsublimation, Direct Injection, µ-dDIHEN, MC-ICP-MS, Transient Signals, Carbonates, Foraminifera, Biomineralisation, Toba volcano, Pleistocene, Interglacial-Glacial

---

À ma maman,

À Gildas,

À Valérie,

REMERCIEMENTS

Et voici la partie que je redoutais le plus d'écrire, plus encore que le reste de ce manuscrit. Probablement est-ce dû au fait qu'elle sera sans aucun doute la plus lue de ce manuscrit et qu'elle implique de beaucoup plus parler avec ses sentiments et non plus avec son cerveau. Cette combinaison rend cet exercice difficile pour la personne aussi terre-à-terre que je suis. Probablement aussi parce que cette partie n'est autre que la conclusion de cette magnifique aventure que fut cette thèse, parenthèse qui s'avère beaucoup plus difficile à fermer que je ne le pensais.

Résumer une thèse après trois ans et demi de travail au-delà de son aspect scientifique n'est pas une chose aisée. Mais si je devais le faire avec un seul mot, je pourrais dire qu'il s'agit avant tout d'un rêve, qui s'est réalisé et qui avait pris racine dès mon plus jeune âge, venant d'un petit garçon qui collectionnait les fiches de dinosaures devant *Jurassic Park* et les minéraux, espérant un jour devenir un des scientifiques interviewés dans *C'est pas sorcier*. Pour cela, mon parcours aura été sinueux pour initier cette thèse, mais j'ai fini par décrocher ce précieux sésame, porte d'entrée de ce monde qui me faisait tant envie. Ce doctorat aura été évidemment en contrepartie une source de perpétuelles phases d'interrogations et remises en question entre la découverte du Neptune et de l'injection directe (ce monstre bicéphale qui a nourri mes premiers cauchemars de thèse), les premières manips de chimie et mesures isotopiques qui ne marchaient pas, l'immense littérature scientifique à absorber, l'apprentissage de la programmation (qui me faisait tant horreur durant mes études), maîtriser l'anglais, rédiger des articles scientifiques ou encore se tenir devant des étudiants lors des travaux dirigés (pour de la chimie organique et de la thermodynamique, avec ma formation de géologue !). Malgré cela, mon enthousiasme durant tout ce temps ne s'est jamais tari, même avec l'arrivée d'une pandémie mondiale qui aura ébranlé cet enthousiasme que très légèrement et ponctuellement. La simple joie d'être là m'aura permis de passer chacun de ces écueils qui ont pavé le chemin menant à ce manuscrit et à la soutenance, et me fait dire aujourd'hui que quelle que soit ma future carrière, mon objectif est déjà rempli en atteignant le bout de ce chemin qui ressemble quand même beaucoup à un voyage initiatique.

On dit souvent que la réussite d'une thèse se joue énormément sur l'entourage, scientifique et personnel. Je ne peux qu'être d'accord avec cette affirmation, tant ces quatre dernières années, qui se sont déroulées à grande vitesse, j'ai été entouré de personnes formidables rencontrées dans le cadre de ce doctorat ou qui étaient présentes depuis bien avant. Je souhaite ainsi dans ces prochains paragraphes exprimer ma plus profonde gratitude à toutes ces personnes qui ont contribué à cette belle odyssée. Ils pourront paraître un peu plus longs que ce qui se fait d'habitude, mais je tenais absolument à personnaliser ces remerciements pour marquer ma reconnaissance voire mon amitié à ces personnes (en espérant surtout ne pas en oublier !).

Je tiens tout d'abord à remercier Éric Douville, Kazuyo Tachikawa, Magali Ader, Damien Cardinal et Markus Raitzsch d'avoir accepté et pris le temps d'évaluer mon travail de thèse en me faisant l'honneur de faire partie de mon jury. Vos commentaires, remarques et questions ont été précieux en me permettant d'approfondir et d'élargir le sujet tout en me montrant le recul nécessaire à avoir face à mon travail.

De plus, j'aimerais adresser mes plus vifs remerciements aux membres de mon comité de thèse, Franck Bassinot, Isabelle Martinez et Guillaume Paris, pour leurs nombreuses suggestions et recommandations toujours bienveillantes et pédagogiques, et qui m'auront ainsi aiguillé tout au long de cette thèse tout en évitant de m'éparpiller, jusqu'à me proposer d'intégrer ce super projet concernant l'éruption du Toba.

Surtout, je souhaite avant tout dire un immense merci à mes directrices de thèse, Claire Rollion-Bard et Pascale Louvat, pour m'avoir accordé leur confiance en m'offrant l'opportunité de réaliser cette thèse, après m'avoir encadré en stage de Master 2. Grâce à vous, j'ai pu réaliser mon désir d'entrer de plain-pied dans le monde de la recherche et de m'avoir ainsi permis de faire la connaissance de toutes ces fantastiques personnes pendant ce doctorat. Pour cela, je vous suis infiniment reconnaissant.

Pascale, un immense merci pour ta gentillesse infinie, ta disponibilité incommensurable (malgré les nombreux aléas instrumentaux !) et ton indéfectible soutien, couplés à tant de conseils avisés qui m'ont toujours permis d'avancer. Merci à ton dévouement inébranlable, ta pédagogie si bienveillante et ton inestimable savoir, qui m'ont permis de tellement apprendre à tes côtés, scientifiquement, par la découverte du monde des isotopes du bore dans la Zone Critique et des grands cycles géochimiques, et techniquement par le "domptage" du Neptune et de l'injection directe, et par la rigueur technique et intellectuelle nécessaire en salle de chimie pour arriver à mesurer des quantités si infimes de bore. Que de chemin parcouru où tu remarquais ma lenteur à calculer un facteur de dilution en stage de Master 2, en me disant "ça viendra" ! C'est aussi par ces qualités que j'ai beaucoup appris humainement à tes côtés. Nos si nombreuses discussions resteront des souvenirs précieux, tant cela m'a permis de cultiver ces dernières années un regard différent sur le monde qui nous entoure.

Claire, un immense merci pour ta grande disponibilité, tes nombreux conseils, encouragements et ton investissement qui m'ont permis d'appréhender ce qu'était la rigueur scientifique, à constamment questionner chaque résultat afin d'avoir le recul suffisant à chaque interprétation. Tu auras su me faire partager ta passion et ton enthousiasme pour le monde des biominéralisateurs et des prox ... traceurs ! géochimiques à partir de ces derniers, grâce notamment à ces nombreux groupes de lecture qui m'ont considérablement permis d'étendre et d'enrichir mes connaissances scientifiques sur ces sujets.

Je tiens également à remercier plus particulièrement tous les membres et ex-membres de l'équipe Géochimie des Enveloppes Externes, cette grande "famille" qui m'a apporté le meilleur environnement de travail que l'on puisse imaginer, se distinguant par sa bonne humeur, sa grande complicité, son altruisme, sa disponibilité et son appui sans faille. Et sans oublier tous ces moments suspendus dans le temps autour d'un café (ou thé !), d'une bière, d'un morceau de Comté, d'une tranche de saucisse de Morteau accompagnés de franches rigolades qui caractérisent si bien l'ambiance G2E.

En rebondissant sur ces évocations culinaires jurassiennes, je souhaite témoigner de ma profonde reconnaissance à Jérôme Gaillardet pour son accueil chaleureux d'un "ventre jaune" dans une équipe à forte couleur jurassienne ! Merci infiniment pour ton aide et de m'avoir fait partager tes inestimables expériences et savoirs, de la chimie isotopique du bore, son cycle géochimique, les évaporites à l'art de la papillote sur bécher, en passant surtout par la Zone Critique, ses processus et la place de l'Homme au sein de celle-ci qui ont alimenté de nombreuses discussions passionnantes avec celles sur le monde de la recherche et de l'enseignement. L'océan est peut-être un peu éloigné des thématiques de la Zone Critique, mais les innombrables interactions que j'ai eues avec tous les membres de l'équipe G2E à ce sujet se sont avérées conséquentes pour ma culture scientifique (et philosophique), sans oublier que ce sont tes captivants cours de Master 2 à ce sujet qui m'ont poussé à frapper la porte de l'équipe pour un stage de Master. Merci également pour ta grande disponibilité, ayant toujours eu la porte ouverte malgré ton emploi du temps de ministre, et surtout pour ton soutien, jusqu'à justifier à l'IPGP un retour à 4 h du matin pour arrêter une session Neptune !

Je voudrais aussi remercier sincèrement Julien Bouchez pour sa grande gentillesse et son entière disponibilité. Un grand merci pour ton aide conséquent, qui s'est étendu du stage de Master avec la mesure des isotopes du strontium dans les halites et le traitement des données associé jusqu'aux derniers mois de thèse avec la modélisation du cycle du bore au Phanérozoïque. De m'avoir redonné, pour la personne aussi allergique que moi lors de mes études, l'envie de toucher à des codes MATLAB, de me lancer un petit peu à Python et la motivation de remettre le nez dans des équations (entre modélisations, traitements statistiques et fractionnements isotopiques), ne font que démontrer la bienveillance et le caractère encyclopédique de tes enseignements. Entre le 5ème, Ivry et la Bretagne, on aura de multiples occasions de continuer nos discussions sport, entre foot, surf, paddle, handball avec l'US Ivry et randonnées VTT, cinéma et séries autour d'une bonne bière !

Je souhaiterais de même profondément remercier Éric Gayer pour ses multiples conseils de grandes valeurs distillés tout au long de ma thèse, de la gestion du temps d'une thèse, le déroulé d'un cours ou TD jusqu'à ses précieuses recommandations de rédaction et de planning dans la dernière ligne droite, mais en passant surtout par le délicat équilibre entre vie privée et vie de recherche et nos différentes conceptions de l'enseignement. Surtout, un grand merci de m'avoir donné définitivement goût à LaTeX et son pendant Overleaf, un gain de temps non négligeable pour moi, qui me prend beaucoup trop la tête dans la forme des documents, et sans quoi le manuscrit n'aurait jamais pris sa jolie forme finale (et je m'en excuse à vous Pascale et Claire de vous avoir infligé cela pour les corrections du manuscrit, Éric en est aussi un peu le responsable !). Tu auras grandement participé à la joie de vivre qui règne dans l'équipe, notamment par ton humour décapant. Nos nombreuses discussions autour du monde du sport auront toujours été passionnantes et de véritables bols d'air tout au long de cette thèse. On a plus qu'à attendre désormais le ballon d'or de Kylian Mbappé pour les conclure de la plus belle des manières ;).

Je tiens également à exprimer ma gratitude à Antoine Lucas pour également sa très grande disponibilité et sa gentillesse. Conjointement avec Julien, en décidant de vous attaquer avec Raphaël à la modélisation du δ^{11}B de l'eau de mer au cours des temps géologiques, tu m'as également redonné un attrait pour la modélisation et les mathématiques par tes explications toujours lumineuses sur des choses qui m'avaient toujours un peu dépassées au cours de ma scolarité. Je te remercie également pour ton aide précieuse sur la façon de traiter des données et les statistiques qui se cachent derrière. Malheureusement, je n'ai pas pu suivre l'intégralité de tes cours à ce sujet, pourtant captivants et surtout indispensables, par un manque de temps et mes difficultés à ce moment-là dans la programmation. J'espère pouvoir un jour rattraper ces cours, qui ne peuvent qu'être fondamentaux pour la suite de mon parcours.

Je remercie enfin tous les autres membres permanents (ou ex-permanents) de l'équipe G2E qui ont chacun à leur manière participé à la réussite de cette thèse et qui ont aussi fortement contribué à ces dernières belles années : un grand merci à Laëtitia Faure (et particulièrement à toi Laëtitia, pour m'avoir appris la chimie sur colonne du strontium et pour m'avoir aidé sur la chimie du bore sur colonne), Caroline Gorge, Delphine Limnois pour leur soutien logistique sur les salles de chimie, sans qui elles ne fonctionneraient tout simplement pas et pour ses conversations autour d'un café à l'arrivée le matin qui permettaient toujours de bien commencer la journée ; un grand merci à Jean-Louis "Bibi" Birck, la figure omnisciente de l'équipe qui a toujours répondu à mes questionnements d'ordre chimique et dont les anecdotes sur les débuts et l'évolution de la géochimie isotopique, de la datation (de la Lune !), des spectromètres de masse mais aussi sur le parapente sont toujours un régal à écouter (très souvent le soir quand on finissait par être les deux derniers) ; un grand merci à Catherine Chauvel pour sa grande disponibilité et ses conseils, un grand merci à Lou Derry pour sa gentillesse, ses discussions scientifiques toujours électrisantes et sa bonne humeur communicative ; un grand merci à Virginie Entringer pour son attention et son rire tout aussi communicatif et un grand merci à Fatim Hankard, présente en ce début de thèse, pour ces moments de plaisanteries et ces joutes verbales d'anthologie avec Éric (et qui auront permis de me sentir plus à l'aise au sein de l'équipe).

Ces dernières années de thèse n'auraient définitivement jamais été les mêmes sans les thésards et les post-docs de l'équipe, sur qui j'ai pu compter avec leur grande gentillesse, camaraderie, un soutien constant, une aide de tous les instants et leurs encouragements, le tout émaillé par de nombreux bons moments salutaires passés ensemble autour d'une bière, d'un café (ou d'un maté !), à base de rigolades et de débats passionnés autour de tout et n'importe quoi (et surtout n'importe quoi !). Tout d'abord, j'aimerais dire un immense merci à Quentin, qui m'aura pris sous son aile dès mon arrivée en stage jusqu'à ma troisième année de thèse (on peut avoir ainsi un "mentor" plus jeune !), en me montrant et m'expliquant toutes les ficelles de la thèse, de l'école doctorale, de l'IPGP en général et surtout l'organisation des soirées Hekla ! On se sera même motivé pour se retrouver aussi sur les terrains de handball, où tu m'auras fait aussi revoir ma façon de tirer, tout en se marrant sur le trajet des histoires de salle de chimie ! Je tiens également à remercier chaleureusement ceux qui furent tour à tour mes colocataires de bureau : Paul (avec qui j'aurais pu être en stage de Master mais l'appel du bore – et non du large – aura été plus fort) pour m'avoir porté secours sur Python et de m'y avoir apporté de nombreux conseils, son enthousiasme et pour ces moments de fou rire autour de ses géniales imitations, Xu, tour à tour banane géante ou Super Mario pour illuminer le bureau et l'étage, pour sa générosité illimitée, Alida, sans qui ce manuscrit aurait pris une tout autre forme (probablement en beaucoup moins joli), pour son aide colossale pour le traitement des données sur les signaux transitoires et surtout la réalisation des figures sur MATLAB (tu avais définitivement raison, cela simplifie beaucoup la vie, un enorme agradecimiento a usted !), pour ces nombreuses séances cinés partagées et dont l'enthousiasme imprégnait l'ambiance du bureau, Nicole pour son entrain communicatif et ses multiples corrections orales et écrites de mon anglais et Nils pour sa grande sympathie. De plus, je souhaite exprimer ma reconnaissance envers Marie, Jean-Sébastien et Jean, toujours attentionnés. J'aurai été enfin heureux de croiser un autre supporter de l'OL dans les labos avec toi Jean, même si c'est actuellement des années olympiennes à manger son pain noir, avec en apothéose cette belle déculottée partagée ensemble dans un bar quasi-désert pour une demi-finale de coupe de France ! Je souhaite ajouter un gigantesque merci au scoïste Damien et Sylvain (qui m'aura convaincu d'essayer un jour l'Ultimate !), pour leur grand altruisme et profonde bienveillance et dont les nombreux encouragements, conseils et recommandations, que ce soit sur le fonctionnement du Neptune, le travail en chimie à la conduite d'une thèse, mais surtout sur la gestion de sa vie professionnelle et personnelle pendant et après la thèse, demeureront précieux et m'auront appris à ne jamais minimiser mes réalisations. Vos saillies humoristiques et moqueries désopilantes auront été de sacrés bols d'air tout au long de cette thèse ! Et j'insiste Damien, ce *Fury Road* est un chef d'œuvre ! Enfin, je tiens à exprimer mon extrême gratitude à ma coéquipière de la *Boron team* Caroline, pour son soutien sans faille, ses nombreux conseils, sa bonne humeur contagieuse, son optimisme à toute épreuve, et dont la volonté d'aller au fond des choses m'aura toujours impressionné, quand il s'agissait de traiter de simples données, de décrire chaque zone d'ombre d'un article scientifique même quand cela concernait la biominéralisation des œufs de poule ou de parler du dernier DC/Marvel. Un grand merci à toi pour cette plongée la tête la première dans le monde de la biominéralisation des foraminifères, moules et autres bryozoaires et pour nos nombreuses discussions sur la place des femmes dans le monde de la recherche. Je terminerai ce paragraphe par une pensée pour Sofia, arrivée cette année, mais avec qui on a déjà partagé de beaux moments de rigolades en cette fin de thèse, et qui en appellent beaucoup d'autres !

Évidemment, remercier la "famille G2E" revient aussi à ne pas omettre les cousins germains du 5ème étage, l'équipe Géochimie des Isotopes Stables, qui au détour d'une pause café, d'une pause déjeuner ou d'un apéro ont su m'apporter culture scientifique, conseils, soutiens et surtout de nombreux moments de légèreté. Je désire ainsi grandement remercier pour cela : Pierre Cartigny, dont les discussions sur l'actualité m'auront toujours passionné et auront été accompagné de conseils lecture qui trônent sur ma table de chevet et avec qui j'aurais beaucoup aimé apprendre à travailler sur les gaz avec cette expérience sur le fractionnement isotopique du bore non aboutie faute de temps, Hans Eggenkamp, pour m'avoir donné l'opportunité de mesurer le δ^{11}B d'une séquence évaporitique entière du Permien engendrant de nombreuses discussions passionnantes mais qui n'a malheureusement pas débouché sur quelque chose de probant, Pierre Agrinier avec ces nombreuses discussions sur les évaporites et leur signature isotopique en chlore mais aussi Giovanni Aloisi, Gérard Bardoux (sans qui le café pour démarrer le matin serait bien plus triste), Vincent Busigny (et sa chemise à "Caro"), Jabrane Labidi, Romaric Tchibinda, et sans oublier Amaury, Arnaud (compagnon de route depuis le M2), Isabelle (merci encore pour ton aide à ce déménagement mémorable !), Étienne et Élodie.

Et surtout, le 5ème étage ne fonctionnerait pas sans le dévouement de toutes les personnes s'occupant des spectromètres de masse, dont leur aide et conseils ont été considérables, et ont ainsi grandement participer aux résultats de ce manuscrit. Je souhaite ainsi tout d'abord fortement remercier Pierre Burckel pour la réalisation des mesures de concentrations élémentaires sur l'ICP-QMS, couplé à son altruisme et sa grande disponibilité, et avec qui j'aurais assidûment pris plaisir à écouter toutes ses nombreuses interventions toujours passionnantes et très pédagogiques sur le fonctionnement du "Quad" et le traitement des données associé. Un grand merci à Mickaël Tharaud, fer de lance avec Pascale du montage µ-dDIHEN, également pour sa gentillesse et grande disponibilité mais aussi pour son aide et pour ses réponses à mes multiples interrogations afin de dompter le µ-dDIHEN et l'injection directe. N'étant pas fan du PSG, j'espère vraiment pour toi qu'ils vont finir par l'avoir cette LDC ! Et mille mercis à Thibaud et Barthélémy pour leur assistance plus que précieux sur les sessions Neptune. Ce fut un réel plaisir de rencontrer de véritables alter egos geeks, respectivement fan absolu du Seigneur des Anneaux et de Star Wars (jusqu'à trouver pas mal la dernière trilogie, y a des limites !) et dont nos conversations et débats passionnés sur les films, séries, comics et autres jeux de société auront été de sacrés bols d'air. Cette séance de *Fury Road* en 4DX, partagé avec Alida et toi, Barthélémy aura été mythique ! Merci infiniment à Pamela, pour tous ces moments de détente partagés aux pauses cafés, déjeuners mais aussi autour d'une bière après le travail ! Je finirai par remercier Julien Moureau pour ses interventions sur le Neptune qui nous ont sauvées la mise plus d'une fois, ainsi que Dimitri (encore merci d'avoir laissé ton bureau pour la soutenance) et Tu-Han (merci pour tes nombreux conseils !), arrivés en cette fin de thèse, pour leur bonhomie et sympathie.

Je remercie enfin Samia Hidalgo, pour l'accès et son aide à la salle des microscopes et loupes binoculaires et mais aussi pour sa contribution indirecte à la rédaction de ce manuscrit, en étant l'élément capital du 4ème et du 5ème étage pour l'approvisionnement du fuel de toute rédaction de thèse et de labo de recherche en général : le café !

Je clôturerai la partie IPGP en exprimant ma gratitude à toutes les personnes qui ont pris part à ces belles années de thèse : à tous mes camarades de promo membres de l'Hekla 2017-2018, Laëtitia, Martin, Edith, Tara et Benjamin, pour tous ces fabuleux moments passés ensemble à organiser puis à profiter des évènements Hekla de cette année-là, mais aussi pour ceux qui ont jalonné les années suivantes, à mon ex-colocataire Giulia (et qui par heureux hasard aura participé aussi au projet Toba par son stage de M2 sur la tephrostratigraphie de la carotte BAR94-25), à ma collègue de TD Charlotte (on en aura fait des sessions zoom pendant le premier confinement à gérer les exercices et les examens de thermo !), mon ancienne camarade de M2 devenue "copine de foraminifères" Siham, à Mathieu, Francisco et aussi aux nombreux membres de l'IPGP FC, Hugo, Julien, Gino, Ariel, ..., pour ces nombreuses parties de foot endiablées ! Je tiens enfin à spécialement remercier Giovanni "Ninto" Occhipinti, qui a su me conseiller et m'aiguiller dans mes choix afin de pouvoir intégrer l'IPGP au niveau du Master 2, à un moment charnière où je cherchais encore ma voie.

Cette thèse, financée par l'ANR franco-allemande B2SeaCarb m'aura donné la fantastique opportunité de réaliser deux séjours au sein de l'équipe de Biogéosciences marines de l'Institut Alfred Wegener à Bremerhaven. Je souhaiterais ainsi dire Herzlichen Dank à Albert Benthien, Jelle Bijma, Beate Müller, Markus Raitzsch, Klaus-Uwe Richter et Grit Steinhoefel pour leur formidable accueil. Et plus particulièrement, je remercie infiniment Markus pour l'apprentissage des différentes espèces de foraminifères, du lavage de ceux-ci (conjointement avec Beate Müller), pour ses nombreuses recommandations et nombreux conseils, toujours avec pédagogie et cordialité, sur la microsublimation, le traitement des échantillons en salle blanche, les blancs de chimie mais aussi les analyses sur le MC-ICP-MS. Ces parenthèses allemandes auront encore été plus réjouissantes grâce à Ruchen et Szabina avec qui j'aurais partagé les joies du "picking" et autres galères de préparations d'échantillons toujours sous le signe de la bonne humeur. Et plus spécialement merci à toi Szabina, pour ces soirées qui auront permis de m'acclimater beaucoup plus facilement, avec les différents doctorants de l'institut, mais aussi pour tout ton soutien sur cette fin de thèse !

Ces dernières années auront été aussi l'objet de nombreuses collaborations, qui m'auront permis de rencontrer tant de personnes épatante, sans qui cette thèse n'aurait jamais pu prendre cette forme actuelle. Je souhaite dire infiniment merci à Guillaume Paris, pour la tenue de tous ces groupes de lecture sur les traceurs géochimiques et le monde de la biominéralisation qui m'auront tant permis d'élargir ma culture scientifique, pour tous tes conseils et suggestions sur les chimies et les analyses, et particulièrement pour avoir été la personne à m'ouvrir les portes du projet Toba. Je souhaite ainsi dire un immense merci à Annachiara Bartolini de m'avoir embarqué dans ce passionnant projet, dont l'enthousiasme, la bienveillance, l'optimisme à toute épreuve, les nombreux conseils et encouragements auront rythmé la dernière partie de ma thèse. Je remercie également les autres membres du projet Toba, Franck Bassinot, Benoît Caron, Anne Le Friant et Eva Moreno pour leurs résultats et données précédemment obtenus à mon introduction au sujet et ayant ainsi servi à l'interprétation des données bore et Mg/Ca. J'aimerais de plus remercier William Gray pour son aide et ses nombreuses suggestions pour la mise en place du lavage des foraminifères à l'IPGP. Enfin, je remercie Mickaël Hermoso et Fabrice Minoletti, qui m'auront permis d'envisager la belle opportunité de mesurer des isotopes du bore dans les coccolithes et fourni quelques échantillons pour cela, sans que cela n'aboutisse malheureusement pour des limites analytiques. Je clôturerai cette partie en évoquant les étudiants en stage avec qui j'ai travaillé : tout d'abord Ana, stagiaire de M2 que j'ai co-encadrée sur le Toba puis devenue collègue en thèse ; ce fut un immense plaisir de t'encadrer sur ce stage, marqué par ta motivation, ton enthousiasme, ta bonne humeur et ta grande rigueur de tous les instants entre chaque session de cracking, lavage de foraminifères, microsublimation, analyses isotopiques et discussions des données. Ces moments auront été ponctués par ses innombrables discussions rafraîchissantes sur tout et n'importe quoi, notamment lors de loooonnngues sessions de lavages, qui auront ainsi permis de faire passer les journées beaucoup plus vite ! Tu m'auras probablement pris pour un grand maniaque en salle blanche au tout début, mais tu auras fini par devenir pareil ahah ! Ensuite, je dis un grand merci à Raphaël, encadré par Julien et Antoine, pour avoir pris à-bras-le-corps toutes ces histoires de modélisation du cycle du bore au cours des temps géologiques, et pour m'avoir ainsi grandement aidé à dénouer le nœud gordien des équations et autres problèmes mathématiques derrière tout ça (il m'aurait fallu plusieurs années je pense !). Enfin, j'ai une pensée pour Aya qui aura permis de valider encore plus la méthode d'analyse des isotopes du bore sur d'autres foraminifères lors de son stage, passé avec succès et une grande motivation pour un sujet par forcément facile en L3.

Je tiens à dire également un grand merci à tous mes amis pour ces multiples moments partagés ensemble et sur qui j'ai toujours pu compter depuis déjà de nombreuses années. Leur ombre aura ainsi planer par leur action indirecte sur tout le déroulé de la thèse en m'ayant apporté énormément par leur présence, leur fidélité, leur affection, leurs encouragements et leurs soutiens, des galères avant thèse jusqu'à la dernière ligne droite. Toutes mes pensées vont ainsi en particulier vers Marine, Xavier, Simon, Mathilde, Juan-David, Manon, François, Takfa, Matuk, Yohan, Florian, Eva, Francesca, Romain, Nicolas, Thibaud, Léa, Domi, Juliette, Coralie, Jordan et Paul-Éloi ...

J'achève enfin ces remerciements en rendant hommage aux quatre piliers de cette aventure, qui auront permis de faire tenir tout l'édifice. Je souhaite ainsi vous dire de tout mon cœur merci de m'avoir épaulé toutes ces années, pour votre attachement, votre amitié, votre irremplaçable dévouement et altruisme, vos inestimables et inconditionnels encouragements, soutiens et aides.

Je pense tout d'abord au pilier de l'IPGP, qu'ont été Paco, Laëtitia, Sarah et William. Merci à vous Paco et Laëti d'avoir tant illuminé mes années au 5ème étage, par ses indénombrables pauses qui m'ont été vitales entre discussions scientifiques, politiques, philosophiques, sur notre futur et à base de grand n'importe quoi (ça penchait plutôt vers ce pôle) et de rigolades, et ses nombreuses soirées (celle du déménagement restera gravé dans ma mémoire !). J'aurai appris beaucoup de choses en biologie à tes côtés Paco, c'est toi que j'aurais dû avoir en prof de SVT (j'aurais moins fait l'impasse au lycée par rapport à la géologie !). Merci à toi Sarah, dont les discussions et encouragements depuis le Master 2 m'ont tout autant été cruciaux, notamment dans les moments de moins bien. On se rappellera de ces super soirées Hekla, organisées et passées ensemble (avec en point d'orgue la remise des diplômes de M2), ou encore de cette formation en pédagogie universitaire sur comment rendre la chimie organique plus attractive en licence Sciences de la Terre à base de *Breaking Bad* ! Merci à toi William, d'avoir été mon compagnon de route lorsque l'on partageait nos galères de spectro et de chimie jusqu'à pas d'heure, à souvent se retrouver à manger des kebabs devant des matchs de coupe de France en attendant que ça se termine tout en évitant les problèmes avec les gardiens ! Mais aussi pour ton soutien et ton aide jusqu'à la dernière ligne droite en direct de Chambéry et pour les nombreuses bouffées d'air frais entre les pauses thés/cafés, les cinémas, les apéros, les repas diététiques à base de kebabs/hamburgers/pizzas (j'avais bien les bonnes adresses !) et les soirées passés ensemble lors de tes nombreux passages à l'IPGP, à bien se marrer entre deux discussions sérieuses sur notre futur dans la recherche !

Je pense ensuite au pilier qu'ont été mes amis proches, et ce depuis tant d'années voire décennies. Un immense merci à vous d'avoir été là depuis le début et tout le temps, pour votre soutien et indispensables encouragements, notamment dans les moments difficiles avant mon entrée à l'IPGP et qui m'ont permis en grande partie d'en arriver là aujourd'hui. Merci à toi Steve, d'avoir tant égayer ces deux décennies passées ensemble, où tu as toujours été à l'écoute des mes nombreux déboires et pendant lesquels on aura fait les 400 coups. Tu auras été pendant toute la durée de cette thèse à l'autre bout du monde, mais tes trop rares visites (foutu COVID) et nombreux appels forcément à l'heure du déjeuner auront fait un bien fou ! Merci à toi Benjamin, mais aussi à Prithvy (qui est rentré plus tard dans ta vie) pour vos si précieux conseils et d'avoir toujours été à l'écoute, mais aussi pour ton inestimable franchise, qui m'aura à la fois fait tant marrer mais aussi toujours permis d'avancer dans la bonne direction.

Je pense également au troisième pilier qu'aura été ma famille et mes proches, qui m'ont constamment soutenu et encouragé dans mes choix, et sans qui rien de tout de cela n'aurait été possible. Mille fois merci à vous d'avoir su éveillé en moi cette passion des sciences, avec la curiosité qui la caractérise tant. Je souhaite ainsi rendre hommage à ma tante Anne, qui a plus que nourri mon appétit des sciences en m'amenant tout petit dans les musées avec en particulier la visite mémorable du Museum d'Histoire Naturelle de Paris, et qui m'aura tant encouragé depuis tout ce temps. Ta présence, ton aide, tes conseils et tes encouragements sans discontinuer auront été très chers à mes yeux. Je voudrais aussi de la même manière profondément remercier mes nombreux cousins et cousines ainsi qu'oncles et tantes, et en particulier Perrine, Hélène et Marie, mes tantes Françoise et Françoise, et Jean-Luc, et surtout mes frères Jean-Clément et Thibault. Avec toi Thibault, on aura partagé ce goût des géosciences jusqu'au Master 2 (jusqu'à partager un lit superposé dans notre appartement parisien pour les études ahah), et maintenant aussi de l'enseignement avec ton arrivée dans les collèges et lycées de France ! Je souhaite également remercier infiniment Christine, Francis et Antoni pour leur extraordinaire accueil, ainsi que pour leurs multiples encouragements et soutiens. Enfin je terminerai pas un hommage infini à mon Papa, qui n'a jamais questionné mes choix et toujours soutenu, sans jamais trouver quoi que ce soit à redire.

Enfin, je terminerai par mon quatrième pilier, sans qui je n'aurais jamais commencé cette thèse et surtout jamais pu la terminer : Manon. Je ne crois pas qu'il existe de mots assez forts pour exprimer ma gratitude à ton égard. Tu m'auras soutenu, épaulé, encouragé, poussé, assisté, réconforté jusqu'au bout, même quand cela signifiait que je devais rentrer à pas d'heure ou y passer mes week-ends pour les analyses, les chimies ou encore la rédaction. Un immense merci du fond du cœur pour ton dévouement et ta compréhension qui auront été les pièces centrales de cette thèse.

En parallèle à ces remerciements, je souhaite dédier cette thèse à mon oncle Gildas et ma cousine Valérie, qui m'avaient toujours soutenu et encouragé depuis mon plus jeune âge (et même en ayant préféré le foot au rugby !). Et surtout, j'aimerais dédier cette thèse à ma maman, qui aurait été très heureuse et fière aujourd'hui, d'autant plus en ayant un autre géologue dans la famille comme son papa.

TABLE DES MATIÈRES

Résumé iii

Abstract v

Remerciements viii

Table des matières xix

Liste des figures xxiii

Liste des tableaux xxxiii

1 Introduction générale **1**
1.1 L'Anthropocène . . . 2
1.2 La paléoclimatologie pour anticiper l'avenir . . . 5
1.3 Problématiques abordées dans ce travail de thèse . . . 10

2 Les isotopes du bore et paléo-pH océaniques **13**
2.1 L'océan et le cycle du carbone . . . 15
2.2 Reconstruction des paléo-pH océaniques à partir des isotopes du bore . . . 17
2.2.a Chimie et isotopie du bore . . . 17
2.2.b Principes des isotopes du bore comme pH-mètre . . . 18
2.2.c Composition isotopique en bore des carbonates : théorie . . . 21
2.2.d Incorporation du bore dans les foraminifères . . . 22

3 Seawater δ^{11}B through the Phanerozoic **27**
3.1 Introduction . . . 29
3.2 Material and methods . . . 32
3.2.a Halites . . . 32
3.2.b Modeling . . . 34

3.3 Results . . . 39
- 3.3.a Halite samples . . . 39
- 3.3.b Modelled [B]$_{sw}$ and δ^{11}B$_{sw}$ . . . 41

3.4 Discussion . . . 43
- 3.4.a Halites as a direct archive of δ^{11}B$_{sw}$ secular variations? . . . 43
- 3.4.b δ^{11}B$_{sw}$ secular variations across the Phanerozoic . . . 50

3.5 Conclusion . . . 62

3.6 Appendix . . . 64
- 3.6.a Halite data . . . 64
- 3.6.b Geological and stratigraphic settings of the halite samples . . . 67
- 3.6.c Fluid inclusions in primary halites: geochemical memory of paleo-oceans 74
- 3.6.d δ^{11}B$_{sw}$ across the Phanerozoic: state of the art . . . 78
- 3.6.e XRD diffractograms . . . 84
- 3.6.f Models . . . 84

4 The μ-dDIHEN setup 89

Avant-propos : analyse des isotopes du bore . . . 90
- Le MC-ICP-MS Neptune . . . 90
- L'injection directe . . . 92
- Le μ-dDIHEN . . . 93

4.1 Introduction . . . 95

4.2 Material and methods . . . 96
- 4.2.a The μ-dDIHEN liquid introduction system . . . 96
- 4.2.b Interfacing ICP-MS with the μ-dDIHEN introduction system . . . 97
- 4.2.c ICP-MS measurements . . . 98
- 4.2.d Reagents and sample preparation . . . 98

4.3 Results and discussion . . . 100
- 4.3.a Uptake rate, stabilization time, reproducibility of the injections and sensitivity . . . 100
- 4.3.b Boron isotope ratio measurements by MC-ICP-MS . . . 103
- 4.3.c Multi-element analysis by HR-ICP-MS . . . 106
- 4.3.d Au nanoparticles characterization by spICPMS . . . 107

4.4 Conclusion . . . 109

5 δ^{11}B determination in low-B biocarbonates 111

5.1 Introduction . . . 114

5.2 Experimental . . . 116
- 5.2.a Reagents, materials and labware . . . 116
- 5.2.b Standard and reference materials . . . 117
- 5.2.c Boron separation from carbonates by microsublimation . . . 118
- 5.2.d The μ-dDIHEN . . . 119
- 5.2.e MC-ICP-MS analyses . . . 119

5.3 Optimisation of the δ^{11}B measurements for low [B] . . . 122
- 5.3.a Sample and skimmer cones combinations . . . 122
- 5.3.b Reduction of the signal/noise ratio with 10^{13} Ω amplifiers . . . 126
- 5.3.c Long-term reproducibility . . . 129

5.4 Boron separation with the microsublimation . . . 131
- 5.4.a Whole procedural blank contamination . . . 131
- 5.4.b Heating duration of the microsublimation . . . 133

5.4.c Microsublimation for different B masses loaded 134
5.5 Application: microsublimation vs ion chromatography 135
5.6 Conclusion 139

6 δ^{11}B measurements in foraminifera 141
6.1 Introduction 143
6.2 Experimental 146
6.2.a Foraminifera samples 146
6.2.b Reagents, Material and Labware 146
6.2.c Foraminifera cleaning 147
6.2.d Boron isotope analysis in continuous mode 148
6.2.e Boron isotope analysis in transient mode 150
6.3 Results and Discussion 151
6.3.a Cleaning efficiency 151
6.3.b δ^{11}B measurements in continuous and transient mode 151
6.3.c Ontogenetic variability of the δ^{11}B in *G.bulloides* 157
6.4 Conclusion 158

7 Impact de la super-éruption Toba sur l'océan 161
7.1 Introduction 163
7.1.a Cadre général 163
7.1.b La super-éruption du volcan Toba 164
7.1.c Impact de la super-éruption du volcan Toba : hypothèses 165
7.2 Matériel et méthodes 168
7.2.a Matériel 168
7.2.b Mesure du δ^{11}B 169
7.2.c Mesure du Mg/Ca et efficacité du lavage des foraminifères 170
7.2.d Données sédimentaires et géochimiques pré-existantes 171
7.3 Résultats 173
7.3.a Données préliminaires sur la super-éruption YTT : âge, niveaux de téphra et dissolution de $CaCO_3$ 173
7.3.b δ^{11}B de *P. obliquiloculata* lors de la phase YTT 174
7.3.c Évolution de la température de la thermocline lors de la phase YTT . . 175
7.4 Discussion préliminaire 176
7.5 Conclusion 179
7.6 Données 180

8 Conclusion générale et perspectives 181
8.1 Conclusion 181
8.2 Perspectives 184

9 Appendix : Single-shell $\delta^{11}B_{C.\ wuellerstorfi}$ analysis 187

Bibliographie 199

LISTE DES FIGURES

1.1 Magnitude et échelle de temps des changements provoqués sur le cycle du carbone par différents processus climatiques et géologiques. La perturbation anthropogénique du cycle du carbone est mise en perspective avec l'extinction massive de la limite Permo-Trias (252 Ma) et le maximum thermal de la limite Palocène-Eocène. D'après Royer (2016). 3

1.2 Proposition du début de l'Anthropocène en fonction de l'évolution de la température, du méthane et du dioxyde de carbone atmosphérique, il y a 5000 ans BP (b), en 1610 (c) et en 1964, par le pic de ^{14}C retrouvé dans les anneaux de croissance des arbres (d). La limite Holocène/Pléistocène est fixée à 11 650 ans (a). D'après Lewis & Maslin (2015). 4

1.3 800 000 ans d'enregistrements de la pCO_2 atmosphérique à partir des bulles de gaz piégées dans les carottes de glace en gris, des alcénones (triangle orange, ± 60 ppm), de l'index stomatique (carré vert, ± 20 ppm), du rapport B/Ca (diamant bleu clair, ± 30 ppm) et des isotopes du bore (diamant bleu foncé, ± 20 ppm) à partir des foraminifères planctoniques. D'après Hönisch *et al.* (2019) et références associées. 6

1.4 Compilation de la pCO_2 atmosphèrique à travers le Phanérozoïque, reconstituée à partir (a) des paléosols (en bleu) et des isotopes du bore (en rouge), (b) des alcénones (en vert) et des indices stomatiques (en kaki) et avec en (c) l'estimation moyenne de l'erreur associée pour chaque traceur géochimique. D'après Mills *et al.* (2019). 7

1.5 Reconstruction de la pCO_2 atmosphérique au cours du Phanérozoïque, à partir du modèle biogéochimique COPSE (A) et du modèle GEOCARBSULF (B) en comparaison avec l'enveloppe des différents traceurs géochimiques de la figure 1.4.c. Les modèles actualisés ont été réalisés à partir de forçages géodynamiques modernisés sur le Phanérozoïque. D'après Mills *et al.* (2019). 9

1.6 Compilation des pCO_2 atmosphériques déterminées à partir des différents traceurs géochimiques (index stomatique, alcénones, carbonates pédogéniques, isotopes du bore) (a,b), des carottes de glace (c,d) et les prédictions pour les prochains siècles, RCP pour les derniers scénarios du GIEC, WINK12K pour le scénario de Winkelmann *et al.* (2015). Modifiée de Foster *et al.* (2017). 10

2.1 "Bjerrum plot" représentant les différentes espèces de carbone dissout dans l'océan en fonction du pH, aux conditions de surface en rouge (T=25°C, S = 35, P = 1 bar) et pour l'océan profond en noir (T = 4 °C, S = 34.8 et P = 401 bar). D'après Hönisch *et al.* (2019). 16

2.2 (a) Influence de la température (rouge), de la salinité (bleu clair) et de la pression (violet) sur la constante de dissociation pK$^*_B$. (b) Influence de la température, la salinité et de la pression sur sur le δ^{11}B de l'ion borate à pH = 8. D'après Foster & Rae (2016). 18

2.3 Concentration (a) et composition isotopique (b) de l'ion borate B(OH)$_4^-$ et acide borique B(OH)$_3$ en fonction du pH océanique, pour une température de 25°C, une salinité de 34,7 psu, un pK$^*_B \approx$ 8.6 et un fractionnement isotopique α_{B3-B4} de 1.0272 (Klochko *et al.*, 2006), une composition isotopique d'eau de mer δ^{11}B$_{sw}$ = 39.61 ‰ (Foster *et al.*, 2010) et un bore total [B]$_{sw}$ = 432,6 x (salinity/35) µmol.kg^{-1} (Lee *et al.*, 2010). Le rectangle gris correspond à la gamme mesurée dans les carbonates biogéniques modernes. Modifié d'après Foster & Rae (2016). 19

2.4 Calibration δ^{11}B$_{carbonate}$ -δ^{11}B$_{borate}$ pour les foraminifères planctoniques Orbulina universa, Globigerinoides ruber, Trilobatus sacculifer, Globigerina bulloides, Globoconella inflata, Neogloboquadrina pachyderma. Mesure ponctuelle pour Pulleniatina obliquiloculata, Globigerinella siphonifera et Neogloboquadrina dutertrei. D'après Henehan *et al.* (2016) et références associées. 23

2.5 Schéma du micro-environnement de calcification d'un foraminifère planctonique avec symbiotes. Si tous les foraminifères sont impactés dans leur micro-environnement par la respiration et la calcification, ceux qui possèdent des symbiotes sont marqués par une séquestration de CO$_2$ et donc une élévation de pH par l'activité synthétique de ces derniers. D'après Hönisch *et al.* (2019). 25

3.1 Halite samples distribution positioned on a map of the major halite basins (modified Warren 2010). The approximate ages are from Horita *et al.* (2002). . . 32

3.2 The global boron geochemical cycle with its main natural reservoirs. Red and blue arrows represent respectively the boron input and output fluxes to the oceans and associated red and blue numbers are the average fluxes and B isotope fractionation factors (Δ^{11}B in ‰). Black numbers are the average B concentrations and δ^{11}B values (‰, bulk) of the reservoirs. Data compiled from: (1) Marschall *et al.* (2017) (2) Marschall (2018) (3) Foster *et al.* (2010) (4) Smith *et al.* (1995) (5) You *et al.* (1993) (6) Leeman & Sisson (1996) (7) Lemarchand *et al.* (2002b) (8) Chetelat *et al.* (2009) (9) Vengosh *et al.* (1991b) (10) Spivack & Edmond (1987) (11) Palmer *et al.* (1987). 35

3.3 Variation of the geodynamic forcings through the Phanerozoic, impacting the boron oceanic budget. (a) Normalized total subduction length (Mills *et al.*, 2017) (b) Normalized runoff (Goddéris *et al.*, 2014) (c) Relative rate of continental erosion (Hay *et al.*, 2006) and its derived 100 Myr moving average (Mills *et al.*, 2019) (d) Normalized carbonate burial rate (Berner & Mackenzie, 2011). 38

3.4 Boron isotopic composition as a function of B concentration for each halite aliquot. 40

3.5 Average boron isotopic composition as a function of halite age. The gray area represents the halite δ^{11}B$_{sw}$ values from Paris *et al.* (2010b) and the blue area the envelope of the δ^{11}B$_{sw}$ estimated from carbonates in the literature (See Fig.3.8 and 3.9 for the references). 40

3.6 ^{87}Sr/^{86}Sr measured in the halite samples, with the addition of the Guérande salt, in light of the seawater ^{87}Sr/^{86}Sr compilation from unaltered carbonates (Veizer *et al.*, 1999 ; Prokoph *et al.*, 2008 ; Halverson *et al.*, 2007). 41

3.7 Modelled seawater boron concentration and isotopic composition across the Phanerozoic with the two scenarios of constant or variable riverine B flux. 42

3.8 Data compilation of seawater boron concentrations (a) and isotopic compositions (b) across the Cenozoic. Lines are for models and calculations from foraminifera data (Lemarchand *et al.* 2002b ; Raitzsch & Hönisch 2013 ; Greenop *et al.* 2017, this study); circles, triangles and yellow areas for determinations from foraminifera studies (Palmer *et al.*, 1998 ; Pearson & Palmer, 1999, 2000 ; Pearson *et al.*, 2009 ; Foster *et al.*, 2012 ; Raitzsch & Hönisch, 2013 ; Martínez-Botí *et al.*, 2015a ; Anagnostou *et al.*, 2016 ; Gutjahr *et al.*, 2017 ; Henehan *et al.*, 2019); ; squares for halite data (Paris *et al.* 2010b, this study). Blue dotted line: variable runoff (Lemarchand *et al.*, 2002b), blue solid line: variable runoff (Lemarchand *et al.*, 2002b), variable pH from foraminifera with fractionation factor=1.0272 (Raitzsch & Hönisch, 2013), orange solid line: variable pH from foraminifera with fractionation factor=1.020 (Raitzsch & Hönisch, 2013). 44

3.9 Data compilation of seawater boron concentrations (a) and isotopic compositions (b) across the Phanerozoic. Lines are for models and calculations from foraminifera data (Lemarchand *et al.* 2002b ; Joachimski *et al.* 2005 ; Raitzsch & Hönisch 2013 ; Greenop *et al.* 2017), this study); diamonds and rectangles from brachiopod data (Lécuyer *et al.*, 2002 ; Joachimski *et al.*, 2005 ; Simon *et al.*, 2006 ; Müller *et al.*, 2020); stars from inorganic carbonate data (Kasemann *et al.*, 2010 ; Ohnemueller *et al.*, 2014 ; Clarkson *et al.*, 2015); and squares for halite data (Paris *et al.*, 2010b) in grey, and this study: AW-86-49 and Ara7. Blue dotted line: variable runoff (Lemarchand *et al.*, 2002b), blue solid line: constant runoff (Lemarchand *et al.*, 2002b), green dotted line: variable continental input (Joachimski *et al.*, 2005), green solid line: constant continental input (Joachimski *et al.*, 2005) variable pH from foraminifera with fractionation factor=1.0272 (Raitzsch & Hönisch, 2013), orange solid line: variable pH from foraminifera with fractionation factor= 1.020 (Raitzsch & Hönisch, 2013). 46

3.10 Sensitivity tests on the δ^{11}B$_{sw}$ with an imposed sinusoidal oscillation for each forcing playing a role in the oceanic boron fluxes. The black line is the boron isotopic composition of seawater reconstructed with a variable runoff. The colour code of the selected forcing chosen to fluctuate are the same as in Fig.3.3. (a) Perturbed oceanic crust alteration. (b) Perturbed hydrothermalism. (c) Perturbed fluids expelling from accretionary prisms. (d) Perturbed continental boron discharge. (e) Perturbed adsorption on the clastic sediments. (f) Perturbed boron coprecipitation. 52

3.11 Comparison between modelled δ^{11}B$_{sw}$ for the "complete" box model (black lines) and "simplified" model (yellow lines) where only the main output, alteration of the oceanic crust, and main input, boron continental discharge, are considered. Both scenarios of constant (solid lines) and variable (dotted lines) runoff are represented. 53

3.12 Normalized oceanic crust production for the Mesozoic and the Cenozoic reconstructed from magnetic anomalies with plate rotations models (Larson, 1991 ; Rowley, 2002 ; Cogné & Humler, 2004, 2006 ; Muller *et al.*, 2008 ; Seton *et al.*, 2009 ; Coltice *et al.*, 2013) and normalized subduction rates from full-plate motion model (Engebretson *et al.*, 1992 ; Van Der Meer *et al.*, 2014 ; East *et al.*, 2020). The distinction between the two estimations by Cogné & Humler (2006) are for an oceanic crust production ($km^2.an^{-1}$, solid green line) and an oceanic crust flux ($km^3.an^{-1}$, dashed green line). For Seton *et al.* (2009), the two orange lines are from two different crust model ages. 54

3.13 Normalized oceanic crust production rate for the Phanerozoic reconstructed from sea-level inversion (Gaffin, 1987 ; Mills *et al.*, 2017), from the mantellic strontium flux (van der Meer *et al.*, 2017) and normalized subduction rates from full-plates motion model (Vérard *et al.*, 2015 ; Merdith *et al.*, 2017 ; Mills *et al.*, 2017 ; Hounslow *et al.*, 2018). The two curves from (Mills *et al.*, 2017) are a reconstruction from updated paleo sea-level (solid pink line) and the total suture length (dashed pink line, as used in this study. 55

3.14 Normalized runoff for the Phanerozoic from Otto-Bliesner (1995), Gibbs (1999) (straight line: control and dashed line elevated CO_2) and (Goddéris *et al.*, 2014) (solid line: full simulation, dashed line: with only a rising solar constant and paleogeography). 56

3.15 Compilation of all the runs computed in this study with all possible combinations of variable runoffs or constant runoff (3.14) and oceanic crust productions (Fig.3.12 and 3.13). The colours correspond to the oceanic crust production rates referenced in the figures (Fig.3.12 and 3.13). 58

3.15 (Previous page.) Seawater chemistry and atmospheric pCO_2 across the Phanerozoic. (a) Modelled seawater boron concentration. (b) Modelled seawater boron isotopic composition. (c) Concentration of Ca^{2+} (red), Mg^{2+} (green) and SO_4^{2-} (blue) calculated from fluid inclusions in primary marine halites (Brennan & Lowenstein, 2002 ; Horita *et al.*, 2002 ; Brennan *et al.*, 2004 ; Lowenstein *et al.*, 2005 ; Brennan *et al.*, 2013 ; Holt *et al.*, 2014) and modelled (Demicco *et al.*, 2005). (d) $^{87}Sr/^{86}Sr$ ratio measured in the halite samples (symbols as in figure 3.6 and modern Guérande salt, grey square), in light of the seawater $^{87}Sr/^{86}Sr$ compilation from unaltered carbonates (Veizer *et al.*, 1999 ; Prokoph *et al.*, 2008 ; Halverson *et al.*, 2007). (e) Modelled atmospheric CO2 concentration from the updated long term carbon cycle box models GEOCARBSULF and COPSE, and from proxy estimations (grey area, Mills *et al.* 2019). $CaCl_2$ and $MgSO_4$ seas correspond to the switch where [Ca^{2+}] is respectively higher and lower than [SO_4^{2-}], and consequently to marine KCl and $MgSO_4$ late evaporite depositions in the geological records (Hardie, 1996). Aragonitic and calcitic seas are respectively set when Mg/Ca in seawater is higher or lower than 2 (Sandberg, 1983 ; Lowenstein *et al.*, 2014). 61

3.16 Seawater density and ionic strength of an evaporating modern seawater and associated evaporite mineral precipitation sequence (McCaffrey *et al.*, 1987 ; Bąbel & Schreiber, 2014). The timing of the evaporite precipitation sequence has been approximated from Shalev *et al.* (2018) (figure modified from Bąbel & Schreiber 2014). 67

3.17 Location of the Pliocene Sedom Lagoon and its associated facies in the Dead Sea Rift (DSB=Dead Sea Basin). Figures from García-Veigas *et al.* (2009). . . . 68

3.18 Paleogeography and paleoclimate of the Late Triassic with a focus on the North Europe. ITCZ: Intertropical Convergence Zone, O: Olenekian, A: Anisian, L: Ladinian, C : Carnian, N : Norian, R: Rhaetian. Figure from McKie 2017. 69

3.19 (A) Paleogeographic map of the Upper Permian (260 Myr, `www.deeptimemaps.com`), with the location of the Delaware basin (red circle); (B) Paleogeography of the Delaware Basin at the same time. Figure from Feng *et al.* (2018). 70

3.20 Paleomap of the Middle Devonian (390 Ma, figure from Domeier & Torsvik 2014); (B) Focus on the paleogeography of the Laurentia palaeocontinent at the same period (Broughton 2018, modified from `www.deeptimemaps.com`). . . 71

3.21 Paleogeographic map of the late Middle- Late Ordovician (452 Myr). The Canning Basin is located by the star. Figure from Spaak *et al.* (2017). 72

3.22 (A) Paleogeography reconstruction of the Lower Cambrian (530 Myr). Figure from (Li *et al.*, 2008); (B) Paleomap of the Siberian Terrane during the Late Cambrian (500 Myr). Figure from Cocks & Torsvik (2007). 73

3.23 (A) Paleogeographic reconstruction of the Mid-Cambrian, the numbers corresponding to the references from which have been extracted the continental margins setting. Figure from Millson *et al.* (1996) and references therin.; (B) Location of the Evaporite Belt on the eastern Gondwanan terranes, 1: Alborz Mountains of northern Iran, 2: Oman, 3: Lesser Himalayas, 4: South China, Om: Oman, K: Kerman area of central Iran, Af: Afghanistan, Pak: Pakistan, SR: Salt Range, P:Punjab. Figure from Allen (2007). 73

3.24 Na^+, Mg^{2+} and Cl^- concentrations of individual primary fluid inclusions in: modern and ancient halite samples (Lowenstein, 2001), measured in an evaporating seawater (pink squares, McCaffrey *et al.* 1987) and theoretically determined alongside a computed evaporation path of a modern seawater (black line, Harvie *et al.* 1984). The drop of [Na^+] and the rise of [Mg^{2+}] at 6000 mmol.kg^{-1} H_2O marks the precipitation onset of NaCl salt, whereas [Cl^-] increases due to its initial level higher than [Na+] in modern and ancient oceans . The [Cl-] threshold at 10 500 mmol.kg^{-1} H_2O characterizes the initiation of the precipitation of the Mg-K potash salts. (Figure from Bąbel & Schreiber 2014, modified from Lowenstein 2001). 76

3.25 Data compilation of seawater boron concentrations (a) and isotopic compositions (b) across the Cenozoic. Lines are for models and calculations from foraminifera data (Lemarchand *et al.*, 2002b ; Raitzsch & Hönisch, 2013 ; Greenop *et al.*, 2017), this study); circles, triangles and yellow areas for determinations from foraminifera studies (Palmer *et al.*, 1998 ; Pearson & Palmer, 1999, 2000 ; Pearson *et al.*, 2009 ; Foster *et al.*, 2012 ; Raitzsch & Hönisch, 2013 ; Martínez-Botí *et al.*, 2015a ; Anagnostou *et al.*, 2016 ; Gutjahr *et al.*, 2017 ; Henehan *et al.*, 2019); ; squares for halite data (Paris *et al.* 2010b, this study). Blue dotted line: variable runoff (Lemarchand *et al.*, 2002b), blue solid line: variable runoff (Lemarchand *et al.*, 2002b), variable pH from foraminifera with fractionation factor=1.0272 (Raitzsch & Hönisch, 2013), orange solid line: variable pH from foraminifera with fractionation factor=1.020 (Raitzsch & Hönisch, 2013). 81

3.26 Data compilation of seawater boron concentrations (a) and isotopic compositions (b) across the Phanerozoic. Lines are for models and calculations from foraminifera data (Lemarchand *et al.*, 2002b ; Joachimski *et al.*, 2005 ; Raitzsch & Hönisch, 2013 ; Greenop *et al.*, 2017); diamonds and rectangles from brachiopod data (Lécuyer *et al.*, 2002 ; Joachimski *et al.*, 2005 ; Simon *et al.*, 2006 ; Müller *et al.*, 2020); stars from inorganic carbonate data (Kasemann *et al.*, 2010 ; Ohnemueller *et al.*, 2014 ; Clarkson *et al.*, 2015); and squares for halite data (Paris *et al.*, 2010b) in grey. Blue dotted line: variable runoff (Lemarchand *et al.*, 2002b), blue solid line: constant runoff (Lemarchand *et al.*, 2002b), green dotted line: variable continental input (Joachimski *et al.*, 2005), green solid line: constant continental input (Joachimski *et al.*, 2005) variable pH from foraminifera with fractionation factor=1.0272 (Raitzsch & Hönisch, 2013), orange solid line: variable pH from foraminifera with fractionation factor= 1.020 (Raitzsch & Hönisch, 2013). 83

3.27 Diffractograms of the Triassic sample Keuper and the Silurian sample Car12-3-3 showing in addition to halite, traces of potassic halite, sylvite (KCl) and especially the presence of ilmenite (Fe and Ti oxide), an accessory mineral in alluvial deposits. 85

3.28 Reconstruction of the boron concentration of seawater with varying runoff (Otto-Bliesner, 1995 ; Gibbs, 1999 ; Goddéris *et al.*, 2014) and varying oceanic crust production. 86

3.29 Reconstruction of the boron isotopic ratio of seawater with varying runoff (Otto-Bliesner, 1995 ; Gibbs, 1999 ; Goddéris *et al.*, 2014) and varying oceanic crust production. 87

4.1 Spectromètre de masse à source plasma à multicollection (MC-ICP-MS) de l'IPGP qui a été utilisé pour l'analyse des isotopes du bore. 90

4.2 Schéma de fonctionnement du MC-ICP-MS Neptune. (1) : le système d'introduction, (2) : la torche et le plasma, (3) : les cônes, (4) : les premières lentilles d'extraction et de focalisation, (5) : la fente source déterminant la résolution de la mesure, (6) : le secteur électrostatique, (7) : les lentilles quadrupôlaires de focalisation, (8) : la fente tube, (9) : la vanne tube, (10) : les lentilles octopôlaires contrôlant la forme des pics (Focus zoom), (11) : le secteur magnétique (aimant), (12) : les lentilles dodécapôlaires dajustement de l'alignement des signaux (dispersion zoom), (13) : les neuf cages de Faraday et (14) : le multiplicateur d'électron. 91

4.3 Schéma (a, Louvat *et al.* 2011a) et photo (b) du dDIHEN (demountable direct injection high efficiency nebulizer), introduit directement dans la torche. l'aiguille et le capillaire peuvent être démontés et changés. La position du capillaire est ajustée à l'extrémité de l'aiguille pour optimiser le spray (stable, non pulsé et avec de fines gouttelettes) sous une binoculaire avant le démarrage des analyses. 92

4.4 The µ-dDIHEN for liquid sample introduction to ICP-MS with: direct injection nebulizer (d-DIHEN), flow injection analysis valve and gas displacement pump. The d-DIHEN is directly plugged into the torch of the ICP-MS, in place of the injector. 97

4.5 Injection peaks with the µ-dDIHEN at different liquid uptake rates and sample loops of 10 and 50 µL. The last peak at 15 µL.min^{-1}) and 50 mL sample loop is commented with start/end of the peak, peak duration and stable signal plateau. the peak duration is used to calculate the liquid uptake rate of the µ-dDIHEN setup. 101

4.6 Liquid uptake rate of the µ-dDIHEN according to the gas flow rate from the mass flow controller (MCF) of the gas displacement pump (GDP) for (a) two different dDIHENs tested on the MC-ICP-MS and (b) the same dDIHEN tested on two different ICP-MS (MC- and HR-) ; c) and d) corresponding signal intensity as a function of the dDIHEN uptake rate. 102

4.7 MC-ICP-MS boron isotope ratio (δ^{11}B) measurements of the standard reference materials SRM AE 120, 121 and 122 (Vogl & Rosner, 2011) at concentrations between 5 and 200 ppb, with the µ-dDIHEN at different uptake rates. . 104

4.8 MC-ICP-MS boron isotope ratio (δ^{11}B) measurements in continuous (50 µL loop, one measurement) versus transient (10 µL loop, triplicate measurements) modes for a series of samples. Both transient and continuous modes required 80 µL of sample and uptake rate was kept at 25 µL.min^{-1}. 105

4.9 Limits of quantification (LOQ) for trace and ultra-trace elements determined with the µ-dDIHEN at 25 µL.min^{-1} and with a PFA nebulizer fitted on a cyclonic spray chamber at 200 µL.min^{-1} ("Spray Chamber") in ng/L (empty circles) and in pg (gray circles). Dots below the 1:1 line indicate µ-dDIHEN LOQs lower than spray chamber LOQs. 107

4.10 Gold nanoparticle characterization using the µ-dDIHEN, with a 50 µL sample loop at an uptake rate of 25 µL/min: calibration curve for dissolved Au (A), raw Au NP (40 nm) signal acquisition (B), and signal frequency histogram (C). 108

5.1 (a) Schematic illustration of the microsublimation protocol adopted for B extraction from carbonate samples after the multiple tests of this study, modified from Gaillardet *et al.* (2001). (b) A microdistillation vial wrapped with aluminium foil, except for the tip. (c) Microsublimation session with the vials placed on the hot plate. 118

5.2 Typical sample-standard-sample bracketing (SSB) sequence for the triplicate measurement of a sample with the µ-dDIHEN. Here [B]$_{solution}$ = 20 ppb, sample loop = 50 µL, uptake rate = 25 µL.min^{-1}. Average δ^{11}B of the sample and "individual" repeatability (2SD) calculated from the five δ^{11}B values thus obtained. R$_{rep\_x}$ = ^{11}B/^{10}B of the reference material or sample solution, R$_{std\_x}$ = ^{11}B/^{10}B of the standard NIST SRM 951, $^{10\ or\ 11}$B$_{blk\_x}$ = $^{10\ or\ 11}$B intensity of the background (HNO$_3$ 0.05 N) and δ^{11}B$_{smp\_x}$ = one of the five δ^{11}B values obtained for the reference material/sample solution. Adapted from Louvat *et al.* (2014b) and Louvat *et al.* (2019). 121

5.3 Reproducibility of the δ^{11}B measured for the reference materials BAM ERM-AE120, AE121 and AE122 at B concentrations between 1 and 50 ppb, using either a H skimmer cone and 10^{11} Ω resistors as amplifiers for a, b and c, or a X skimmer cone associated with 10^{13} Ω resistors for d, e and f. Light grey areas represent the reference values (Vogl & Rosner, 2011). Dark grey areas are for IPGP long-term values, updated from Louvat *et al.* (2019). 125

5.4 Change in instrumental mass bias with B concentration by using X or H skimmer cones with 10^{11} Ω (a) or 10^{13} Ω (b) amplifiers. Left Y-axis for ^{11}B/^{10}B ratio of NIST SRM 951 (after blank correction) and right Y-axis for the associated mass fractionation factor from its theoretical value of 4.04362 (Catanzaro *et al.*, 1970). 126

5.5 Internal standard errors (‰, 2σ) of the ^{11}B/^{10}B measurements according to the ^{10}B signal intensity, with 10^{11} Ω (red) or 10^{13} Ω (blue) amplifiers. σ = standard deviation/$\sqrt{n}$ * 1000, with n = 12 cycles of 8 s. Each data point corresponds to one injection of a reference material (NIST SRM 951, BAM ERM-AE120, AE121 or AE122). The database gathers roughly one year of measurements. Theoretical internal error curves are calculated according for Johnson-Nyquist plus Poisson noises (John & Adkins, 2010 ; Dellinger *et al.*, 2020). 128

5.6 δ^{11}B long-term reproducibility of BAM ERM-AE121 (Vogl & Rosner, 2011) that was measured together with carbonate samples at 1 $\leq$ [B] $\leq$ 50 ppb, using the Jet + X cones and the 10^{13} Ω amplifiers for [B] $\leq$ 35 ppb, otherwise 10^{11} Ω amplifiers. Each data point represents a triplicate analysis through the standard-sample bracketing described in the figure 5.2. Only 1.2 ng of boron is required at 5 ppb, and 0.5 ng at 2 ppb (0.4 ng and 0.17 ng respectively per injection). The colour bar represents the boron concentration at which the solution were measured. 130

5.7 Boron procedural blank in pg reported for ion exchange chromatography (Foster 2008 ; Wang *et al.* 2010 ; Louvat *et al.* 2011a ; Rae *et al.* 2011 ; Henehan *et al.* 2013 ; Louvat *et al.* 2014a, in green), for automated ion exchange chromatography (Vega *et al.* 2020, in orange) and for microsublimation (Wang *et al.* 2010 ; Misra *et al.* 2014b ; Raitzsch *et al.* 2018, in blue), compared with contamination values assessed with our microsublimation protocol. Those values are dissociated in circles and diamonds, representing respectively the determination of the whole procedural blank just after the microsublimation and after a longer storage (> one week) of the distillate in PP tubes. The squares reflect the maximum contamination values when the blank contamination range was not mentioned. 132

5.8 Reproducibility of δ^{11}B measurements on the carbonate reference material MVS-1 (15.95 $\pm$ 0.19 ‰, 2SD, n=46, Jurikova *et al.* 2019, dashed and solid lines) in a and b (15.94 $\pm$ 0.21 ‰, 2SD, n=148) and the synthetic carbonate reference material NIST RM 8301 Foram (14.51 $\pm$ 0.17 ‰, Stewart *et al.* 2021, dashed and solid lines) in c. B extraction was performed by the microsublimation technique for (a) different heating durations (with fixed 20 ng boron in a 40 µL droplet, i.e. [B]=40 ppb); (b): different boron masses loaded on the sublimation beaker lids (with fixed heating duration of 24 hours). (c): for 2.5 and 5 ng of boron loaded on the sublimation beaker lids (with fixed heating duration of 24 hours). Each data point represents average $\pm$ 2SD for a triplicate sample-standard bracketing measurement with the µ-dDIHEN setup, the Jet + X cones and the 10^{11} Ω (if [B] $\geq$ 35 ppb) or 10^{13} Ω amplifiers. The blue box plots depict the statistical parameters for nine to ten aliquots (orange dots) with median in red. 134

5.9 (a) Cross plot of δ^{11}B of different modern biogenic carbonates (Tab.5.3) obtained after microsublimation or B extraction by ion exchange chromatography. (b) δ^{11}B difference between microsublimation and ion exchange chromatography extractions according to the δ^{11}B values after ion exchange chromatography. Colour code gives the concentration at which the samples have been measured after microsublimation. The dark grey band represents the 0.4 ‰ envelope and the lightest grey band the 1 ‰ envelope around the 1:1 black line. 138

6.1 Picture of one of the picked Globigerina bulloides shells 147

6.2 Reproducibility of the δ^{11}B measured for the reference material ERM AE121 according to the concentration for (a) continuous measurements mode and (b) transient measurements mode. The light gray band corresponds to the reference value, 19.6 ± 0.6 ‰ (Vogl & Rosner, 2011), and the dark gray band the IPGP long-term reproducibility, 19.56 ± 0.17 ‰ (2SD, n=90, Louvat *et al.* 2019, Chap.5). 149

6.3 (a): Example of an injection peak with a 10 µL sample loop and a sample uptake rate at 25 µL.min^{-1}. (b) Evolution of the ^{11}B/^{10}B ratio during the 180 s measurement. (c): linear regression between the ^{11}B and the ^{10}B signals from the 180 measurements to determine the ^{11}B/^{10}B ratio. 150

6.4 Crossplots between the Al/Ca and the δ^{11}B measured in continuous (50 µL loop, a) and transient (10 µL loop, b) mode for the foraminifera samples to check possible contamination, with the red line for the threshold of 100 µmol/mol (Rae *et al.*, 2011). 152

6.5 δ^{11}B of the foraminifera samples measured in continuous (50 µL loop, a) and transient (10 µL loop, b) according to the depth of the sample in the core PS97-122. 154

6.6 Closs plot between the δ^{11}B measured in continuous mode with a 50 µL sample loop and the δ^{11}B measured in transient mode with 10 µL sample loop. The colour code provides the B concentration at which the samples have been measured for the continuous mode. The dark gray band represents the 0.25 ‰ enveloppe around the 1:1 line. 155

6.7 Comparison of the δ^{11}B measured in *G. bulloides* planctonic foraminifera against the δ^{11}B of the borate in seawater, calculated from the carbonate chemistry of the locations from where the foraminifera samples were collected. The literature data reported come from Martínez-Botí *et al.* (2015b) and Raitzsch *et al.* (2018). The red line correspond to the calibration proposed for this species, $\delta^{11}B_{G. bulloides}$ = 1.09 (± 0.65)*$\delta^{11}B_{Borate}$ - 3.58 (± 11.77) from Raitzsch *et al.* (2018) and the black line, the 1:1 line (sample value on this line means correct determination of the seawater borate, within the classical δ^{11}B - paleo-pH hypotheses). The mean of the different fraction sizes are also reported with their associated $\delta^{11}B_{Borate}$, as well as the mean value measured at the AWI (see text for more details). 156

6.8 Violin plots illustrating the distribution of the δ^{11}B for the planctonic foraminifera *G. bulloides* in three size fractions: 250-315 µm, 315-400 µm and > 400 250-315 µm. 158

7.1 Effets sur le climat des grandes éruptions volcaniques dite stratosphériques. D'après Timmreck (2012). 164

7.2 (a) Localisation et contexte géodynamique de l'île de Sumatra, Indonésie. (b) Localisation du complexe de caldeiras Toba sur l'île de Sumatra. Les lignes pointillées correspondent à l'emplacement des différentes caldeiras, résultantes de plusieurs phases éruptives. HDT (marron, 1,2 Ma): *Haranggoal Dacite Tuff*, OTT (jaune, 0,840 Ma): *Oldest Toba Tuff*, MTT (bleu foncé, 0,501 Ma): *Middle Toba Tuff* and YTT (rouge, 0,074 Ma) : *Younger Toba Tuff*. Les traits pleins sont pour les dômes de laves Samsoir (orange) et ceux de Parepur (bleu clair), et des cryptodômes (orange). PV = volcan Pusikbukit, PD = dômes de lave Pardepur, TT = dômes de lave TukeTuk, TV = volcan Tandukbenua, SV = volcan Singgalang, SF = Faille de Sumatra. D'après Chesner (2012) 165

7.3 Occurence de l'éruption YTT dans la région de l'océan Indien, l'Asie du Sud et dans la mer de Chine méridionale. D'après Lane *et al.* (2013). 166

7.4 Localisation de la carotte sédimentaire BAR94-25 et du volcan Toba sur l'île de Sumatra. D'après van der Kaars *et al.* (2012). 167

7.5 Tests de P. obliquiloculata observé à la loupe binoculaire. D'après Alves (2020).169

7.6 Relation entre le δ^{11}B mesuré dans les échantillons de P. obliquiloculata et les indices de contamination que sont les rapports Al/Ca et Mn/Ca. La ligne rouge en pointillés correspond au seuil admis par Rae *et al.* (2011) 171

7.7 (A) Modèle d'âge de la carotte sédimentaire BAR94-25. (B) δ^{18}O de la carotte sédimentaire BAR94-25 (van der Kaars *et al.*, 2012). D'après Alves (2020). . . . 172

7.8 Évolution de l'abondance de téphra et de la teneur en carbonate de calcium entre 100 et 50 ka pour la carotte BAR94-25, lors de la phase YTT (del Manzo, 2018 ; Caron *et al.*, submitted). D'après Alves (2020). 173

7.9 Evolution du δ^{11}B mesuré (avec l'erreur ± 2SD en zone grisée) sur des échantillons de foraminifères planctoniques P. obliquiloculata entre 100 et 50 ka lors de la super-éruption YTT. Les chiffres 1 à 6 correspondent aux six évènements identifiés de la phase YTT en figure 7.8 (del Manzo, 2018 ; Caron *et al.*, submitted). D'après Alves (2020). 174

7.10 Évolution de la température de la thermocline calculée à partir du rapport Mg/Ca mesuré sur des échantillons de foraminifères planctoniques P. obliquiloculata entre 100 et 50 ka lors de la super-éruption YTT (del Manzo, 2018 ; Caron *et al.*, submitted). D'après (Alves, 2020). 176

7.11 Evolution de plusieurs marqueurs climatiques et géochimiques dans la carotte BAR94-25 entre 82 et 57 ka: δ^{18}O, pourcentage de téphra, pourcentage de carbonate de calcium dans le sédiment (del Manzo, 2018 ; Caron *et al.*, submitted), δ^{11}B mesuré à partir de P.obliquiloculata et température déterminée à partir des rapports Mg/Ca dans P.obliquiloculata. Ces données sont mises en regard des pCO_2 mesurées dans des carottes de glace Antarctique (Bereiter *et al.*, 2012).D'après Alves (2020). 177

LISTE DES TABLEAUX

3.1 Location, formation, stratigraphy, age, $^{87}Sr/^{86}Sr$ and mineralogy of the halite samples and [B], $\delta^{11}B$ for each subsample. 66

4.1 Gas displacement pump (GDP) and FIA (FAST) programs (SC-FAST Autosampler, ESI) 98

4.2 Operating parameters of the ICP-MS instruments 99

5.1 Operating parameters of the MC-ICP-MS instrument 120

5.2 Boric acid reference materials BAM ERM-AE120, AE121 and AE122 measurements at B concentrations between 1 and 50 ppb, using either a H skimmer cone and 10^{11} Ω resistors as amplifiers or a X skimmer cone associated with 10^{13} Ω resistors. " * " symbol: outliers. 124

5.3 Comparison of the microsublimation protocol and the ion exchange chromatography (Lemarchand *et al.*, 2002a ; Paris *et al.*, 2010a) to separate boron from its carbonate matrix on a variety of modern biogenic carbonate. The " * " symbol marks the sample with a 1 ‰ discrepancy between the two separation methods. The percentage of the different mineralogies were determined by XRD (Calc.: Calcite, Arag.: Aragonite, Mg Calc.: High Mg calcite) and the boron concentrations in the carbonate matrix were measured by ICP-QMS. . 136

6.1 $\delta^{11}B$ measurements for *G. bulloides* from the PS97-122 coretop 153

7.1 Données géochimiques de l'espèce *P. obliquiloculata* sur la fraction > 315 µm provenant de la carotte BAR94-25. L'erreur sur le Mg/Ca est de 1,02 %, celle du $\delta^{18}O$ 0,05 ‰ 180

CHAPITRE 1

INTRODUCTION GÉNÉRALE

Sommaire

1.1 L'Anthropocène 2
1.2 La paléoclimatologie pour anticiper l'avenir 5
1.3 Problématiques abordées dans ce travail de thèse 10

1.1 L'Anthropocène

La composition chimique de l'atmosphère, telle que nous la connaissons aujourd'hui, est le fruit d'une perpétuelle évolution depuis la formation de la Terre il y a 4,5 milliards d'années. C'est elle, alors que la Terre recevait 30 % d'énergie solaire en moins (Paradoxe du Soleil jeune, Feulner 2012), qui aurait évité la formation d'une planète entièrement gelée sur les deux premiers milliard d'années de son histoire. Ce qu'on appelle ainsi l'effet de serre aurait été mis en place par un intense dégazage volcanique à l'Archéen et aurait ainsi endigué la perte des radiations thermiques ré-émises par la surface terrestre en les absorbant, les redistribuant et créant ainsi un gradient de température plus chaud dans l'atmosphère. Ce phénomène, décrit pour la première fois il y a un siècle (Arrhenius & Holden, 1897) s'inscrit donc comme étant le régulateur principal du système Terre. explique la différence entre ce que devrait être la température à la surface de la Terre avec seulement la réception de l'énergie solaire (-17°C) et celle qui est ou a été observée au cours des temps géologiques (pour la surface des océans : 60-100 °C à l'Archéen, 40-70 °C au début du Paléozoïque, et une moyenne pour le Phanérozoïque de 17 °C, qui est aussi la moyenne actuelle, Vérard & Veizer 2019). Les principaux responsables de cet effet de serre sont la vapeur d'eau et les nuages à plus de 75 % ainsi que les gaz à effet de serre non condensables, dominés par le dioxyde de carbone CO_2 et le méthane CH_4, pour environ 25 % (Lacis *et al.*, 2010). Le couple irradiance solaire - gaz à effet de serre s'inscrit donc comme le paramètre majeur guidant l'évolution du climat terrestre. Cependant, aux pressions et aux températures rencontrées sur Terre, les nuages et la teneur en vapeur d'eau dans l'atmosphère sont une corollaire de l'effet de serre, laissant les gaz non condensables comme principal forçage (Lacis *et al.*, 2010). Il s'avère en fait que l'impact du méthane est intimement lié à la concentration du CO_2 (Bartdorff *et al.*, 2008), le gaz à effet de serre majeur des derniers 500 millions d'années (e.g., Lacis *et al.*, 2010 ; Beerling *et al.*, 2011 ; Anagnostou *et al.*, 2016).

A très grande échelle de temps, la concentration de dioxyde de carbone a été régulée par un jeu de balance entre les apports issus du volcanisme, du métamorphisme et l'altération de la matière organique, et la consommation par l'altération des silicates et l'enfouissement de la matière organique (Walker *et al.*, 1981). La tectonique des plaques à l'échelle de plusieurs dizaines de millions d'années, par son effet sur le climat, devient également un acteur majeur du cycle du carbone (Berner, 2006). A des échelles de temps plus courtes, il a été mis en évidence que les deux derniers millions d'années ont été caractérisés par de larges oscillations cycliques de la pCO_2 dans l'atmosphère, notamment grâce à l'analyse des bulles de gaz piégées dans les carottes de glace (Dansgaard *et al.*, 1993 ; Petit *et al.*, 1999 ; Lüthi *et al.*, 2008 ; Yan *et al.*, 2019). Ces variations, entre périodes dites glaciaires et interglaciaires, ont été associées à des changements orbitaux de la Terre qui ont fait varier de manière saisonnière et spatiale l'énergie incidente du Soleil sur Terre, et ont été amplifiées par la production biologique à la surface des océans (Sigman & Boyle, 2000 ; Sigman *et al.*, 2010).

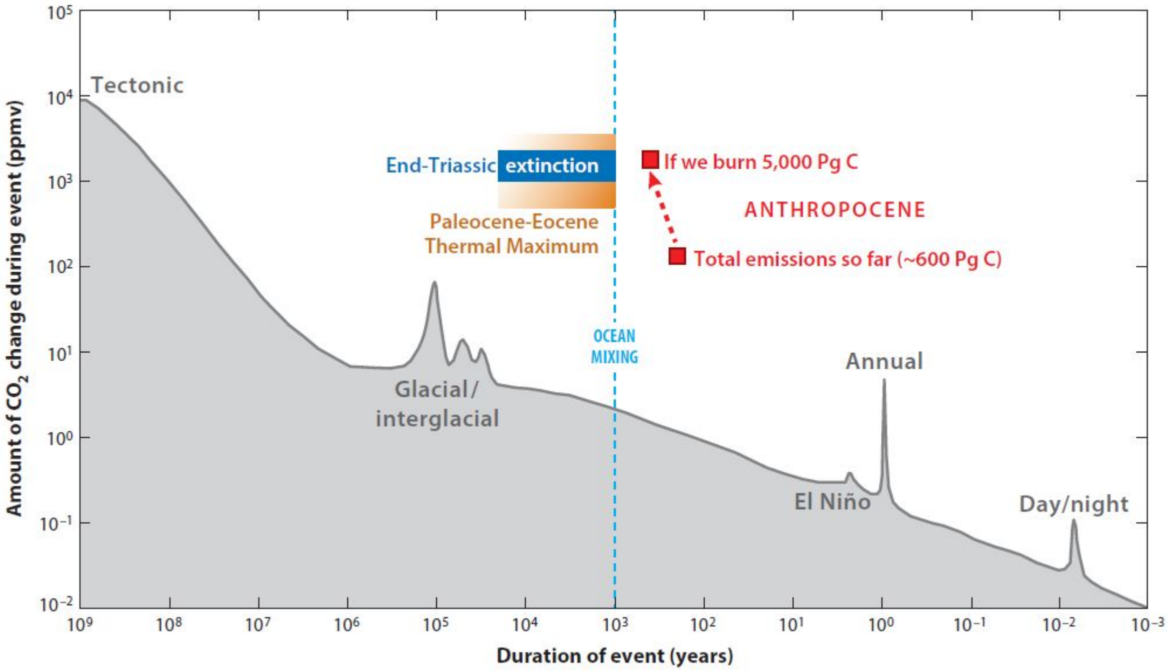

FIGURE 1.1 : *Magnitude et échelle de temps des changements provoqués sur le cycle du carbone par différents processus climatiques et géologiques. La perturbation anthropogénique du cycle du carbone est mise en perspective avec l'extinction massive de la limite Permo-Trias (252 Ma) et le maximum thermal de la limite Palocène-Eocène. D'après Royer (2016).*

Les paramètres orbitaux sont au nombre de trois : l'excentricité (forme des orbites, période de 100 000 ans), l'obliquité (l'inclinaison de l'axe de rotation, période de 42 000 ans) et la précession (rotation autour de l'axe de la Terre, période de 23 000 ans) et correspondent à ce qu'on appelle les cycles de Milankovitch (Hays *et al.*, 1976). Ces trois processus, jouant à différentes échelles de temps, ont ainsi rythmé l'énergie solaire arrivant à la surface de la Terre et donc sa température (Fig.1.1). L'intensité lumineuse du Soleil, augmentant de 7 % par milliard d'années, a cependant été neutralisée sur le long terme au cours des 420 derniers millions d'années par un long déclin de la pCO_2 atmosphérique lié à la rétroaction négative et continue de l'altération des silicates et à l'apparition des végétaux terrestres, mettant ainsi en évidence son importance capitale sur la régulation du climat (Schwartzman & Volk, 1989 ; Berner, 1992 ; Foster *et al.*, 2017). Ces actions et rétro-actions entre irradiance solaire, tectonique des plaques et paramètres orbitaux, qui ont rythmé l'histoire climatique terrestre et l'ont divisée en périodes géologiques distinctes (dont les limites sont souvent liées à des extinctions de masse), ont été peu à peu bouleversées par l'émergence de l'humanité. Celle-ci en a totalement modifié l'équilibre par ses activités et s'est imposée comme une nouvelle force géologique, à l'échelle du siècle (Fig.1.1), donnant naissance à une nouvelle ère géologique, l'Anthropocène (Crutzen, 2002).

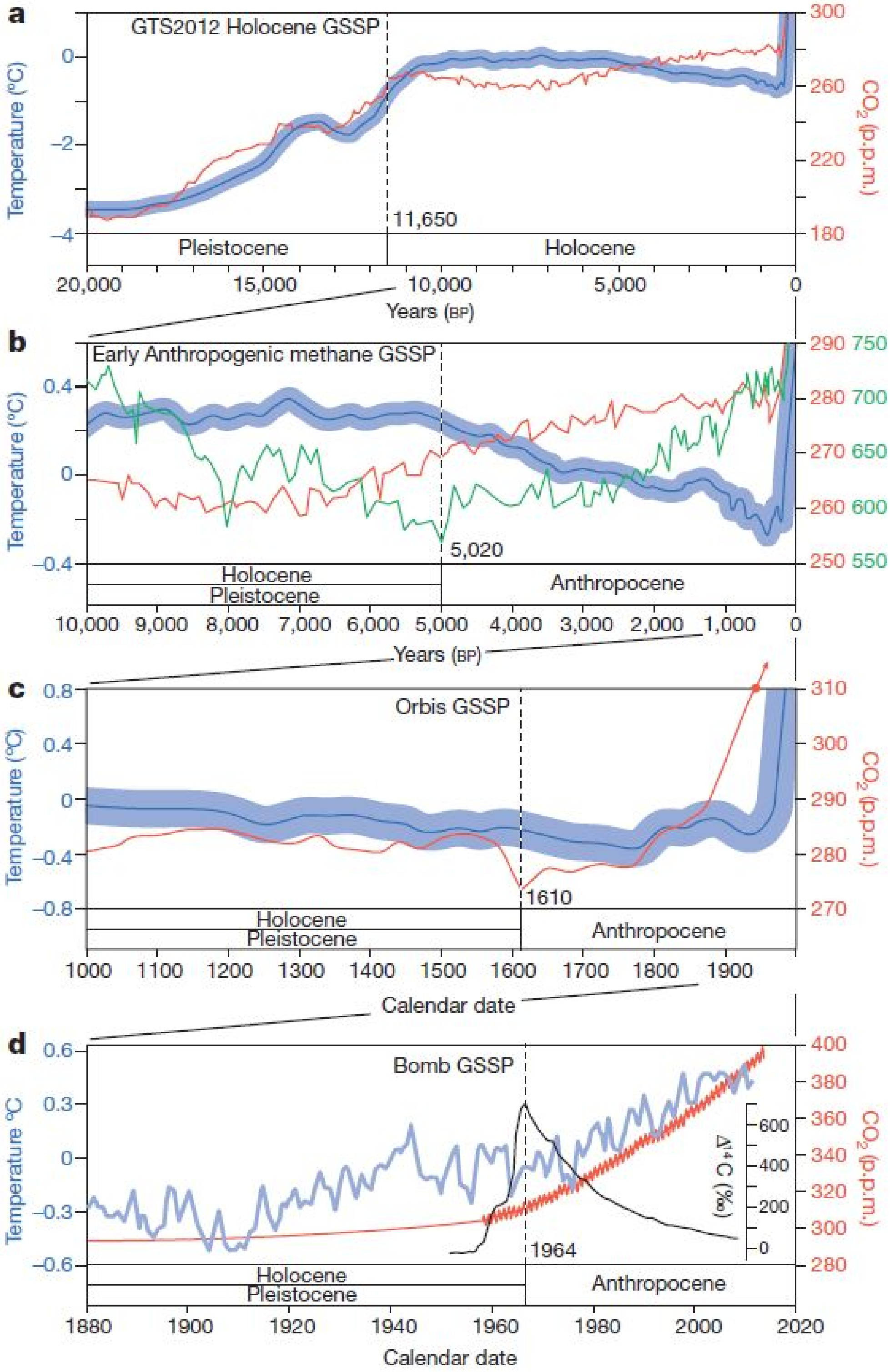

FIGURE 1.2 : *Proposition du début de l'Anthropocène en fonction de l'évolution de la température, du méthane et du dioxyde de carbone atmosphérique, il y a 5000 ans BP (b), en 1610 (c) et en 1964, par le pic de ^{14}C retrouvé dans les anneaux de croissance des arbres (d). La limite Holocène/Pléistocène est fixée à 11 650 ans (a). D'après Lewis & Maslin (2015).*

L'intervalle le plus récent de l'histoire terrestre, l'Holocène, démarre il y a précisément 11 650 ans, marqué par les premiers signes géochimiques de réchauffement dans les carottes de glace après la période froide du Younger Dryas (Walker *et al.* 2009, Fig.1.2.a). Le début de l'Holocène est marqué par une stabilité de la pCO_2 atmosphérique (Monnin, 2001), qui va être bouleversée au dernier millénaire par l'accroissement des activités humaines se traduisant par des phases d'augmentation successives dans l'atmosphère (Lewis & Maslin, 2015 ; Zalasiewicz *et al.*, 2015). Cependant, le début stratigraphique de l'Anthropocène fait l'objet de débats. Lewis & Maslin (2015) ont ainsi proposé d'en placer le début soit au commencement des pratiques agricoles, qui ont peu à peu remplacé une végétation hautement captatrice de CO_2 (forêts, savanes) et auraient retardé voire annulé la transition vers une période glaciaire (Fig.1.2.b), soit au moment du développement de la mondialisation et des échanges commerciaux à l'échelle planétaire lors de la découverte de l'Amérique (Fig.1.2.c), ou encore à l'entrée dans l'ère industrielle au XVIII^{ème} siècle avec les premières exploitations d'énergies fossiles. Le début de l'Anthropocène a finalement été placé au début de ce qui a été appelé la “grande accélération” (Steffen *et al.* 2015, Fig.1.2.d), avec un début stratigraphique placé en 1964 par le pic de ^{14}C associé au maximum des essais nucléaires, retrouvé dans les carottes de glace et les anneaux de croissance des arbres. Ce point d'inflexion au milieu du XX^{ème} siècle est associé à une forte croissance de la population, au développement de nouveaux matériaux comme les plastiques mais surtout à de larges bouleversements dans les cycles naturels. La concentration de CO_2 dans l'atmosphère a ainsi gagné 100 ppmv à l'échelle d'un demi-siècle (passant de 300 à 400 ppmv, Le Quéré *et al.* 2018) et pourrait avoir amené le climat terrestre à un point de non retour (Steffen *et al.*, 2018), avec des conséquences sur les sociétés humaines comme la fonte des glaces (notamment aux pôles) et l'élévation du niveau marin (Winkelmann *et al.*, 2015 ; M. DeConto & Pollard, 2016), un taux d'extinction d'espèces supérieur à ce que la Terre a connu (Barnosky *et al.*, 2011), des évènements climatiques de plus en plus extrêmes et plus fréquents (Mora *et al.*, 2017, 2018) ou encore les migrations, et les apparitions de nouvelles maladies (Short *et al.*, 2017 ; Caminade *et al.*, 2019).

1.2 La paléoclimatologie pour anticiper l'avenir

Les bouleversements associés à ces émissions de gaz à effet de serre d'origine anthropique, sont encore une fois une question d'échelle de temps, car la combustion des énergies fossiles injecte de façon massive un CO_2 dans l'atmosphère qui n'aurait jamais dû sortir du cycle long lié à l'érosion des continents et au volcanisme (Le Quéré *et al.*, 2018). La compréhension du cycle du carbone, à ces deux échelles de temps, devient alors primordiale afin d' estimer l'ampleur de la perturbation et de mieux anticiper l'évolution future du climat. La paléoclimatologie prend de ce fait une place de plus en plus centrale (Haywood *et al.*, 2011 ; Tierney *et al.*, 2020). L'enregistrement direct de la pCO_2 atmosphérique dans les carottes de glace s'arrête au delà de 800 000 ans à 2 Ma (Dansgaard *et al.*, 1993 ; Petit *et al.*, 1999 ; Lüthi *et al.*, 2008 ; Yan *et al.*, 2019) et il est donc nécessaire de trouver d'autres témoins de cette pCO2 atmosphérique pour des temps plus anciens (Fig.1.3). Les traceurs géochimiques, à partir d'enregistrements sédimentaires, deviennent alors un outil précieux afin de reconstituer les paramètres physico-chimiques d'un milieu au cours des temps géologiques. Ces traceurs géochimiques reposent sur des principes physiques et chimiques. Ils sont très étudiés et continuellement affinés, mais peuvent aussi être sources d'incertitudes car ces traceurs reposent généralement sur de nombreuses hypothèses et sont souvent modifiés par des processus biologiques (appelés effet vital, Urey *et al.* 1951).

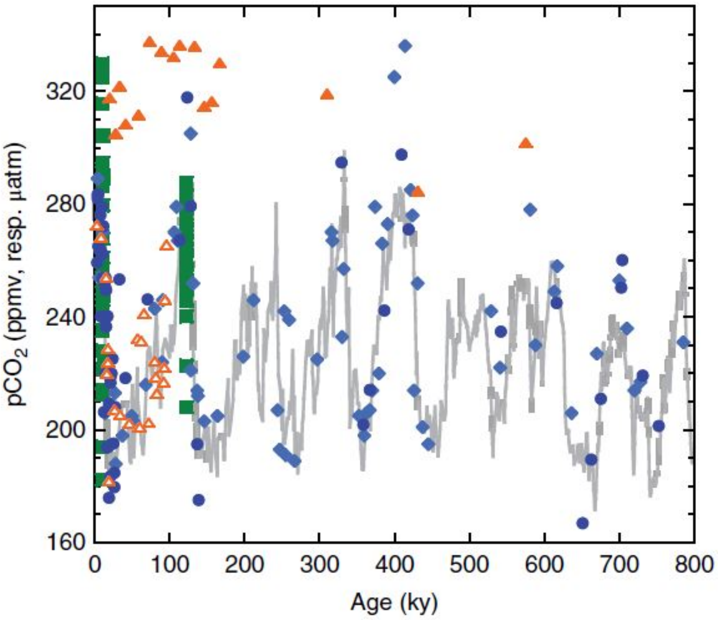

FIGURE 1.3 : *800 000 ans d'enregistrements de la pCO$_2$ atmosphérique à partir des bulles de gaz piégées dans les carottes de glace en gris, des alcénones (triangle orange, ± 60 ppm), de l'index stomatique (carré vert, ± 20 ppm), du rapport B/Ca (diamant bleu clair, ± 30 ppm) et des isotopes du bore (diamant bleu foncé, ± 20 ppm) à partir des foraminifères planctoniques. D'après Hönisch et al. (2019) et références associées.*

Le premier traceur géochimique utilisé pour le cycle du carbone exploite la relation entre la densité de stomates des plantes vasculaires de type C3 et les valeurs de pCO$_2$ dans l'atmosphère (e.g., Woodward, 1987 ; Konrad *et al.*, 2020). Les stomates sont des petits trous situés dans l'épiderme des feuilles et sont le principal lieu d'échanges gazeux pour les plantes vasculaires. Leur nombre, par unité de surface, est ainsi régulé pour maximiser la prise du CO$_2$ et minimiser la perte en eau. Pour de nombreuses plantes modernes, cette densité de stomates est ainsi inversement corrélée à la concentration de CO$_2$ dans l'atmosphère. L'index stomatique a ainsi été appliqué à des fossiles de feuilles pour reconstruire la pCO$_2$ de l'atmosphère dans laquelle elles avaient vécu (e.g., Royer *et al.*, 2001 ; Steinthorsdottir & Vajda, 2015 ; Barclay & Wing, 2016). Cependant, ce traceur est sujet à de nombreuses incertitudes, car d'autres paramètres environnementaux peuvent rentrer en jeu sur cette densité, comme la luminosité, la pression atmosphérique et donc la paléo-latitude, la température, l'humidité, mais aussi le fait que les calibrations d'espèces éteintes sont faites à partir de leur plus proche parent moderne (Royer *et al.*, 2001 ; Sundquist & Ackerman, 2014 ; Konrad *et al.*, 2020).

Les isotopes du carbone (δ^{13}C) ont aussi été utilisés afin de retracer la pCO_2 atmosphérique. Dans un premier temps, ils ont été mesurés dans des carbonates pédogéniques, en se basant sur des modèles de diffusion de CO_2 dans les sols et en estimant la différence entre la composition isotopique du CO_2 respiré par le sol et celui qui a été diffusé ainsi qu'un équilibre isotopique entre le carbonate qui précipite et le CO_2 des solutions présentes dans le sol (Cerling, 1991, 1992 ; Ekart *et al.*, 1999 ; Breecker *et al.*, 2010). Mais là aussi, ce traceur est source de nombreuses incertitudes, tant la diffusion de CO_2 dans les sols est dépendante aussi de l'humidité et de la température. La différence isotopique du CO_2 respiré varie également selon le métabolisme d'une plante C3 ou C4 (Sundquist & Ackerman, 2014).

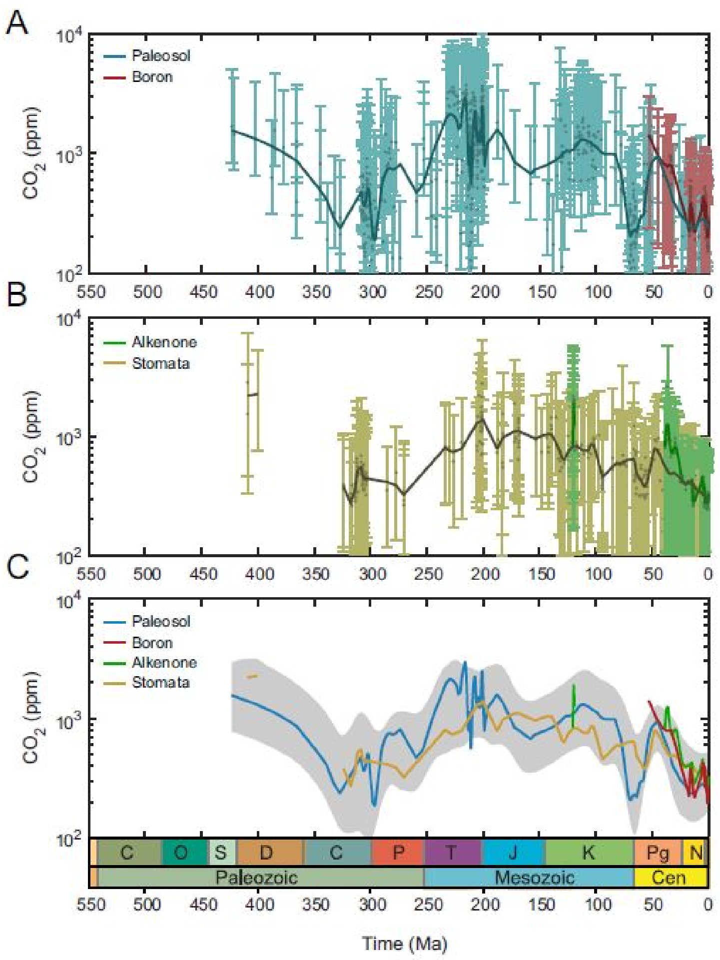

FIGURE 1.4 : *Compilation de la pCO_2 atmosphèrique à travers le Phanérozoïque, reconstituée à partir (a) des paléosols (en bleu) et des isotopes du bore (en rouge), (b) des alcénones (en vert) et des indices stomatiques (en kaki) et avec en (c) l'estimation moyenne de l'erreur associée pour chaque traceur géochimique. D'après Mills et al. (2019).*

En parallèle, les reconstructions de la pCO$_2$ à partir du δ^{13}C des alcénones se fondent sur le fractionnement isotopique qui se produit lors de la photosynthèse d'algues unicellulaires, les haptophytes, entre le [CO$_2$]$_{aqueux}$ et la matière organique, qui se retrouve préservée dans le sédiment (e.g., Freeman & Hayes, 1992 ; Pagani, 2002 ; Seki *et al.*, 2010). Malheureusement, cette méthode souffre aussi d'incertitudes, notamment pour relier le CO$_2$ dissous dans l'océan et celui de l'atmosphère, avec des effets de salinité, de physiologie (taille de la cellule, et croissance de l'organisme) et encore une fois de température (Sundquist & Ackerman, 2014).

Bien que marqués par de nombreuses incertitudes, demandant notamment le couplage d'autres traceurs géochimiques pour connaître la température (i.e. δ^{18}O, Mg/Ca), ces traceurs précédemment décrits de la pCO$_2$ ont pu être validés en comparant les pCO$_2$ déduites avec les valeurs mesurées dans les bulles piégées dans les carottes de glace (Fig.1.3), puis ont permis de reconstruire la pCO$_2$ sur le Phanérozoïque (Fig.1.4).

Au-delà des enregistrements des carottes de glace, à défaut d'avoir un enregistrement direct, les traceurs géochimiques peuvent avoir comme support la modélisation (Berner *et al.*, 1983 ; Berner, 2004, 2006). Celle-ci repose sur un système à l'équilibre, avec des échanges et des boucles de rétroactions sur le CO$_2$ atmosphérique, décrite par un simple bilan de masse (Goddéris *et al.*, 2014 ; Sundquist & Ackerman, 2014) :

$$F_{vol} + F_{MOR} + F_{cw} + F_{ow} = F_{cd} + F_{od} \tag{1.1}$$

avec F$_{vol}$ le flux de CO$_2$ issu du volcanisme "subaérien", F$_{MOR}$ le dégazage de CO$_2$ au niveau des rides océniques, F$_{cw}$ le flux de CO$_2$ issu de la dissolution des carbonates, F$_{ow}$ le flux de CO$_2$ provenant de l'oxydation de roches sédimentaires réduites, tandis que le CO$_2$ est stocké au niveau de la croûte océanique par la sédimentation de carbonate F$_{cd}$ (avec F$_{cd}$ = F$_{swo}$ + F$_{swy}$ + F$_{cw}$, respectivement le flux d'alcalinité par l'altération d'anciens silicates cratoniques, par l'altération de roches jeunes volcaniques et la dissolution des carbonates) et l'enfouissement de la matière organique dans les sédiments F$_{od}$. Chaque paramètre est ainsi fonction de la tectonique, de la paléogéographie, du relief, du climat ou encore de la végétation, et repose donc sur de nombreuses hypothèses, qui deviennent de plus en plus incertaines en remontant dans le temps. Cependant, les modèles se sont affinés au fur et à mesure avec une meilleure compréhension des processus qui régissent le cycle du carbone, ainsi que par des avancées sur les reconstructions tectoniques. Ces modèles s'appuient d'ailleurs eux aussi sur tous les traceurs géochimiques disponibles pour valider les modèles (i.e. δ^{18}O, δ^{13}C, δ^{34}S, ^{87}Sr/^{86}Sr, Van Der Meer *et al.* 2014 ; Royer 2014 ; Mills *et al.* 2017 ; Lenton *et al.* 2018). La dernière compilation de données a ainsi permis de réconcilier à plus de 75 % les traceurs géochimiques et les différents modèles biogéochimiques du CO$_2$ (Mills *et al.* 2019, Fig.1.5).

Du fait du caractère unique de la combustion d'énergies fossiles perturbant le cycle actuel du carbone, il n'existe malheureusement pas d'analogue direct dans le passé. Cependant, les traceurs géochimiques et les modélisations ont permis de mettre en évidence des périodes où la concentration en dioxyde de carbone dans l'atmosphère était plus élevée. Ces périodes sont donc très activement étudiées afin de comprendre les processus climatiques qui les ont régis et ainsi de mieux appréhender ce que pourrait être un monde avec une forte concentration de CO_2 dans l'atmosphère (Haywood *et al.*, 2011 ; Tierney *et al.*, 2020). Les valeurs prévisionnelles de pCO_2 pour les prochaines années ont ainsi été évaluées comme étant sans précédents depuis le début de l'Eocéne (51-53 Ma, Pearson & Palmer 2000 ; Anagnostou *et al.* 2016 ; Zeebe *et al.* 2016 ; Foster *et al.* 2017).

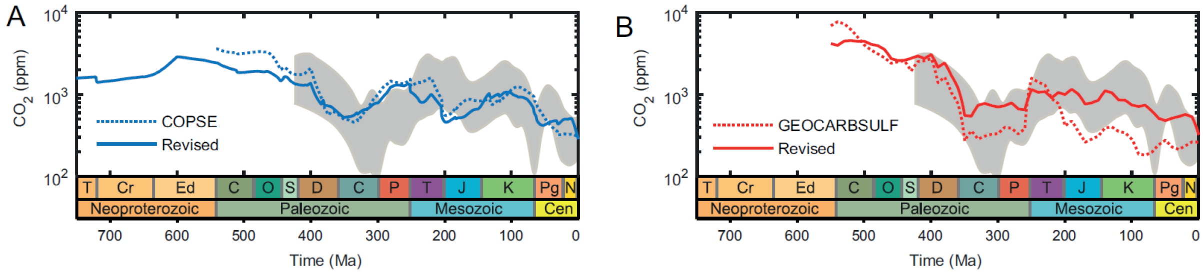

Figure 1.5 : *Reconstruction de la pCO_2 atmosphérique au cours du Phanérozoïque, à partir du modèle biogéochimique COPSE (A) et du modèle GEOCARBSULF (B) en comparaison avec l'enveloppe des différents traceurs géochimiques de la figure 1.4.c. Les modèles actualisés ont été réalisés à partir de forçages géodynamiques modernisés sur le Phanérozoïque. D'après Mills et al. (2019).*

En parallèle, un intérêt accru s'est porté sur les perturbations du cycle du carbone à courtes échelles de temps dans l'histoire géologique de la Terre (entre le millier et la dizaine de milliers d'années), qui sont de plus associées à des crises biologiques. Mais elles restent éloignées de la rapidité des émissions anthropogéniques (à l'échelle du siècle, Fig. 1.1). Citons par exemple :

- la limite Permo-Trias (252 Ma), la crise biologique la plus massive que la Terre ait connue, due à des émissions de gaz à effet de serre par la mise en place des trapps de Sibérie, dont l'émission en gaz volcaniques est pourtant estimée comme étant 14 fois moins élevée que les émissions anthropogéniques (Payne & Clapham, 2012 ; Jurikova *et al.*, 2020).
- la limite Crétacé-Paléogène (66 Ma), marquée à la fois par l'impact d'une météorite et par l'intense activité volcanique des trapps du Deccan, faisant passer en un temps très court (quelques dizaines de milliers d'années) la concentration de CO_2 de 900 à 1600 ppmv (Henehan *et al.*, 2019).
- le maximum thermal à la limite Paléocène-Eocène (56 Ma), avec une forte émission de gaz à effet de serre dont l'origine est débattue (entre la déstabilisation des hydrates de méthane au fond des océans, la fonte du permafrost et une large oxydation de la matière organique sédimentaire), avec un pic très important de la pCO2 passant de $\sim$ 850 ppmv à $\sim$ 2200 ppmv en $\sim$ 25 000 ans (Gutjahr *et al.*, 2017).
- les alternances glaciaires-interglaciaires du Plio-Pléistocène (suivant les cycles de

Milankovitch, Dansgaard *et al.* 1993 ; Petit *et al.* 1999 ; Lüthi *et al.* 2008), ayant été massivement étudiées du fait de leur proximité temporelle et de leur enregistrement direct dans les carottes de glace (e.g. Foster, 2008 ; Martínez-Botí *et al.*, 2015a ; Rae *et al.*, 2018 ; Chalk *et al.*, 2019 ; Shuttleworth *et al.*, 2020).

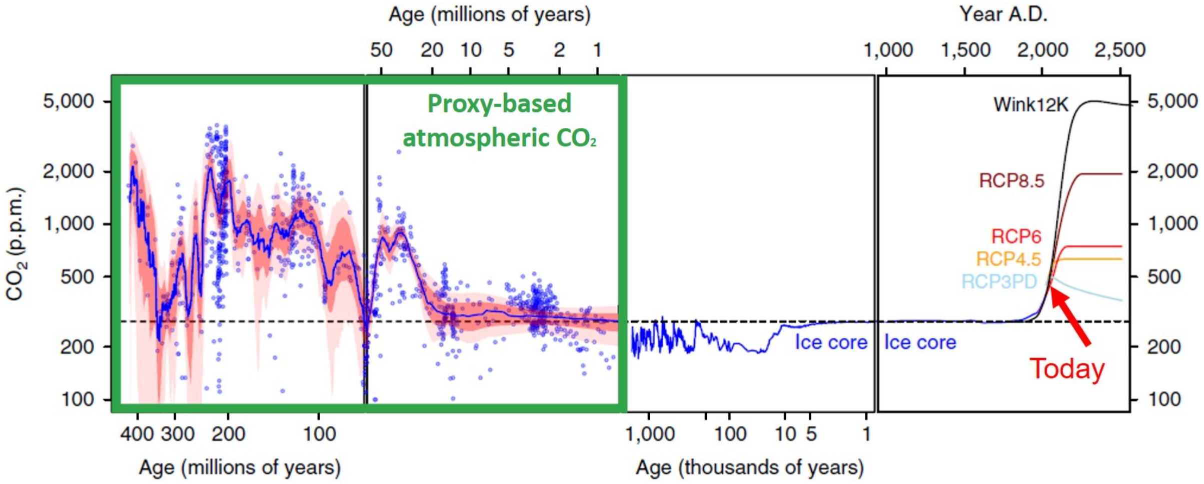

FIGURE 1.6 : *Compilation des pCO_2 atmosphériques déterminées à partir des différents traceurs géochimiques (index stomatique, alcénones, carbonates pédogéniques, isotopes du bore) (a,b), des carottes de glace (c,d) et les prédictions pour les prochains siècles, RCP pour les derniers scénarios du GIEC, WINK12K pour le scénario de Winkelmann et al. (2015). Modifiée de Foster et al. (2017).*

1.3 Problématiques abordées dans ce travail de thèse

La plupart des ces études remontant jusqu'à la limite Permo-Trias (voire jusqu'au Néo-Protérozoïque, Kasemann *et al.* 2010 ; Ohnemueller *et al.* 2014), reposent sur un quatrième traceur géochimique : les isotopes du bore (δ^{11}B) dans les carbonates biogéniques (Fig.1.3 et 1.4), qui ont connu un intérêt grandissant depuis le début des années 1990 (Vengosh *et al.*, 1991b ; Hemming & Hanson, 1992) et sont massivement utilisés aujourd'hui afin de reconstruire la pCO_2 atmosphérique (Pearson & Palmer, 1999, 2000 ; Foster, 2008 ; Pearson *et al.*, 2009). Leur grand intérêt, c'est qu'avant de reconstruire la pCO_2 dans l'atmosphère, il s'agit d'un traceur direct du pH océanique qui permet ainsi de se concentrer sur un acteur majeur du cycle du carbone qui n'a été que brièvement mentionné jusque là : l'océan. Les isotopes du bore dans les carbonates marins deviennent alors un outil précieux pour comprendre le climat, les dynamiques des écosystèmes marins et donc les mécanismes qui gouvernent le cycle du carbonate dans l'océan, et qui, couplés à un second paramètre comme l'alcalinité, permettent donc de reconstruire la pCO_2 à partir du pH (Zeebe *et al.*, 2001). Cependant, le rapport B/Ca dans les carbonates a été utilisé par le passé comme un traceur du système carbonate dans l'océan pour reconstruire la pCO_2 (Yu *et al.*, 2007b ; Tripati *et al.*, 2009) mais est aujourd'hui sujet à caution, car il n'est pas encore bien clair comment le système des carbonates joue sur l'incorporation du bore (Foster, 2008 ; Allen *et al.*, 2012 ; Henehan *et al.*, 2015 ; Haynes *et al.*, 2017). Cependant, comme tout traceur géochimique, l'utilisation du δ^{11}bore pour des applications géologiques repose sur de nombreuses hypothèses concernant l'environnement de l'échantillon utilisé, tandis que les processus chimiques, physiques qui régissent ce traceur doivent être bien connus afin de limiter les incertitudes (Pagani *et al.*, 2005).

La relation δ^{11}B$_{carbonates}$-pH a ainsi été le fil conducteur de ce travail de thèse afin d'en explorer les différents paramètres, relation qui a été par la suite appliquée sur des foraminifères planctoniques. Ce travail a été réalisé au sein de l'ANR franco-allemande B2SeaCarb dont la thématique principale est de mieux comprendre le rôle de l'océan dans les fluctuations du réservoir de carbone dans l'Océan Austral lors des alternances glaciaires-interglaciaires du Plio-Pléistocène.

Ce fil conducteur peut être résumé en une seule équation, qui relie le δ^{11}B$_{carb}$ au pH de l'océan, et donc certains paramètres la constituant ont été étudiés,

$$pH = pK_B - log\left(\frac{\delta^{11}B_{carb} - \delta^{11}B_{sw}}{\delta^{11}B_{sw} - \alpha_{B3-B4}\delta^{11}B_{carb} - 1000 * (\alpha_{B3-B4} - 1)}\right), \tag{1.2}$$

Avec δ^{11}B$_{carb}$ la composition isotopique mesurée du carbonate étudié, δ^{11}B$_{sw}$ la composition isotopique de l'eau de mer dans lequel ce-dit carbonate a précipité, pK$_B$ la constante de dissociation entre l'acide borique et l'ion borate dans l'océan et enfin α_{B3-B4} le fractionnement isotopique entre ces deux espèces chimiques.

◇ Tout d'abord, le chapitre 2 s'attardera à présenter les processus physiques et chimiques qui régissent la relation δ^{11}B$_{carb}$-pH (notamment à partir de foraminifères planctoniques), en l'inscrivant dans le cycle plus global du CO$_2$ dans l'océan.

◇ Le chapitre 3 se concentrera sur la composition isotopique en bore de l'océan (δ^{11}**B**$_{sw}$) au cours du Phanérozoïque. En effet, l'utilisation des isotopes du bore dans les carbonates demande également de connaître la composition isotopique de l'eau de mer dans laquelle ils ont précipité. Hors, celle-ci a varié au cours des temps géologiques. Cette étude a été commencée au sein de l'ANR Carboric et a été continuée lors de ce projet. Ce chapitre présente deux méthodes pour évaluer les variations du δ^{11}**B**$_{sw}$ au cours du Phanérozoïque, par l'analyse d'inclusions fluides contenues dans les halites primaires et par la modélisation.

◇ La mesure du bore dans les carbonates (δ^{11}**B**$_{carb}$) est un défi analytique, d'autant plus quand les échantillons sont peu concentrés en bore et de très petites tailles comme peuvent l'être les foraminifères planctoniques, alors que les erreurs analytiques doivent être minimisées afin d'assurer des reconstitutions de paléo-pH à haute fréquence. Le chapitre 4 présente dans un système d'injection directe des échantillons dans le spectromètre de masse MC-ICP-MS Neptune, le µ-dDIHEN, qui permet de mesurer le δ^{11}B sur de très faibles volumes d'échantillon.

◇ Le chapitre 5, quant à lui, s'appuie sur ce développement analytique en l'adaptant pour la mesure du $\delta^{11}\mathbf{B}_{carb}$ à très faibles concentrations en bore, et en le couplant à un protocole d'extraction du bore de la matrice carbonatée, à très bas niveau de blanc, la microsublimation, développée au cours de cette thèse.

◇ Le chapitre 6 concerne la mise en place de ce protocole pour mesurer des échantillons carbonatés de petites tailles et à faible concentration en bore. Ceci a abouti aux premières mesures du $\delta^{11}\mathbf{B}_{carb}$ de foraminifères à partir du protocole mis en place lors de ce travail de thèse, et plus particulièrement sur l'espèce planctonique *Globigerina bulloides*, avec la mise en oeuvre d'une stratégie alternative d'analyses isotopiques à des niveaux de concentration et de volume jamais égalés jusque là pour ce type d'échantillon.

◇ Enfin, le chapitre 7 montre les premiers reconstitutions paléo-**pH** réalisées à la suite de ce développement analytique sur l'espèce de foraminifère planctonique *Pulleniatina obliquiloculata*, vivant au niveau de la thermocline. Cette étude a pour objectif d'essayer de comprendre quel impact aurait eu la super-éruption du volcan Toba (Indonésie) il y a 73 000 ans sur la dernière transition interglaciaire-glaciaire et notamment sur la chimie de l'océan.

CHAPITRE 2

LES ISOTOPES DU BORE ET PALÉO-PH OCÉANIQUES

Sommaire

2.1 L'océan et le cycle du carbone 15

2.2 Reconstruction des paléo-pH océaniques à partir des isotopes du bore 17

  2.2.a Chimie et isotopie du bore 17

  2.2.b Principes des isotopes du bore comme pH-mètre 18

  2.2.c Composition isotopique en bore des carbonates : théorie 21

  2.2.d Incorporation du bore dans les foraminifères 22

L'introduction générale nous a permis de mettre en lumière le rôle du cycle du carbone en tant que thermostat terrestre et ainsi le besoin crucial de connaître tous les processus qui l'ont gouverné, hier et aujourd'hui, afin de comprendre ce qu'il en sera demain à l'ère de l'Anthropocène. Dans cette partie, je vais me pencher sur le devenir du dioxyde de carbone dans l'océan, et de ce fait m'intéresser plus en détail à son corollaire, le pH océanique. Il s'agit ici de comprendre comment les isotopes du bore, mesurés dans les organismes à test carbonaté que sont par exemple les foraminifères, permettent de le reconstruire. Je développerai donc les principes physico-chimiques qui gouvernent la relation δ^{11}B$_{carbonate}$-pH et les processus biologiques qui impactent cette relation, demandant une correction de ce que l'on appelle l'effet vital (Urey *et al.*, 1951), effet commun à toute reconstruction paléoclimatique à partir de matériels biologiques.

LES ISOTOPES DU BORE DANS LES FORAMINIFÈRES : UN TRACEUR DES PALÉO-PH OCÉANIQUES ET DE LA PCO$_2$ ATMOSPHÉRIQUE

2.1 L'océan et le cycle du carbone

La forte émission du CO$_2$ d'origine anthropique dans l'atmosphère a également des conséquences sur l'océan qui peuvent s'avérer désastreuses à l'avenir. En plus des augmentations de température qui peuvent fortement affecter les écosystèmes marins (Bijma *et al.*, 2013 ; Cheung *et al.*, 2013), ces fortes émissions causent ce que l'on appelle le "jumeau maléfique" du réchauffement climatique : l'acidification des océans (Pelejero *et al.*, 2010). En effet, cette injection massive de dioxyde de carbone dans l'atmosphère a été freinée par les océans qui ont déjà absorbé 30 % du CO$_2$ anthopogénique déjà émis (Sabine *et al.*, 2004 ; Gruber *et al.*, 2019), ce qui a provoqué une réduction du pH de 0.1 unité (entre 1750 et 2000) et la modification en conséquence des équilibres chimiques dans l'océan (Zeebe, 2012). Le carbonate de calcium (CaCO$_3$), dont la plupart des organismes marins se servent pour construire leur coquille ou leur squelette s'en retrouve déstabilisé et les répercussions se font déjà sentir aujourd'hui (e.g. Riebesell *et al.*, 2000 ; De'ath *et al.*, 2009 ; Doney *et al.*, 2009 ; Gazeau *et al.*, 2013 ; Fox *et al.*, 2020). Il est alors important d'étudier le comportement du CO$_2$ dans les océans, qui en contient 60 fois plus que l'atmosphère, et ses conséquences sur le pH, d'autant plus que, dans le registre fossile, les grandes crises biologiques comme la crise Permo-Trias ou Crétacé-Paléogène ont été associées à des phases intenses d'acidification des océans (Hönisch *et al.*, 2012 ; Henehan *et al.*, 2019 ; Jurikova *et al.*, 2020). Le dioxyde de carbone, CO$_2$, se présente dans l'océan sous trois formes : le dioxyde de carbone aqueux CO$_2$ (aq), l'ion bicarbonate HCO$_3^-$ et l'ion carbonate CO$_3^{2-}$. Au pH de l'océan, HCO$_3^-$ est l'espèce majoritaire, à plus de 85 %. Lors des échanges entre l'atmosphère et l'océan, l'équilibre thermodynamique qui régit le passage du dioxyde de carbone gazeux au dioxyde de carbone aqueux est relié par la loi de Henry :

$$[CO_2]\ (aq) = K_0\ (T,S) * pCO_2 \tag{2.1}$$

avec K$_0$ la constante de solubilité du CO$_2$ dans l'eau de mer, dépendante de la température et de la salinité, [CO$_2$] (aq) la concentration de CO$_2$ dans l'océan et pCO$_2$ la pression partielle de dioxyde de carbone dans l'atmosphère. Le [CO$_2$] (aq) est ensuite hydraté puis va réagir avec l'eau afin de se dissocier en ion bicarbonate HCO$_3^-$, ion carbonate CO$_3^{2-}$ et en proton H$^+$ (avec pH=-log[H$^+$]). Ces réactions, acido-basiques, sont gouvernées par les constantes d'équilibres K$^*{}_1$ et K$^*{}_2$, dépendantes elles aussi de la pression, de la température et de la salinité selon :

$$CO_2 + H_2O \xrightleftharpoons{K_1^*} H^+ + HCO_3^- \xrightleftharpoons{K_2^*} 2H^+ + CO_3^{2-} \tag{2.2}$$

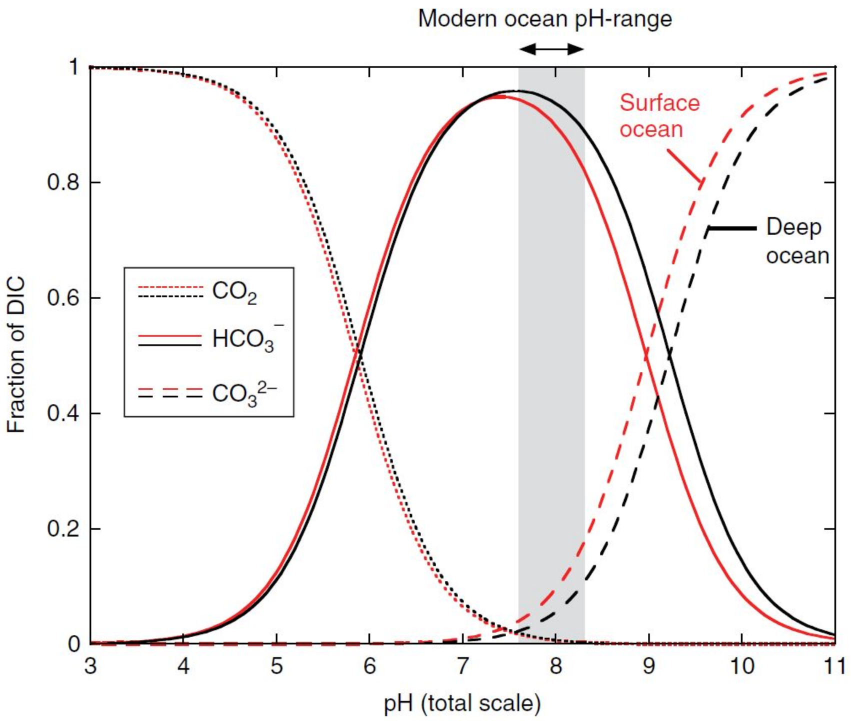

FIGURE 2.1 : "Bjerrum plot" *représentant les différentes espèces de carbone dissout dans l'océan en fonction du pH, aux conditions de surface en rouge (T=25°C, S = 35, P = 1 bar) et pour l'océan profond en noir (T = 4 °C, S = 34.8 et P = 401 bar). D'après Hönisch et al. (2019).*

$$K_1^* = \frac{[HCO_3^-][H^+]}{[CO_2]} \quad et \quad K_2^* = \frac{[CO_3^{2-}][H^+]}{[HCO_3^-]}. \tag{2.3}$$

Le pK$^*_1$ [= -log (K$^*_1$] et pK$^*_2$ [= -log (K$^*_2$] sont respectivement égales dans l'eau de mer à 5.94 et 9.13 pour une température de 15°C, de salinité S = 35 g/L et une pression de 1 atm. Ainsi à un pH océanique de 8.2, la proportion de [CO_2],[HCO_3^-] et [CO_3^{2-}] sont d'environ 0,5 %, 89 % et 10,5 % (Fig. 2.1). La somme de ces trois espèces va composer ce qu'on appelle le DIC (*Dissolved Inorganic Carbon*) :

$$DIC = [CO_2] + [HCO_3^-] + [CO_3^{2-}]. \tag{2.4}$$

Enfin, un dernier paramètre permet de décrire le système des carbonates dans l'océan : l'alcalinité (Alk), qui correspond à une mesure de la balance de charge de l'océan :

$$Alk = [HCO_3^-] + 2[CO_3^{2-}] - [H^+]. \tag{2.5}$$

Le DIC et l'alcalinité (en mol.kg^{-1}) sont des paramètres conservatifs et ne sont donc pas affectés par les changements de pression et de température. Ce sont ainsi ces variables qui sont plus souvent utilisées dans les modèles qui reconstruisent le cycle du carbone dans les océans. De tous les paramètres évoqués précédemment, seuls la pCO_2, le pH, le DIC et l'Alk peuvent être déterminés analytiquement. Six variables ([CO_2], [HCO_3^-],[CO_3^{2-}], Alk, pH et le DIC) permettent donc de décrire le système des carbonates, qui présente ainsi deux degrés de liberté. De ce fait, si le pH et un autre paramètre sont connus, il est possible de reconstruire les autres paramètres du système des carbonates, comme par exemple, ici avec le DIC :

$$[CO_2] = DIC\frac{[H^+]^2}{[H^+]^2 + [H^+]K_1^* + K_1^*K_2^*} \tag{2.6}$$

Enfin, en ayant la concentration de CO_2 dissout, il est alors possible de reconstruire la pCO_2 en utilisant l'équation 2.1. Couplés à un autre paramètre du système des carbonates, les isotopes du bore, en tant que traceur des paléo-pH, permettent de reconstruire les compositions en dioxyde de carbone de l'atmosphère au cours des temps géologiques.

2.2 Reconstruction des paléo-pH océaniques à partir des isotopes du bore

2.2.a Chimie et isotopie du bore

Le bore est un élément semi-métallique appartenant au groupe 13 du tableau périodique qui possède un unique état redox, + III, le rendant insensible aux variations d'oxydo-réduction de son environnement. Il s'agit d'un élément qui est peu abondant sur Terre ($\sim$ 0.3 ppm, McDonough & Sun 1995), mais étant facilement soluble dans les fluides de moyenne à haute température, il est plutôt concentré dans la croûte terrestre ($\sim$ 15 ppm, Leeman & Sisson 1996).

Le bore a une masse atomique de 10,81 et possède deux isotopes stables, ^{10}B et ^{11}B d'une abondance respective de 19.8 et 80.2 %. Les variations isotopiques en bore sont exprimées en notation δ, correspondant au rapport ^{11}B/^{10}B mesuré dans un échantillon rapporté au ^{11}B/^{10}B d'un acide borique de référence, le *National Institute of Standards and Technology (NIST) Standard Reference Material (SRM) 951 boric acid*, selon l'équation :

$$\delta^{11}B = (\frac{(^{11}B/^{10}B)_{sample}}{(^{11}B/^{10}B)_{NIST\ SRM\ 951}} - 1) * 1000. \tag{2.7}$$

Le bore se comporte comme un acide de Lewis en s'associant principalement avec l'oxygène. Dans les systèmes naturels, il est majoritairement sous forme d'acide borique $B(OH)_3$ (trigonal plan) ou d'ion borate $B(OH)_4^-$ (tétraèdrique). Du fait de la grande différence de masse entre ces deux isotopes (10 %), de la différence de spéciation et la grande mobilité du bore dans les fluides, le δ^{11}B est couramment utilisé pour retracer les processus géochimiques à la surface de la Terre, avec une gamme de 145 ‰ (-70 à +75 ‰) observé dans la nature (Barth, 1993 ; Hogan & Blum, 2003 ; Williams & Hervig, 2004). L'un de ces processus qui va nous intéresser ici est l'incorporation du bore dans les carbonates marins, dont la mesure du δ^{11}B va permettre de reconstruire le pH de l'eau de mer à partir de laquelle ces carbonates se sont formés (Vengosh *et al.*, 1991b ; Hemming & Hanson, 1992).

2.2.b Principes des isotopes du bore comme pH-mètre

Le principe des isotopes du bore pour retracer le pH, repose sur l'équilibre acido-basique de celui-ci en solution (Foster & Rae, 2016). Dans cette partie, nous développons ainsi l'aspect théorique de ce traceur géochimique.

Dans l'océan, la concentration en bore totale $[\mathrm{B}]_{sw}$ n'est représentée majoritairement que par l'acide borique et l'ion borate, selon :

$$[B]_{sw} = [B(OH)_3] + [B(OH)_4^-], \tag{2.8}$$

dont les proportions varient avec le pH :

$$B(OH)_3 + H_2O \rightleftarrows B(OH)_4^- + H^+. \tag{2.9}$$

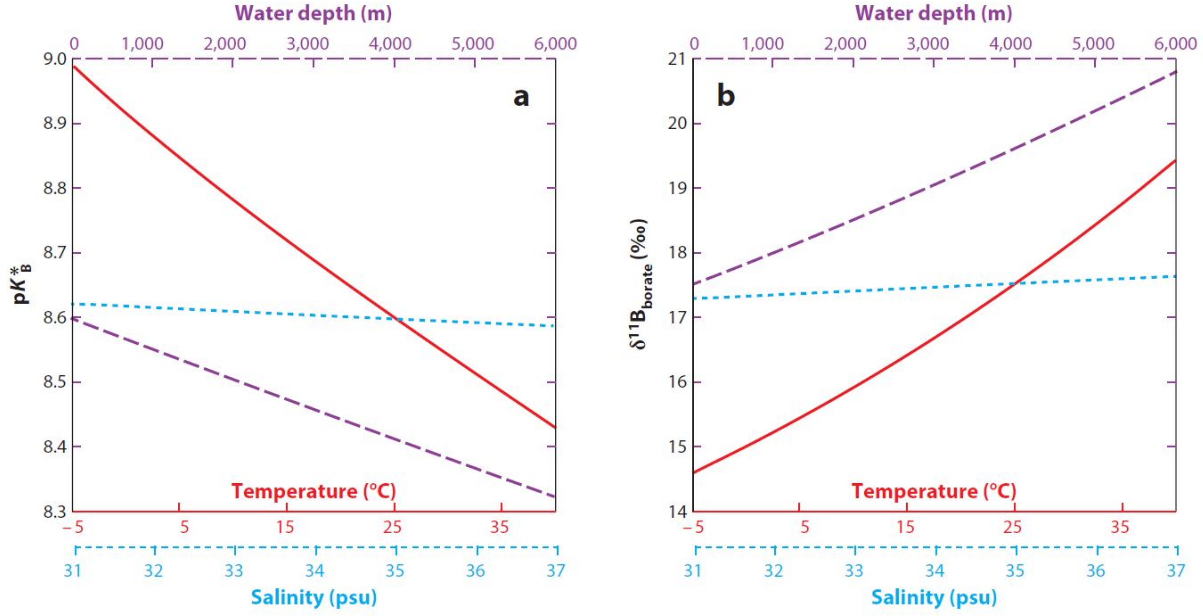

FIGURE 2.2 : *(a) Influence de la température (rouge), de la salinité (bleu clair) et de la pression (violet) sur la constante de dissociation pK$^*_B$. (b) Influence de la température, la salinité et de la pression sur sur le δ^{11}B de l'ion borate à pH = 8. D'après Foster & Rae (2016).*

La constante d'équilibre stoechiométrique s'exprime par :

$$K_B^* = \frac{[B(OH)_4^-][H^+]}{[B(OH)_3]} \tag{2.10}$$

et sa valeur est $\sim 10^{-8.6}$ (pK$^*_B \approx 8.6$) à 25 °C, 35 psu et pression atmosphérique. L'influence de la température, de la salinité et de la pression sur cette constante est mineure (Fig.2.2), tandis qu'avec un pK$^*_B$ proche du pH océanique (8,1-8,2), les proportions de [B(OH)$_3$] et de [B(OH)$_4^-$] vont fortement fluctuer avec le pH (Fig.2.3.a) :

$$[B(OH)_3] = \frac{[B]_{sw}}{1 + K^*_B/[H^+]} \tag{2.11}$$

et

$$[B(OH)_4^-] = \frac{[B]_{sw}}{1 + [H^+]/K^*_B}. \tag{2.12}$$

Le bore total dans l'océan, quant à lui, demeure conservatif (Lee *et al.*, 2010) :

$$[B]_{sw} = 432,6 \frac{\mu mol}{kg} * \frac{salinity}{35}. \tag{2.13}$$

La composition isotopique en bore des océans δ^{11}B$_{sw}$ est égale à 39.61 ± 0.04 ‰ et est homogène quelque soit la température, la salinité et la pression à cause de son grand temps de résidence (14 Ma), supérieur au temps de mélange des océans (1000 ans, Lemarchand *et al.* 2002b ; Foster *et al.* 2010).

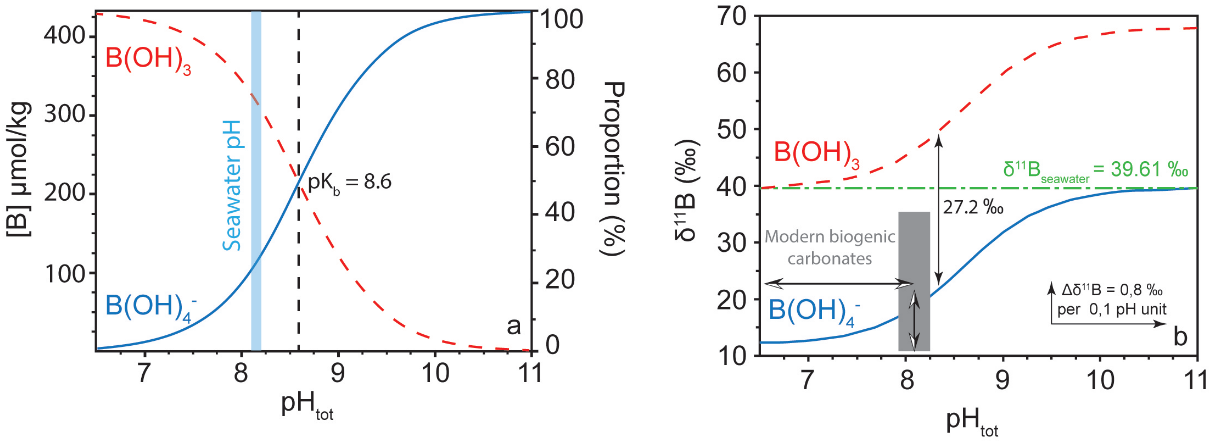

FIGURE 2.3 : *Concentration (a) et composition isotopique (b) de l'ion borate B(OH)$_4^-$ et acide borique B(OH)$_3$ en fonction du pH océanique, pour une température de 25°C, une salinité de 34,7 psu, un pK$^*_B \approx$ 8.6 et un fractionnement isotopique α_{B3-B4} de 1.0272 (Klochko et al., 2006), une composition isotopique d'eau de mer δ^{11}B$_{sw}$ = 39.61 ‰ (Foster et al., 2010) et un bore total [B]$_{sw}$ = 432,6 x (salinity/35) µmol.kg^{-1} (Lee et al., 2010). Le rectangle gris correspond à la gamme mesurée dans les carbonates biogéniques modernes. Modifié d'après Foster & Rae (2016).*

L'acide borique est plus enrichi en ^{11}B que l'ion borate à cause des différences dans la géométrie moléculaire et les énergies de vibration entre ces deux espèces chimiques créant ainsi un fort fractionnement isotopique (Kakihana *et al.*, 1977 ; Klochko *et al.*, 2006). L'échange isotopique entre l'acide borique et l'ion borate peut être décrit comme :

$$^{10}B(OH)_3 +^{11} B(OH)_4^- \rightleftarrows^{11} B(OH)_3 +^{10} B(OH)_4^- \tag{2.14}$$

avec un fractionnement isotopique α_{B3-B4} :

$$\alpha_{B3-B4} = \frac{[^{11}B(OH)_3][^{10}B(OH)_4^-]}{[^{10}B(OH)_3][^{11}B(OH)_4^-]} = \frac{^{11}_{10}R_{B(OH)_3}}{^{11}_{10}R_{B(OH)_4^-}} \tag{2.15}$$

où $^{11}_{10}$R est le rapport ^{11}B/^{10}B. Le facteur de fractionnement, pour sa part, est exprimé selon :

$$\epsilon_B = (\alpha_{B3-B4} - 1) * 1000. \tag{2.16}$$

Ainsi, en connaissant le fractionnement isotopique entre l'acide borique et l'ion borate, dont les proportions dans l'océan dépendent du pH, et tout en conservant constante la concentration [B]$_{sw}$ et le rapport isotopique δ^{11}B$_{sw}$ dans l'océan, il est alors possible de connaître la composition isotopique de B(OH)$_4^-$ ou de B(OH)$_3$ et donc de remonter directement au pH de l'océan, selon le bilan de masse :

$$^{11}_{10}R_{B_{sw}} * [B]_{sw} = ^{11}_{10} R_{B(OH)_4^-}[B(OH)_4^-] + ^{11}_{10} R_{B(OH)_3}[B(OH)_3]. \tag{2.17}$$

En se plaçant ainsi à des pH inférieurs à 7 ou supérieurs à 10, l'océan ne serait composé que d'acide borique ou d'ion borate (Fig.2.3.a), chacun d'eux représentant ainsi la quasi totalité de la concentration en bore avec une valeur isotopique égale à la valeur actuelle, 39.61 ‰. Le faible pourcentage de l'acide ou de la base restante serait ainsi fractionnée de α_{B3-B4}, par rapport à cette valeur de 39.61 ‰ (Fig.2.3.b).

La composition isotopique de l'acide borique et l'ion borate peut-être ainsi calculée en réarrangeant l'équation 2.17 puis en substituant dans l'équation 2.15 :

$$^{11}_{10}R_{B(OH)_4^-} = \frac{^{11}_{10}R_{B_{sw}} * [B]_{sw}}{[B(OH)_4^-] + \alpha_{B3-B4}[B(OH)_3]}, \tag{2.18}$$

qui peut être par la suite convertie en notation δ en substituant les équations 2.7, 2.8 et 2.16 pour obtenir :

$$\delta^{11}B_{B(OH)_3} = \delta^{11}B_{B(OH)_4^-} * \alpha_{B3-B4} + \epsilon_B \tag{2.19}$$

Au final, parce que la proportion de B(OH)$_4^-$ et B(OH)$_3$ varie en fonction du pH, le δ^{11}B de chaque espèce est ainsi contrôlé par ce paramètre (Fig.2.3.b) :

$$\delta^{11}B_{B(OH)_4^-} = \frac{\delta^{11}B_{sw} + (\delta^{11}B_{sw} - \epsilon_B) * 10^{pK_B^* - pH}}{1 + \alpha_{B3-B4} * 10^{pK_B^* - pH}}, \tag{2.20}$$

Comme la constante de dissociation pK$^*_B$ est dépendante de la pression, la température et la salinité, cela implique également que le δ^{11}B de chaque espèce peut évoluer avec ces paramètres. Ainsi, si on peut avoir accès soit au δ^{11}B de l'ion borate, soit au δ^{11}B de l'acide borique, il est possible, par cette succession d'équations de remonter au pH de l'océan. Et c'est justement sur cette constatation que va se fonder la relation δ^{11}B$_{carbonate}$-pH. En effet, il a été émis l'hypothèse que les carbonates marins incorporaient préférentiellement l'ion borate, pouvant facilement se substituer à l'ion carbonate, de par leurs similarités chimiques (voir section suivante). Partant de ce postulat, en mesurant le δ^{11}B d'un carbonate, il est alors possible de reconstruire le pH océanique, et, couplé à un autre paramètre du système carbonate, de reconstituer la pCO$_2$ atmosphérique.

L'utilisation de ce traceur isotopique (Eq. 2.20) demande ainsi la connaissance de chacun des paramètres physico-chimiques qui le constitue. Ainsi, par des calculs *ab initio* ou des méthodes empiriques, le α_{B3-B4} a pu ainsi être estimé (e.g. Kakihana *et al.*, 1977 ; Pagani *et al.*, 2005 ; Sanchez-Valle *et al.*, 2005 ; Klochko *et al.*, 2006 ; Rustad *et al.*, 2010), mais avec des valeurs de fractionnement assez disparates. Ce paramètre a néanmoins pu être affiné par sa mesure directe et donner une valeur de α_{B3-B4} égale à 1.0260 ± 0.00010 (Nir *et al.*, 2015), en accord avec la première mesure qui avait été faite par (Klochko *et al.*, 2006), autour de 1.025-1.036. L'influence de la température sur le fractionnement n'a cependant pas pu être déterminée avec précision, mais dans le domaine des carbonates cette incertitude est probablement insignifiante face aux incertitudes qu'engendre l'utilisation de ce traceur géochimique (Foster & Rae, 2016).

2.2.c Composition isotopique en bore des carbonates : théorie

Le principe de base sur lequel repose la relation δ^{11}B$_{carbonate}$-pH est donc l'incorporation préférentielle d'ions borate dans le système cristallin (Vengosh *et al.*, 1991b ; Hemming & Hanson, 1992). Étant le seul chargé des deux espèces de bore, il va pouvoir se mettre sur des surfaces réactives comme un cristal de calcite ou d'aragonite en pleine croissance, pour qu'il puisse être incorporé sous forme HBO$_3^{2-}$ en se substituant à l'ion carbonate, de taille et de charge quasi similaire, selon :

$$CaCO_3 + B(OH)_4^- \Rightarrow Ca(HBO_3) + HCO_3^- + H_2O. \tag{2.21}$$

Ceci implique donc un changement de coordination, où le tétraèdrique B(OH)$_4^-$ devient le trigonal plan HBO$_3^{2-}$, avec l'hypothèse que ce changement n'implique pas de fractionnement isotopique (Hemming & Hanson, 1992 ; Branson *et al.*, 2015), tandis que dans l'aragonite, l'ion borate pourrait s'y intégrer directement sans changement de coordination, ce qui pourrait expliquer les plus hautes concentrations trouvées dans ces carbonates (Hemming *et al.*, 1995, 1998). Il est alors possible, à partir de la composition isotopique d'un carbonate, d'obtenir le pH de l'eau de mer dans laquelle il a précipité selon l'équation, en connaissant la température, la salinité, la pression (jouant sur le pK$^*_B$) et la composition isotopique de l'eau de mer δ^{11}B$_{sw}$ (Zeebe & Wolf-Gladrow, 2001) :

$$pH = pK*_B - log\left(\frac{\delta^{11}B_{carb} - \delta^{11}B_{sw}}{\delta^{11}B_{sw} - \alpha_{B3-B4}\delta^{11}B_{carb} - 1000*(\alpha_{B3-B4} - 1)}\right). \tag{2.22}$$

Nous retrouvons ainsi l'équation qui relie le δ^{11}B$_{carbonate}$ et le pH, et qui est donc le fil rouge de ce manuscrit.

2.2.d Incorporation du bore dans les foraminifères

Les forminifères planctoniques sont des micro-organismes unicellulaires et eucaryotes (0.50 µm - 1 mm), faisant partie du zooplancton, qui vivent en surface de la colonne, généralement dans les 200 premiers mètres. Apparus au Jurassique il y a 170 Ma, ils ont colonisé tous les océans depuis le Crétacé Moyen (Schiebel & Hemleben, 2017). Leur intérêt premier en paléocéanographie et paléoclimatologie, c'est de posséder une coquille (test) en carbonate de calcium qui se préserve dans le sédiment marin, et qui a surtout lors de sa formation incorporé de nombreux éléments chimiques (majeurs, mineurs, traces et isotopes) dont la teneur peut-être mesurée afin de remonter aux paramètres physico-chimiques de l'océan (Kucera, 2007). Cependant la relation entre la chimie de l'océan et la chimie du test n'est pas directe, car il faut prendre en compte le contrôle qu'a l'organisme sur sa calcification et qui peut donc modifier la chimie de l'océan initiale. Cet effet biologique doit être pris en compte et correspond à ce qu'on appelle l'effet vital (Urey *et al.*, 1951). Pour le corriger, on réalise des calibrations en mesurant le paramètre géochimique visé à partir de foraminifères cultivés, collectés dans la colonne d'eau ou dans des sommets de carottes sédimentaires, dont les paramètres physico-chimiques du milieu de vie sont connus. Pour la mesure des isotopes du bore, ces calibrations ont donc été réalisées sur plusieurs espèces qui ont été cultivées ou collectées de façon à couvrir la plus large gamme possible de pH (e.g. Sanyal *et al.*, 2001 ; Foster, 2008 ; Henehan *et al.*, 2013 ; Martínez-Botí *et al.*, 2015b ; Henehan *et al.*, 2016 ; Raitzsch *et al.*, 2018 ; Guillermic *et al.*, 2020). Afin de s'affranchir des effets environnementaux sur la constante de dissociation pK$^*_B$, les calibrations ne sont pas faites classiquement selon la relation δ^{11}B$_{carbonate}$ - pH mais selon la relation δ^{11}B$_{carbonate}$ -δ^{11}B$_{borate}$ du milieu de vie (Foster, 2008 ; Rae *et al.*, 2011 ; Henehan *et al.*, 2013), avec des équations de type :

$$\delta^{11}B_{B(OH)_4^-} = \frac{\delta^{11}B_{CaCO_3} - c}{m} \tag{2.23}$$

Le gradient (m) et l'intercepte (c) du δ^{11}B$_{carbonate}$ sont ainsi indépendants de la température, de la pression ou de la salinité (Fig.2.4). Si les foraminifères n'incorporaient que l'ion borate, ils seraient donc sur la droite 1 :1 (Fig.2.4). Cependant, bien qu'ils en soient très proches, démontrant que l'incorporation préférentielle d'ion borate est le mécanisme principale, il y a un décalage qui doit de fait être corrigé afin de reconstruire le pH océanique (Fig.2.4). C'est pour cela que les calibrations sont réalisées, qu'elles sont intra-spécifiques et qu'entre les différentes espèces les mécanismes physiologiques expliquant ce décalage doivent être différents, car certains sont au dessus de droite 1 :1, et d'autres non.

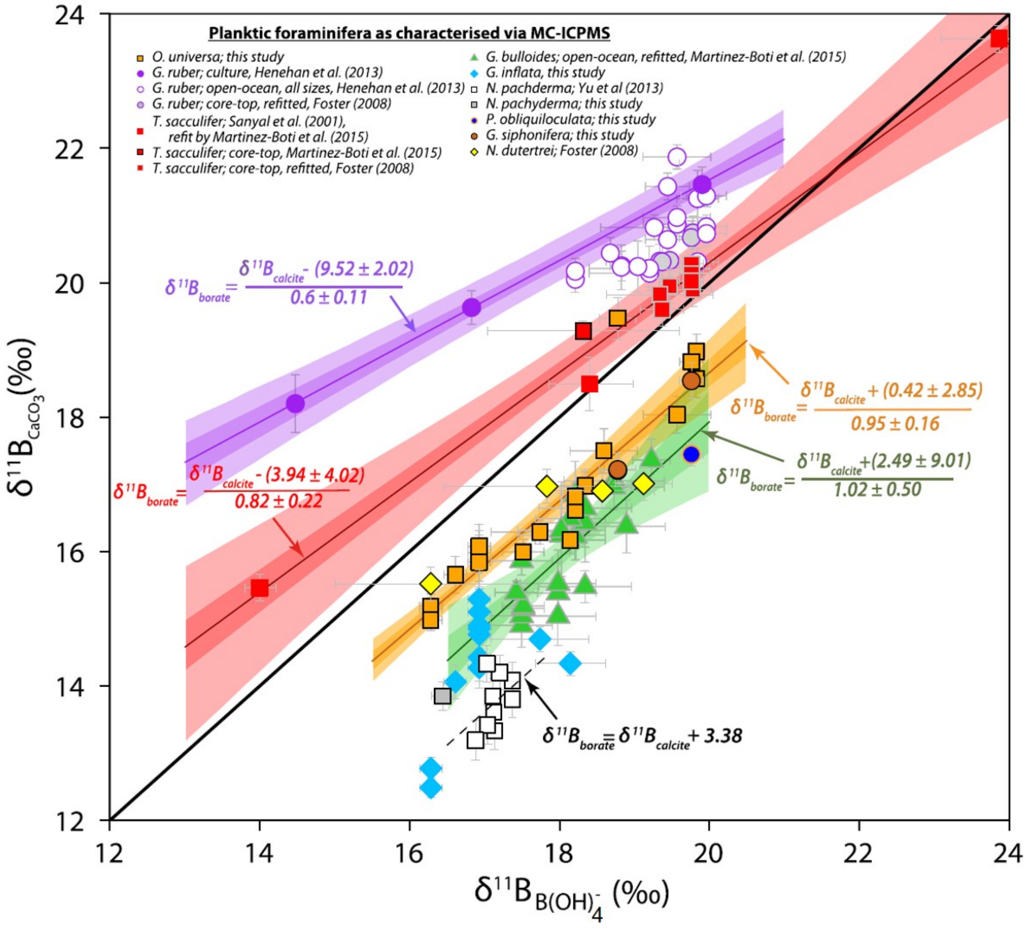

FIGURE 2.4 : *Calibration $\delta^{11}B_{carbonate}$ -$\delta^{11}B_{borate}$ pour les foraminifères planctoniques Orbulina universa, Globigerinoides ruber, Trilobatus sacculifer, Globigerina bulloides, Globoconella inflata, Neogloboquadrina pachyderma. Mesure ponctuelle pour Pulleniatina obliquiloculata, Globigerinella siphonifera et Neogloboquadrina dutertrei. D'après Henehan et al. (2016) et références associées.*

D'un point de vue inorganique, deux processus pourrait en être la cause : une incorporation également d'acide borique, plus enrichie en ^{11}B (Klochko *et al.*, 2009 ; Rollion-Bard *et al.*, 2011 ; Noireaux *et al.*, 2015 ; Uchikawa *et al.*, 2015) ou un fractionnement isotopique, à l'équilibre ou cinétique, lors de l'incorporation de l'ion borate (Pagani *et al.*, 2005). Certaines études réfutent l'hypothèse d'incorporation d'acide borique, ne mettant en évidence que la forme trigonale HBO_3^{2-} tandis la seconde hypothèse a été invalidée, car le temps d'équilibration pour les isotopes du bore entre $B(OH)_4^-$ et $B(OH)_3$ est de 100 µs, ce qui est 3 à 4 fois plus rapide que le taux de croissance des cristaux de carbonates biogéniques (Zeebe *et al.*, 2001). Des fractionnements isotopiques d'origine cinétique sont donc à exclure.

D'un point de vue biologique, ce décalage pourrait être expliqué par les mécanismes de biominéralisation des foraminifères, qui se feraient à partir de la vacuolisation d'eau de mer par endocytose (Erez, 2003), et dont les vacuoles sont modifiées chimiquement afin de favoriser la précipitation de carbonate de calcium, avec une élévation de pH pouvant aller jusqu'à 9 (Nehrke *et al.*, 2013 ; de Nooijer *et al.*, 2014) et ainsi causer un δ^{11}B plus élevé de 12 ‰ par rapport au δ^{11}B de l'ion borate. Ceci ne peut donc pas être la cause de ce léger décalage, en sachant notamment que les foraminifères benthiques ne montrent aucun écart par rapport à cette droite 1 :1 (Rae *et al.*, 2011). Enfin, l'autre possibilité serait la modification du micro-environnement du foraminifère, qui est une région où le transport de nutriments, d'oxygène et des espèces dissoutes du carbone se fait par diffusion. Celle-ci étant marquée par de faible temps d'équilibration et de diffusion des espèces dissoutes de carbone, elle est hautement influençable par les processus physiologiques que sont (Fig.2.5, Zeebe *et al.* 2003) :

1. La photosynthèse des symbiotes

$$CO_2 + H_2O = CH_2O + O_2 \tag{2.24}$$

2. La respiration des foraminifères

$$CH_2O + O_2 = CO_2 + H_2O \tag{2.25}$$

3. La calcification des foraminifères

$$Ca^{2+} + 2HCO_3^- = CaCO_3 + CO_2 + H_2O \tag{2.26}$$

$$Ca^{2+} + CO_3^{2-} = CaCO_3 \tag{2.27}$$

Cette dernière hypothèse est celle qui est la plus communément admise et qui explique très bien les écarts avec la courbe 1 :1 de la relation δ^{11}B$_{carbonate}$ -δ^{11}B$_{borate}$ (Fig.2.4). Par exemple, les espèces qui possèdent des symbiotes comme *G. ruber* ou *G. sacculifer* vont voir le pH de leur microenvironnement augmenter du fait de la photosynthèse (Eq.2.24, Sanyal *et al.* 2001 ; Foster 2008 ; Henehan *et al.* 2016 ; Raitzsch *et al.* 2018) tandis que celles sans symbiotes, par exemple *G. bulloides* ou *T. dutertrei* ont le pH de leur microenvironnement qui augmente à cause de la respiration (Eq.2.25) et de la calcification (Eq.2.26 et 2.27, Foster 2008 ; Martínez-Botí *et al.* 2015b ; Raitzsch *et al.* 2018). L'espèce *O. Universa* illustre également cet équilibre entre ces trois processus dans le microenvironnement : en possédant des symbiontes, elle est pourtant en dessous de la droite 1 :1 (Fig.2.4), et cette acidification serait marquée par une respiration et une calcification plus intenses que l'activité photosynthétique des symbiotes (Henehan *et al.*, 2016).

Ce chapitre nous a permis d'explorer les mécanismes physico-chimiques et biologiques qui permettent de calculer le pH océanique à partir des isotopes du bore mesurés sur des foraminifères planctoniques. Il permet ainsi de mettre également en lumière les limites qui peuvent caractériser l'utilisation de ce traceur géochimique. Ainsi, il a été montré que la composition isotopique en bore dans l'océan est un paramètre fondamental dans les équations montrées ci-dessus. Hors, certaines études paléoclimatiques remontant jusqu'à plusieurs millions d'années dans le passé, conserver la valeur moderne du δ^{11}B de l'océan n'est plus tenable car les flux qui régissent le cycle du bore dans les océans ont probablement variés aussi. Le prochain chapitre va ainsi se porter sur cette thématique afin d'évaluer la variation de $\delta^{11}\text{B}_{sw}$ au cours des temps géologiques.

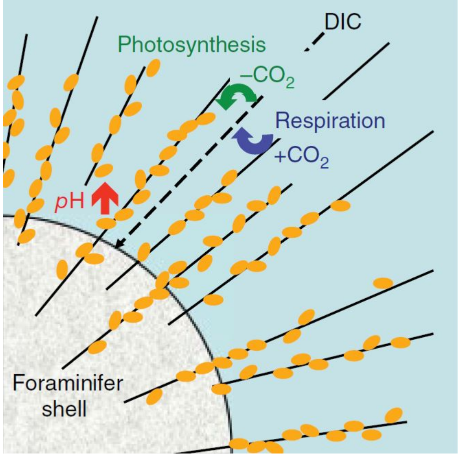

FIGURE 2.5 : *Schéma du micro-environnement de calcification d'un foraminifère planctonique avec symbiotes. Si tous les foraminifères sont impactés dans leur micro-environnement par la respiration et la calcification, ceux qui possèdent des symbiotes sont marqués par une séquestration de CO_2 et donc une élévation de pH par l'activité synthétique de ces derniers. D'après Hönisch et al. (2019).*

CHAPITRE 3

SEAWATER δ^{11}B THROUGH THE PHANEROZOIC

Sommaire

3.1 Introduction 29
3.2 Material and methods 32
  3.2.a Halites 32
  3.2.b Modeling 34
3.3 Results 39
  3.3.a Halite samples 39
  3.3.b Modelled $[B]_{sw}$ and $\delta^{11}B_{sw}$ 41
3.4 Discussion 43
  3.4.a Halites as a direct archive of $\delta^{11}B_{sw}$ secular variations ? 43
  3.4.b $\delta^{11}B_{sw}$ secular variations across the Phanerozoic 50
3.5 Conclusion 62
3.6 Appendix 64
  3.6.a Halite data 64
  3.6.b Geological and stratigraphic settings of the halite samples 67
  3.6.c Fluid inclusions in primary halites : geochemical memory of paleo-oceans . 74
  3.6.d $\delta^{11}B_{sw}$ across the Phanerozoic : state of the art 78
  3.6.e XRD diffractograms 84
  3.6.f Models 84

Le chapitre précédent nous a montré l'importance de connaître le δ^{11}B$_{sw}$ dans l'océan afin d'utiliser la relation δ^{11}B$_{carbonate}$-pH. Par son long temps de résidence, 14 millions d'années - supérieur au temps de mélange des océans (d'environ 1000 ans), la concentration et la composition isotopique en bore de l'océan est aujourd'hui homogène quelque soit la pression, la salinité ou la température (Lemarchand *et al.*, 2002b; Foster *et al.*, 2010). Cependant, les flux qui régissent le cycle océanique du bore au cours des temps géologiques ont varié. Il devient alors nécessaire de reconstruire l'évolution du δ^{11}B$_{sw}$ au cours du Phanérozoïque. Ces reconstructions ont été faites à partir de trois manières différente : la mesure du δ^{11}B$_{carb}$ dans les carbonates avec des hypothèses sur le pH (i.e Pearson & Palmer, 2000; Raitzsch & Hönisch, 2013; Clarkson *et al.*, 2015; Anagnostou *et al.*, 2016; Jurikova *et al.*, 2020), la modélisation en faisant varier au cours du temps par un simple modèle de boite les flux entrants et sortants à l'océan (Lemarchand *et al.*, 2002b; Joachimski *et al.*, 2005) et enfin à partir de halites primaires (Paris *et al.*, 2010b). Cependant, cette dernière est controversée car elle donne une tendance du δ^{11}B$_{sw}$ qui est différente de celle qui est donnée par la mesure des carbonates tandis qu'il n'existe que peu d'enregistrements après le Cénozoïque.

Je me suis attaché dans ce chapitre à retracer cette évolution à partir de ces deux dernières méthodes et de notamment tenter de valider l'hypothèse selon laquelle les halites peuvent enregistrer directement le δ^{11}B$_{sw}$ de l'eau de mer. Pour cela j'ai d'abord étudié sept échantillons de halite primaires, allant du Néoprotérozoïque (550 Ma) au Plio-Pléistoce (3-5 Ma), en passant par le Cambrien (520-540 Ma), le Silurien (434-444 Ma), le Permien (250 Ma) et le Trias (230 Ma) et dont les inclusions fluides se sont révélées être le témoin de la chimie de l'eau de mer dans laquelle elles se sont formées. J'ai ensuite exploré les différentes possibilités qui aurait expliqué pourquoi une halite aurait conservé ou non la signature géochimique de l'océan, bien que les données sur le sujet (le bore en zone évaporitique) sont rares. Dans un second temps, j'ai étendu le modèle réalisé par Lemarchand *et al.* (2002b) à partir de flux géodynamiques mis à jour avec les publications les plus récentes afin de reconstruire la première courbe continue du δ^{11}B$_{sw}$ sur le Phanérozoïque. Ce chapitre est en préparation pour une publication dans *Geochimica et Cosmochimica Acta*.

RECONSTITUTION OF THE SEAWATER BORON ISOTOPIC COMPOSITION OVER GEOLOGICAL TIMES

Matthieu Buisson[1], Raphaël Guignard[1], Pascale Louvat[1], Julien Bouchez[1], Antoine Lucas[1], Claire Rollion-Bard[1], Juske Horita[2], Jérôme Gaillardet[1]

[1]*Université de Paris, Institut de physique du globe de Paris, CNRS, F-75005 Paris, France*

[2]*Department of Geosciences, Mail Stop 1053, Texas Tech University, Lubbock, TX 79409-1053, USA*

Abstract

The reconstruction of seawater paleo-pH based on the boron isotopic composition (δ^{11}B) of fossil carbonate shells requires the knowledge of the δ^{11}B$_{sw}$ of the seawater in which the calcifying organisms lived. Boron has a long residence time in the ocean (14 Ma) and its δ^{11}B$_{sw}$ has changed throughout the Phanerozoic, resulting from changes in the source (continental weathering) and sink (adsorption onto ocean floor sediments and oceanic crust alteration) fluxes. In this study we provide direct determinations of the δ^{11}B$_{sw}$ variations from the historical collection of primary halites, that allowed the reconstruction of the ocean paleochemistry over the Phanerozoic, and a modeling of the secular vation of the δ^{11}B$_{sw}$ for the whole Phanerozoic.

3.1 Introduction

The boron isotopic composition of marine biogenic carbonates (δ^{11}B$_{carb}$) has proven to be a powerful geochemical proxy to reconstruct seawater pH (Vengosh *et al.*, 1991b; Hemming & Hanson, 1992; Sanyal *et al.*, 1996; Lécuyer *et al.*, 2002; Hönisch *et al.*, 2004). Because of the link between ocean pH and the atmospheric partial pressure of CO$_2$, investigating δ^{11}B$_{carb}$ to track the past perturbations of the atmosphere-continent-ocean carbon cycle is one of the keystones to face the Anthropocene's climate change and the other CO2 problem: ocean acidification (Pelejero *et al.*, 2005; Doney *et al.*, 2009; Wei *et al.*, 2009; Hönisch *et al.*, 2012; Liu *et al.*, 2014; Wu *et al.*, 2018; Tierney *et al.*, 2020). This proxy has thereby been widely applied to study the past climate changes in the geological record, investigating the paleo-climatic crises (Gutjahr *et al.*, 2017; Henehan *et al.*, 2019; Müller *et al.*, 2020; Jurikova *et al.*, 2020) or reconstructing the atmospheric pCO2 across the Cenozoic (Pearson & Palmer, 1999, 2000; Foster *et al.*, 2012; Anagnostou *et al.*, 2016; Greenop *et al.*, 2019; Henehan *et al.*, 2020) and the Plio-Pleistocene glacial-interglacial periods (Sanyal & Bijma, 1999; Hönisch & Hemming, 2005; Foster, 2008; Hönisch *et al.*, 2009; Martínez-Botí *et al.*, 2015b; Chalk *et al.*, 2017; Shuttleworth *et al.*, 2020; de la Vega *et al.*, 2020).

Boron has two stable isotopes in nature, ^{10}B and ^{11}B, whose large mass difference generates large boron isotopic fractionations responsible for the 145 ‰ wide range in δ^{11}B observed on Earth (Hogan & Blum, 2003; Williams & Hervig, 2004). Boron isotope ratio is thus also largely used to track geochemical processes at the surface of the Earth (Gaillardet & Lemarchand, 2018; Marschall, 2018). The ^{11}B/^{10}B ratio (δ^{11}B) is expressed as the per mil (‰) deviation of the sample ^{11}B/^{10}B ratio relative to the NBS SRM 951 standard ^{11}B/^{10}B ratio (NIST, USA, Catanzaro *et al.* 1970), following:

$$\delta^{11}B = (\frac{(^{11}B/^{10}B)_{sample}}{(^{11}B/^{10}B)_{SRM\ 951}} - 1) * 1000. \tag{3.1}$$

The δ^{11}B$_{carb}$-pH proxy relies on well-known inorganic chemistry principles. In the aqueous environment, boron dominant species are boric acid B(OH)$_3$ and borate anion B(OH)$_4^-$, with pH-dependent proportions (Dickson, 1990; Zeebe *et al.*, 2001). Between these two species, differences in vibrational frequencies and molecular coordination are responsible of a strong and constant isotopic fractionation (Δ^{11}B$_{3-4}$ of 27.2 ± 0.6 ‰), B(OH)$_4^-$ being depleted in ^{11}B (e.g., Klochko *et al.*, 2006). As B(OH)$_4^-$ is preferentially incorporated during carbonate precipitation, measuring the δ^{11}B of carbonates allows to reconstruct the pH of the fluids these minerals have precipitated from (Hemming & Hanson, 1992), using the equation:

$$pH = pK_B - log\left(\frac{\delta^{11}B_{carb} - \delta^{11}B_{sw}}{\delta^{11}B_{sw} - \alpha_{B3-B4}\delta^{11}B_{carb} - 1000 * (\alpha_{B3-B4} - 1)}\right), \tag{3.2}$$

This relationship between seawater pH and δ^{11}B$_{B(OH)_4^-}$ requires that the dissociation constant of boron (pK$_B$), the isotopic fractionation between B(OH)$_4^-$ and B(OH)$_3$ (α_{B3-B4}) and the boron isotopic ratio of seawater δ^{11}B$_{sw}$ in which the carbonate has precipitated are constrained (Vengosh *et al.*, 1991b; Hemming & Hanson, 1992; Pagani *et al.*, 2005). This study investigates the possible variations of δ^{11}B$_{sw}$ over geologic timescales.

As boron in seawater is a quasi-conservative element with a modern residence time of 14 Myr (Lemarchand *et al.*, 2000, 2002b), higher than the ocean's mixing time (1 kyr), seawater boron concentration ([B]$_{sw}$ = 4.68 ± 0.01 ppm) and isotopic composition (δ^{11}B$_{sw}$ = 39.61 ± 0.04 ‰) are homogeneous today, regardless of depth, salinity or temperature (Spivack & Edmond, 1987; Foster *et al.*, 2010; Lee *et al.*, 2010; Gonzalez, 2014). This steady state in the oceanic boron budget stems from a balance between input and output boron fluxes, that have fluctuated over time scales of million of years and therefore modified the δ^{11}B$_{sw}$ values in the past. Several authors investigated δ^{11}B$_{sw}$ variations during the Cenozoic, by either measuring the pore fluids of marine sediments (Spivack *et al.*, 1993), modelling the variations of the boron fluxes (Lemarchand *et al.*, 2000, 2002b; Simon *et al.*, 2006) or coupling the δ^{11}B of benthic and/or planktonic foraminifera living at different depths and assuming a surface to bottom pH gradient (Palmer *et al.*, 1998; Pearson & Palmer, 1999, 2000; Foster *et al.*, 2012; Raitzsch & Hönisch, 2013; Anagnostou *et al.*, 2016; Greenop *et al.*, 2017; Gutjahr *et al.*, 2017; Henehan *et al.*, 2019).

Only few studies examined the secular variation of $\delta^{11}B_{sw}$ beyond 65 Myr. Joachimski *et al.* (2005) expanded the B flux modelling to the whole Phanerozoic and validated the computed $\delta^{11}B_{sw}$ variations with $\delta^{11}B_{carb}$ measurements of brachiopods from Silurian to Permian (Joachimski *et al.*, 2005) and Jurassic (Lécuyer *et al.*, 2002). $\delta^{11}B_{sw}$ has also been determined from brachiopods for the Cretaceous (Simon *et al.*, 2006), Toarcian Oceanic Anoxic Event (Early Jurassic, Müller *et al.* 2020) and Permian-Triassic Boundary (Jurikova *et al.*, 2020); from cap carbonates in the Neoproterozoic (Kasemann *et al.*, 2010; Ohnemueller *et al.*, 2014); and from shallow marine platform carbonates at the Permo-Trias transition (Clarkson *et al.*, 2015).

Because the aforementioned indirect methods (from $\delta^{11}B_{carb}$) are based on different oceanic paleo-pH scenarios, Paris *et al.* (2010b) proposed to directly reconstruct the boron isotope composition of seawater from primary halite samples. Indeed, evaporite deposits record the changes of ocean's chemistry (Hardie, 1996; Holland *et al.*, 1996; Hay *et al.*, 2006) and the fluid inclusions trapped in primary halites are the Rosetta stone to seawater paleo-chemistry decryption (Lowenstein, 2001; Horita *et al.*, 2002; Brennan *et al.*, 2004, 2013; Holt *et al.*, 2014; Spear *et al.*, 2014). The possibility of fluid inclusions to record the chemistry of seawater was confirmed for modern samples (Timofeeff *et al.*, 2001). With regard to boron, Liu *et al.* (2000) and Fan *et al.* (2015) showed that there are no or minor isotopic fractionation between halite and brine, as boron is only concentrated in the brine inclusions (it hardly enters the halite matrix). Paris *et al.* (2010b) confirmed this assumption by showing that modern halites have the bulk $\delta^{11}B$ of modern seawater and proposed $\delta^{11}B_{sw}$ values from Cenozoic and Devonian primary halites.

However, $\delta^{11}B_{sw}$ determinations from primary halites are still debated as Paris *et al.* (2010b) proposed $\delta^{11}B_{sw}$ values decrease to globally lower values as those modelled from $\delta^{11}B_{carb}$ or from input/output budgets, which also suffer from several uncertainties and model-dependence outputs (Raitzsch & Hönisch, 2013; Greenop *et al.*, 2017). Boron budget $\delta^{11}B_{sw}$ models have not been updated since the works of Lemarchand *et al.* (2002b) and Joachimski *et al.* (2005). Because of the yet established utility of the $\delta^{11}B_{carb}$-pH proxy for paleoclimatology studies (Mills *et al.*, 2019), it is essential to know the $\delta^{11}B_{sw}$ variations over geological times. Here we complete the investigations of Paris *et al.* (2010b) to cover the whole Phanerozoic with primary halites from the collection of Horita *et al.* (2002) and assess the validity of the $\delta^{11}B_{sw}$ derived from evaporites. We then re-evaluate the secular variations through the Phanerozoic of modelised boron concentration and $\delta^{11}B_{sw}$ in oceans with updated geodynamics fluxes. We ultimately put into perspective our modelled $\delta^{11}B_{sw}$ with the geodynamic history of the Earth.

3.2 Material and methods

3.2.a Halites

Halite sample preparation

We studied seven halite samples originated from the historical collection of Horita *et al.* (2002), which primary nature has been extensively established, and which stratigraphic, geological, paleo-geographical and climatic framework have been fully described. These salts cover a period between the end of the Proterozoic (Ara 7) and the Plio-Pleistocene (IZ-3), and were collected from Cambrian (Sib4), Silurian (Car12-3-3), Devonian (AW-86-49), Permian (WIPP-3), and Triassic (Keuper) basins (Fig.3.1). The Silurian salt (Car12-3-3) has been divided in two sub-parts, one being transparent and colourless and the second one opaque orange-coloured and bearing clays.

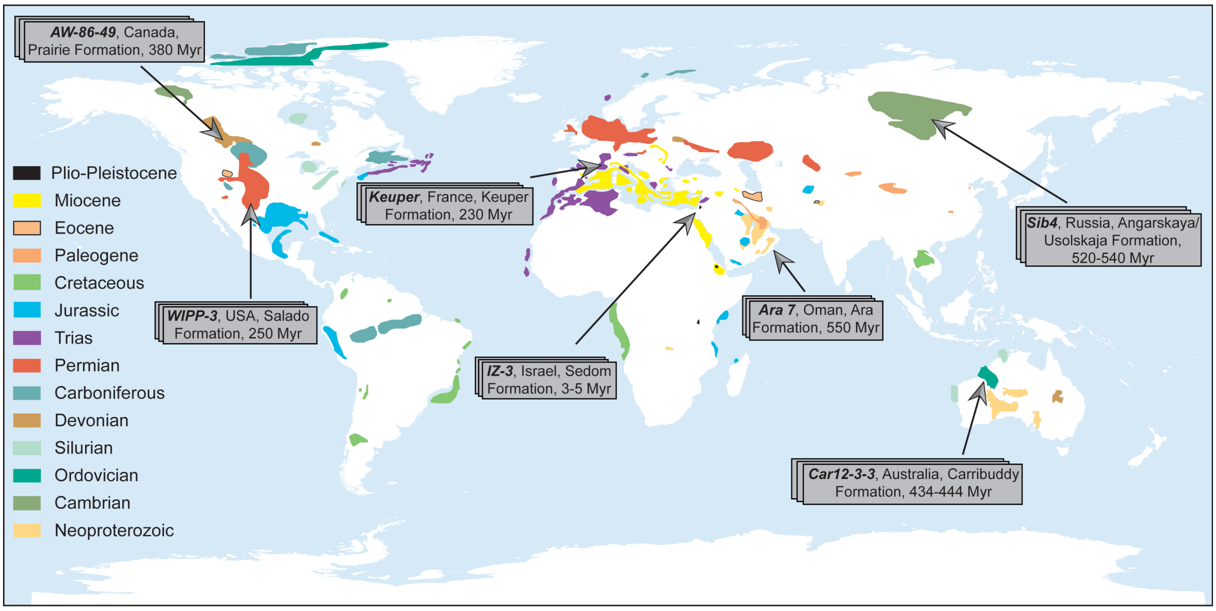

Figure 3.1 : *Halite samples distribution positioned on a map of the major halite basins (modified Warren 2010). The approximate ages are from Horita et al. (2002).*

After a superficial cleaning of the sample surface with MilliQ water and drying with Kimwipe paper, the halites were crushed. For each sample, 10 aliquots of salt were prepared: for each aliquot 0.35 mg of salt was dissolved in 10 mL of MilliQ water to reach actual seawater salinity. Because B is almost absent in the halite matrix and is enriched in brine inclusions (Liu *et al.*, 2000; Fan *et al.*, 2015), bulk halite analysis must yield an average δ^{11}B value of the brine inclusions within the sample. For each aliquot, a small fraction is collected and diluted in 10 mL HNO_3 0.5 N to measure major and trace element concentrations by Inductively Coupled Plasma Mass Spectrometry (ICPMS, Agilent 7900).

Boron isotope analysis

Boron has been extracted from the salt samples by ion-exchange chromatography columns filled with 50 µL of Amberlite 743 resin at 200-400 mesh (Lemarchand *et al.*, 2002a; Paris *et al.*, 2010a). Prior to the separation, the salt aliquots were basified to pH 8-9 with distilled ammoniac. The column resin was washed with 30 mL of 0.5 N HNO_3, then rinsed and conditioned with 0.2 mL MilliQ water basified at pH 9 with NH_4OH. The sample was then introduced and the resin was rinsed again with pH 9 water (0.1 mL), saturated with 0.6 M NaNO3 (0.1 mL), and finally rinsed with basified MilliQ water (0.2 mL). Boron was eluted with 0.05 mL of nitric acid at 0.5 N and 0.6 mL of HNO_3 0.1 N. The eluted solution is diluted to 0.05 N HNO3, introduction matrix for the MC-ICPMS analyses (Louvat *et al.*, 2011a). B from seawater NASS 6 was regularly extracted to verify the extraction yield. For optimized analyses, 100-400 ng of boron are usually aimed in the eluted solutions. According to B concentrations measured in the halites, 5 to 7 mL of the sample solutions were introduced to the columns. To ensure that large volumes of NaCl do not interfere with boron extraction, introduction of 0.5, 1 and 5 mL of seawater reference material NASS 6 have been tested.

The halite's δ^{11}B were measured on a MC-ICPMS (multicollector ICPMS, Neptune, ThermoFischer Scientific) with a direct injection nebulizer, the d-DIHEN (demountable-direct injection high-efficiency nebulisation, Louvat *et al.* 2011a) plugged in the torch in place of the injector. This introduction system showed good cross calibration with other methods for δ^{11}B determinations on standards, seawater and carbonates samples (Foster *et al.*, 2013; Gutjahr *et al.*, 2020). During our measurements the ^{11}B signal was around 2 V for 200 ppb. Each sample is measured three times in alternance with the bracketing standard solution NBS SRM 951 (NIST, USA, Catanzaro *et al.* 1970) at the same concentration (± 5 %) to keep identical conditions in the plasma (Louvat *et al.*, 2011a, 2014b). Five δ^{11}B values can be calculated from the triplicate sample-standard bracketing of one sample enabling to calculate individual repeatability as 2 standard deviation (2SD, Louvat *et al.* 2014b). The reference solutions from Vogl & Rosner (2011) ERM-AE120 (-20.2 ± 0.6 ‰), ERM-AE121 (19.9 ± 0.6 ‰) and ERM-AE122 (39.7 ± 0.6 ‰) were measured together with the halite samples, resulting in average values of -20.27 ± 0.02 ‰ (n=4, 2SD), 19.75 ± 0.11 ‰ (n=9, 2SD) and 39.35 ± 0.29 ‰ (n=6, 2SD). For the different seawater volumes tested (0.5, 1 and 5 mL), the δ^{11}B values were respectively 39.57 ± 0.13 ‰, 39.75 ± 0.19 ‰ and 39.72 ± 0.07 ‰ (2SD), in agreement with Foster *et al.* (2010) (39.61 ± 0.04 ‰) and the two years IPGP average (39.87 ± 0.25 ‰, Louvat *et al.* 2014b), indicating no volume effect for boron extraction from large volume of seawater.

Strontium isotope analysis

The ^{87}Sr/^{86}Sr ratio of the halites has been measured to verify their marine origin (Veizer *et al.*, 1999; Paris *et al.*, 2010b). According to the measured Sr concentrations, 0.01 to 2 mL of the initial halite solutions (for a final concentration of 200 ppb) were evaporated, taken in 50 µL of 16 N nitric acid and evaporated again. The residue was then dissolved in 0.1 mL of 3 N HNO_3. The strontium is extracted from its natural matrix with 100 µL of ion exchange resin Sr-SPEC (Eichrom Technologies) of 50-100 µm grain size (Horwitz *et al.*, 1991; Pin & Bassin, 1992). The protocol has been adapted in order to avoid calcium and barium in the eluted solution due to their similar chemical behaviour (Scher *et al.*, 2014). Prewashed with HNO_3 5 N (2.5 mL), MilliQ water (5 mL), HCl 3 N (2.5 mL) and finally MilliQ water (10 mL), the columns are conditioned with 3 N HNO_3 (0.1 mL). After loading the sample, the resin is washed with HNO_3 3 N (0.2 mL) and 6 N (4 mL) to remove the unwanted elements whereas strontium is immobilized. Finally, Sr is eluted with milliQ water (2 mL) and the solution is acidified to 0.5 N HNO_3 (Hajj *et al.*, 2017).

The ^{87}Sr/^{86}Sr ratios of the salt samples have been determined on the MC-ICP-MS Neptune Plus (ThermoFischer Scientific). The samples were introduced with an APEX (ESI) desolvating unit paired with a PFA nebulizer with an uptake rate of 50 µL.min^{-1}. Isobaric interferences ^{86}Kr and ^{87}Rb were corrected by background subtraction for ^{86}Kr and by subtracting ^{87}Rb from ^{87}Sr (measuring ^{85}Rb and applying the ^{87}Rb/^{85}Rb ratio that had been measured from a Rb standard solution at the start of each session). Instrumental mass bias was corrected with the exponential law of Russel, on the supposedly invariant ^{88}Sr/^{86}Sr ratio of 8.375209 (Russell & Papanastassiou, 1978) and samples were further bracketed with the carbonate standard SRM 987 (NIST, USA, accepted value of 0.71024). The SRM 987 standard yielded a ^{87}Sr/^{86}Sr value of 0.710281 $\pm$ 0.000066 (n=8). Modern seasalt (Guérande, France) as a witness of actual seawater yielded ^{87}Sr/^{86}Sr of 0.709208 $\pm$ 0.000030 (n=2) in agreement with the modern seawater values (0.709176, Veizer *et al.* 1999; Paris *et al.* 2010b).

Mineralogy

In combination with the chemical and isotopic analyses, X-ray diffraction analyses have been performed to evaluate qualitatively if the halite samples were associated with other minerals. XRD analyses were performed in Laboratoire Paléoenvironnemements Paléoclimats, Bassins (Institut des Sciences de la Terre) of Sorbonne University on a X-ray diffractometer D2 PHASER (BRUKER) equipped with a detector LYNXEYE. Diffractogrammes were interpreted thanks to the MacDiff®4.2.5 software.

3.2.b Modeling

Boron geochemical cycle

The boron oceanic budget can be established for [B] but also for B isotope ratio. The main B sources to the ocean are continental weathering, hydrothermal vents at mid-ocean ridges and accretion prisms, while the main oceanic B sinks are adsorption on the sediments of the oceanic floor, oceanic crust alteration and coprecipitation in carbonates (Fig.3.2).

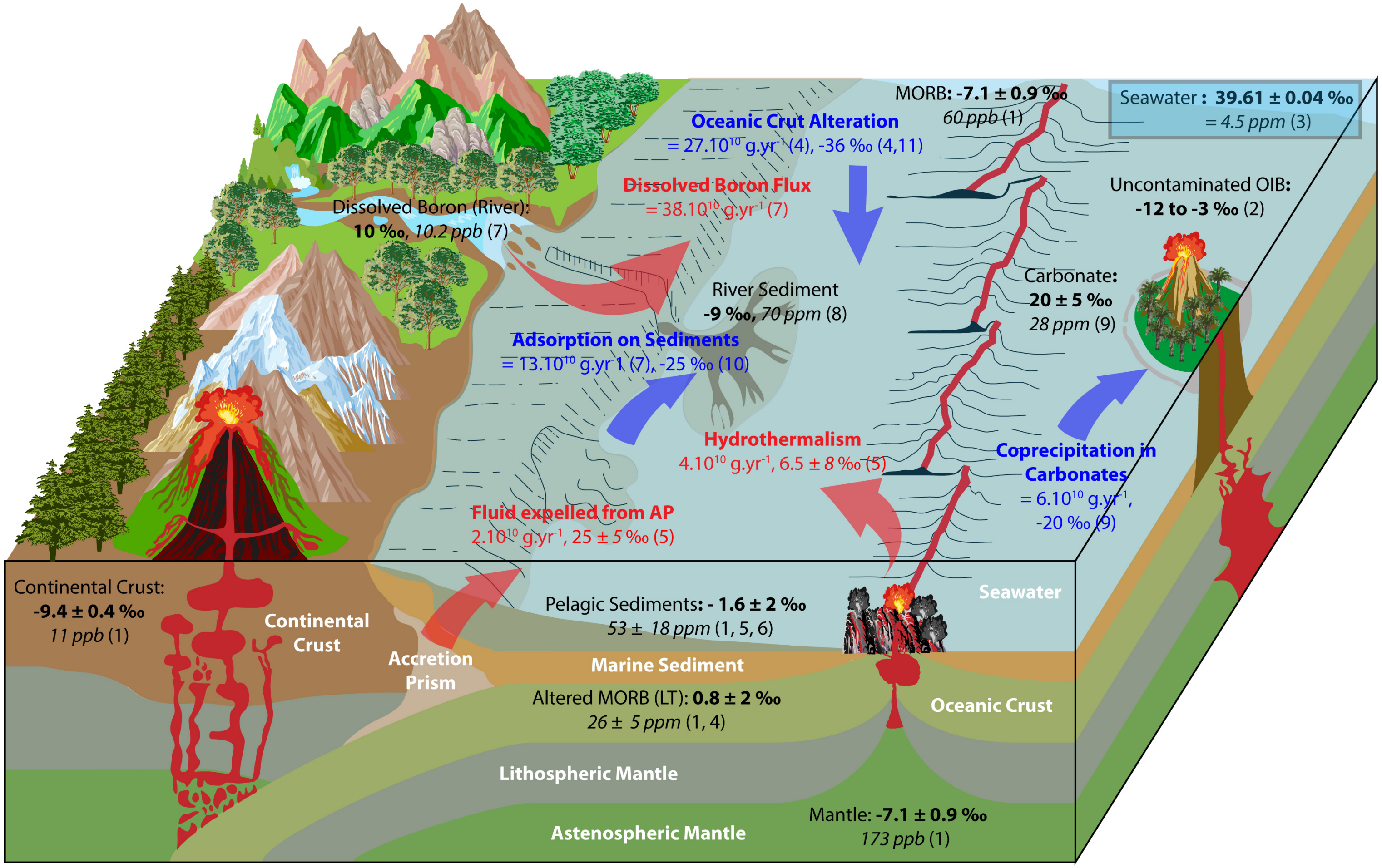

Figure 3.2 : *The global boron geochemical cycle with its main natural reservoirs. Red and blue arrows represent respectively the boron input and output fluxes to the oceans and associated red and blue numbers are the average fluxes and B isotope fractionation factors ($\Delta^{11}B$ in ‰). Black numbers are the average B concentrations and $\delta^{11}B$ values (‰, bulk) of the reservoirs. Data compiled from: (1) Marschall et al. (2017) (2) Marschall (2018) (3) Foster et al. (2010) (4) Smith et al. (1995) (5) You et al. (1993) (6) Leeman & Sisson (1996) (7) Lemarchand et al. (2002b) (8) Chetelat et al. (2009) (9) Vengosh et al. (1991b) (10) Spivack & Edmond (1987) (11) Palmer et al. (1987).*

At steady state, incoming or outgoing fluxes represent 45.10^{10} g.year^{-1} (Lemarchand *et al.*, 2002b). In the isotopic budget of oceanic boron, seawater has the highest δ^{11}B value, 39.61 ± 0.04 ‰ (Foster *et al.*, 2010), which could be surprising given that the main input flux by continental weathering has an average δ^{11}B value of 10 ‰ (Lemarchand *et al.*, 2002b), but is due to the boron sink processes, which preferentially take the charged and reactive borate, enriched in ^{10}B. Indeed, the major sinks correspond to the low alteration of the newly formed oceanic crust, (27.10^{10} g.year^{-1}, Spivack *et al.* 1987; Smith *et al.* 1995; Lemarchand *et al.* 2002b), followed by adsorption on clastic sediments (13.10^{10} g.year^{-1}, Palmer *et al.* 1987; Spivack *et al.* 1987; Lemarchand *et al.* 2002b), which together are termed as "reverse weathering" with the formation of marine authigenic aluminosilicate clays. Based on adsorption experiments on sediments and clays, their related isotopic fractionations are respectively -36 and -25 ‰, in agreement with δ^{11}B analyses of altered oceanic basalts (Palmer *et al.*, 1987; Spivack *et al.*, 1987; Smith *et al.*, 1995). Comparatively, B coprecipitation in carbonates is a minor output flux, estimated at 6.10^{10} g.year^{-1}, with an average fractionation of -20 ‰ (Vengosh *et al.*, 1991b).

Concerning B input to the oceans, low-temperature continental weathering, through the dissolved boron in rivers, represents more than 85 % of the flux with a discharge-weighted average B flux for the 22 largest rivers (39 % of the water discharge to ocean) evaluated at 38.10^{10} g.year^{-1} (Lemarchand *et al.*, 2002b). Atmospheric and anthropogenic B inputs to rivers are thought to be negligeable (Lemarchand *et al.*, 2002b; Chetelat *et al.*, 2009; Gaillardet & Lemarchand, 2018). The contribution of mid-ocean ridge hydrothermal vents and fluids expelled from accretion prisms are considered to be marginal, with incoming B fluxes of 4 and 2.10^{10} g.year^{-1} and average δ^{11}B values of 6.5 and 25 ‰, respectively (Spivack & Edmond, 1987; You *et al.*, 1993; Smith *et al.*, 1995; You *et al.*, 1995).

Modeling the marine boron secular evolution across the Phanerozoic

The assessment of the input and output fluxes and their isotopic fractionation regulating the boron geochemical cycles allows us to model [B]$_{sw}$ and δ^{11}B$_{sw}$ fluctuations across the Phanerozoic. As the intensity of these fluxes changed in the past according to the geodynamic history of Earth and consequently impacted the boron chemistry, we reconstructed the oceanic boron content (Eq. 3.3) and the oceanic boron isotopic budget (Eq.3.4) with a simple box model according to:

$$\frac{dB_{sw}}{dt} = \sum \phi_{in} - \sum \phi_{out} \tag{3.3}$$

$$\frac{dR_{sw}}{dt} = \left(\sum \frac{\phi_{in}}{B_{sw}}\right)\left(\frac{1+R_{sw}}{1+R_{in}}\right)(R_{in} - R_{sw}) - \left(\sum \frac{\phi_{out}}{B_{sw}}\right)\left(\frac{1+R_{sw}}{1+R_{out}}\right)(R_{out} - R_{sw}) \tag{3.4}$$

where B_{sw} and R_{sw} are respectively the total boron content and the ^{11}B/^{10}B ratio in seawater, ϕ_{in} and ϕ_{out} the total boron input and output fluxes for the ocean, R_{in} and R_{out} their associated ^{11}B/^{10}B, and *t* the time in years. All the δ^{11}B values have been transposed to ^{11}B/^{10}B ratios in the modelling and the reconstructed seawater ^{11}B/^{10}B ratios back to δ^{11}B (Eq. 3.1) with ^{11}B/^{10}B$_{NISTSRM951}$ = 4.04362 (Catanzaro *et al.*, 1970). To estimate the amplitude of the changes in the boron fluxes across the geological times, we considered the most recent evaluations of the geodynamic forcings (normalized to the present), which have been intensively studied as inputs into the box models of carbon and oxygen cycles, and are governed at long time scale by plate tectonics (Berner, 2004; Royer, 2014; Mills *et al.*, 2017; Lenton *et al.*, 2018; Mills *et al.*, 2019). The model is initialized with the modern [B]$_{sw}$ and δ^{11}B$_{sw}$ values, and resolved going back in time.

The rate of B sink through alteration of the oceanic crust is controlled by the exposure of fresh basaltic materials to seawater and is thus linked to the oceanic crust spreading rate. To modulate this B output in the Phanerozoic, we selected the total global length of subduction zones as a proxy of the total crustal addition and destruction rates (Van Der Meer *et al.*, 2014), which was used in the last updated Earth pCO$_2$ and temperature models that have sensibly reconciled CO$_2$ and temperature reconstructions with geological and geochemical proxies (Mills *et al.*, 2019). Directly linked to this forcing, the intensity of the B input flux through mid-ocean ridge hydrothermalism and accretion prisms is also derived from the length of the subduction zones (Fig.3.3.a). For the B output flux by adsorption on clastic sediments, the magnitude is assimilated to fluctuations of the global erosion rate over geological times, built from a compilation of dated global sediment masses (over continents and oceans) that allowed to determine a long-term polynomial fit to calculate the missing parts, lost by erosion (Hay *et al.*, 2002, 2006). We selected for our model the 100 Myr moving average also used by Mills *et al.* (2019) (Fig.3.3.c). The coprecipitation of boron in carbonates has been associated to the burial rate of carbonate sediments over the Phanerozoic established with the GEOCARBSULFvolc model (Fig.3.3.d), which calculates the atmospheric O$_2$ and CO$_2$ driven by the geochemical proxy data (δ^{13}C, δ^{18}O, δ^{34}S, ^{87}Sr/^{86}Sr) of the geological records (Berner, 2006; Berner & Mackenzie, 2011).

In contrast to the boron fluxes mentioned above, whose reservoirs and processes are pretty much well defined in the modern ocean realm and therefore can be simply assimilated to changes in geodynamics forcings (Lemarchand *et al.*, 2002b; Marschall *et al.*, 2017; Marschall, 2018), the relationships in the critical zone between the riverine dissolved boron input, coming from the chemical weathering of the continents, and climate, lithology, hydrology, biology or hydrothermal activity remain unclear (Gaillardet & Lemarchand, 2018).

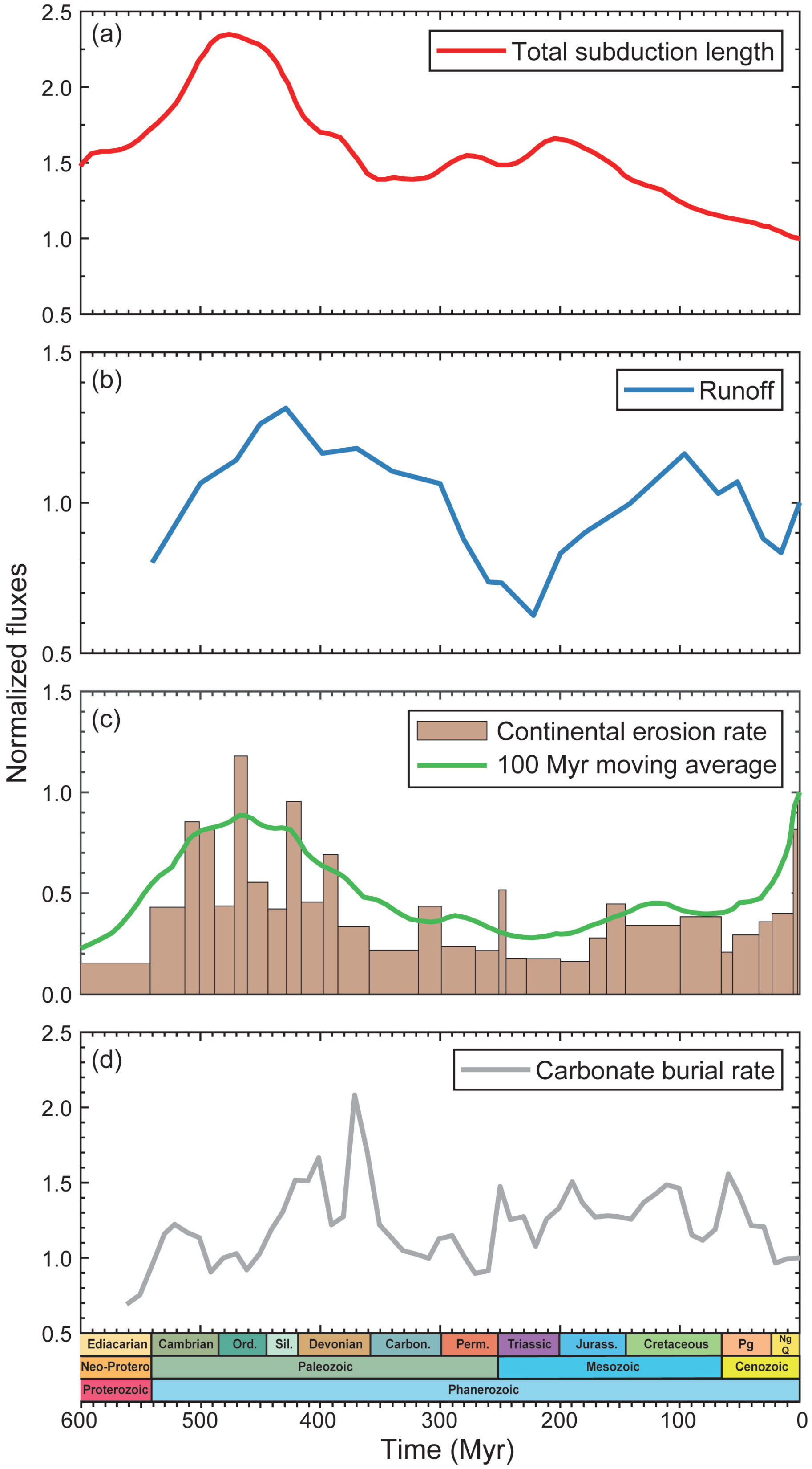

Figure 3.3 : *Variation of the geodynamic forcings through the Phanerozoic, impacting the boron oceanic budget. (a) Normalized total subduction length (Mills et al., 2017) (b) Normalized runoff (Goddéris et al., 2014) (c) Relative rate of continental erosion (Hay et al., 2006) and its derived 100 Myr moving average (Mills et al., 2019) (d) Normalized carbonate burial rate (Berner & Mackenzie, 2011).*

Following Lemarchand *et al.* (2002b), we modelled the boron secular variation in seawater with a first scenario that kept the modern riverine B flux and average δ^{11}B constant through time. For lack of better, these present-day values offer the advantage of gathering a large diversity of weathering contexts at the Earth surface (lithologies, relief, climate, geomorphology, weathering environments...). The second scenario involves past fluctuations of the boron continental discharge with the runoff (Lemarchand *et al.*, 2002b). Defined as the difference between rainfall and evapotranspiration, and therefore driven by temperature, the runoff strongly controls weathering rates and fluxes, and thus the chemical composition of the rivers. Runoff relies on the hydrological cycle and the palaeogeographical settings. Unfortunately, for now, there is no proxy for runoff in the geological records, but runoff is usually resolved from atmospheric general circulation models that couple atmospheric CO_2, solar energy and the continental paleo-configurations (Otto-Bliesner, 1995; Gibbs, 1999). For the second scenario of our modelling we introduced the last runoff reconstruction from the GEOCLIM simulation (Fig.3.3.b), which contains a long-term CO_2 cycle (Goddéris *et al.*, 2014). Elaborating these two scenarios allowed to build two δ^{11}B curves for the Phanerozoic. We have to keep in mind that the two scenarios do not relate independent stories of the seawater boron isotopic composition, but complement each other; the main uncertainty remains the variation of the boron isotopic composition of rivers across geological times.

3.3 Results

3.3.a Halite samples

The large B concentration variations over three orders of magnitude among the halite samples reflect the diversity of the fluid inclusion density between samples, but also between aliquots of a same sample. Despite these variations, δ^{11}B values of the aliquots are quite homogeneous for each salt sample (Fig.3.4), arguing against a difference in δ^{11}B between the halite matrix and the fluid inclusions and/or in favor of absence of B in the halite matrix. Indeed, if matrix and inclusions both contained B at different δ^{11}B values, the aliquots of a same sample salt (unless extremely homogeneous) would show a mixing between two different B reservoirs. The different salts display large variations in the δ^{11}B throughout the ages, ranging from 28.3 ± 2.3 ‰ (n=10, 2SD) in the late Neo-Proterozoic to 39.2 ± 3.7 ‰ (n=10, 2SD) in the Plio-Pleistocene, with 11.2 ± 5.5 ‰ (n=10, 2SD) in the Lower Cambrian, 3.74 ± 9.4 ‰ (n=17, 2SD) in the lower Silurian, 31.7 ± 3.0 ‰ (n=10, 2SD) in the Middle Devonian, 17.2 ± 1.5 ‰ (n=10, 2SD) in the Upper Permian and 9.4 ± 2.2 ‰ (n=9, 2SD, without the outlier) in the Upper Triassic (Fig.3.5). The measured 2SDs of the halite samples are very high, too high for paleo-pH reconstructions where a 1 ‰ fluctuation of the $\delta^{11}B_{sw}$ results in a deviation of 0.1 pH unit.

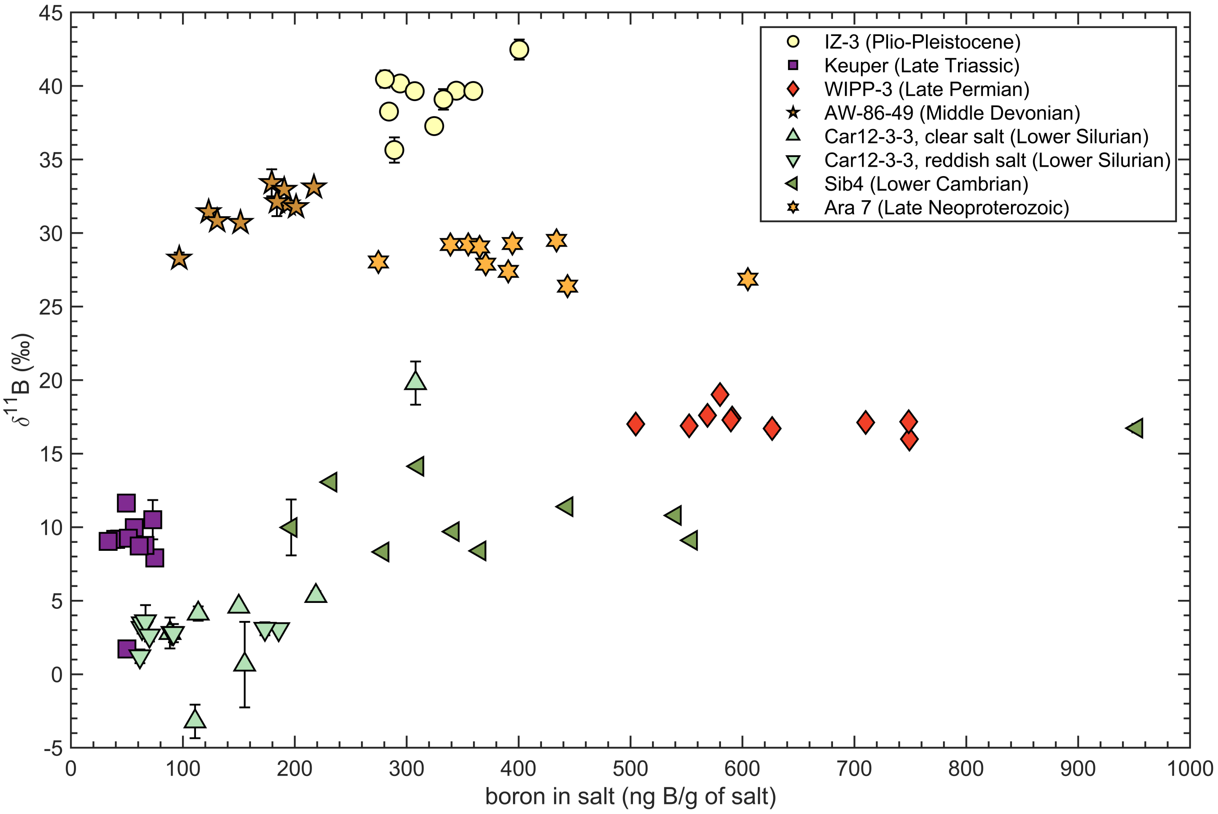

Figure 3.4 : *Boron isotopic composition as a function of B concentration for each halite aliquot.*

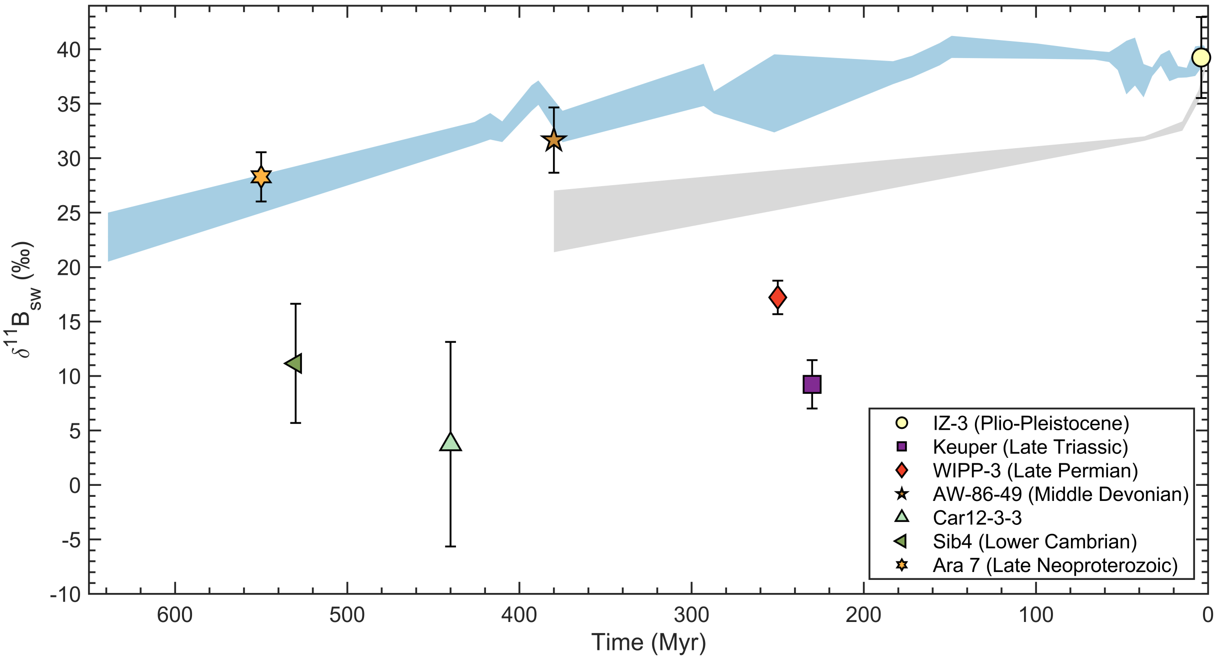

Figure 3.5 : *Average boron isotopic composition as a function of halite age. The gray area represents the halite $\delta^{11}B_{sw}$ values from Paris et al. (2010b) and the blue area the envelope of the $\delta^{11}B_{sw}$ estimated from carbonates in the literature (See Fig.3.8 and 3.9 for the references).*

^{87}Sr/^{86}Sr ratios for WIPP-3 (Late Permian), AW-86-49 (Middle Devonian) and Sib4 (Lower Cambrian) yielded 0.706895 ± 0.000004, 0.708014 ± 0.000019 and 0.708685 ± 0.000006, respectively, in agreement with the ^{87}Sr/^{86}Sr seawater records (Veizer *et al.* 1999, Fig.3.6) and the Prairie Devonian halite value reported by Paris *et al.* (2010b) (0.70787-0.70788). The IZ-3 (Plio-Pleistocene, 0.708277 ± 0.000008), Keuper (Late Triassic, 0.708515 ± 0.000008) and Car-12-3-3 (Lower Silurian, 0.709230 ± 0.0000016 and 0.709171 ± 0.000007) halites displayed ^{87}Sr/^{86}Sr outside the seawater trend (Fig.3.6).

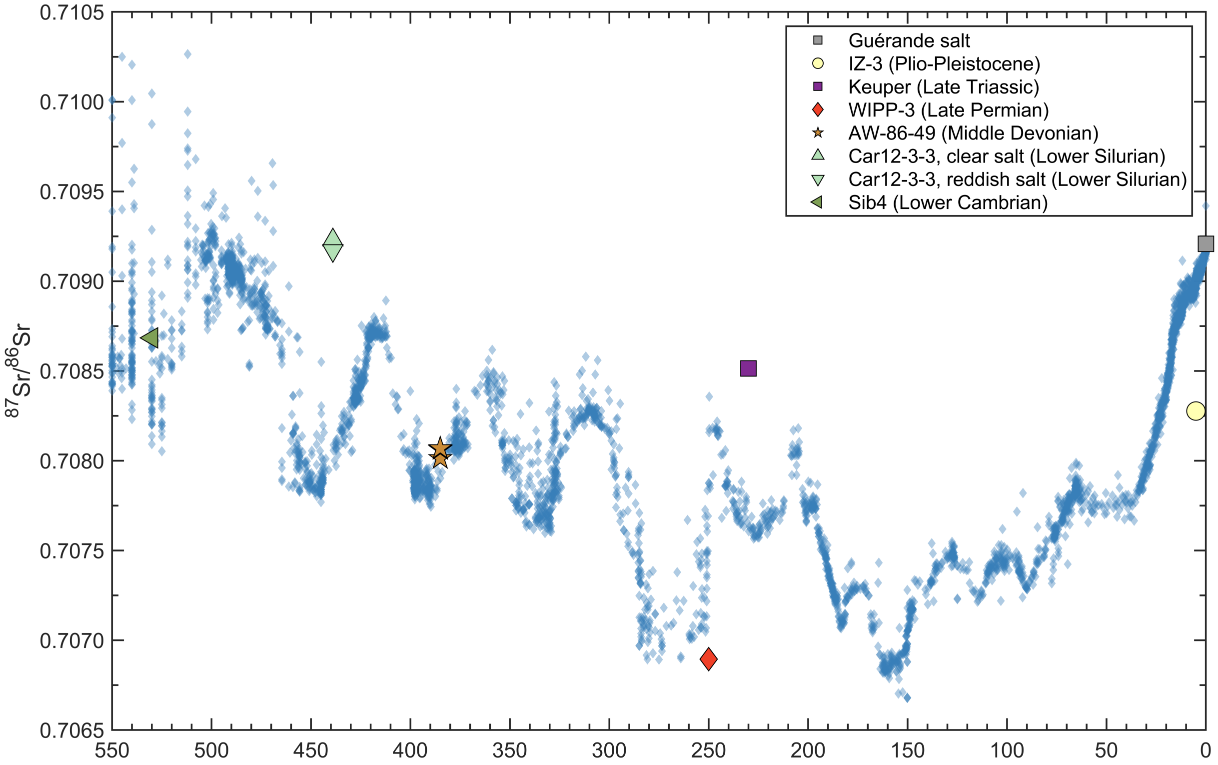

Figure 3.6 : *^{87}Sr/^{86}Sr measured in the halite samples, with the addition of the Guérande salt, in light of the seawater ^{87}Sr/^{86}Sr compilation from unaltered carbonates (Veizer et al., 1999; Prokoph et al., 2008; Halverson et al., 2007).*

The XRD diffractograms of the different samples exhibited a mineralogy composed mainly of halite, with traces of anhydrite (in Keuper, WIPP-3, Car-12-3-3 and Sib4), sylvite (in all except Car-12-3-3 and Sib4) and potassic halite with Na substituted by K (in all except Sib4). It was not possible to quantify the amounts of the minor minerals, but the halite mineral is clearly dominant. The reddish aspect of the second subset of the Silurian salt appeared to be due to the presence of iron and aluminium oxides, though this did not seem to alter the δ^{11}B values, similar between the two subsets.

3.3.b Modelled [B]$_{sw}$ and δ^{11}B$_{sw}$

The modelled [B]$_{sw}$ and δ^{11}B$_{sw}$ through the Phanerozoic interestingly highlight four major periods in their secular variations, regardless of the selected scenario (constant or varying riverine B input - runoff), although variations are much less pronounced at constant runoff and some small disparities between the two scenarios are observed, with timings slightly shifted. According to both story-lines, $[B]_{sw}$ oscillated between 3 or 3.4 and 4.8 or 5.4 ppm during the Phanerozoic, and $\delta^{11}B_{sw}$ between 38.2 or 37.5 and 42.9 or 43.9 ‰ (Fig.3.7), the larger variation range being always for the second scenario, with variable runoff.

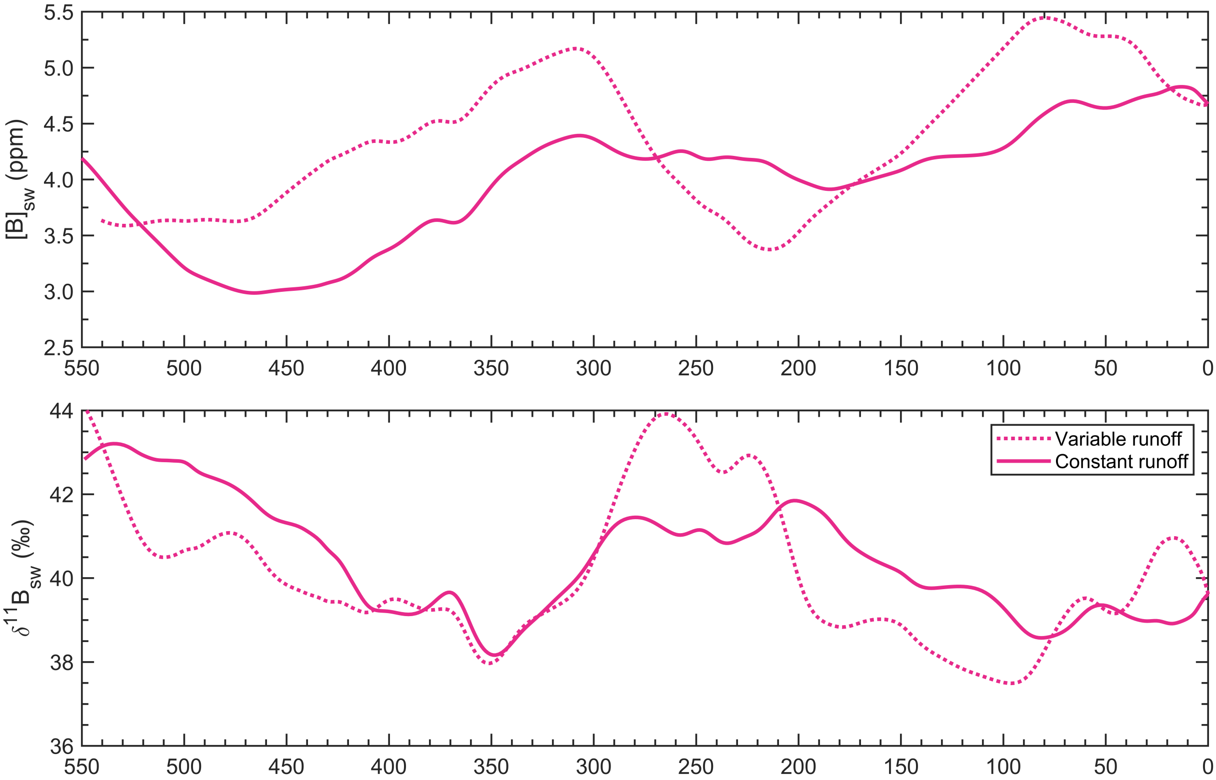

Figure 3.7 : *Modelled seawater boron concentration and isotopic composition across the Phanerozoic with the two scenarios of constant or variable riverine B flux.*

In more details, for this second scenario (variable runoff), the boron concentration increased from 3.6 ppm at 540 Myr to 5.2 ppm at 310 Myr, then decreased to 3.4 ppm at 220 Myr, rose again to 5.4 ppm at 80 Myr and finally reached the contemporary value (4.68 ppm). The boron isotopic ratio follows a similar pattern, starting at 43.8 ‰ 540 Myr ago, decreasing to 38.0 ‰ at 350 Myr, then rising to 43.9 ‰ at 260 Myr, decreasing again toward 37.5 ‰ at around 95 Myr and rising again to the modern $\delta^{11}B_{sw}$ value (39.61 ‰). The first scenario with constant riverine B input is slightly different and smoother. The seawater boron concentration began to decline from 4.1 to 3.0 ppm between 540 and 465 Myr with , increased thereafter towards 4.4 ppm at 310 Myr, is marginally lowered towards 3.9 ppm at 180 Myr and ultimately extended to the present $[B]_{sw}$. For $\delta^{11}B_{sw}$, the constant runoff scenario reconstructed a drop between 43 ‰ at 540 Myr and 38.2 ‰ at 350 Myr, like the second scenario, then an increase towards 41.8 ‰ at 200 Myr with in between a small reduction to 40.8 ‰ at 235 Myr. The $\delta^{11}B_{sw}$ declined again to reach 38.6 ‰ at 80 Myr and ultimately slowly went up to today's value. Focusing on the Cenozoic $\delta^{11}B_{sw}$, we can observe two smaller oscillations, the oldest one is almost identical between the two scenarios (39.3-39.5 ‰ at 60 Myr) but the second is in phase opposition with a maximum δ^{11}B$_{sw}$ of 40.9 ‰ at 18 Myr for the varying runoff model output, while almost no fluctuations are present for the constant runoff scenario (minimum value 38.9 ‰ at 18 Myr).

3.4 Discussion

3.4.a Halites as a direct archive of δ^{11}B$_{sw}$ secular variations?

Comparison of the halite derived δ^{11}B$_{sw}$ with literature values

The first study of δ^{11}B$_{sw}$ in halites by Paris *et al.* (2010b) was challenged due to the low δ^{11}B$_{sw}$ values they proposed for the Cenozoic, much lower than those estimated from foraminifera and models (Fig.3.8.b). Raitzsch & Hönisch (2013) pointed out that the Priabonian halite value for the Eocene/Oligocene transition (31.8 ± 0.2 ‰) coupled with their benthic foraminifera data gives an unrealistic deep-sea pH of $\sim$ 8.5, which would suggest an oversaturation with respect to calcite for the whole water column, in contradiction with the carbonate record from this time. For the same period, Hönisch *et al.* (2019) used the foraminifera data from Pearson *et al.* (2009) to also demonstrate the impossibility of the Paris *et al.* (2010b) Cenozoic δ^{11}B to reflect δ^{11}B$_{sw}$, as such δ^{11}B$_{sw}$ values lead to incoherent calculated pH and pCO$_2$. Can halites truly capture the δ^{11}B signature of the seawater from which they precipitated ?

First of all, the Plio-Pleistocene halite sample has a δ^{11}B value of 39.2 ± 3.7 ‰ 3-5 Myr ago, very close to the Plio-Pleistocene value 39.2 ‰ used by Martínez-Botí *et al.* (2015a) for pCO$_2$ reconstructions and in line with the values of Pearson & Palmer (2000); Raitzsch & Hönisch (2013) and the model of Lemarchand *et al.* (2002b) (Fig.3.8.a). Subsamples of this salt allowed ten independent analyses to constrain the salt δ^{11}B variability (2SD of almost 4 ‰), which largely encompasses possible B isotope fractionation during salt precipitation ($\leq$ 5 ‰, Liu *et al.* 2000). ^{87}Sr/^{86}Sr ratio is lower than the late Pliocene seawater value (Fig.3.6), likely due to brine-rock interactions with late Cretaceous carbonates in the evaporitic lagoon (Stein *et al.*, 2000). However, the sulphur and chlorine isotope ratio for this halite coming from the Sedom Formation is consistent with the late Cenozoic seawater values and definitely confirm, with the fluid inclusion data of Horita *et al.* (2002), that the original water was marine (Raab *et al.*, 2000; Stein *et al.*, 2000; Horita *et al.*, 2002; Eggenkamp *et al.*, 2019a). Paris *et al.* (2010b) proposed a value between 35.5 ± 0.3 and 36.1 ± 0.2 ‰ for Messinian salts 5.5 Myr ago (Fig.3.8). Although they strictly respected the mineralogical and stratigraphic criteria to select their primary halites, other processes may have affected the brine inclusions and led to low δ^{11}B.

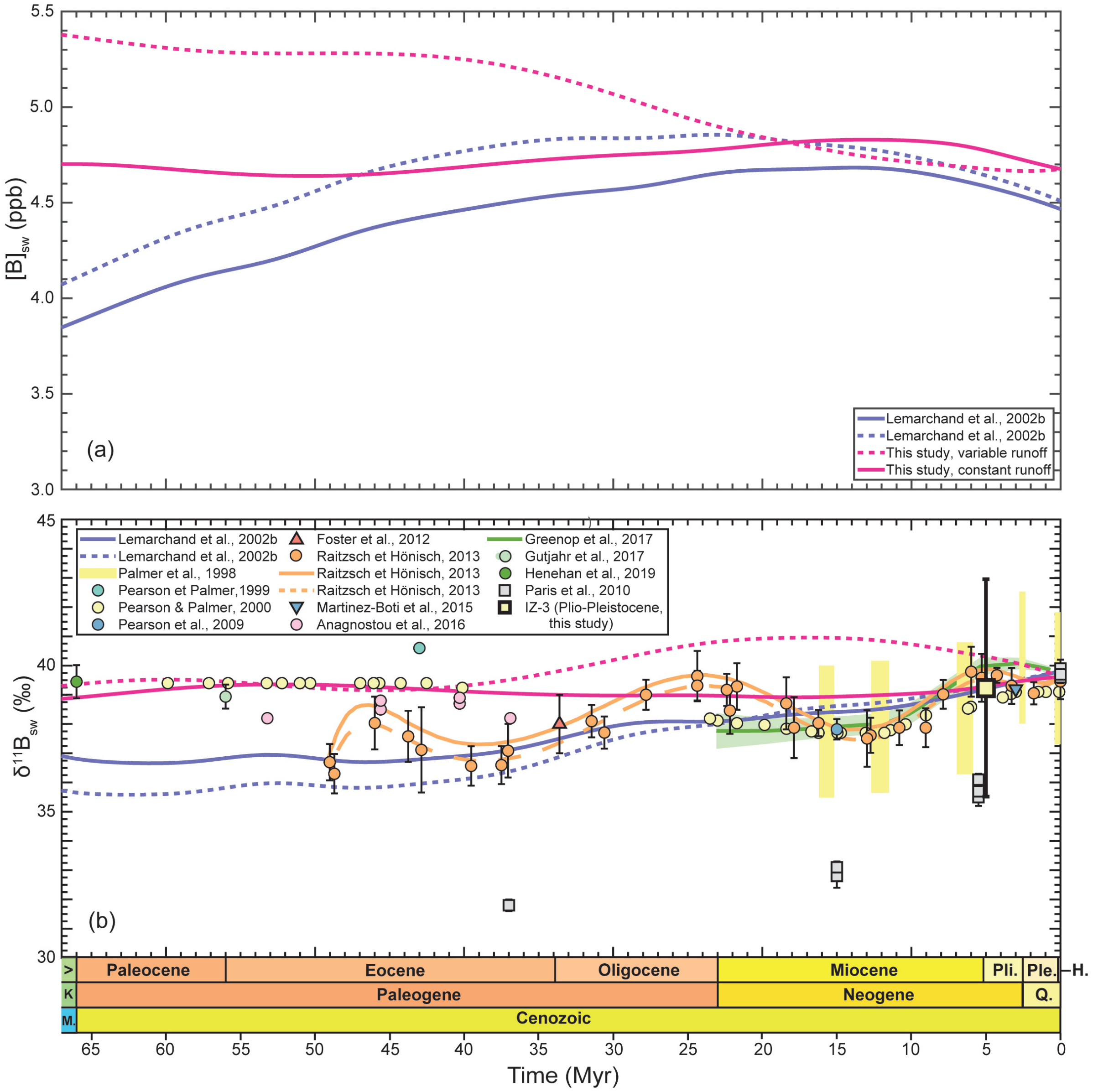

Figure 3.8 : *Data compilation of seawater boron concentrations (a) and isotopic compositions (b) across the Cenozoic. Lines are for models and calculations from foraminifera data (Lemarchand et al. 2002b; Raitzsch & Hönisch 2013; Greenop et al. 2017, this study); circles, triangles and yellow areas for determinations from foraminifera studies (Palmer et al., 1998; Pearson & Palmer, 1999, 2000; Pearson et al., 2009; Foster et al., 2012; Raitzsch & Hönisch, 2013; Martínez-Botí et al., 2015a; Anagnostou et al., 2016; Gutjahr et al., 2017; Henehan et al., 2019); ; squares for halite data (Paris et al. 2010b, this study). Blue dotted line: variable runoff (Lemarchand et al., 2002b), blue solid line: variable runoff (Lemarchand et al., 2002b), variable pH from foraminifera with fractionation factor=1.0272 (Raitzsch & Hönisch, 2013), orange solid line: variable pH from foraminifera with fractionation factor=1.020 (Raitzsch & Hönisch, 2013).*

This is also probably the case for the Devonian samples. The salts of Paris *et al.* (2010b) and this study come from the same Prairie evaporite deposit (Canada), but display a δ^{11}B difference of up to 7 ‰ between the two studies (Fig.3.9.b). However, our value (31.7 ± 3.0 ‰) is in agreement with the estimations of Joachimski *et al.* (2005) from brachiopod δ^{11}B. This strengthens the idea that AW-86-49 (Prairie) halite could trace the boron isotopic composition of the Devonian seawater (Fig.3.9b.), its marine signature being further consolidated with the ^{87}Sr/^{86}Sr ratio (Fig.3.6). The Neoproterozoic/Phanerozoic transition recorded a significant increase with time of the seawater boron isotopic composition (Joachimski *et al.*, 2005; Kasemann *et al.*, 2010; Ohnemueller *et al.*, 2014). Despite a lack of data between the model of Joachimski *et al.* (2005) and the δ^{11}B deduced from cap carbonates (Kasemann *et al.*, 2010; Ohnemueller *et al.*, 2014), the δ^{11}B of the halite sample for Neoproterozoic (Ara formation) fits in this rise and could also faithfully reflect the δ^{11}B signature of seawater during this transition. The ^{87}Sr/^{86}Sr of this sample could not be measured but the marine origin was indeed previously established by the δ^{37}Cl signature (Eggenkamp *et al.*, 2019a).

Processes that can influence the δ^{11}B of halites

Originally, δ^{11}B measurements in evaporites have been used to determine the marine or the non-marine origin of the salt deposits (Swihart *et al.*, 1986; Oi *et al.*, 1989; Vengosh *et al.*, 1991a, 1995; Wei *et al.*, 2014; Zhao *et al.*, 2020). A marine salt δ^{11}B is assumed to be between 10 and 40 ‰, while δ^{11}B is rather between -30 and 5 ‰ for a non-marine evaporite (Mao *et al.*, 2019; Zhao *et al.*, 2020). Except for the Silurian salt (Car12-3-3), all other δ^{11}B values fall within this marine origin criteria. However, the strong disparity between δ^{11}B for some of these halites and the $\delta^{11}B_{sw}$ proposed in literature, despite the rigorous mineralogical selection, highlights that other processes may occur during or after their formations, as supported by the strontium isotope ratios and the XRD data. However, the δ^{11}B signature of the Triassic (Keuper), Permian (WIPP-3), Silurian (Car12-3-3) and Cambrian (Sib4) samples still have to be clarified.

Only few studies have addressed boron isotopic fractionation between brine and evaporite minerals: δ^{11}B data in halites are limited, whereas none exists for epsomite ($MgSO_4.7H_2O$), kainite ($4KCl.MgSO_4.11H_2O$) or carnallite ($MgKCl_3.6H_2O$), minerals precipitating jointly with halite at higher degree of evaporation of the marine brines. Furthermore, the few existing studies do not agree: Vengosh *et al.* (1992) proposed a δ^{11}B difference of -30 ‰ between brine and halite, based on seawater evaporation experiments, while Liu *et al.* (2000) measured an offset of only $\leq$ -5 ‰, also from evaporation experiments but with artificial seawater solutions and salt lake brines; and finally studies of salt lake brines and associated halite or modern marine halite analyses concluded to no δ^{11}B fractionation during salt formation (Liu *et al.*, 2000; Paris *et al.*, 2010b; Fan *et al.*, 2015). In order to explained δ^{11}B fractionation they observe, Vengosh *et al.* (1992) proposed that borate (enriched in ^{10}B) was dominantly incorporated in the salts, while Liu *et al.* (2000) suggested that boron was almost exclusively present in fluid inclusions, and not in the salt matrix.

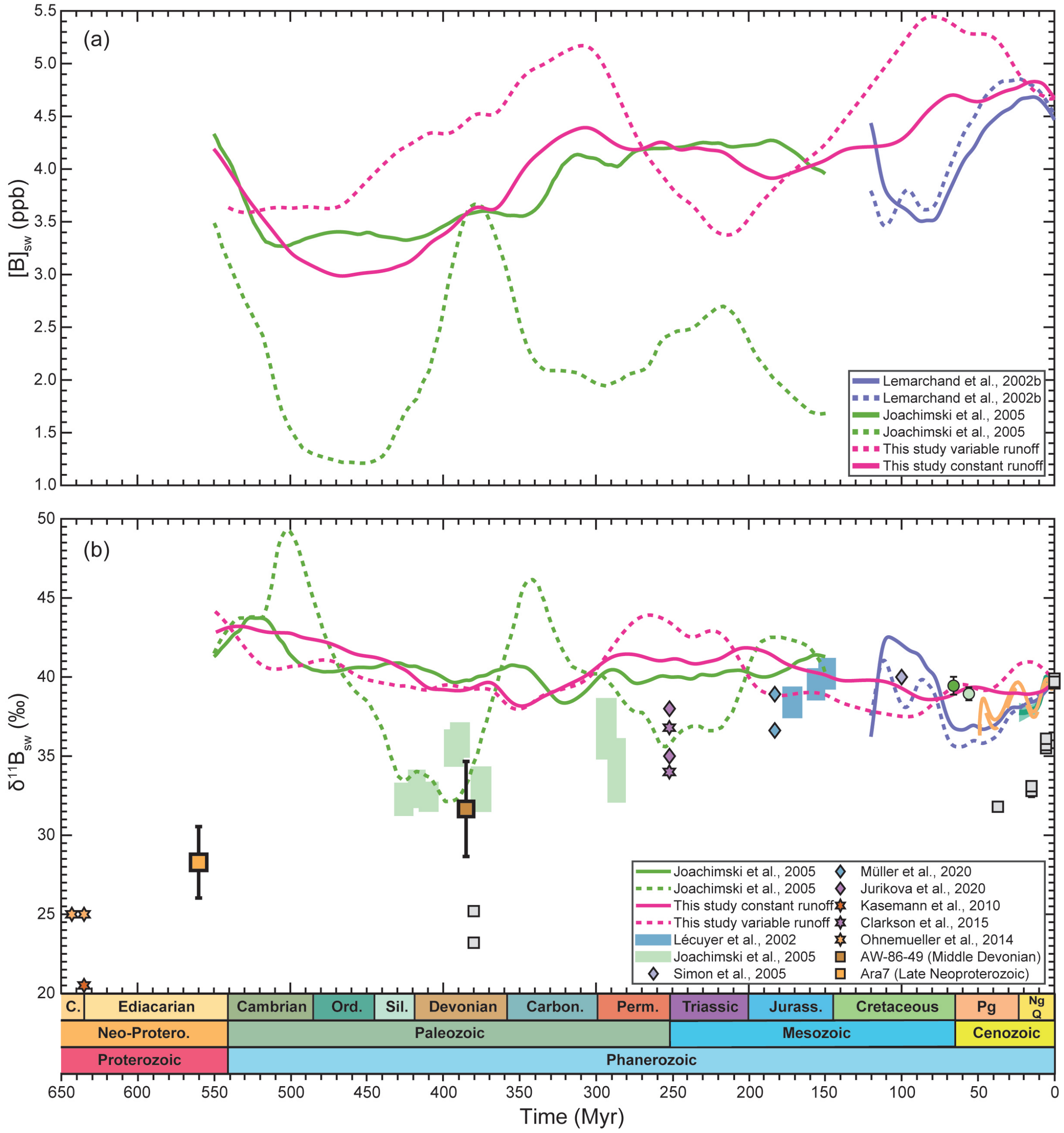

Figure 3.9 : *Data compilation of seawater boron concentrations (a) and isotopic compositions (b) across the Phanerozoic. Lines are for models and calculations from foraminifera data (Lemarchand et al. 2002b; Joachimski et al. 2005; Raitzsch & Hönisch 2013; Greenop et al. 2017), this study); diamonds and rectangles from brachiopod data (Lécuyer et al., 2002; Joachimski et al., 2005; Simon et al., 2006; Müller et al., 2020); stars from inorganic carbonate data (Kasemann et al., 2010; Ohnemueller et al., 2014; Clarkson et al., 2015); and squares for halite data (Paris et al., 2010b) in grey, and this study: AW-86-49 and Ara7. Blue dotted line: variable runoff (Lemarchand et al., 2002b), blue solid line: constant runoff (Lemarchand et al., 2002b), green dotted line: variable continental input (Joachimski et al., 2005), green solid line: constant continental input (Joachimski et al., 2005) variable pH from foraminifera with fractionation factor=1.0272 (Raitzsch & Hönisch, 2013), orange solid line: variable pH from foraminifera with fractionation factor= 1.020 (Raitzsch & Hönisch, 2013).*

The slight fractionation between brine and halite may then be related to coprecipitation of boron with $CaSO_4$ salts at an early evaporation stage; the amplitude of the δ^{11}B fractionation being therefore dependent upon the brine chemistry (Liu *et al.*, 2000): small fractionation ($\sim$ 0-1 ‰) for pH > 7.5 and [Ca^{2+}] < 1 g.L^{-1}, and larger fractionation (-5 ‰) for pH < 7.5 and [Ca^{2+}] > 1 g.L^{-1}. Nevertheless, due to the low partition coefficient between the brine and the halite, the δ^{11}B of the brine along the evaporation path changes only very slightly (Vengosh *et al.*, 1992; Liu *et al.*, 2000; Zhao *et al.*, 2020). The large 2SD errors we determined from the 10 aliquots of each salt sample might nonetheless echoes these slight δ^{11}B fractionation during brine evaporation up to halite formation.

The -5 ‰ fractionation between brine and halite may reconcile the halite δ^{11}B data of Paris *et al.* (2010b) with literature $\delta^{11}B_{sw}$ (Fig.3.8.b), especially since they showed a very good relationship between the δ^{11}B of their halites and the Mg/Ca data of fluid inclusions, where high halite δ^{11}B are associated with high Mg/Ca. Hönisch *et al.* (2019) proposed then that the halites were more enriched in ^{10}B when the seawater Ca concentration was higher, which was the case at the beginning of the Cenozoic, with a lower [Mg^{2+}] and higher [Ca^{2+}] than today (Horita *et al.*, 2002; Brennan *et al.*, 2013). While ocean pH during the Phanerozoic probably did not decrease below the pH threshold value of 7.5 (Hönisch *et al.*, 2012; Halevy & Bachan, 2017) fixed by Liu *et al.* (2000), the concentration of calcium has never increased beyond the cut-off of 1 g.L^{-1} mentioned by Liu *et al.* (2000), but was however very close during the Paleogene, the beginning of the Mesozoic and the end of the Paleozoic (Horita *et al.*, 2002; Lowenstein *et al.*, 2014). As a result, the -5 ‰ observed for Devonian halite of Paris *et al.* (2010b) compared to the $\delta^{11}B_{sw}$ determined from brachiopods (Joachimski *et al.*, 2005) and the agreement of our Devonian salt (AW-86-49) value with that from brachiopods Fig.3.9.b) could be explained by salt precipitation at different evaporation degrees. The fluid inclusion chemistry of sample AW-86-49 showed that this salt had precipitated in the early to middle stages of the seawater evaporation sequence (Horita *et al.*, 1996). If on the other hand the halite sample of Paris *et al.* (2010b) comes from a salt precipitated at an earlier stage, it could entrapped anhydrite or gypsum and therefore exhibit a lower δ^{11}B signature, consistently with the study of Liu *et al.* (2000). The Devonian salt of the present study could have been formed at a middle evaporation stage, assumption supported by the lack of $CaSO_4$ detection in the XRD analysis, and consequently record more faithfully the boron isotopic composition of seawater with the absence of this $CaSO_4$ disruption. An other way to explain the difference of the Devonian δ^{11}B between this study and Paris *et al.* (2010b) could be linked to the rate of salt precipitation, higher rate enabling more trapping of fluid inclusions. At lower temperature, the rate of halite formation is slow, causing low density of fluid inclusions and conversely more removal of boron through co-precipitation of early mineral phases in halite. Accordingly, the δ^{11}B of halite would be a result of a binary mixing between pure halite, where boron is only in fluid inclusions, and halite with few fluid inclusions and more co-precipitated phases (Liu *et al.*, 2000). Depending on the dynamic of the basin during its closure, the Devonian halite of Paris *et al.* (2010b) could be closer of the pole with a low fluid inclusions density and co-precipitated phase.

In general terms, our samples tend to argue against a -30 ‰ δ^{11}B fractionation during halite precipitation (Vengosh *et al.*, 1992). Indeed, the Plio-Pleistocene, the Devonian and the Neo-Proterozoic NaCl salts are close to an agreement with $\delta^{11}B_{sw}$ from previous studies (Pearson & Palmer, 2000; Lemarchand *et al.*, 2002b; Joachimski *et al.*, 2005; Kasemann *et al.*, 2010; Raitzsch & Hönisch, 2013; Ohnemueller *et al.*, 2014; Martínez-Botí *et al.*, 2015a) whereas the gradual increase of the $\delta^{11}B_{sw}$ since 540 Myr evidenced in the literature would result in halites with a δ^{11}B signature of -10 to 5 ‰ between the Neo-Proterozoic and the end of the Paleozoic, if the -30 ‰ fractionation factor was applied, which is inconsistent with all marine halites that have been measured to date. Additionally, with the exception of the Silurian samples, the relative homogeneity of the δ^{11}B salts (Fig.3.4) combined to the mineralogy observations seem to support the hypothesis of Liu *et al.* (2000) that boron is almost exclusively located in the halite fluid inclusions and that B can coprecipitate in the minor solid phases as a trace element, but not as borate salts as suggested by Vengosh *et al.* (1992). Moreover, borate salts were not detected in our XRD analysis and those of Fan *et al.* (2015). However, δ^{11}B data from marine gypsum or anhydrite salts are lacking to corroborate this assumption of coprecipitated phases.

In a similar study attempting to reconstruct the magnesium isotopic composition of seawater from the same pool of primary halites with the same assumption that Mg is only concentrated in fluid inclusions, Xia *et al.* (2020) showed that the precipitation of epsomite, kainite and carnallite obviously affects the δ^{26}Mg of the evolving brine, as Mg is their major constituent. The mechanisms impacting the halite δ^{11}B during precipitation of late stage evaporites from an evolved brine are currently unknown. Vengosh *et al.* (1992) proposed a -20 ‰ δ^{11}B fractionation between brines and K-$MgSO_4$ salts but without mineral distinction. The presence of these entrapped minerals could decrease the δ^{11}B of halites if we consider this δ^{11}B fractionation: the precipitation of halites from a brine more depleted in ^{10}B than during the $CaSO_4$ and (early) halite evaporation stages, due to a massive incorporation of boron in these late stage minerals and/or their entrapment in the halite crystal, the tetrahedral coordination of the borate anion being favoured during the crystallisation of these sulphate minerals (Liu *et al.*, 2000; Xia *et al.*, 2020). The first assumption can be rule out as δ^{11}B values are systematically lower (not higher) than previous estimations.

Except for the Permian salt (WIPP-3) and to a lesser extent the Devonian salt (AW-86-49), the fluid inclusion chemistry of the samples revealed that they all have been formed in a highly evolved brine, in which K-Mg sulphates could also have precipitated alongside (Horita *et al.*, 1991, 1996, 2002). The high evaporation degree of the brine for these samples is supported by Br/Cl and δ^{37}Cl data, which translate the salt evolution during crystallisation (Eggenkamp *et al.*, 2019a). The presence of solid inclusions of K-$MgSO_4$ salts, detected by XRD analyses for the whole pool of samples in this study, could have decreased the bulk halite δ^{11}B, if the brine to K-MgSO$_4$ salt δ^{11}B fractionation of –20 ‰ is valid (Vengosh *et al.*, 1992); however it is apparently not valid for brine to halite. The K-MgSO$_4$ salts may originate from co-precipitation during the evaporation sequence (Eggenkamp *et al.*, 2019b) or from diapiric entrapments during post-depositional deformations, in relation with the weak mechanical resistance of salts (Hudec & Jackson, 2007; Xia *et al.*, 2020). As all the halites studied here exhibit these solid inclusions but not all have δ^{11}B values lower than the supposed $\delta^{11}B_{sw}$ signatures, K-MgSO$_4$ salt traces can not be the only reason for low δ^{11}B values recorded in some halites. For example the Plio-Pleistocene sample appears to have recorded the $\delta^{11}B_{sw}$ whereas the Permian sample, with a validated marine origin, did not.

Alternatively, the salt deposits could also have been altered by non-marine inputs to the closed sea basin, some constituents being more affected than others, depending on their concentrations and isotopic signatures in these non-marine inputs. This could have been the case for the Triassic (Keuper) and Silurian (Car12-3-3) salts, that display non-marine (too high) ^{87}Sr/^{86}Sr ratios (Fig.3.6). The δ^{11}B of these samples may reflect a mixing between seawater and freshwater in the evaporitic basin, at any period of its formation, through dissolution – reprecipitation sequences in the closed basin. If we assume an average δ^{11}B at 10 ‰ for the modern boron continental flux (Lemarchand *et al.*, 2002b), which could however have been lower in the past in light of the boron continental reservoirs (Fig.3.2) or be much higher or much lower depending on the local geologic and weathering contexts (variability -6 to 45 ‰ for modern rivers, Gaillardet & Lemarchand 2018), this mixed brine could have a δ^{11}B much lower than seawater. Also groundwaters (e.g. δ^{11}B: -15.9 to 2.2 ‰ Vengosh *et al.* 1991a) and continental hydrothermal springs (e.g. δ^{11}B: -4 to 10 ‰ Louvat *et al.* 2011b, 2014a) inputs could decrease evaporite δ^{11}B (Zhao *et al.*, 2020). Because continental waters have B concentrations 100 to 1000 times lower than seawater, the freshwater influx must have been huge (or long) in order to lower the δ^{11}B of the brine by a few ‰. Such a scenario of sequential dissolution-precipitation would probably have lowered the B content of the halite (purification of the salts, less trace elements being incorporated), which is consistent for the Keuper and CAR12-3-3 samples (Fig.3.4). Moreover, CAR12-3-3 sample turned out to be of clayey aspect and XRD showed traces of iron and aluminium oxides probably of detrital origin, which can contain ^{10}B enriched borate anions (Lemarchand *et al.*, 2007). Consequently, for these samples, the low δ^{11}B cannot be interpreted as a marine signature.

The Permian (WIPP-3) and Cambrian (Sib4) salt δ^{11}B are higher than those for the Triassic and Silurian samples, but still seem unrealistic seawater values (Fig.3.5), despite their marine Sr signature (Fig.3.6). Regarding boron isotopes, other processes (especially during salt preservation) could alter the chemistry of the fluid inclusions. Particularly the Sib4 salt comes from the Siberian Platform Basin, seat of flood basalt magmatism responsible for the Permo-Trias mass-extinction and that affected most of the underlying evaporite deposits (Grishina *et al.*, 1992), as halite is a good heat conductor (Hudec & Jackson, 2007). Otherwise, it is difficult to assess how diagenesis influences the boron chemistry of evaporites deposits, boron fractionation mechanisms during water/rock interactions in the Critical Zone being yet not totally understood (e.g., Gaillardet & Lemarchand, 2018). Dissolution-reprecipitation from groundwaters in the sedimentary layers could also decrease the δ^{11}B signature halite (Vengosh *et al.*, 1991a).

Many research projects nowadays aim at understanding how the gigantic evaporite basins could have been deposited and some of them question evaporation as the only process. Another hypothesis involving hydration of the oceanic crust during serpentinization has been proposed (Scribano *et al.*, 2017; Hovland *et al.*, 2018; Manuella *et al.*, 2018). In such a case, oceanic crust fluids could exchange with local brines and might imprint a different chemical and isotopic signature to the salts, in particular for trace elements (Pinto *et al.*, 2017). Why not for boron?

3.4.b δ^{11}B$_{sw}$ secular variations across the Phanerozoic

Comparison of the modelled [B]$_{sw}$ and δ^{11}B$_{sw}$ with the literature data

The boron concentrations of seawater modelled in Lemarchand *et al.* (2002b) and this study do not show the same trends for the Cenozoic. Our scenario with a constant runoff points out almost no variation, while with a variable runoff [B]$_{sw}$ steadily decreases during this period. These two scenarios for Lemarchand *et al.* (2002b) follow the same trend, with a constant rise up to the Miocene and then a decrease towards today. The four curves (two scenarios in Lemarchand *et al.* (2002b) and two for this study) are quite close for the last 20 Myr b.p. but after they drift apart (Fig.3.8.a). The scenario with a constant runoff remains also similar to the [B]$_{sw}$ modelled with changes in runoff by Lemarchand *et al.* (2002b) for the last 50 Myr. The differences between the two models are related to the choice of the geodynamic forcings. Our modelled [B]$_{sw}$ with a constant runoff is consistent with the general rise observed from foraminifera data and also with the Plio-Pleistocene halite data for the last 30 Myr, but fails to catch, like Lemarchand *et al.* (2002b), the δ^{11}B$_{sw}$ oscillations at higher frequencies (Fig.3.8.b) underscored by Raitzsch & Hönisch (2013) and to a lesser extent Pearson & Palmer (2000). This scenario diverges from the prediction of Lemarchand *et al.* (2002b) and Raitzsch & Hönisch (2013) for the beginning of the Cenozoic but reproduces precisely the published high δ^{11}B$_{sw}$ values for the Eocene and the Paleocene (Pearson & Palmer, 2000; Anagnostou *et al.*, 2016; Gutjahr *et al.*, 2017; Henehan *et al.*, 2019). Our second scenario, with variable runoff, also agrees with the values proposed for these periods. However, for the last 30 Myr b.p., it points out an increase above 40 ‰ in the early Miocene and then a decrease towards the modern value (Fig.3.8.b), a pattern opposed to that shown by Raitzsch & Hönisch (2013). Additionally, our two scenarios match with δ^{11}B$_{sw}$ estimations from brachiopods data (Lécuyer *et al.*, 2002) in the Jurassic, while the variable runoff scenario duplicates the higher threshold for the OAE event fixed by Müller *et al.* (2020) (Fig.3.9.b).

The first observation that jumps out for the Phanerozoic is that the δ^{11}B$_{sw}$ and the [B]$_{sw}$

modelled trends of our variable runoff scenario are systematically almost in antiphase with the model by Joachimski *et al.* (2005), with also a low seawater boron concentration for the latter (Fig.3.9.a, green dotted line). The discrepancy between the two models relies again on the choice of the forcings that cause the fluctuations of the boron continental discharge. Joachimski *et al.* (2005) associated these changes to the continental erosion rate (Fig.3.3) supposing a correlation between mechanical and chemical erosions. This assumption is however too simple, for example a decline of the weathering intensity is not necessarily joined with a diminution of the silicate erosion fluxes (Caves Rugenstein *et al.*, 2019). Although there are not direct records but only modelling, runoff remains the best forcing to express the oscillations of the dissolved boron continental discharge in the Phanerozoic (Lemarchand *et al.*, 2002b). The reconstruction of Joachimski *et al.* (2005) succeeds however to explain the δ^{11}B$_{sw}$ values they reconstructed from brachiopods data, as well as that of Jurikova *et al.* (2020) and from inorganic carbonates (Clarkson *et al.*, 2015) in the Triassic, when our simulations do not. But these δ^{11}B$_{sw}$ reconstructions, as those from Neoproterozoic cap-carbonates (Kasemann *et al.*, 2010; Ohnemueller *et al.*, 2014), must be moderated: 1) a modern δ^{11}B-pH calibration (Lécuyer *et al.*, 2002) was used to correct potential vital effects for the brachiopod extinct species; 2) the use of shallow water carbonates as a pH proxy is challenged due to evidences of microbially-mediated carbonate precipitation (Zhang *et al.*, 2017) and 3) the hypothesis of the incorporation of borate only into inorganic carbonates is questionned (Mavromatis *et al.*, 2015; Noireaux *et al.*, 2015; Saldi *et al.*, 2018). Finally, even with updated forcings, our δ^{11}B$_{sw}$ built on a constant continental input across the Phanerozoic is almost comparable to the model of Joachimski *et al.* (2005). As mentioned, the δ^{11}B$_{sw}$ we modelled across the Phanerozoic with a constant and a variable runoff are in agreement with some of the previously proposed δ^{11}B$_{sw}$ variations, but are sometimes unsuccessful to reproduce δ^{11}B$_{sw}$ data reconstructed by other studies. We therefore investigate hereafter how each of the forcing parameters affects the construction of our models.

Model sensitivities

- **Sensitivity of the boron fluxes**

To evaluate the sensitivity of the modelled δ^{11}B$_{sw}$ against changes in the B input and output fluxes, we integrated sinusoidal perturbations for each of the forcings. We set a perturbation amplitude at 20 % of the associated flux and a fluctuation period of 20 Myr, corresponding roughly to the boron residence time in the oceans (Fig.3.10). It appears that the oceanic boron geochemical cycle across the Phanerozoic is mostly controlled by the oceanic crust alteration as the major sink and by the continental weathering as the major source, as the resulting modelled δ^{11}B$_{sw}$ directly imprints the imposed sinusoidal perturbations for these two fluxes (Fig.3.10.a and d). Hydrothermalism and the adsorption on clastic sediments seem also to impact the $\delta^{11}B_{sw}$ (Fig.3.10.b and e) but with a much less intense amplitude. On the other hand, the B flux fluctuations for fluids expelled from accretionary prisms and coprecipitation in carbonates have only marginal effects on the $\delta^{11}B_{sw}$ modelled curve (Fig.3.10.c and f). These results were expected, as oceanic alteration and continental weathering are respectively the major sink and source of the boron cycle (Fig.3.2).

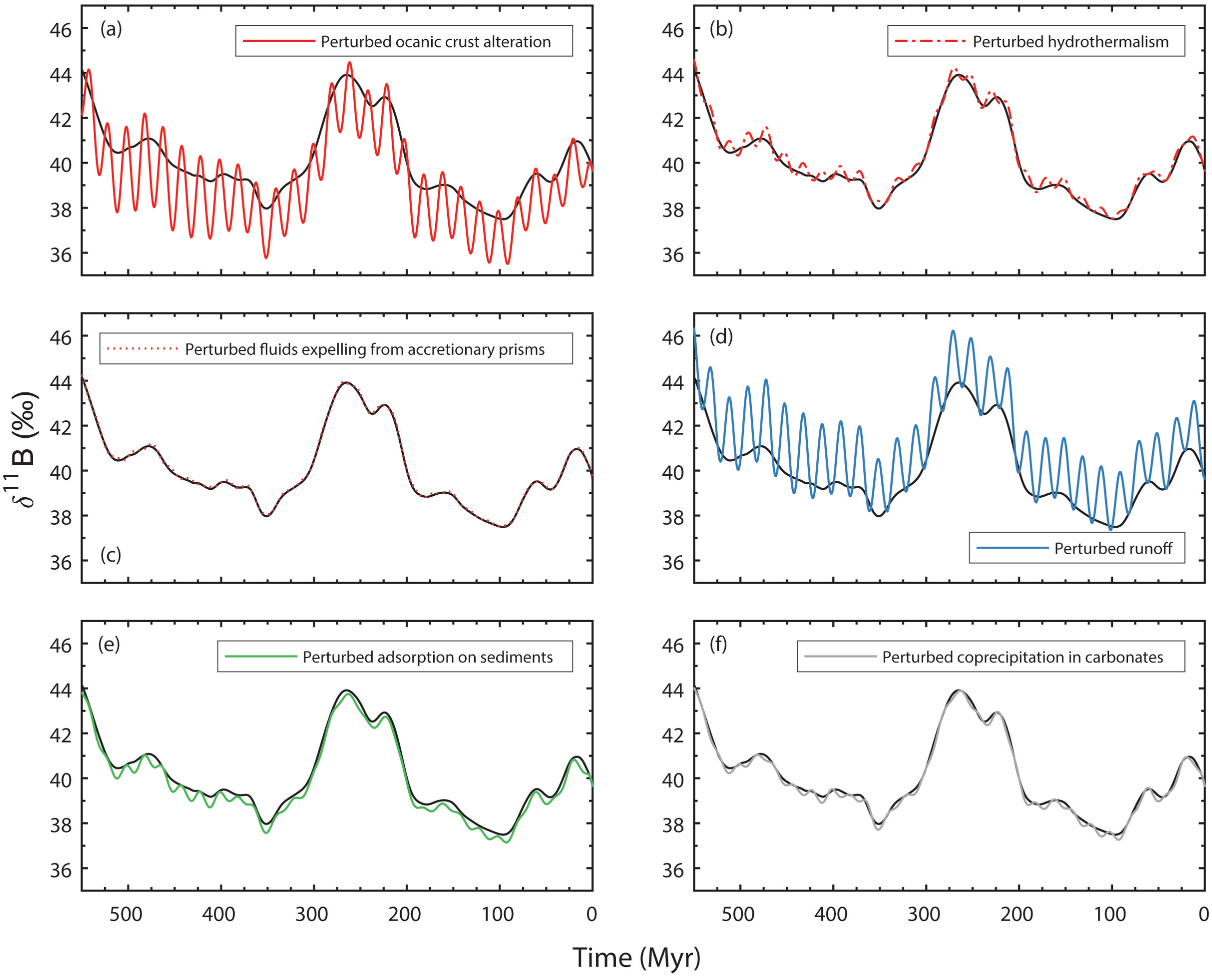

Figure 3.10 : *Sensitivity tests on the $\delta^{11}B_{sw}$ with an imposed sinusoidal oscillation for each forcing playing a role in the oceanic boron fluxes. The black line is the boron isotopic composition of seawater reconstructed with a variable runoff. The colour code of the selected forcing chosen to fluctuate are the same as in Fig.3.3. (a) Perturbed oceanic crust alteration. (b) Perturbed hydrothermalism. (c) Perturbed fluids expelling from accretionary prisms. (d) Perturbed continental boron discharge. (e) Perturbed adsorption on the clastic sediments. (f) Perturbed boron coprecipitation.*

The relative importance of the different fluxes can also be demonstrated by "simplifying" the boron isotopic budget, taking into account only the major sink, the alteration of the oceanic crust, and major source, the continental weathering. The resulting simplified $\delta^{11}B_{sw}$ curves are very similar to the "complete" $\delta^{11}B_{sw}$ curves (Fig.3.11). However, differences of 0 to 2 ‰ between the complete and the simplified $\delta^{11}B_{sw}$ sets of curves can be explained by the secondary boron fluxes, adsorption on the clastic sediments and hydrothermal vents, across geological times. We observed that for the scenario with a variable run-off, the higher divergences are correlated to higher continental erosion rates at the beginning of the Paleozoic and during the last 65 Myr (Fig.3.3.c), whereas the differences for the scenario with a constant runoff seem guided by the intensity of the crust production (Fig.3.3.a), i.e. a more active MORB alteration during the Cambrian, the Ordovician and the Permo-Trias transition, which overtake the continental input. However, crust production rate also impacts B input flux by hydrothermalism. As this flux has a low δ^{11}B signature, a more intense oceanic crust production would significantly decrease the seawater δ^{11}B. However, during these periods, we observe an increase, i.e. a strengthening of the ^{10}B uptake through alteration of the oceanic crust. Altogether, the δ^{11}B$_{sw}$ fluctuations during the Phanerozoic reflect the balance between boron uptake governed by newly formed oceanic crust, which preferentially removes ^{10}B and increases consequently the δ^{11}B$_{sw}$, and continental weathering bringing light boron to the ocean, which decreases the δ^{11}B$_{sw}$. Boron adsorption on clastic sediments exerts however a more localized control when continental erosion rates are higher.

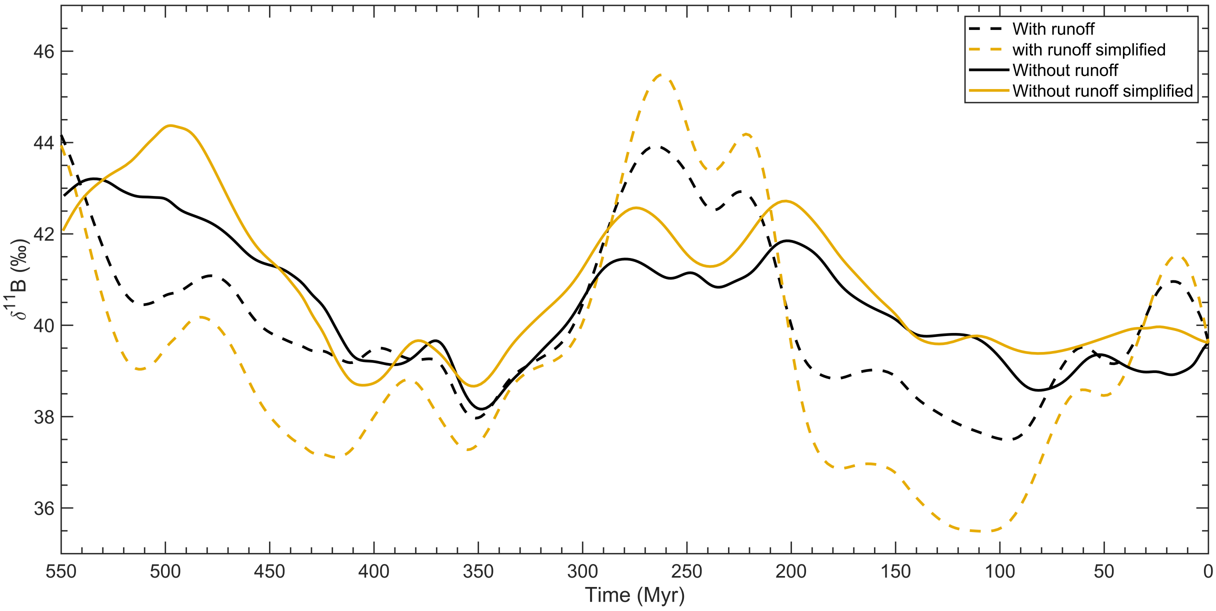

Figure 3.11 : *Comparison between modelled $\delta^{11}B_{sw}$ for the "complete" box model (black lines) and "simplified" model (yellow lines) where only the main output, alteration of the oceanic crust, and main input, boron continental discharge, are considered. Both scenarios of constant (solid lines) and variable (dotted lines) runoff are represented.*

- **Choice of the forcing parameters**

To construct the δ^{11}B$_{sw}$ for the last 550 Myr, one question emerged: which forcing parameters to choose? By selecting the most up-to date forcings proposed in other continent-ocean-atmosphere and climate models (total subduction length, runoff and carbonate burial rate, Berner & Mackenzie 2011; Goddéris *et al.* 2014; Mills *et al.* 2017, 2019), we managed to replicate most of the previously measured and modelled $\delta^{11}B_{sw}$ data from different studies, but without being able to explain all of them (Part. 3.4.b). We therefore performed a succession of $\delta^{11}B_{sw}$ modelling with the different forcings available in the literature. Discussing the accuracy and the confidence in the different forcing reconstructions that wre proposed by these previous studies is beyond the scope of this study. As aforementioned, we focused only on crust production rate and runoff, which are the main drivers of $\delta^{11}B_{sw}$. Those different forcings were integrated in our model while keeping: 1) the same carbonate burial rate as in our initial model (Fig.3.3.d), although other suggestions exist (Opdyke & Wilkinson 1988; Mackenzie & Morse 1992; François & Goddéris 1998; Berner 2004; Li & Elderfield 2013), but we showed that this flux has in any case negligeable impact on $\delta^{11}B_{sw}$ fluctuations (Fig.3.10.f); and 2) the same continental erosion rate, i.e. runoff (Fig.3.3.b) as previously, because, to our knowledge, only one study addressed this parameter (Hay *et al.*, 2002, 2006).

□ Oceanic crust production rate

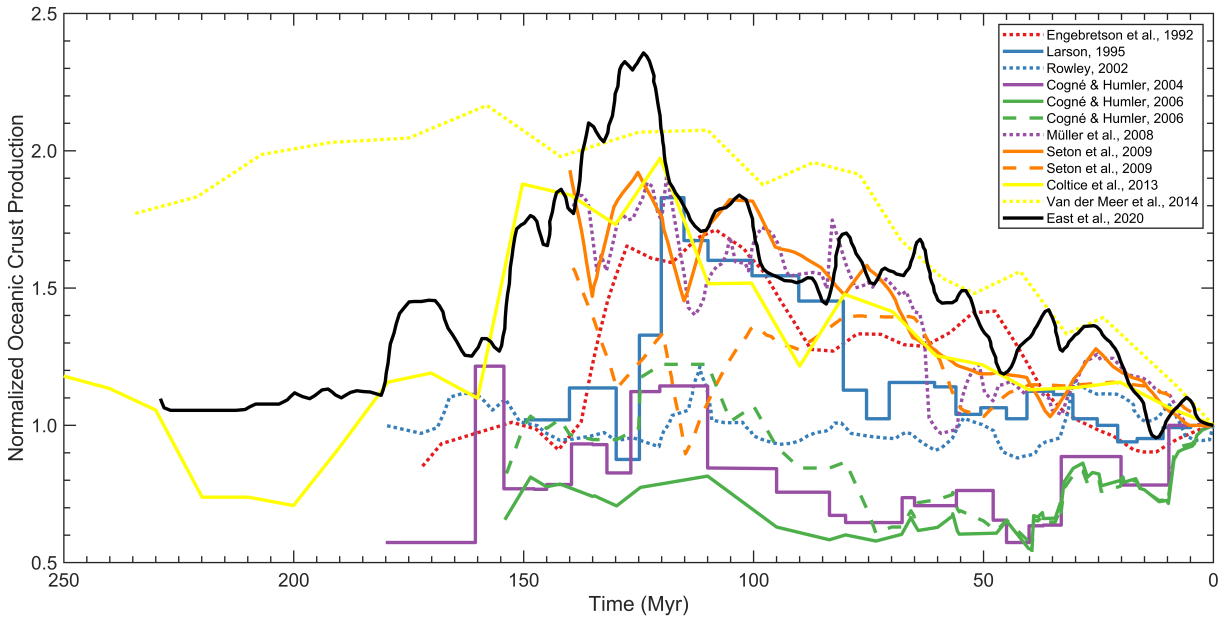

Figure 3.12 : *Normalized oceanic crust production for the Mesozoic and the Cenozoic reconstructed from magnetic anomalies with plate rotations models (Larson, 1991; Rowley, 2002; Cogné & Humler, 2004, 2006; Muller et al., 2008; Seton et al., 2009; Coltice et al., 2013) and normalized subduction rates from full-plate motion model (Engebretson et al., 1992; Van Der Meer et al., 2014; East et al., 2020). The distinction between the two estimations by Cogné & Humler (2006) are for an oceanic crust production (km^2.an^{-1}, solid green line) and an oceanic crust flux (km^3.an^{-1}, dashed green line). For Seton et al. (2009), the two orange lines are from two different crust model ages.*

The oceanic crust production rate is reconstructed from marine magnetic anomalies with plate rotation models (Fig.3.12, Larson 1991; Cogné & Humler 2004, 2006; Muller *et al.* 2008; Seton *et al.* 2009; Coltice *et al.* 2013; Müller *et al.* 2016). However, this method is confined to the first 140 Myr as pre-Cretaceous oceanic crust has been recycled through the subduction (Seton *et al.*, 2012; Müller *et al.*, 2016). Beyond 140 Myr, it has been proposed to calculate the oceanic crust production rates from the paleo sea-level changes (Gaffin, 1987; Mills *et al.*, 2017) or to use the mantellic strontium component flux curve, which is deconvoluted from the seawater ^{87}Sr/^{86}Sr records through the Phanerozoic, with respect to its weathering part (van der Meer *et al.*, 2017). Recently, subduction fluxes from long-term CO_2 models replaced the oceanic crust production rate, as they provide a quantification of the CO_2 degassing at subduction arcs in addition to mid-ocean ridges, and therefore turn into a proxy of the total crustal addition and removal rates (Van Der Meer *et al.*, 2014; Mills *et al.*, 2017). Subduction rates have been estimated from mantle tomography for the last 250 Myr (Van Der Meer *et al.*, 2014), full-plate motion models (Engebretson *et al.*, 1992; Vérard *et al.*, 2015; Merdith *et al.*, 2017; Hounslow *et al.*, 2018; East *et al.*, 2020) or length of subduction zones from plate tectonics reconstructions (van der Meer *et al.*, 2017). They are in concordance with the oceanic crust production rate, especially in that the secular average plate velocity remained roughly unchanged during the Phanerozoic (Fig.3.13). The fluctuations of the oceanic crust production rates, whatever the way they were determined, are expected to have a huge impact on the reconstruction of the $\delta^{11}B_{sw}$. For example, at 50 Myr the oceanic crust production rate is assumed to be between 0.6 and 1.5 times the modern value (Fig.3.12), between 0.7 and 3 times at 125 Myr (Fig.3.12 and 3.13) and between 0.8 and 3.2 500 million years ago (Fig.3.13).

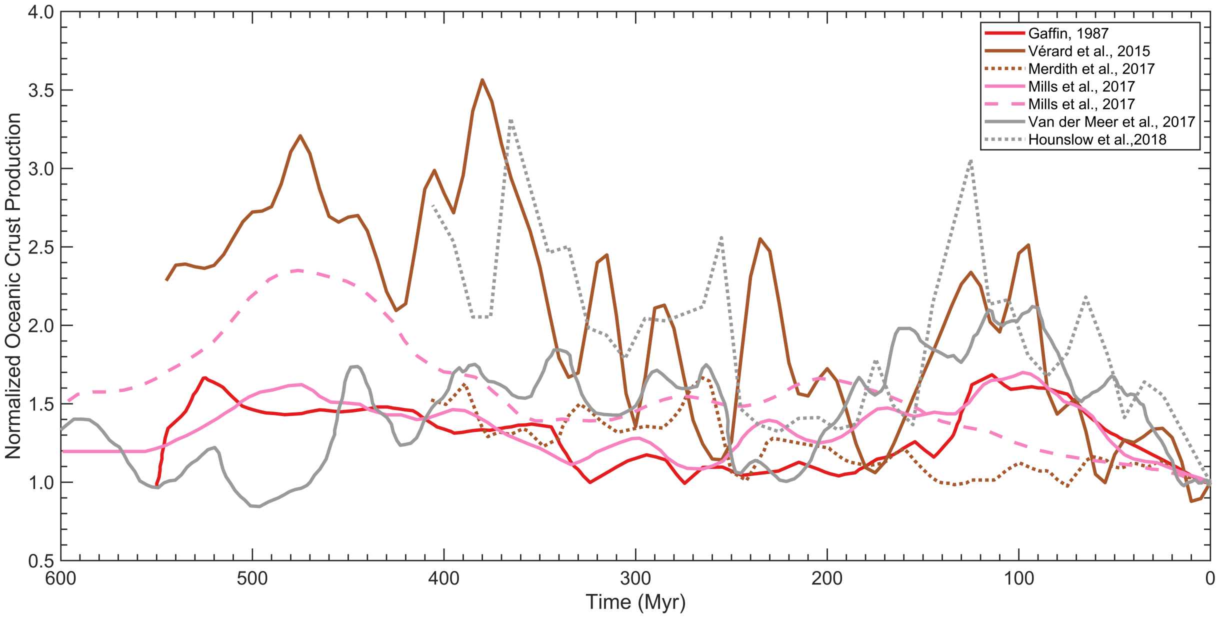

Figure 3.13 : *Normalized oceanic crust production rate for the Phanerozoic reconstructed from sea-level inversion (Gaffin, 1987; Mills et al., 2017), from the mantellic strontium flux (van der Meer et al., 2017) and normalized subduction rates from full-plates motion model (Vérard et al., 2015; Merdith et al., 2017; Mills et al., 2017; Hounslow et al., 2018). The two curves from (Mills et al., 2017) are a reconstruction from updated paleo sea-level (solid pink line) and the total suture length (dashed pink line, as used in this study.*

If we focus on the oceanic crust production reconstruction of Larson (1991) (Fig.3.12), used by the previous $\delta^{11}B_{sw}$ modelling for the last 120 Myr (Lemarchand *et al.*, 2002b), we can see that its decrease is very limited for the first 80 Myr, remaining close to the modern spreading rate. This is not the case for the other proposed production rates rates, and especially for the total suture length of Mills *et al.* (2017), that we used in this study, which shows a constant reduction since the Triassic and is 1.5 times higher than the value by Larson (1991) at this time (Fig.3.3.a and Fig.3.13). This explains why our $\delta^{11}B_{sw}$ curve is systematically higher than that of Lemarchand *et al.* (2002b) in the Cenozoic for both scenarios, with a higher crustal production rate removing more ^{10}B (Fig.3.8). For the Cretaceous, the $\delta^{11}B_{sw}$ proposed by Lemarchand *et al.* (2002b) is conversely higher than ours, due to a faster spreading rate (Fig.3.9, 3.12, 3.13). The $\delta^{11}B_{sw}$ determination of Joachimski *et al.* (2005) for the period between 150 and 550 Myr was based on the oceanic crust production reconstruction of Gaffin (1987), and is quite in concordance with our $\delta^{11}B_{sw}$ evolution for constant continental weathering flux (Fig.3.9, solid green and pink lines), due to minimal differences in oceanic crust production rates (Fig.3.13, red line and solid pink line), both determined from sea level inversion. This also illustrates once again that taking the total subduction length can faithfully track the changes in the crustal production rate (Van Der Meer *et al.*, 2014; Mills *et al.*, 2017).

☐ Runoff

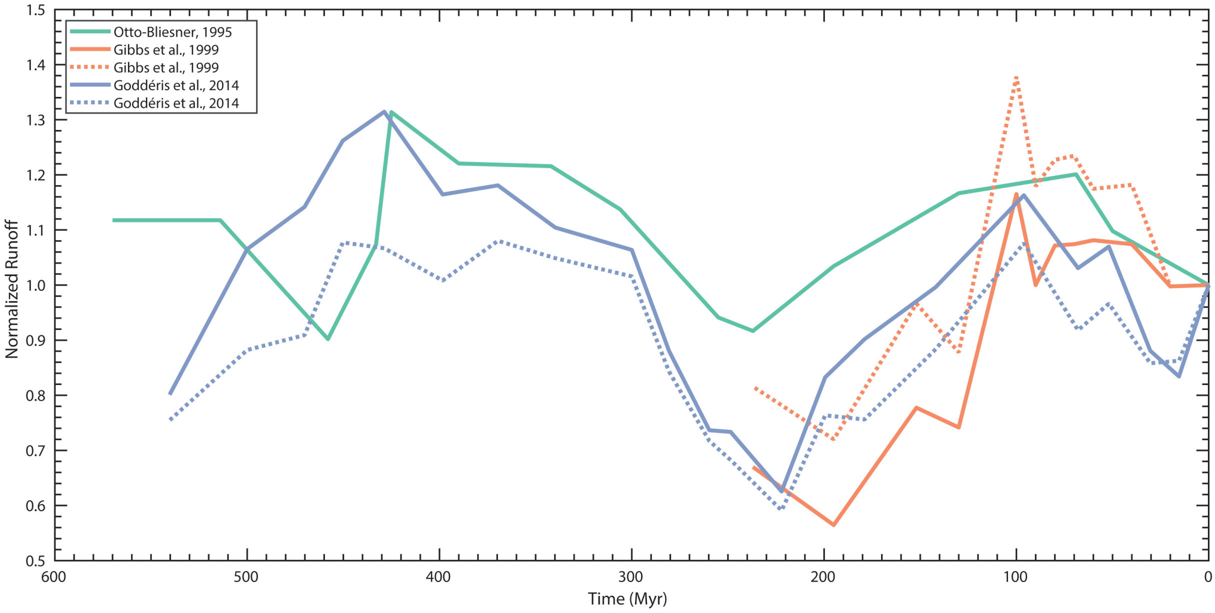

Figure 3.14 : *Normalized runoff for the Phanerozoic from Otto-Bliesner (1995), Gibbs (1999) (straight line: control and dashed line elevated CO_2) and (Goddéris et al., 2014) (solid line: full simulation, dashed line: with only a rising solar constant and paleogeography).*

Concerning the runoff, as mentioned earlier, there are only simulations based on atmospheric general circulation models coupling atmospheric CO_2, solar energy and the continental paleo-configurations. The variations between the modelled runoffs rely essentially on improvements in the parameter inputs. Otto-Bliesner (1995) initially used 14 time slices spanning the Phanerozoic with a fixed pCO_2 at 280 ppm, the modern solar constant and flat continents, whereas Gibbs (1999) kept also the modern solar constant and performed for the last 250 Myr two simulations, one with a constant pCO_2 at 340 ppmv and the other with an elevated pCO_2 (between 2 and 4.5 times 340 ppmv for different time slices) coming from the GEOCARB box model (Berner, 1991). Finally, Goddéris *et al.* (2014) investigated the global CO_2 cycle through the Phanerozoic by combining climatic and paleogeographic models, with either a full simulation, or combining only a rising of solar constant and paleogeography reconstruction (no atmospheric CO_2 model, Fig 3.14). The resulting runoff intensity evolved between 0.6 and 1.3 times the current value during the Phanerozoic, with no fundamental difference between the two simulations.

□ Combining the forcings for oceanic crust production and runoff

We ran the box model for each combination of the previously proposed oceanic crust production and runoff forcings in order to provide numerous $[B]_{sw}$ and $\delta^{11}B_{sw}$ estimations across the Phanerozoic (Fig.3.15). They are extremely variable, with $3 \leq [B]_{sw} \leq 7$ ppm and $28\ ‰ \leq \delta^{11}B_{sw} \leq 50\ ‰$ illustrating the large impact of the forcing selection on the model results (Fig.3.15 and Annex Fig.3.29 and 3.29). As the few different estimations of the runoff variations are all very similar in shape (Fig 3.14), there are also no strong differences in the $\delta^{11}B_{sw}$ general shape for a fixed oceanic crustal production rate (lines of same colour in Fig.3.15), but some in the amplitudes, due to the somehow changing intensity of the applied runoff (Fig 3.14). The exception remains the runs at constant runoff, showing a different trend compared to the others (Annex Fig.3.29 and 3.28). We can observe a general pattern in the $[B]_{sw}$ evolution across the Phanerozoic: an increase of the concentration almost for the whole Paleozoic, a decline between the Permian and the Triassic and finally a global rise towards the present.

□ Towards a reconciliation of modelled and measured $\delta^{11}B_{sw}$?

For the first 100 Myr we observe that $\delta^{11}B_{sw}$ reconstructions with oceanic crust productions from Cogné & Humler (2004, 2006) (green curves in Fig.3.15) stand out with a rise steeper than in the other reconstructions, starting at only 28-32 ‰ to reach the modern value. These curves are for example in agreement with the $\delta^{11}B_{sw}$ measured by Paris *et al.* (2010b) from primary halites (Fig.3.8). Furthermore, the beginning of the Devonian exhibits lower $\delta^{11}B_{sw}$ values for some runs built with the variable runoff of Otto-Bliesner (1995) (Annex Fig.3.29), around 36 ‰, which are also in agreement with the $\delta^{11}B_{sw}$ reconstructions from brachiopods (Joachimski *et al.*, 2005) and with the Devonian halite $\delta^{11}B$ of this study, but not the halite of Paris *et al.* (2010b). However, all the performed simulations fail to reproduce the low δ^{11}B thresholds at 34-35 ‰ estimated for the Permo-Triassic transition from brachiopods and inorganic carbonates (Fig.3.9 and 3.15, Clarkson *et al.* 2015; Jurikova *et al.* 2020).

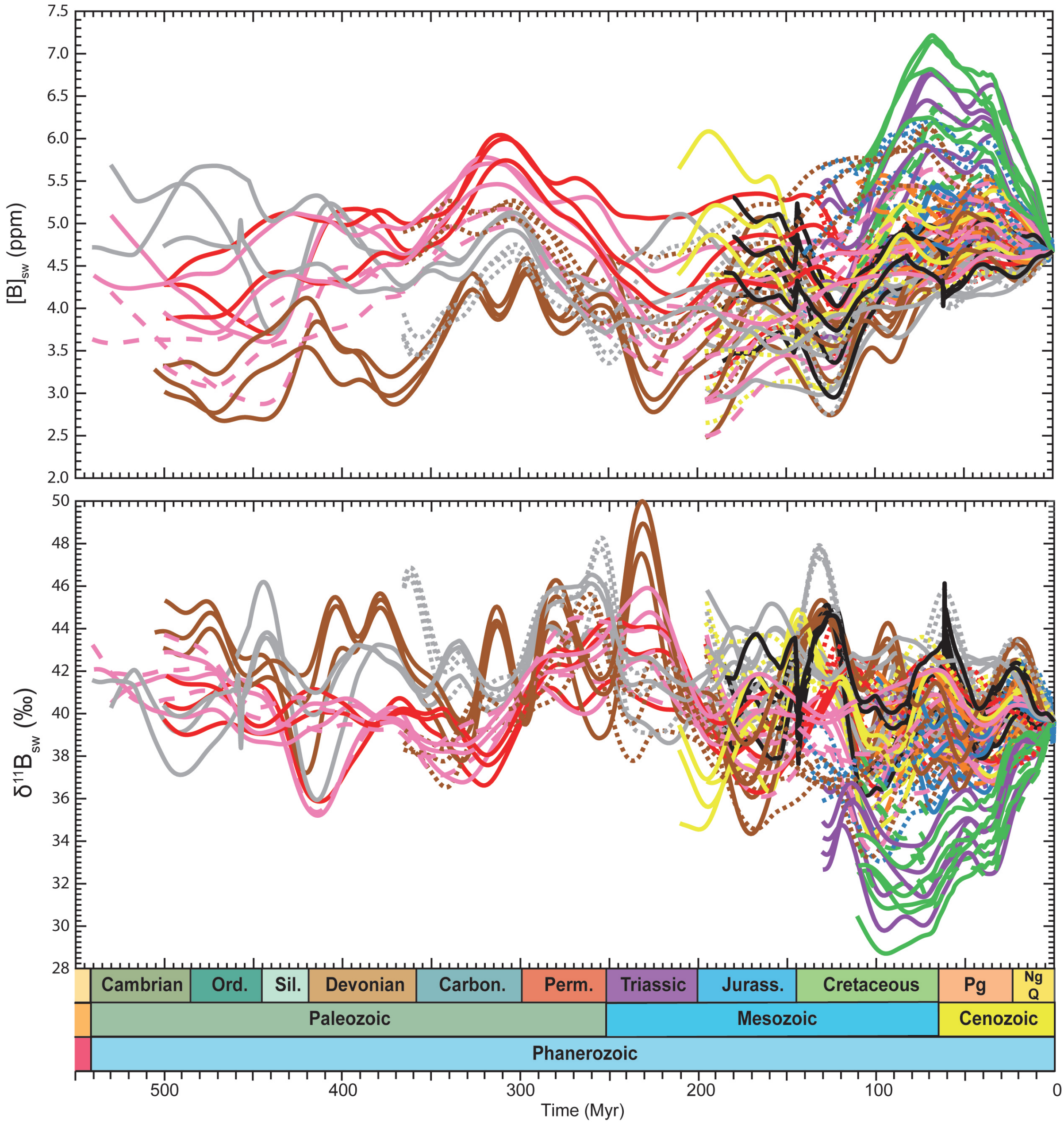

Figure 3.15 : *Compilation of all the runs computed in this study with all possible combinations of variable runoffs or constant runoff (3.14) and oceanic crust productions (Fig.3.12 and 3.13). The colours correspond to the oceanic crust production rates referenced in the figures (Fig.3.12 and 3.13).*

This is probably because the box model is constructed on long term geodynamical forcings and therefore does not sometimes capture punctual geochemical perturbations in the ocean that are due to a global climatic crisis. The end of the Permian experimented indeed the biggest environmental crisis of the geological record, linked to a huge emission of greenhouse gases from the Siberian traps (Burgess & Bowring, 2015; Jurikova *et al.*, 2020). These gases have increased the chemical weathering (Jurikova *et al.*, 2020), which could therefore probably provide additional light boron to the oceans through the dissolved boron continental discharge (Gaillardet *et al.*, 1999; Lemarchand *et al.*, 2002b).

Finally, at the beginning of the Cambrian, all the runs display $\delta^{11}B_{sw}$ values between 40 and 43 ‰, while $\delta^{11}B_{sw}$ was only 20-25 ‰ for the Cryogenian, as inferred from the cap carbonates (Kasemann *et al.*, 2010; Ohnemueller *et al.*, 2014); it is very difficult to clarify what would have cause this huge leap. Like for the punctual and global crisis of the Permo-Triassic transition, these Cryogenian values are contemporaneous to the Sturtian and Marinoan glaciations, which resulted in an Earth entirely covered by ice (Snowball Earth, Hoffman *et al.* 1998) and a temporary increase of the continental weathering at the end of the glaciation, bringing again additional light continental B to the oceans (Kasemann *et al.*, 2014). Moreover, although the boron isotopic composition of the rivers across the geological times is unknown, we can expect for the Neoproterozoic, seat of an intense continental crust formation (Rino *et al.*, 2008) and a high atmospheric pCO_2 (Mills *et al.*, 2019), that the continental weathering would be more important and with a boron continental discharge at a much lower $\delta^{11}B$, due to the weathering of unrecycled materials (around -7 ‰ for the continental crust, Marschall *et al.* 2017) and yet poorly vegetated continental surfaces. This would also explain the low $\delta^{11}B$ value of our Neoproterozoic halite close to 28 ‰ at 565 Myr.

Global geodynamic implications

We are conscious that the $\delta^{11}B$-pH proxy requires precise $\delta^{11}B_{sw}$ values (Pagani *et al.*, 2005) and that our $\delta^{11}B_{sw}$ simulations do not respond to this request. However, by using the latest forcings available in the literature for oceanic crust production and continental runoff, we could propose from all our iterations a secular variation of the $\delta^{11}B_{sw}$, which approximates some of the $\delta^{11}B_{sw}$ reconstructions based on geochemical proxies measured in carbonates or salt samples. Beyond its use for the paleo-pH, the $\delta^{11}B_{sw}$ fluctuations allow us to track the global geodynamical cycles in the Earth history, related to the Wilson cycle. We evidenced four different periods of time in these fluctuations, which have been correlated to the seawater $^{87}Sr/^{86}Sr$, ocean chemical composition from halite fluid inclusions and the atmospheric pCO2 (Fig.3.15). They interestingly compare to the periods define by Turchyn & DePaolo (2019). The four isolated period are also more and less correlated to the oceanic chemistry, with the alternance of $CaCl_2/MgSO_4$ and aragonitic/calcitic seas. As mentioned earlier, the boron oceanic cycle is a balance between the continental weathering and the alteration of the oceanic crust, both processes closely linked to the long-term CO_2 cycle; continental weathering being the main negative feedback and degassing through volcanism (correlated to the oceanic production rate at the oceanic ridges) the main positive feedback (Walker *et al.*, 1981; Berner *et al.*, 1983; Sundquist & Ackerman, 2014).

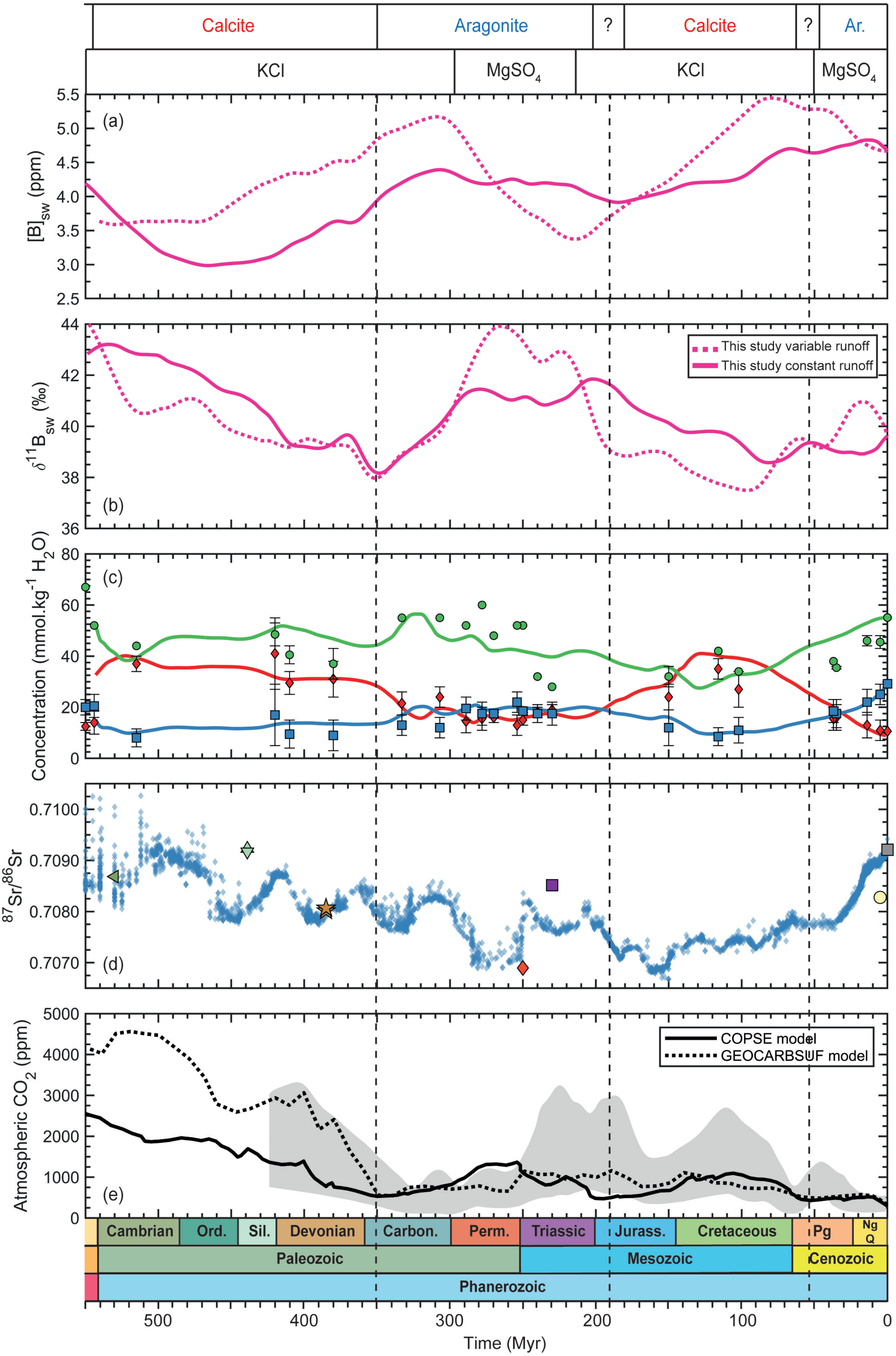

(Caption next page.)

Figure 3.15 : *(Previous page.) Seawater chemistry and atmospheric* pCO_2 *across the Phanerozoic. (a) Modelled seawater boron concentration. (b) Modelled seawater boron isotopic composition. (c) Concentration of* Ca^{2+} *(red),* Mg^{2+} *(green) and* SO_4^{2-} *(blue) calculated from fluid inclusions in primary marine halites (Brennan & Lowenstein, 2002; Horita et al., 2002; Brennan et al., 2004; Lowenstein et al., 2005; Brennan et al., 2013; Holt et al., 2014) and modelled (Demicco et al., 2005). (d)* $^{87}Sr/^{86}Sr$ *ratio measured in the halite samples (symbols as in figure 3.6 and modern Guérande salt, grey square), in light of the seawater* $^{87}Sr/^{86}Sr$ *compilation from unaltered carbonates (Veizer et al., 1999; Prokoph et al., 2008; Halverson et al., 2007). (e) Modelled atmospheric CO2 concentration from the updated long term carbon cycle box models GEOCARBSULF and COPSE, and from proxy estimations (grey area, Mills et al. 2019).* $CaCl_2$ *and* $MgSO_4$ *seas correspond to the switch where* $[Ca^{2+}]$ *is respectively higher and lower than* $[SO_4^{2-}]$*, and consequently to marine KCl and* $MgSO_4$ *late evaporite depositions in the geological records (Hardie, 1996). Aragonitic and calcitic seas are respectively set when Mg/Ca in seawater is higher or lower than 2 (Sandberg, 1983; Lowenstein et al., 2014).*

The seawater $^{87}Sr/^{86}Sr$ ratio, recorded in marine carbonates, reflects in the first order this CO_2 balance as a mixing between a river input (0.7136) and mantellic input from mid-ocean ridges and volcanic arcs (0.7030, Allègre *et al.* 2010; Van Der Meer *et al.* 2014; Vérard *et al.* 2015; van der Meer *et al.* 2017). The chemical composition of seawater through time is roughly balanced between inputs from continental weathering and reverse weathering and outputs from precipitations of minerals, either biologically mediated, incorporated into sedimentary rocks on the oceanic crust, or secondarily formed by hydrothermalism (Walker *et al.*, 1981; Berner *et al.*, 1983; Horita *et al.*, 1991; Isson & Planavsky, 2018; Turchyn & DePaolo, 2019). All these combined parameters can highlight what were the interplays that conduced to the long-term $\delta^{11}B_{sw}$ oscillations.

The beginning of the Paleozoic, until the beginning of the Carboniferous, is characterized by a $\delta^{11}B_{sw}$ decline coupled with a general decrease of the atmospheric pCO_2, of the $^{87}Sr/^{86}Sr$ ratio and Ca concentration ($[Ca^{2+}]$, Fig.3.15). In the early Paleozoic, high $[Ca^{2+}]$ is due to low seawater pH induced by the high atmospheric pCO_2 (Zeebe, 2012). The seawater $^{87}Sr/^{86}Sr$ variations are nevertheless marked by peaks, corresponding to orogeny onsets (forming the Pangea), which more efficiently consume atmospheric CO_2 through increased continental erosion and weathering, and have probably been even enhanced by the apparition of the first continental plants (Goddéris *et al.*, 2017). This tectonic scenario probably supplied a larger quantity of boron isotopically much lighter through the riverine dissolved charge (Lemarchand *et al.*, 2002b; Marschall *et al.*, 2017; Marschall, 2018), in line with an increase of the seawater boron concentration from the late Ordovician.

Between the end of the Carboniferous and the start of the Jurassic, a weak positive peak of pCO_2 is correlated to the major positive peak of the $\delta^{11}B_{sw}$, while $^{87}Sr/^{86}Sr$ and $[Ca^{2+}]$ display low values. The latter is linked to the preceeding decline of the pCO_2, which increased the seawater pH (Zeebe, 2012). The formation of the Pangea supercontinent peneplain coupled with arid climatic conditions at its center led to a rise of the pCO_2 and lowered consequently the seawater ^{87}Sr/^{86}Sr and the runoff (Goddéris *et al.*, 2014, 2017). With less continental inputs, δ^{11}B$_{sw}$ became mainly controlled by the alteration of the oceanic crust, removing preferentially the ^{10}B isotope. This is also illustrated by the decrease of the boron concentration as well as [Mg2+], Mg being incorporated in secondary minerals during oceanic crust alteration. The Permo-Triassic limit is defined by a sudden increase of ^{87}Sr/^{86}Sr, and punctual changes in the concentrations of calcium, sulphates and magnesium probably caused by the Siberian trap's emissions, also increasing continental weathering.

The period between the onset of the Jurassic and the beginning of the Paleogene is marked by the Pangea break-up with a stronger seafloor generation, which again decreased [Mg^{2+}]. At the start of this period, the seawater ^{87}Sr/^{86} is minimal alongside a high pCO$_2$, mirroring the lack of orogens. The pH is therefore lower and consequently [Ca^{2+}] is higher. We should expect an increased borate uptake through oceanic crust alteration, but this period is also characterised by an increasing runoff (Fig.3.14), which contributed to slightly diminish δ^{11}B$_{sw}$, even with high oceanic crustal production rate, as also shown by the increase of the boron concentration. This stands for the scenario with a variable runoff. But in the scenario with a constant runoff, the beginning of the Jurassic exhibits the higher δ^{11}B$_{sw}$ and a small decrease of [B]$_{sw}$, which can be explained by an intense oceanic crust alteration.

Finally, for the last and most recent period, the ^{87}Sr/^{86} increased in conjunction with a decline of the atmospheric pCO$_2$, due to the Himalayas formation that caused a stronger erosion and weathering, providing more magnesium to the oceans (Misra & Froelich, 2012). [Ca^{2+}] is consecutively lowered with the pH increase. The scenario with a variable runoff exhibits a stronger rise of δ^{11}B$_{sw}$ than the scenario with a fixed runoff, which remains more or less constant at the onset. In this case, as shown by Lemarchand *et al.* (2002b) and Paris *et al.* (2010b), boron adsorption on the clastic sediments overrides the continental discharge, as the runoff forcing is by construction weaker. The δ^{11}B$_{sw}$ oscillation at the end of the Cenozoic for the scenario with a variable runoff is caused by a steep increase of the runoff over the last 10 Myr, after 80 Myr of decline.

3.5 Conclusion

As the boron isotopic composition is a key parameter to apply δ^{11}B proxy on biogenic carbonates for paleo-pH and pCO$_2$ reconstruction in the geological times, we investigated two ways to determine the δ^{11}B$_{sw}$ across the Phanerozoic : a direct record through primary halites, from seven samples covering the last 560 Myr, and a boron cycle modeling with updated geodynamic forcings.

We firstly underscored the relative δ^{11}B homogeneity regardless of the B concentration in the NaCl salt with the measurement of ten subsamples, supporting the assumption that boron is only concentrated in fluid inclusions. We then evaluated if the average δ^{11}B of the halites could directly reflect the $\delta^{11}B_{sw}$, with the assistance of annex analysis, XRD and the $^{87}Sr/^{86}Sr$ ratio, to assess respectively the mineralogy and the marin origin of the samples. We showed that the primary halites from the Neoproterozoic (Ara 7, 550 Myr, $\delta^{11}B$ = 28.3 ± 2.3 ‰), the Devonian (AW-86-49, 380 Myr, $\delta^{11}B$ = 31.7 ± 3.0 ‰) and the Pleistocene (IZ-3, 3-5 Myr, $\delta^{11}B$ = 39.2 ± 3.7 ‰) are in agreement with previous $\delta^{11}B_{sw}$ estimations, established from modeling and carbonates samples (inorganic and biogenic). The Pleistocene sample exhibited a non marine $^{87}Sr/^{86}Sr$ signature, which has been fully explained in the end by brine-rock interactions with older carbonates in the basin. These three halites, which marin origin was confirmed (with the $^{87}Sr/^{86}Sr$ ratio and/or $\delta^{37}Cl$ from a previous study) could therefore represent a direct measurement of the $\delta^{11}B$ of seawater and give precious indications on the seawater from which they precipitated. However, the $\delta^{11}B$ variability among the sub-samples of a halite sample, between 2.3 and 3.7 ‰, precludes their use in paleo-pH applications, as an uncertainty of 1 ‰ on the $\delta^{11}B_{sw}$ parameter causes a deviation of 0.1 pH unit. On the contrary, the four other samples, Cambrian (Sib4, 520-540 Myr, $\delta^{11}B$ = 11.2 ± 5.5 ‰), Silurian (Car12-3-3, 434-444 Myr, $\delta^{11}B$ = 3.74 ± 9.4 ‰), Permian (WIPP-3, 250 Myr, $\delta^{11}B$ = 17.2 ± 1.5 ‰) and Triassic (WIPP-3, 250 Myr, $\delta^{11}B$ = 9.4 ± 2.2 ‰), have $\delta^{11}B$ values much lower than the literature trend, although the Permian and the Cambrian sample exhibit seawater $^{87}Sr/^{86}Sr$ signatures. This was also the case for the first controversial study on primary halites by Paris *et al.* (2010b). We then explored the different processes which can affect the $\delta^{11}B$ fingerprint of halites, without really being able to discriminate: the rate of crystallisation; coprecipitation of boron in associated phases (which have been documented with the XRD analyses) such as $CaSO_4$ at early stages of evaporation and K-$MgSO_4$ salts at final stages, minerals taking preferentially the light borate anion; external continental inputs in the basin with low $\delta^{11}B$; or post-depositional preservation as halites display mechanical, thermal and chemical properties prone to easily modify the salt deposits. Finally, our study on primary halite contribute to promote the absence or the slight fractionation between brine and halites, and rule out the -30 ‰ fractionation which have been previously proposed, but the boron isotopes behaviour during seawater evaporation have to be more fully constrained in future studies.

In a second part, we reconstructed the boron isotopic composition in seawater from a simple box model with the last updated geodynamic forcings that are generally used in atmospheric CO_2 reconstruction models across the geological times. We considered two scenarios, at constant runoff (modern value) and at varying runoff. We therefore propose two alternatives storylines compared to what was previously proposed in the literature, but covering the entire Phanerozoic and reproducing faithfully most of $\delta^{11}B_{sw}$ data for the last 200 Myr. We then explore the possibilities which can outline the observed discrepancies, by questionning the $\delta^{11}B_{sw}$ reconstructions from biogenic or inorganic carbonates or the selection of the geodynamic forcings used in the boron cycle models. Consequently, we performed a series of sensitivity tests to estimate which parameters have a dominant impact on the models. It turned out that the boron concentration and isotopic ratio in seawater are mainly controlled by continental riverine input through weathering and the oceanic crust alteration through boron adsoption on marine sediments, with a secondary control, but much less important, of the adsoption on clastic sediments. We also demonstrated that the initial selection of the geodynamic forcings to construct the model plays a substantial role in the suggested scenarios for δ^{11}B$_{sw}$ across the Phanerozoic, but the compilation we proposed in this study can explain almost all the δ^{11}B$_{sw}$ reported so far. However, it highlights the inability of long term models to catch short environmental perturbations in the geological records. Modeling does not bring a straightforward answer for a precised δ^{11}B$_{sw}$ in the past, as is requested for paleo-pH applications, but can provide, as do halites, supplementary informations on the evolution of the seawater chemistry in the past, in connection with the geodynamic, climatic and ecological history of the Earth.

3.6 Appendix

3.6.a Halite data

Sample	Location	Formation	Stratigraphy	Age (Myr)	[B] (ngB/g Salt)	δ^{11}B (‰)	2σ	^{87}Sr/^{86}Sr	2σ	Mineralogy
IZ-3-1	Israel	Sedom	Plio-Pleistocene	3-5	344	39.68	0.21	0.708277	0.000008	Halite (major peaks) potassic halite and sylvite as remainders
IZ-3-2					294	40.17	0.09			
IZ-3-3					281	40.47	0.58			
IZ-3-4					401	42.47	0.69			
IZ-3-5					289	35.65	0.86			
IZ-3-6					307	39.65	0.07			
IZ-3-7					360	39.66	0.12			
IZ-3-8					325	37.27	0.20			
IZ-3-9					333	39.09	0.69			
IZ-3-10					284	38.26	0.14			
Keuper-1	France	Keuper	Upper Triassic	230	75	7.91	0.16	0.708515	0.000003	Halite (major peaks) Potassic halite, sylvite and anhydrite as remainders
Keuper-2					40	9.18	0.59			
Keuper-3					50	1.72	0.34			
Keuper-4					66	8.76	0.26			
Keuper-5					57	9.97	0.18			
Keuper-6					51	9.25	0.39			
Keuper-7					49	11.64	0.35			
Keuper-8					61	8.72	0.17			
Keuper-9					33	9.04	0.33			
Keuper-10					73	10.51	1.33			
WIPP-3-1	USA	Salado	Upper Permian	250	710	17.12	0.18	0.706895	0.000004	Halite (major peaks) Potassic halite, sylvite and anhydrite as remainders
WIPP-3-2					749	15.99	0.22			
WIPP-3-3					580	19.02	0.12			
WIPP-3-4					591	17.43	0.09			
WIPP-3-5					749	17.17	0.15			
WIPP-3-6					505	17.01	0.09			
WIPP-3-7					626	16.71	0.37			
WIPP-3-8					552	16.89	0.11			
WIPP-3-9					590	17.29	0.08			
WIPP-3-10					569	17.60	0.08			
AW-86-49-1	Canada	Prairie	Middle Devonian	380	194	31.96	0.14	0.708014	0.000019	Halite (major peaks) Potassic halite and sylvite as remainders
AW-86-49-2					123	31.44	0.20			
AW-86-49-3					179	33.42	0.92			
AW-86-49-4					191	32.96	0.20			
AW-86-49-5					131	30.83	0.11			
AW-86-49-6					217	33.12	0.11			
AW-86-49-7					201	31.78	0.27			
AW-86-49-8					97	28.28	0.39			
AW-86-49-9					184	32.12	0.97			
AW-86-49-10					151	30.71	0.00			

Sample	Location	Formation	Stratigraphy	Age (Myr)	[B] (ngB/g Salt)	δ^{11}B (‰)	2σ	^{87}Sr/^{86}Sr	2σ	Mineralogy
Car12-3-3 (clear)-1	Australia	Carribuddy	Lower Silurian	434-444	308	19.79	1.47	0.70923	0.000016	Halite (major peaks) Potassic halite as remainders
Car12-3-3 (clear)-2					219	5.32	0.32			
Car12-3-3 (clear)-3					155	0.66	2.91			
Car12-3-3 (clear)-4					150	4.59	0.21			
Car12-3-3 (clear)-5					114	4.12	0.49			
Car12-3-3 (clear)-6					111	-3.21	1.14			
Car12-3-3 (clear)-7					88	2.81	1.05			
Car12-3-3 (reddish)-1	Australia	Carribuddy	Lower Silurian	434-444	186	3.07	0.10	0.709171	0.000007	Halite (major peaks) Potassic halite and anhydrite as remainders Traces of iron and aluminium oxide
Car12-3-3 (reddish)-2					173	3.09	0.44			
Car12-3-3 (reddish)-3					90	2.81	0.16			
Car12-3-3 (reddish)-4					62	1.22	0.47			
Car12-3-3 (reddish)-5					64	3.15	0.38			
Car12-3-3 (reddish)-6					64	3.46	0.36			
Car12-3-3 (reddish)-7					62					
Car12-3-3 (reddish)-8					67	3.60	1.10			
Car12-3-3 (reddish)-9					70	2.63	0.40			
Car12-3-3 (reddish)-10					92	2.80	0.62			
Sib4-1	Russia	Angarskaja/Usolskaja	Lower Cambrian	520-540	342	9.70	0.11			Halite (major peaks) Anhydrite as remainders
Sib4-2					443	11.40	0.09			
Sib4-3					279	8.32	0.14			
Sib4-4					197	9.98	1.90			
Sib4-5					555	9.11	0.18			
Sib4-6					232	13.06	0.12			
Sib4-7					540	10.80	0.05	0.708685	0.000005	
Sib4-8					952	16.73	0.29			
Sib4-9					366	8.39	0.10			
Sib4-10					310	14.14	0.12			
Ara7-1	Oman	Ara	Late Neo-Proterozoic	550	371	27.88	0.09			Halite (major peaks) Potassic halite and sylvite as remainders
Ara7-2					339	29.22	0.27			
Ara7-3					434	29.50	0.21			
Ara7-4					275	28.03	0.27			
Ara7-5					355	29.23	0.16			
Ara7-6					605	26.86	0.10			
Ara7-7					391	27.39	0.13			
Ara7-8					444	26.39	0.09			
Ara7-9					394	29.29	0.08			
Ara7-10					365	29.06	0.19			

Table 3.1 : *Location, formation, stratigraphy, age, ^{87}Sr/^{86}Sr and mineralogy of the halite samples and [B], δ^{11}B for each subsample.*

3.6.b Geological and stratigraphic settings of the halite samples

Evaporites are sedimentary rocks and minerals produced by solar (and wind) -driven concentration of a brine. As a result of the large concentration of Na and Cl in the oceans, halite is the predominant mineral starting to precipitate after $CaCO_3$ (calcite and aragonite) and $CaSO_4$ (gypsum and anhydrite) when seawater is concentrated ten to eleven times, and before Mg-K potash salts minerals (Fig.3.16, Bąbel & Schreiber 2014; Shalev *et al.* 2018). These three minerals represent 90-95 % of salt deposits (Hay *et al.*, 2006; Warren, 2010). The evaporitic formations require particular climatic, tectonic and eustatic conditions, which explain their sparse distribution and their variable basin size in the geological times, also due to their soluble nature and thus a poor preservation over geological times (Warren, 2010). It is as well difficult to obtain their absolute dating, especially for halite layers. Datation by the cosmogenic isotope ^{10}Be is limited due to its half life time of 1.39 Myr (Belmaker *et al.*, 2013) whereas ^{40}Ar/^{39}Ar dating can be used only for K rich evaporitic minerals (Renne *et al.*, 2001).

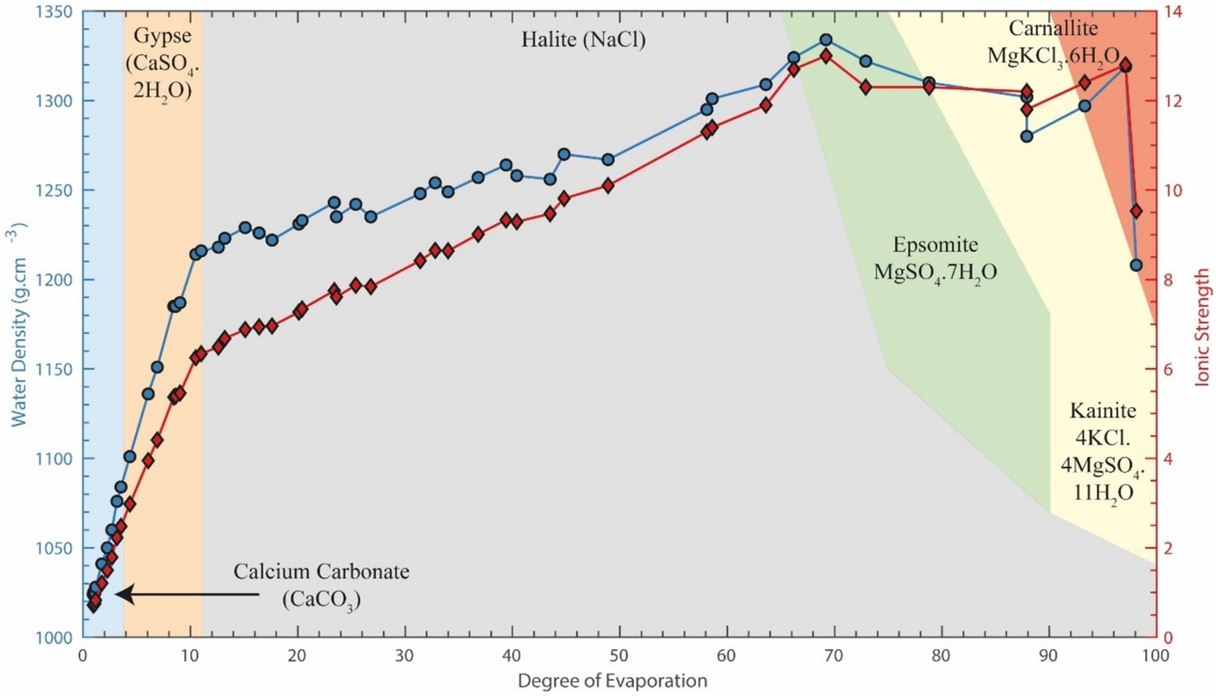

Figure 3.16 : *Seawater density and ionic strength of an evaporating modern seawater and associated evaporite mineral precipitation sequence (McCaffrey et al., 1987; Bąbel & Schreiber, 2014). The timing of the evaporite precipitation sequence has been approximated from Shalev et al. (2018) (figure modified from Bąbel & Schreiber 2014).*

Sedom formation

The Sedom formation, a 2000 m deep sedimentary deposit composed mostly of salts (halites in majority with some layers of gypsum and anhydrite) and minor interbeds of carbonates rocks (dolomite) and clastic materials, is localized in the Dead Sea Rift, a pull-apart basin (Stein *et al.* 2000, Fig.3.17). This basin results from tectonic movements during the Miocene along the Dead Sea Transform fault system separating the Arabian plate from the Sinai sub-plate Freund *et al.* (1970). This formation is one of the remnants (like the Dead Sea) of the Sedom marine lagoon connecting the Mediterranean Sea and the Dead Sea Rift Valley and comes from water evaporation in its subsiding distal part (Stein *et al.*, 2000; García-Veigas *et al.*, 2009). The reasons of the ingression, the disconnection (eustatic changes or uplift) and their associated timing, between the late Pliocene or the late Neogene and the early Pleistocene, are not well characterized (Stein, 2001). However, Belmaker *et al.* (2013) showed that seawater beryllium is incorporated into the halite and used the ^{10}Be datation to estimate an age between 3 and 5 Myr for the Sedom formation.

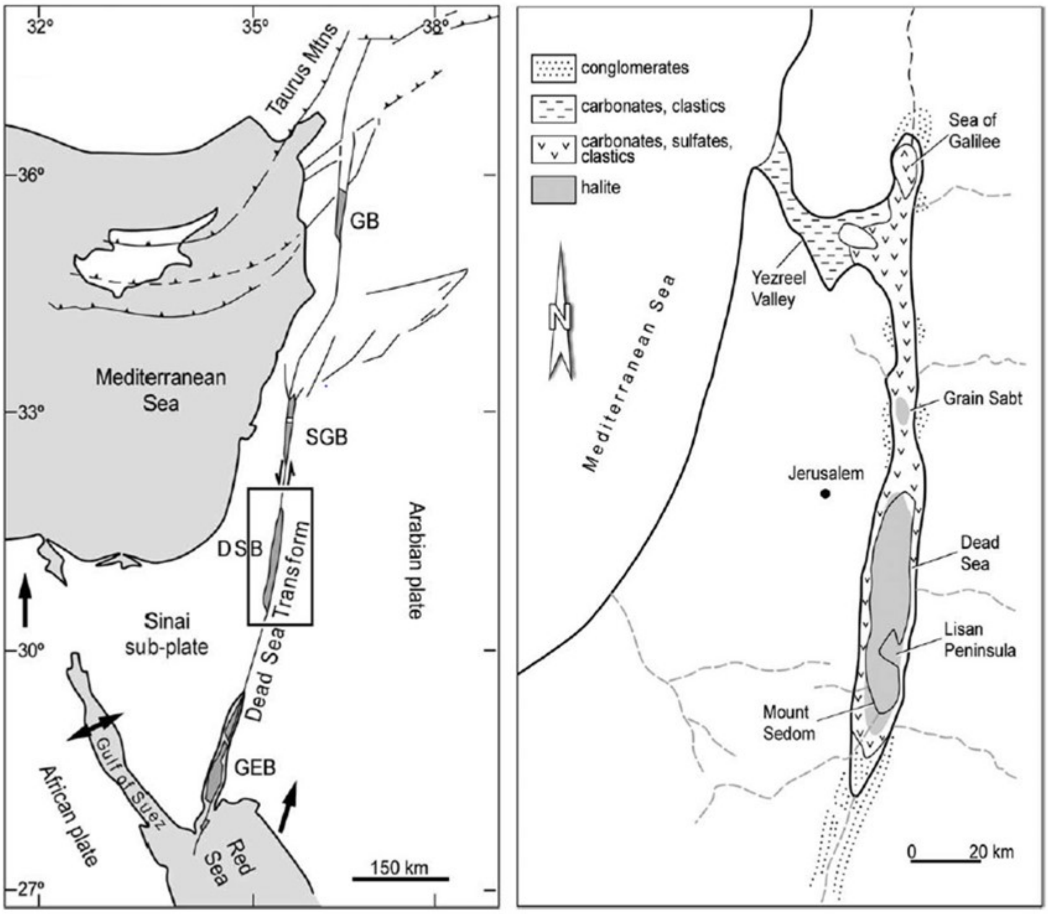

Figure 3.17 : *Location of the Pliocene Sedom Lagoon and its associated facies in the Dead Sea Rift (DSB=Dead Sea Basin). Figures from Garcia-Veigas et al. (2009).*

Keuper formation

The Keuper formation is one of the lithostratigaphic units deposited in the German Basin, an epicontinental platform in the northwestern front of the Tethys Ocean during the Triassic (Fig.3.18). The sedimentation occurred in a rifting context during the Pangea break-up leading to a large sediment accumulation due to the subsidence (Golonka, 2007). This formation consists in continental and predominantly coastal sediments (siliciclastics, marine carbonates and evaporites). It is the final part of the "germanic trilogy" in the Central Europe, a stratigraphic succession produced by a marine transgression-regression cycle and is thereby preceded by the continental Buntsandstein (alluvial sediments) and the shallow marine Muschelkalk carbonates (Aigner & Bachmann, 1992). The salt used in this study comes from the Lorraine Basin, in the east of the Paris Basin which itself was a western inlet of the German Basin (Fig.3.18.B). The Lorraine Basin is characterized by a thick evaporite sequence up to 150 m, formed in a coastal plain environment with anhydrite and dolomite depositions at the start of the Early Carnian (Upper Triassic). The halite accumulation within the evaporite formation took place in the regions with the strongest subsidence (Bourquin *et al.*, 1995; Fanlo & Ayora, 1998).

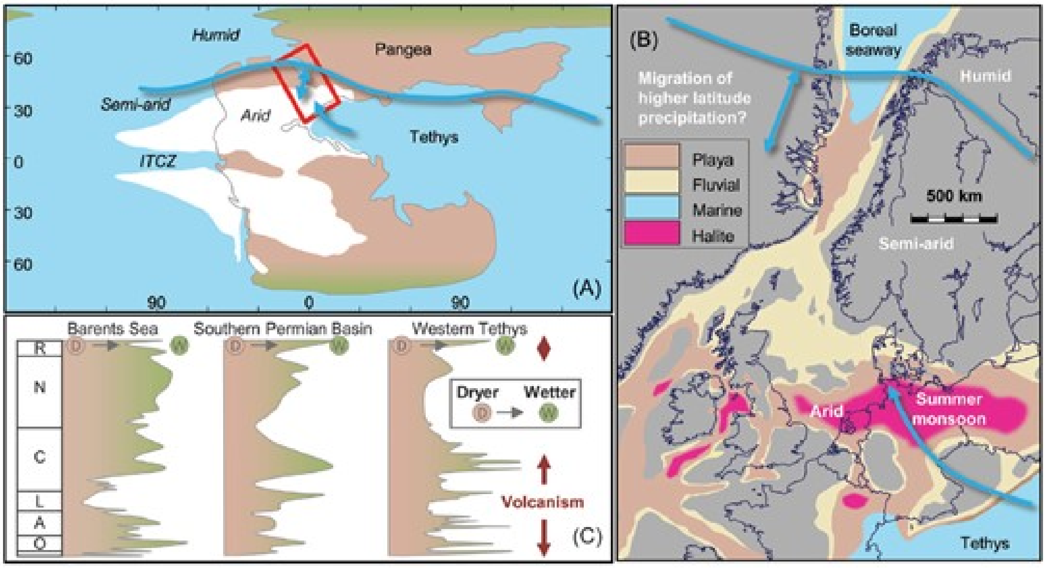

Figure 3.18 : *Paleogeography and paleoclimate of the Late Triassic with a focus on the North Europe. ITCZ: Intertropical Convergence Zone, O: Olenekian, A: Anisian, L: Ladinian, C : Carnian, N : Norian, R: Rhaetian. Figure from McKie 2017.*

Salado formation

The Salado formation is located in the Delaware Basin covering the west part of Texas and south-east part of New Mexico and is a sub-basin with the Midland Basin of the Permian Basin (Ward *et al.*, 1986). The sedimentation of the latter started to the end of the Pennsylvanian and ended at the end of the Permian and is the result of the formation of the Pangea caused by the collision between the Laurasia and the Gondwana creating foreland arc basins and reliefs. The Permian Basin was in the lower Permian on the western coast of the Pangea at 5-10°of the Paleo-Equator (Fig.3.19, Scholle *et al.* 1992). At the start of this era, this place was a sea (as a foreland basin) in connection with the Panthalassa ocean. A marine regression occurred successively at the end of the Lower Permian, increasingly disconnecting the Permian Basin from the Panthalassa ocean and isolating the Delaware and the Midland Basin. Only one entrance to the ocean remained, the Hovey Channel in the south of the basin, which closed definitely after closure-opening cycles during the Upper Permian (Hill, 1999). Due to the Variscan and then the Marathon orogeneses, a significant subsidence occurred at the Lower Permian in particular supplied by the uplift of the carbonate Central Basin Platform splitting the Delaware and the Midland Basins and which then declined all along the Permian (Hills, 1984). The Salado Formation, comprising a 700 m thick evaporite sequence, belongs to the Ochoan lithostratigraphic unit, deposited at the Late Permian at closing time of the Hovey Channel with other evaporite sequences in-between the underlying Castile Formation and the overlying Rustler Formation (Lowenstein, 1988; Lucas & Anderson, 1993).

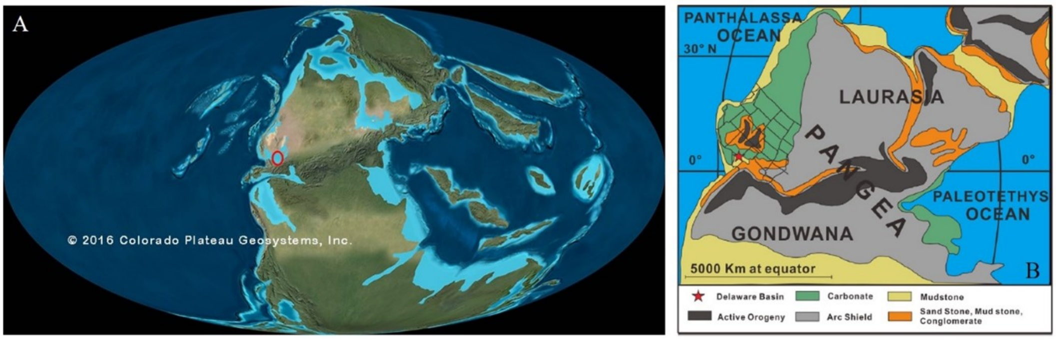

Figure 3.19 : *(A) Paleogeographic map of the Upper Permian (260 Myr,* `www.deeptimemaps.com`*), with the location of the Delaware basin (red circle); (B) Paleogeography of the Delaware Basin at the same time. Figure from Feng et al. (2018).*

Evaporite Prairie formation

The Evaporite Prairie formation, a 150 m thick layer, was deposited in the Elk Point Basin during the Middle Devonian, covering today the western part of the Canada (Alberta) to the Montana and the North Dakota. This basin was found on the Laurentia paleo-continent (North American Craton) separated from the Gondwana by the Rheic Ocean in a closure process throughout the Devonian, initiating the Pangea formation at the Early Carboniferous (Fig.3.20). The Elk Point Basin was more precisely located in the northern margin of the Laurentia at the Equator and is the memory of a shallow epicontinental sea, inlet of the Panthalassic Ocean, penetrating the continent southward (Broughton, 2018). At the end of the Middle Devonian, the development of a continuous reef barrier, the Presqu'île Barrier, coupled with a marine regression closed almost the basin at the mouth, with restricted marine water influx through the barrier and caused the Evaporite Prairie deposition after the carbonate Keg River Formation (Day *et al.*, 1996; Jin & Bergman, 1999; Rogers & Pratt, 2017).

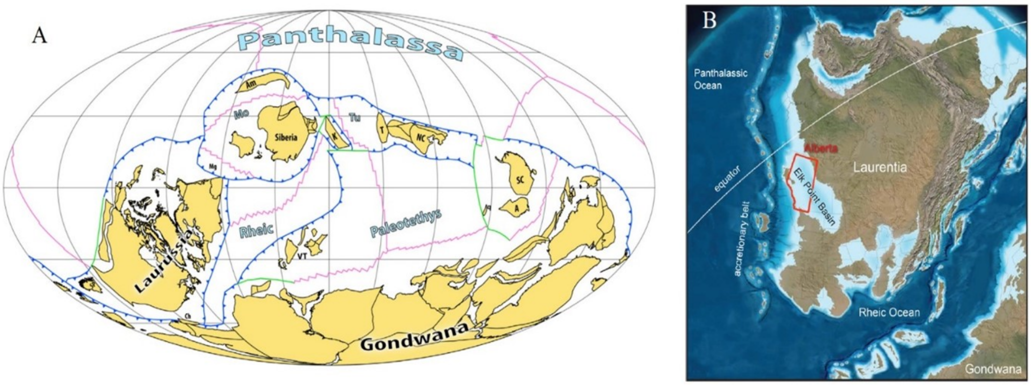

Figure 3.20 : *Paleomap of the Middle Devonian (390 Ma, figure from Domeier & Torsvik 2014); (B) Focus on the paleogeography of the Laurentia palaeocontinent at the same period (Broughton 2018, modified from* `www.deeptimemaps.com`*).*

Carribuddy Group

The marginal-marine and evaporitic Carribuddy Group is a sedimentary formation settled in the onshore Canning Basin in the northern of Western Australia during the Ordovician-Silurian transition. This basin, surrounded by Proterozoic and Archean cratons such as the Pilbara Craton, has a NW-SE orientation with an offshore spreading in the northern part and was active between the Early Ordovican to the Cretaceous (Haines & Wingate, 2005). The salt sample originates specifically from the halite-rich Mallowa Salt Formation, a layer up to 800 m thick penultimate of five mudstone, evaporite, and dolomite formations (Cathro *et al.*, 1992; Haines & Wingate, 2005). Between the Ordovician and the Silurian, Australia was part of Gondwana, which was situated mostly on the South Pole and hosted the Late Ordovician-Early Silurian glaciation (Fig.3.21). Australia was at this time in the Northern-Eastern margin of the paleo-continent at equatorial latitudes and underwent the opening of the Larapinta Rift (480-460 Myr) followed by the intra-continental Alice Springs Orogeny for the Ordovician-Carboniferous period in the central part of Australia (Haines *et al.*, 2001; Silva *et al.*, 2018).

This first step of rifting splited Australia from east to west, from the Canning Basin to the central Australia and was overwhelmed by the epicontinental Larapintine sea (Webby, 1978). Immediately after, the second step of orogeny in its early stages created an extension phase and initiated the opening of the Canning Basin around 460-430 Myr (Roberts & Houseman, 2001). These two extension phases are concomitant with a significant marine transgression at the late Middle Ordovician, reaching the highest level in the geological records, immediately followed by a sharp regression in the Last Ordovician associated with the glaciation (Haq & Schutter, 2008). Coupling the tropical climate, the tectonic elevation and the major regression at the Ordovician-Silurian transition in this region caused the trap of marine water and therefore evaporite depositions such as the Mallowa salt (Williams, 1991; Haines & Wingate, 2005).

Figure 3.21 : *Paleogeographic map of the late Middle- Late Ordovician (452 Myr). The Canning Basin is located by the star. Figure from Spaak et al. (2017).*

Angarskaja and Usolskaya formations

The Angarskaja and the Usolskaya formations, 15-450 m and 200 m thick, respectively, are two salt deposition phases of the Early Cambrian East Siberian Platform Basin, located in the North-West of the Baikal Lake (Petrychenko *et al.*, 2005). At the end of the Neoproterozoic, the supercontinent Rodinia broke-up to form, among other smaller continents, Siberia in equatorial-subtropical latitudes (in the south of paleo-equator), which drifted northly during the Paleozoic and merged with other continents to form Pangea. During the whole Cambrian, Siberia crossed thereby the tropical zone and was separated from Laurentia by the Paleoasian Ocean while the big paleocontinent Gondwana set up in the South Pole (Fig.3.22A, Gordienko 2006; Cocks & Torsvik 2007). The evaporite deposits were more precisely identified in the southern margins of the Siberian craton (Grishina *et al.*, 1992). During the Neoproterozoic-Cambrian transition, Siberia was bordered to the North-West by an active margin with its associated volcanic arc islands and a back arc basin when the south was characterized by shelf basins of passive continental margins (Fig.3.22B, Metelkin *et al.* 2012). These southern areas were favourable for lagoon developments and associated carbonate shelves allowing large evaporite depositions coinciding with sea level fluctuations at hight frequency (Ulmishek, 2001; Haq & Schutter, 2008).

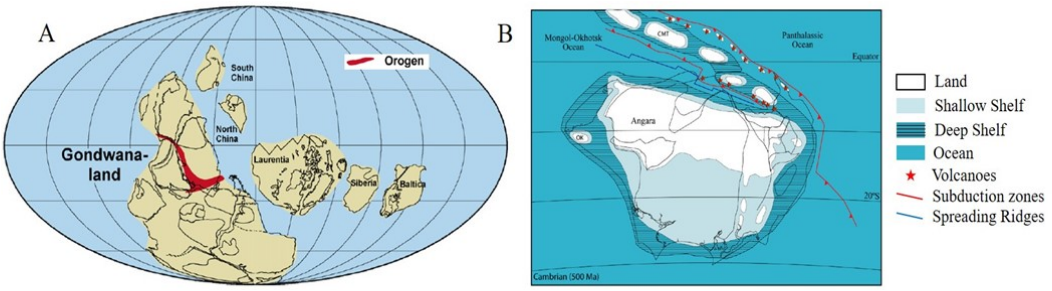

Figure 3.22 : *(A) Paleogeography reconstruction of the Lower Cambrian (530 Myr). Figure from (Li et al., 2008); (B) Paleomap of the Siberian Terrane during the Late Cambrian (500 Myr). Figure from Cocks & Torsvik (2007).*

Ara Group

The evaporite-carbonate sequences of the Terminal Neoproterozoic-Early Cambrian (547-540 Myr) Ara Group, up to 1700 m thick, lies in a belt of salt basins in the interior of the sultanate of Oman (Mattes & Conway Morris, 1990; Bowring *et al.*, 2007). It belongs to the Huqf Supergroup, build up during Cryogenian and the Early Cambrian (725- 540 Myr) and subdivided by three groups: the glacial sedimentary Abu Mahara Group, the Nafun Group (cap carbonates then shelf clastics and carbonates) and finally the Ara Group (Gorin *et al.*, 1982; Bowring *et al.*, 2007). At the end of the Neoproterozoic, Oman is on the Arabian-Nubian shield, one of the blocks accreted on the North-Eastern margin to form Gondwana at equatorial latitudes (Fig.3.23, Millson *et al.* 1996; Allen 2007). The large sediment accumulation in these precambrian basins has been thereby allowed by the last pulse of the consequential Pan-African orogenic collision between Africa/Arabia creating extension zones (grabbens, Mattes & Conway Morris 1990; Allen 2007).

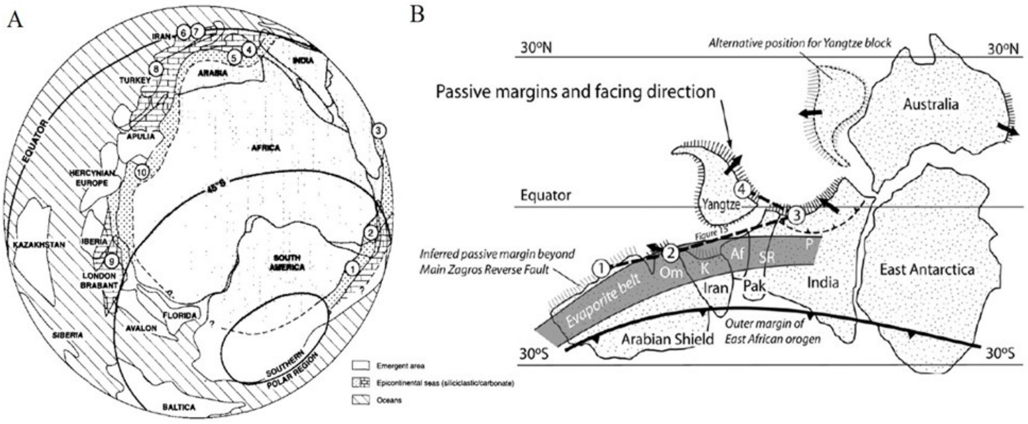

Figure 3.23 : *(A) Paleogeographic reconstruction of the Mid-Cambrian, the numbers corresponding to the references from which have been extracted the continental margins setting. Figure from Millson et al. (1996) and references therin.; (B) Location of the Evaporite Belt on the eastern Gondwanan terranes, 1: Alborz Mountains of northern Iran, 2: Oman, 3: Lesser Himalayas, 4: South China, Om: Oman, K: Kerman area of central Iran, Af: Afghanistan, Pak: Pakistan, SR: Salt Range, P:Punjab. Figure from Allen (2007).*

Afterwards, the Ara group deposition was enabled by the turn of a passive margin basin to a retro-arc basin because of a subduction onset of the Proto-Thethyan ocean floor along the former passive continental margin in the Northern-Eastern Gondwana, trapping Oman between the subduction and the East-African Orogen (Allen, 2007). A large and thick latitudinal evaporite belt could be thereby set up along the Arabian Shield (and the eastern neighbouring blocks such as Iran, Pakistan or India) in this context by repeated flooding episodes (glacio and tectono-eustatism) and by tectonic subsidence (Schröder *et al.*, 2003; Allen, 2007; Bowring *et al.*, 2007).

3.6.c Fluid inclusions in primary halites: geochemical memory of paleo-oceans

Identification of marine primary halites and their fluid inclusions to reconstruct the ocean paleo-chemistry

To examine fluid inclusions in halites as a geochemical fingerprint of ancient oceans, various criteria have to be respected to firstly determine the marine character of the halites samples and secondly assess the viability of the brine inclusions (Hardie, 1984; Horita *et al.*, 1996; Lowenstein, 2001; Timofeeff *et al.*, 2001; Zimmermann, 2001; Horita *et al.*, 2002; Lowenstein *et al.*, 2014). First of all, these minerals have to be sampled just above the last evaporites preceding the NaCl deposition in the evaporitic sequence, so just above the gypsum and anhydrite (calcium sulphates) layers (Fig.3.16). The salts are consequently and crucially supposed to be a product of the least altered brine near a seawater inlet in basins and supposed to preserve a marine signature, signal also supported by the associated non-evaporitic deposits, the surrounding stratigraphy or palaeontology. In addition, these evaporitic basins must also be devoided of any tectonic activity after their deposition, diagenesis and its associated fluid circulation, metamorphism, presence of carbonate platform (that might cause chemistry changes in the brines with dolomitization) and detrital supply (Hardie, 1984; Timofeeff *et al.*, 2001; Horita *et al.*, 2002; Lowenstein *et al.*, 2014).

In more details, the sampled halites must display some mineralogical and geochemical features typical of marine deposits. Primary salt layers are crystallographically characterized by cumulate cubic and hopper crystals (resulting from the development of NaCl floating crystals – or rafts – at the air-brine interface prior to sink, with a rapid growth rate providing numerous fluid inclusions) and bottom-grown crust showing chevrons structures (alternating bands rich in inclusions, with a cloudy aspect, and bands poor in single-phase brine inclusions, with a clear aspect) , picturing perennial depositional and subaqueous conditions without perturbations, redissolution or recycling (Horita *et al.*, 1996, 2002; Timofeeff *et al.*, 2006; Lowenstein *et al.*, 2014). Additionally, geochemical and isotopic features provide further indicators to discriminate marine and non-marine origins of the NaCl salt, such as Br concentration due to its long residence time of 100 Myr (Taberner *et al.*, 2000; Siemann, 2003; Brennan *et al.*, 2013; Holt *et al.*, 2014), ^{87}Sr/^{86}Sr (Stein *et al.*, 2000; Kloppmann *et al.*, 2001;

Paris *et al.*, 2010b), δ^{11}B (Vengosh *et al.*, 1992; Liu *et al.*, 2000; Kloppmann *et al.*, 2001; Paris *et al.*, 2010b), δ^{34}S (Stein *et al.*, 2000), δ^{37}Cl (Eggenkamp *et al.*, 1995; Eastoe *et al.*, 2001, 2007; Eggenkamp *et al.*, 2019a), as well as chemical (Lowenstein, 2001; Timofeeff *et al.*, 2001; Zimmermann, 2001; Horita *et al.*, 2002; Brennan *et al.*, 2013) and isotopic (δ^2H and δ^{18}O, Knauth & Beeunas 1986; Horita 1990; Yang *et al.* 1995; Rigaudier *et al.* 2011) compositions of the brine inclusions. Especially, fluid inclusions in halites are considered as the best and reliable witnesses of the brine in which the mineral has crystallized.

The major elements chemistry in the brine inclusions can thus reflect this syn-depositionnal recycling, with marine or non-marine water inflows dissolving the pre-existing evaporite and changing consequently the chemistry of seawater derived parent brine and leading to increasing concentrations of Na^+, Cl^-, K^+ and Mg^{2+} (Timofeeff *et al.*, 2001, 2006). Any evidence of such phenomenon that alter the primary character of the halites must discard the salt layers from the studies. But, without petrographic evidence of secondary precipitation, it is difficult to truly exclude recycling or water inflows modifying the parent brine chemistry. To dispel the doubts, the major ion chemistry of one fluid inclusion have to follow an evaporation curve ($[Na^+]$ vs $[Cl^-]$ or $[Mg^{2+}]$ vs $[Cl^-]$ for example) built from the set of fluid inclusions of the entire sample. Any inclusion outside of this curve probably derives from a modified brine (Zimmermann, 2001; Timofeeff *et al.*, 2001). Furthermore, if the comparison of these plots (adding also other elements like $[SO_4^{2-}]$ or $[K^+]$) between different basins with the same age indicates identical evaporation paths, the brine inclusions derive from a same parent brine with a uniform chemical composition, which is very likely the paleo-seawater. As a validation, brine inclusions in modern halites are consistent with data and theory for the compositional evaporation path from seawater with present-day chemical composition (Fig.3.24, Lowenstein 2001; Timofeeff *et al.* 2001; Bąbel & Schreiber 2014). Thereby it was demonstrated that Permian and late Precambrian seawaters were close to the modern ocean chemistry, whereas Cambrian, Silurian and Cretaceous seawaters shared the same ocean chemistry but different from today's (Lowenstein, 2001; Horita *et al.*, 2002). Different geological periods were subsequently studied more closely: Neoproterozoic (Spear *et al.*, 2014), early Cambrian (Brennan *et al.*, 2004), Silurian (Brennan & Lowenstein, 2002), Devonian (Horita *et al.*, 1996), Carboniferous (Holcomb *et al.*, 2014), Permian (Lowenstein *et al.*, 2005), Cretaceous (Timofeeff *et al.*, 2006) and the last 36 Myr (Brennan *et al.*, 2013).

Seawater paleo-chemistry reconstruction from the halite samples

As demonstrated in the figure 3.24 and explained just above, the offset in chemical composition between fluid inclusions in ancient primary halites and the evaporation path of present seawater, supported by modern halites, highlights that the chemistry of the parent seawater was different across the geological times.

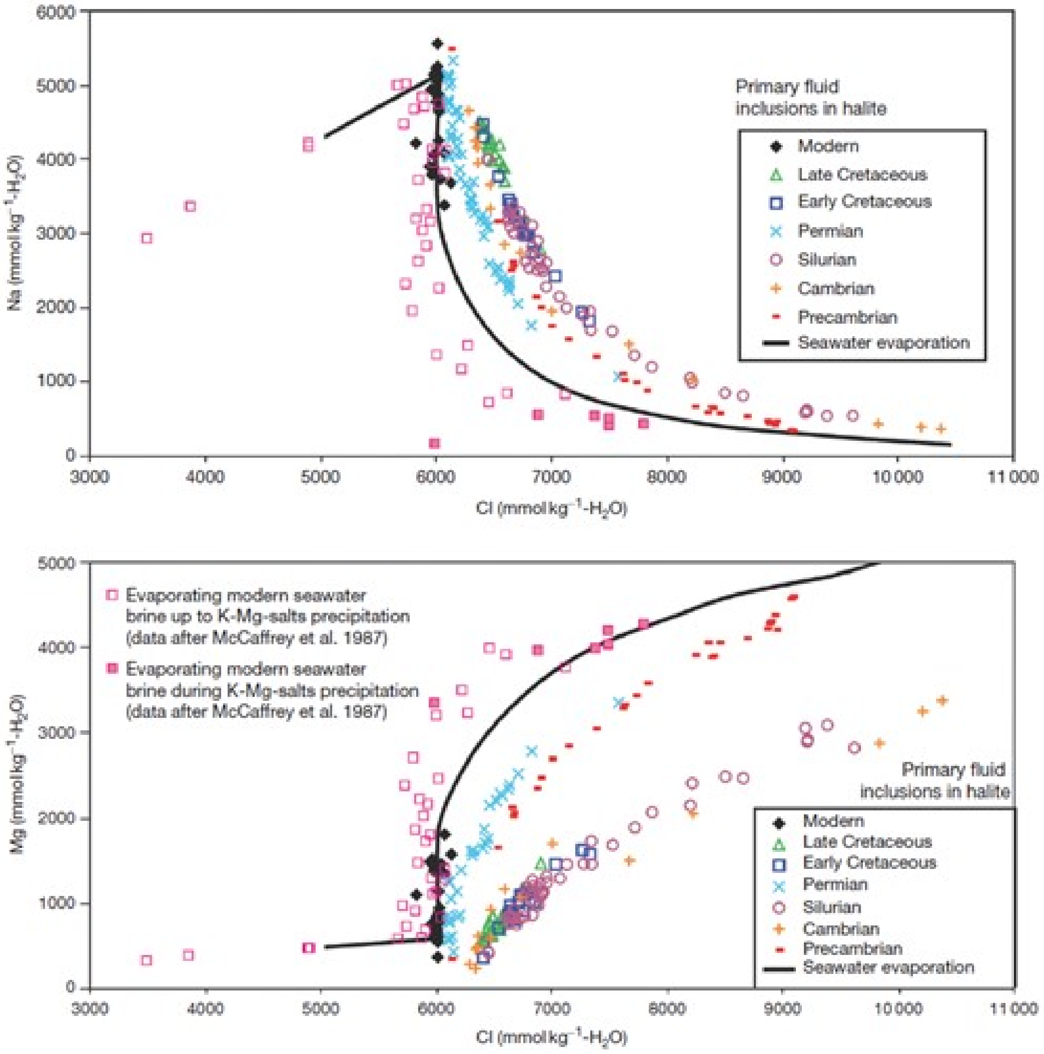

Figure 3.24 : *Na^+, Mg^{2+} and Cl^- concentrations of individual primary fluid inclusions in: modern and ancient halite samples (Lowenstein, 2001), measured in an evaporating seawater (pink squares, McCaffrey et al. 1987) and theoretically determined alongside a computed evaporation path of a modern seawater (black line, Harvie et al. 1984). The drop of [Na^+] and the rise of [Mg^{2+}] at 6000 mmol.kg^{-1} H_2O marks the precipitation onset of NaCl salt, whereas [Cl^-] increases due to its initial level higher than [Na+] in modern and ancient oceans . The [Cl-] threshold at 10 500 mmol.kg^{-1} H_2O characterizes the initiation of the precipitation of the Mg-K potash salts. (Figure from Bąbel & Schreiber 2014, modified from Lowenstein 2001).*

Initially, the degree of evaporation (DE) can be estimated from conservative elements such as Li, B or Br. Particularly, the concentration of bromine in seawater did probably not fluctuate during the Phanerozoic due to its long residence time (100 Myr) and its present-day concentration can therefore be used at any geological period to estimate the DE, according to:

$$DE_{Br} = (M_{Br})_{FluidInclusion}/(M_{Br})_{Seawater} \tag{3.5}$$

with M in mmol.kg^{-1} H_2O. On this basis, Horita *et al.* (2002) showed that the K^+ concentration of seawater did not evolve across the Phanerozoic (11 mmol.kg^{-1} H_2O) and proposed that this element be also used to reconstruct the DE all through the halite precipitation stages, given that potassium is not involved in the precipitation of carbonates and calcium sulphates or in dolomitization processes (Fig.3.16). This naturally implies to exclude brine inclusions exhibiting saturation in respect with Mg-K potash minerals (Fig.3.24). [Mg^{2+}] of seawater can then be calculated from [Mg^{2+}] in fluid inclusion and the calculated DE following the equation 3.5. Concerning calcium and sulphate concentrations, numerous studies pointed out that the brine inclusions were depleted in either one or the other because of the precipitation of $CaSO_4$ salts, consuming the less abundant of the two ions, while carbonate precipitation is assumed to have a negligeable impact on [Ca^{2+}] in fluid inclusions, representing today a loss of only 10 % (Horita *et al.*, 2002; Brennan & Lowenstein, 2002; Lowenstein *et al.*, 2005; Timofeeff *et al.*, 2006; Brennan *et al.*, 2013; Holt *et al.*, 2014). These authors thereby demonstrated that that [Ca^{2+}] and [SO_4^{2-}] oscillated during the geological times, in concordance with the alternation of $MgSO_4$ and KCl evaporites in the sedimentary record, which precipitated respectively in "MgSO4" and "$CaCl_2$" seas. [Ca^{2+}] or [SO_4^{2-}] thus estimated with the DE from brine inclusions do not represent seawater concentrations but the residual concentration after $CaSO_4$ crystallisation and must be consequently corrected using:

$$Ca_{Fluid\ Inclusion} = Ca^{2+}_{seawater} - (SO^{2-}_{4\ seawater} + HCO_3^-) \tag{3.6}$$

$$SO_{4\ Fluid\ Inclusion} = SO^{2-}_{4\ seawater} - (SO^{2-}_{4\ seawater} + HCO_3^-) \tag{3.7}$$

The consumed component can be derived from (Ca^{2+})(SO_4^{2-}), the saturation degree of anhydrite $CaSO_4$, whilst the HCO_3^- concentration is disregarded due to its low levels compared to the other elements (2.5 mmol.kg^{-1} H_2O). This anhydrite saturation degree in ancient seawater is supposed to be between 0.5 and 1.5 times (150-450 (mmol.kg^{-1} $H_2O)^2$) that in modern ocean, 319 (mmol.kg^{-1} $H_2O)^2$, assuming that seawater salinity did not significantly change (Hay *et al.*, 2006). As the excess of one element relative to the other and the boundaries of (Ca^{2+})(SO_4^{2-}), are defined, [Ca^{2+}] and [SO_4^{2-}] ranges can be restricted and formulated with a value derived from the modern (Ca^{2+})(SO_4^{2-}) more and less a value derived respectively from 0.5(Ca^{2+})(SO_4^{2-}) and 1.5(Ca^{2+})(SO_4^{2-}) (Brennan & Lowenstein, 2002; Horita *et al.*, 2002; Lowenstein *et al.*, 2005; Brennan *et al.*, 2013; Holt *et al.*, 2014). The chlorinity (565 mmol.kg^{-1}) and the salinity are considered constant through the Phanerozoic (565 mmol.kg^{-1}), allowing to assess the Na^+ concentration (Brennan & Lowenstein, 2002; Horita *et al.*, 2002; Lowenstein *et al.*, 2005; Brennan *et al.*, 2013; Holt *et al.*, 2014), following the charge balance equation:

$$Na^+ = Cl^- + 2(SO_4^{2-}) - K^+ - 2(Mg^{2+}) - 2(Ca^{2+}) \tag{3.8}$$

However, if dolomitization occurred in the studied basin, the recrystalized carbonate is more enriched in magnesium and less in calcium, which impacted accordingly the brine chemistry during NaCl precipitation (Horita *et al.*, 1996; Brennan & Lowenstein, 2002). The magnesium and calcium concentrations of seawater reconstructed from the brine inclusion chemistry thus represent only respectively a lower and an upper limit, and result in a lower limit for the Mg/Ca ratio. The upper limit of [Mg^{2+}] is approximated using the Mg/Ca value at which the calcitic sea switches to aragonitic sea (1.5-2 mol/mol), and provides a degree of dolomitization to also identify the lower limit of [Ca^{2+}] (Horita *et al.*, 2002). This reconstruction is only possible for halites which have been crystallized in calcitic sea because there is no upper threshold for aragonitic seas, as during Jurassic, Devonian and Silurian (Horita *et al.*, 2002). Finally, as a verification, the evaporation path of the paleo-seawater has been reconstructed with a computer program (Harvie *et al.*, 1984; Risacher & Clement, 2001) that fits the chemistry of the fluid inclusions with the modelled path of evaporation from the calculated seawater chemical compositions (Brennan & Lowenstein, 2002; Horita *et al.*, 2002; Lowenstein *et al.*, 2005; Timofeeff *et al.*, 2006; Brennan *et al.*, 2013; Holt *et al.*, 2014).

3.6.d $\delta^{11}B_{sw}$ across the Phanerozoic: state of the art

Knowing $\delta^{11}B_{sw}$ as precisely as possible is crucial for palaeoceanographic and paleoclimatic reconstructions at high frequency. Indeed, a $\delta^{11}B_{sw}$ difference of 1 ‰ induces a deviation of 0.1 pH units, which is the magnitude for the Anthropocene ocean acidification (Orr *et al.*, 2005), whereas glacial/interglacial transitions impacted ocean pH by 0.2 units (Hönisch *et al.*, 2009). Different methods have been used to assess the paleo- $\delta^{11}B_{sw}$ values.

Originally, Spivack *et al.* (1993) assumed that δ^{11}B in pore fluids of a marine sediment core could be interpreted as the boron isotopic ratio of seawater. They estimated for the last 21 Ma a $\delta^{11}B_{sw}$ approximatively constant around 34 ± 1.5 ‰. But marine sediments are the seat of fluid circulations and the δ^{11}B of pore fluids rather records boron isotope fractionation between seawater and clays through preferential adsorption of $B(OH)_4^-$ (Spivack *et al.*, 1987; Ishikawa & Nakamura, 1993; Gaillardet & Lemarchand, 2018).

In the early 2000s, Lemarchand *et al.* (2000, 2002b) updated the modern continental boron flux to the oceans by analysing the world's main rivers covering 40 % of the world water discharge. Firstly, they balanced the oceanic boron budget, defined a mean δ^{11}B for rivers, assessed that continental weathering is the main source of boron and subsequently refined its residence time (14 Myr), previously estimated at 20 Myr (Spivack & Edmond, 1987). With these breakthroughs and previous estimations of the others boron fluxes in literature, their corresponding B isotope fractionation and their fluctuations through time, the changes of $[B]_{sw}$ and $\delta^{11}B_{sw}$ during the last 100 Ma have been modelled with two mass balance equations, one for the total B mass and one for the B isotopic budget. These authors finally showed that $\delta^{11}B_{sw}$ increased by 0.1 ‰/Myr over the last 100 Myr, with a variation magnitude of 5 ‰. More precisely, three periods were identified: around 110-118 Myr, δ^{11}B$_{sw}$ increased from 39.5 to 42.5 ‰, then decreased to 37 ‰ at the Early Cenozoic (60 Myr), and increased again to achieve the modern value of 39.6 ‰. Demonstration of the large impact of the weathering processes on the boron mass budget, this last variation is due to the Himalaya formation during the Cenozoic, delivering to the oceans a large amount of sediments and accordingly promoting boron adsorption on clays, with a preferential incorporation of B(OH)$_4^-$ (Palmer *et al.*, 1987). Lemarchand *et al.* (2002b) reaffirmed that keeping δ^{11}B$_{sw}$ constant is not sustainable for paleo-pH reconstructions beyond 1 Myr. Simon *et al.* (2006) refined the model, re-investigating oceanic crust production rate, seawater-crust ratio and the residence time of boron, combining temperature and porosity profiles wih B distribution coefficients and isotope fractionation factors during water-rock interactions at oceanic ridges. They proposed respectively a crust production rate of 3 cm.yr^{-1}, a seawater-crust ratio between 1-3 and a B residence time of 10 Myr to fulfill the steady state budget of B in seawater and moderated the utilisation of δ^{11}B$_{carb}$ as a paleo-pH proxy, pointing out strong variations in the δ^{11}B$_{sw}$ (between 30 and 50 ‰) due to changes in oceanic crust permeability, varying expansion rate and closure time of the hydrothermal systems. However their model considered constant B input and output fluxes, which is not realistic.

A third approach has been extensively applied, based on the difference in δ^{11}B$_{carb}$ for contemporaneous planktonic foraminifera living at different depths. The resulting Δ^{11}B, coupled to the assumed surface-to-deep pH gradient (ΔpH$_{sw}$), allows to recover a unique plausible δ^{11}B$_{sw}$ value. This approach overcomes the problem of depending on faithful pH values to reconstruct δ^{11}B$_{sw}$ from δ^{11}B$_{carb}$ but makes a strong assumption on the pH gradient and depth at which planktonic foraminifera species lived, that can vary somehow. Using this method, Palmer *et al.* (1998), could reconstruct that δ^{11}B$_{sw}$ increased from 37.7 ± 0.6 ‰ in the middle Miocene (15.2-16.2 Myr) to 39.6 ± 2.26 ‰ during Pleistocene (85 kyr), assuming constant temperature and pH gradients in the upper water column. Pearson & Palmer (1999) refined this methodology for Eocene-aged planktonic foraminifera. They enhanced the pH gradient with assessments on the biological productivity and proposed the value of 40.6 ‰ for the boron isotopic ratio of seawater at 43 Myr. From a broader perspective, Pearson & Palmer (2000) extended the δ^{11}B$_{sw}$ determination for the last 60 Myr however with a gap between 40 and 23 Myr: δ^{11}B$_{sw}$ remained constant between 60 and 42 Myr (39.40 ‰), then decreased towards 16 Ma (37.70 ‰), remained constant again between 16 and 12 Ma and lastly increased to achieve 39.10 ‰ 85 kyr ago.

Foster *et al.* (2012) instead used benthic foraminifera for the middle Miocene with a constant pH gradient in the first place, leading to a δ^{11}B$_{sw}$ of $37.6^{+0.4}_{-0.5}$ ‰. In a second place, they attempted to reconstruct this pH gradient with the δ^{13}C measured in the planktonic and benthic foraminifera. The δ^{13}C and pH gradients are both controlled by the weakening of the biological pump with depth and are therefore well correlated. They proposed a δ^{11}B$_{sw}$ of $38.0^{+0.1}_{-0.1}$ ‰ and finally averaged these two values to 37.82 ± 0.35 ‰ for the Miocene.

Later, Anagnostou *et al.* (2016) implemented this nonlinear surface-to-deep $\delta^{11}B_{borate}$-pH relationship approach, defining two boundaries to constrain $\delta^{11}B_{sw}$ in the early Cenozoic (in five periods of time from 53.2 to 36.9 Myr). The upper $\delta^{11}B_{sw}$ threshold was determined from the lowest $\delta^{11}B_{carb}$ of seventeen foraminifera species at 39.5 ‰. For the lowest $\delta^{11}B_{sw}$ value, the modern surface-to-deep pH gradient was considered as the minimum gradient in Eocene, supported by a larger δ^{13}C gradient between surface and deep-dwelling foraminifera due to a more active biological pump under hotter climate (Foster *et al.*, 2012). From the smallest $\delta^{11}B_{carb}$ difference at 53.2 Myr and the smallest pH gradient, they were able to determine the lower threshold $\delta^{11}B_{sw}$ at 38.2 ‰, or 38.6 ‰ if the shift between the $\delta^{11}B_{carb}$ of these extinct foraminifera species and $\delta^{11}B_{borate}$ due to vital effects is taken into account. Moreover, they further enhanced their own $\delta^{11}B_{sw}$ upper limit for each of the five ages in this Eocene interval, by compiling dissolved inorganic carbon (DIC) profiles between the deepest and the shallowest-dwelling planktonic foraminifera with carbonate chemistry modelling, and varying the $\delta^{11}B_{sw}$ between 38.2 ‰ and 39.6 ‰, the modern value. They finally propose a $\delta^{11}B_{sw}$ upper thershold at 38.8 ‰ at 45.6 Ma and 39.9 ‰ at 40.3 Myr. Ultimately, Greenop *et al.* (2017) also used δ^{13}C and δ^{11}B of benthic and planktik foraminifera, and two carbon cycle box models to determine the most plausible oceanic δ^{13}C versus pH gradient relationship and reconstruct $\delta^{11}B_{sw}$ for the entire Neogene. Their estimation conforms to the limits of Lemarchand *et al.* (2000)'s model and the higher frequencies oscillations of Raitzsch & Hönisch (2013), except for the first part of Miocene. Between 23 et 15 Myr, $\delta^{11}B_{sw}$ continues to decrease from 37.9 ± 1 ‰ to 37.7 ± 1 ‰, whereas the Raitzsch & Hönisch (2013)'s $\delta^{11}B_{sw}$ value at this time increases. Another approach was developped by Raitzsch & Hönisch (2013) for the whole Cenozoic from the $\delta^{11}B_{carb}$ of benthic foraminifera from two different oceans (Atlantic and Pacific) and embracing different depths. Deep-sea pH was kept constant through time, while sea-surface pH was modelled, but with a constant surface-deep gradient of 0.3. The resulting $\delta^{11}B_{sw}$ increases over the last 50 Myr by 3 ‰, with three oscillations (peaks at: 47 Ma with ≈ 38.7 ‰, 24 Ma with ≈ 39.6 ‰, and 5 Ma with ≈ 39.9 ‰) that were not recognized before; Lemarchand *et al.* (2002b) having proposed a constant $\delta^{11}B_{sw}$ rise over this period. .

All these studies follow the same $\delta^{11}B_{sw}$ trends and provide a robust pattern for the secular variation of $\delta^{11}B_{sw}$ during the Cenozoic. Pearson *et al.* (2009) applied $\delta^{11}B_{sw}$ = 37-39 ‰ (Lemarchand *et al.*, 2002b) for their pCO$_2$ reconstruction at the Eocene-Oligocene transition and revealed a good agreement with the literature by using a $\delta^{11}B_{sw}$ value of 38 ‰. Martínez-Botí *et al.* (2015a) extrapolated $\delta^{11}B_{sw}$ between the modern value and the Foster *et al.* (2012)'s value at the middle Miocene for pCO$_2$ estimations in the Plio-Pleistocene, leading to a $\delta^{11}B_{sw}$ value of 39.2 ‰ at 3 Myr, consistent with the previous data. Gutjahr *et al.* (2017) combined Earth system modelling to establish the surface pH of Northeast Atlantic just before the onset of the Paleocene-Eocene Thermal Event (PETM) and their foraminifera data without any vital effect correction to estimate a $\delta^{11}B_{sw}$ at 38.94 ± 0.41 ‰, in agreement with the Eocene $\delta^{11}B_{sw}$ of Anagnostou *et al.* (2016). By applying a vital effect calibration, the value falls to 37.6 ± 0.5 ‰. Finally, Henehan *et al.* (2019) restricted $\delta^{11}B_{sw}$ between 39.05 and 39.85 ‰ during the Cretaceous-Paleogene transition.

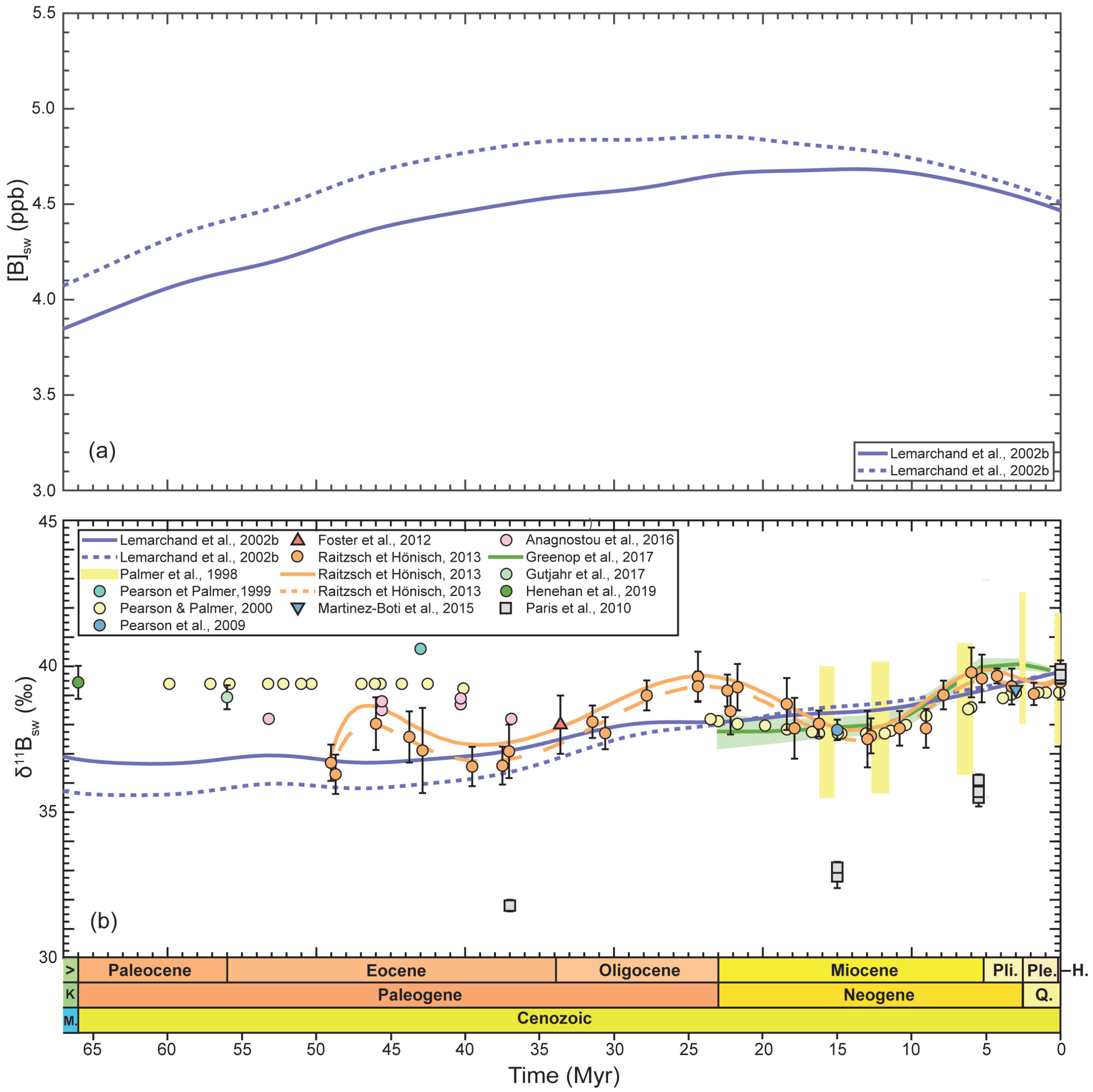

Figure 3.25 : *Data compilation of seawater boron concentrations (a) and isotopic compositions (b) across the Cenozoic. Lines are for models and calculations from foraminifera data (Lemarchand et al., 2002b; Raitzsch & Hönisch, 2013; Greenop et al., 2017), this study); circles, triangles and yellow areas for determinations from foraminifera studies (Palmer et al., 1998; Pearson & Palmer, 1999, 2000; Pearson et al., 2009; Foster et al., 2012; Raitzsch & Hönisch, 2013; Martínez-Botí et al., 2015a; Anagnostou et al., 2016; Gutjahr et al., 2017; Henehan et al., 2019); ; squares for halite data (Paris et al. 2010b, this study). Blue dotted line: variable runoff (Lemarchand et al., 2002b), blue solid line: variable runoff (Lemarchand et al., 2002b), variable pH from foraminifera with fractionation factor=1.0272 (Raitzsch & Hönisch, 2013), orange solid line: variable pH from foraminifera with fractionation factor=1.020 (Raitzsch & Hönisch, 2013).*

Only few studies focused on $\delta^{11}B_{sw}$ beyond 65 Myr, but they pursued the same approaches, modelling ocean B budgets calibrated from $\delta^{11}B$ of marine biocarbonates. To go further in Phanerozoic, calcite brachiopods shells are studied, corals and foraminifera becoming more limited in the sedimentary records (Schiebel & Hemleben, 2017). Brachiopods present many advantages: they emerged during the Cambrian Explosion, survived different extinctions (Carlson, 2016), present a significant fossil record (Veizer *et al.*, 1999; Vollstaedt *et al.*, 2014) and their low Mg-calcite shells have been particularly well preserved, thus preserving the primary geochemical signals (Brand & Veizer, 1980, 1981), among which δ^{11}B$_{carb}$ that can also be used to deduce ocean pHs (Lécuyer *et al.*, 2002; Penman *et al.*, 2013; Jurikova *et al.*, 2019). Joachimski *et al.* (2005) measured low δ^{11}B$_{carb}$ values of Silurian, Devonian, Carboniferous and Permian brachiopods that could not only reflect ancient oceanic pH at these times (unrealistic pH considering the carbonate system as a buffer), but also a change of the δ^{11}B$_{sw}$. They completed the modelled δ^{11}B$_{sw}$ secular variation of Lemarchand *et al.* (2002b), with a constant and a variable continental boron flux, for the Palaeozoic and the beginning of the Mesozoic, and showed three oscillations across this period, within a range between 31 and 42 ‰. Using these δ^{11}B$_{sw}$ values to reconstruct the δ^{11}B$_{carb}$ curve together with the pH-dependent calibration between pH and δ^{11}B$_{carb}$ of modern brachiopod calcite from Lécuyer *et al.* (2002) they found a quite good agreement with their sample δ^{11}B$_{carb}$. Concomitantly, Simon *et al.* (2006) measured Cretaceous brachiopod δ^{11}B$_{carb}$ values similar to modern shells and mentioned an oceanic boron composition close to nowadays at this time. In the same way, by assuming a pre-event pH of 7.8 and 7.7 following Ridgwell (2005), Jurikova *et al.* (2020) and Müller *et al.* (2020) suggested two δ^{11}B$_{sw}$ values respectively for the Permian-Triassic boundary (PTB) and for the Toarcian Oceanic Anoxic Event (T-OAE, Early Jurassic), with a vital effect corrected from Lécuyer *et al.* (2002) and without correction (δ^{11}B$_{Brachiopod}$ = δ^{11}B$_{Borate}$). PTB exhibited thereby δ^{11}B$_{sw}$ between 35 and 38 ‰ whereas T-OAE δ^{11}B$_{sw}$ were between 36.6 and 38.9 ‰.

Kasemann *et al.* (2010) and Ohnemueller *et al.* (2014) reconstructed Neoproterozoic oceanic paleo-pH profiles by analysing shallow marine inorganic carbonate section crossing the Sturtian and Marinoan glaciations ("Snowball Earth", 720-650 and 650-635 Myr) and their post-glacial transitions. These carbonates (cap carbonates) consisted in dolostone or limestone with different particles sizes precipitated in a shallow marine platform or a deeper-marine slope and exhibited no evidence of secondary alteration or recrystallisation. The average δ^{11}B$_{carb}$ value of only 4 ‰ in Kasemann *et al.* (2010) involved an equilibrium with a Cryogenian seawater with a δ^{11}B of 25 ‰, whereas Ohnemueller *et al.* (2014) suggested a value of 20.5 ‰ for the Marinoan deglaciation stage at 635 Myr, applying Equation 3.2 with an hypothesis on the pre-Cambrien pH value. These values are reasonable in the light of Joachimski *et al.* (2005)'s Paleozoic δ^{11}B$_{sw}$ trend. Similarly, Clarkson *et al.* (2015) worked on a shallow marine platform carbonates succession from the Late Permian to Early Triassic to evaluate ocean acidification during the Permo-Triassic mass extinction. They modelled atmospheric pCO$_2$ and oceanic pH by combining carbonate and silicate weathering, pyrite deposition, marine changes in calcification coupled with CO$_2$ and SO$_2$ perturbations (terrestrial and marine carbon burial, Siberian traps volcanism and contact metamorphism) and suggested two possible values of $\delta^{11}B_{sw}$, 34 and 36.8 ‰, to reproduce their $\delta^{11}B_{Carb}$ data.

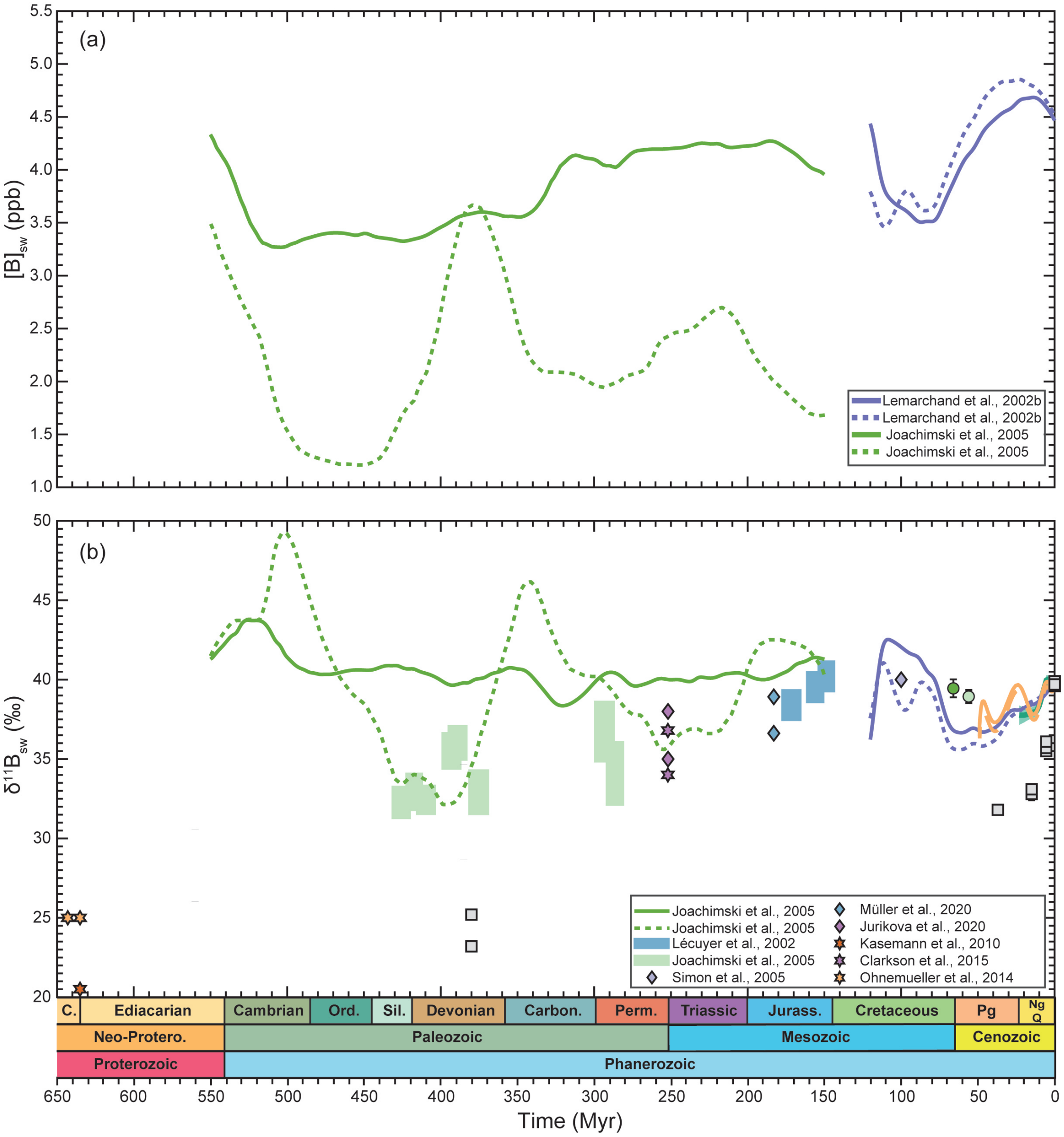

Figure 3.26 : *Data compilation of seawater boron concentrations (a) and isotopic compositions (b) across the Phanerozoic. Lines are for models and calculations from foraminifera data (Lemarchand et al., 2002b; Joachimski et al., 2005; Raitzsch & Hönisch, 2013; Greenop et al., 2017); diamonds and rectangles from brachiopod data (Lécuyer et al., 2002; Joachimski et al., 2005; Simon et al., 2006; Müller et al., 2020); stars from inorganic carbonate data (Kasemann et al., 2010; Ohnemueller et al., 2014; Clarkson et al., 2015); and squares for halite data (Paris et al., 2010b) in grey. Blue dotted line: variable runoff (Lemarchand et al., 2002b), blue solid line: constant runoff (Lemarchand et al., 2002b), green dotted line: variable continental input (Joachimski et al., 2005), green solid line: constant continental input (Joachimski et al., 2005) variable pH from foraminifera with fractionation factor=1.0272 (Raitzsch & Hönisch, 2013), orange solid line: variable pH from foraminifera with fractionation factor= 1.020 (Raitzsch & Hönisch, 2013).*

Marginally, hydrothermally altered oceanic rocks may record the boron isotopic composition of seawater. Under a high water/rock ratio, their δ^{11}B is mainly controlled by the pH and δ^{11}B$_{sw}$ and a strong Rayleigh effect is avoided. In a similar way to brachiopod shells, Simon *et al.* (2006) showed that modern seafloor and Cretaceous ophiolitic peridotites share the same range of δ^{11}B, testimony of a Cretaceous ocean δ^{11}B around 40 ‰, as today.

3.6.e XRD diffractograms

3.6.f Models

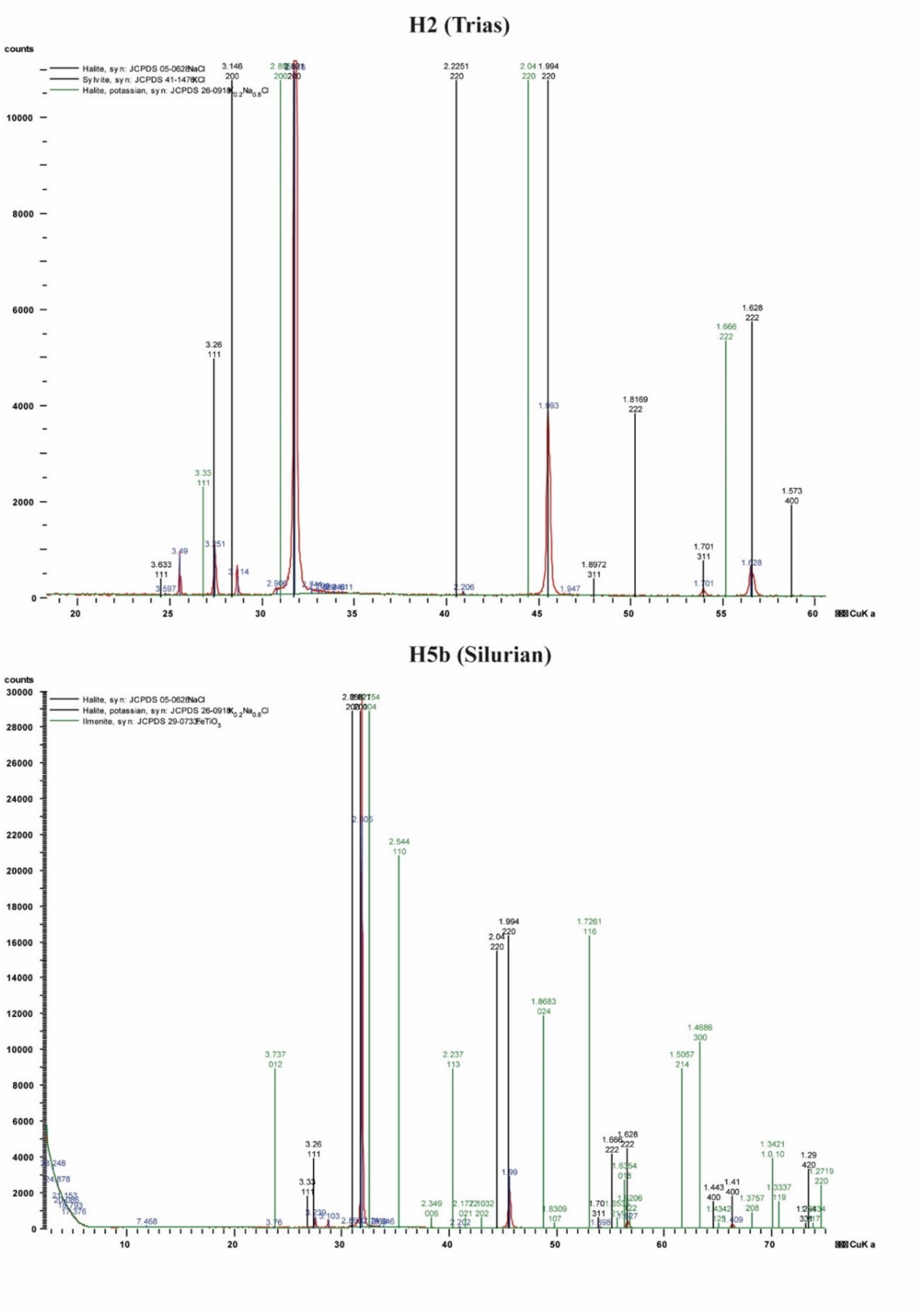

Figure 3.27 : *Diffractograms of the Triassic sample Keuper and the Silurian sample Car12-3-3 showing in addition to halite, traces of potassic halite, sylvite (KCl) and especially the presence of ilmenite (Fe and Ti oxide), an accessory mineral in alluvial deposits.*

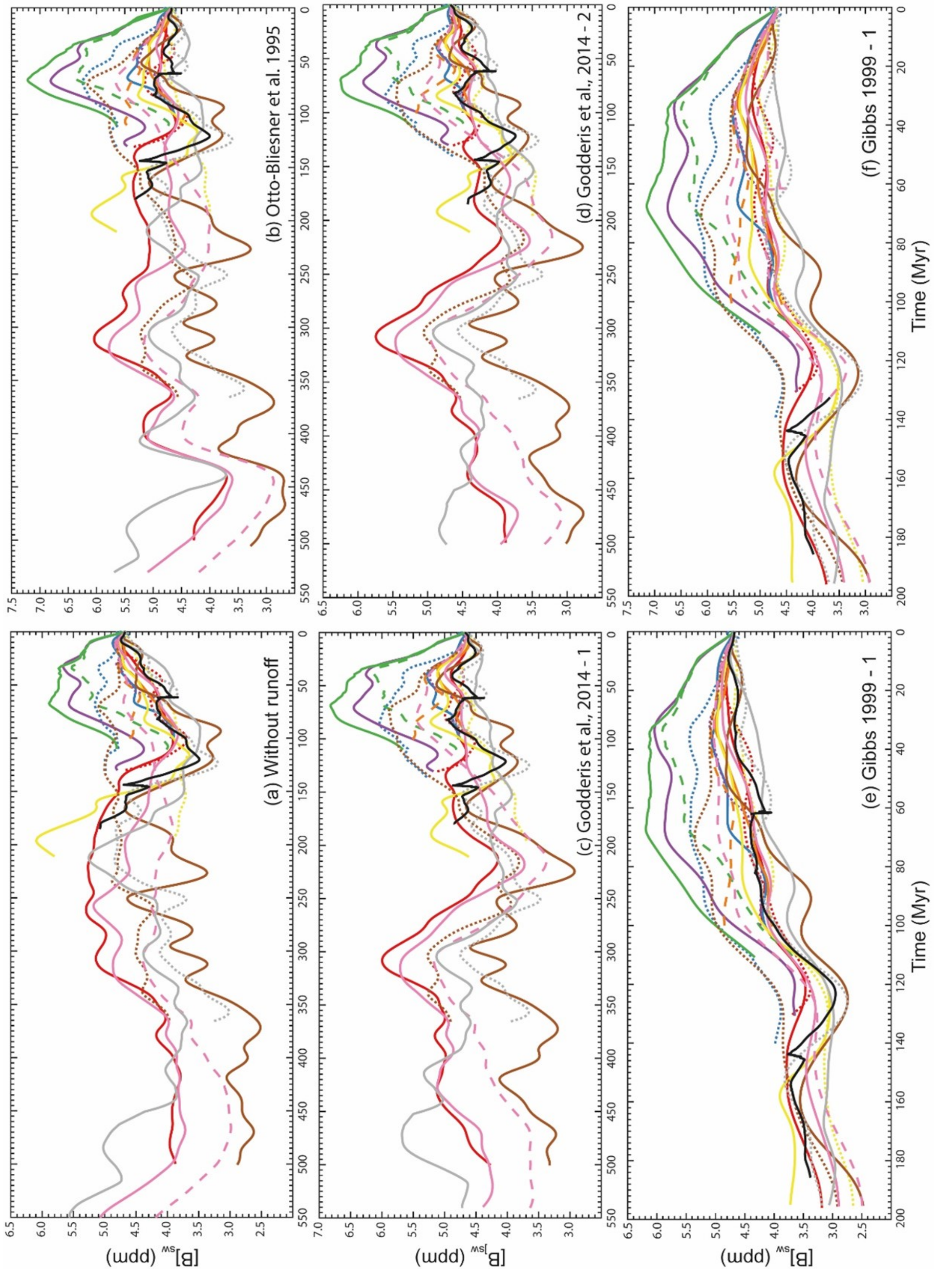

Figure 3.28 : *Reconstruction of the boron concentration of seawater with varying runoff (Otto-Bliesner, 1995; Gibbs, 1999; Goddéris et al., 2014) and varying oceanic crust production.*

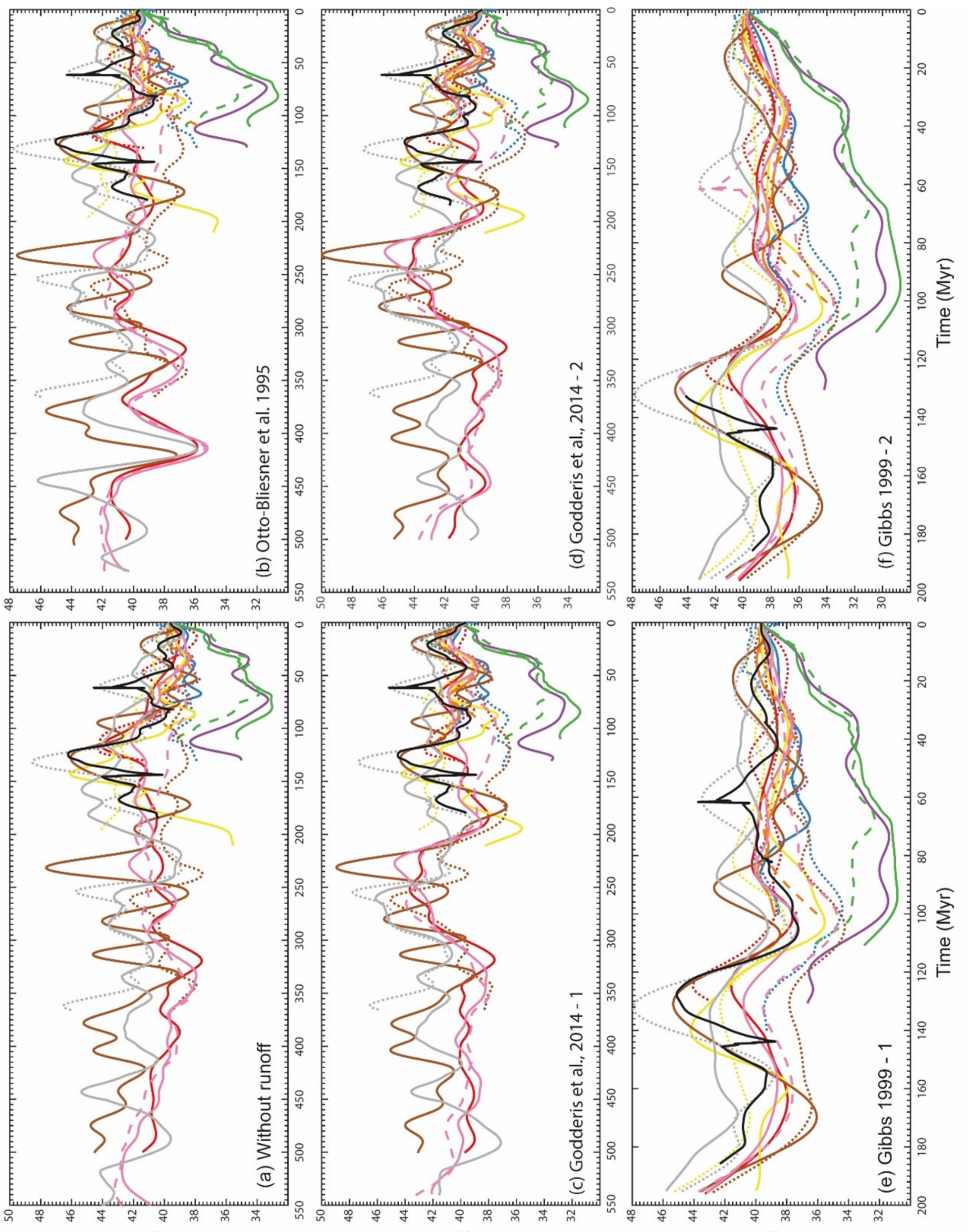

Figure 3.29 : *Reconstruction of the boron isotopic ratio of seawater with varying runoff (Otto-Bliesner, 1995; Gibbs, 1999; Goddéris et al., 2014) and varying oceanic crust production.*

CHAPTER 4

THE µ-DDIHEN SETUP

Sommaire

Avant-propos : analyse des isotopes du bore 90
  Le MC-ICP-MS Neptune 90
  L'injection directe 92
  Le µ-dDIHEN 93
4.1 Introduction 95
4.2 Material and methods 96
  4.2.a The µ-dDIHEN liquid introduction system 96
  4.2.b Interfacing ICP-MS with the µ-dDIHEN introduction system 97
  4.2.c ICP-MS measurements 98
  4.2.d Reagents and sample preparation 98
4.3 Results and discussion 100
  4.3.a Uptake rate, stabilization time, reproducibility of the injections and sensitivity 100
  4.3.b Boron isotope ratio measurements by MC-ICP-MS 103
  4.3.c Multi-element analysis by HR-ICP-MS 106
  4.3.d Au nanoparticles characterization by spICPMS 107
4.4 Conclusion 109

Avant-propos : analyse des isotopes du bore

Les prochains chapitres de thèse, à partir de celui-ci porteront ou seront basés sur la mesure du δ^{11}B$_{carb}$ dans des petits échantillons à faible concentration de bore. Les mesures des isotopes du bore ont été réalisées sur un MC-ICP-MS Neptune avec la méthode dite de l'injection directe, dont les principes seront décrits ici, avant d'évoquer dans les chapitres 4, 5 et 6 les différents développements analytiques qui ont permis les premières mesures de δ^{11}B$_{carb}$ dans des foraminifères planctoniques à l'IPGP à de très faibles concentrations.

Le MC-ICP-MS Neptune

Les mesures du δ^{11}B ont été réalisées sur un MC-ICP-MS (*Multi Collector Inductively Coupled Plasma Mass Spectrometer*) de type Neptune, de ThermoFisher Scientific (Fig.4.1).

Figure 4.1 : *Spectromètre de masse à source plasma à multicollection (MC-ICP-MS) de l'IPGP qui a été utilisé pour l'analyse des isotopes du bore.*

L'échantillon est pompé sous forme liquide et introduit dans la source ICP à travers un nébuliseur. Les fines gouttelettes produites sont portées par le gaz de nébulisation (argon) jusqu'à la torche où le plasma d'argon se forme (8000 K, Fig.4.2, 2). Après évaporation immédiate de la matrice, les atomes sont plus ou moins ionisés selon leur potentiel d'ionisation. Pour le bore, l'énergie de première ionisation étant de 8,3 eV, l'ionisation n'est pas très efficace. Ensuite, les cônes (Fig.4.2, 3), disques de nickel percés au centre, prélèvent la partie centrale du plasma. Ces derniers permettent également la transition entre une zone à pression atmosphérique (le système d'introduction et le plasma) et une zone sous vide, autour de 10^{-8} mbar, dans le spectromètre de masse. Le prélèvement des ions positifs est assuré par la lentille d'extraction à - 2 kV (Fig.4.2, 4), induisant une différence de potentiel avec la partie ICP qui est neutre. Par la suite, les ions sont accélérés par une tension de -5 kV et focalisés par plusieurs lentilles (dont des quadrupoles) jusqu'à un premier système de fentes (Fig.4.2, 5). Celui-ci présente des fentes de différentes tailles, de 16, 30, ou 250 μm, correspondant aux différents modes de résolution, de haute, moyenne et basse résolution. Les isotopes du bore sont mesurés avec la fente de basse résolution.

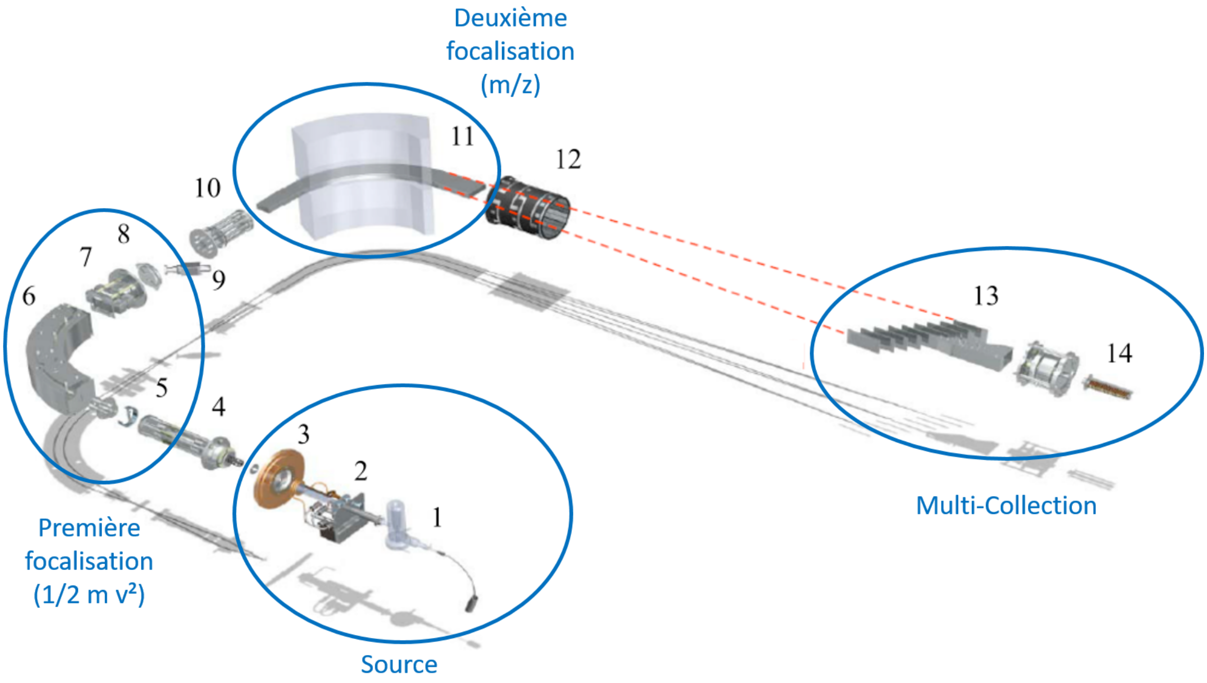

Figure 4.2 : *Schéma de fonctionnement du MC-ICP-MS Neptune. (1) : le système d'introduction, (2) : la torche et le plasma, (3) : les cônes, (4) : les premières lentilles d'extraction et de focalisation, (5) : la fente source déterminant la résolution de la mesure, (6) : le secteur électrostatique, (7) : les lentilles quadrupôlaires de focalisation, (8) : la fente tube, (9) : la vanne tube, (10) : les lentilles octopôlaires contrôlant la forme des pics (Focus zoom), (11) : le secteur magnétique (aimant), (12) : les lentilles dodécapôlaires dajustement de l'alignement des signaux (dispersion zoom), (13) : les neuf cages de Faraday et (14) : le multiplicateur d'électron.*

Ce système de fentes marque aussi l'entrée dans l'analyseur électrostatique (Fig.4.2, 6), l'ESA, où les ions sont accélérés à travers un gradient de potentiel électrique (jusqu'à 10 kV). Cet analyseur permet de filtrer la dispersion en énergie de ces ions. A sa sortie, un champ électrostatique permet de focaliser le faisceau d'ions selon leur énergie avant d'entrer dans un champ magnétique. Après les premières lentilles quadrupôlaires de focalisation, une seconde série de fente et de plaques à forte charge électrostatique (Fig.4.2, 8) stabilisent et créent un spectre d'énergie constant dans le faisceau d'ions tandis que la vanne tube (Fig.4.2, 9) sert à isoler la partie où les signaux sont mesurés (avec aimant et collecteurs) et où le vide est le plus poussé. Enfin, à travers le secteur magnétique (aimant, Fig.4.2,11), les ions sont séparés en fonction de leur rapport masse sur charge (m/z). Avant et après ce secteur magnétique, deux multipôles permettent l'un de refocaliser (Fig.4.2, 10) les ions et l'autre de concentrer ou de disperser (Fig.4.2, 12) le faisceau. Les ions arrivent alors dans les 4+4 cages de Faraday mobiles (Fig.4.2,13), de chaque coté d'une cage de Faraday centrale fixe. Les faibles courants d'ions collectés simultanément par les cages de Faraday sont amplifiés par des résistances de 10^{11} ou 10^{13} Ω. Pour l'analyse du bore, les cage de Faraday L3 et H3 sont utilisées pour mesurer respectivement les isotopes ^{10}B et ^{11}B.

L'injection directe

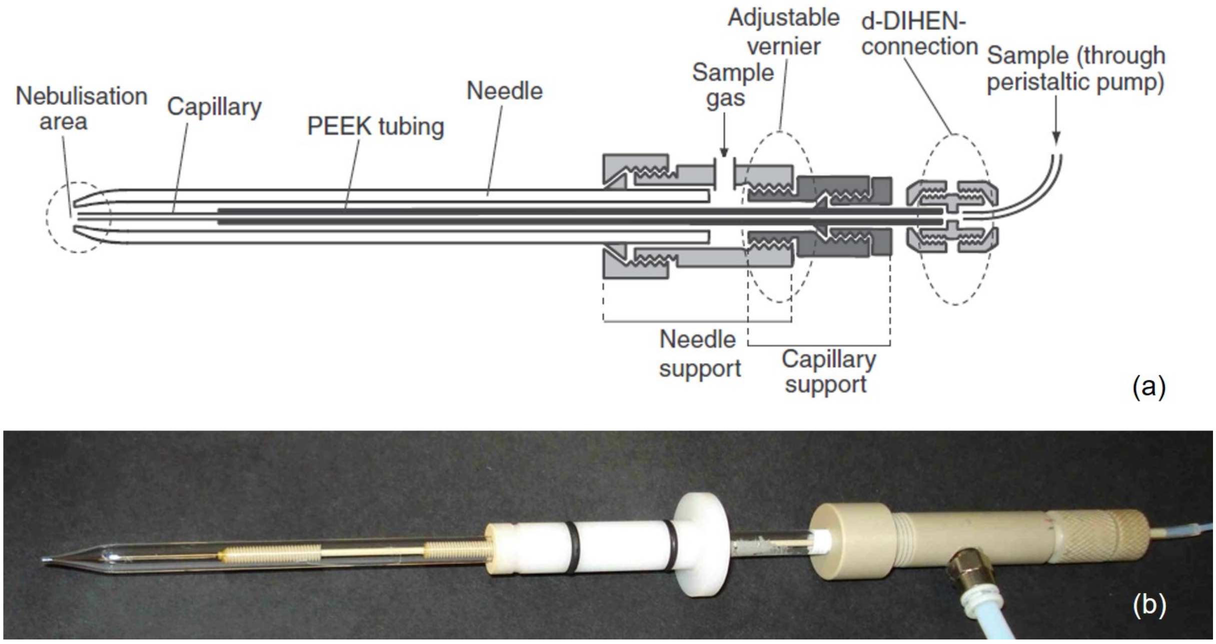

Figure 4.3 : *Schéma (a, Louvat et al. 2011a) et photo (b) du dDIHEN (demountable direct injection high efficiency nebulizer), introduit directement dans la torche. l'aiguille et le capillaire peuvent être démontés et changés. La position du capillaire est ajustée à l'extrémité de l'aiguille pour optimiser le spray (stable, non pulsé et avec de fines gouttelettes) sous une binoculaire avant le démarrage des analyses.*

Les systèmes d'introduction d'échantillons au MC-ICP-MS sont généralement caractérisés par un nébuliseur, convertissant la solution liquide en un aérosol, qui est soit introduit dans une chambre de nébulisation, où les plus fines gouttelettes d'aérosol sont sélectionnées, soit introduit dans un système de désolvation, consistant par exemple en une chambre cyclonique chauffée et un condenseur à refroidissement Peltier (APEX, ESI) ou bien en une chambre de pulvérisation suivie d'une membrane avec un flux de gaz de direction inverse au flux de l'échantillon (Aridus, Cetac). Le nébulisat est ensuite injecté dans la torche à plasma. Fruits de décennies de développement analytique visant à améliorer l'efficacité de l'ionisation, la stabilité du signal et à minimiser le fractionnement isotopique instrumental en ICP-MS pour des éléments multiples, ces systèmes offrent à la fois une grande sensibilité et une bonne stabilité. Mais pour les analyses du bore, parce qu'il est collant et volatile, les chambres de nébulisation souffrent d'effets de mémoire et les désolvateurs entraînent une perte de signal. Ces systèmes d'introduction ne sont donc pas optimaux, à moins que des méthodes de lavage spéciales ne soient mises en œuvre (par exemple avec de l'HF, Misra *et al.* 2014b, ou de l'ammoniac Foster 2008).

Depuis maintenant plus de 10 ans, la nébulisation par injection directe avec le dDIHEN (*demountable-Direct Injection High-Efficiency Nebulizer)* a été mise en place avec succès à l'IPGP pour mesurer les isotopes du bore (Fig.4.3). Le nébuliseur étant introduit directement dans la torche du MC-ICP-MS à la place de l'injecteur, il permet de réduire les surfaces de contact, les temps de lavage entre deux échantillons, mais également les volumes d'échantillons nécessaires pour l'analyse. L'échantillon est ainsi entièrement pulvérisé dans le plasma, ce qui augmente la sensibilité du bore. Ce système a été ensuite automatisé afin d'éviter les bulles d'air qui éteignaient le plasma, mais surtout pour assurer des mesures en continu et pour permettre un encadrement des échantillons avec les standards ou matériaux de référence beaucoup plus efficace.

Le µ-dDIHEN

Ce chapitre présente le développement analytique mis en oeuvre au cours de cette thèse (µ-dDHIEN), pour réduire davantage le volume utilisé lors de l'injection directe, afin de l'appliquer par la suite à la mesure de $\delta^{11}\mathrm{B}_{carb}$ dans de petits échantillons tels que les foraminifères planctoniques. Le volume consommé dans le plasma est ainsi limité par une boucle d'injection (50 ou 10 µL), tandis que le débit d'introduction est contrôlé par un flux de gaz, jusqu'à de très bas niveaux. Cette méthode a été utilisée avec succès sur des échantillons contenant 10 à 20 ppb de bore pour une consommation d'échantillon comprise seulement entre 80 et 240 µL. Elle a été publiée en 2019 dans *Journal of Analytical Atomic Spectrometry* (***Louvat, P., Tharaud, M., Buisson, M., Rollion-Bard, C., Benedetti, M. F., 2019.µ-dDIHEN: A New Micro-Flow Liquid Sample Introduction System for Direct Injection Nebulization in ICP-MS, Vol.34(8), p. 1553–1563, Louvat et al. 2019***).

µ-dDIHEN: A NEW MICRO-FLOW LIQUID SAMPLE INTRODUCTION SYSTEM FOR DIRECT INJECTION NEBULIZATION IN ICP-MS.

Pascale Louvat[1], Mickaël Tharaud[1], Matthieu Buisson[1], Claire Rollion-Bard[1], Marc F. Benedetti[1]

[1]*Institut de physique du globe de Paris, UMR 7154, Université Paris Diderot, Université de Paris, 1 rue Jussieu, 75232 Paris Cedex 05*

Abstract

The µ-dDIHEN is a new liquid sample introduction device for ICP-MS (inductively coupled plasma mass spectrometry) analyses allowing for the direct nebulization of the sample into the plasma, without any spray chamber, at flow rate down to 5 µL.min^{-1}. It is composed of a demountable direct injection high efficiency nebulizer (d-DIHEN), a flow injection analysis (FIA) valve and a gas displacement pump (GDP) connected to a µ-mass-flow meter that allows very stable liquid flow rates. The system was successfully tested with sample loop sizes of 10 and 50 µL and for liquid flow rates between 5 and 50 µL.min^{-1} on two different ICP-MS instruments, an HR-ICP-MS and an MC-ICP-MS, and for three different applications:boron isotopic ratio measurement of geological samples, multi-element analysis of natural water samples and gold nanoparticles characterization by single particle ICPMS (sp-ICPMS).

The liquid uptake rate of the µ-dDIHEN was proportional to the gas flow rate of the GDP, and signal sensitivity was increasing with uptake rate, but not anymore above 30 µL.min^{-1}, due to the deterioration of the ionization conditions within the plasma at high uptake rate (extra-wet plasma conditions). We successfully measured boron isotopic ratios (δ^{11}B) for reference material solutions with B concentrations between 10 and 200 ppb, the reproducibility of the measurements depending on both the B concentration of the sample and the uptake rate: 10B signals below 20-30 mV (with 10^{11} ohms amplifiers) gave 2SD reproducibility $\geq$ 0.5 ‰ (n=5). Thus, the best measurement conditions were not necessarily with very low uptake rate of 5-7 µL.min^{-1}, but rather at 25 µL.min^{-1}, allowing for a higher signal. We also tested transient versus continuous measurement modes for a serie of natural samples, by setting the sample loop size either at 10 or 50 µL, with a same uptake rate of 25 µL.min^{-1}. The two modes gave fully comparable results but the transient mode allows the triplicated δ^{11}B measurement of very small samples ($\leq$ 100 µL) with a B content of a few ng. Concerning the multi-element analyses by HR-ICP-MS, the LOQs of the majority of the trace and ultra-trace elements were lower (up to 15 times) than with the classical concentric nebulizer and spray chamber, due to the much lower volume of sample needed with the µ-dDIHEN. Lastly, the newly developed system is highly promising for nanoparticles (NP) characterization by sp-ICPMS. The first set of measurements for gold NPs of 40 nm certified size at 25 µL.min^{-1} led to a transport efficiency of 85 %.

4.1 Introduction

In spite of improvements in signal detection and interference resolution for inductively coupled plasma (ICP) analyses, efficient sample introduction to the plasma remains one of the weaknesses of ICP technics. The mostly used liquid introduction system in ICP consists in spraying the sample with a pneumatic concentric nebulizer, selecting the finest spray droplets in a spray chamber and directing this fine aerosol to the plasma through an injector in the centre of the torch. This results in an analyte transfer efficiency to the plasma of only 1 to 2 %, with a potential increase of memory and matrix effects as well as an extension of sample uptake and wash times. An alternative system is direct injection, where the sample is directly sprayed into the plasma without a spray chamber, the long nebulizer being directly plugged in the torch in place of the injector. Direct injection nebulizer was first proposed in 1984 (Lawrence *et al.*, 1984) and had a lot of developments and applications since. Its main advantage is an analyte transfer efficiency of 100 % and lower sample flow rates (typically <100 µL.min^{-1}), increasing the analyte sensitivity significantly (by a factor of typically 5, Jorabchi *et al.* 2005) and decreasing limits of quantification (LOQ, Nam *et al.* 1994; Zoorob *et al.* 1995). The two first commercialized direct injection nebulizers, the DIN (Cetac, USA) and the DIHEN (for direct injection high efficiency nebulizer, Meinhard, USA) where successfully used for hyphenated technics, such as liquid chromatography and HPLC or capillary electrophoresis (Bendahl *et al.*, 2001; Wind *et al.*, 2002; Jensen *et al.*, 2003; Stefánka *et al.*, 2006; Grotti *et al.*, 2014; Bernardin *et al.*, 2018). Direct injection was also valuable for the measurement of samples with a high matrix load or even petroleum samples (Sánchez *et al.*, 2013; Leclercq *et al.*, 2015; Bernardin *et al.*, 2018). In some of these applications low flow rates down to a few µL.min^{-1} were mandatory and where achieved mostly through peristaltic pump, syringe pump (Becker *et al.*, 1999) or HPLC (high performance liquid chromatography) pump (Acon *et al.*, 2000), sometimes through self-aspiring. Gas displacement pump (GDP) was the default pump for the DIN (Wiederin *et al.*, 1991), but this GDP-DIN set-up was not maintained because of its cost and difficulty of use (Bendahl *et al.*, 2001). The last generation of direct injection nebulizer, the dDIHEN (demountable direct injection high efficiency nebulizer, now sold by Analab, France) has the advantage of being low-cost, still with a low dead volume, but less prone to clogging or melting and above all finely adjustable to optimize the spray (Westphal *et al.*, 2004). The dDIHEN is used at IPGP (Institut de Physique du Globe de Paris) for over ten years for boron isotope ratio measurements in geological samples at an uptake rate of 50 µL.min^{-1} (Louvat *et al.*, 2011a, 2014b).

With the wide spread utilization of inductively coupled plasma mass spectrometry (ICP-MS) for environmental samples and the need for analysing smaller samples and lower concentrations, there is a growing interest in developing new introduction systems with increased sensitivity, smaller sample consumption rates and higher transport efficiency. Some preceding studies promoted devices such as the torch integrated sample introduction system (Paredes *et al.*, 2009), that allowed sample uptake rates down to 5 or 10 µL.min^{-1} for isotope ratio measurements by MC-ICP-MS (Paredes *et al.*, 2011, 2013). Flow injection analysis (FIA) is another way to reduce the amount of sample consumed per analysis (Pergantis *et al.*, 1995; McLean *et al.*, 1998; Westphal *et al.*, 2002), speed up the analyses (Fischer *et al.*, 2014), but also allow direct ICP-MS analysis of small biological samples with high matrix salt load (Takasaki *et al.*, 2011; Zhang *et al.*, 2018), dilution or on-line separation (Wang & Hansen, 2003). In a previous paper, we automatized a direct injection introduction setup, with an autosampler and a FIA 6-port valve (Louvat *et al.*, 2014b), in order to avoid the introduction of air bubbles when moving the autosampler probe from one sample tube to the next. The sample was pushed to the dDIHEN nebulizer through a peristaltic pump. The use of a peristaltic pump precluded flow rates below 30 µL.min^{-1} due to instabilities in the signal. In the present work we describe the µ-dDIHEN, an original set-up for sample introduction in ICP-MS with direct injection nebulizer (d-DIHEN) at flow rates down to 5 µL.min^{-1} thanks to a gas displacement pump (GDP) for flow injection analyses (FIA), and that could be used for many ICP applications. Here we tested its performances for two different ICP-MS instruments (HR-ICP-MS Element and MC-ICP-MS Neptune) with applications to multi-elemental analyses, determination of nanoparticles sizes and number concentrations by spICPMS, and boron isotope ratio measurements with MC-ICP-MS, in both continuous and transient signal analysis modes.

4.2 Material and methods

4.2.a The µ-dDIHEN liquid introduction system

The direct injection nebulizer (d-DIHEN, Analab, France) was connected to an autosampler (SC, ESI, USA) through a 6-port valve (FAST, ESI, USA, Louvat *et al.* 2014b) with a sample loop of adjustable size (here 10 and 50 µL). The sample or carrier delivery to the d-DIHEN was done by a gas displacement pump, which consists in a 8-port valve with two carrier loops that were alternatively filled with a carrier by a peristaltic pump (12 rods, Spetec, Germany, with 0.76 mm inner diameter - i.d., “black-black” PVC tube) and emptied by an Ar gas flow controlled by a micro mass flow controller (0.015 to 1 mL.min^{-1}, El Flow, Bronkorst, France). The carrier solution was thus pushed from the GDP toward the FIA valve and the dDIHEN nebulizer. The FIA sample loop was filled thanks to the aspiration of the sample by the autosampler vacuum (SC-DX, ESI, USA).

Because sample introduction with dDIHEN is very sensitive to air bubbles that switch off the plasma, the whole set-up must be carefully tuned in terms of tubing diameters and timing of the FIA and GDP valves, in order to get rid of any air bubble during filling of the carrier and sample loops and transfers to the dDIHEN nebulizer. The inner diameters of the carrier and sample tubes were of decreasing size towards the nebulizer. The two GPD pump carrier loops had a volume of 200 µL with 0.8 mm i.d. tubing, the GDP to FIA tube was 0.5 mm i.d. The autosampler probe and sample loop i.d. were 0.25 mm, while the FIA valve to dDIHEN connecting tube was 0.2 mm i.d. The autosampler probe and FIA valve to autosampler vacuum tube diameters were also optimized in order to maintain regular and reproducible uptake rate (i.e. slow enough to consume the lowest possible sample volume but quick enough to allow fast analyses). The best compromise was for autosampler probe of 0.25 mm i.d. and tube to the autosampler vacuum of 0.5 mm i.d. and length of 1 m. The sample loop volume was tested at 50 and 10 µL (0.25 mm i.d.).

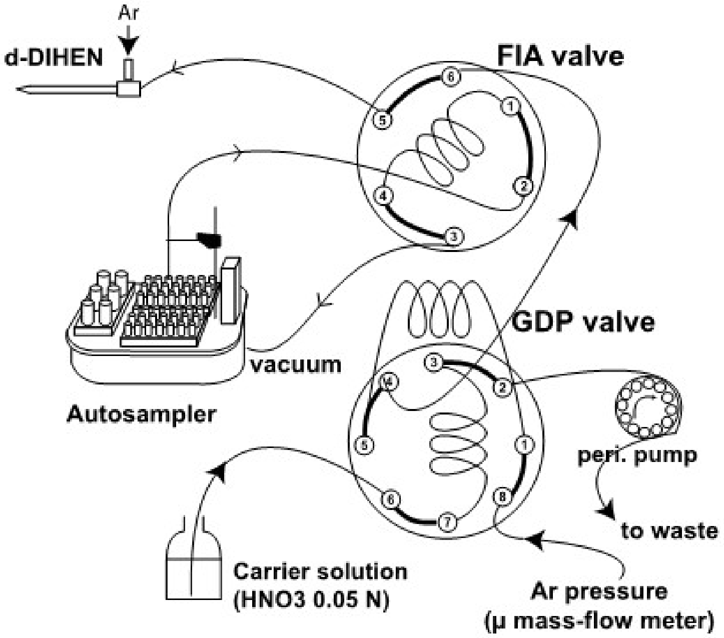

Figure 4.4 : *The µ-dDIHEN for liquid sample introduction to ICP-MS with: direct injection nebulizer (d-DIHEN), flow injection analysis valve and gas displacement pump. The d-DIHEN is directly plugged into the torch of the ICP-MS, in place of the injector.*

4.2.b Interfacing ICP-MS with the µ-dDIHEN introduction system

Both valves (FIA and GDP) were controlled by the ESI autosampler software (GDP and FAST programs, Table 4.1), which was synchronized with the ICP-MS software for automatic acquisition during sequence measurement. The GDP valve program switches the carrier delivery pushed by the Ar flow from one loop to the other every 8s, allowing stable sample flow rates between 5 and 75 µL.min^{-1}. The FAST program switches the FIA valve to LOAD as soon as the autosampler goes to the next sample, turns on the autosampler vacuum during 23s to aspire the sample (volume large enough to slightly overfill the sample loop), sends the autosampler probe to the wash station, waits for another 8s that the sample loop is completely filled by the sample volume, switches the FIA valve to INJECT and leaves the autosampler vacuum ON for 10 additional seconds to rinse the probe and FIA valve (except the sample loop). The autosampler probe stays in the wash station until the instrument software starts the next sample acquisition.

Table 4.1 : *Gas displacement pump (GDP) and FIA (FAST) programs (SC-FAST Autosampler, ESI)*

	GDP	
Sub method		
Start loop		
	Toggle valve	Valve 1
	Delay	30 s
End loop		
	FIA/FAST	
Event	**Action**	**Parameter**
On probe down	Load valve 2	
On probe down	Vacuum on	
On probe down	Timer A	23 s
Timer A expires	Move rinse	
Timer A expires	Timer B	8 s
Timer B expires	Inject vale 2	
Rinse completed	Vacuum off	
	Rinse	
Rinse 1 2 s	Rinse 2 20 s	Max vacuum time 30 s

4.2.c ICP-MS measurements

Two ICP-MS instruments were used during this study. Multi-element analyses and nanoparticles characterization were performed on a HR-ICP-MS Element (ThermoScientific, USA), while boron isotope analyses were done on a MC-ICP-MS Neptune (ThermoScientific, USA). The ICP operating parameters for the three applications were quite similar (Table 4.2), with globally lower sample gas and higher auxiliary gas flow rates compared to the classical micro-concentric nebulizer + spray chamber sample introduction system. Optimization of the dDIHEN spray was performed visually out of the torch assembly. It consists in finding the best distance between the inner dDIHEN capillary and the outer dDIHEN needle, in order to achieve a stable spray with fine droplets, as described in Louvat *et al.* (2011a).

4.2.d Reagents and sample preparation

All analyte solutions were prepared with MilliQ water (resistivity > 18 MΩ.cm^{-1}, Millipore, USA) in polypropylene bottles and tubes that have been pre-washed in distilled (DST-1000, Savillex, USA) HNO_3 or HCl solutions at 0.5 N and rinsed with MilliQ water. Multi-elemental standards (1 ppt to 10 ppb) were made from 1g.L^{-1} mono-elemental stock solutions (SCP Sciences, Canada) and diluted in a 1 % distilled HNO_3 solution. This latter was measured several times in order to determine the limit of quantification (LOQ) for each element. For spICPMS measurements, citrate capped AuNPs with a nominal diameter of 40 nm were purchased at British Biocell International (Cardiff, UK).

Table 4.2 : *Operating parameters of the ICP-MS instruments*

	MC-ICP-MS Neptune (boron isotope ratios)	**HR-ICP-MS Element II (multi-elem. & Au NPs)**
Cones	Ni: regular skimmer, Jet sampler	Ni: regular skimmer and sampler
Introduction system	µd-DIHEN	µd-DIHEN
Uptake rate	5 to 100 µL.min^{-1}	5 to 100 µL.min^{-1}
RF power	1200 W	1295 W
Ar Cool gas	15 L.min^{-1}	16 L.min^{-1}
Ar auxiliary gas	1.2 to 1.5 L.min^{-1}	1.2 to 1.5 L.min^{-1}
Ar sample gas	0.3 to 0.4 L.min^{-1}	0.3 to 0.4 L.min^{-1}
Detection	Faraday cups, 10^{11} Ω amplifiers	Secondary Electron Multiplier
Resolution	Low (400)	Low, Medium, High
Extraction lens	-2000 V	-2000 V
B isotope measurement	15 cycles 8 s integration	
Multi-elementary meas.		3 runs of 3 passes
Au NPs measurement		20000 runs of 1 pass with a 1 ms dwell-time
Oxides		UO/U $\leq$ 10%
Doubly charged		$Ba^+/Ba^{2+} \leq 0.3\%$

The mean diameter and the concentration provided by the supplier were 40 nm with a coefficient of variation of $\leq$ 8 % and 9.00 x 10^{10}particles per mL, respectively. Prior to measurements, suspensions were freshly prepared to calculate the nebulisation efficiency using the size method based on the TEM-measured median size of 40 nm particles (Pace *et al.*, 2011). For dissolved gold calibration, a 1 g.L^{-1} mono-elemental standard from SCP Science (Quebec, Canada) was diluted to 10, 100 and 1000 ppb in 1 % HCl. Boron isotope ratio measurements on the MC-ICP-MS Neptune were first tested on the reference standard materials AE120, AE121 and AE122 (BAM, Germany, Vogl & Rosner 2011) at concentrations between 5 and 200 ppb. A series of 35 samples from an experience on boron adsorption onto silica (similar to the experience onto carbonate, Saldi *et al.* 2018) has been prepared for δ^{11}B analyses: boron was extracted from the samples by ion exchange chemistry (Lemarchand *et al.*, 2002a; Louvat *et al.*, 2011a). Boron isotopic ratios were measured with the sample-standard bracketing method (Louvat *et al.*, 2014b) and are expressed as δ^{11}B in per mil unit (‰) relative to SRM 951 (NIST, USA, Catanzaro *et al.* 1970):

$$\delta^{11}B = (\frac{(^{11}B/^{10}B)_{sample}}{(^{11}B/^{10}B)_{SRM\ 951}} - 1) * 1000. \tag{4.1}$$

4.3 Results and discussion

4.3.a Uptake rate, stabilization time, reproducibility of the injections and sensitivity

Some examples of the injection peaks obtained with the µ-dDIHEN are shown in Figure 4.5 for liquid uptake rates of 5 to 30 µL.min^{-1} and sample loops of 50 and 10 µL. After plasma switches on, the sample gas is slowly increased to 0.35 L.min^{-1} and the auxiliary gas to 1.5 L.min^{-1}. The GDP is then started with a gas flow rate of typically 40 µL.min^{-1}, which will be then adjusted according to the needs of the application. It takes approximately one hour to stabilize the liquid flow rate, while the gas flow rate (from the µ-mass-flow meter) is immediately stable. When the gas flow rate is increased or decreased, the system needs another hour to stabilize. So, for regular operation (real sample measurements), the GDP gas flow-rate is usually fixed. The peak width and height (Fig.4.5) are proportional to the liquid uptake rate, with flat tops when the ratio sample loop volume (µL) to sample uptake rate (µL.min^{-1}) was higher than 2, and a rather transient shape when lower. Figure 4.5 shows that the injection peaks are very reproducible, after a stabilisation time of almost one hour. The liquid flow rates were calculated from the injection peaks by dividing the known sample loop volume (10 or 50 µL) by the time between the beginning of signal increase and the beginning of signal decrease. We tested the linearity of the liquid uptake rates according to the GDP gas flow rates (from mass flow controller, MFC) between 20 and 200 µL.min^{-1} for two different dDIHEN nebulizers (Fig.4.6.a and 4.6.c) on the MC-ICPMS and between 15 and

75 µL.min^{-1} on the MC-ICPMS and the HR-ICPMS (Fig.4.6.b and 4.6.c) with the same dDIHEN. The liquid uptake rate was globally higher for dDIHEN 1 than for dDIHEN 2 for a given gas flow. Both dDIHEN are similar but the quartz nebulizer and inner capillary tips can differ slightly in shape and surface roughness due to ageing. Moreover, the spray is optimized at the beginning of each measurement session and the tuning may be a bit different between two measurement sessions. As a consequence the liquid uptake rate has to be calibrated at the beginning of each measurement session. For gas flows above 100 µL.min^{-1}, we observe that the liquid uptake rate does not increase linearly anymore (Fig.4.6.a).

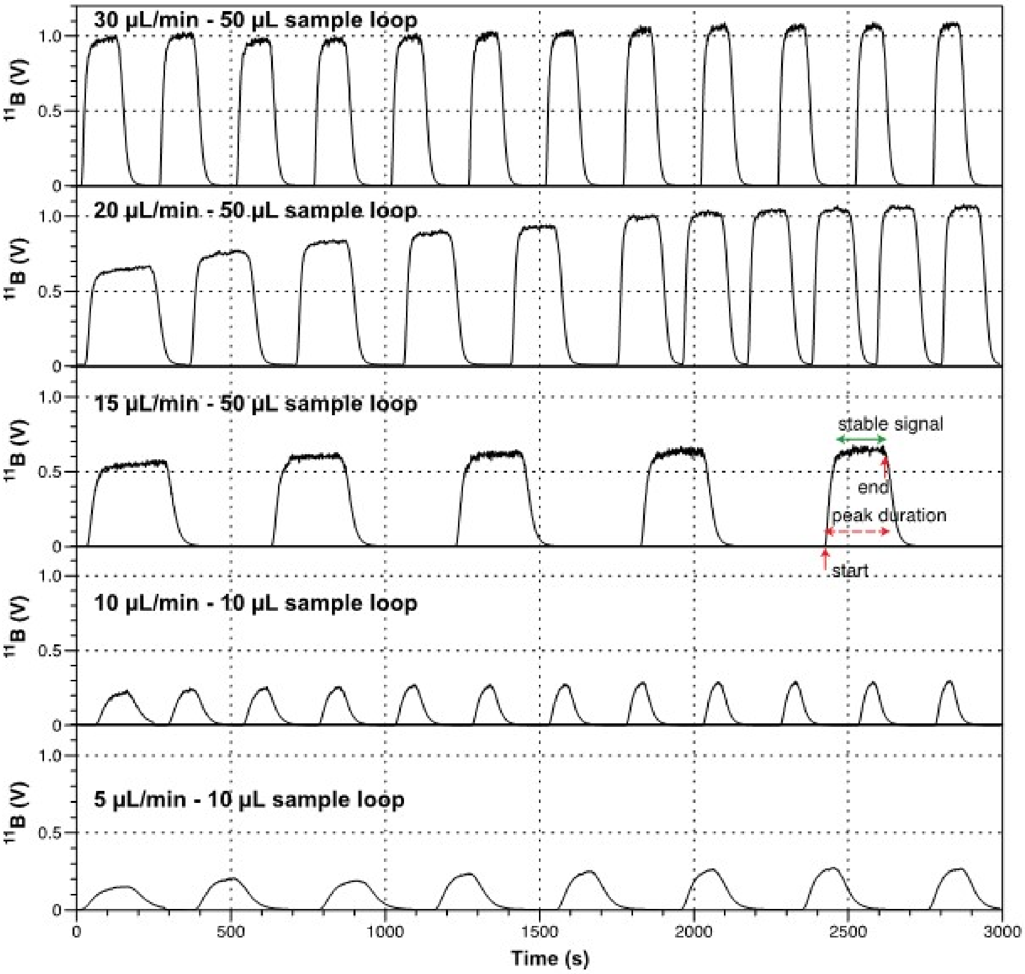

Figure 4.5 : *Injection peaks with the µ-dDIHEN at different liquid uptake rates and sample loops of 10 and 50 µL. The last peak at 15 µL.min^{-1}) and 50 mL sample loop is commented with start/end of the peak, peak duration and stable signal plateau. the peak duration is used to calculate the liquid uptake rate of the µ-dDIHEN setup.*

For the tests with dDIHEN 2, the measurements were started at a gas flow rate of 100 µL.min^{-1}, then decreased to 50 and 20 µL.min^{-1}, and increased again to 30, 40, 75 and 150 µL.min^{-1}. The signal was refocused many times during the tests (due to the stabilisation of the instrument through time after plasma ignition), and in particular the sample gas flow and torch positions, for better ^{11}B signal sensitivity and stability. For the tests with dDIHEN 1 the gas flow rate was started at 20 µL.min^{-1} and successively increased to 30, 50, 100 and 200 µL.min^{-1}, without retuning of the ^{11}B signal, as the plasma had already been on for a few hours. This might explain why the gas flow versus liquid flow rates (Fig.4.6.a) and ^{11}B signal versus liquid flow rate (Fig.4.6.c) relationships are not as linear for dDIHEN 2 as for dDIHEN 1. When investigating the lower gas flow range of the MCF (15 to 75 µL.min^{-1}, (Fig.4.6.b), the liquid uptake rates and gas flow rates are linearly proportionate, and for the two instruments, but the liquid uptake rates were a little bit smaller for the MC-ICPMS than for the HR-ICPMS, probably due again to slightly different tuning of the dDIHEN spray and sample gas between the two instruments.

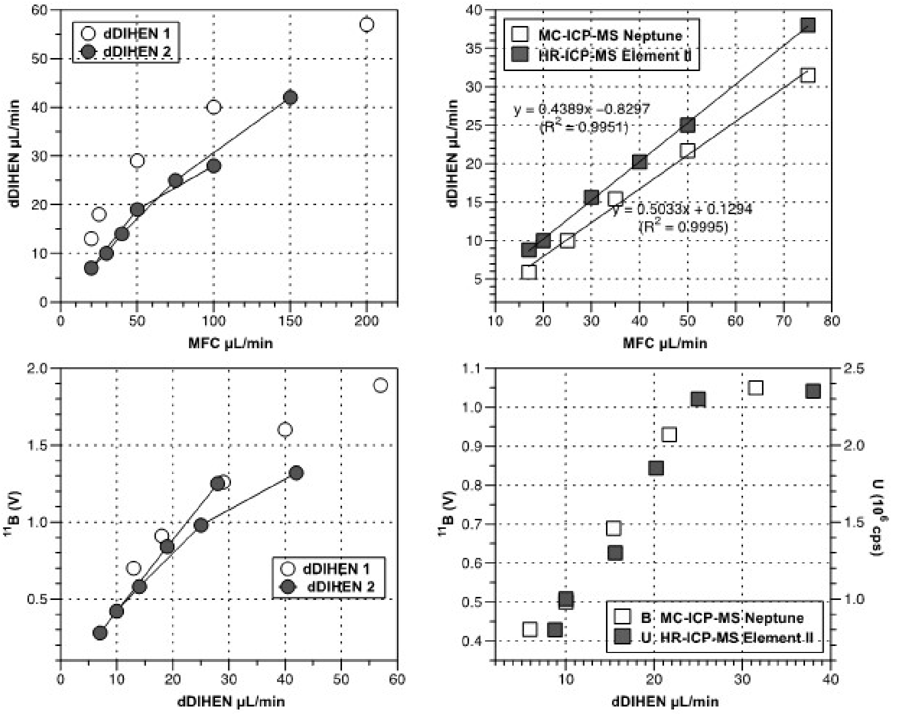

Figure 4.6 : *Liquid uptake rate of the µ-dDIHEN according to the gas flow rate from the mass flow controller (MCF) of the gas displacement pump (GDP) for (a) two different dDIHENs tested on the MC-ICP-MS and (b) the same dDIHEN tested on two different ICP-MS (MC- and HR-) ; c) and d) corresponding signal intensity as a function of the dDIHEN uptake rate.*

What is striking is the almost linear increase of signal sensitivity (on ^{11}B for MC-ICPMS and on ^{238}U on HR-ICPMS) below 25 µL.min^{-1} liquid uptake rate and attenuation or almost stagnation of the signal above (Fig.4.6.d). When liquid uptake rate is increased, more ions are introduced to the MS, thus increasing the signal, but when too much liquid is sprayed to the plasma, extra-wet conditions worsen the ionisation efficiency within the plasma and the signal does not increase as much anymore. Nebulisation conditions have been extensively discussed for the precursors of the dDIHEN nebulizer, namely the DIHEN (McLean *et al.*, 1998) and LB-DIHEN (Acon *et al.*, 2000), and depend on the droplet velocity and size distributions:

the ideal aerosol should be composed of very small, mono-dispere droplets of uniform velocities to enhance desolvation-vaporization-excitation-ionization of the sample droplets in the plasma (Mclean *et al.*, 1998). Many parameters combine together to control the aerosol quality. For example, higher sample gas flow favours smaller droplets but reduce the droplet residence time within the plasma and thus sensitivity (Minnich *et al.*, 2001); very small uptake rates induce a rotation of the aerosol that can generate satellite droplets and thus less uniform size and velocity distributions (Minnich *et al.*, 2001). The present observation that at increasing uptake rate, but with a constant sample gas flow, sensitivity increases up to a knickpoint value and then plateaus is in agreement with these previous works. Laser light scattering measurements of the dDIHEN aerosol under various tuning conditions (capillary-needle tip distance, sample uptake rate and sample gas flow) would be necessary to fully understand these processes and accordingly optimize the µ-dDIHEN setup for a given application.

4.3.b Boron isotope ratio measurements by MC-ICP-MS

Reference materials at different concentrations and rates

Three standard reference materials (AE120, AE121 and AE122, Vogl & Rosner 2011 were measured at concentrations between 5 and 200 ppb at liquid uptake rates of 7, 15 and 25 µL.min^{-1} with a sample loop of 50 µL and at an uptake rate of 14 µL.min^{-1} in transient mode with a loop of 10 µL (Fig.4.6). When the ^{10}B signal was lower than 20 mV (with 10^{11} ohms amplifiers), standard errors of the measurement were high (>0.5 ‰, 2SD, and up to 5 ‰ for only 2mV on ^{10}B) but the measurements were always accurate, within the 2SD limits. For higher ^{10}B signals, the measured δ^{11}B values were in perfect agreement with the certified and long-term measured values. This shows that we were able to measure accurate and precise boron isotope ratios for these standard reference materials with the new µ-dDIHEN liquid introduction system, at much lower flow rates (7 to 25 µL.min^{-1}) and with much smaller sample volumes (<300 µL) than with the previous method (50 µL.min^{-1} and 1.5 mL, Louvat *et al.* 2014b). At an uptake rate of 25 µL.min^{-1}, the minimum boron concentration necessary for δ^{11}B measurements with 2SD errors below 0.5 ‰ was 10 ppb. At 15 µL.min^{-1} it was 30 ppb and at 7 µL.min^{-1} 50 ppb.

What would be the best uptake rate and sample loop volume for the δ^{11}B measurement of a small sample? The measurements here lasted 2 minutes (15 cycles of 8s each), so the minimum sample loop volumes are respectively 15, 30 and 50 µL for uptake rates of 7, 15 and 25 µL.min^{-1}. The volume of sample needed to fill the loop has to be larger than the loop. With a good optimization of the FIA program timers (Table 4.2) and of the tubing diameter and lengths between the autosampler, the FIA valve and the autosampler vacuum, we determined that 80 µL were necessary to fill the 50 µL loop, and 24 µL for the 10 µL loop.

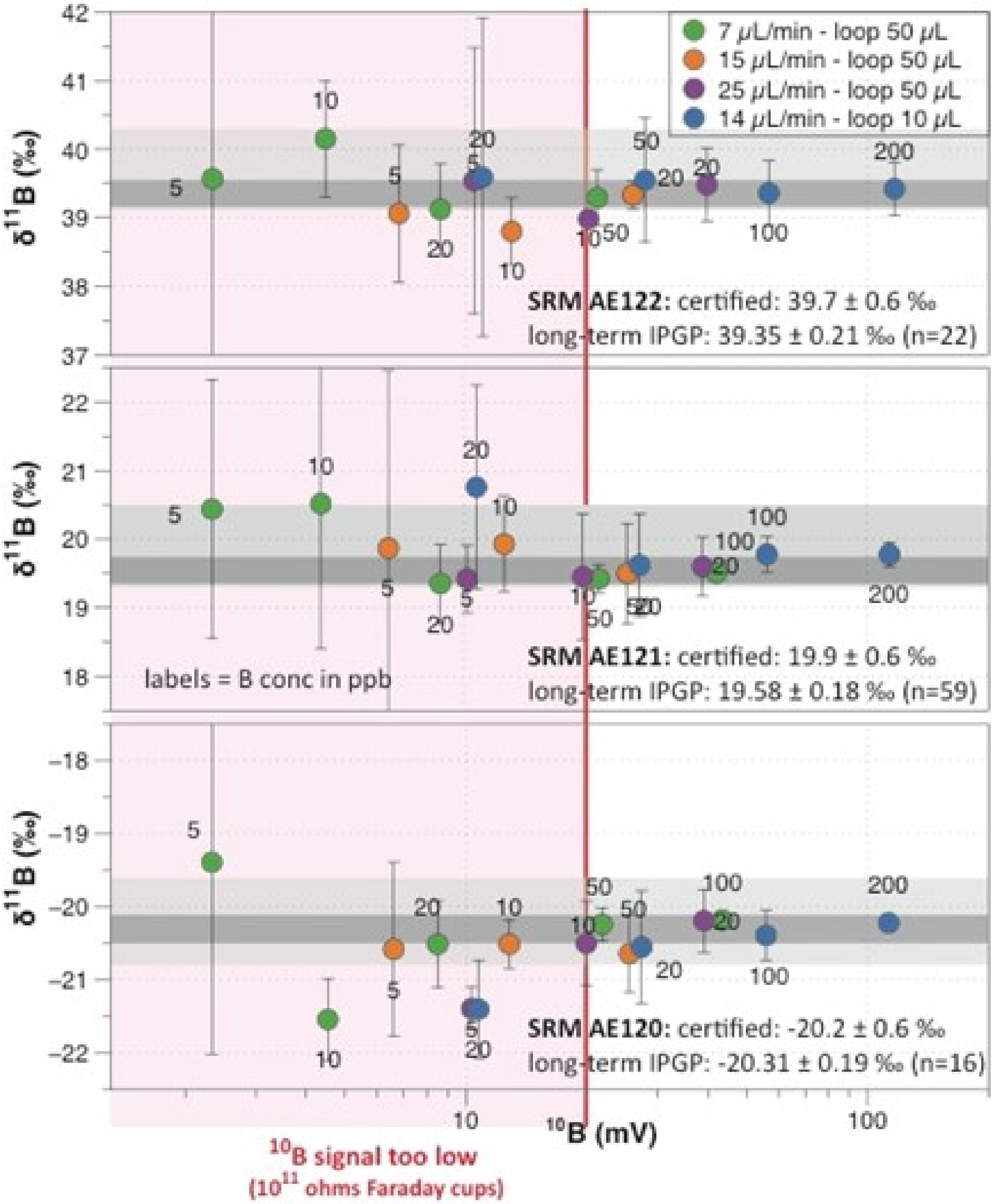

Figure 4.7 : *MC-ICP-MS boron isotope ratio (δ^{11}B) measurements of the standard reference materials SRM AE 120, 121 and 122 (Vogl & Rosner, 2011) at concentrations between 5 and 200 ppb, with the μ-dDIHEN at different uptake rates.*

Thus for the measurement of one sample in triplicate, as was done for the reference materials here (Fig.4.7), the minimum volume of sample needed would be 90, 150 and 240 μL respectively for the uptake rates at 7, 15 and 25 μL.min^{-1}. As minimum B concentrations for $\leq$ 0.5 ‰ 2SD δ^{11}B measurements were respectively 40, 30 and 10 ppb for an uptake rate of 7, 15 and 25 µL.min^{-1}, the minimum B amount that can be measured at each rate is respectively 4.5, 4.5 and 2.4 ng. These "back of the envelope" estimations show that there is no real difference between the three uptake rates that were tested, as the required minimum B concentration increases with decreasing uptake rate, and that the limiting factors are more likely the stability of the signals, their amplification and both the instrument and B extraction procedure blanks. Above this minimum sample amount of 2 ng B, we would recommend an uptake rate of 25 µL.min^{-1} and sample loop of 50 µL, with the advantage of timings easier to adjust for the FIA valve (loop filling with a minimum sample volume) and for the transport to the plasma compared to smaller uptake rates (and smaller loops).

Continuous (50 µL loop) versus transient (10 µL loop) measurements for small samples

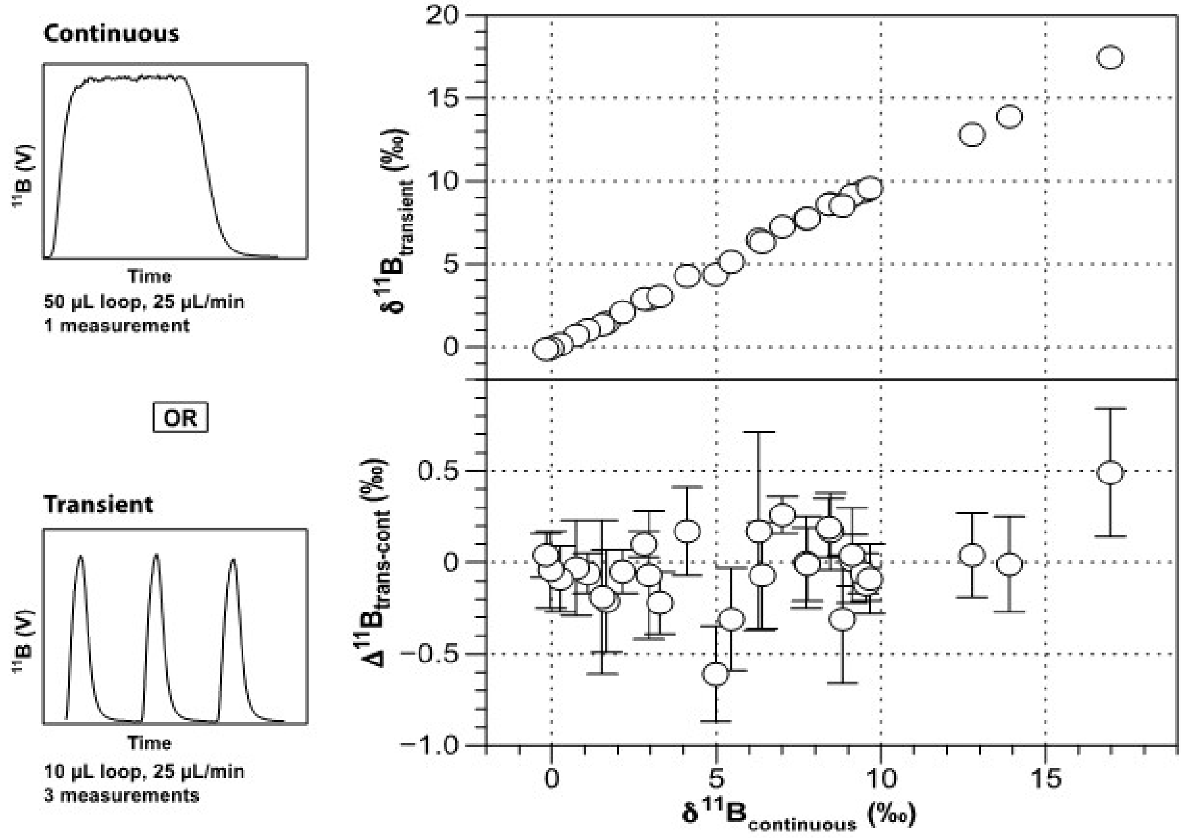

Figure 4.8 : *MC-ICP-MS boron isotope ratio (δ^{11}B) measurements in continuous (50 µL loop, one measurement) versus transient (10 µL loop, triplicate measurements) modes for a series of samples. Both transient and continuous modes required 80 µL of sample and uptake rate was kept at 25 µL.min^{-1}.*

In the case of very small samples (<2 ng B and sample volume <100 µL), it becomes impossible to have a triplicate measurement in the above-mentioned conditions with a stable continuous signal lasting for 2 min. For such samples, and at a fixed liquid uptake rate of 25 µL.min^{-1} allowing for optimized sensitivity, we could either measure the δ^{11}B value once in continuous mode with the 50 µL sample loop or thrice but on a smaller loop of only 10 µL and as transient signal. The test was made on real samples issued from a study on B adsorption to silica at different pH (similar conditions as Saldi *et al.* 2018). The test samples (not limited in volume nor B concentration) were first measured by standard-sample bracketing in continuous mode, i.e. with a long enough plateau on the injection peaks to measure 15 cycles of 8s, with the 50 µL loop and at an uptake rate of 25 µL.min^{-1}. Then the loop volume was reduced to 10 µL (uptake rate kept at 25 µL.min^{-1}) and the measurements were made in transient mode (injection peaks without plateaus), with 150 cycles of 1s (Fig.4.8). Blanks were measured before and after each triplicated standard-sample bracketing sequence. For each sample or standard, the ^{11}B/^{10}B ratio was determined as the slope of the linear regression (Epov *et al.*, 2010) between ^{11}B and ^{10}B signals (from the 150 measurements), after subtraction of the average ^{11}B and ^{10}B blank intensities. For these samples the B concentrations were adjusted to 200 µg.L^{-1}, so that the maximum ^{10}B signal was about 100 mV in transient mode and 150 mV in continuous mode, high enough for correct δ^{11}B measurement with the 10^{11} ohms amplifiers (Fig.4.7). Both modes of measurement give comparable δ^{11}B results within $\pm$ 0.5 ‰ (Fig.4.8). The advantage of the transient signal mode is the possibility of estimating for each sample measured a 2SD error out of the five δ^{11}B values calculated from the triplicated standard sample measurements (Louvat *et al.*, 2014b). For the same 80 µL sample volume only one measurement is possible in continuous mode and no specific reproducibility can be reported. So we would encourage the transient mode if needed for small volume samples with low B content.

4.3.c Multi-element analysis by HR-ICP-MS

The developed micro-introduction device was also tested on the HR-ICP-MS Element II for the multi-elementary measurement of small sample volumes. The limits of quantification (LOQ) for trace and ultra-trace elements were determined for continuous introduction using a PFA nebulizer fitted on a cyclonic spray chamber at an uptake rate of 200 µL.min^{-1} and for the µ-dDIHEN at 25 µL.min^{-1} with a 50 µL loop (Fig.4.9). When expressed in ng.L^{-1}, the LOQ with the µ-dDIHEN were globally slightly higher than that with the classical spray chamber and this is because the signal intensities where lower. However, when LOQ is expressed as pg, taking into account the uptake rate (thus the volume of sample consumed for one analysis), for most of the considered elements, the LOQs with the µ-dDIHEN were significantly lower than those with the spray chamber, as the required volume of sample was much lower. No particular trend is observed depending on the element type or resolution of analysis (high *versus* low-resolution).

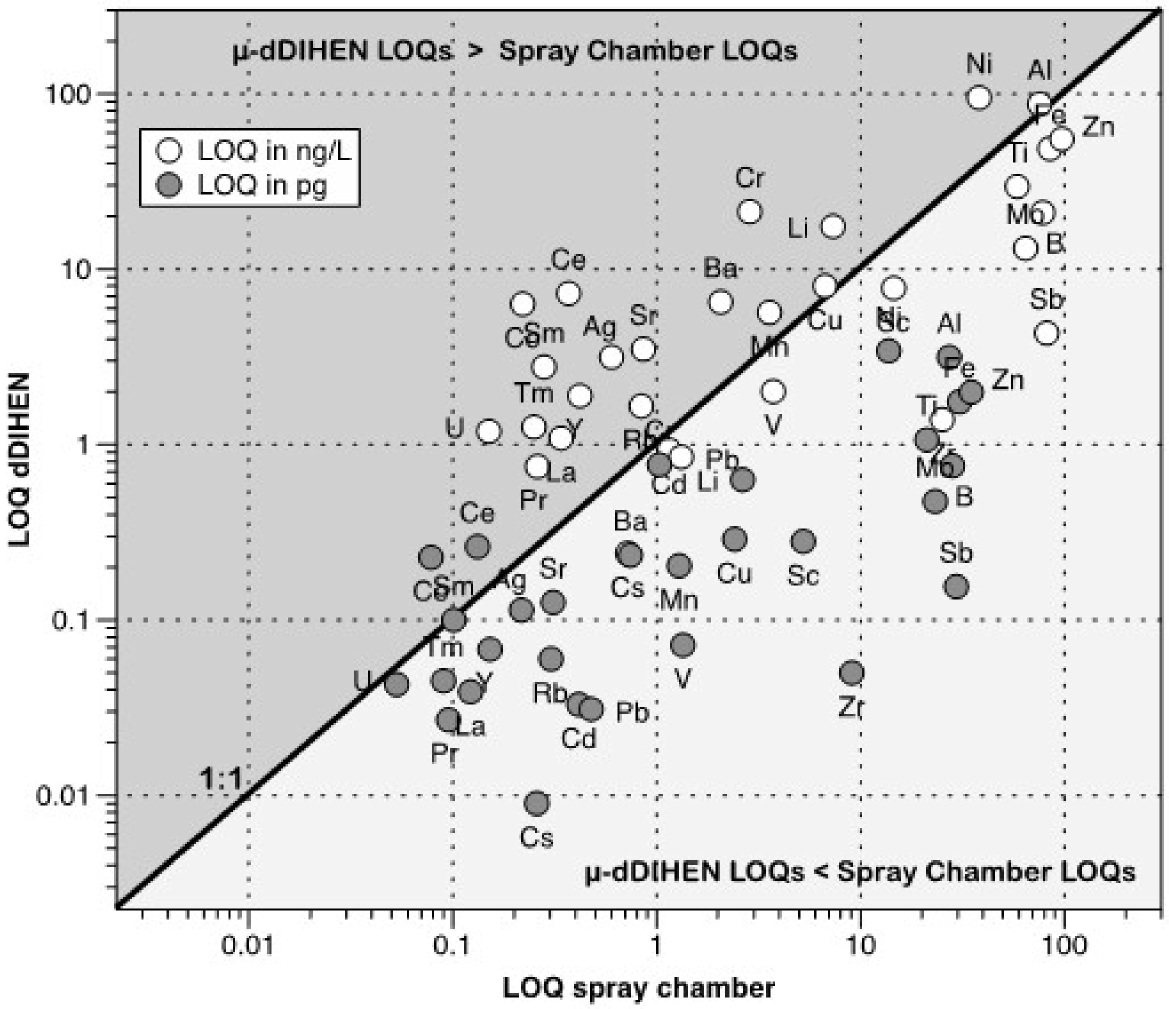

Figure 4.9 : *Limits of quantification (LOQ) for trace and ultra-trace elements determined with the µ-dDIHEN at 25 µL.min^{-1} and with a PFA nebulizer fitted on a cyclonic spray chamber at 200 µL.min^{-1} ("Spray Chamber") in ng/L (empty circles) and in pg (gray circles). Dots below the 1:1 line indicate µ-dDIHEN LOQs lower than spray chamber LOQs.*

4.3.d Au nanoparticles characterization by spICPMS

The single-particle ICP-MS (spICPMS) allows the measurement of events produced by individual particles at milli-second rate (Degueldre *et al.*, 2006). For usual spICPMS analyses the nanoparticles (NPs) suspended in an aqueous solution are nebulized into a spray chamber and only a fraction of the aerosolized suspension reaches the plasma. This fraction, also called "transport efficiency" needs to be calculated to relate concentration of dissolved element used for the calibration range (intensity vs concentration) to a total mass observed per event. Pace *et al.* (2011) described three different methods to calculate the transport efficiency. In this study, we used the second method, based on the particle size (Pace *et al.*, 2011). In a previous study (Tharaud *et al.*, 2017) determined that the transport efficiency for continuous introduction using a PFA nebulizer fitted on a cyclonic spray chamber at an uptake rate of µL.min^{-1} is about 10 %. This efficiency was calculated using the following equation:

$$\eta_{Transport} = \frac{d^3_{AuNPs} * Slope_{Au^{3+}} * f_a * \pi * \rho}{(I_{AuNPs} - I_{dissolved}) * t_d * q * 6} \tag{4.2}$$

Where d$_{AuNPs}$, the certified diameter of the AuNPs used in nm; Slope$_{Au^{3+}}$, the slope calculated for the calibration range in cps.ng^{-1}.L^{-1} (from the dissolved Au calibration solutions); f$_a$, the mass fraction (here 100 %); ρ, the density of the AuNPs (here 19.3 x 10^{-11} ng.nm^3); I$_{AuNPs}$ and I$_{dissolved}$, respectively the mean intensity obtained for the measurement of AuNPs and of the dissolved Au background in cps; t_d, the dwell-time in second; and q, the flow-rate in L.s^{-1}.

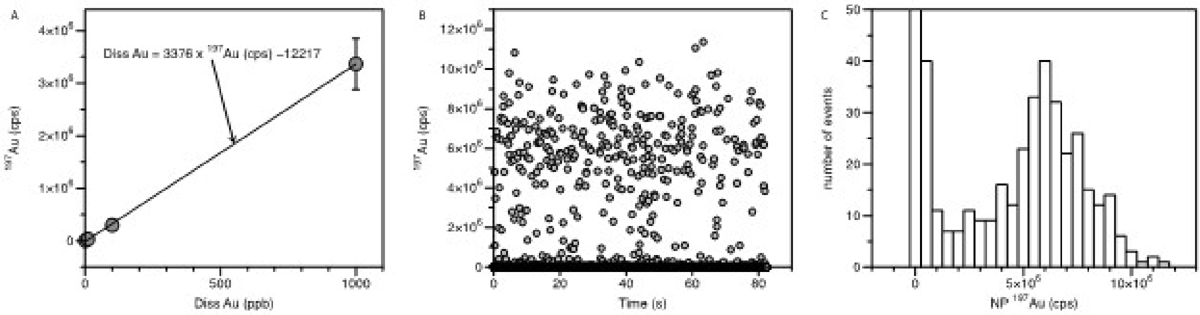

Figure 4.10 : *Gold nanoparticle characterization using the µ-dDIHEN, with a 50 µL sample loop at an uptake rate of 25 µL/min: calibration curve for dissolved Au (A), raw Au NP (40 nm) signal acquisition (B), and signal frequency histogram (C).*

Using the µ-dDIHEN at a flow-rate of 25 µL.min^{-1} and a 50 µL loop, the instrument was first calibrated with the dissolved Au standard solutions (Fig.4.10.a). The fitting parameters, calculated using the least square method, indicate a very good correlation between intensity and dissolved concentration (R^2 = 0.99981). A suspension of the 10^6 diluted reference 40 nm AuNPs (British Biocell International) was then injected through the µ-dDIHEN to the MS. The time-resolved signal we obtained (Fig.4.10.b) is identical to that usually obtained using a cyclonic spray chamber with a signal spike each time an ion cloud coming from an ionized NP reaches the detector (according to an appropriate dilution to avoid AuNP signal coincidences at millisecond dwell-times). Once converted into a histogram (Fig.4.10.c), the Gaussian-like shape is confirmed by a Kolmogorov-Smirnov test showing that NP intensities are normally distributed (p = 1.33 x 10^{-15} with N = 270 and a = 0.05, Massey 1951). Thus, this result is assessed again for a correct nebulization–vaporization–ionization of the mono-dispersed 40 nm AuNPs into the plasma with the µ-dDIHEN. However, in order to verify that the size distribution is not broader than the one provided by the manufacturer, further experiments are needed with different NP sizes and compositions.

Based on the slope obtained with the dissolved Au (3.4 x 10^3 cps.ng^{-1}.L^{-1}), the mean intensity of the 40 nm AuNPs distribution (6.4 x 10^6 cps) and the dissolved background (8.6 x 10^3 cps), the calculated transport efficiency is about 85 %. The 8.5-fold increase of the transport efficiency looks very promising and so far, such a high efficiency was never reached using a nebulizer to aerosolize the NP suspension. Further investigations should allow us to find the best set of parameters (uptake rates and dwell time) to reach 100 % transport efficiency.

4.4 Conclusion

We have demonstrated here that the newly developed direct injection nebulisation setup, the µ-dDIHEN, allows the introduction to ICP-MS of small volumes of liquid samples, under very stable conditions for uptake rates down to 5-7 µL.min^{-1}. These tests were successfully and reproducibly conducted on two different instruments, MC-ICP-MS Neptune and HR-ICP-MS Element II, for two dDIHEN injectors, and were validated for three different applications: for isotope ratio measurements (here for boron), for multi-element analyses of trace and utra-trace elements, and for sp-ICPMS (here for gold nanoparticles).

Because the signal intensity is linearly correlated with the uptake rate and too low signals hamper precise measurements, very low uptake rates might not always provide the best measurements, if signal detection of the instruments is not designed for very small signal. Investigating detection systems dedicated to very small signals (10^{12} or 10^{13} ohms amplifiers for Faraday cups or multi- Secondary Electron Multipliers) would allow to go a step forward in miniaturising ICP-MS measurements for µ-samples. For small B amounts in small volume samples (typically 100 µL) we propose that transient signal measurements with smaller flow injection loops (of typically 10 µL) can achieve the same performance as continuous (but unique) signal measurement on a larger loop, but with the big advantage of having multiple measurements and thus an estimation of the measurement uncertainty for each sample.

Overall, the big advantage of direct injection nebulization is the introduction of 100 % of the uptaken sample to the plasma. And combined with low uptake rates, the µ-dDIHEN can really be a method of choice to characterize nanoparticles by spICP-MS and overcome uncertainties due to the estimation of the low transport efficiencies of actual methods. Altogether the newly developed µ-dDIHEN system for liquid introduction to ICP-MS is very promising for a large variety of applications that require low sample uptake rates and/or small volumes, and for hyphenated technics.

CHAPTER 5

δ^{11}B DETERMINATION IN LOW-B BIOCARBONATES

Sommaire

5.1 Introduction . . . 114

5.2 Experimental . . . 116

- 5.2.a Reagents, materials and labware . . . 116
- 5.2.b Standard and reference materials . . . 117
- 5.2.c Boron separation from carbonates by microsublimation . . . 118
- 5.2.d The µ-dDIHEN . . . 119
- 5.2.e MC-ICP-MS analyses . . . 119

5.3 Optimisation of the δ^{11}B measurements for low [B] . . . 122

- 5.3.a Sample and skimmer cones combinations . . . 122
- 5.3.b Reduction of the signal/noise ratio with 10^{13} Ω amplifiers . . . 126
- 5.3.c Long-term reproducibility . . . 129

5.4 Boron separation with the microsublimation . . . 131

- 5.4.a Whole procedural blank contamination . . . 131
- 5.4.b Heating duration of the microsublimation . . . 133
- 5.4.c Microsublimation for different B masses loaded . . . 134

5.5 Application: microsublimation vs ion chromatography . . . 135

5.6 Conclusion . . . 139

La mise en place du µ-dDIHEN a permis de réduire les volumes analysés et a présenté d'excellentes reproductibilités. Cependant, celles-ci n'étaient atteintes que pour des échantillons à [B] > 20 ppb. Ce chapitre présente ainsi la seconde partie du développement analytique qui a permis la mesure du δ^{11}B$_{carb}$ dans des carbonates à très faible niveau de bore. J'ai ainsi mis en oeuvre un protocole qui a d'abord consisté à développer la séparation du bore de sa matrice carbonatée par la microsublimation, avec un important travail de réduction des blancs de chimie et de validation de la reproductibilité de cette méthode. En adaptant le montage µ-dDIHEN/MC-ICP-MS Neptune avec des cônes Jet + X et des amplificateurs à 10^{13} Ω, j'ai pu abaisser considérablement les quantités de bore nécessaires à la mesure du δ^{11}B. J' ai réussi de cette manière à mesurer des échantillons de carbonates contenant jusqu'à 1 à 2,5 ng de bore, à de très faibles niveaux de blanc de l'ordre de la dizaine de picogrammes. Ce chapitre rédigé sous forme d'article a été accepté à *Journal of Analytical Atomic Spectrometry*.

HIGH PRECISION MC-ICP-MS MEASUREMENTS OF ^{11}B/^{10}B RATIOS FROM NG AMOUNTS IN CARBONATE SAMPLES, USING MICROSUBLIMATION AND DIRECT INJECTION (µ-DDIHEN)

Matthieu Buisson[1], Pascale Louvat[1], Caroline Thaler[1], Claire Rollion-Bard[1]

[1]*Université de Paris - Institut de physique du globe de Paris - CNRS, UMR 7154, Paris, France*

Abstract

The boron isotopic ratio (δ^{11}B) of marine biogenic carbonates is a proxy for oceanic pH through the geological times, provided that δ^{11}B measurements reach precisions better than 0.8 ‰ (2SD), corresponding to 0.1 pH-unit (magnitude of the Anthropocene ocean acidification). This level of precision is challenging for the small size and low B content of the samples used in paleoceanographic reconstitutions. We developed a protocol combining (i) the fast-handling and very low blanks (9 ± 7 pg, 1SD, n=7) microsublimation technique to purify boron from the carbonate matrix and (ii) the direct injection of the samples to the MC-ICP-MS plasma with the new µ-dDIHEN device, allowing for small sample volumes and low uptake rates. We further used Jet sampler and X skimmer cones and implemented two 10^{13} Ω amplifiers to respectively increase the sensitivity and enhance the signal/noise ratio, enabling the precise measurement of small B signals. Our protocol, that consumes only 240 µL for a triplicate sample-standard bracketing (SSB) measurement, was validated through repeated B extractions and measurements of the carbonate reference material MVS-1 at different B concentrations. It yielded 15.93 ± 0.24 ‰ (2SD, n=10) with only 1.2 ng consumed for a triplicate SSB measurement, with individual external repeatabilities (n=5, 2SD) of 0.19 ± 0.14 ‰. We further measured δ^{11}B of modern biogenic carbonates (arthropods, brachiopods, molluscs, red algae and recifal carbonate mix) down to 0.5-0.7 ng of B and successfully compared these δ^{11}B values with those obtained after B extraction of the same samples through ion exchange chromatography.

5.1 Introduction

The boron isotopic ratio $^{11}B/^{10}B$ has been widely used to explore geochemical processes on Earth owing to the large atomic mass disparity (10 %) between ^{10}B and ^{11}B leading to large fractionations (De Hoog & Savov, 2018; Gaillardet & Lemarchand, 2018; Marschall, 2018; Trumbull & Slack, 2018). One of boron isotope studie's major contributions is the possibility to infer the oceanic pH from biogenic carbonates (Vengosh *et al.*, 1991b; Hemming & Hanson, 1992). This permits to track ocean acidification during past climatic crises (Hönisch *et al.*, 2012; Clarkson *et al.*, 2015; Henehan *et al.*, 2019; Jurikova *et al.*, 2020), atmospheric pCO_2 variations across the last 65 Myr (Pearson & Palmer, 2000; Hönisch *et al.*, 2009; Anagnostou *et al.*, 2016; Chalk *et al.*, 2017; Rae *et al.*, 2018), until today's acidification caused by anthropogenic CO_2 emissions (Wei *et al.*, 2009; Fietzke *et al.*, 2015; Wu *et al.*, 2018). The relationship between $^{11}B/^{10}B$ and pH is based on the preferential incorporation into the carbonate lattice of the tetrahedral borate anion $B(OH)_4^-$ (Vengosh *et al.*, 1991b; Hemming & Hanson, 1992), isotopically lighter by 27.2 ± 0.6 ‰ than its weak conjugate acid, the trigonal boric acid $B(OH)_3$ (Klochko *et al.*, 2006), the proportion of these two dissolved species in seawater fluctuating with pH. Reliable oceanic pH reconstitutions require high accuracy of the δ^{11}B measurements and reproducibility of at least 0.8 ‰ (2SD), roughly equivalent to 0.1 pH unit (Foster *et al.*, 2006). This indeed corresponds to the observed amplitude of anthropogenic ocean acidification (Caldeira & Wickett, 2003; Orr *et al.*, 2005), bearing in mind that for the last 300 Myr oceanic pH has oscillated between 7.5 and 8.2 (Hönisch *et al.*, 2012), whereas during the Pleistocene glacial/interglacial transitions the shift was about 0.2 pH unit (Hönisch *et al.*, 2009).

However the challenges inherent in measuring δ^{11}B with ICP-MS are manifold: (1) a low sensitivity, due to the high first ionization energy of boron (8.3 eV); (2) long washout times triggered by the strong memory effect of boron (Al-Ammar *et al.*, 2000); (3) a large instrumental mass bias, due to the 10 % atomic mass discrepancy between the two isotopes, inducing large space charge effects during ion transfers in the MC-ICP-MS plasma (Aggarwal *et al.*, 2003; Foster, 2008); (4) $^{40}Ar^{4+}$, $^{20}Ne^{2+}$ isobaric interferences on $^{10}B^+$ and $^{10}B^1H^+$ on $^{11}B^+$ (Foster, 2008); (5) chemistry and laboratory blank issues caused by the volatility of $B(OH)_3$ (Misra *et al.*, 2014b) ; (6) residual matrix effects resulting in varying instrumental mass fractionation (Louvat *et al.*, 2011a). It is thus highly challenging to deal with small carbonate samples with very low boron concentration like foraminifera ([B] ≈ 10 ppm), for which tens to hundreds individual shells are required to gather a sufficient amount of material for B isotope ratio determination (Rae *et al.*, 2011). Breakthroughs in palaeoceanographic and paleoclimatic reconstructions during the last twenty years have been therefore supported by technological and scientific achievements in mass spectrometric analysis of the boron isotopic ratio (Aggarwal & You, 2016; Foster *et al.*, 2018).

While interferences are easily and fully resolved at low resolution ($m/\Delta m$=400, e.g. $^{40}Ar^{4+}$ on $^{10}B^+$; $^{10}B^1H^+$ impact being negligible, Foster 2008) and the sensitivity can be enhanced five times with the combination of Jet sample cone and X skimmer cone to extract ions (Misra *et al.*, 2014b; He *et al.*, 2016), separate approaches have been pursued to counteract the memory effect of boron, i.e. the addition of gaseous ammonia to maintain a basic environment in the spray chamber and convert thereby $B(OH)_3$ to the non-volatile $B(OH)_4^-$ (Al-Ammar *et al.*, 2000; Foster, 2008; Farmer *et al.*, 2016) or the selection of different rinse solutions: water followed by NH_4OH (Wang *et al.*, 2010), HNO_3 (McCulloch *et al.*, 2014), HF (Misra *et al.*, 2014b), or NaF (He *et al.*, 2019). According to the washing protocol, Foster (2008), Misra *et al.* (2014b) and He *et al.* (2019) observed blanks dropped to 2 % of the initial boron signal in less than 200 seconds. Decreasing the washout time between samples allowed consequently the implementation of the sample-standard bracketing technique (SSB) to correct for mass bias drift (Foster, 2008; Louvat *et al.*, 2014b). More recently the reduction of the signal/noise ratio through the use of 10^{12} Ω and more specifically the newly released 10^{13} Ω resistors as amplifiers has facilitated the δ^{11}B determination at high precision for low ion beam intensities (Lloyd *et al.*, 2018; Sadekov *et al.*, 2019).

Nevertheless, for boron analyses, because it is sticky and volatile, spray chambers suffer from memory effects, while desolvators (e.g. APEX or Aridus) lead to signal loss. Such introduction systems are thus not optimum, unless special wash methods are implemented, as stated above. An alternative strategy, the direct injection nebulization, has been adopted at Institut de physique du globe de Paris (IPGP) to circumvent the spray chamber and its related memory effects, and successfully implemented during the last decade with continuous upgrades to automate the setup and decrease the uptake rate, leading to the best individual reproducibility ($\sim$ 0.1 ‰, 2SD) and lowest sample volume needed (100 µL) published so far for boron isotope measurements (Louvat *et al.*, 2011a, 2014b, 2019). It consists of spraying the sample directly into the plasma by placing a demountable direct injection high efficiency nebulizer (d-DIHEN, Westphal *et al.* 2004) directly into the torch, in place of the injector, thus increasing the sensitivity by a factor of two to five and drastically decreasing washout times and blank signal (Louvat *et al.*, 2011a). Automation of sample introduction to the d-DIHEN allowed to measure faster, continuously and to provide accordingly a more efficient SSB than spray chamber (Louvat *et al.*, 2014b), and its recent miniaturization (µ-dDIHEN) now enables the analysis of very small sample volumes (Louvat *et al.*, 2019).

The critical point remains that “bulk” δ^{11}B analysis methods involve a chemical extraction of boron from the constituents of the samples prior to analyses, otherwise matrix effects affect the accuracy of the measurements. This extraction requires that the boron recovery from the sample is close to 100 % to avoid any isotopic fractionation (Gaillardet *et al.*, 2001; Lemarchand *et al.*, 2002a; Misra *et al.*, 2014b) and necessitates a cautious and specific handling of the samples. Initially, boron was extracted from samples by ion exchange chromatography, using the boron-specific resin Amberlite IRA-743 (Kiss, 1988; Vengosh *et al.*, 1991b; Hemming & Hanson, 1992, 1994). However, ion exchange chromatography suffers from several shortcomings: it is time consuming, taking place over several hours, which also boosts the boron loss by this long air exposure, and the multitude of reagents used for dissolution, buffering, conditioning, washing and elution are as many possible sources of contamination, despite the recent progress to automate ion exchange extractions (Vega *et al.*, 2020). A substitute to this separation procedure, the microsublimation (or microdistillation) technique, initially dedicated to remove organic contamination as final purification step after ion chromatography for TIMS measurements (Gaillardet *et al.*, 2001; Lemarchand *et al.*, 2002a), re-emerged ten years ago in the literature (Wang *et al.*, 2010). Due to its volatility, $B(OH)_3$ is "distilled" in a single step at low temperature (70-100 °C) from digested samples in an acidic matrix (Wang *et al.*, 2010; Liu *et al.*, 2014; Misra *et al.*, 2014b; Raitzsch *et al.*, 2018). Consequently to the small volume of sample solution needed (< 50 µL), the fast handling and the reduction in the number of reagents used, the risks of contamination are radically reduced.

In this study, we introduce a new protocol to achieve accurate and high precision δ^{11}B determination in low-volume, low [B] solutions of dissolved carbonate samples, by coupling the microsublimation B extraction and the miniaturized direct injection nebulization system (µ-dDIHEN) for sample introduction to MC-ICP-MS, designed for low volume consumption (Louvat *et al.*, 2019). Firstly, the optimisation of the δ^{11}B analyses with the µ-dDIHEN for low [B] has been achieved by the implementation of an X skimmer cone, which enhanced the sensitivity, and of two 10^{13} Ω amplifiers, which improved the signal/noise ratio and thus the precision of the measurements for small signals. Secondly, the optimal temperature, time of heating, sample volume and B amounts have been carefully calibrated for the microsublimation protocol to extract boron from small carbonate samples. Those experiments were conducted on a carbonate reference material (MVS-1, Jurikova *et al.* 2019), and multiple separations have been performed at several boron concentrations to test reproducibility. The protocol finally established has been tested on marine carbonate samples of different B concentrations and mineralogies.

5.2 Experimental

5.2.a Reagents, materials and labware

Because of the ubiquity of boron, drastic precautions must be taken to avoid contamination during the chemical preparations and measurements of the solutions and during air-handling of the samples, by using reagents as pure as possible and performing intensive cleaning of the vessels. The whole chemical handling has been hence conducted in an over-pressured and air filtered cleanroom with boron-free H14 HEPA filters (Megacell III, AAF, Vincennes, France). Nitric acid HNO_3 was distilled with a DST1000 device (Savillex, Eden Prairie, MN, USA), then diluted with Milli-Q (MQ) water (resistivity > 18 MΩ/cm) from a Q-Pod distributor comprising 0.22 µm Millipak Express filter (Millipore, Burlington, MA, USA) and finally stored in pre-washed polypropylene bottles.

All 5 mL Savillex Teflon fin legged conical vials used for microsublimation are initially rinsed thrice with MQ water and successively boiled in 3 N and 0.5 N HNO_3 in a Teflon jar placed on a hotplate at 95°C during four days, with three MQ water rinses after each cleaning step. The sealing of these vials was monitored to ensure there are no leaks and prevent any future boron loss: the beakers were filled with a volume of ethanol, weighted and placed on a hotplate at 100°C for 24 hours. If no leakage was noticed (no weight loss), the beakers and their caps were numbered to keep the same beaker-cap association for the microsublimation. Other consumables, polypropylene (PP) tubes for MC-ICP-MS analyses and pipette tips were bathed in a 0.5 N HNO_3 and rinsed in MQ water before use.

5.2.b Standard and reference materials

The boron isotopic ratio $^{11}B/^{10}B$ of reference materials and samples is conventionally expressed in delta notation ($\delta^{11}B$) as parts per thousand (‰) deviation relative to the ratio of the boric acid standard reference material NIST SRM 951 (NIST, USA, by definition at 0 ‰, Catanzaro *et al.* 1970) diluted at the sample/reference material concentration (within ± 5 %) in 0.05 N HNO_3 (Louvat *et al.*, 2011a), following

$$\delta^{11}B = (\frac{(^{11}B/^{10}B)_{sample}}{(^{11}B/^{10}B)_{NIST\ SRM\ 951}} - 1) * 1000. \tag{5.1}$$

Three boric acid reference materials (BAM, Germany, Vogl & Rosner 2011) ERM-AE120 (AE120; $\delta^{11}B$ = -20.2 ± 0.6 ‰), ERM-AE121 (AE121; $\delta^{11}B$ = +19.9 ± 0.6 ‰) and ERM-AE122 (AE122; $\delta^{11}B$ = +39.7 ± 0.6 ‰) have been measured alongside with the samples to test the accuracy and reproducibility of the $\delta^{11}B$ measurements. AE121 was more often measured; as its $\delta^{11}B$ value is close to the values for marine biogenic carbonates, it was consistently incorporated in the carbonate sample analytical sessions.

Microsublimation experiments were carried out with the carbonate reference material MVS-1 ([B] ≈ 38 ppm, B/Ca ≈ 310 µmol.mol^{-1}, $\delta^{11}B$ = 15.95 ± 0.19 ‰, n=46) elaborated in GEOMAR Helmholtz-Zentrum für Ozeanforschung (Kiel, Germany, Jurikova *et al.* 2019). As the traditional carbonate reference materials JCp-1 (coral *Porites*, B/Ca ≈ 460 µmol.mol^{-1}) and JCt-1 (giant clam *Tridacna gigas*, B/Ca ≈ 190 µmol.mol^{-1}) are no longer available due to their animal origins (Gutjahr *et al.*, 2020; Stewart *et al.*, 2021), MVS-1, which we had in large quantities, represents a good intermediate in terms of B/Ca ratios. Delivered in the powdered form, previously pre-treated with MQ water and an oxidative cleaning to remove organic matter following Barker *et al.* (2003), this carbonate reference material (66 mg) was dissolved in 0.5 N HNO_3 in order to obtain a stock solution with a boron concentration of about 500 ppb. This concentration corresponds e.g. to 20 ng of boron in a 40 µL droplet. Lately, we added to our carbonate measurement sessions the new synthetic marine carbonate reference material NIST RM 8301 Foram ([B] ≈ 2.5 ppm, B/Ca ≈ 140 µmol.mol^{-1}, $\delta^{11}B$ = 14.51 ± 0.17 ‰, Stewart *et al.* 2021). This reference material is provided dissolved in HNO_3 3.3 N and was consequently diluted to HNO_3 0.5 N, leading to a B concentration of 370 ppb, close to that prepared from the MVS-1 reference material and used for the experiments.

5.2.c Boron separation from carbonates by microsublimation

Boron is extracted from the carbonate matrix and rid of its various sources of contamination (organic matter, clays and/or oxides, Barker *et al.* 2003) by a microsublimation technique modified from Gaillardet *et al.* (2001), Misra *et al.* (2014b) and Raitzsch *et al.* (2018). A droplet (volume < 70 µL) of the carbonate sample or reference material, dissolved in HNO_3 0.5 M, is deposited in the lid of a pre-cleaned 5 mL Savillex Teflon fin legged conical vial. The vial, used as a distillation reservoir, is tightly and rapidly closed in the upside-down position and then coated completely with an aluminium foil, except the top of the beaker where the distillate will condense in this colder tip (Fig.5.1). It is thereafter positioned on a hotplate for 24 hours at 95°C (fixed after the heating duration tests). The beaker is then removed from the hot plate, carefully flipped, and allowed to cool for 15 min.

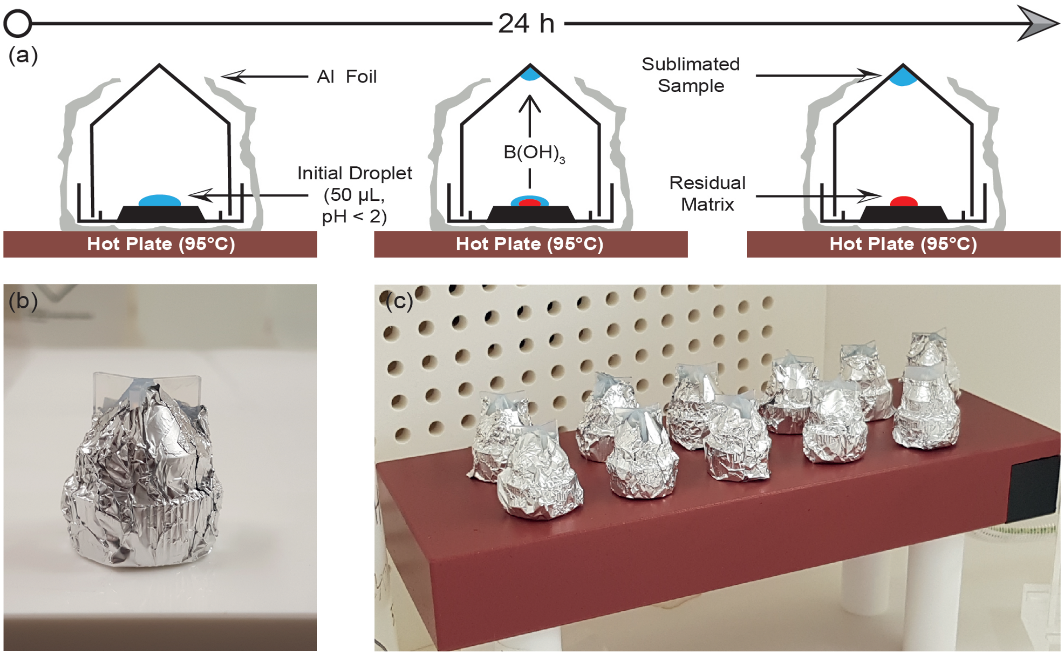

Figure 5.1 : *(a) Schematic illustration of the microsublimation protocol adopted for B extraction from carbonate samples after the multiple tests of this study, modified from Gaillardet et al. (2001). (b) A microdistillation vial wrapped with aluminium foil, except for the tip. (c) Microsublimation session with the vials placed on the hot plate.*

Thanks to its volatility, $B(OH)_3$, the only B species at this low pH (< 2), is exclusively found in the distillate while the matrix remains on the cap. The distillate solution is immediately diluted with MQ water to 0.05 N HNO_3 (according to the droplet size, e.g. 450 µL of MQ water for an initial 50 µL droplet) and transferred to a 5 mL PP tube for boron isotope analysis. A volume of 0.05 N HNO_3 was further added to the samples, which initial droplet volumes were below 50 µL, to ensure a volume large enough ($\sim$ 0.5 mL) for at least four injections with the FAST sample loop of the µ-dDIHEN. The boron concentration of the sample is first determined (with the MC-ICP-MS) in order to prepare a bracketing standard solution at the same concentration ($\pm$ 5 %).

5.2.d The µ-dDIHEN

The d-DIHEN (demountable Direct Injection High Efficiency Nebuliser, Analab, Strasbourg, France) consists of a long Meinhard-like quartz nebulizer plugged in the torch instead of a regular injector, and for which quartz needle and capillary can be dismounted and changed separately (Westphal *et al.*, 2004). The spray can be easily adjusted by changing the relative position of the capillary and needle tip, and this optimisation takes place outside the torch under a binocular microscope (Louvat *et al.*, 2011a), before ignition of the plasma. Originally, the solutions were delivered into the d-DIHEN through a peristaltic pump. Because the introduction of air bubbles between samples lead to plasma extinction and possibly torch melting (Louvat *et al.*, 2011a), the d-DIHEN was then fully automated with a 6-port valve (FAST, ESI, USA), a carrier solution (0.05 N HNO_3) being introduced when the autosampler probe moves from a sample to another (Louvat *et al.*, 2014b).

The µ-dDIHEN setup has been recently developed for low sample uptake rates and small sample volumes. It is fully described in Louvat *et al.* (2019). In this setup, the sample is pushed to the nebulizer by a gas displacement pump (GDP, an 8-port valve — ESI, USA — with two carrier solution loops and fed by an adjustable argon flux from a micro mass flow controller — El Flow, Bronkhorst, France —) in place of the peristaltic pump. In summary, the sample solution probed by the autosampler fills the 50 µL sample loop of the FAST valve and is then pushed toward the plasma by the carrier solution (HNO_3 0.05 N) from the GDP at a controlled uptake rate (5 to 25 µL.min^{-1}). During filling-up of the sample loop, this carrier solution directly supplies to the plasma, washing at the same time the system between the FAST valve and the d-DIHEN nebulizer. Conversely, while the sample from the sample loop is pushed to the plasma, the autosampler probe and second half of the FAST valve are washed.

In this study, a peristaltic pump (Spetec, Erding, Germany) is used to fill alternatively the two loops of the GDP valve with the carrier solution, but also the 50 µL sample loop, instead of the autosampler vacuum used in Louvat *et al.* (2019). This allowed a slower but more reproducible filling-up of the FAST sample loop, and a further reduction of the sample volume needed. The timings to toggle the GDP and FAST valves are set within the ESI autosampler software, synchronized with the ICP-MS software (Louvat *et al.*, 2019).

5.2.e MC-ICP-MS analyses

Boron isotope measurements have been conducted at IPGP on a MC-ICP-MS Neptune (ThermoScientific, MA, USA), all the settings being listed in the Table 5.1. The measurements were done at low resolution ($m/\Delta m \approx 400$). The signals of the ^{10}B and ^{11}B isotopes are respectively captured by the Faraday cups L3 and H3, amplified with 10^{11} or 10^{13} Ω resistors according to the boron concentration of the analyte, consistently in HNO_3 at 0.05 N (Louvat *et al.*, 2011a, 2014b, 2019). The ^{11}B signal for a boron concentration of 20 ppb was generally between 0.2 and 0.4 V (depending on d-DIHEN nebulizer and MC-ICP-MS tuning from one session to the next). The ^{11}B signal of 0.05 N HNO_3 blank solutions is typically between 0.4 and 0.9 mV, contributing less than 0.8-1.8 % to a signal at 50 mV ($\simeq$ 5 ppb) whereas the ^{11}B/^{10}B blank ratios interestingly converge towards values of 1-2 when low boron concentrations were analyzed. Additional washout of the system during measurements is unnecessary as it is already cleaned with the carrier solution between two injections: the signal drops below 1 % of the previous injection signal in 1 minute.

Table 5.1 : *Operating parameters of the MC-ICP-MS instrument*

Instrument	Operating parameters
Nebulizer	Direct injection nebulizer (d-DIHEN)
Autosampler	SC-2DX (ESI)
Automation valves	6-port FAST valve/8-port GDP valve (ESI)
Sample matrix	0.05 N HNO_3
Uptake rate	25-30 µL.min^{-1}
Sample cone	Ni - JET
Skimmer cone	Ni – H or X
Plasma RF power	1300 W
Extraction voltage	-2000 V
Ar cool gas	15 L.min^{-1}
Ar auxiliary gas	1.2 to 1.5 L.min^{-1}
Ar sample gas	0.4 to 0.5 L.min^{-1}
Cup configuration	^{10}B in L3 and ^{11}B in H3
Amplifier resistors	10^{11} or 10^{13} Ω
Resolution	Low (400)
Baseline	30 cycles of 1 s integration
B isotope measurements	12 cycles of 8 s integration
Uptake time	40 s
Wash time	(0 s), during uptake
Sensitivity	0.2 to 0.3 V for [B] $\approx$ 20 ppb on ^{11}B mass

After installing the µ-dDIHEN assembly, verifying all loops are correctly filled with the carrier solution, adjusting the timings for filling the 50 µL sample loop on the FAST valve for minimum sample volume consumption (the timing of the GDP valve being fixed, Louvat *et al.* 2019) and optimizing the d-DIHEN spray, the plasma is switched on. The peristaltic pump is in the aftermath turned on, followed by the GDP at a gas flow rate of 45 µL.min^{-1}, whereas the RF power, the auxiliary and the sample gas are slowly increased to the values listed in Table 5.1. One hour is necessary to stabilize the µ-dDIHEN uptake rate, during which the instrument is tuned to maximize the sensitivity and stability of the signal.

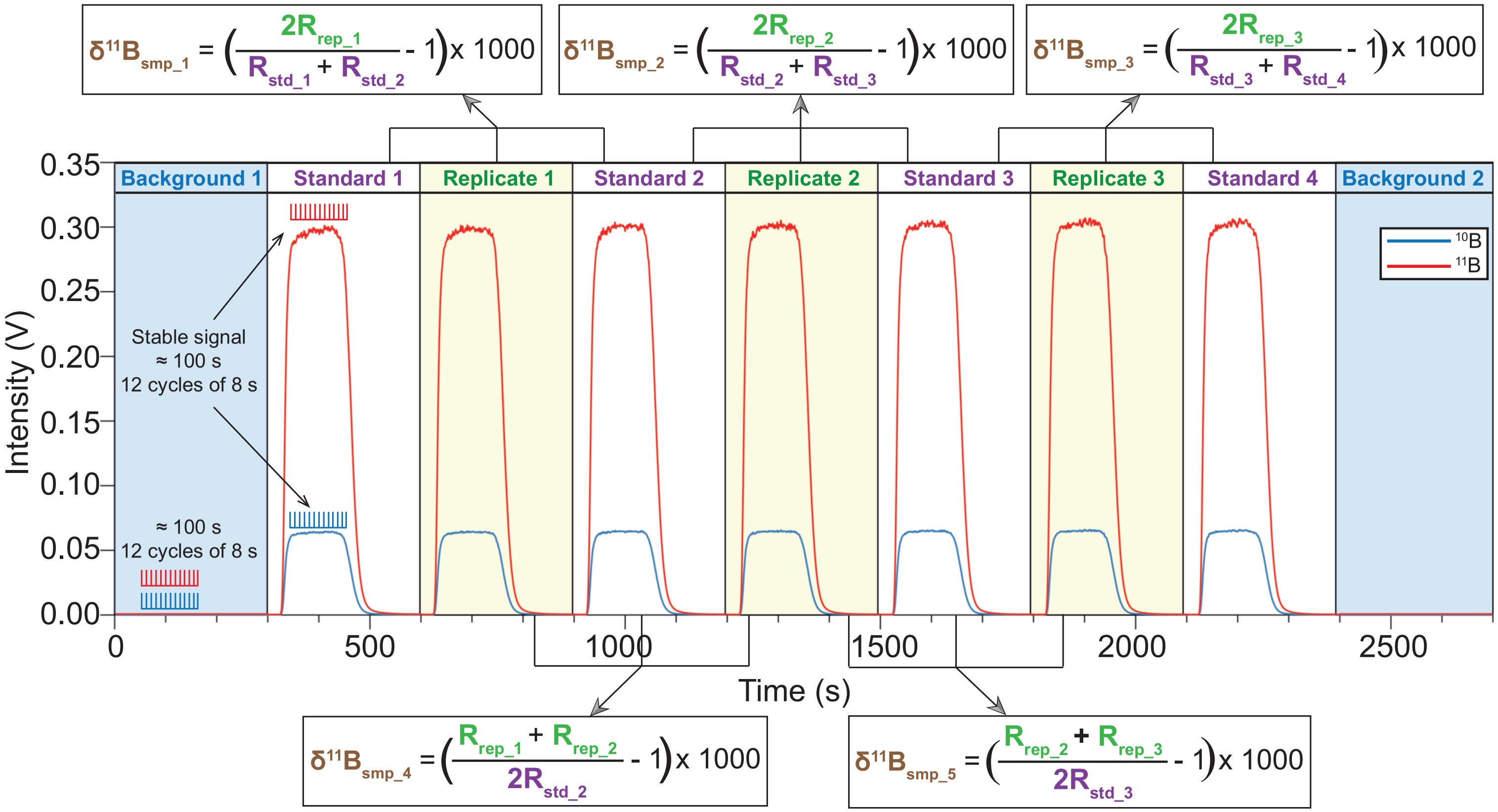

$$\delta^{11}B_{smp\_1} = \left(\frac{2R_{rep\_1}}{R_{std\_1} + R_{std\_2}} - 1\right) \times 1000$$

$$\delta^{11}B_{smp\_2} = \left(\frac{2R_{rep\_2}}{R_{std\_2} + R_{std\_3}} - 1\right) \times 1000$$

$$\delta^{11}B_{smp\_3} = \left(\frac{2R_{rep\_3}}{R_{std\_3} + R_{std\_4}} - 1\right) \times 1000$$

$$\delta^{11}B_{smp\_4} = \left(\frac{R_{rep\_1} + R_{rep\_2}}{2R_{std\_2}} - 1\right) \times 1000$$

$$\delta^{11}B_{smp\_5} = \left(\frac{R_{rep\_2} + R_{rep\_3}}{2R_{std\_3}} - 1\right) \times 1000$$

$$\text{with } \mathbf{R} = \frac{{}^{11}B_{measured} - ({}^{11}B_{bkg\_1} + {}^{11}B_{bkg\_2})/2}{{}^{10}B_{measured} - ({}^{10}B_{bkg\_1} + {}^{10}B_{bkg\_2})/2}$$

$$\delta^{11}B_{sample} = \text{Average}\ (\delta^{11}B_{smp\_1}, \delta^{11}B_{smp\_2}, \delta^{11}B_{smp\_3}, \delta^{11}B_{smp\_4} \text{ and } \delta^{11}B_{smp\_5})$$

$$2SD_{sample} = 2 \times \text{Standard Deviation}\ (\delta^{11}B_{smp\_1}, \delta^{11}B_{smp\_2}, \delta^{11}B_{smp\_3}, \delta^{11}B_{smp\_4} \text{ and } \delta^{11}B_{smp\_5})$$

Figure 5.2 : *Typical sample-standard-sample bracketing (SSB) sequence for the triplicate measurement of a sample with the μ-dDIHEN. Here* $[B]_{solution}$ *= 20 ppb, sample loop = 50 μL, uptake rate = 25 μL.min*$^{-1}$*. Average* $\delta^{11}B$ *of the sample and "individual" repeatability (2SD) calculated from the five* $\delta^{11}B$ *values thus obtained.* R_{rep_x} *=* $^{11}B/^{10}B$ *of the reference material or sample solution,* R_{std_x} *=* $^{11}B/^{10}B$ *of the standard NIST SRM 951,* $^{10\ or\ 11}B_{blk\_x}$ *=* $^{10\ or\ 11}B$ *intensity of the background (*HNO_3 *0.05 N) and* $\delta^{11}B_{smp\_x}$ *= one of the five* $\delta^{11}B$ *values obtained for the reference material/sample solution. Adapted from Louvat et al. (2014b) and Louvat et al. (2019).*

As recommended in Louvat *et al.* (2019), an uptake rate of 25-30 µL.min^{-1} is selected by fixing the gas flow rate of the mass flow meter of the GDP at 45-50 µL.min^{-1}. These parameters correspond to the best compromise to have the highest sensitivity while displaying the most stable signal and to achieve injection peaks comprising a stable signal plateau long enough (around 100 s) to provide a statistical determination of the ^{11}B/^{10}B ratio with 12 cycles of 8 seconds with the 50 µL sample loop (Fig.5.2).

The sample is measured thrice in a row, alternately with NIST SRM 951 standard, following the SSB technique (Galy *et al.*, 2001). A 0.05 N HNO_3 blank solution is measured before the first standard and after the last standard of the SSB sequence for [B] < 50 ppb (Fig.5.2) to take into consideration the slight incremental contamination that is mainly due to B evaporation from the opened vials in addition to the initial background. The blank solution signals proved to be stable during a SSB sequence, meaning that blank intensity and ratio are not affected by the ^{11}B/^{10}B value of the sample or standard that was measured just before. Acidity and concentration of the sample, reference material and standard solutions are matched to within ± 5 % in order to maintain similar mass bias conditions in the plasma. Five δ^{11}B values, background corrected, can be therefore extracted from the SSB sequence (Fig.5.2) allowing to calculate an average δ^{11}B value and "individual" repeatability (2SD) for each sample, as described in Louvat *et al.* (2014b). This procedure also allows to assess potential mass bias induced by residual matrix in the sample B solution or to take into account abrupt drifts of the machine and to accordingly exclude outlier δ^{11}B values. The two additional $\delta^{11}B_{smp\_4}$ and $\delta^{11}B_{smp\_5}$ (Fig.5.2) have consequently an important role to play in the averaged δ^{11}B and 2SD results. Only 240 µL of sample are needed for the whole triplicate SSB sequence, each injection consuming only 80 µL of liquid (Louvat *et al.*, 2019).

5.3 Optimisation of the δ^{11}B measurements for low [B]

5.3.a Sample and skimmer cones combinations

At the interface between the ICP part at atmospheric pressure and high temperature and the mass spectrometer part under vacuum at low temperature, the sampler and skimmer cone's function is to extract the ions formed in the argon plasma. Accordingly, the geometry of these nickel cones strongly impacts the instrumental mass fractionation and the sensitivity, and hence the precision and accuracy of the measurements. Two types of sampler and skimmer cones are available for the MC-ICP-MS Neptune (Thermo Scientific): the 0.8 mm cylindrical orifice Standard sampler cone and the 1.2 mm cylindrical orifice Jet sampler cone; the 0.8 mm cylindrical orifice H skimmer cone and the 0.8 mm orifice X skimmer cone, inducing four possible combinations of sampler-skimmer cones. The first three cones are characterized by a trumpet-shaped base, whereas the X skimmer cone exhibits a completely trumpet-shaped geometry (not cylindrical at the top, He *et al.* 2016). The combination Jet sampler cone + X skimmer cone enhanced the sensitivity by a factor 4 to 10 compared to the Standard + H combination for the heavy elements Sr, Nd, Hf, Pb and U (Newman, 2012) and by 2 to 7 times for lighter elements like Li and Mg (Gou *et al.*, 2018, 2019) in solution mode. This is due to the larger sampling of the plasma among the four cone combinations, allowed by the larger orifice of the Jet sampler cone and to the trumpet-shaped geometry of the X cone. However, the Jet + X cone combination also causes an increase of polyatomic interferences and of ion repulsion due to a larger space charge effect in the increased volume behind the X cone orifice, impacting Li and Mg isotope measurements, especially at low concentrations (Gou *et al.*, 2018, 2019).

Although B sensitivity during δ^{11}B measurement sessions is a critical point especially due to its poor ionization, no tests have really been carried out and no consensus was reached on the best association of cones for δ^{11}B measurements. He *et al.* (2016) evidenced boron sensitivity increase of 3 to 4 times with the Jet + X cones and of 2 times with the Standard + X cones, compared to the Standard + H cones. At IPGP, previous δ^{11}B measurements using direct injection were first performed with Standard + X cones (Louvat *et al.*, 2014b), and then with Jet + H cones for the µ-dDIHEN (Louvat *et al.*, 2019) after upgrading of the MC-ICP-MS Neptune with the Jet-interface (the X skimmer cone was initially abandoned because of frequent switch off of the extraction lens). Misra *et al.* (2014b) reported a 5 times enhanced sensitivity using the Jet + X cones. They, and later Lloyd *et al.* (2018) allowed to reduce the boron mass required for analysis with improved precisions.

We measured the δ^{11}B values of the reference materials AE120, AE121 and AE122 at different B concentrations, between 1 and 50 ppb, for two combinations of cones: the Jet + H and the Jet + X cones (Fig.5.3, Table.5.2). We also used 10^{11} or 10^{13} Ω amplifiers, which performances will be discussed in the next section. We observed an increase of 2 to 5 fold of the B signal using the X skimmer cone compare to the H cone, in agreement with Misra *et al.* (2014b) and He *et al.* (2016). As an example, the ^{10}B signal increased from around 4-10 to 21-23 mV for 5 ppb B solutions and from 8-23 mV to 40-48 mV for 10 ppb B. Given that the sample volume required for a triplicate analysis with the µ-dDIHEN is 240 µL, 5 and 10 ppb correspond to only 1.2 and 2.4 ng of boron analysed. The use of the X skimmer cone therefore allows for such low amounts to step over the threshold ^{10}B signal of 20-30 mV necessary to ensure reasonable external precisions (< 0.5 ‰, 2SD) with the µ-dDIHEN and with 10^{11} Ω amplifiers (Louvat *et al.*, 2019). The "extra-wet plasma" conditions when using the µ-dDIHEN (nebulization of the sample directly in the plasma) do not seem to hamper the performances of the Jet sample + X skimmer cone combination for δ^{11}B measurements.

The best boron isotope measurements achieved with the Jet + X cones can be explained by two reasons. As opposed to the observations of Gou *et al.* (2018) on δ^{7}Li and Gou *et al.* (2019) on δ^{26}Mg, the δ^{11}B determination with X skimmer cone is not impacted by the simultaneously amplified polyatomic interferences, $^{40}Ar^{4+}$ and $^{20}Ne^{2+}$ on $^{10}B^{+}$, that are still easily resolved at low resolution (m/Δm = 400), whereas $^{10}B^{1}H^{+}$ is insignificant (Foster, 2008; Misra *et al.*, 2014b).

Table 5.2 : *Boric acid reference materials BAM ERM-AE120, AE121 and AE122 measurements at B concentrations between 1 and 50 ppb, using either a H skimmer cone and 10^{11} Ω resistors as amplifiers or a X skimmer cone associated with 10^{13} Ω resistors. " * " symbol: outliers.*

ERM-AE120				**ERM-AE121**				**ERM-AE122**			
^{10}B intensity (mV)	[B]meas (ppb)	$\delta^{11}B$ (‰)	2SD (‰)	^{10}B intensity (mV)	[B]meas (ppb)	$\delta^{11}B$ (‰)	2SD (‰)	^{10}B intensity (mV)	[B]meas (ppb)	$\delta^{11}B$ (‰)	2SD (‰)
With H skimmer cone and 10^{11} Ω amplifiers											
4	5	-19.01*	1.54	4	5	22.15*	4.66	4	5	36.82*	5.92
5	5	-19.21*	1.64	5	5	17.63*	3.48	5	5	38.98*	3.62
5	5	-17.60*	4.58	5	5	21.28*	2.22	5	5	38.56*	2.99
5	5	-21.22	4.94	5	5	20.09	3.07	5	5	40.40	1.59
6	5	-20.51	0.81	6	5	19.24	0.69	7	5	40.11	0.73
7	5	-20.58	1.19	6	5	19.87	2.59	7	5	39.06	1.00
10	5	-20.44	0.35	9	5	19.59	0.67	10	5	39.81	0.77
10	5	-21.39	0.30	10	5	19.42	0.49	10	5	39.54	1.94
8	10	-20.18	1.35	8	10	19.39	2.98	8	10	38.09	1.21
9	10	-20.73	1.79	8	10	19.38	3.93	8	10	39.43	0.80
10	10	-20.74	1.16	9	10	19.96	1.05	9	10	37.78	0.48
10	10	-20.49	1.38	9	10	20.30	1.48	10	10	40.70	2.35
13	10	-20.51	0.33	12	10	19.93	0.70	13	10	38.80	0.49
14	10	-19.90	0.75	13	10	18.99	0.30	13	10	38.62	0.59
20	10	-20.50	0.58	19	10	19.45	0.92	20	10	38.98	0.05
23	10	-20.26	0.45	22	10	19.77	0.24	22	10	39.47	0.13
16	20	-19.89	0.62	16	20	19.61	0.40	15	20	39.25	1.25
17	20	-19.93	1.07	16	20	20.06	0.62	16	20	39.50	0.43
18	20	-19.92	0.30	17	20	19.00	1.19	18	20	39.75	0.63
19	20	-19.92	2.00	18	20	20.02	0.60	18	20	39.25	0.75
19	20	-20.03	0.89	18	20	19.84	0.96	18	20	39.82	0.54
26	20	-20.64	0.53	25	20	19.50	0.73	25	20	39.29	0.46
27	20	-20.05	0.44	26	20	19.57	0.18	26	20	39.33	0.20
40	50	-19.83	0.33	39	50	19.92	0.66	40	50	39.57	0.19
40	50	-19.76	0.23	40	50	19.98	0.27	41	50	39.66	0.28
46	50	-19.74	0.48	45	50	20.11	0.37	45	50	39.79	0.24
With X skimmer cone and 10^{13} Ω amplifiers											
4	1	-20.57	0.92	4	1	19.15	1.06	4	1	38.55	1.27
5	1	-19.89	0.38	5	1	19.94	0.65	5	1	39.02	0.86
8	2	-20.66	0.44	8	2	19.15	0.44	8	2	39.05	0.87
9	2	-21.00	0.06	8	2	19.48	0.43	9	2	39.21	0.22
9	2	-19.90	0.44	8	2	19.76	0.43	9	2	39.35	0.50
9	2	-20.09	0.56	9	2	19.69	0.50	9	2	38.64	0.35
21	5	-19.89	0.18	21	5	19.74	0.18	21	5	39.55	0.09
22	5	-20.41	0.39	21	5	19.63	0.13	21	5	39.23	0.19
23	5	-19.58	0.37	22	5	19.80	0.07	22	5	39.41	0.51
23	5	-19.89	0.14	23	5	19.75	0.16	23	5	39.21	0.21
42	10	-20.26	0.19	23	5	19.44	0.21	41	10	39.32	0.40
43	10	-20.28	0.13	40	10	19.59	0.19	41	10	39.35	0.16
45	10	-20.15	0.06	41	10	19.41	0.16	43	10	39.17	0.22
46	10	-20.24	0.13	42	10	19.45	0.27	45	10	39.25	0.11
82	20	-20.13	0.12	44	10	19.50	0.20	84	20	39.19	0.11
88	20	-20.13	0.11	48	10	19.74	0.17	86	20	39.20	0.14
93	20	-20.03	0.15	73	20	19.28	0.13	91	20	39.34	0.15
				83	20	19.57	0.12				
				86	20	19.56	0.17				
				91	20	19.61	0.08				

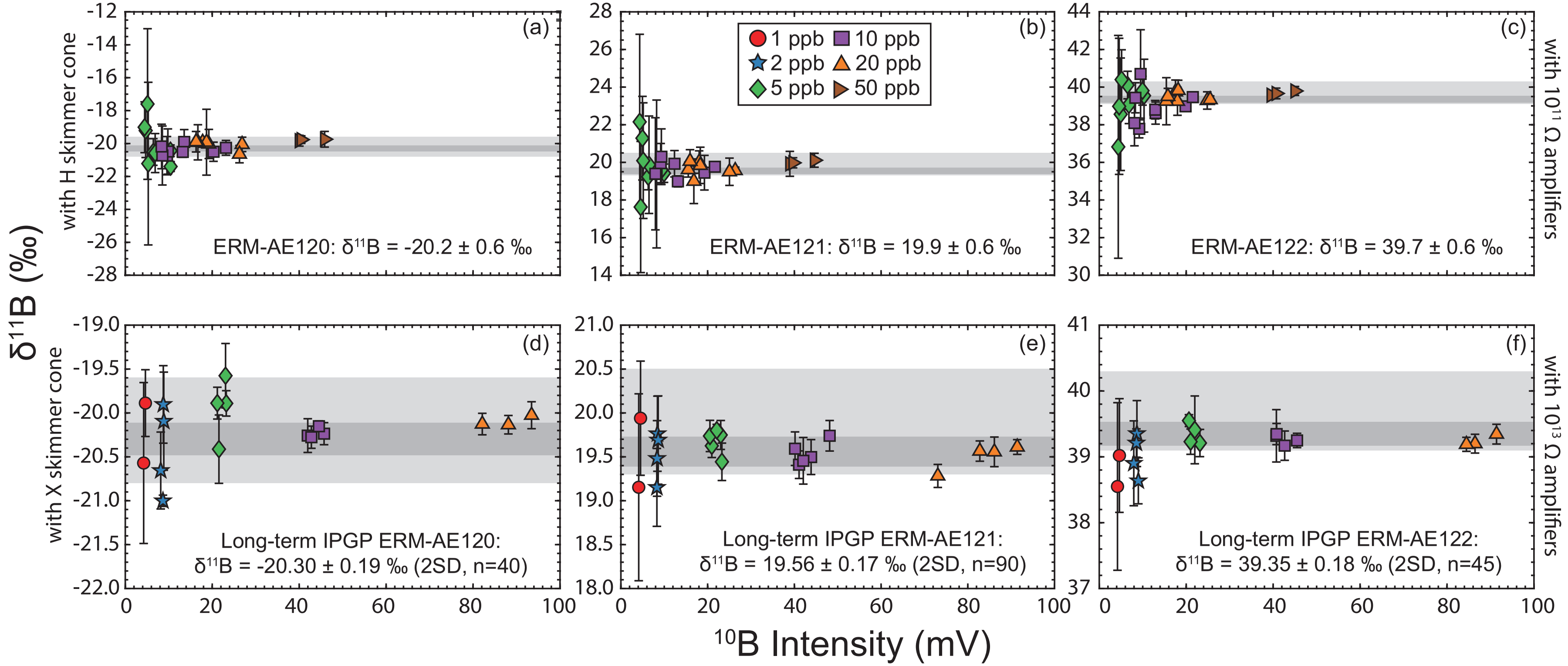

Figure 5.3 : *Reproducibility of the δ^{11}B measured for the reference materials BAM ERM-AE120, AE121 and AE122 at B concentrations between 1 and 50 ppb, using either a H skimmer cone and 10^{11} Ω resistors as amplifiers for a, b and c, or a X skimmer cone associated with 10^{13} Ω resistors for d, e and f. Light grey areas represent the reference values (Vogl & Rosner, 2011). Dark grey areas are for IPGP long-term values, updated from Louvat et al. (2019).*

As the space charge effect (charge repulsion) affects more light isotopes than heavy ones (Niu & Houk, 1996), the measured ^{11}B/^{10}B ratio is much higher than the true ^{11}B/^{10}B value (Fig.5.4). This mass discrimination is strengthened when using the X skimmer cone (increase by ~0.7-1.5 %), but not as much as for lithium (increase by 8 %, Gou *et al.* 2018), while it was reduced for magnesium (~2.5 %, Gou *et al.* 2019). This highlights the "element-dependent" nature of the instrumental mass bias caused by the type of cones used and that boron is less vulnerable than lithium to this additional mass discrimination effect with the Jet + X cones. Incidentally no relationship emerges between B concentration and the measured ^{11}B/^{10}B ratio, in opposition to the slight mass bias increase with concentration (between 20 and 800 ppb), which was reported for Li and Mg; more ions introduced in the plasma leading to larger charge repulsion effect (Gou *et al.*, 2018, 2019). The concentrations investigated in this study are probably too low to observe this influence. However slight shifts of ^{11}B/^{10}B between 1 and 50 ppb can be noted, which underlines once again the necessity to match the boron concentrations of standard and sample during the SSB procedure.

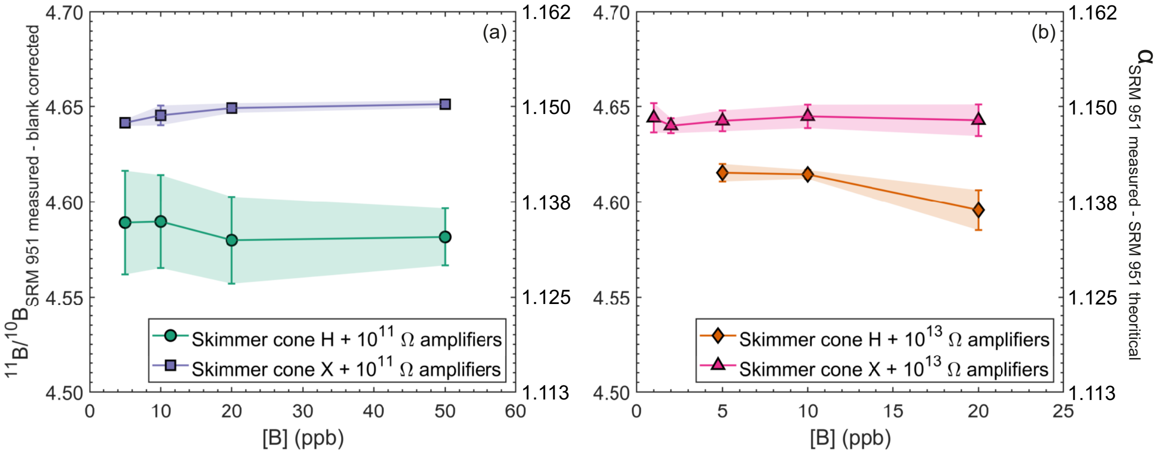

Figure 5.4 : *Change in instrumental mass bias with B concentration by using X or H skimmer cones with 10^{11} Ω (a) or 10^{13} Ω (b) amplifiers. Left Y-axis for ^{11}B/^{10}B ratio of NIST SRM 951 (after blank correction) and right Y-axis for the associated mass fractionation factor from its theoretical value of 4.04362 (Catanzaro et al., 1970).*

5.3.b Reduction of the signal/noise ratio with 10^{13} Ω amplifiers

The Faraday cup detectors of the MC-ICP-MS collect simultaneously the small ion beam currents, which are converted to voltages by amplifiers with high-ohmic resistances. This detection mode generates two sources of noises, the counting statistics (Poisson noise) and the thermal Johnson-Nyquist noise (JN noises) that lessen the internal precision (Wieser & Schwieters, 2005). The thermal JN noise, especially, originates from the high ohmic resistance and is critical for small ion beams (typically $\leq$ 100 mV for the mostly used 10^{11} Ω amplifiers, Wielandt & Bizzarro 2011).

JN noises can be understood as oscillations of the background voltage (in absence of ion beams) and is expressed as:

$$\Delta V_{JN} = \sqrt{\frac{4k_B RT}{t}}, \tag{5.2}$$

where ΔV$_{JN}$ is the 1 SD of the JN noise in voltage, k$_B$ the Boltzmann's constant (1.38.10^{-23} J.K^{-1}), T the temperature in K, t the integration time in s and R the resistance in Ω. It follows that if the resistance value is increased linearly by one (10^{12} Ω) or two (10^{13} Ω) orders of magnitude (and hence the signal voltage, even if it is translated back to 10^{11} Ω resistance by applying the amplifier's gain factors), the noise is only amplified by $\sqrt{10}$ or $\sqrt{100}$, which means a theoretical signal/noise ratio improved respectively by a factor 3 or 10 (Wieser & Schwieters, 2005; Koornneef *et al.*, 2014).

10^{12} Ω amplifiers have been set up on MC-ICP-MS for solution analysis, such as for Li (Lin *et al.*, 2019), S (Makishima & Nakamura, 2012), Fe (John & Adkins, 2010), Sr (Bazzano *et al.*, 2017), Hf, W and Pt (Peters *et al.*, 2015) and naturally for B (Henehan *et al.*, 2016; Greenop *et al.*, 2017; Vega *et al.*, 2020). It turned out that the benefits on the signal to noise ratio was lower than expected (Wieser & Schwieters, 2005; John & Adkins, 2010), whereas those amplifiers precluded the analyses of ion beam below < 10^{-13} A, the signal being still too noisy. The secondary electron multipliers (SEM) were therefore favoured for such small signals. SEMs are able to quantify the smallest ion beams without electronic noise but result in poorer internal precisions occasioned by their instabilities in the high-precision counting statistic, requiring thus corrections and repeated calibrations of the gains (Koornneef *et al.*, 2014). Raitzsch *et al.* (2018) mentioned for instance a 2 ‰ (2σ) internal precision for δ^{11}B measurements with SEMs for 4 ppb B solutions.

To measure low abundance isotopes and/or scarce samples, 10^{13} Ω amplifiers fill the gap between SEM and 10^{11} Ω amplifiers. Primarily installed on TIMS instruments, they reached unprecedented internal and external precisions for strontium and neodymium isotope analysis of small samples (Koornneef *et al.*, 2014). Their use for MC-ICP-MS in solution mode has been successfully validated for tantalum (Pfeifer *et al.*, 2017) and rhenium (Dellinger *et al.*, 2020). Lloyd *et al.* (2018) reached high precision δ^{11}B measurements (2SD < 0.2 ‰) with 10^{13} Ω amplifiers for a boron mass down to 0.8 ng (for a single measurement). Meanwhile they also clarified that δ^{11}B measurements are not affected by the very slow response time of these amplifiers (a lag between the detection of the signal and the electronic transcription, increasing with resistance, Gourgiotis *et al.* 2015), if both Faraday cups have the same amplifier resistance. In contrast, the response time gap between two different amplifiers preclude δ^{11}B analysis with combinations on the Faraday cups such as 10^{11} Ω amplifiers on H3 and 10^{13} Ω on L3. For our measurements of the reference materials AE120, AE121 and AE122 at [B] between 1 and 50 ppb, ^{10}B signals (Fig.5.3) are all below the 100 mV threshold, at which the JN noise interferes for the 10^{11} Ω amplifiers (Wielandt & Bizzarro, 2011). Louvat *et al.* (2019) established a critical limit at 20-30 mV with those amplifiers, below which the individual external 2SD were systematically > 0.5 ‰. The accuracy, internal and external reproducibilities of the measurements are thereby strongly affected. The 2SD values start to be acceptable (0.2 – 1.2 ‰, except for one AE120 solution > 2 ‰) only for [B] $\geq$ 20 ppb and are significantly better at 50 ppb (< 0.7 ‰, 2SD, Fig.5.3a-c). Thanks to the 10^{13} Ω amplifiers, the internal standard errors (Fig. 5.5) have been considerably reduced, compared to 10^{11} Ω amplifiers, and we recommend their use for ^{10}B signals $\leq$ 100 mV.

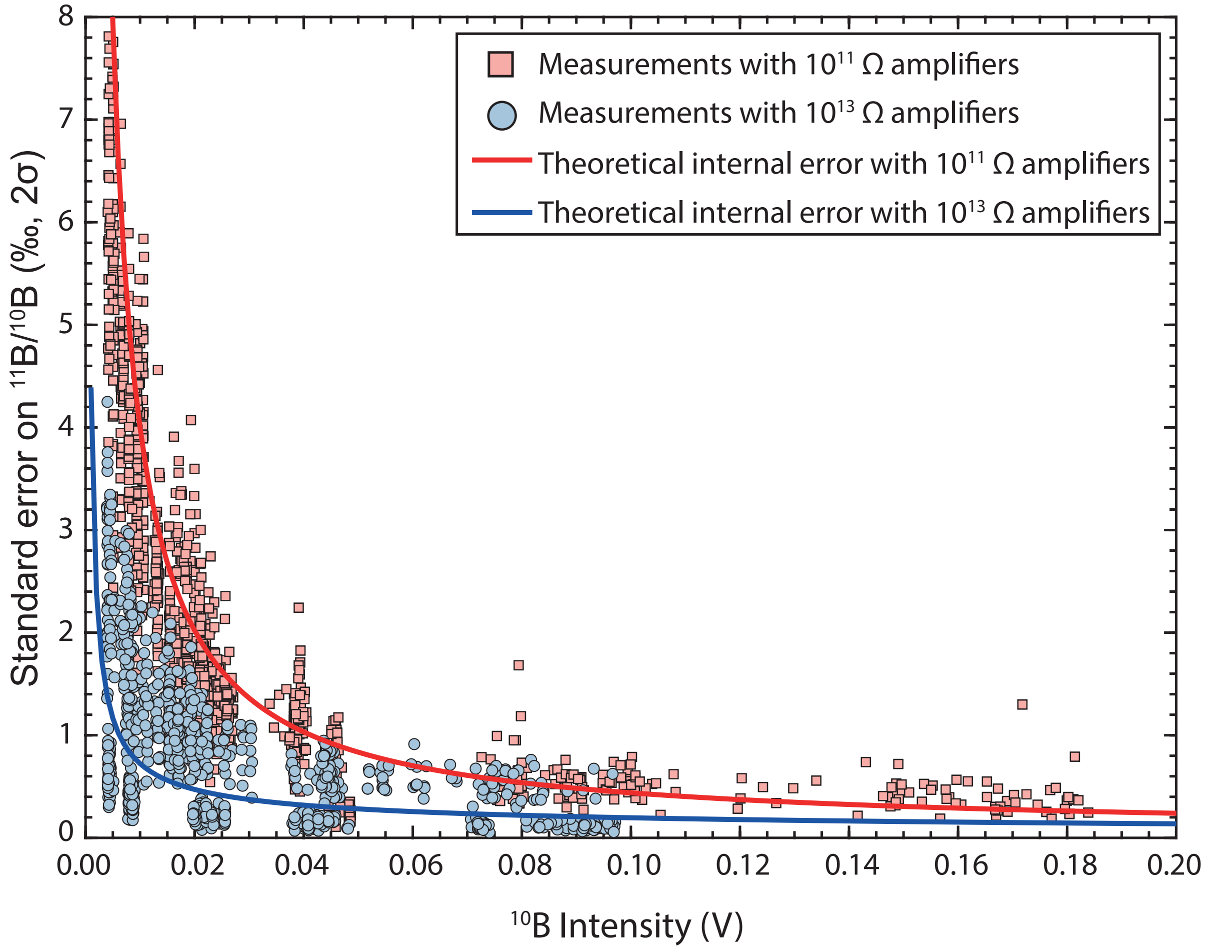

Figure 5.5 : *Internal standard errors (‰, 2σ) of the ^{11}B/^{10}B measurements according to the ^{10}B signal intensity, with 10^{11} Ω (red) or 10^{13} Ω (blue) amplifiers. σ = standard deviation/$\sqrt{n}$ * 1000, with n = 12 cycles of 8 s. Each data point corresponds to one injection of a reference material (NIST SRM 951, BAM ERM-AE120, AE121 or AE122). The database gathers roughly one year of measurements. Theoretical internal error curves are calculated according for Johnson-Nyquist plus Poisson noises (John & Adkins, 2010; Dellinger et al., 2020).*

Combining the use of 10^{13} Ω amplifiers and a X skimmer cone, δ^{11}B measurements of solutions with [B] $\leq$ 5 ppb are now possible. Except for one measurement of AE122 (2SD at 0.87 ‰, Fig.5.3f), all the 2 ppb solutions measured under these optimised conditions had individual external repeatability $\leq$ 0.5 ‰ (2SD, Fig. 5.3d-f). Given the volume of sample required for a triplicate SSB analysis with the 50 µL sample loop of the µ-dDIHEN, only 0.5 ng of boron were necessary to achieve these measurements. δ^{11}B accuracy below 2 ppb is also in agreement with the certified values, although some values (solutions at 1 ppb) are slightly shifted towards lower δ^{11}B for AE122. This is probably due to the instrumental blank, highly enriched in ^{10}B, that impacts more visibly high δ^{11}B samples at low [B], i.e. lower sample/blank signal ratio (Louvat *et al.*, 2014b). δ^{11}B data of reference materials at 1 ppb, with individual 2SD between 0.4 and 1.3 ‰, illustrate this difficulty of correcting for instrument memory effect for [B] < 1 ppb and set a cut-off from which the blank correction is no longer effective to achieve accurate measurements. While the 10^{13} Ω amplifiers overcame the noise issues for very small ion beams, the underlying lightness and memory effect of boron complicate the δ^{11}B determination for B concentration below 1 ppb, and once again controlling B contaminations in the instrument environment becomes a limiting step.

5.3.c Long-term reproducibility

Given these previous results on reference material solutions, the Jet + X cones have been set up for the δ^{11}B measurement of natural samples. The 10^{13} Ω amplifiers were used for [B] < 35 ppb to respect the 0.5 V upper limit for ^{11}B signal (transposed as 10^{11} Ω amplifier signal through the gain factor) and 10^{11} Ω amplifiers for [B] $\geq$ 35 ppb. For each measurement session, essentially dedicated to carbonate samples, reference material AE121 was measured every few samples ($\sim$ 5) at the same concentration as the samples. Altogether AE121 has been measured more than 100 times in one year (Fig.5.6), at 1 $\leq$ [B] $\leq$ 50 ppb, yielding a long-term δ^{11}B value of 19.55 $\pm$ 0.34 ‰ (2SD, n=103), in total agreement with the literature (Vogl & Rosner, 2011; Misra *et al.*, 2014b; Lloyd *et al.*, 2018), and with 2SD slightly higher than for the long-term ($\geq$ 10 years) IPGP reproducibility (δ^{11}B = 19.56 $\pm$ 0.17 ‰, 2SD, n=90, but for [B] of 100-200 ppb, Louvat *et al.* 2019). The median individual external precision (2SD) for these 103 replicates is 0.18 ‰ (0.22 $\pm$ 0.15 ‰, 1SD).

More specifically, for AE121 solutions with 4 $\leq$ [B] $\leq$ 10 ppb (B amount analysed between 1 ng and 2.4 ng for triplicate SSB analysis, i.e. between 0.3 and 0.8 ng per sample injection), average δ^{11}B for AE121 becomes 19.60 $\pm$ 0.23 ‰ (2SD, n=43), with an average individual external precision (2SD) of 0.19 $\pm$ 0.14 ‰ (2SD). With the µ-dDIHEN, we thus reiterated the same analytical performances achieved by Lloyd *et al.* (2018), but we also significantly decreased the amount of boron analysed per measurement (here injection) from 0.8 ng to 0.4 ng for reference material solutions at 5 ppb, with half the injected volume ($\sim$ 150 µL against 80 µL here).

For solutions with 2 $\leq$ [B] $\leq$ 3.5 ppb (0.5 $\leq$ B $\leq$ 0.85 ng), average δ^{11}B for AE121 is 19.47 $\pm$ 0.51 ‰ (2SD, n=19). The one-year 2SD reproducibility value gathering all concentrations (19.55 $\pm$ 0.34 ‰, 2SD) is therefore slightly pulled up by this pool of low [B] solution samples, when compared with those of Lloyd *et al.* (2018) or Louvat *et al.* (2019).

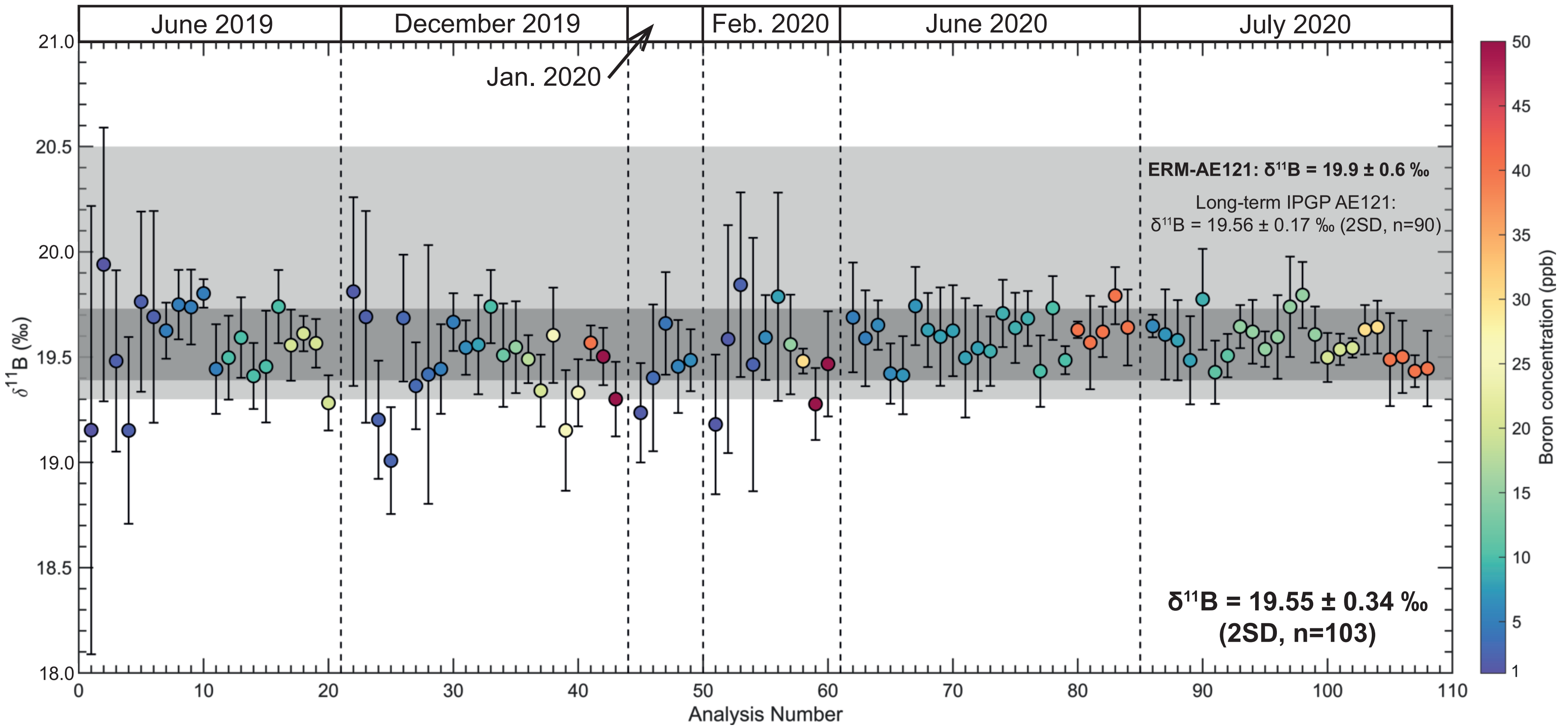

Figure 5.6 : *$\delta^{11}B$ long-term reproducibility of BAM ERM-AE121 (Vogl & Rosner, 2011) that was measured together with carbonate samples at 1 $\leq$ [B] $\leq$ 50 ppb, using the Jet + X cones and the 10^{13} Ω amplifiers for [B] $\leq$ 35 ppb, otherwise 10^{11} Ω amplifiers. Each data point represents a triplicate analysis through the standard-sample bracketing described in the figure 5.2. Only 1.2 ng of boron is required at 5 ppb, and 0.5 ng at 2 ppb (0.4 ng and 0.17 ng respectively per injection). The colour bar represents the boron concentration at which the solution were measured.*

Without them, the long-term reproducibility is 19.56 ± 0.26 ‰ (2SD, n=84), much closer to the long-term IPGP reproducibility (19.56 ± 0.17 ‰, Louvat *et al.* 2019). By their very low concentrations, these solutions were more sensitive to the instrument B memory or to contamination during the dilutions. The individual external precisions are by extension impacted with an average of 0.45 ± 0.25 ‰ (2SD). Additionally, it should be noted that the AE121 measurements starting December 2019 have been performed along with carbonate samples and therefore some residual matrix effects (from the carbonate samples) could have affected the δ^{11}B determination. However, at such low concentrations and measured in between natural samples, these AE121 δ^{11}B still match with the certified values, and all the individual 2SD are below 0.6 ‰. Transposed to marine carbonates, this level of precision could enable paleo-pH reconstructions on the lowest amount of boron ever reached to date, thus reducing the amount of material required for each sample measurement.

5.4 Boron separation with the microsublimation

Multiple microsublimation experiments have been carried out on a stock solution of the reference carbonate MVS-1 (Jurikova *et al.*, 2019) to evaluate the best combination of temperature, heating duration and B amount to achieve a full boron recovery in a nitric acid medium. Gaillardet *et al.* (2001) originally recommended 70°C for 12-14 hours. Wang *et al.* (2010) proposed to raise the temperature to 98°C because of the temperature gradient between the beakers and their homemade hotplate and the use a coated graphite rack instead of aluminium foil. Using the same protocol as Wang *et al.* (2010), Misra *et al.* (2014b) fixed the temperature at 95°C for 15-18 hours, whereas Raitzsch *et al.* (2018) used a temperature of 100°C during 24 hours.

In our case, we initially choose to set the heating of the hot plate at 95°C in order to be consistent with Misra *et al.* (2014b), temperatures above 100°C being wilfully avoided to prevent potential bubbling on the upside-down beaker's lid. We then conducted our microsublimation protocol with different heating durations and boron loads, and measured the δ^{11}B of the distillates exploring alongside the µ-dDIHEN method on carbonate samples. For each heating duration or B mass, nine to ten aliquots from the stock solution have been prepared, thanks to the fast handling, and analysed to establish robust statistics to validate our protocol.

5.4.a Whole procedural blank contamination

The installation of boron-free H14 HEPA filters in the over-pressured cleanroom allowed initially to prevent boron contaminations coming from the filtered air. A Teflon vial filled with HNO_3 0.05 N was left open on the bench during 48 h, and indicated that the air B contamination was only 4 pg per hour.

The whole procedural blanks (complete microsublimation protocol with a 50 µL droplet of nitric acid at 0.5 N) were processed as any other sample until the MC-ICP-MS measurements. However, the blank beakers were always the last prepared for the microsublimation, thus integrating B contamination from reagents, materials or volatilization from the distilled analytes during the handling time of the whole series of samples to microsublimate. This blank represents thus a "maximum" value.

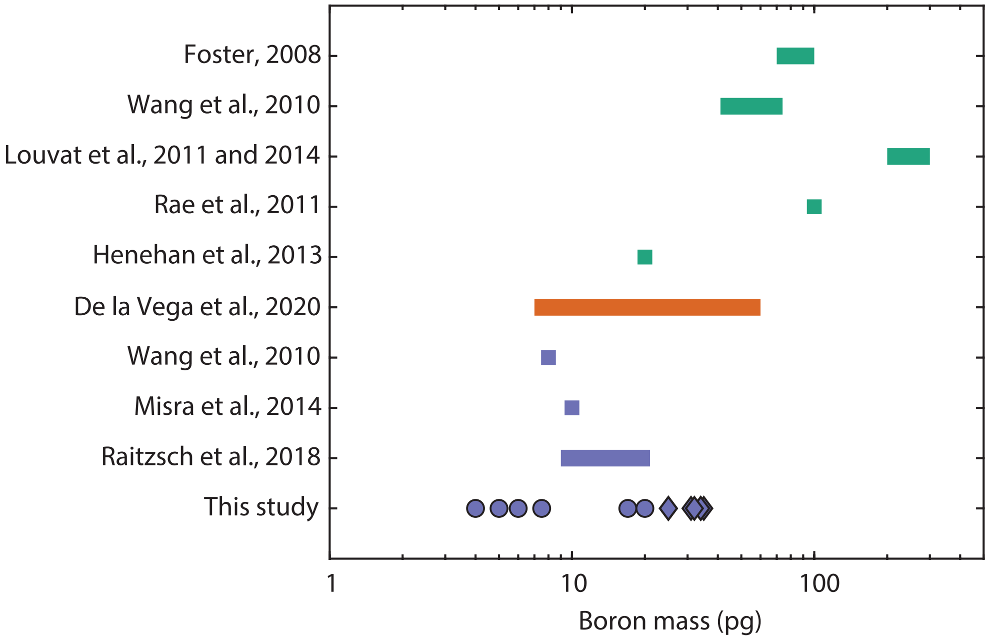

Figure 5.7 : *Boron procedural blank in pg reported for ion exchange chromatography (Foster 2008; Wang et al. 2010; Louvat et al. 2011a; Rae et al. 2011; Henehan et al. 2013; Louvat et al. 2014a, in green), for automated ion exchange chromatography (Vega et al. 2020, in orange) and for microsublimation (Wang et al. 2010; Misra et al. 2014b; Raitzsch et al. 2018, in blue), compared with contamination values assessed with our microsublimation protocol. Those values are dissociated in circles and diamonds, representing respectively the determination of the whole procedural blank just after the microsublimation and after a longer storage (> one week) of the distillate in PP tubes. The squares reflect the maximum contamination values when the blank contamination range was not mentioned.*

Our microsublimation blanks exhibit a median of 23 pg (20 ± 12 pg B, 1SD, n=14), which represent only ~ 0.9 % of a solution with 2.5 ng of boron. These blanks are 2 to 10 times lower than those reported for B extraction by ion exchange chromatography with the Amberlite resin in micro-columns (Foster, 2008; Wang *et al.*, 2010; Louvat *et al.*, 2011a; Rae *et al.*, 2011; Louvat *et al.*, 2014a; Vega *et al.*, 2020), in the same order of magnitude as Henehan *et al.* (2013) with ion exchange chromatography and the lowest values of Vega *et al.* (2020) with automated ion exchange chromatography or Raitzsch *et al.* (2018) with microsublimation, and higher than those of Wang *et al.* (2010) and Misra *et al.* (2014b) with microsublimation (Fig.5.7). We nevertheless observed that the higher microsublimation blanks were for series that had been stored for a longer time (> one week) in PP tubes before δ^{11}B analysis. That is why the microsublimation separations were then performed the day before the MC-ICP-MS sessions, and the procedural blanks drop below 20 pg of boron (9 ± 7 pg, 1SD, n=7), reaching the lowest values mentioned in the literature (Wang *et al.*, 2010; Misra *et al.*, 2014b).

5.4.b Heating duration of the microsublimation

As the protocol slightly differs from Misra *et al.* (2014b) by the use of aluminium foil (Gaillardet *et al.*, 2001), different heating durations between 12 and 24 hours with steps of two hours (Fig.5.8.a) have been tested on the stock solution of the reference material MVS-1 (Jurikova *et al.*, 2019), with droplet volumes of 40 µL (containing 20 ng of boron for a final concentration of 40 ppb in the analysed solution). A supplementary test for 87 hours ($\approx$ 3.5 days) has also been conducted. It appears that the full recovery has been almost achieved after 12 hours, also reported by Wang *et al.* (2010), as the MVS-1 reference value has already been reached (15.95 ± 0.19 ‰, 2SD, n=46, Jurikova *et al.* 2019). [B] measurements on residues were also very close to the blanks whereas the desired boron concentration were systematically found during the isotopic measurement with the MC-ICP-MS according to the type of sample and the size of the droplet that we loaded. Misra *et al.* (2014b) also noticed a near recovery after 12 hours but a full recovery only after 14 hours, however with a lower temperature of 75°C during their initial tests. When the recovery is not complete, the distillate contains more of the heavier isotope compared to the certified value due to its preferential condensation from the vapor phase or its distillation as the volatile boric acid is preferentially enriched in ^{11}B (Chetelat *et al.*, 2005; Misra *et al.*, 2014b).

On the other hand, our results show that a prolonged heating, even after several days, does not affect the δ^{11}B measurements, as our values yielded 15.87 ± 0.12 ‰ (n=10, 2SD). This validates that, even after long heating times, no significant sublimation of other elements from the carbonate matrix occurs, that could generate matrix effects during δ^{11}B measurements and therefore shift the isotopic values. We finally adopted, for practical reasons, a microsublimation duration of 24 hours, which can be interestingly extended if needed (e.g. over weekends) according to the operator's schedule. Finally, this set of experiments allows us to define for this carbonate reference material MVS-1 an average δ^{11}B value of 15.95 ± 0.22 ‰ (2SD, n=78) for final solutions containing 40 ppb B (i.e. only 10 ng B per triplicate analysis). This emphasizes that coupling microsublimation with the µ-dDIHEN device consistently reproduced Jurikova *et al.* (2019)'s values, that was obtained after B extraction with ion-exchange resin Amberlite IRA-743 in microcolumns, and by MC-ICP-MS measurements using a spray chamber with [B] between 10 and 50 ppb. This is also a step towards an interlaboratory consensus on δ^{11}B analyses for carbonates; intercomparisons that showed initially a great variability (Foster *et al.*, 2013) but now tend towards reduced or even absent differences between laboratories (Gutjahr *et al.*, 2020). Furthermore, with an average 2SD of 0.12 ± 0.11 ‰ (2SD, n=78), the individual external errors reach a noteworthy level for carbonate sample δ^{11}B analyses at such low boron amount (10 ng for triplicate analysis).

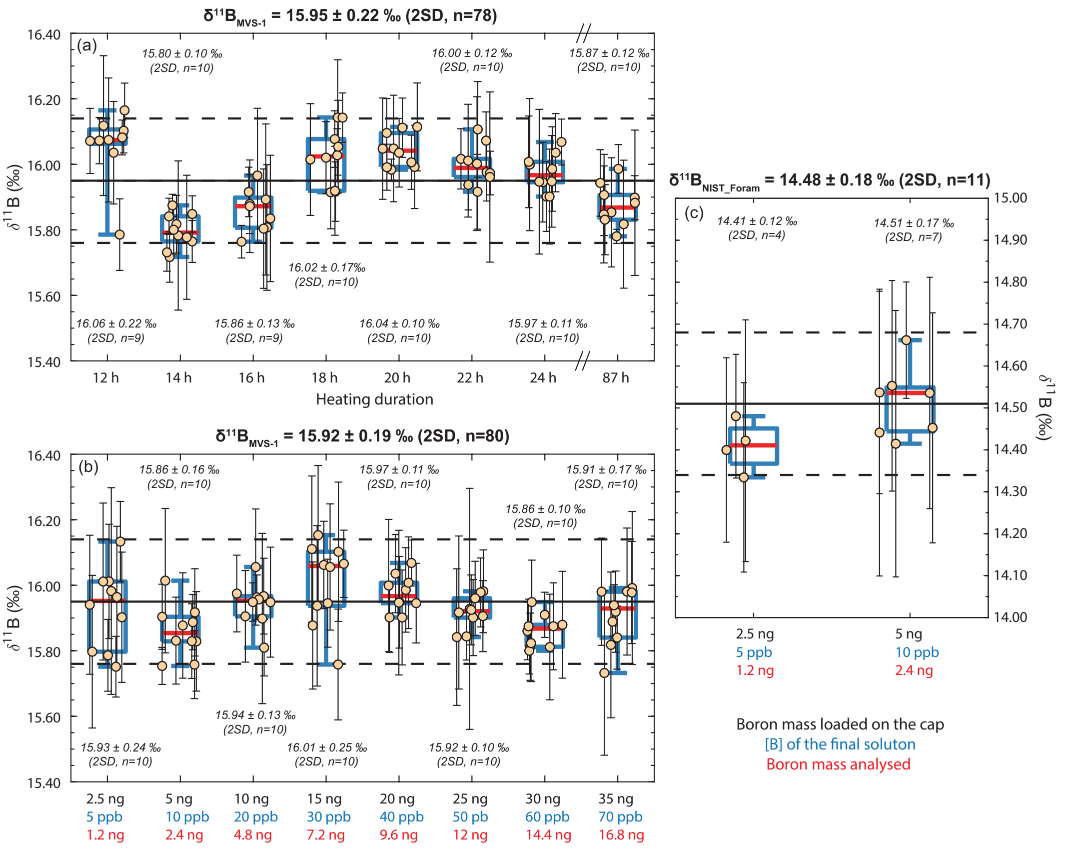

Figure 5.8 : *Reproducibility of δ^{11}B measurements on the carbonate reference material MVS-1 (15.95 ± 0.19 ‰, 2SD, n=46, Jurikova et al. 2019, dashed and solid lines) in a and b (15.94 ± 0.21 ‰, 2SD, n=148) and the synthetic carbonate reference material NIST RM 8301 Foram (14.51 ± 0.17 ‰, Stewart et al. 2021, dashed and solid lines) in c. B extraction was performed by the microsublimation technique for (a) different heating durations (with fixed 20 ng boron in a 40 µL droplet, i.e. [B]=40 ppb); (b): different boron masses loaded on the sublimation beaker lids (with fixed heating duration of 24 hours). (c): for 2.5 and 5 ng of boron loaded on the sublimation beaker lids (with fixed heating duration of 24 hours). Each data point represents average ± 2SD for a triplicate sample-standard bracketing measurement with the µ-dDIHEN setup, the Jet + X cones and the 10^{11} Ω (if [B] $\geq$ 35 ppb) or 10^{13} Ω amplifiers. The blue box plots depict the statistical parameters for nine to ten aliquots (orange dots) with median in red.*

5.4.c Microsublimation for different B masses loaded

We thereafter conducted microsublimation at 95°C for 24 hours (as selected above) still on the stock solution of the reference material MVS-1 (Jurikova *et al.*, 2019) in order to assess the boron recovery (with an isotopic fractionation expressed if the recovery is not total), explore the µ-dDIHEN achievements (with Jet + X cones and 10^{13} Ω amplifiers) at different boron concentrations and secondarily test the impact of the droplet size. The boron masses loaded on the caps of the beakers vary according to the droplet volume of the stock solution at 500 ppb B (e.g. 50 µL = 25 ng B).

It turned out that the droplet size must be carefully monitored. During our first experiments, we noted that for droplets larger than 70 µL (35 ng of boron) the distillate droplet did not remain in the conical top of the beaker and fell down to the beaker cap. On the other side, droplets smaller than 30 µL exhibited δ^{11}B with larger offsets relative to the reference value, as part of the boron remained probably trapped within the matrix during the sublimation. Consequently, an additional volume of HNO_3 at 0.5 N was added to these sample droplets to reach a constant droplet volume of 50 µL on the cap. For experiments with 2.5 and 5 ng of boron, in order to have a better reproducibility on the sample volume taken, two daughter solutions were diluted from the stock solution to respectively 50 and 100 ppb. In the same way, two daughter solutions for NIST RM 8301 Foram (Stewart *et al.*, 2021) were prepared at the same concentrations. The distillates are finally diluted to 0.5 mL in 0.05 N HNO_3, and only half of this volume (240 µL) is used for triplicate analysis.

All the MVS-1 δ^{11}B results for droplets comprising 2.5 to 35 ng B (Fig.5.8.b) are in complete agreement with the reference value (15.95 ± 0.19 ‰, 2SD, n=46, Jurikova *et al.* 2019), with a global average δ^{11}B of 15.92 ± 0.19 ‰ (2SD, n=80). The individual repeatabilities (2SD) are also very low at 0.15 ± 0.13 ‰ (2SD). More specifically, for only 5 and 10 ng B loaded on the microsublimation cap (i.e., 2.4 and 4.8 ng analysed), the average values are respectively δ^{11}B = 15.86 ± 0.16 ‰ (2SD, n=10) and δ^{11}B = 15.94 ± 0.13 ‰ (2SD, n=10), and external reproducibilities are as good as those at higher concentrations, thanks to the X skimmer cone and the 10^{13} Ω amplifiers. Regarding the droplets loaded with only 2.5 ng of boron, the δ^{11}B values are slightly more scattered (δ^{11}B = 15.93 ± 0.24 ‰, 2SD, n=10) with individual 2SD marginally higher than for the other tests (0.19 ± 0.14 ‰, 2SD, with a maximum at 0.32 ‰). In parallel, the δ^{11}B measurements for NIST RM 8301 Foram with only 2.5 and 5 ng B in the loaded droplet (Fig.5.8.c) are as well in full agreement with the reference value (14.51 ± 0.17 ‰, Stewart *et al.* 2021), with a value of 14.48 ± 0.18 ‰ (2SD, n=11). As for the MVS-1 carbonate at these low concentrations, the individual repetabilities are hardly worsened (0.25 ± 0.13 ‰, 2SD, with a maximum at 0.34 ‰). All these results reach an outstanding degree of reproducibility and accuracy, especially for 2.5 ng B and 5 ng B in the initial droplet for respectively only 1.2 and 2.4 ng B analysed, i.e. 0.4 and 0.8 ng of boron per injection.

5.5 Application: comparison between the new developed method and ion chromatography separation

The microsublimation technique was applied on a range of modern marine biogenic carbonate organisms belonging to four different phylum and different recifal carbonate mixes (Tab.5.3) that were sampled on the French coasts. In order to compare the microsublimation to the common method of B extraction by ion exchange chromatography using the anionic resin Amberlite IRA-743 in micro-columns (Lemarchand *et al.*, 2002a; Paris *et al.*, 2010a), boron from these samples was extracted using the two methods and δ^{11}B was measured with the µ-dDIHEN technique.

Table 5.3 : *Comparison of the microsublimation protocol and the ion exchange chromatography (Lemarchand et al., 2002a; Paris et al., 2010a) to separate boron from its carbonate matrix on a variety of modern biogenic carbonate. The " * " symbol marks the sample with a 1 ‰ discrepancy between the two separation methods. The percentage of the different mineralogies were determined by XRD (Calc.: Calcite, Arag.: Aragonite, Mg Calc.: High Mg calcite) and the boron concentrations in the carbonate matrix were measured by ICP-QMS.*

Carbonate samples					Ionic Chromatography			Microsublimation		
Phylum/Carbonate type	Species/Genus	Mineralogy	B/CaCO$_3$ (ppm)	2SD (%)	[B]$_{meas}$ (ppb)	δ^{11}B (‰)	2SD (‰)	[B]$_{meas}$ (ppb)	δ^{11}B (‰)	2SD (‰)
Arthropoda	*Balanus* sp.	Calc. (100 %)	10	1.2	60	20.39	0.38	3	19.95	0.10
Arthropoda	*Balanus* sp.	Calc. (100 %)	11	2	51	17.66	0.25	2	18.23	0.50
Brachiopoda	*Mergelia truncata (low. valve)*	Calc. (100 %)	40	3	50	18.47	0.28	40	18.06	0.08
Brachiopoda	*Mergelia truncata (upper valve)*	Calc. (100 %)	48	3	74	18.11	0.07	15	17.60	0.17
Mollusca	*Anomia* sp.	Calc. (100 %)	7	7	44	18.72	0.29	12	18.45	0.06
Mollusca	*Patella vulgata*	Calc. (90 %) + Arag. (10 %)	8	2	32	20.87	0.32	2	20.57	0.53
Mollusca	*Mytillus edulis (blue layer)*	Calc. (91 %) + Arag. (9 %)	8	2	33	14.61	0.23	9	14.00	0.21
Mollusca	*Mytillus edullis*	Calc. (70 %) + Arag. (30 %)	10	1	36	14.55	0.20	8	15.28	0.17
Mollusca	*Mytillus edullis (white layer)*	Calc. (7 %) + Arag. (93 %)	15	2	65	15.15	0.06	18	15.60	0.08
Recifal carbonate mix*	*n.d.*	Calc. (41 %) + Mg Calc. (59 %)	49	2	85	19.62	0.11	15	18.39	0.12
Recifal carbonate mix	*n.d.*	Calc. (100 %)	57	2	61	18.62	0.17	15	18.33	0.26
Recifal carbonate mix	*n.d.*	Arag. (19 %) + Mg Calc. (81 %)	58	4	50	20.88	0.25	35	20.82	0.13
Recifal carbonate mix	*n.d.*	Arag. (36 %) + Mg Calc. (64 %)	59	3	51	18.62	0.25	15	18.21	0.13
Recifal carbonate mix	*n.d.*	Calc. (58 %) + Mg Calc. (42 %)	61	3	78	20.67	0.03	15	20.80	0.13
Recifal carbonate mix	*n.d.*	Arag. (36 %) + Mg Calc. (64 %)	64	9	56	19.62	0.25	46	19.40	0.13
Recifal carbonate mix	*n.d.*	Arag. (23 %) + Mg Calc. (77 %)	64	4	66	18.54	0.20	50	18.00	0.13
Recifal carbonate mix	*n.d.*	Mg Calc. (100 %)	68	1	30	21.06	0.58	8	20.91	0.26
Recifal carbonate mix	*n.d.*	Arag. (70 %) + Mg Calc. (30 %)	79	10	103	19.29	0.28	39	19.55	0.21
Recifal carbonate mix	*n.d.*	Mg Calc. (100 %)	84	17	112	19.54	0.12	115	19.53	0.11
Recifal carbonate mix	*n.d.*	Arag. (23 %) + Mg Calc. (77 %)	90	4	85	22.33	0.23	50	21.84	0.23
Recifal carbonate mix	*n.d.*	Mg Calc. (100 %)	142	4	131	22.19	0.13	85	22.06	0.14
Rhodophyta	*Corallina* sp.	Mg Calc. (100 %)	39	8	83	28.57	0.09	31	29.05	0.36
Rhodophyta	*n.d.*	Arag. (25 %) + Mg Calc. (75 %)	65	2	21	22.82	0.29	6	22.96	0.28

These samples also provide the opportunity to test the microsublimation on $CaCO_3$ matrices with a wide spectrum of mineralogies (calcite, aragonite, magnesian calcite and sometimes combined) and boron concentrations (7 ± 7 % to 142 ± 4 % ppm).

After a preliminary oxidative cleaning to remove organic matter with the alkaline-buffered H_2O_2 method (Barker *et al.*, 2003), two fractions of each powdered calcium carbonate sample have been dissolved in 0.5 M HNO_3 before boron extractions: 2 to 20 mg of sample in 0.2 to 1 mL 0.5 M HNO_3 for ion exchange chromatography and 0.4 to 30 mg of sample in 0.15 to 1.15 mL 0.5 M HNO_3 for microsublimation and major and trace element analysis in ICP-QMS. For some of the samples the very low amount of material aimed at checking the µ-dDIHEN performances at very low boron concentrations. One advantage of the microsublimation is that an aliquot of the dissolved sample can be directly use for separation, while ion exchange chromatography requires basification of the sample solution to pH 6-8 by addition of 0.5 to 2 mL of NH_4OH 4M prior to their introduction in the micro-columns. Another ion exchange chromatography protocol (Foster, 2008; Rae *et al.*, 2011; Vega *et al.*, 2020) buffers sample solutions with Na acetate (2 M $NaCH_3CO_2$)/acetic acid (0.5 M CH_3CO_2H), which requests an addition of twice the volume of 0.5 N HNO_3 used for carbonate dissolution. These bufferings can contribute significantly to total procedural blanks. Moreover the addition of large amounts of Na might lead to residual Na in the B eluted fractions and consequently to different instrumental mass fractionation during the δ^{11}B measurements between the sample solutions and the pure boric acid bracketing standard NIST SRM 951 (Foster, 2008; Rae *et al.*, 2011). Microsublimation avoids such additional contamination and matrix effects.

For the marine biogenic carbonate samples investigated here δ^{11}B values varied between 14.55 and 29.05 ‰, in agreement with published values for biomineralisers: e.g. 22-40 ‰ (Hemming & Hanson, 1992; Zhang *et al.*, 2017; Sutton *et al.*, 2018) for high-Mg calcite coralline algae, and 11-19 ‰ (Heinemann *et al.*, 2012; Liu *et al.*, 2020; Lécuyer *et al.*, 2002; Penman *et al.*, 2013; Jurikova *et al.*, 2019) for mussels (*Mytillus edulis*) and brachiopods (*Myriapora truncata*). Recifal carbonate mixes show B concentrations between 49 ± 2 % and 142 ± 4 % ppm and δ^{11}B between 18.00 ± 0.13 and 22.33 ± 0.23 ‰. Barnacles (*Balanus* sp.) and limpet (*Patella vulgata*) δ^{11}B were measured for the first time (Tab.5.3). They have a low B content (around 10 ppm), similar to bivalves. The large variety of B contents and δ^{11}B values of these marine calcifiers could reflect different biomineralisation processes, which will be discussed in another publication.

The two methods of B extraction globally show for most of the samples an excellent agreement within ± 0.4 ‰ (Fig.5.9), consistent with our analytical uncertainties. One recifal carbonate δ^{11}B value is nevertheless slightly away by roughly 1 ‰ (Fig.5.9.b, marked with an asterisk in Tab.5.3). Given the relatively high boron concentrations at which this sample was measured (15 ppb after microsublimation, 85 ppb after ion exchange chromatography), measurement issues can be excluded. The difference between the two methods could be rather due an incomplete recovery during ion exchange chromatography extraction (loss of ^{10}B at the end of the elution, Lemarchand *et al.* 2002a), leading to δ^{11}B value 1 ‰ higher than after microsublimation. The presence of organic matter in the carbonate sample could possibly have deteriorated the performances of ion exchange B extraction (Gutjahr *et al.*, 2020).

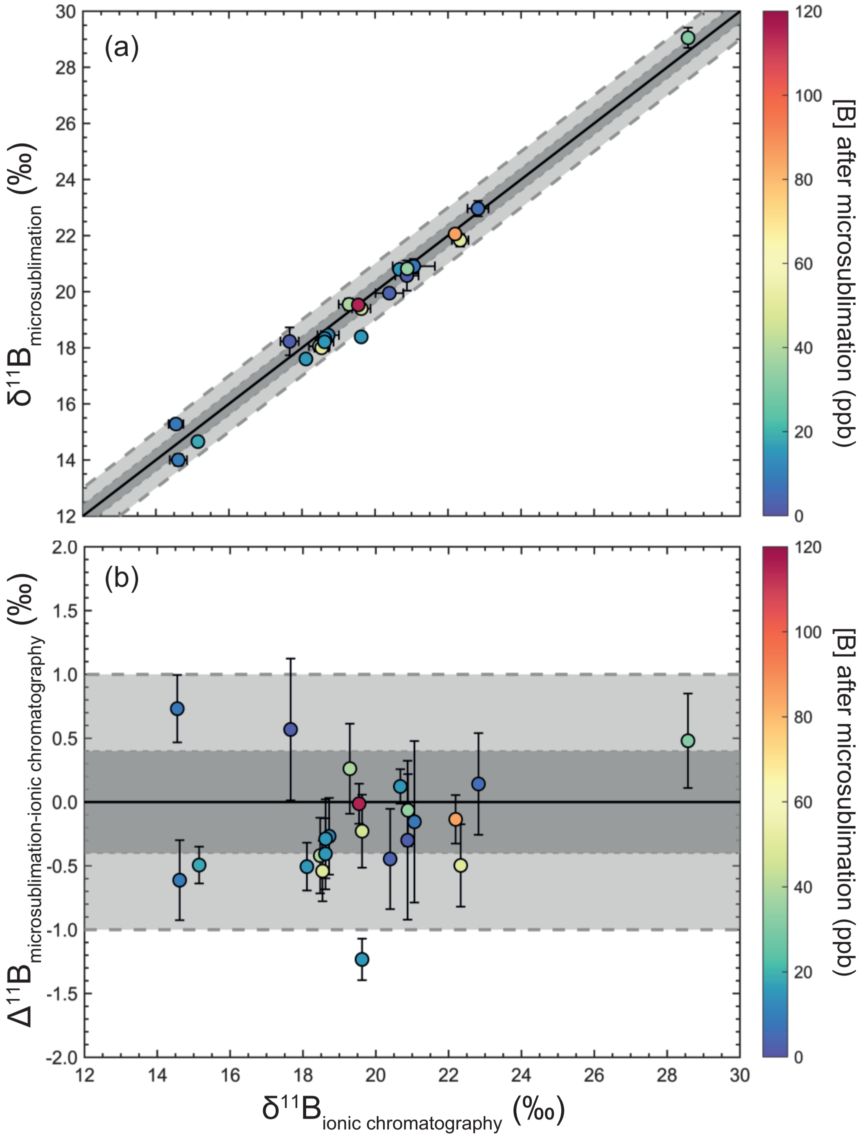

Figure 5.9 : *(a) Cross plot of δ^{11}B of different modern biogenic carbonates (Tab.5.3) obtained after microsublimation or B extraction by ion exchange chromatography. (b) δ^{11}B difference between microsublimation and ion exchange chromatography extractions according to the δ^{11}B values after ion exchange chromatography. Colour code gives the concentration at which the samples have been measured after microsublimation. The dark grey band represents the 0.4 ‰ envelope and the lightest grey band the 1 ‰ envelope around the 1:1 black line.*

The barnacle and limpet samples exhibit three of the lowest boron concentrations (10-11 and 8 ppm, respectively). Their δ^{11}B measurements after microsublimation have been achieved on final solutions comprising only 1 and 1.5 ng of boron (2 and 3 ppb; the triplicate SSB measurement consumed respectively 0.5 and 0.7 ng B). Despite this low B amount, the

δ^{11}B values are in agreement within uncertainties with those measured at higher concentration (30-60 ppb) after ion exchange chromatography, and the individual external errors for each sample are still very low: 0.1 ‰ for 1.5 ng B and 0.5 ‰ for 1 ng B. Overall, this demonstrates that microsublimation can efficiently extract boron from biogenic calcium carbonates independently of their mineralogy (aragonite, calcite and high-Mg calcite) or boron content (down to 8 ppm in this study), and that our δ^{11}B measurement protocol with the miniaturized direct injection introduction of the samples (µ-dDIHEN), Jet+X cones and 10^{13} Ω amplifiers can reproducibly be applied to such low [B] natural samples.

5.6 Conclusion

To circumvent the analytical issues intrinsic to boron isotope analysis on MC-ICP-MS for small carbonate samples at low boron concentration, we provided a new protocol coupling the direct injection of the sample in the plasma torch with the µ-dDIHEN device allowing both low uptake rates and small sample volumes, and the microsublimation technique for the preliminary extraction of boron from the samples.

The δ^{11}B measurements were improved for small B concentrations by using the combination of a sampler Jet cone and a skimmer X cone, which increased the boron sensitivity by a factor of 2 to 5, and by implementing 10^{13} Ω amplifiers, which raised the signal/noise ratio by a factor of 10 compared to the 10^{11} Ω resistors. Our optimized microsublimation protocol (heating at 95°C during 24 hours, sample droplet volume of 40-50 µL) proved to be a reliable alternative to the traditional ion exchange chromatography for boron extraction from $CaCO_3$ matrices. Beyond the lowest procedural blank levels (9 $\pm$ 7 pg, 1SD, n=7) and the simplicity of a single-step procedure, this method offers the opportunity to treat smaller volumes of sample and became at this point the adequate complement to the µ-dDIHEN setup for the determination of the δ^{11}B in small carbonate samples with low B content.

The long-term δ^{11}B reproducibility for the carbonate reference materials MVS-1 (Jurikova *et al.*, 2019) and NIST RM 8301 Foram (Stewart *et al.*, 2021) has been respectively assessed at 15.94 $\pm$ 0.21 ‰ (2SD, n=148), for boron masses between 2.5 and 35 ng, and 14.48 $\pm$ 0.18 ‰ (2SD, n=11), for boron masses at 2.5 and 5 ng. This optimised analytical protocol enables also to establish accurate δ^{11}B measurements for boron concentration down to 2 ppb for boric acid reference materials, but most importantly, for carbonates, down to a mass of 1 ng of boron in the final solution after microsublimation. With a total volume of only 240 µL injected during the triplicate Sample Standard Bracketing measurement this corresponds to an exceptionally low overall mass of boron consumed of 0.5 ng. Furthermore, the individual repeatabilities for the sample δ^{11}B measurements hardly ever exceeded 0.2 ‰ for solutions containing at least 2.5 ng of boron and up to 0.5 ‰ with 1 ng B.

These analytical performances, elaborated at such low amount of sample and boron concentration, could allow in the future to refine the oceanic paleo-pH reconstitutions from less sample material (e.g. for the benthic foraminifera, less abundant in the sedimentary records) or to better constrain the biomineralization processes by subsampling different sections of larger organisms, such as corals or brachiopods.

CHAPTER 6

δ^{11}B MEASUREMENTS IN FORAMINIFERA

Sommaire

6.1 Introduction . . . 143

6.2 Experimental . . . 146

  6.2.a Foraminifera samples . . . 146

  6.2.b Reagents, Material and Labware . . . 146

  6.2.c Foraminifera cleaning . . . 147

  6.2.d Boron isotope analysis in continuous mode . . . 148

  6.2.e Boron isotope analysis in transient mode . . . 150

6.3 Results and Discussion . . . 151

  6.3.a Cleaning efficiency . . . 151

  6.3.b δ^{11}B measurements in continuous and transient mode . . . 151

  6.3.c Ontogenetic variability of the δ^{11}B in *G.bulloides* . . . 157

6.4 Conclusion . . . 158

Après avoir mis en place la mesure du δ^{11}B$_{carb}$ pour des échantillons de carbonates contenant de faibles concentrations de bore, je me suis attelé à réaliser les premières mesures d'échantillons de foraminifères planctoniques. Celles-ci ont été également permises par de nombreux tests réalisés sur le lavage des échantillons, car toute trace de contaminants comme la matière organique, les argiles ou les oxydes de manganèse ou de fer peuvent fortement impacter le rapport δ^{11}B$_{carb}$. Ce chapitre présente donc les premiers résultats obtenus sur l'espèce de foraminifère *Globigerina bulloides*, l'une des moins concentrées en bore (B/Ca $\approx$ 40 µmol/mol, Henehan *et al.* 2016), sur trois fractions de tailles différentes: 250-315 µm, 315-400 µm et > 400 µm. Comme les échantillons préparés contenaient très peu de matériel, certains étant même trop faiblement concentrés en bore, j'ai utilisé avec succès l'alternative évoquée dans le chapitre 4, consistant à les mesurer en signal transitoire, avec un volume trois fois plus petit que la méthode en signal dit continu expliquée dans le chapitre 5. Cette méthode a permis ainsi d'avoir d'excellentes précisions pour des échantillons ne contenant que 1 ng de bore, pour une consommation totale de 80 µL. La validation de mes résultats au regard de précédentes études sur les foraminifères m'a finalement permis de discuter de potentiel effet de taille sur le δ^{11}B$_{carb}$ chez *Globigerina bulloides*. Ce chapitre rédigé sous forme d'article est en préparation pour *Biogeosciences*, en *technical note*.

δ^{11}B DETERMINATION IN FORAMINIFERA AT VERY LOW B CONCENTRATION: APPLICATION ON THE ONTOGENETIC VARIABILITY WITHIN *GLOBIGERINA BULLOIDES*

Matthieu Buisson[1], Pascale Louvat[1], Szabina Karancz[2,3], Ruchen Tian[2], Markus Raitzsch[2,4], Jelle Bijma[2,5], Claire Rollion-Bard[1]

[1] *Université de Paris, Institut de physique du globe de Paris, CNRS, F-75005 Paris, France*

[2] *Alfred-Wegener-Institut Helmholtz-Zentrum für Polar- und Meeresforschung, Bremerhaven, Germany*

[3] *Royal Netherlands Institute for Sea Research, Utrecht University, Texel, The Netherlands*

[4] *MARUM - Centre for Marine Environmental Sciences, University of Bremen, Bremen, Germany*

[5] *Jacobs University, Bremen, Germany*

Abstract

Since the 1990s the isotopic ratio of boron (δ^{11}B) in calcitic shells of planktic foraminifera has proven to be a powerful geochemical proxy to determine the oceanic paleo-pH and its link to atmospheric CO2 level over geological times. However, the use of planktonic foraminifera in paleoclimatic reconstructions requires calibrations of the pH – δ^{11}B relationships to correct what is known as « vital effect »: each species controls differently its calcification process and consequently slightly modifies the seawater chemistry during biomineralization. Moreover, shell size effect on δ^{11}B has been reported for some symbiont-bearing species due to photosynthetic increase of pH. Calibrations for the symbiont-barren *Globigerina bulloides* have been already determined but sparse data have been reported so far for the test size effect on δ^{11}B. Here we measured the δ^{11}B of three different fractions (250-315, 315-400 and >400 µm) of *G. bulloides* sampled along the coretop PS97-122 from the Chilean margin (54.10°S, 74.91°W), by using a new protocol developed at IPGP and dedicated to small samples which couples a microsublimation technique and a micro-direct injection device (µ-dDIHEN). This allowed to perform δ^{11}B mesurements for solutions containing only 1 ng of boron, corresponding to an analyse on 400 pg of boron, with only 80 µL injected for a triplicate analysis. After validating our δ^{11}B measurements on foraminifera, we showed that there are no δ^{11}B size effect on *G. bulloides*, which is coherent for this specis where the microenvironment is only affected by respiration and calcification, compared to other symbiont bearing species where photosynthesis is at play, impacting δ^{11}B according to the symbionts' density.

6.1 Introduction

Since the pioneering work based on the oxygen and carbon isotopes (Epstein *et al.*, 1953; Emiliani, 1955), foraminifera emerged during the last 60 years as an important archive since the Lower Cretaceous for paleoceanographic and paleoclimatological reconstructions due to their ubiquity in the oceans (Schiebel *et al.*, 2018). During the precipitation of their calcite test, foraminifera entrap various minor and trace elements (i.e Li, B, Na, Mg, Sr, Ba, $\sim 1\,\%$ of the weight) from the seawater, which is closely related to the physical and chemical conditions of their living environment (Lea, 2003; Katz *et al.*, 2010). Biomineralisation mechanisms have been investigated to better apprehend the processes of their incorporation in the carbonate lattice (e.g., Elderfield, 1996; Erez, 2003; Bentov & Erez, 2005; Nehrke *et al.*, 2013; de Nooijer *et al.*, 2014; Toyofuku *et al.*, 2017; Evans *et al.*, 2018), while the relationships between the chemical compositions of the shell and seawater have widely explored in laboratories and field studies (e.g., Delaney *et al.*, 1985; Sanyal *et al.*, 1995; Lea *et al.*, 1999; Anand *et al.*, 2003; Russell *et al.*, 2004; Yu *et al.*, 2007a; Gray *et al.*, 2018), allowing to shed light on the "biological black box". Empirical proxies have thus been calibrated based on these relationships between the surrounding physico-chemical parameters and the carbonate geochemistry of the foraminifera's tests, in an attempt to correct the so-called vital effects i.e the modification by the foraminifera of the seawater chemistry prior to calcification (Urey *et al.*, 1951).

One of the most robust proxies applied in paleoceanographic reconstructions is the boron isotopic ratio as tracer of the seawater pH (Sanyal *et al.*, 1996; Pearson & Palmer, 2000; Sanyal *et al.*, 2001; Foster, 2008; Rae *et al.*, 2011; Henehan *et al.*, 2013, 2016; Raitzsch *et al.*, 2018; Guillermic *et al.*, 2020). The basis of the ^{11}B/^{10}B (δ^{11}B)-pH proxy relies on the constant equilibrium fractionation of 27.2 ± 0.6 ‰ (Klochko *et al.*, 2006) between the two pH-dependent species: the trigonal weak acid $B(OH)_3$ and its conjugated base, the borate anion $B(OH)_4^-$ (Dickson, 1990; Roy *et al.*, 1993), the latter being almost solely incorporated as a substitute of the carbonate ion in the calcium carbonate lattice of many biocalcifiers (Vengosh *et al.*, 1991b; Hemming & Hanson, 1992; Sen *et al.*, 1994; Branson *et al.*, 2015; Balan *et al.*, 2016). Other proxies, such as the B/Ca ratio for the seawater carbonate system, are however still lacking concensus (e.g., Ni *et al.*, 2007; Yu *et al.*, 2007b; Tripati *et al.*, 2009; Allen *et al.*, 2012; Babila, 2014; Henehan *et al.*, 2015; Haynes *et al.*, 2017).

However, measuring δ^{11}B of foraminifera is challenging due to their small size and low boron concentration. The lower and upper B/Ca ratios reported in the literature for planktonic foraminifera are 40-60 µmol/mol for *Globigerina bulloides* and 80-120 µmol/mol for *Globigerinoides ruber* (Henehan *et al.*, 2016; Guillermic *et al.*, 2020), which involves to gather respectively $\sim$ 400 specimens and $\sim$ 100 specimen for one bulk sample at $\sim$ 2-20 ng (Rae, 2018). For the benthic foraminifera with higher B/Ca ratios (100-250 µmol/mol), 2-20 individual tests are sufficient but their occurence is generally limited in the sediments (Rae *et al.*, 2011; Raitzsch *et al.*, 2011, 2020). The imperative to clean the foraminifera samples from organic matter, clays and oxides contaminants leads to a further loss of more than 30 % of the sample mass, through its partial dissolution, fraction that can be even higher if a reductive cleaning step is operated after the oxidative cleaning (Barker *et al.*, 2003; Yu *et al.*, 2007a; Pang *et al.*, 2020). The shell cleaning procedures must therefore be considered for the sample preparation. In order to fully resolve the pH value from δ^{11}B measurements in foraminifera, annex analysis such as the paleo-thermometer Mg/Ca ratio is essential to determine the seawater temperature and calculate consequently the dissociation constant of the boric acid (e.g., Martínez-Botí *et al.*, 2015a; Gutjahr *et al.*, 2017; Raitzsch *et al.*, 2018; Henehan *et al.*, 2019).

Moreover the δ^{11}B measurement required precision that must not exceed 0.8 ‰ (2SD, Foster *et al.* 2006), corresponding to $\simeq$ 0.1 pH units (where for example the ΔpH in the whole surface oceans is only 0.3 pH units), which is quite challenging given the difficulties encountered during boron wet chemistry (blank issues for low level samples) and mass spectrometer measurements (volatility in acid medium, stickiness, large instrumental mass fractionation and poor ionization). Various approaches in the last decades have been commonly used to measure δ^{11}B in carbonate samples alongside a continual, challenging ever decrease in the boron mass needed and increase in the precision needed (Aggarwal & You, 2016; Foster *et al.*, 2018).

The bulk δ^{11}B analysis are performed either on TIMS (Thermal Ionization Mass Spectrometer) or MC-ICP-MS (Multi-Collector Inductively Plasma Source Mass Spectrometer), after dissolution of the carbonate samples and extraction of the boron to be analysed. For the former, two versions have been used on carbonates with Positive-TIMS (Gaillardet & Allègre, 1995; Wei *et al.*, 2009) and Negative TIMS (Vengosh *et al.*, 1989; Hemming & Hanson, 1992, 1994; Hönisch *et al.*, 2004; Clarkson *et al.*, 2015). Those technics are somehow antinomic because PTIMS provides the best precision (0.1 ‰, 2SD) but with a substantial boron mass (100 ng, Ishikawa & Nagaishi 2011), whereas NTIMS consumes the lowest amount of boron, 1 ng for a precision of 0.3 ‰ (2SD, Foster *et al.* 2013). An alternative NTIMS method consists in ionizing the whole sample (Total Evaporation NTIMS, Foster *et al.* 2006; Ni *et al.* 2010; Liu *et al.* 2013), substantially decreasing the B amount to 0.3 ng but at the expense of the precision, 0.7 ‰ (Foster *et al.*, 2006). Concurrently δ^{11}B determination with MC-ICP-MS (and more marginally with High Resolution HR-ICP-MS, Misra *et al.* 2014b) has been developed since the early 2000s (Lécuyer *et al.*, 2002; Foster, 2008; Louvat *et al.*, 2011a; Rae *et al.*, 2011; McCulloch *et al.*, 2014). It gradually supplanted NTIMS, with higher ionisation yields, a more stable mass bias and higher analysis throughput. Significant disparities have been reported for data from different laboratories and for inter-laboratory comparisons between NTIMS and MC-ICP-MS, although the reasons are not well established (Foster *et al.*, 2013; Farmer *et al.*, 2016). The last strategies and upgrades on MC-ICP-MS have reach their apogee with 0.2 ‰ (2SD) for samples containing only 3 ng of boron (Lloyd *et al.*, 2018).

The best precision ever reported in the literature for plasma MC-ICP-MS, 0.1 ‰, was achieved at Institut de Physique du Globe de Paris (IPGP) for pure boric acid solutions and samples with boron mass higher than $\sim$ 20 ng (Louvat *et al.*, 2014b), with an automated direct injection nebulizer (d-DIHEN, Louvat *et al.* 2011a). This sample introduction system has been recently miniaturized (μ-dDIHEN, Louvat *et al.* 2019) to reach the lowest amount of solution consumed for a δ^{11}B measurement, 300 µL with their usual method and 100 µL with a new calculation strategy based on transient signal measurements never used so far for boron isotopes. This new µ-dDIHEN device, combined with the microsublimation technique to extract boron from the carbonate matrix (Gaillardet *et al.*, 2001; Wang *et al.*, 2010; Misra *et al.*, 2014b; Raitzsch *et al.*, 2018) resulting in low procedure blanks, has been successfully tested for carbonate samples, with unprecedented performances: 2SD precision of 0.2 ‰ for 2.5 ng of boron, and 0.5 ‰ for sample solutions containing only 1 ng (Chap.5).

In this study, we tested the validity on this analytical breakthrough for the planktonic foraminifera species *Globigerina bulloides* (d'Orbigny, 1826). We propose a new approach aiming to minimize the required sample amount while increasing the number of chemical analyses possible on the same sample; a need for tiny and precious samples that require considerable times of preparation and rigorous analytical protocols. These foraminifera are the first to be analyzed at IPGP for their boron isotope ratio at such boron concentrations. Originating from the top of a marine sediment core, they were sieved at different sizes, allowing us to investigate the δ^{11}B ontogenetic variability within *G. bulloides*.

6.2 Experimental

6.2.a Foraminifera samples

The sediment material come from the core PS97/122-1 (Lamy, 2016), collected along the Chilean margin (54.10 °S, 74.91 °W), at a water depth of 2558 m for a length of 10.77 m and sampled every centimeter. Each sample was freeze-dried, wet sieved at 63 µm and dried in an oven at 40 °C for two to three days. For the purpose of this study, we used the Holocene coretop samples between 7 and 37 cm sieved at >400 µm, 400-315 µm and 250-125 µm, in which we handpicked under optical microscope only well preserved shells of the shallow dwelling planktonic foraminifera *G. bulloides* ($\sim$ 120-190 shells per sample), a species living in temperate to sub-polar water and upwelling zones (Schiebel & Hemleben, 2017).

6.2.b Reagents, Material and Labware

The foraminifera cleaning, dissolution, boron extraction and the preparation of standards and reference materials have been carried out with supra-pure chemicals reagents, distilled nitric acid HNO_3 (DST1000 device) and Milli-Q water (resistivity > 18 MΩ and Q-pod with 0.22 µm Millipak Express filter), in an over-pressured and air filtered clean room with boron-free H14 HEPA filters. All the Eppendorf vials (for foraminifera cleaning) and 0.5 mL polypropylene tubes have been boiled in HCL 3N, then rinsed with MQ water and soaked in HNO3 0.5 N. For the Savillex teflon vials boiling was in HNO_3 3N but the rest of the procedure was the same. The polypropylene tubes for MC-ICP-MS measurements were filled with 0.5 N HNO_3

for a few days. After the acid treatments, all the labware is rinsed with MQ water and dried at room temperature. The pipettes tips were washed just before use by pipetting three times 0.5N HNO_3 and then milliQ water.

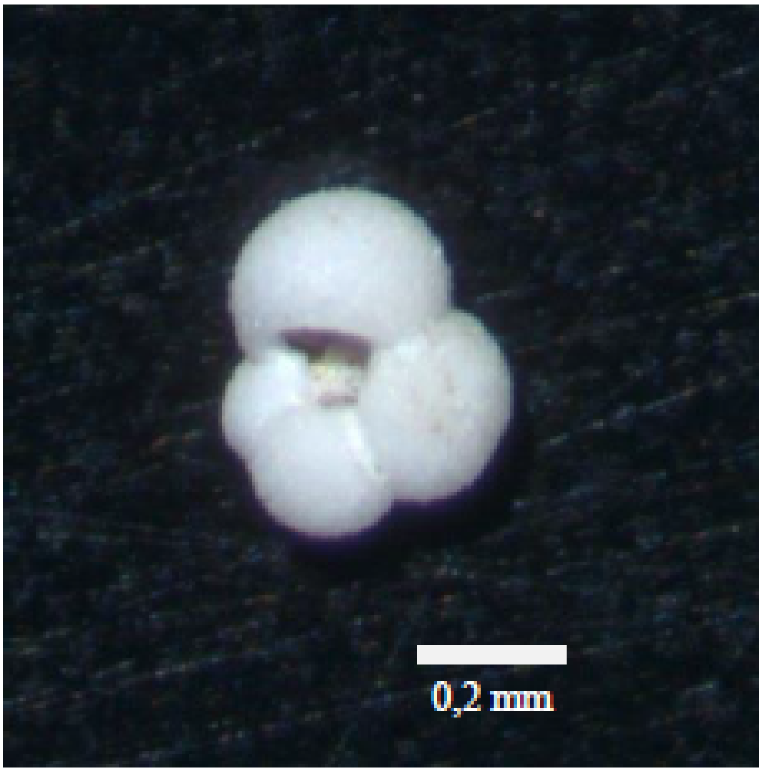

Figure 6.1 : *Picture of one of the picked* Globigerina bulloides *shells*

6.2.c Foraminifera cleaning

The picked foraminifera samples are cleaned following a modified protocol from Barker *et al.* (2003) and Rae *et al.* (2011). They were initially gently crushed between two clean glass slides under a binocular to open the foraminifera test chambers. The shell fragments are then transferred to 500 µL Eppendorf vials with MQ water. The samples are rinsed and ultrasonicated 6 to 8 times with MQ water until there is visually no clay residue. The organic matter is then oxidised with 0.1 N NaH_4OH buffered-1% H_2O_2 in a hot water bath at 80°C. They are immediately after rinsed three times with MQ water and transferred in 1.5 mL eppendorf vials for leaching with 0.0005 N HNO_3 to remove any adsorbed contaminants. They are finally rinsed again with MQ water and gradually (drop by drop) dissolved with HNO_3 0.5N, for a final solution at $\sim$ 100-200 µL and ultimately stocked in a teflon vial. The reductive cleaning step with ammonia-ammonium acetate buffer, citric acid and hydrazine for ferromanganese oxy-hydroxides removal is delicate as it decreases the Mg/Ca ratio through partial dissolution (Barker *et al.*, 2003; Yu *et al.*, 2007b; Pang *et al.*, 2020), without however impacting B/Ca ratio and $\delta^{11}B$ (Yu *et al.*, 2007a; Misra *et al.*, 2014a,b). In the context of paleo-pH reconstructions, because we generally need the Mg/Ca ratio from which is deduced the seawater temperature required to calculate the acid boric / borate dissociation constant, we chose to omit this step. To check the efficient of the cleaning protocol, the Al/Ca and the Mn/Ca ratio have been measured with a quadrupole inductively coupled plasma mass spectrometer (ICP-MS, Agilent 7900) at IPGP, following a protocol modified from Yu *et al.* (2005)

6.2.d Boron isotope analysis in continuous mode

The whole protocol for boron purification and isotope ratio measurement is fully described in the Chapter.5. The boron isotopes are originally separated from the carbonate matrix by the microsublimation method (Gaillardet *et al.*, 2001; Wang *et al.*, 2010; Misra *et al.*, 2014b; Raitzsch *et al.*, 2018). A 50 µL droplet of the dissolved sample was loaded on a cap of a pre-cleaned 5 mL Savillex Teflon fin legged conical vial. The vial was rapidly and tightly closed, then coated in an aluminium foil entirely except for the upper tip, and placed (still upside down) on a hotplate for 24 hours at 95°C. Vials are then carefully removed from the hot plate, flipped and allowed to cool for 15 min. The distillate (recovered in the vial bottom) is finally diluted with 450 µL of MQ water for a final HNO_3 concentration at 0.05 N, the chosen medium for δ^{11}B analysis (Louvat *et al.*, 2011a, 2014b). The 0.5 mL final solution is transferred to 5 mL propylene tubes to be analysed immediately.

The δ^{11}B measurements were carried out at low mass resolution (m/Δm=400) on a MC-ICP-MS Neptune (Thermoscientific) at IPGP. The instrument has been customized for low signals, with the combination of Jet sampler and X skimmer cones, and two 10^{13} ohm resistor positioned on Faraday cups H3 and L3 to collect respectively the ^{11}B and the ^{10}B isotope signals. The solution samples were introduced directly into the plasma with a fully automated direct injection nebulizer (d-DIHEN, Louvat *et al.* 2011a, 2014b) in flow injection analysis mode, and supplied by a gas displacement pump (GDP), the whole system constituting the µ-dDIHEN set-up (Louvat *et al.* 2019, Chap.4). Briefly, a 50 µL sample loop is filled with the solution, standard or reference material and then driven to the nebulizer with a 0.05 HNO_3 carrier solution from the GDP fed by an argon micro-flow rate. We fixed the mass flow meter of the GDP at 45-50 µL.min^{-1} to obtain sample uptake rate of 25-30 µL.min^{-1} and achieve a stable signal plateau lasting $\sim$ 100 s for the injections peaks, which allows to measure the ^{11}B/^{10}B ratio with 12 cycles of 8 seconds (Louvat *et al.*, 2019). Prior the δ^{11}B analysis, B concentration are measured on the MC-ICP-MS in order to match within $\pm$ 5% the concentrations of the sample, standard and reference material solutions. For each sample, the average boron isotopic ratio and its associated repeatability (2SD) is calculated from five δ^{11}B values (background corrected) obtained after three successive sample-standard bracketing measurements (Louvat *et al.*, 2014b), consuming in total only 240 µL. Boron isotopic ratios are reported as δ^{11}B, relative to the boric acid international standard reference NIST SRM 951

(Catanzaro *et al.*, 1970):

$$\delta^{11}B = (\frac{(^{11}B/^{10}B)_{sample}}{(^{11}B/^{10}B)_{NIST\ SRM\ 951}} - 1) * 1000. \tag{6.1}$$

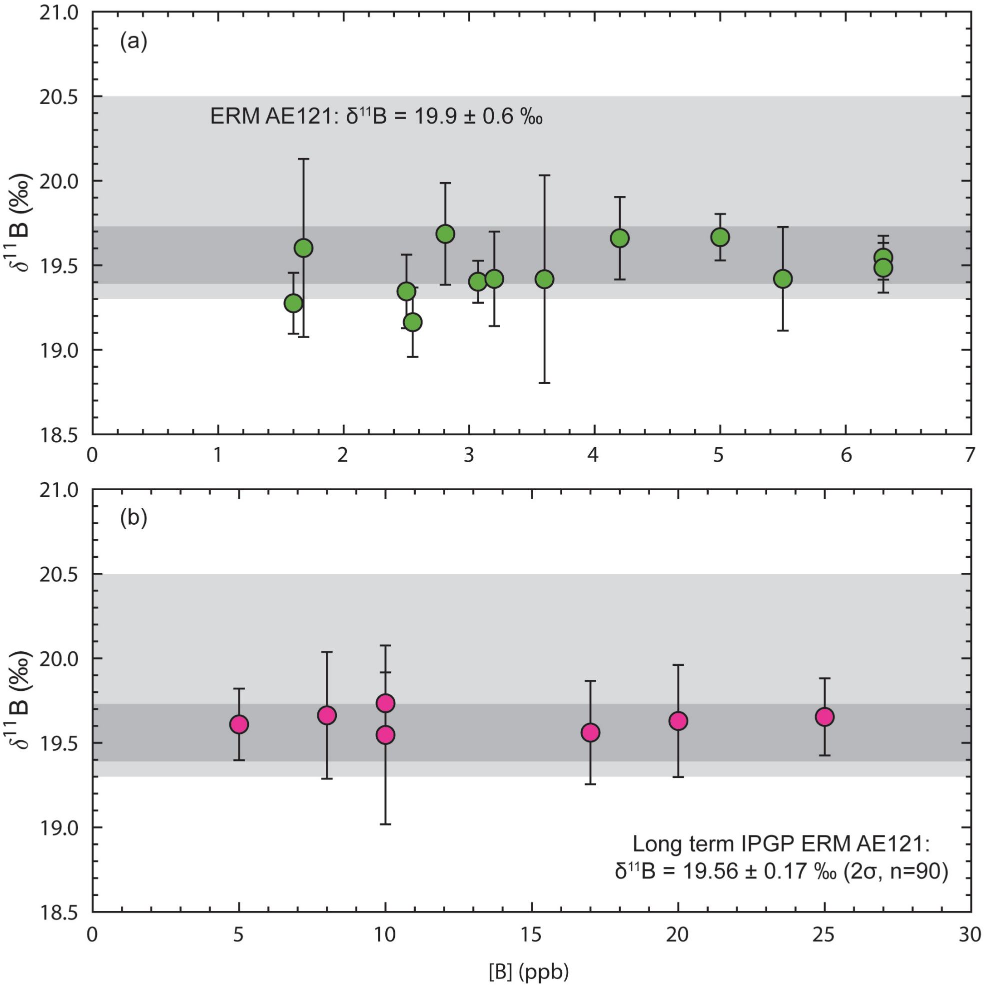

Figure 6.2 : *Reproducibility of the $\delta^{11}B$ measured for the reference material ERM AE121 according to the concentration for (a) continuous measurements mode and (b) transient measurements mode. The light gray band corresponds to the reference value, 19.6 ± 0.6 ‰ (Vogl & Rosner, 2011), and the dark gray band the IPGP long-term reproducibility, 19.56 ± 0.17 ‰ (2SD, n=90, Louvat et al. 2019, Chap.5).*

The foraminifera samples exhibited [B] between 1.5 ppb (0.75 ng) and 6.5 ppb (3.25 ng), corresponding to a ^{11}B signal between ∼ 20 mV and ∼ 100 mV. The whole procedural blank was 12 ± 4 pg (1SD, n=4), representing ≈ 1.5 % of the B content for a sample with 0.75 ng of boron. For each B concentration range, the quality of the δ^{11}B measurement was supported with the measurement at the same concentration of the boric acid reference material ERM-AE121 (δ^{11}B=+19.9 ± 0.6 ‰, Vogl & Rosner 2011). All ERM-AE121 measurements during the study yielded 19.47 ± 0.31 ‰ (2SD, n=13) in concordance with the long-term IPGP value (δ^{11}B=19.56 ± 0.17 ‰, 2SD, n= 90 for 200 ppb solutions, Chap.5) but with a reproducibility slightly higher due to the very low concentrations addressed here (Fig.6.2.a). The carbonate reference material MVS-1 (δ^{11}B=15.95 ± 0.19 ‰, 2SD, n= 46, Jurikova *et al.* 2019) was also measured during this study, giving a value of 15.96 ± 0.09 ‰ (2SD, n=3).

6.2.e Boron isotope analysis in transient mode

As the B concentrations of the foraminifera samples were very low (between 1.6 and 6.9 ppb) after microsublimation extraction, we attempted an alternative measurement strategy in order to reduce the sample volume consumption while keeping the same boron amount: δ^{11}B were measured in transient mode for some of the samples (Louvat *et al.*, 2019).

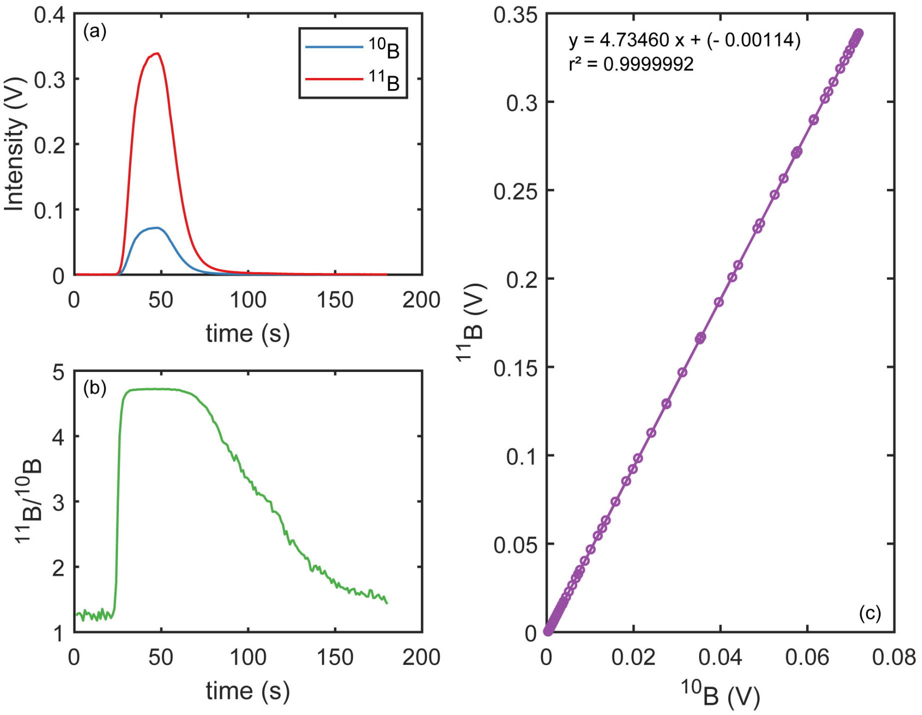

Figure 6.3 : *(a): Example of an injection peak with a 10 μL sample loop and a sample uptake rate at 25 μL.min^{-1}. (b) Evolution of the ^{11}B/^{10}B ratio during the 180 s measurement. (c): linear regression between the ^{11}B and the ^{10}B signals from the 180 measurements to determine the ^{11}B/^{10}B ratio.*

From the same foraminifera solutions (after cleaning and dissolution), we repeated the microsublimation protocol by sampling again 50 μL, but after the purification we added only 150 μL of 0.5 HNO_3 and transferred the diluted distillate in a 0.5 mL polypropylene tube to be analysed. Consequently, all the solutions, standards, reference materials, samples, as well as the carrier solution are prepared in HNO_3 0.5 N medium instead of HNO_3 0.05 N. We changed also the 50 μL sample loop for a 10 μL loop. At this sample loop volume, the injection peaks are not long enough for continuous stable signal measurements; the ^{11}B and ^{10}B signals are transient and consequently the whole peaks are measured in 180 cycles of 1 s, including baseline signals before and after the B peak (Fig.6.3a and b). For each sample, standard or reference material injection, the ^{11}B/^{10}B ratio is calculated from the slope of a linear fit (using the fit linear regression model, fitlm, in *Matlab*, Fig.6.3c) between the 180 measurements of ^{11}B and ^{10}B signals, described by the equation

$$^{11}B = (a \pm u_a)^{10}B + (b \pm u_b), \tag{6.2}$$

with a the slope of the linear regression representing the ^{11}B/^{10}B ratio, u$_a$ the uncertainty of the slope corresponding to the internal precision of the ^{11}B/^{10}B ratio, b the intercept of the regression and u$_b$ the uncertainty of the intercept (Fietzke *et al.*, 2008; Epov *et al.*, 2010). This allows us to determine a ^{11}B/^{10}B for each B injection and performs a sample-standard bracketing in triplicate for one foraminifera sample following Louvat *et al.* (2014b). The triplicate measurement consumes only 80 µL, i.e. ∼ 27 µL per injection (Louvat *et al.*, 2019). The use of the 10 µL sample loop instead of 50 µL allowed to significantly increase the B concentration of the samples to between 5 ppb (1 ng) and 25 ppb (5 ng), for a maximal intensity on the ^{11}B signal of between 70 and 350 mV. For example, only 400 pg of boron is analysed during standard-sample bracketing in triplicate measurement for a 5 ppb solution, i.e. ∼ 125 pg for one peak injection, reaching the lowest amount of boron ever analysed in the literature.

6.3 Results and Discussion

6.3.a Cleaning efficiency

Potential clay and Fe-Mn oxides contamination were screen with the Al/Ca and Mn/Ca ratio. Mn/Ca ratio was very low for all foraminifera sample solutions, <16.7 ± 5.4 µmol/mol (2SD), lower than the acceptable limit of 30 µmol/mol determined by (e.g. Martin & Lea, 2002), but almost all the samples exhibited high Al/Ca, most of them above the threshold generally fixed, 100 µmol/mol (Rae *et al.*, 2011). When plotting this clay contamination indicator against the δ^{11}B (measured in continuous mode and transient mode) (Fig.6.4), we observe no correlation between elevated Al/Ca ratios and low δ^{11}B. This allows us to exclude a potential impact of residual clay on the determination of our sample's δ^{11}B (e.g. Rae *et al.*, 2011; Gutjahr *et al.*, 2017).

6.3.b δ^{11}B measurements in continuous and transient mode

In the rest of the discussion, we chose to address the mean of the measured values. However, considering that we obtained on MVS-1 a reproducibility of 0.09 ‰ in continuous mode and in transient mode, it is likely that a part of the measured variability in our sample is due to natural variability (mostly pH change through the studied time period).

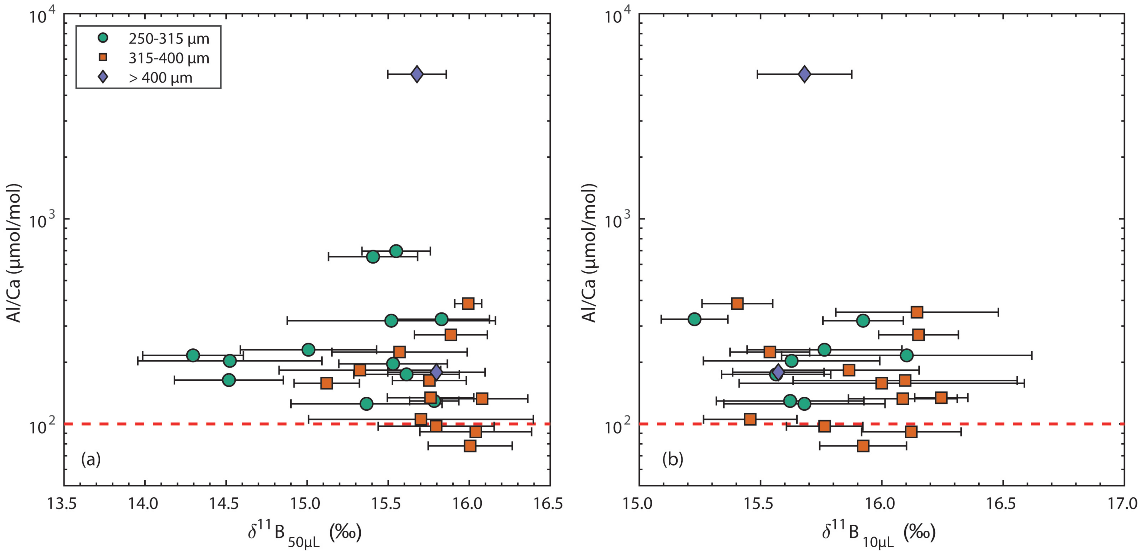

Figure 6.4 : *Crossplots between the Al/Ca and the δ^{11}B measured in continuous (50 µL loop, a) and transient (10 µL loop, b) mode for the foraminifera samples to check possible contamination, with the red line for the threshold of 100 µmol/mol (Rae et al., 2011).*

δ^{11}B results in continuous mode

The *G. bulloides* δ^{11}B determined from the continuous mode measurements exhibits values between 14.52 and 15.83 ‰ with an average of 15.25 ± 1.06 ‰ (2SD, n=12) for the 125-250 µm fraction. The two other fractions have very similar values, with 15.78 ± 0.60 ‰ (2SD, n=13, between 15.12 and 16.10 ‰) for the 315-400 µm and 15.74 ± 0.17 ‰ (2SD, n=2) for the > 400 µm fraction (Fig.6.5. a). As mentioned earlier, picking of at least 400 individual shells per sample is usually recommended for providing enough boron to analyse (e;g., Martínez-Botí *et al.*, 2015b). Our samples contain half as much shells (180 to 200) and the measurements were performed on solutions with very low concentrations, especially for the smallest fraction containing naturally less material. Our protocol coupling the µ-dDIHEN setup and the microsublimation has highlighted a threshold at 1-2 ppb (Chap. 5), where the measurement reproducibility starts to worsen, due to too low signals and higher impact of boron memory effect, contamination during the dilutions or residual matrix effects, lowering the δ^{11}B values, our blank being more enriched in ^{10}B (Louvat *et al.*, 2014b).

The > 400 µm and 315-400 µm fractions have been very little concerned by these effects, with concentrations after microsublimation between 2.6 and 6.9 ppb, whereas the 250-315 µm fraction is more impacted with seven [B] values below 2.5 ppb. We observe that there almost no difference within uncertainties between the 315-400 and > 400 µm and also between the 250-315 µm and 315-400 µm where the values of the 250-315 µm fraction are not pulled down because of their low content.

Table 6.1 : $\delta^{11}B$ *measurements for G. bulloides from the PS97-122 coretop*

G. bulloides		**Continuous mode**			**Transient mode**			**AWI measurements**		Al/Ca	Mn/Ca
Depth (cm)	Fraction size (µm)	[B] (ppb)	δ^{11}B (‰)	2SD (‰)	[B] (ppb)	δ^{11}B (‰)	2SD (‰)	δ^{11}B (‰)	2SD (‰)	(µmol/mol)	(µmol/mol)
15-16	250-315	3.1	15.37	0.47	10	15.68	0.33			125	10
17-18	250-315	1.6	14.52	0.34						164	19
19-20	250-315	2.5	14.52	0.57	10	15.63	0.36			203	18
21-22	250-315	3.6	15.41	0.28						653	14
23-24	250-315	1.7	15.01	0.42	5	15.76	0.32			230	13
25-26	250-315	1.6	14.30	0.31	5	16.10	0.52			216	15
27-28	250-315	2.4	15.52	0.64	10	15.92	0.17			319	14
29-30	250-315	3.5	15.78	0.15	10	15.62	0.30			129	13
31-32	250-315	2.3	15.53	0.33						196	17
33-34	250-315	2.5	15.61	0.33	8	15.56	0.23			174	16
35-36	250-315	3	15.55	0.21						696	16
37-38	250-315	4.2	15.83	0.30	10	15.23	0.14			324	16
7-8	315-400	6.8	16.01	0.26	20	15.92	0.18			78	26
11-12	315-400	6.7	15.89	0.22	20	16.15	0.16			272	30
15-16	315-400	6.7	15.99	0.08	20	15.40	0.15			386	13
17-18	315-400	5.5	15.80	0.36	25	15.76	0.16			98	16
19-20	315-400	5.3	15.70	0.69	17	15.46	0.19	15.91	0.25	105	14
21-22	315-400	4.3	15.57	0.42	17	15.54	0.16	15.67	0.25	224	15
23-24	315-400	3.1	15.75	0.23	10	16.10	0.46			163	13
25-26	315-400	2.6	15.12	0.20	10	16.00	0.59	16.06	0.46	158	23
27-28	315-400	2.8	15.76	0.27	10	16.24	0.11			134	12
29-30	315-400	3.8	15.33	0.50	20	15.86	0.29	15.92	0.25	183	13
31-32	315-400	4.6	16.10	0.23	25	16.24	0.27			43	14
33-34	315-400	6.4	16.04	0.34	20	16.12	0.21			92	16
35-36	315-400				25	16.15	0.34			351	15
37-38	315-400	6.9	16.08	0.28	25	16.09	0.22			133	15
7-8	> 400	6	15.68	0.18	20	15.68	0.19			5071	34
11-12	> 400	6.4	15.80	0.30	20	15.57	0.19			179	16

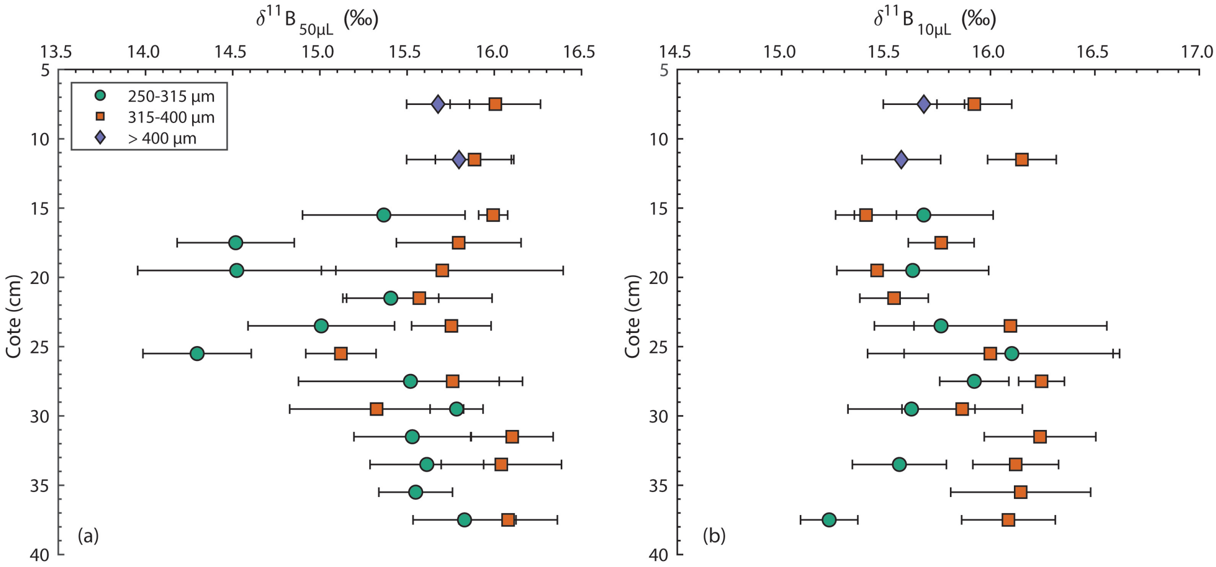

Figure 6.5 : *δ^{11}B of the foraminifera samples measured in continuous (50 µL loop, a) and transient (10 µL loop, b) according to the depth of the sample in the core PS97-122.*

δ^{11}B results in transient mode

The new measurement method through transient signal mode has been validated with the reference material ERM-AE121 at each foraminifera sample concentration, and with the carbonate reference material MVS-1, yielding δ^{11}B average values of respectively 19.63 ± 0.13 ‰ (2SD, n=7, Fig.6.2b) and 15.75 ± 0.09 ‰ (2SD, n=2).

The average δ^{11}B for the samples measured in transient mode is 15.93 ± 0.57 ‰ (2SD, n=14, between 15.40 and 16.24 ‰) for the >400 µm fractions and 15.63 ± 0.15 ‰ (2SD, n=2) for the 400-315 µm fractions, very close of the continuous mode values (Fig.6.5. b). On the other hand, the δ^{11}B reproducibility for the 125-250 µm size is improved, and the average increased, with 15.69 ± 0.52 ‰(2SD, n=8), now in agreement with the other sample size fractions. In fact, this transient measurement approach (with the 10 µL sample loop of the µ-dDIHEN) shows an excellent agreement with the traditional and continuous mode above 2 ng boron, but additionally offers the possibility to measure samples with very low B concentrations at higher precision (Fig.6.6), by reducing the initial sample volume and therefore concentrating boron. The too low δ^{11}B values obtained with the continuous mode for sample solutions with [B] close to the 2 ppb threshold, are more accurately measured with the transient mode, because in better concordance with the analysis of the other sample size fractions (Fig.6.6). Moreover, with the same pool of low B foraminifera samples (independantly of the size fraction, the external reproducibilities with the transient mode are improved and less scattered, with an average of 0.26 ± 0.25 ‰ (2SD), against 0.33 ± 0.29 ‰ (2SD) for the continuous mode. Considering the lowest concentrations measured in transient mode — 5 ppb (1 ng B in 200 µL)— this corresponds to an unprecedented low level of boron analysed of 400 pg (80 µL for a sample standard bracketing in triplicate, i.e. 125 pg of boron per injection), for 2SD external reproducibilities reaching 0.32 and 0.52 ‰ (2SD), in addition to providing more consistent data.

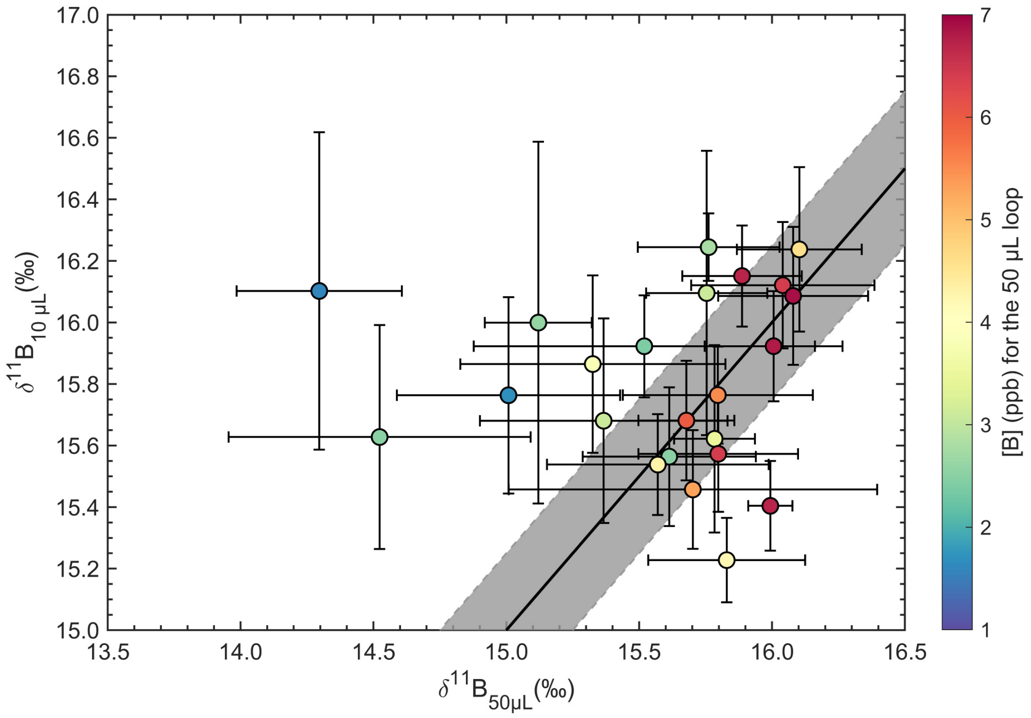

Figure 6.6 : *Closs plot between the $\delta^{11}B$ measured in continuous mode with a 50 µL sample loop and the $\delta^{11}B$ measured in transient mode with 10 µL sample loop. The colour code provides the B concentration at which the samples have been measured for the continuous mode. The dark gray band represents the 0.25 ‰ enveloppe around the 1:1 line.*

Validity of foraminifera δ^{11}B

In the following, we assume the same climate conditions for all the studied time period and therefore the >400 µm, 400-315 µm and 250-125 µm of the whole depth interval were averaged for δ^{11}B. The precise calcification depths, as well as the natural changes in water chemistry are therefore not taken into account by averaging, but can perfectly explain the small variations observed in the δ^{11}B values between samples in the studied period, as the seawater carbonate chemistry changes with these parameters (Raitzsch *et al.*, 2018).

To compare our data with the existing *G.bulloides* calibration, we calculated the δ^{11}B of the seawater borate at the sampling location conditions with the following relationship (Zeebe & Wolf-Gladrow, 2001):

$$\delta^{11}B_{Borate} = \frac{\delta^{11}B_{sw} * B_T - 1000(\alpha_B - 1)[B(OH)_3]}{[B(OH)_4^-] + \alpha_B[B(OH)_3]}, \tag{6.3}$$

The total alkalinity (TA, 2267 ± 7 µmol/kg, 2SD) and the dissolved inorganic carbon (DIC, 2021 ± 16 µmol/kg) are derived from the GLODAPv 1.1 dataset through Ocean Data

View (Schlitzer, 2015), whereas the annual temperature (7.56 ± 0.15 °C, 2SD) and salinity (33.47 ± 0.36 psu, 2SD) are from the TCO2 +TALK gridded database (Goyet *et al.*, 2000). This allows to calculate the pH using CO2sys Excel program (8.235 ± 0.030, Pierrot *et al.* 2011), with the dissociation constants for the carbonate system from Lueker *et al.* (2000). $[\mathrm{B(OH)_3}]$ and $[\mathrm{B(OH)_4^-}]$ are derived from the calculated pH and the boron concentration in seawater (B_T = 432.6 x S/35 µmol/kg, Lee *et al.* 2010). The dissociation constant of boric acid pK^*_B, temperature and salinity dependant, is calculated with the equation of Dickson (1990). The boron isotope fractionation factor between boric acid and borate (α_B) is taken as 1.0272 (Klochko *et al.*, 2006) and the boron isotopic composition of seawater $\delta^{11}\mathrm{B}_{sw}$ as 39.61 ± 0.04 ‰ (Foster *et al.*, 2010). Here the assumption was made that there was no change in carbonate chemistry and temperature through the studied interval of time. The calculated $\delta^{11}\mathrm{B}_{Borate}$ is 17.68 ± 0.30 ‰ (2SD).

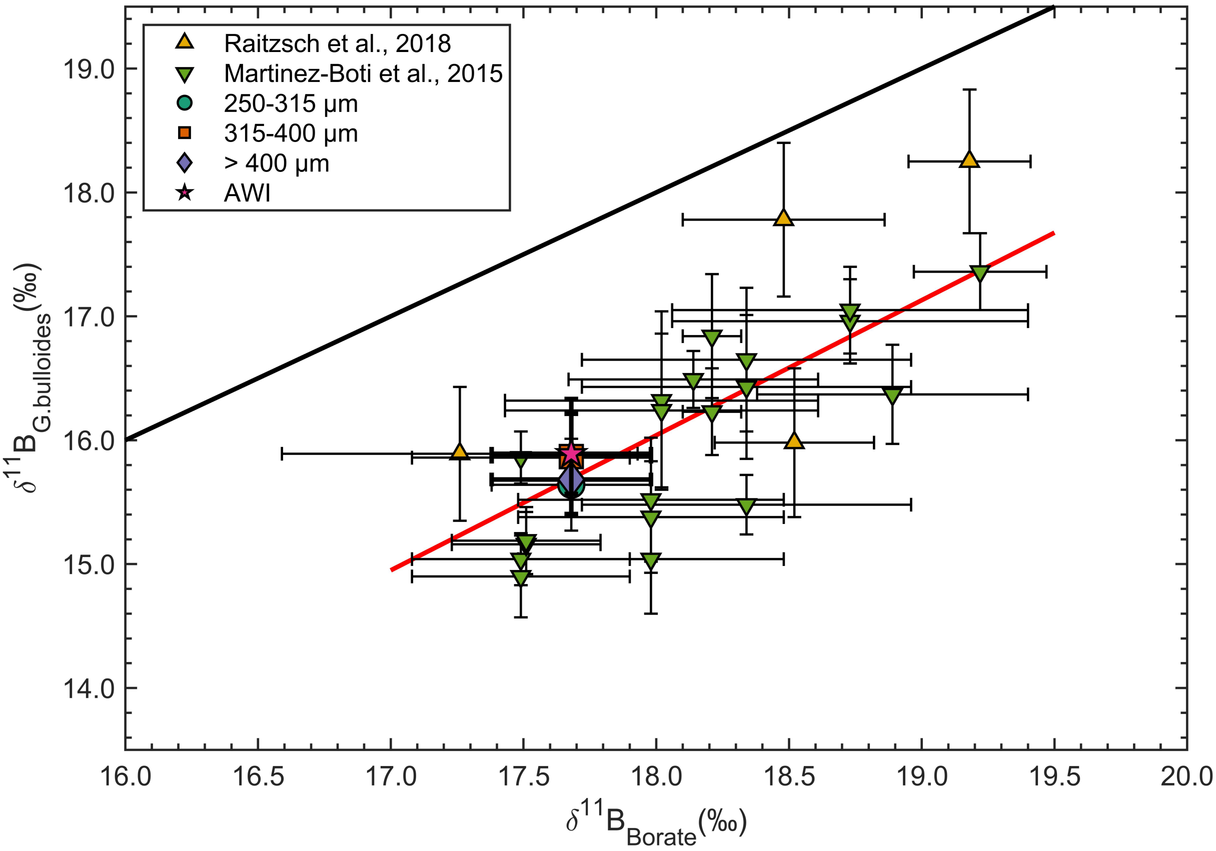

Figure 6.7 : *Comparison of the δ^{11}B measured in G. bulloides planctonic foraminifera against the δ^{11}B of the borate in seawater, calculated from the carbonate chemistry of the locations from where the foraminifera samples were collected. The literature data reported come from Martínez-Botí et al. (2015b) and Raitzsch et al. (2018). The red line correspond to the calibration proposed for this species, $\delta^{11}\mathrm{B}_{G.\ bulloides}$ = 1.09 (± 0.65)*$\delta^{11}\mathrm{B}_{Borate}$ - 3.58 (± 11.77) from Raitzsch et al. (2018) and the black line, the 1:1 line (sample value on this line means correct determination of the seawater borate, within the classical δ^{11}B - paleo-pH hypotheses). The mean of the different fraction sizes are also reported with their associated $\delta^{11}\mathrm{B}_{Borate}$, as well as the mean value measured at the AWI (see text for more details).*

As the transient and continuous modes of δ^{11}B measurement are in agreement (at least for solutions with [B]> 2 ppb), they offered two independent values for each foraminifera sample. These values were then averaged, with the exception of the δ^{11}B values in continuous mode at too low [B] that the transient mode discarded. The 250-315 µm fraction exhibits a value of 15.64 ± 0.37 ‰ (2SD, n=11), the 315-400 µm 15.87 ± 0.46 ‰ (2SD, n=14) and the >400 µm 15.68 ± 0.01 ‰ (2SD, n=2). These δ^{11}B values for each size fraction perfectly plot in the the linear regression of the species-specific $\delta^{11}B_{Borate}$-$\delta^{11}B_{G.bulloides}$ calibration (Martínez-Botí *et al.* 2015b; Raitzsch *et al.* 2018, Fig.6.7). Moreover, four samples of the size fraction 315-400 µm (at 19-20 cm, 21-22 cm, 25-26 cm and 29-30 cm) have been also measured at the Alfred-Wegener-Institut (AWI) in Bremerhaven (Germany) following the protocol of Raitzsch *et al.* (2018), giving an average value of 15.89 ± 0.33 ‰ (2SD), in full agreement with our value and the *G.bulloides* calibration. This further validates our analytical protocol to measure δ^{11}B of foraminifera samples.

6.3.c Ontogenetic variability of the δ^{11}B in *G.bulloides*

After these validations of the measurement of the boron isotope ratios, the results allow us to investigate potential size effects on the δ^{11}B values. We averaged the continuous and transient mode measurements. Outlier values that could be assigned to analytical issues with the second measurements were discarded. The δ^{11}B median for the 250-315 µm fraction (15.59 ‰) is slightly smaller than that for the 315-400 µm fraction (15.94 ‰), but the 0.3 ‰ difference is insignificant in terms of paleo-pH reconstructions and also because this corresponds roughly to the analytical uncertainty reported for δ^{11}B measurements (Fig.6.7, Fig.6.8). A shift toward lower values could be explained by the lower boron concentrations and therefore possibly a blank bias (Louvat *et al.*, 2014b), however the coarse fraction, with more carbonate material and higher [B], exhibit δ^{11}B between 15.68 and 15.69 ‰, closer to the finer size fraction and pull out this hypothesis. Nevertheless, it has to be taken into account that we need to measure more foraminifera from the >400µm fraction, as here it is difficult to rule out a size effect with only two measurements for this fraction. We can also observe this lack of size effect individually at each depth of the core-top, showing that the δ^{11}B difference within uncertainities is negligeable (Fig.6.5 and 6.6).

The boron signatures, related to the pH, recorded in the foraminifera do not directly reflect those of the seawater but rather the foraminifera microenvironment, likely modified by physiology (active modification of the calcifying medium, photosynthesis and respiration, Hönisch *et al.* 2003; Zeebe *et al.* 2003). In opposition to symbiont-bearing foraminifera (e.g. *G. ruber* and *G. sacculifer*), which symbionts' photosynthetic activity increases the microenvironment pH (Foster, 2008; Henehan *et al.*, 2016), for symbiont-barren foraminifera such as *G.bulloides* the pH is decreased due to calcification and respiration processes (Martínez-Botí *et al.*, 2015b; Raitzsch *et al.*, 2018). Size effects have been therefore reported for *G. ruber* and *G. sacculifer* in conjunction with the density of symbionts around the shells, whereas the lack of symbionts leads to an absence of this physiological influence here (Babila, 2014; Henehan *et al.*, 2016; Osborne *et al.*, 2020).

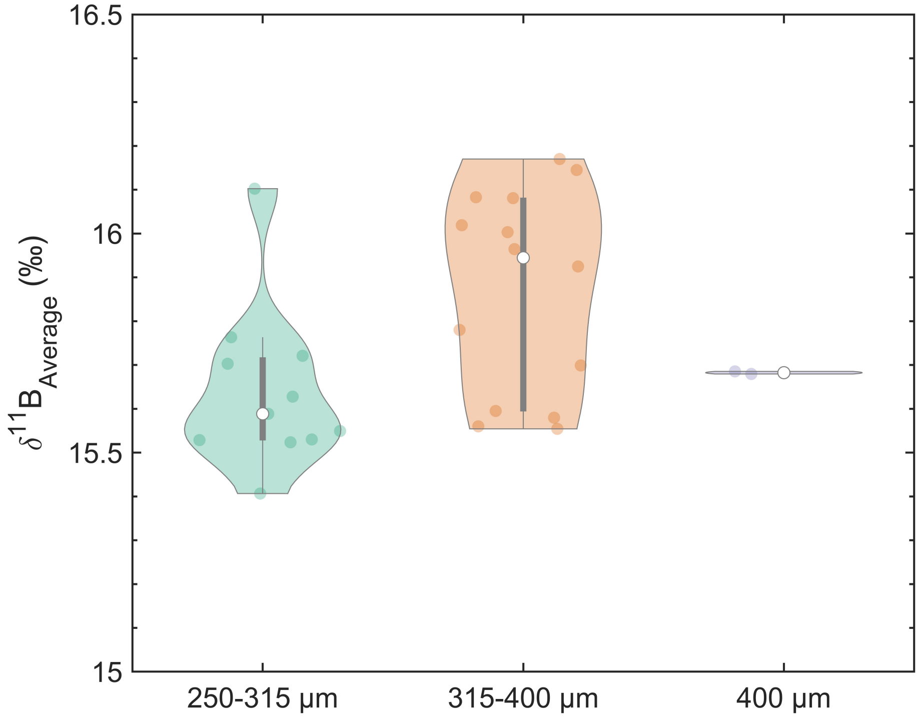

Figure 6.8 : *Violin plots illustrating the distribution of the δ^{11}B for the planctonic foraminifera G. bulloides in three size fractions: 250-315 µm, 315-400 µm and > 400 250-315 µm.*

6.4 Conclusion

After the implementation of a protocol coupling the µ-dDIHEN setup and the microsublimation purification for biocarbonates with low B concentrations, we tested it in this study to measure our first foraminifera samples. We successfully measured for [B] > 2 ppb, the δ^{11}B of planktonic foraminifera *G. bulloides* with only half of the material usually used for such studies (i.e. 180-200 shells against 400). For sample solutions with [B] below a threshold of 2 ppb, where the δ^{11}B measurements were impacted by higher relative blank contribution, boron was extracted again by microsublimation and the condensates were diluted to a smaller volume of 0.25 mL, thus increasing the [B] of the solutions. These samples δ^{11}B were measured in a transient signal mode through a 10 µL sample loop, allowing for more accurate δ^{11}B values with only 1 ng of boron and 80 µL consumed for a whole standard sample bracketing method in triplicate. Such transient signal δ^{11}B analyses have been realized down to 400 pg of boron for reproducibilities reaching between 0.3 and 0.5 ‰. This is the lowest amount of boron ever analysed for such precisions on carbonate samples with MC-ICP-MS. The δ^{11}B values of the foraminifera samples we analysed perfectly matched with the δ^{11}B$_{\textit{G. bulloides}}$-δ^{11}B$_{borate}$ calibration.

By measuring three size fractions of the symbiont-barren *G. bulloides* along the upper 0-30 cm of a sediment core from the Chilean margin, we highlighted no statistical variations between the three studied size fractions for the δ^{11}B. The lack of variation with size for the δ^{11}B, directly linked to the pH, may be explained by the absence of symbionts for this species.

The δ^{11}B determination in transient mode with only 1 ng of B and consuming only 80 µL of sample for precise and accurate measurements open the path towards a protocol with limited amount of sample required and then increasing the number of possible geochemical analyses. The recuperation of the microsublimation residues could for example be explored for trace and minor elements, or isotope ratio measurements and it could be coupled with the boron isotopic analysis to bring more constraints to the paleclimatological and paleoceanographic reconstructions.

CHAPTER 7

IMPACT DE LA SUPER-ÉRUPTION TOBA SUR L'OCÉAN

Sommaire

7.1 Introduction . . . 163
  7.1.a Cadre général . . . 163
  7.1.b La super-éruption du volcan Toba . . . 164
  7.1.c Impact de la super-éruption du volcan Toba : hypothèses . . . 165
7.2 Matériel et méthodes . . . 168
  7.2.a Matériel . . . 168
  7.2.b Mesure du δ^{11}B . . . 169
  7.2.c Mesure du Mg/Ca et efficacité du lavage des foraminifères . . . 170
  7.2.d Données sédimentaires et géochimiques pré-existantes . . . 171
7.3 Résultats . . . 173
  7.3.a Données préliminaires sur la super-éruption YTT : âge, niveaux de téphra et dissolution de $CaCO_3$ . . . 173
  7.3.b δ^{11}B de *P. obliquiloculata* lors de la phase YTT . . . 174
  7.3.c Évolution de la température de la thermocline lors de la phase YTT . . . 175
7.4 Discussion préliminaire . . . 176
7.5 Conclusion . . . 179
7.6 Données . . . 180

Le développement analytique réalisé tout au long de de cette thèse a permis d'aboutir à une première application paléo-océanographique, qui est toujours en cours de réalisation. Celle-ci se penche sur l'influence de la super-éruption du Toba (Sumatra, Indonésie) il y a 74 000 ans sur le pH et la température de surface au niveau de la mer d'Andaman, à proximité du complexe volcanique. Cette éruption s'est également déroulée en concomitance avec la dernière transition interglaciaire-glaciaire et son influence sur celle-ci demeure vivement débattue, alors qu'elle est considérée comme la plus grande éruption volcanique du Quaternaire. Pour lever le voile sur les potentielles conséquences de la super-éruption Toba sur l'océan, nous avons ainsi étudié dans un premier temps l'espèce de foraminifère planctonique *Pulleniatina obliquiloculata* vivant au niveau de la thermocline, afin de mesurer le rapport isotopique du bore (traceur du pH océanique), mais aussi le rapport Mg/Ca (traceur de la température océanique). Les premiers résultats permettent en outre d'illustrer la mise en place désormais routinière à l'IPGP du protocole de lavage sur des foraminifères ainsi que le succès des premières mesures en Mg/Ca, alors que les concentrations en bore obtenues pour ces échantillons après séparation, entre 5 et 10 ppb (2.5-5 ng), sont dorénavant devenues confortable pour déterminer le δ^{11}B. Cette première étape s'inscrit dans un projet plus large visant à évaluer la dynamique de l'océan lors de la super-éruption du Toba, et plus particulièrement le gradient de pH et de température entre la thermocline et la surface. Il est donc ainsi prévu de coupler les données acquises de δ^{11}B et de Mg/Ca issues de *P. obliquiloculata* avec celles à venir du foraminifère planctonique vivant plus en surface *Globigerinoides ruber*, à partir des mêmes échantillons sédimentaires. Cette espèce, par conséquence, pourra également permettre de déduire la pCO_2 atmosphérique lors de cette période charnière. Parallèlement, le travail effectué sur *P. obliquiloculata* nous a amené à vouloir prochainement affiner la calibration δ^{11}B$_{carbonate}$-δ^{11}B$_{borate}$ pour cette espèce à partir de sommets de carottes provenant de divers océans et couvrant une large gamme de pH. En effet, la calibration existante n'est portée que par six points de mesure, dont 5 dans une gamme de pH très étroite. Elle permettra éventuellement de déconvoluer les possibles effets du pH sur le paléo-thermomètre géochimique Mg/Ca, comme cela avait été démontré pour d'autres espèces de foraminifères planctoniques, et de spécifier s'il existe un effet de taille sur le δ^{11}B pour *P. obliquiloculata*. La convergence de ce développement analytique avec la thématique de la super-éruption Toba est le fruit d'une collaboration avec Annachiara Bartolini (MNHN), Franck Bassinot (LSCE), Benoît Caron (ISTeP), Giulia Del Manzo (IPGP), Anne Le Friant (IPGP), Eva Moreno (LOCEAN) et Guillaume Paris (CRPG). Elle a abouti au co-encadrement du stage de Master 2 d'Ana Alves commencé en Février 2020, dont sont issus les résultats et discussion de ce chapitre, prenant plus la forme d'une ouverture. Aujourd'hui en thèse sur cette même thématique, Ana continuera de travailler avec moi afin de terminer ce projet, stoppé dans son élan par les confinements successifs.

IMPACT DE LA SUPER-ÉRUPTION DU VOLCAN TOBA (74 000 ANS) SUR LA TEMPÉRATURE ET LE PH DE L'OCÉAN À PROXIMITÉ DE L'ÎLE DE SUMATRA

7.1 Introduction

7.1.a Cadre général

Comme évoqué en introduction (Chap.1), les émissions de CO_2 volcanique jouent un rôle important dans la régulation à long terme du thermostat terrestre, balancées par l'altération des continents, et plus particulièrement des roches silicatées (Walker *et al.*, 1981). Des phases intenses d'activité magmatique ont cependant perturbé cet équilibre au cours des temps géologiques. Il a été ainsi documenté que sur les 350 derniers millions d'années, les principales crises biologiques d'extinction de masse et d'anoxie dans l'océan étaient corrélées à la mise en place de grandes provinces basaltiques dites LIP (*Large Ignous Province*). Ces dernières ont provoqué des changements environnementaux drastiques liés à des injections volumineuses de gaz à effet de serre, avec dans un premier temps un fort impact du SO_2 causant refroidissements, régressions marines, extinctions de masse et crises de la production carbonatée, suppléé dans un second temps par un fort impact du CO_2, entraînant des réchauffements plus extrêmes, des transgressions marines, des périodes d'anoxie et d'autres phases d'extinction de masse (Courtillot & Renne, 2003 ; Burgess & Bowring, 2015 ; Guex *et al.*, 2016 ; Black *et al.*, 2018 ; Müller *et al.*, 2020 ; Jurikova *et al.*, 2020). Les conséquences climatiques des éruptions volcaniques (celles surtout des "supervolcans", Self & Blake 2008) se déroulant à plus court terme (plusieurs années à plusieurs décennies) sont provoquées par l'émission de cendres et de gaz, mais plus particulièrement d'aérosols soufrés (acide sulfurique, H_2SO_4) dans la stratosphère. Ceux-ci peuvent bloquer la lumière transmise par le soleil et donc créer un refroidissement, alors que dans la basse atmosphère ces particules sont rapidement évacuées (Fig.7.1, Robock *et al.* 2009). Les dynamiques récentes océan-atmosphère s'en trouvent déréglées, comme peuvent l'être les phénomènes climatiques El Niño (Khodri *et al.*, 2017) ou les moussons (Liu *et al.*, 2016) tandis que l'injection de soufre dans l'océan provoque une acidification de celui-ci (Doney *et al.*, 2007).

Les conséquences sur les sociétés humaines peuvent être désastreuses, comme l'ont été documentées dans les registres historiques les années "sans été" en Europe de l'Ouest suite aux éruptions des volcans Samalas (Indonésie, 1257, Lavigne *et al.* 2013) et Tambora (Indonésie, 1815, Luterbacher & Pfister 2015) qui ont entraîné des pluies incessantes, de grandes inondations et de très mauvaises récoltes. Plus proche de nous, l'éruption du Pinatubo aux Phillipines en Juin 1991 aurait abaissé la température moyenne sur Terre de 0,5 °C l'année qui a suivi (Parker *et al.*, 1996). Comprendre les mécanismes sous-jacents à ces perturbations naturelles de la dynamique océan-atmosphère qui ont eu lieu dans notre histoire récente nous offre une opportunité unique d'appréhender les changements climatiques et environnementaux dont l'humanité est responsable par l'injection massive de gaz à effets de serre mais aussi de soufre dans l'atmosphère par la combustion des énergies fossiles (Doney *et al.*, 2007). Les isotopes du bore et le rapport Mg/Ca, mesurés dans les foraminifères planctoniques, vont s'avérer être des outils précieux afin de quantifier les potentiels changements de pH et de température dans l'océan suite à ce type de manifestation climatique. Notre cas d'étude s'est donc porté sur les éventuelles perturbations qu'auraient engendrées la super-éruption du Volcan Toba (Sumatra).

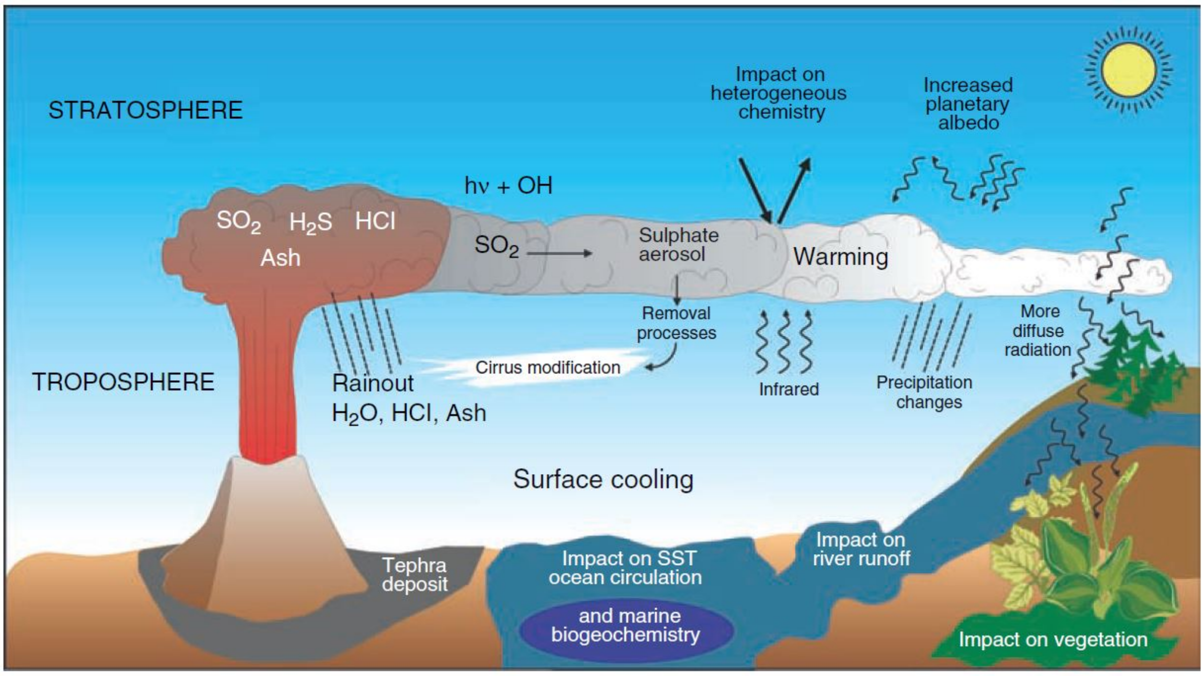

Figure 7.1 : *Effets sur le climat des grandes éruptions volcaniques dite stratosphériques. D'après Timmreck (2012).*

7.1.b La super-éruption du volcan Toba

Le super-volcan Toba se situe sur l'île de Sumatra en Indonésie et plus particulèrement dans la ceinture de feu du Pacifique, une des zones les plus actives tectoniquement sur Terre concentrant neuf dixièmes des volcans mondiaux en contexte de subduction (Fig.7.2.a, Chesner 2012). Ce complexe de caldeiras, le plus grand daté du Quaternaire, est la résultante de quatre éruptions volcaniques ayant démarré il y a 1,2 millions d'années (Chesner, 2012).

Sa phase paroxysmale, la plus récente, correspond à l'éruption YTT (*Younger Toba Tuff*, Fig.7.2.b, Ninkovich *et al.* 1978). Elle est à l'origine du plus grand lac volcanique du monde, le lac Toba (100 x 30 km^2), et aurait émis plus de 8600 km^3 de matériel volcanique couvrant ainsi jusqu'à 40 millions de km^2 avec 5 mm de cendres (Costa *et al.*, 2014), faisant d'elle la plus grande éruption volcanique du Quaternaire avec un indice d'explosivité de 8 (sur une échelle de 8, l'éruption du volcan Tambora, en 1815, se situant par exemple à 7, Ninkovich *et al.* 1978 ; Oppenheimer 2002 ; Chesner 2012). Situées autour de 73 500 ans (Rampino & Self, 1992), les datations ^{40}Ar/^{39}Ar à partir des téphra volcaniques (ou pyroclastes, fragments de roche magmatique expulsés lors de l'éruption) ont plus précisément établi un âge entre 73,88 ± 0,32 ka (1σ, Storey *et al.* 2012) et 75,0 ± 0,9 ka (1σ, Mark *et al.* 2014). Ces téphra ont été dispersés dans une vaste zone géographique des deux cotés de l'équateur, de l'Asie du Sud-Est à la côte est et au sud de l'Afrique, en passant par l'Inde (Fig.7.3, Ninkovich *et al.* 1978 ; Lane *et al.* 2013 ; Smith *et al.* 2018) et se retrouvent dans les carottes marines de l'Océan Indien (Pattan *et al.*, 1999), en mer d'Arabie (Schulz *et al.*, 2002) ou encore en mer de Chine Méridionale (Huang *et al.*, 2001).

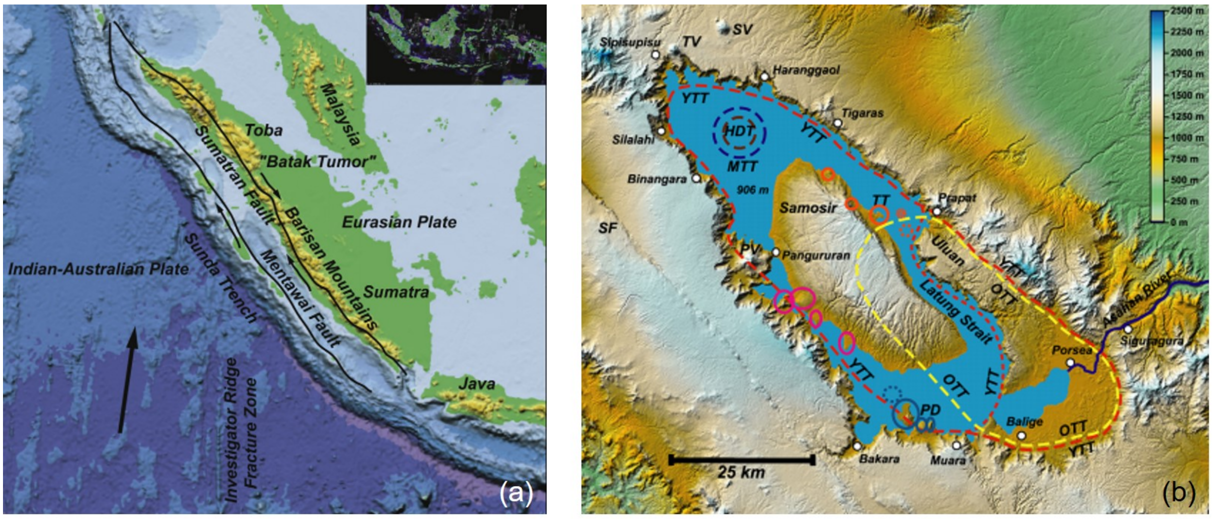

Figure 7.2 : *(a) Localisation et contexte géodynamique de l'île de Sumatra, Indonésie. (b) Localisation du complexe de caldeiras Toba sur l'île de Sumatra. Les lignes pointillées correspondent à l'emplacement des différentes caldeiras, résultantes de plusieurs phases éruptives. HDT (marron, 1,2 Ma): Haranggoal Dacite Tuff, OTT (jaune, 0,840 Ma): Oldest Toba Tuff, MTT (bleu foncé, 0,501 Ma): Middle Toba Tuff and YTT (rouge, 0,074 Ma) : Younger Toba Tuff. Les traits pleins sont pour les dômes de laves Samsoir (orange) et ceux de Parepur (bleu clair), et des cryptodômes (orange). PV = volcan Pusikbukit, PD = dômes de lave Pardepur, TT = dômes de lave TukeTuk, TV = volcan Tandukbenua, SV = volcan Singgalang, SF = Faille de Sumatra. D'après Chesner (2012)*

7.1.c Impact de la super-éruption du volcan Toba : hypothèses

L'impact climatique de l'éruption YTT, et notamment sa nature stratosphérique fait aujourd'hui l'objet de débats, d'autant plus que l'éruption s'inscrit entre la période interglaciaire (stade isotopique MIS 5) et la période glaciaire (stade isotopique MIS 4), dont la transition est l'évènement le plus important de la fin du Quaternaire, marquée par la plus rapide accumulation de glace et la plus grande amplitude de température pour le dernier cycle glaciaire dans l'Hémisphère Nord (Ninkovich *et al.*, 1978 ; Rampino & Self, 1992 ; Khodri *et al.*, 2001 ; Schulz *et al.*, 2002). Pour certains auteurs, l'éruption du Toba aurait ainsi pu permettre d'accélérer cette transition vers un régime glaciaire déjà en cours (Rampino & Self, 1992), avec un refroidissement entre 3 à 15°C, tandis que d'autres réfutent cette hypothèse (Oppenheimer, 2002 ; Jones *et al.*, 2005 ; Lane *et al.*, 2013) ou proposent un refroidissement limité (Robock *et al.*, 2009). Les conséquences sur la population humaine auraient ainsi été une perte de la diversité génétique, avec la décimation de nombreuse populations d'Hommes modernes en dehors des zones tropicales (Ambrose, 1998).

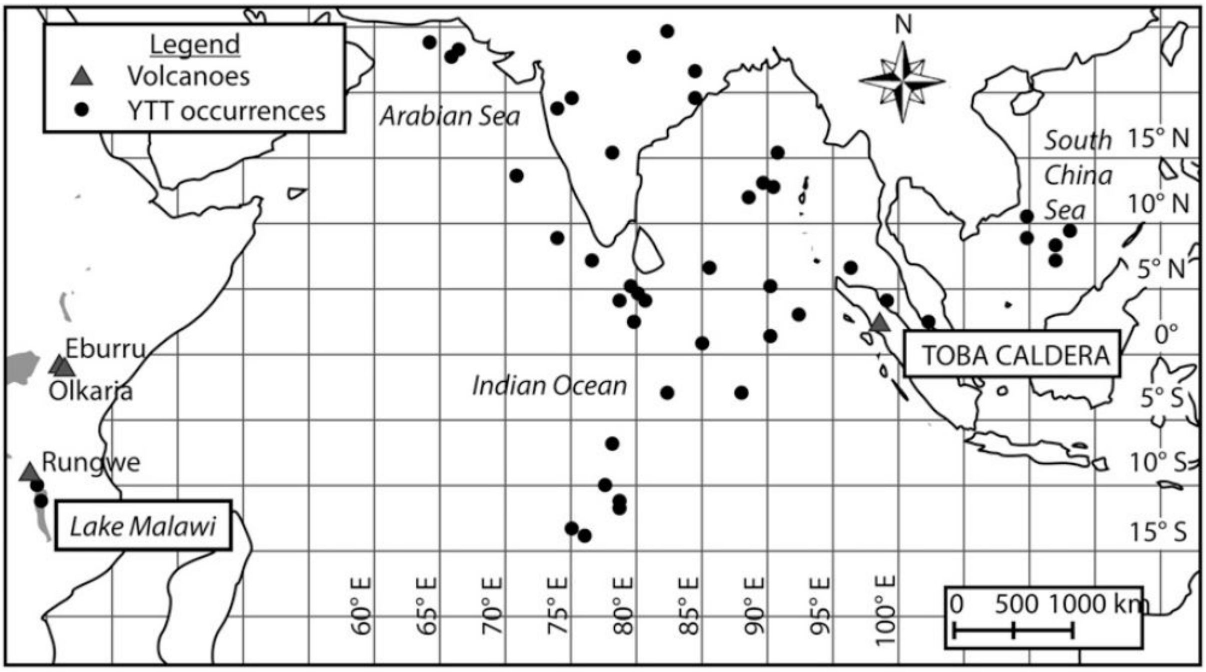

Figure 7.3 : *Occurence de l'éruption YTT dans la région de l'océan Indien, l'Asie du Sud et dans la mer de Chine méridionale. D'après Lane et al. (2013).*

Les quantités de soufre émis dans l'atmosphère sont également faiblement contraintes, variant de plusieurs ordres de grandeurs (0,35-33 Tg —Oppenheimer 2002—, 1700-3500 Tg —Costa *et al.* 2014—). Les carottes de glace permettent à la fois de contraindre la durée des éruptions et de retracer les éruptions stratosphériques, grâce la présence de sulfates volcaniques avec une signature isotopique en soufre indépendante de la masse (Δ^{33}S) et issus de l'oxydation photochimique du dioxyde de soufre (SO_2) en acide sulfurique (H_2SO_4) en quelques mois après l'éruption (Baroni *et al.*, 2007). En Arctique et en Antarctique, des pics de sulfates datés entre 74,6 et 70 ka ont ainsi pu être identifiés, malgré l'absence de matériel volcanique (Svensson *et al.*, 2013). Le Δ^{33}S de certains de ces pics de sulfate contemporains à l'éruption YTT a mis en évidence des évènements éruptifs de type stratosphérique (Crick *et al.*, 2021). Cependant, une absence de consensus demeure sur le nombre d'évènements volcaniques et leur temporalité lors de l'éruption YTT (Caron *et al.*, submitted). Une éruption multi-phasée du YTT aurait en fait plus d'impact qu'une seule et grande super-éruption (Swingedouw *et al.*, 2015).

L'éruption YTT a d'abord été considérée comme un seul évènement éruptif extrême, qui aurait duré entre 9 et 14 jours (Ninkovich *et al.*, 1978). Cette durée a servi de base aux nombreuses simulations qui ont suivi (e.g., Jones *et al.*, 2005). Une étude géochronologique a cependant montré une phase de résurgence qui a suivie la super-éruption YTT entre 70 et 65 ka (Mucek *et al.*, 2017). De même, ce ne sont pas moins de neuf pics de soufre, d'amplitude équivalente, contemporains à l'éruption YTT qui sont répertoriés dans les carottes de glace sur une fenêtre de 2000 ans. Mais à nouveau l'absence de verres volcaniques ne permet pas de corroborer cette relation (Zielinski, 2000 ; Svensson *et al.*, 2013). Il a aussi été mis en évidence dans des spéléothèmes de Bornéo plusieurs évènements volcaniques sur une courte période autour de 74 ka, qui auraient pu modifier la circulation océanique au niveau régional et affaiblir la mousson d'été Indienne sur une durée de 1000 ans (Cobb *et al.*, 2017). Enfin, l'étude de la carotte sédimentaire BAR94-25 prélevée au large de Sumatra (Fig.7.4), et qui est celle qui a été utilisée au cours de ce travail, a suggéré que l'éruption du Toba ne soit pas un unique évènement mais une succession d'éruptions très rapprochées, avec 17 niveaux de téphra calibrés temporellement par la stratigraphie isotopique (δ^{18}O) sur une période de 50 ka (entre 100 et 50 ka avant l'actuel), avec une phase paroxysmale de 10 ka (75-65 ka, correspondant à la phase YTT), et dont l'analyse des éléments majeurs et la morphologie des verres volcaniques ne laissent aucun doute quant à la provenance des dépôts (del Manzo, 2018 ; Caron *et al.*, submitted).

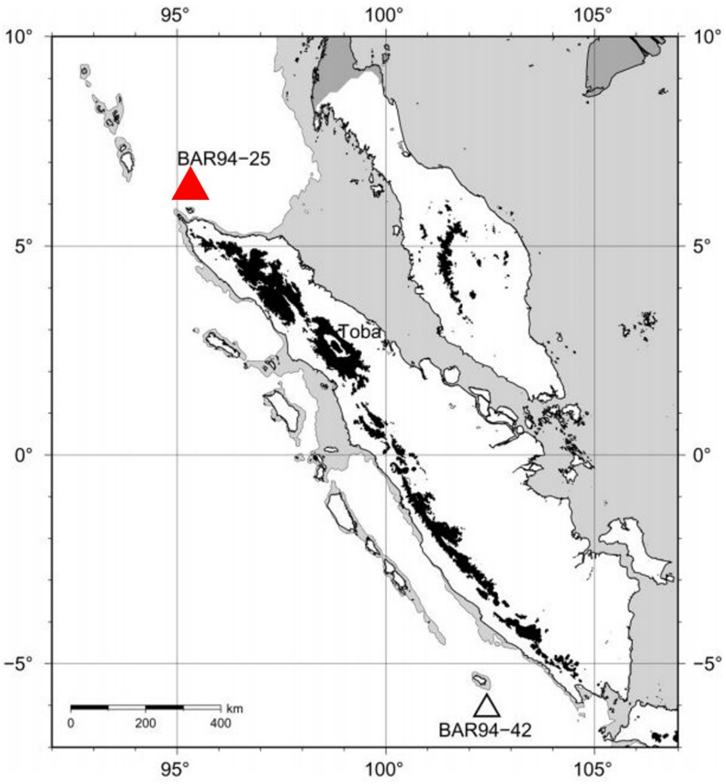

Figure 7.4 : *Localisation de la carotte sédimentaire BAR94-25 et du volcan Toba sur l'île de Sumatra. D'après van der Kaars et al. (2012).*

Cependant, aucune étude ne s'est penchée sur les conséquences de la super-éruption du Toba sur l'océan. Si la phase paroxysmale YTT était de nature stratosphérique, il serait attendu que la surface de l'océan se refroidisse à cause de la forte émission d'aérosols sulfatés dans la stratosphère, augmentant l'albédo terrestre et diminuant ainsi le rayonnement solaire arrivant sur Terre (Fig.7.1). Mais du fait de la succession d'éruptions, sur 10 ka, un effet cumulatif pourrait avoir eu lieu et ainsi provoquer un refroidissement durable sur l'échelle de plusieurs milliers d'années, là où dans le cas des éruptions plus courtes, le refroidissement s'estompe au bout de quelques années (Timmreck, 2012). Ces émissions soufrées peuvent aussi avoir une autre conséquence : l'acidification des océans. Le dioxyde de soufre (SO_2) émis se transforme en acide sulfurique H_2SO_4 dans l'eau, se dissociant très rapidement (Doney *et al.*, 2007). Cette acidification par les arérosols soufrés, en plus de celle liée au dégazage volcanique de CO_2, peut en conséquence réduire la saturation du carbonate de calcium à la surface de l'océan, la concentration de $[CO_3^{2-}]$ diminuant au profit de $[HCO_3^-]$. La superposition de ces deux phénomènes pourrait ainsi avoir fortement affecté la biocalcification des foraminifères planctoniques (Davis *et al.*, 2017) et la préservation de la production carbonatée pélagique, dissoute plus facilement à faible profondeur (Schiebel, 2002).

Cette étude a ainsi pour objectif d'évaluer le potentiel effet de l'éruption multi-phases YTT sur la température et le pH de l'océan au niveau de la thermocline, par l'étude couplée du rapport Mg/Ca et de $\delta^{11}B_{carb}$ sur l'espèce de foraminifère planctonique *Pulleniatina obliquiloculata* (Fig.7.5, Parker & Jones 1865). Ces mesures ont également été corrélées avec la teneur en $CaCO_3$ mesurée dans le sédiment (Caron *et al.*, submitted).

7.2 Matériel et méthodes

7.2.a Matériel

La carotte sédimentaire marine BAR94-25 utilisée pour cette étude, d'une longueur de 5,95 m, a été prélevée dans la mer d'Andaman, à 600 km au nord de la caldeira de Toba, à une profondeur de 1558 m (95°.5'E, 6°26.09'N, Fig.7.4). Quarante huit échantillons ont été sélectionnés entre 258 et 353 cm, comprenant les phases éruptives YTT et post-YTT, préparés de la même façon décrite dans la section 6.2.a puis au final tamisés pour ne garder que la fraction > 315 µm. De cette fraction, une centaine de tests de l'espèce *P. obliquiloculata* a été collectée afin de réaliser un échantillon analysable (Fig.7.5). Il s'agit d'une espèce qui vit dans les régions tropicales à subtropicales, et qui est résistante à la dissolution (Schiebel & Hemleben, 2017), ce qui fait d'elle l'espèce idéale pour notre étude. Son cycle de vie se situe au niveau supérieur de la thermocline, entre 50 et 100 m de profondeur, et son abondance est de ce fait aussi un traceur de la variation de la thermocline (Dang *et al.*, 2018).

Figure 7.5 : *Tests de P. obliquiloculata observé à la loupe binoculaire. D'après Alves (2020).*

7.2.b Mesure du δ^{11}B

Les échantillons de foraminifères ont été nettoyés de leurs contaminants en suivant le protocole de la section 6.2.c, sans étape réductrice afin de ne pas affecter le rapport Mg/Ca (Barker *et al.*, 2003 ; Yu *et al.*, 2007a ; Pang *et al.*, 2020). Le volume d'acide nitrique 0,5 N utilisé pour les dissoudre a oscillé entre 100 et 175 µL selon la masse de matériel après le lavage. 50 µL ont été ensuite prélevés afin d'extraire le bore par microsublimation (matériel décrit section 5.2.a et 6.2.b et protocole décrit en section 5.2.c et 6.2.d), puis de mesurer le δ^{11}B sur le MC-ICP-MS Neptune à l'aide du montage µ-dDIHEN (décrit en détail dans le chapitre 4, 5 et la section 6.2.d). Les analyses du δ^{11}B des échantillons de *P. obliquiloculata* ont été réalisées à des concentrations en bore plutôt confortables comparées à celles du chapitre 6, entre 5 ppb (2.5 ng) et 11 ppb (5.5 ng) et n'ont donc pas nécessité le recours à l'analyse en mode transitoire. Les différentes microsublimations ont montré une contamination moyenne en bore de 30 $\pm$ 16 pg (1SD, n=8), soit $\sim$ 1 % du bore total pour les solutions de 5 ppb. Pour chaque gamme de concentration des échantillons, la solution de référence d'acide borique, le standard ERM-AE121 (Vogl & Rosner, 2011), a été mesurée à la même concentration. Entre 5 et 11 ppb, la valeur moyenne pour ce standard était de 19.59 $\pm$ 0.24 ‰ (2SD, n=25), en accord total avec la valeur de référence (19.9 $\pm$ 0.6 ‰, Vogl & Rosner 2011) et avec la moyenne à long terme de l'IPGP sur 10 ans (19.56 $\pm$ 0.17 ‰, 2SD, n=90, pour [B]=200 ppb, Louvat *et al.* 2019 et Chap. 5). Le carbonate de référence MVS-1 (Jurikova *et al.*, 2019) a quant à lui accompagné chaque session de microsublimation, et après mesure isotopique, a donné une valeur moyenne de 15.84 $\pm$ 0.12 permil (2SD, n=8) pour des concentrations entre 8 et 11 ppb, et une valeur de 15.87 $\pm$ 0.05 ‰ (2SD) à 40 ppb, en accord avec sa valeur de référence (15.95 $\pm$ 0.19 ‰, n=46, Jurikova *et al.* 2019). Ces résultats illustrent la robustesse des mesures réalisées sur ces échantillons de foraminifères.

7.2.c Mesure du Mg/Ca et efficacité du lavage des foraminifères

Les rapports Mg/Ca et les indicateurs de contaminations que sont les rapports Al/Ca (pour les argiles) et Mn/Ca (pour les oxydes de fer et manganèse) ont été mesurés sur l'ICP-MS (*Inductively Coupled Mass Spectrometer*) Agilent 7900 à l'IPGP, en suivant un protocole modifié de Yu *et al.* (2005). Les échantillons sont introduits dans le spectromètre par un µ-nébuliseur à travers une chambre cyclonique de Scott. Les teneurs en magnésium, calcium, aluminium et manganèse ont été analysées avec l'ajout d'hélium dans une cellule de collision afin de réduire les interférences polyatomiques.

Tout d'abord, 5 µL de la solution initiale de foraminifères dissous ont été prélevés puis dilués dans 2 mL d'acide nitrique 0,5 N afin de mesurer approximativement la concentration de calcium de la solution mère. Puis 5 à 20 µL sont prélevés de nouveau selon la concentration initiale afin d'obtenir une solution fille de 4 mL avec 25 ppm de calcium, toujours en HNO_3 0.5 N. Les carbonates de référence MVS-1 (Jurikova *et al.*, 2019) et JCt-1 (Hathorne *et al.*, 2013) sont également préparés à la même concentration. Homogénéiser la concentration de calcium permet ainsi de conserver les mêmes conditions d'ionisation dans le plasma pour ces matrices carbonatées (Yu *et al.*, 2005). Une solution d'acide nitrique 0,5 N est mesurée entre chaque échantillon afin de soustraire le blanc au signal mesuré, et les matériaux de référence sont mesurés tous les trois échantillons. Le carbonate MVS-1 est utilisé afin de corriger les échantillons de la dérive instrumentale, tandis que JCt-1 apporte la reproductibilité long-terme de la mesure. Les concentrations en Mg, Al, Ca et Mn sont déterminées par une courbe de calibration réalisée par la mesure de deux solutions élémentaires, une pour les éléments traces et mineurs et une pour les éléments majeurs, à plusieurs concentrations. Les rapports élémentaires sont ensuite exprimés en mmol ou en µmol/L. La valeur mesurée de JCt-1 sur toute la session d'analyse pour le Mg/Ca est de 1,32 $\pm$ 0.01 mmol/mol (2SD, n=21), en accord avec la valeur de référence (1,289 $\pm$ 0.045 mmol, Hathorne *et al.* 2013) ou celle par exemple mesurée par Raitzsch *et al.* (2018), 1,32 $\pm$ 0,05 mmol (2SD, n=7). Cette reproductibilité de $\pm$ 0.01 mmol/mol (2SD), soit $\pm$ 1.02 % (2RSD, n=21) est considérée comme représentative pour la mesures des échantillons.

A part pour sept échantillons, toutes les valeurs de Al/Ca sont en-dessous du seuil fixé pour un lavage efficace (< 100 µmol/mol, Rae *et al.* 2011, Fig. 7.6.a). Aucune tendance ne se dégage entre le rapport Al/Ca et le δ^{11}B (e.g. Rae *et al.*, 2011 ; Gutjahr *et al.*, 2017), permettant d'exclure l'influence d'un quelconque contaminant argileux sur la composition isotopique en bore (Fig. 7.6.a). Cependant, les données de Mn/Ca, entre 300 et 750 µmol/mol (Fig.7.6.b), sont largement au-dessus des seuils communément admis, 30 µmol/mol (Martin & Lea, 2002) ou 80 µmol/mol (Raitzsch *et al.*, 2018). Le contexte volcanique de notre étude permet de nuancer ces valeurs seuils car une grande quantité de métaux a été émise dans l'océan. Des bandes intra-tests enrichies en Mn ont été ainsi observées dans les tests contemporains de l'éruption YTT de l'espèce planctonique *Globorotalia menardii* (Lemelle *et al.*, 2020). La présence d'oxydes entraînerait de plus une signature isotopique plus enrichie en ^{10}B (Lemarchand *et al.*, 2007). De la même manière que les argiles avec le rapport Al/Ca, aucune relation n'est constatée entre le rapport Mn/Ca et le δ^{11}B, éliminant l'hypothèse de la présence de ces minéraux contaminants (Fig.7.6.b). Ces données montrent en tout cas la robustesse des mesures de Mg/Ca, et la qualité des lavages par l'absence de contamination en argiles ou oxydes pour la mesure de δ^{11}B.

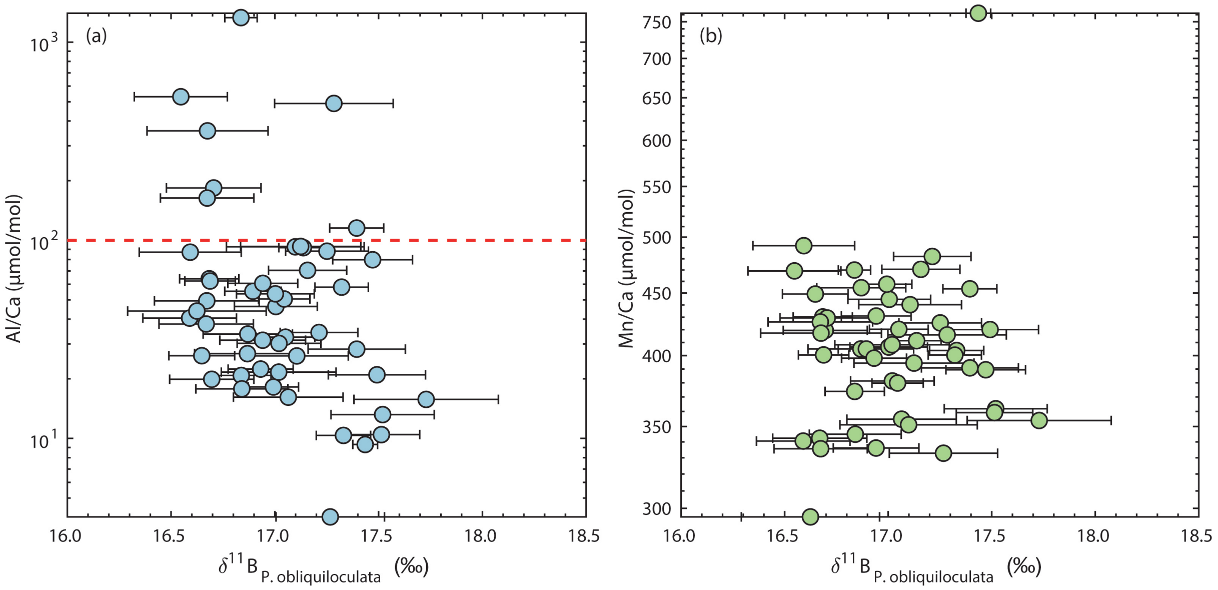

Figure 7.6 : *Relation entre le δ^{11}B mesuré dans les échantillons de P. obliquiloculata et les indices de contamination que sont les rapports Al/Ca et Mn/Ca. La ligne rouge en pointillés correspond au seuil admis par Rae et al. (2011)*

7.2.d Données sédimentaires et géochimiques pré-existantes

Cette partie va présenter les analyses géochimiques et sédimentaires de la carotte BAR94-25, obtenus précédemment à notre étude sur *P. obliquiloculata*, et dont les résultats, présentés dans la partie suivante, serviront à caler les données de δ^{11}B et de Mg/Ca stratigraphiquement et à les interpréter dans le cadre des différentes phases éruptives du YTT. Ces données proviennent des études réalisées par van der Kaars *et al.* (2012), del Manzo (2018) et Caron *et al.* (submitted).

Les isotopes stables de l'oxygène

La mesure des isotopes stables de l'oxygène (δ^{18}O) a permis de reconstruire un modèle d'âge pour la carotte BAR94-25 (Fig.7.7). La mesure a été menée à partir de 6 à 10 tests du foraminifère planctonique *Globigerinoides ruber* (d'Orbigny, 1839), de la fraction 250-315 µm. Le prélèvement s'est effectué tous les 10 cm (van der Kaars *et al.*, 2012), et a été affiné sur la zone 298-400 cm avec un prélèvement tous les 2 cm, afin de capturer plus en détail la transition MIS 5 et MIS 4 (Caron *et al.*, submitted). Les foraminifères ont été lavés dans un bain à ultrason plongé dans du méthanol, pour éliminer les argiles et autres contaminants possibles puis passés dans un four à 380 ° sous vide pendant 45 min afin d'éliminer la matière organique. Enfin, les échantillons ont été analysés au Laboratoire des Sciences du Climat et de l'Environnement (LSCE), sur un Thermo Finnigan Delta Plus et le δ^{18}O est exprimé par rapport au standard V-PDB, avec une reproductibilité analytique interne de 0,05 ‰ (1 σ) établi sur un matériau de référence du laboratoire (marbre de Carrare).

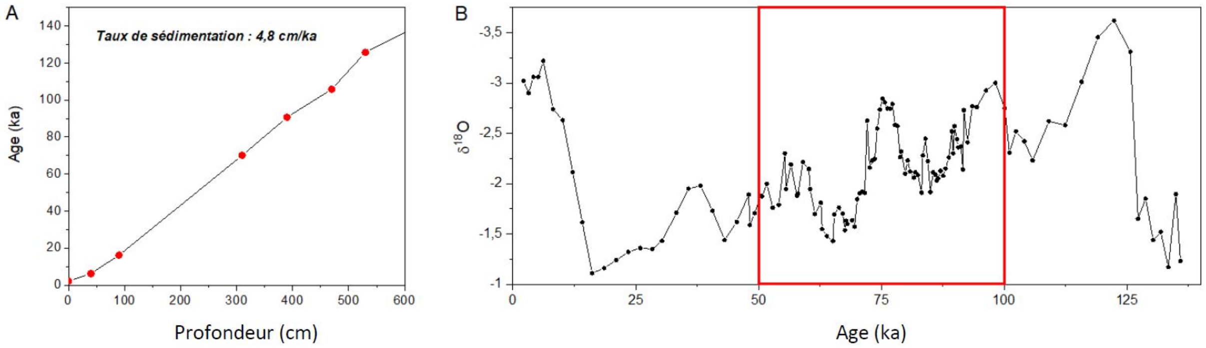

Figure 7.7 : *(A) Modèle d'âge de la carotte sédimentaire BAR94-25. (B) δ^{18}O de la carotte sédimentaire BAR94-25 (van der Kaars et al., 2012). D'après Alves (2020).*

Pourcentage de téphra

L'abondance de téphra, comprenant donc les esquilles de verres et les microponces émis en grande quantité par les éruptions volcaniques, a été obtenu par un comptage des grains à la loupe binoculaire sur la fraction > 63 µm dépourvue de sa phase sédimentaire carbonatée, et rapporté sur un total de 300 grains (del Manzo, 2018 ; Caron *et al.*, submitted). Il a ainsi permis de mettre en évidence les épisodes éruptifs enregistrés dans la carotte et de déterminer leur origine par l'analyse des éléments majeurs, mineurs et traces par microsonde électronique (SX FIVE de la plateforme CAMPARIS) et LA-ICP-MS (Ablation Laser Teledyne Analyte G2 et ICP-MS 8800 de chez Agilent).

Teneur en carbonate de calcium dans le sédiment

La teneur en $CaCO_3$, exprimée en pourcentage, a été mesurée le long de la carotte, sur 100 mg de sédiments séchés, broyés puis placés dans un calcimètre Méliès. Dans un flacon hermétique, le sédiment est mis en contact avec de l'acide chlorhydrique et le volume de CO_2 ainsi émis, proportionnel à la quantité de $CaCO_3$ présente, est mesuré à l'aide d'un manomètre. La teneur en calcium a également été mesurée par fluorescence des rayons X (XRF), par un scanner SRF Avaatech, lors de l'échantillonnage de la carotte. Celle-ci est bombardée avec des rayons X (de faible longueur d'onde et de forte énergie) afin d'exciter les atomes, qui en revenant à leur état initial vont émettre un rayon X en retour (sous forme de photons) dont l'intensité de l'énergie est proportionnelle aux éléments chimiques présents. La combinaison de ces deux techniques a ainsi permis d'obtenir une courbe de la teneur en carbonate de calcium dans le sédiment à haute résolution (données acquises par Eva Moreno, Caron *et al.* submitted).

7.3 Résultats

7.3.a Données préliminaires sur la super-éruption YTT : âge, niveaux de téphra et dissolution de $CaCO_3$

Tout d'abord, le modèle d'âge a été obtenu en comparant la stratigraphie isotopique en δ^{18}O mesuré sur la carotte BAR94-25 avec la courbe chronostratigraphique de référence *Low-Latitude Stack* du δ^{18}O de l'océan Indien (Bassinot *et al.*, 1994 ; van der Kaars *et al.*, 2012). La zone temporelle qui concerne notre étude se situe entre 50 et 100 ka, chevauchant les stades MIS 3, MIS 4 et MIS 5 et comprenant donc la phase pré-YTT, YTT et post-YTT (Fig.7.7).

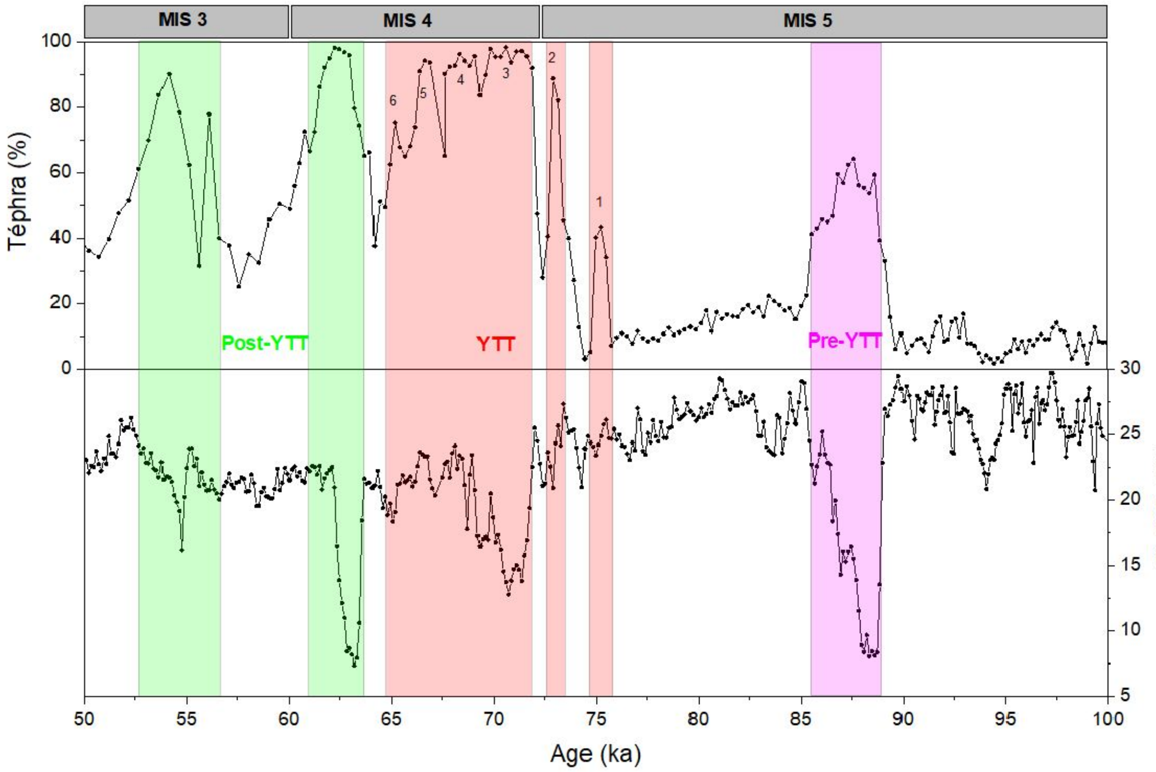

Figure 7.8 : *Évolution de l'abondance de téphra et de la teneur en carbonate de calcium entre 100 et 50 ka pour la carotte BAR94-25, lors de la phase YTT (del Manzo, 2018 ; Caron et al., submitted). D'après Alves (2020).*

Les niveaux de téphra, dont la composition élémentaire a confirmé qu'ils étaient bien originaire de la super-éruption Toba, permettent de distinguer trois phases distinctes, mettant ainsi en évidence le caractère multi-phasé de la super-éruption YTT : la phase YTT entre 75 et 65 ka (entre la période MIS 5 et MIS 4), marquée par six évènements éruptifs et étant considérée comme la phase paroxysmale, encadrée par la phase pré-YTT entre 100 et 76 ka (avec sept éruptions distinctes) et la phase post-YTT avec quatre éruptions entre 65 et 50 ka (Fig.7.8, del Manzo 2018 ; Caron *et al.* submitted).

De plus, les phases de plus forte diminution de $CaCO_3$ dans le sédiment se corrèlent parfaitement avec ces phases éruptives (Caron *et al.*, submitted). La phase pré-YTT est ainsi marquée par une chute de plus de 20 % de la teneur en carbonates. La phase YTT quant à elle présente une chute moins drastique, de l'ordre de 12 % (surtout au niveau de l'évènement 3 de la phase YTT) tandis que pour les deux éruptions (62 et 55 ka) de la phase post-YTT, la chute est respectivement d'environ 15 % et d'un peu moins de 10 % (Fig.7.7).

7.3.b δ^{11}B de *P. obliquiloculata* lors de la phase YTT

Les valeurs de δ^{11}B mesurées à partir des foraminifères *P. obliquiloculata* couvrant la super-éruption YTT entre 81 et 57 ka montrent de nombreuses oscillations, entre 16,55 ± 0,22 et 17,73 ± 0,35 ‰ (Fig.7.9). Ces valeurs sont parfaitement dans la gamme de ce qui est connu pour cette espèce dans la littérature, sur des sommets de carottes, bien qu'il n'existe que six points de mesures : les cinq premiers sont entre 16,14 ± 0,18 ‰ et 16,52 ± 0,18 ‰ et ne couvrent qu'une faible gamme de pH (Guillermic *et al.*, 2020), tandis que le dernier unique point a été mesuré à 17,44 ± 0,17 ‰ (Henehan *et al.*, 2016).

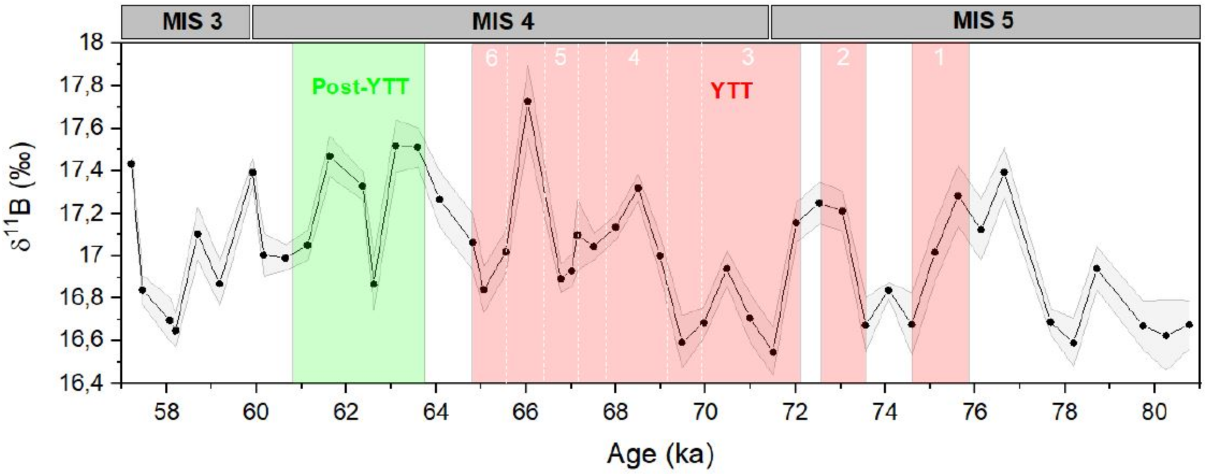

Figure 7.9 : *Evolution du δ^{11}B mesuré (avec l'erreur ± 2SD en zone grisée) sur des échantillons de foraminifères planctoniques P. obliquiloculata entre 100 et 50 ka lors de la super-éruption YTT. Les chiffres 1 à 6 correspondent aux six évènements identifiés de la phase YTT en figure 7.8 (del Manzo, 2018 ; Caron et al., submitted). D'après Alves (2020).*

Pour le stade MIS 5, les valeurs de δ^{11}B au niveau de la thermocline sont entre 16,59 et 17,28 ‰. Le début de la super-éruption YTT à 76 ka se caractérise par une diminution entre 17,16 et 16,67 ‰. Ensuite, le δ^{11}B remonte à 17,25 ‰ (évènement 2) puis l'entrée dans la phase glaciaire (MIS 5-MIS 4) est corrélée à une baisse du δ^{11}B, la plus importante de l'enregistrement, à 16,55 ‰, associée à l'évènement 3. La transition entre l'évènement 5 et 6 mettent également en évidence une baisse, à 16,89 ‰ alors que suit juste derrière le point le plus élevé de la série, à 17,73 ‰. Enfin, la phase post-YTT, est marquée par une chute du δ^{11}B à 16,87 ‰ autour de 62 ka et une autre à 16,65 ‰ à 58 ka.

7.3.c Évolution de la température de la thermocline lors de la phase YTT

Le rapport Mg/Ca mesuré dans les foraminifères planctoniques est communément utilisé pour reconstruire la température de l'eau de mer dans laquelle ils ont vécu, un paramètre essentiel à toute reconstruction paléo-océanographique. L'incorporation de Mg^{2+} dans le réseau cristallin à la place de Ca^{2+} est ainsi plus importante quand la température est plus élevée (e.g. Elderfield & Ganssen, 2000 ; Anand *et al.*, 2003 ; Russell *et al.*, 2004). Cependant la salinité (e.g. Russell *et al.*, 2004 ; Kısakürek *et al.*, 2008 ; Mathien-Blard & Bassinot, 2009) ainsi que la chimie des carbonates de l'eau de mer (e.g. Russell *et al.*, 2004 ; Allen *et al.*, 2016 ; Evans *et al.*, 2016) exercent une influence secondaire sur cette relation Mg/Ca-température. Une correction doit être ainsi réalisée afin de soustraire ces paramètres avec un Mg/Ca qui a tendance à augmenter avec la salinité ou quand le pH est plus faible (Gray *et al.*, 2018).

Comme pour les isotopes du bore, la valeur du Mg/Ca pour une même température varie selon les espèces de foraminifères, du fait d'une incorporation différente du magnésium selon la physiologie de l'espèce (effet vital, Urey *et al.* 1951 ; Erez 2003). Chaque espèce demande une calibration Mg/Ca-température (T) spécifique, reconstituée à partir de culture de foraminifères prélevés dans la colonne d'eau ou à partir d'échantillons de foraminifères provenant des sommets de carottes (e.g. Lea *et al.*, 1999 ; Gray *et al.*, 2018). Concernant *P. obliquiloculata*, nous avons utilisé la dernière calibration réalisée par Dang *et al.* (2018) à partir de nombreux échantillons de sommets de carotte dans la zone Indo-Pacifique :

$$Mg/Ca = (0.245 \pm 0.041)e^{(0.088 \pm 0.009)T} \tag{7.1}$$

La salinité ne semble pas avoir d'influence sur cette relation tandis que celle du pH n'a pas encore été déterminée (Dang *et al.*, 2018). Les températures ainsi calculées à partir de nos échantillons de *P. obliquiloculata* sont cohérentes avec ce qui est connu aujourd'hui de la mer d'Andaman (Dang *et al.*, 2018).

Dans notre cas d'étude, en moyenne la température de la thermocline ainsi reconstituée fluctue entre 25,6 et 27,7 °C (Fig.7.10). La phase MIS 5 est ainsi d'abord marquée par des hautes températures, 27,5-27,7 °C autour de 78-80 ka, puis diminue tout au long de cette période interglaciaire jusqu'à 26 °C à 72 ka. A l'entrée de la phase glaciaire, les températures au niveau de la thermocline remontent juste après progressivement, jusqu'à 27,2 °C à la fin de la phase YTT (85 ka), puis 27,5 °C lors de la phase post- YTT (82 ka), en exhibant un refroidissement brusque lors de l'évènement 4 de la phase YTT, redescendant à 26 °C à 68 ka. Elle diminue de nouveau brusquement lors de la transition MIS4-MIS3, pour atteindre 25,5°C.

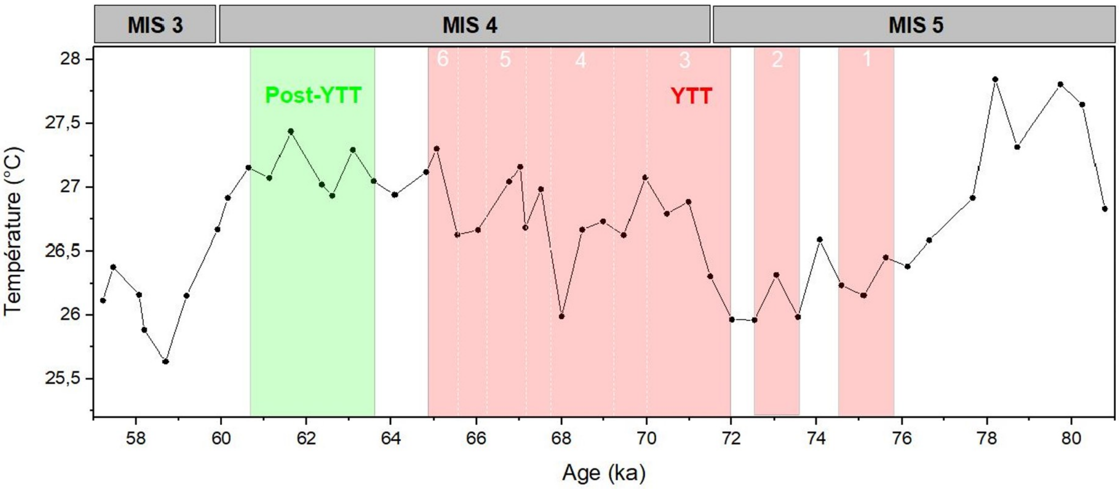

Figure 7.10 : *Évolution de la température de la thermocline calculée à partir du rapport Mg/Ca mesuré sur des échantillons de foraminifères planctoniques P. obliquiloculata entre 100 et 50 ka lors de la super-éruption YTT (del Manzo, 2018 ; Caron et al., submitted). D'après (Alves, 2020).*

7.4 Discussion préliminaire

Les données acquises en température à travers le Mg/Ca et les variations de pH à travers le δ^{11}B sur l'espèce *P. obliquiloculata* ont permis de donner de premières indications sur la chimie de l'océan au niveau de la thermocline à proximité du volcan Toba lors de sa phase paroxysmale YTT, en les mettant en relation avec la teneur en $CaCO_3$ et en téphra dans le sédiment marin (Fig.7.11). La concentration en dioxyde de carbone atmosphérique obtenue à partir de carottes de glace en Antarctique (Bereiter *et al.*, 2012) est mise en relation à titre indicatif avec les données géochimiques obtenues, bien que nous soyons conscients que ces dernières sont représentatives de la thermocline et non de la subsurface, et que le modèle d'âge entre les carottes de glace et la carotte BAR94-25 est différent, ne permettant pas de faire des corrélations précises. Cela nous permet néanmoins de discuter de l'évolution générale. L'évolution relative du pH sera ainsi discutée en fonction du δ^{11}B mesuré dans les tests de *P.obliquiloculata*, où une baisse de ce rapport est associée à une diminution du pH (Chap.2).

Les données de δ^{11}B et de Mg/Ca, entre 81 et 57 ka, couvrent ainsi les six évènements qui constituent la phase YTT (entre 75 et 65 ka) ainsi que la phase géochimiquement distincte post-YTT (entre 64 et 58 ka), et couvrent donc également la transition entre le glaciaire MIS 5 et l'interglaciaire MIS 4 (del Manzo, 2018 ; Caron *et al.*, submitted), appuyant l'hypothèse d'une histoire éruptive multiphasée et non unique, et sur des périodes de temps plus longues que les quelques jours initialement proposés dans la littérature (Ninkovich *et al.*, 1978).

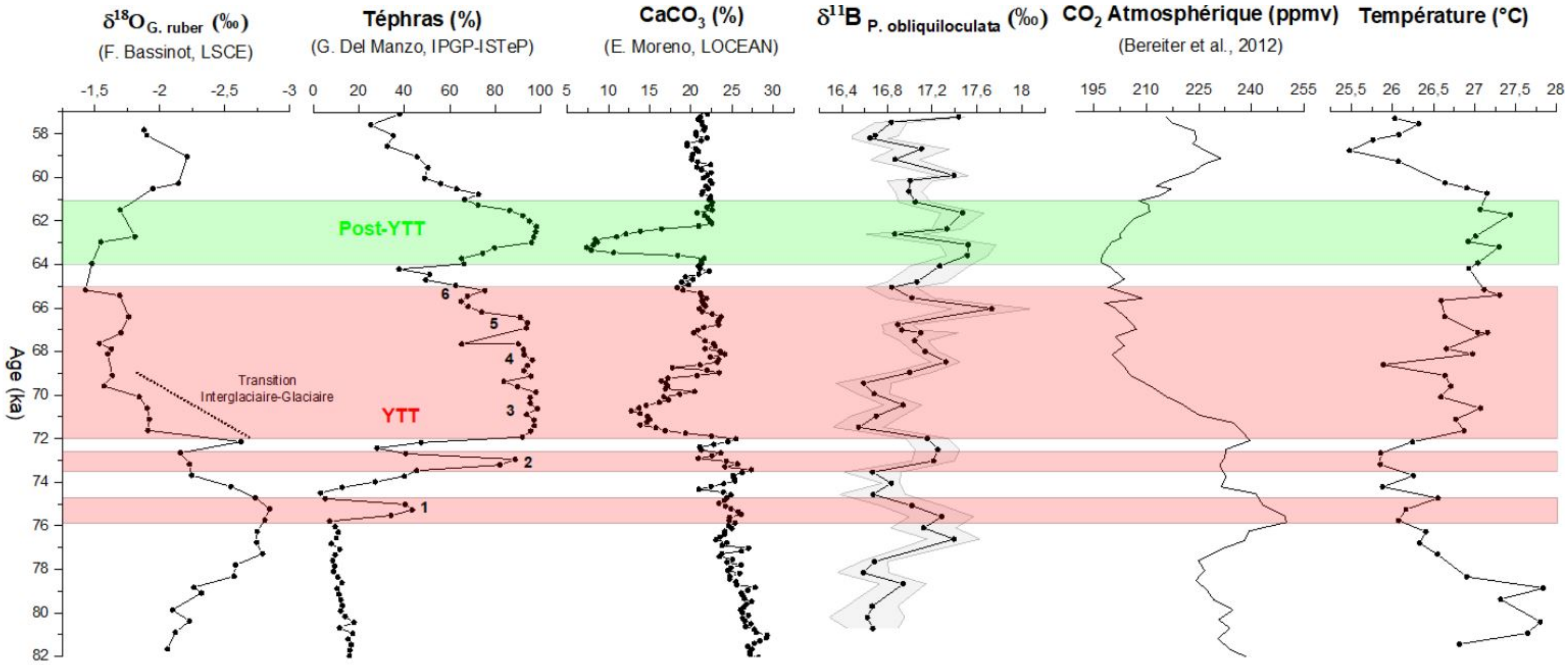

Figure 7.11 : *Evolution de plusieurs marqueurs climatiques et géochimiques dans la carotte BAR94-25 entre 82 et 57 ka: δ^{18}O, pourcentage de téphra, pourcentage de carbonate de calcium dans le sédiment (del Manzo, 2018 ; Caron et al., submitted), δ^{11}B mesuré à partir de P.obliquiloculata et température déterminée à partir des rapports Mg/Ca dans P.obliquiloculata. Ces données sont mises en regard des pCO$_2$ mesurées dans des carottes de glace Antarctique (Bereiter et al., 2012).D'après Alves (2020).*

Ces données nouvellement acquises mettent surtout en évidence une période d'acidification importante (de l'ordre de 0,6 ‰ en δ^{11}B, correspondant environ à 0,1 unité pH) lors du troisième et quatrième évènement de la phase YTT entre 72 et 70 ka, contemporain à la transition interglaciaire-glaciaire. Elle est ainsi associée à de fortes teneurs en téphra (~ 100 %) ainsi qu'à une phase de forte diminution de la teneur en carbonates dans le sédiment marin, perdant plus de 15 % de $CaCO_3$. La phase post-YTT est également marquée par un pic de diminution de $CaCO_3$ dans le sédiment, accompagnée également par une diminution brusque du pH, de l'ordre de 0.8 ‰ en δ^{11}B (à 61 ka), alors que la fin de la phase YTT était caractérisée par une remontée progressive du pH de la thermocline. Cependant, cette faible valeur de δ^{11}B est également observée dans la période interglaciaire qui précède l'entrée dans la phase YTT. La concomitance de tous ces évènements : diminution de la teneur en carbonate de calcium, niveau de cendres et δ^{11}B est donc peut-être à nuancer, mais la synchronicité entre téphra, diminution du pourcentage de $CaCO_3$ et acidification de la thermocline laisse à penser que la phase YTT a joué un rôle sur la chimie de l'océan. Une phase d'acidification aurait ainsi bouleversé la calcification des producteurs carbonatés (de Moel *et al.*, 2009 ; Davis *et al.*, 2017) ou une diminution de l'état de saturation des carbonates (Feely, 2004). Une autre explication, mais qui dédouanerait le volcan Toba, serait que la forte émission de cendres n'ait entraîné qu'une "dilution" des sédiments carbonatés dans le sédiment marin, et la baisse de pH observée n'aurait alors eu aucun impact sur la calcification.

Les températures de la thermocline, quant à elles, affichent de façon intéressante une tendance anti-corrélée sur tout l'intervalle avec le CO_2 atmosphérique et le δ^{18}O mesuré sur *G. ruber*, ces deux derniers épousant donc les variations glaciaires et interglaciaires. Ainsi les valeurs Mg/Ca montrent un réchauffement de la thermocline en période glaciaire (72-61 ka) alors que les phases interglaciaires sont marquées par un refroidissement (82-72 ka et 61-57 ka). Ceci illustre probablement plus le caractère local de la température enregistrée, ne s'inscrivant donc pas dans la tendance climatique générale, d'autant qu'il ne s'agit pas de la surface, mais de la thermocline, et illustre ainsi plus des processus qui ont lieu dans la colonne d'eau. Cette température peut ainsi plutôt refléter une dynamique d'upwellings, et n'est ainsi pas directement liée à la tendance générale climatique de la période.

Durant la phase YTT et post-YTT, tandis qu'une acidification des eaux est associée à la diminution du pourcentage de $CaCO_3$ et à de forts niveaux de téphra, il était attendu que la température de l'eau soit plus basse du fait de l'entrée en période glaciaire. En effet si l'éruption était stratosphérique, les aerosols sulfatés auraient bloqué les rayons du soleil et ainsi fait baisser la température de surface (Timmreck, 2012). Ce qui ne nous permet donc pas de statuer sur la nature stratosphérique de l'éruption YTT, tant, encore une fois la thermocline est probablement découplée de la surface. Cependant il a été démontré, que si la tendance climatique globale est au refroidissement, les zones tropicales peuvent à l'inverse être sujettes à un réchauffement par la baisse de l'intensité des vents (Sicre *et al.*, 2017) et ainsi expliquer cette anti-corrélation entre la température dérivée du rapport Mg/Ca et le couple δ^{18}O-CO$_2$ atmosphérique.

7.5 Conclusion

En couplant les analyses du δ^{11}B et du rapport Mg/Ca du foraminifère planctonique *P. obliquiloculata* avec les données géochimiques et sédimentaires (pourcentage de téphra et de carbonates) et un modèle d'âge de la carotte BAR94-25, cette étude a ainsi apporté des indications sur l'impact de la super-éruption du volcan Toba sur la chimie de l'océan, et particulièrement celui de la phase paroxysmale multi-phasée YTT entre 75 et 65 ka. Les analyses préliminaires sur l'abondance de téphra dans les sédiments ayant éliminé l'hypothèse d'un évènement unique à courte durée, il était alors attendu que des effets plus long terme sur le climat se fassent ressentir sur l'océan, avec notamment six évènements éruptifs sur 10 000 ans entre 75 et 65 ka lors de l'éruption YTT. Le pic éruptif daté de 72 ka environ (évènement 3) marque ainsi une période de forte diminution de la teneur en carbonates dans les sédiments marins associée à une phase d'acidification des eaux océaniques au niveau de la thermocline, ce qui est observé aussi lors de la phase volcanique post-YTT vers 62 ka. Alors qu'un hiver volcanique, suite à une éruption stratosphérique, aurait probablement causé un refroidissement des eaux de surfaces, nous observons au contraire un réchauffement de la thermocline lors de la phase YTT et post-YTT, ce qui serait plutôt cohérent étant donné qu'un refroidissement global entraînerait plutôt une phase de réchauffement localisé en zone tropicale suite à la diminution de l'intensité des vents et des upwellings. Il est à noter que cette étude préliminaire s'est portée sur la thermocline, qui est probablement découplée des processus qui ont lieu en surface et illustre plus des processus océanographiques dans la colonne d'eau. Il reste cependant à apporter plus de données pour la calibration δ^{11}B$_{borate}$-δ^{11}B$_{foraminifère}$ de *P. obliquiloculata* afin de pouvoir reconstruire avec précision le pH de la thermocline et potentiellement extraire l'influence du pH sur le rapport Mg/Ca, qui a été documentée chez de nombreux foraminifères planctoniques (Gray *et al.*, 2018). Ainsi, à l'avenir, coupler ces analyses avec le rapport Mg/Ca et le δ^{11}B du foraminifère *G. ruber*, nous permettrait à la fois de déduire la dynamique de la colonne d'eau (avec deux profondeurs différentes), mais également de déterminer le pH des eaux de surfaces (la calibration δ^{11}B$_{borate}$-δ^{11}B$_{foraminifère}$ est bien établie pour *G. ruber* dans la littérature Henehan *et al.* 2013 ; Raitzsch *et al.* 2018) et en conséquence la concentration en dioxyde de carbone de l'atmosphère. L'abondance de *G. bulloides* (Chap.6) dans le sédiment pourrait également être utilisée comme indicateur de l'intensité des upwellings dans cette région, tandis que la préservation des foraminifères, ainsi que leur forme pourraient également être regardées pour observer les potentiels effets de la diminution de l'état de saturation en carbonate de l'eau de mer et des perturbations environnementales sur la biologie des organismes et la calcification.

7.6 Données

Table 7.1 : *Données géochimiques de l'espèce P. obliquiloculata sur la fraction > 315 μm provenant de la carotte BAR94-25. L'erreur sur le Mg/Ca est de 1,02 %, celle du* δ^{18}*O 0,05 ‰*

Section	Cote	Profondeur	Âge	δ^{18}O	δ^{11}B	2SD	Mg/Ca	Al/Ca	Mn/Ca
	(cm)	(cm)	(ka)	(V-PDB, ‰)	(‰)	(‰)	(mmol/mol)	(μmol/mol	(μmol/mol)
II	108-109	258	57,33		17,44	0,06	2,50	9	762
II	109-110	259	57,58	-1,88	16,84	0,14	2,56	21	374
II	110-111	260	58,07	-1,9	16,70	0,20	2,51	20	419
II	112-113	262	58,31		16,65	0,16	2,43	26	449
II	114-115	264	58,80	-2,21	17,11	0,25	2,37	26	440
II	116-117	266	59,30		16,87	0,22	2,50	34	455
II	119-120	269	60,28	-2,14	17,39	0,13	2,61	115	454
II	120-121	270	60,52	-1,95	17,00	0,20	2,67	46	445
II	122-123	272	60,77		16,99	0,12	2,73	18	458
II	124-125	274	61,50	-1,7	17,05	0,14	2,72	32	420
II	126-127	276	61,75		17,47	0,19	2,81	80	389
II	129-130	279	62,73	-1,81	17,33	0,13	2,71	10	404
II	130-131	280	62,97	-1,55	16,87	0,26	2,69	27	405
II	132-133	282	63,22		17,52	0,25	2,78	13	362
II	134-135	284	63,95	-1,48	17,51	0,18	2,72	10	359
II	136-137	286	64,20		17,27	0,26	2,68	4	333
II	139-140	289	65,18	-1,43	17,06	0,26	2,73	16	355
II	140-141	290	65,42	-1,69	16,84	0,22	2,77	18	345
II	142-143	292	65,67		17,02	0,20	2,60	30	381
II	144-145	294	66,40	-1,76	17,73	0,35	2,61	16	354
II	147-148	297	67,14	-1,81	16,89	0,14	2,71	55	405
II	148-149	298	67,14		16,93	0,16	2,75	22	398
III	0-1	300	67,87	-1,63	17,10	0,33	2,63	93	351
III	1-2	301	68,12	-1,6	17,05	0,12	2,70	51	380
III	3-4	303	68,61		17,14	0,12	2,47	92	411
III	5-6	305	69,10	-1,64	17,32	0,13	2,64	58	400
III	7-8	307	69,59	-1,57	17,00	0,19	2,65	54	406
III	9-10	309	70,08	-1,77	16,59	0,25	2,61	87	492
III	11-12	311	70,60	-1,9	16,68	0,14	2,72	64	430
III	13-14	313	71,11	-1,92	16,94	0,17	2,65	61	431
III	15-16	315	71,63	-1,91	16,71	0,23	2,66	184	429
III	17-18	317	72,14	-2,63	16,55	0,22	2,52	530	469
III	19-20	319	72,66	-2,3	17,16	0,19	2,44	71	471
III	21-22	321	73,17	-2,23	17,25	0,20	2,44	88	425
III	23-24	323	73,69	-2,24	17,21	0,19	2,53	34	482
III	25-26	325	74,20	-2,55	16,67	0,25	2,45	49	426
III	27-28	327	74,72	-2,74	16,84	0,08	2,61	1330	470
III	29-30	329	75,23	-2,81	16,68	0,29	2,52	357	417
III	31-32	331	75,74	-2,81	17,02	0,28	2,50	22	408
III	33-34	333	76,26	-2,75	17,28	0,29	2,57	491	416
III	35-36	335	76,77	-2,74	17,12	0,29	2,55	93	394
III	37-38	337	77,29	-2,79	17,39	0,23	2,60	28	391
III	41-42	340	78,32		16,69	0,12	2,67	62	401
III	43-44	343	78,83		16,59	0,23	2,90	40	341
III	45-46	345	79,35		16,94	0,21	2,77	31	336
III	47-48				17,49	0,23	2,43	21	420
III	49-50	349	80,38		16,67	0,23	2,90	38	342
III	51-52	351	80,89		16,62	0,33	2,86	44	295
III	53-54	353	81,41		16,67	0,23	2,66	163	336

CHAPTER 8

CONCLUSION GÉNÉRALE ET PERSPECTIVES

Sommaire

8.1 Conclusion 181
8.2 Perspectives 184

8.1 Conclusion

Dans un contexte de plus en plus pressant demandant de comprendre les bouleversements anthropiques que le climat terrestre subit actuellement, la paléoclimatologie s'est de plus en plus imposée comme une discipline clé. Celle-ci repose notamment sur la mesure dans les archives géologiques de traceurs géochimiques dont la connaissance et la grande précision analytique avancent de paire. Mon travail de thèse, portant sur les isotopes du bore mesurés dans les foraminifères planctoniques, traceurs du paléo-pH océanique et de la pCO_2 atmosphérique, s'est donc pleinement inscrit dans ces thématiques, repoussant les limites de l'utilisation de ce traceur. Il avait quatre objectifs : reconstruire le δ^{11}B$_{sw}$ de l'océan au cours des temps géologiques, mesurer le δ^{11}B$_{carb}$ dans des petits échantillons de carbonates à faible concentration en bore, mesurer et valider les premiers δ^{11}B$_{carb}$ obtenus sur des foraminifères planctoniques et appliquer cette méthode d'analyse optimisée à une carotte sédimentaire prélevée au large de Sumatra, afin de contraindre l'impact de la super-éruption Toba il y a 74 000 ans. Ces objectifs ont ainsi été parfaitement remplis, tandis que l'application, prometteuse, appelle à continuer les analyses.

Tout d'abord, l'utilisation du δ^{11}B$_{carb}$, mesuré dans les carbonates biogéniques, pour reconstruire les pH de l'océan, requiert une connaissance précise du δ^{11}B$_{sw}$ de l'eau de mer au moment où ce-dit carbonate s'est formé. Alors que cette composition isotopique dans l'océan est aujourd'hui homogène, dû au long temps de résidence du bore dans l'océan par rapport au temps de mélange des océans, le δ^{11}B$_{sw}$ a varié au cours des temps géologiques. Il est donc nécessaire de le reconstruire, avec d'autant plus de précision, car une variation de 1 ‰ de ce paramètre entraîne une variation de 0.1 unité pH, équivalent par exemple à l'ordre de grandeur correspondant à l'acidification des océans d'origine anthropique. J'ai ainsi dans un premier temps étudié la possibilité que les halites primaires, sels marins emprisonnant en leur sein des inclusions fluides témoins de l'eau de mer dans laquelle ils se sont formés, puissent enregistrer directement ce δ^{11}B$_{sw}$. Sur sept échantillons mesurés, couvrant le Phanérozoïque, j'ai montré que seulement trois ont potentiellement enregistré le δ^{11}B$_{sw}$, au Plio-Pleistocène (3-5 Ma), au Dévonien (380 Ma) et au Néoprotrozoïque (560 Ma), car leurs valeurs sont en accord avec les estimations faites dans la littérature à partir de carbonates marins. Cependant, la variabilité au sein d'un même échantillon, supérieur à 1 ‰, empêche d'utiliser ce matériel géologique à des fins de reconstructions paléocéanographiques. Les autres halites étudiées, quant à elles, avaient des δ^{11}B beaucoup plus bas que ceux estimés dans la bibliographie. D'une part, le comportement du bore et de ses isotopes n'est encore aujourd'hui que très peu défini dans les systèmes évaporitiques, et des phases minérales mineures co-précipitées avec la halite pourraient avoir affecté l'enregistrement marin de δ^{11}B. D'autre part, ces quatre halites illustrent probablement en plus la forte difficulté de ces minéraux à conserver un signal primaire de la chimie des océans du fait de leur facilité à se dissoudre, à se déformer et à conduire la chaleur dans les dépôts sédimentaire. Afin de pallier aux incertitudes qu'engendraient l'utilisation des halites pour remonter au signal marin, j'ai modélisé l'évolution du δ^{11}B$_{sw}$ au cours du Phanérozoïque en faisant varier au cours du temps les sources et les puits de bore à l'océan selon le forçage géodynamique qui les régit. J'ai pour cela utilisé les forçages les plus récents et qui sont utilisés dans les grands modèles climatiques et de reconstruction de la pCO$_2$ atmosphèrique au cours de l'histoire terrestre. En utilisant deux scénarios, l'un à *runoff* constant puis l'autre à *runoff* fluctuant au cours du temps, permettant de proposer deux hypothèses sur la grande inconnue qu'est le flux dissous de bore des rivières à l'océan au cours du temps, j'ai construit le premier modèle continu du δ^{11}B$_{sw}$ sur tout le Phanérozoïque, modèle en grande partie en accord avec les données recueillies sur des carbonates marins pour les 200 derniers millions d'années. J'ai ainsi mis en évidence par des tests de sensibilité du modèle que sur le Phanérozoïque, les deux principaux contrôles sur le cycle du bore étaient l'altération de la croûte océanique par l'adsorption sur les sédiments et les apports continentaux par les rivières, marqueurs de l'altération des roches continentales. J'ai aussi mis en lumière l'importance fondamentale du choix des paramètres géodynamiques introduits dans le modèle tant ils font varier le δ^{11}B$_{sw}$, typiquement de plusieurs pour mille pour un âge donné. En effet, la grande variabilité dans les reconstructions proposées de la croûte océanique au cours des temps géologiques, qui est le puits majeur du bore dans l'océan, expliquent ces grandes variations. L'échec de notre modèle à reproduire les données de la littérature sur la première partie du Phanérozoïque peut ainsi s'expliquer par les incertitudes de ces reconstructions géodynamiques en remontant plus loin dans le temps. Comme pour les halites, la modélisation ne répond pas à la précision demandée sur le δ^{11}B$_{sw}$ pour les applications de paléo-pH. Je montre cependant que reconstruire le δ^{11}B$_{sw}$, par son cycle géochimique, peut apporter de précieuses informations sur les processus qui ont fait varier la chimie des océans au cours des temps géologiques.

Cette réflexion sur l'évolution de la composition isotopique du bore dans les océans a été réalisée en parallèle de ce qui était le second objectif de cette thèse : mesurer les isotopes du bore dans des petits échantillons carbonatées à faible concentration en bore afin de l'appliquer sur des foraminifères planctoniques. Le défi était double : la taille de l'échantillon et la concentration en bore, sachant qu'un échantillon de foraminifère planctonique ne contient qu'entre 2 et 20 ppm de bore pour une masse de carbonate de calcium de seulement 5 mg. Ce défi était d'autant plus important que le bore n'est pas un élément facile à analyser : volatile en milieu acide tandis qu'il est sujet à de forts effets mémoire lors de la mesure du δ^{11}B, entraînant des blancs analytiques élevés et des contaminations croisées. Nous avons donc mis en place un protocole couplant la technique de microsublimation, rapide, à faible volume et très peu contaminante pour extraire le bore de sa matrice carbonatée et le dispositif µ-dDIHEN sur MC-ICP-MS, un système d'injection directe automatisé et miniaturisé, adapté pour de faibles volumes et débits. Ce résultat, fruit de nombreux tests et d'expérimentations au cours de cette thèse, a permis d'obtenir des précisions inégalées pour des analyses en triplicat de 1-2,5 ng de bore dans seulement 300 µL.

Le troisième objectif - réaliser les premières mesures de foraminifères planctoniques - est venu tout naturellement après. Cependant, avant les phases d'extraction du bore par microsublimation et d'analyse isotopique, ces échantillons doivent subir un nettoyage méticuleux afin de retirer la matière organique, les argiles ou encore les oxydes de manganèse ou fer pouvant perturber la signature isotopique du bore des carbonates. Celle-ci est délicate car elle peut tout simplement résulter en la perte pure et simple de l'échantillon. Après de nombreux essais de lavages, j'ai réalisé avec succès les premières mesures de δ^{11}B$_{carb}$ sur des foraminifères. Ces échantillons, correspondant à trois fractions de tailles différentes de l'espèce *G. bulloides*, ont été mesurés à de très faibles concentrations et notamment par la technique alternative des signaux transitoires. Celle-ci a permis de mettre en oeuvre une modalité de mesure jamais réalisée jusque là pour les isotopes du bore et d'obtenir d'excellentes précisions de mesure sur seulement 80 µL d'échantillon contenant 400 pg de bore. L'analyse de ces foraminifères avec trois fractions de taille différentes a également permis de regarder la variation ontogénétique du δ^{11}B$_{carb}$ de cette espèce, mettant en évidence comme d'autres études antérieures, que l'absence de symbiontes chez *G.bulloides* induit une grande homogénéité des δ^{11}B$_{carb}$ indépendamment de la taille, alors que la densité des symbiontes peut jouer sur le microenvironnement par la photosynthèse pour les espèces qui en ont.

Enfin, tout ce processus analytique m'a mené à ma première reconstitution paléoclimatique, en étudiant les conséquences climatiques qu'aurait eu la super-éruption du Toba (Sumatra, Indonésie, phase YTT) il y a 74 000 ans avec, en toile de fond, la dernière transition interglaciaire-glaciaire. Pour cela, 48 échantillons de foraminifères planctoniques *P. obliquiloculata*, vivants au niveau de la thermocline, ont été analysés pour leur rapport isotopique du bore mais aussi pour leur rapport élémentaire Mg/Ca, qui est un paléo-thermomètre géochimique en première approche dans les carbonates. La mesure de ce rapport élémentaire a également résulté de la mise en place d'un autre protocole analytique : la mesure précise des concentrations des éléments traces et majeurs dans les foraminifères à l'ICP-QMS. Ces analyses des rapports δ^{11}B et Mg/Ca, bien que préliminaires, ont été couplées aux teneurs en téphras et en carbonate de cette carotte sédimentaire, et semble montrer des phases d'acidification des océans associées à des évènements éruptifs qui auraient entraîné une baisse de la saturation des carbonates dans la colonne d'eau. Les données de température semblent découplées des éruptions volcaniques et sont anti-corrélées aux données climatiques globales que sont le δ^{18}O et la pCO_2 atmosphérique, marqueurs des climats glaciaires et interglaciaires. A l'échelle locale, cette anti-corrélation peut très bien s'expliquer par une diminution de l'intensité des vents et upwellings et qui auraient entraîné ce réchauffement en zone tropicale en période glaciaire.

8.2 Perspectives

Bien naturellement, cette application sur la super-éruption du volcan Toba n'en étant qu'à ses balbutiements, le projet va reprendre dans les mois qui viennent. Après avoir mesuré le foraminifère planctonique *P. Obliquiloculata*, il s'agit de réaliser une calibration δ^{11}B$_{foraminifère}$-δ^{11}B$_{borate}$ pour cette espèce, la calibration actuelle étant très parcellaire, avec seulement cinq analyses dont quatre dans une gamme de pH très étroite (Henehan *et al.*, 2016 ; Guillermic *et al.*, 2020). Cette nouvelle calibration sera établie à partir d'une quinzaine voire une vingtaine d'échantillons provenant de sommets de carottes à travers le globe. Peut-être sera-t-il possible de déconvoluer également l'influence secondaire que peut avoir le pH sur le rapport Mg/Ca, et apporter un affinage sur la validité de la courbe de température ainsi obtenue (Gray & Evans, 2019). Ensuite, il est prévu de mesurer l' espèce *G. bulloides*, dont le milieu de vie est beaucoup plus proche de la surface (*P. Obliquiloculata* vivant plutôt au niveau de la thermocline), et qui pourra nous donner des indications sur la chimie de la surface de l'océan, et sur la concentration en dioxyde de carbone dans l'atmosphère lors de la phase paroxysmale du Toba. En recoupant ces nouvelles données avec celles obtenues pour *P. Obliquiloculata* et avec l'abondance *G. bulloides* nous pourrons également apporter des informations sur la dynamique de la colonne d'eau. Toutes ces calibrations, corrections et données mises ensemble vont ainsi pouvoir être reliées afin d'avoir des estimations précises de la température, du pH et de la pCO_2 atmosphérique avant, pendant et après les différentes phases de l'éruption du Toba, en utilisant notamment des modèles informatiques pour propager les incertitudes. Bien évidemment, l'impact planétaire du volcan Toba ne pourra se définir que par l'étude de plusieurs carottes sédimentaires. La très petite quantité d'échantillon maintenant nécessaire pour les analyses isotopiques du bore et la mesure des éléments majeurs et traces permet d'économiser de l'échantillon et d'autres analyses isotopiques seront aussi couplées aux isotopes du bore. Notamment les isotopes du soufre pourraient permettre de caractériser l'origine des aérosols sulfatés qui seraient arrivés dans l'océan.

Notre étude sur les halites primaires a aussi pointé du doigt le manque criant d'informations sur les processus d'incorporation du bore et de fractionnement de ses isotopes lors de la formation des évaporites. Des expérimentations d'évaporation d'eau de mer ou de solutions synthétiques (reproduisant les compositions chimiques de l'eau de mer aux différentes périodes géologiques en suivant les données Horita *et al.* 2002) permettraient de mieux comprendre s'il y a un fractionnement isotopique ou non entre l'eau de mer et la halite (e.g. Eggenkamp *et al.*, 2016 ; Shalev *et al.*, 2018), mais aussi pour les autres sels formés au cours de la séquence d'évaporation. Ces expérimentations couplées à la mesure des isotopes du bore dans les gypses ou les évaporites de type epsomite, kainite ou carnallite naturels, pourraient ainsi donner de précieuses informations sur le comportement du bore dans ces systèmes climatiques extrêmes, et peut-être nous permettre de remonter pour de bon au $\delta^{11}\text{B}_{sw}$ de l'océan. Elles pourraient également être utilisées afin de résoudre le mystère de la formation de ces dépôts d'évaporites de plusieurs km d'épaisseur, qui ne peuvent pas être expliqués simplement par des processus d'évaporation-remplissage. Il a été ainsi évoqué des processus hydrothermaux (Scribano *et al.*, 2017 ; Hovland *et al.*, 2018) dont les isotopes du bore sont un excellent traceur (Louvat *et al.*, 2011b, 2014a). De plus, le développement analytique réalisé au cours de cette thèse pour de très faibles volumes et concentrations en bore pourrait être utilisé pour mesurer des inclusions fluides que l'on aurait préalablement extraites des halites afin de s'affranchir de sa matrice (e.g. Lazar & Holland, 1988). Alternativement, la mesure des inclusions fluides pourrait être réalisée avec des méthodes in situ comme le Laser-ICP-MS.

Par ailleurs, notre compilation bibliographique du $\delta^{11}\text{B}_{sw}$ au cours des temps géologiques pourraient nous permettre, par des méthodes d'inversion, de reconstruire les variations possibles de la composition isotopique en bore des rivières au cours du Phanérozoïque et ainsi apporter de précieuses informations sur les régimes d'altération et de ce fait sur le climat au cours des temps géologiques.

CHAPITRE 9

APPENDIX : SINGLE-SHELL $\delta^{11}B_{C.\ WUELLERSTORFI}$ ANALYSIS

Biogeosciences, 17, 5365–5375, 2020
https://doi.org/10.5194/bg-17-5365-2020

Biogeosciences Open Access EGU

Technical note: Single-shell δ^{11}B analysis of *Cibicidoides wuellerstorfi* using femtosecond laser ablation MC-ICPMS and secondary ion mass spectrometry

Markus Raitzsch[1,2,3], Claire Rollion-Bard[4], Ingo Horn[1], Grit Steinhoefel[2], Albert Benthien[2], Klaus-Uwe Richter[2], Matthieu Buisson[4], Pascale Louvat[4], and Jelle Bijma[2]

[1]Institut für Mineralogie, Leibniz Universität Hannover, Callinstraße 3, 30167 Hannover, Germany
[2]Alfred-Wegener-Institut, Helmholtz-Zentrum für Polar- und Meeresforschung, Am Handelshafen 12,
27570 Bremerhaven, Germany
[3]MARUM – Zentrum für Marine Umweltwissenschaften, Universität Bremen, Leobener Straße 8, 28359 Bremen, Germany
[4]Institut de physique du globe de Paris, CNRS, Université de Paris, 75005 Paris, France

Correspondence: Markus Raitzsch (mraitzsch@marum.de)

Received: 13 July 2020 – Discussion started: 16 July 2020
Revised: 22 September 2020 – Accepted: 1 October 2020 – Published: 10 November 2020

Abstract. The boron isotopic composition (δ^{11}B) of benthic foraminifera provides a valuable tool to reconstruct past deep-water pH. As the abundance of monospecific species might be limited in sediments, microanalytical techniques can help to overcome this problem, but such studies on benthic foraminiferal δ^{11}B are sparse. In addition, microanalytics provide information on the distribution of δ^{11}B at high spatial resolution to increase the knowledge of biomineralization processes, for example. For this study, we investigated the intra- and inter-shell δ^{11}B variability of the epibenthic species *Cibicidoides wuellerstorfi*, which is widely used in paleoceanography, by secondary ion mass spectrometry (SIMS) and femtosecond laser ablation multicollector inductively coupled plasma mass spectrometry (LA-MC-ICPMS). While the average δ^{11}B values obtained from these different techniques agree remarkably well with bulk solution values to within ±0.1 ‰, a relatively large intra-shell variability was observed. Based on multiple measurements within single shells, the SIMS and LA data suggest median variations of 4.8 ‰ and 1.3 ‰ (2σ), respectively, while the larger spread for SIMS is attributed to the smaller volume of calcite being analyzed in each run. When analytical uncertainties and volume-dependent differences in δ^{11}B variations are taken into account for these methods, the intra-shell variability is estimated to be on the order of ∼ 3 ‰ and ∼ 0.4 ‰ (2σ) on a ∼ 20 and 100 µm scale, respectively. In comparison, the δ^{11}B variability between shells exhibits a total range of ∼ 3 ‰ for both techniques, suggesting that several shells need to be analyzed for accurate mean δ^{11}B values. Based on a simple resampling method, we conclude that ∼ 12 shells of *C. wuellerstorfi* must be analyzed using LA-MC-ICPMS to obtain an accurate average value within ±0.5 ‰ (2σ) to resolve pH variations of ∼ 0.1. Based on our findings, we suggest preferring the conventional bulk solution MC-ICPMS over the in situ methods for paleo-pH studies, for example. However, SIMS and LA provide powerful tools for high-resolution paleoreconstructions, or for investigating ontogenetic trends in δ^{11}B.

1 Introduction

The boron isotopic composition (δ^{11}B) of benthic foraminifera has been used to reconstruct deep-water pH (Hönisch et al., 2008; Rae et al., 2011; Raitzsch et al., 2020; Yu et al., 2010) and to estimate the Cenozoic evolution of seawater δ^{11}B (Raitzsch and Hönisch, 2013). The underlying mechanism behind the boron isotope method lies in the constant equilibrium fractionation of 27.2 ‰ ± 0.6 ‰ between the pH-dependent speciation of trigonal boric acid and the tetrahedral borate in seawater (Klochko et al., 2006), where only the borate ion is incorporated into

Published by Copernicus Publications on behalf of the European Geosciences Union.

the foraminifera test (Branson et al., 2015; Hemming and Hanson, 1992).

However, while the number of studies on planktonic foraminiferal δ^{11}B to estimate surface-ocean pH has rapidly increased within the last decade, deep-sea pH reconstructions based on benthic foraminifera are relatively rare (Hönisch et al., 2008; Rae et al., 2011; Raitzsch et al., 2020; Yu et al., 2010). Possible reasons for this might be the lower abundance of benthic foraminifera, compared to planktonic species, and a limited selection of species that truly record bottom-water rather than pore-water conditions (Rae et al., 2011). Fortunately, there are two suitable candidates, *Cibicidoides wuellerstorfi* and *Cibicidoides mundulus*, that cover a relatively large oceanographic and stratigraphic range, and which have a high boron content of $\sim$ 12–27 ppm (Raitzsch et al., 2011; Yu and Elderfield, 2007). Although their high [B] may partly compensate for the low abundance in the sediments, in many cases the availability of enough specimens for δ^{11}B analysis remains limiting.

Here, microanalytical techniques such as laser ablation multicollector inductively coupled plasma mass spectrometry (LA-MC-ICPMS) and secondary ion mass spectrometry (SIMS) can help to overcome the problem of sample limitation. These techniques have already been successfully used for a variety of biogenic carbonates to gain information on biomineralization processes or seasonal pH variations (e.g., Blamart et al., 2007; Fietzke et al., 2015; Howes et al., 2017; Kaczmarek et al., 2015a; Mayk et al., 2020; Rollion-Bard and Erez, 2010; Sadekov et al., 2019). However, microanalytical analysis of δ^{11}B is usually afflicted with larger uncertainties in terms of repeatability and reproducibility, as well as of natural δ^{11}B heterogeneity within single shells and within a population. In addition, some recent studies using LA-MC-ICPMS suggest correction modes for measured δ^{11}B values because detected interferences on the ^{10}B peak, possibly due to scattered Ca ions from the carbonate sample, can result in large offsets from the expected value (Thil et al., 2016; Sadekov et al., 2019; Standish et al., 2019), whereas in other studies this matrix-induced effect was not observed (Fietzke et al., 2010; Kaczmarek et al., 2015b; Mayk et al., 2020).

Also, the reported analytical reproducibility for δ^{11}B in biogenic carbonate using LA-MC-ICPMS differs considerably among different studies, ranging between ± 0.22 ‰ and 1.60 ‰ ($2\sigma = 2$ standard deviations), determined from repeated measurements of either a carbonate or glass standard (Fietzke et al., 2010; Kaczmarek et al., 2015b; Mayk et al., 2020; Sadekov et al., 2019; Standish et al., 2019; Thil et al., 2016). As there is no standardized protocol nor a commercially available homogenized δ^{11}B carbonate standard for determining the analytical uncertainty of LA-MC-ICPMS, this issue remains the most challenging task to compare the different labs and instruments. The most commonly used carbonate standards with well-constrained boron isotopic compositions are samples from a coral (JCp-1) and a giant clam (JCt-1), provided by the Geological Survey of Japan (e.g., Inoue et al., 2004; Okai et al., 2004). However, for microanalytical analysis the standard is usually powdered in a mortar and finally pressed to a pellet, which is produced individually in each laboratory, thus potentially resulting in different heterogeneities (e.g., through different grain sizes or applied pressures) in each pellet. This issue is also true for SIMS analyses, and the reported reproducibility is strongly linked to the in-house reference material used (e.g., Kaseman et al., 2009; Rollion-Bard and Blamart, 2014).

In this study, we investigate a population of 23 specimens of *C. wuellerstorfi*, which is a widely used benthic foraminifer species in paleoceanographic studies, to extend our knowledge of δ^{11}B variability within and between individuals. The aim of our study is to demonstrate the capabilities and limitations of δ^{11}B analyses in *C. wuellerstorfi* on a microscale. For this purpose, we used the femtosecond LA-MC-ICPMS and SIMS techniques and compared the results with bulk-solution MC-ICPMS. Finally, we examine the size of population required for targeted δ^{11}B uncertainty levels in paleoceanographic studies using LA-MC-ICPMS.

2 Material and methods

2.1 Foraminifer samples

For this study, we used sediment samples from GeoB core 1032-3, taken in the Angola Basin on the Walvis Ridge at a water depth of 2505 m. From a Holocene interval (6–8 cm, 5.6 ka), 23 pristine (glassy) shells of the benthic foraminifer species *C. wuellerstorfi* from the size fraction > 350 µm were picked and prepared for subsequent microanalytical analysis. Five large specimens (> 400 µm) were embedded in epoxy and polished down to a planar surface for SIMS analyses, while the remaining 18 specimens were mounted on carbon tape for LA measurements. From these 18 individuals, two large tests were analyzed for detailed chamber-to-chamber variability, while the remaining 16 tests were used to measure quasi-bulk δ^{11}B by ablating large shell areas, preceded by measurements of the smaller umbilical knob area.

2.2 Secondary ion mass spectrometry

For the ion microprobe analyses, we used the same technique as described in Rollion-Bard et al. (2003) and Blamart et al. (2007). Boron isotopic compositions were measured with the Cameca ims 1270 ion microprobe at CRPG-CNRS, Nancy, France. A primary beam of ^{16}O^{-} ions generated using a radio frequency plasma source (Malherbe et al., 2016) with an intensity of 50 nA was focused to a spot of about 20 µm. A mass resolution of 3000 was used for B isotope analyses, allowing the elimination of all isobaric interferences. Boron isotopes were analyzed in mono-collection mode using the central electron multiplier. The dead time of the electron multiplier was determined before the analytical session and set to

65 ns. A pre-sputtering of 120 s was applied before the analysis itself. The typical intensities of $^{11}B^+$ in foraminifer tests were between 2000 and 4500 counts per second (cps), depending on the boron concentration. The analysis consists of 60 cycles of 10 s for $^{10}B^+$ and 6 s for $^{11}B^+$, respectively. The reference material was a calcium carbonate with a B concentration of 22 ppm and a δ^{11}B of 16.76 ‰ ± 0.11 ‰, relative to the standard reference material (SRM) NIST 951 (WP22, value determined at IPGP using the method of Louvat et al., 2014). The reproducibility, as estimated by multiple measurements of the reference material, was 2.48 ‰ (2σ, $n = 8$) and is very close to the predicted 2σ uncertainty derived from counting statistics.

2.3 Femtosecond laser ablation MC-ICPMS

Boron isotope measurements were performed using a customized UV-femtosecond laser ablation system coupled to a Plasma II MC-ICPMS (Nu Instruments) at the AWI, Bremerhaven. The laser ablation system is based on a Ti:sapphire regenerative amplifier system (Solstice, Spectra-Physics, USA) operating at the fundamental wavelength of 775 nm with a pulse width of 100 fs and pulse energy of 3.5 mJ per pulse. Consecutive frequency conversion results in an output beam with a wavelength in the UV spectra (193 nm) and a pulse energy of 0.08 mJ. The short femtosecond pulses were shown to have major advantages over nanosecond pulses for a wide range of element and isotope ratios with respect to laser-induced and particle-size-related fractionation, thus enabling non-matrix-matched calibrations (e.g., Horn and von Blanckenburg, 2007; Steinhoefel et al., 2009).

The sample and standard materials were mounted in an ablation chamber with an active volume of ca. 45 cm^3 and ablated in a helix-mode scan at a speed of 2 mm s^{-1} by using a laser spot size of ~ 40 µm. This technique allows ablation craters of almost any diameter to be produced, in this study ranging from ~ 80 µm for analysis of single chambers to ~ 400 µm to cover whole shells. The aerosol was transported via a He gas flow (~ 0.5 L min^{-1}) and admixed with Ar gas (~ 0.5 L min^{-1}) before entering the MC-ICP-MS. Torch position, ion optics and gas flows were optimized to gain maximum signal intensity and stability on ^{10}B and ^{11}B peaks. The mass spectrometer was equipped with standard Ni sample and skimmer cones for dry plasma conditions. The radio frequency power was set to 1300 W. Boron isotopes were determined on Daly detectors, where high-mass D5 was used for ^{11}B and D0 for ^{10}B. Each measured sample $^{11}B/^{10}B$ was normalized to $^{11}B/^{10}B$ measurements of the glass standard NIST SRM 610 ($\delta^{11}B = 0$ ‰ NBS 951), using the standard-sample-bracketing technique. The analyses were performed at low mass resolution ($M/\Delta M \sim 2000$, 5 ‰), which was sufficient to resolve all interferences.

We performed mass scans on the peaks of ^{10}B and ^{11}B for both gas blanks (laser off) and measurements on carbonate (laser on) (Fig. 1) to investigate possible effects by scattered ions of matrix elements as observed in some recent studies (Sadekov et al., 2019; Standish et al., 2019). For our set-up, we can exclude such matrix-induced effects, which is in line with Fietzke et al. (2010) and Mayk et al. (2020). Hence, there was no need to correct the raw LA data as done in the recent studies by Sadekov et al. (2019) and Standish et al. (2019). Before analysis, sample and standard materials were pre-ablated to remove potential surface contamination. Laser repetition rates ranged between 12 and 60 Hz to match the signal intensity between carbonate samples and standard material NIST SRM 610 (~ 300 000 cps on ^{11}B). As ablation efficiency and hence signal intensity may vary with progressively increasing surface roughness and crater depth, we adjusted the repetition rate, if required, to target intensity matching between sample and standard. Whereas this approach could result in bulgy time-resolved isotope signals, as shown in Fig. 2, clean calcium carbonate was identified from a plateau-like $^{11}B / ^{10}B$ signal. Conversely, any contaminated phase from partial ablation of clay infillings, indicated by dropping $^{11}B / ^{10}B$ ratios accompanied by rising [B], were excluded from further data treatment (Fig. 2).

Each analysis was preceded by an on-peak gas blank measurement of 60 s on ^{10}B and ^{11}B, which was subtracted from the LA signal. The LA analysis itself was assessed by calculating the mean of the blank-corrected $^{11}B/^{10}B$ signal within an interval of up to 370 cycles (1 s each), where all data exceeding two standard deviations were removed as outliers. After analysis, B was washed out for 120 to 180 s until reaching background levels before a new measurement was started. A typical blank had ~ 7000 cps on ^{11}B at the beginning of a session but decreased to less than 3000 cps during the course of a day. As signal intensity on ^{11}B was aimed at ~ 300 000 cps, the signal-to-noise ratio was on the order of ~ 100.

Accuracy of boron isotope measurements was frequently checked by ablating an in-house carbonate standard that was also used for SIMS analysis (i.e. WP22, Rollion-Bard et al., 2003). The average δ^{11}B of 16.49 ‰ ± 1.26 ‰ (2σ, $n = 20$) for WP22 is very close to the bulk solution values ($\delta^{11}B = 16.60$ ‰ ± 0.30 ‰ (2σ, $n = 6$) measured at AWI, and $\delta^{11}B = 16.76$ ‰ ± 0.11 ‰ measured at IPGP). As the measurement uncertainty is mainly dependent on the ablation time, we report measurement uncertainties (as 2σ) for each δ^{11}B analysis as a function of analysis time, which was determined from multiple measurements of NIST glass standards and carbonate standards, and which is very close to the predicted uncertainty based on counting statistics (Fig. 3).

2.4 Bulk solution MC-ICPMS

After LA analyses, the 18 shells were carefully removed from the carbon tape and cleaned following the procedure outlined by Raitzsch et al. (2018). Briefly, foraminifer shells were gently crushed under a binocular between two glass slides and transferred to Eppendorf vials. After the clay re-

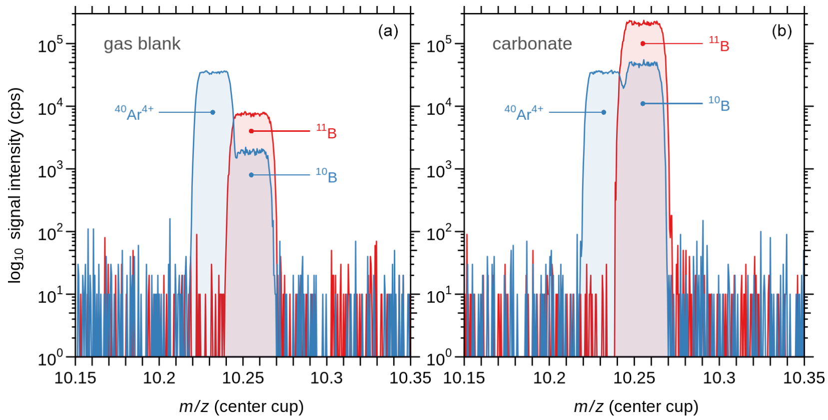

Figure 1. Mass scans over atomic masses 10 (blue) and 11 (red) using Daly detectors, where peak center coincidence appears at ~ 10.25 amu in the center cup. **(a)** Gas blank (laser off), showing the typical double peak of $^{40}Ar^{4+}$ and ^{10}B, and the ^{11}B peak. **(b)** Signal of ablated calcium carbonate (laser on). The baseline exhibits only electronic noise from the Daly detectors, but no sign of unresolved interferences on ^{10}B as matrix-induced scattered Ca ion. Note that the signal intensity is on a logarithmic scale.

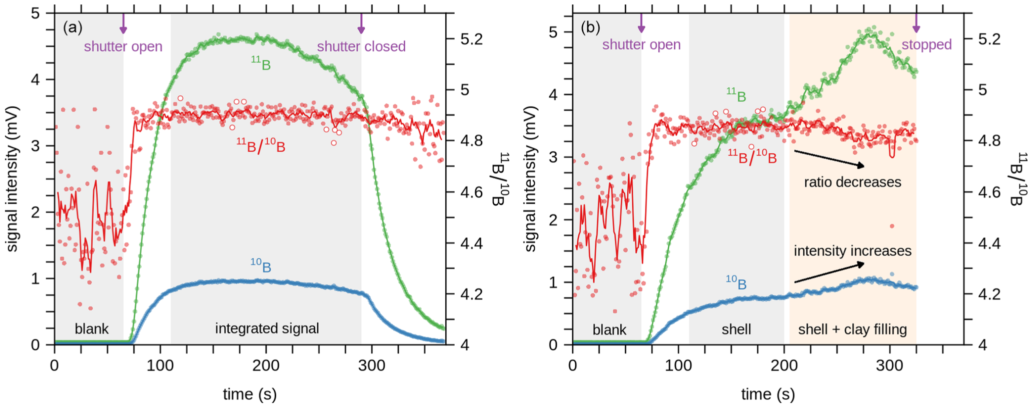

Figure 2. **(a)** Example of time-resolved laser ablation analysis for ^{10}B and ^{11}B of a *C. wuellerstorfi* shell using Daly detectors, preceded by a ~ 60 s blank measurement. Dots represent 1 s cycles, and lines 5-point running averages. Open symbols are data that are excluded by the 2σ outlier test. **(b)** Example of a shell that was penetrated by the laser beam, resulting in the ablation of clay infillings.

moval and oxidative cleaning steps, the samples were leached in 0.001 N HNO_3 and finally dissolved in 60 µL of 1 N HNO_3.

Prior to boron isotope analysis, we used the microdistillation technique to separate B from the calcium carbonate matrix (Gaillardet et al., 2001; Misra et al., 2014; Raitzsch et al., 2018; Wang et al., 2010). The distillate was diluted with 400 µL of 0.3 N HNO_3. The B concentration of a small aliquot was determined using a quick (20 s) on-peak measurement of ^{11}B on Faraday cup H9 using a Nu Plasma II MC-ICPMS (AWI, Bremerhaven). The remainder of the sample was then diluted to yield a solution with a [B] of 3 ppb and concentration-matched with the SRM NBS 951 to within ±3 %.

For isotope ratio measurements, boron was collected on Daly detectors, where high-mass D5 was used for ^{11}B and D0 for ^{10}B. Boron isotope data were measured in triplicate using the standard-sample-bracketing technique and reported in delta notation normalized to SRM NBS 951:

$$\delta^{11}B_{\text{sample}} = \left(\frac{^{11}B/^{10}B_{\text{sample}}}{^{11}B/^{10}B_{\text{NIST951}}} - 1 \right) \cdot 1000. \tag{1}$$

When 2σ of the mean derived from the triplicate was smaller than the long-term reproducibility (0.30 ‰), we report the latter as the measurement uncertainty. In addition, a small fragment of an in-house carbonate reference material WP22, used for our SIMS and LA-MC-ICPMS study, was cleaned and measured exactly the same way as the foraminifera sample to obtain a bulk $\delta^{11}B$ value for comparison (16.60 ‰ ±

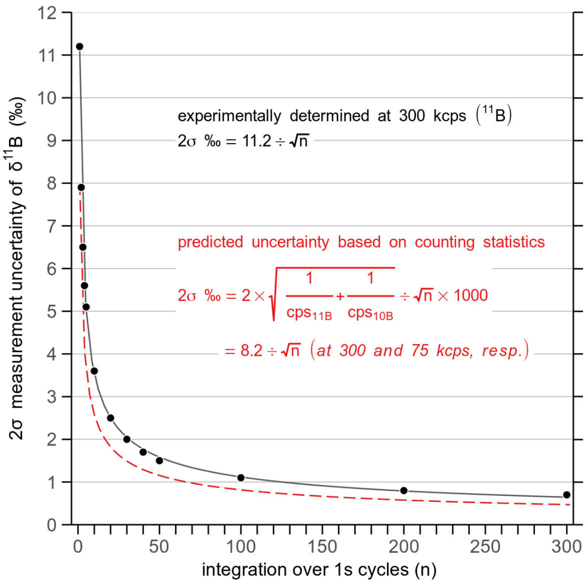

Figure 3. Measurement uncertainty of ^{11}B/^{10}B (2σ) at count rates of 300 000 cps (^{11}B) as a function of the laser ablation time. The uncertainty of each boron isotope measurement is calculated based on this relationship (black solid line). A major portion (∼ 70 %) of the measurement uncertainty is related to Poisson-distributed counts (red dashed line).

0.30 ‰). This value is almost identical to that measured at IPGP using the bulk solution ICP-MS (16.76 ‰ ± 0.11 ‰).

3 Results and discussion

3.1 Intra-shell δ^{11}B variability

The results from SIMS measurements conducted on five large specimens reveal a high δ^{11}B variability ranging between 4.6 and 6.8 (mean 5.2) ‰ (2σ, 2 standard deviation of n individual measurements) within single shells, based on 8 to 19 single-spot analyses on each shell. A similar variability of 4.4 ‰ (2σ) on average is observed for measurements within single chambers (Fig. 4). Since it is difficult to distinguish between the very small (i.e. the juvenile) chambers in the central part, we allocated these measurements to the umbilical "knob", which is also equivalent to the thick central part of the spiral side used for LA measurements. If δ^{11}B is averaged for each chamber (one to three analyses per chamber), the mean variability between chambers is 4.2 ‰ (2σ) (Fig. 4). The two specimens measured chamber by chamber with LA also show variable δ^{11}B, but with a much lower variation of ∼ 1.1 ‰ (2σ), compared to the SIMS data (Fig. 4). The average δ^{11}B variability from all 16 shells measured multiple times is ∼ 1.3 ‰ (2σ).

Here the question arises of whether the difference in δ^{11}B variability between the two methods is due to differences in analytical uncertainty or different scales of natural heterogeneity. If we consider an average uncertainty of ±0.9 ‰ for LA (Fig. 3), intra-shell variability is reduced from 1.3 ‰ to 0.4 ‰. As the 2σ measurement uncertainty for SIMS is roughly ±2.5 ‰, the remaining difference in variability between SIMS and LA methods of ∼ 2.3 ‰ is likely due to the different sampling volumes and hence related to heterogeneous boron isotopic distribution in the test. While the spot size for the SIMS method is ∼ 20 and ∼ 1 µm at depth, the laser-ablated volume ranges from 80 to 100 µm in diameter (Fig. 4) and approximately 10 µm at depth. Consequently, the ∼ 200 times larger volume analyzed by LA would reduce the δ^{11}B variability detected by SIMS to $\sim 0.2 (= 2.3/\sqrt{200})$ ‰. Hence we argue that the "true" δ^{11}B heterogeneity is scale-dependent and assumedly on the order of ∼ 3 and ∼ 0.4 ‰ (2σ) on a ∼ 20 and 100 µm grid, respectively.

To examine potential systematic trends in δ^{11}B among successive chambers, we calculated the residual boron isotopic composition $\Delta\delta^{11}$B for each site within each shell by comparing the B isotopic composition of a single-chamber $\delta^{11}\mathrm{B}_{\mathrm{single}}$ with the mean value of the shell $\delta^{11}\mathrm{B}_{\mathrm{mean}}$:

$$\Delta\delta^{11}\mathrm{B} = \delta^{11}\mathrm{B}_{\mathrm{single}} - \delta^{11}\mathrm{B}_{\mathrm{mean}}. \qquad (2)$$

The SIMS data suggest that $\Delta\delta^{11}$B tends to decrease from the penultimate chamber ($f-1$) towards chamber $f-5$ by roughly 4 ‰ (Fig. 4), whereas no systematic change exists between chambers $f-6$ and the juvenile chambers. However, it is compelling that also the LA results suggest a decreasing trend in $\Delta\delta^{11}$B from the final chambers towards chamber $f-5$ by more than 0.5 ‰, while in the earlier chambers no systematic change can be observed (Fig. 4). For both methods, Wilcoxon–Mann–Whitney tests and Welch's t tests suggest that the $\Delta\delta^{11}$B change between the final chambers and $f-5$ is statistically insignificant at a 95 % significance level (p values ≥ 0.07). However, decreasing δ^{11}B from the final chamber towards earlier chambers would be in line with the LA study by Sadekov et al. (2019) showing a ∼ 2 ‰ decrease along the last whorl of *C. wuellerstorfi*. A similar pattern was also observed for B/Ca, with the highest value in the final chamber (Raitzsch et al., 2011; Sadekov et al., 2019), suggesting a strong biological influence or kinetic (i.e. growth rate) effect on boron incorporation. An in-depth discussion of biological and calcification processes is beyond the scope of this study, but the discovery of such high variability has implications for the use of δ^{11}B-microanalytical techniques in paleoceanographic studies (e.g., Rollion-Bard and Erez, 2010).

Another notable feature derived from LA and SIMS is the elevated δ^{11}B (by ∼ 0.5 ‰ on average) of the umbilical knob, compared to the whole-shell δ^{11}B. This is confirmed by supplementary ablation of the knob of individuals, which were used for whole-shell analysis in Sect. 3.2. On average, umbilical knob δ^{11}B was ∼ 0.4 ‰ higher than the value derived

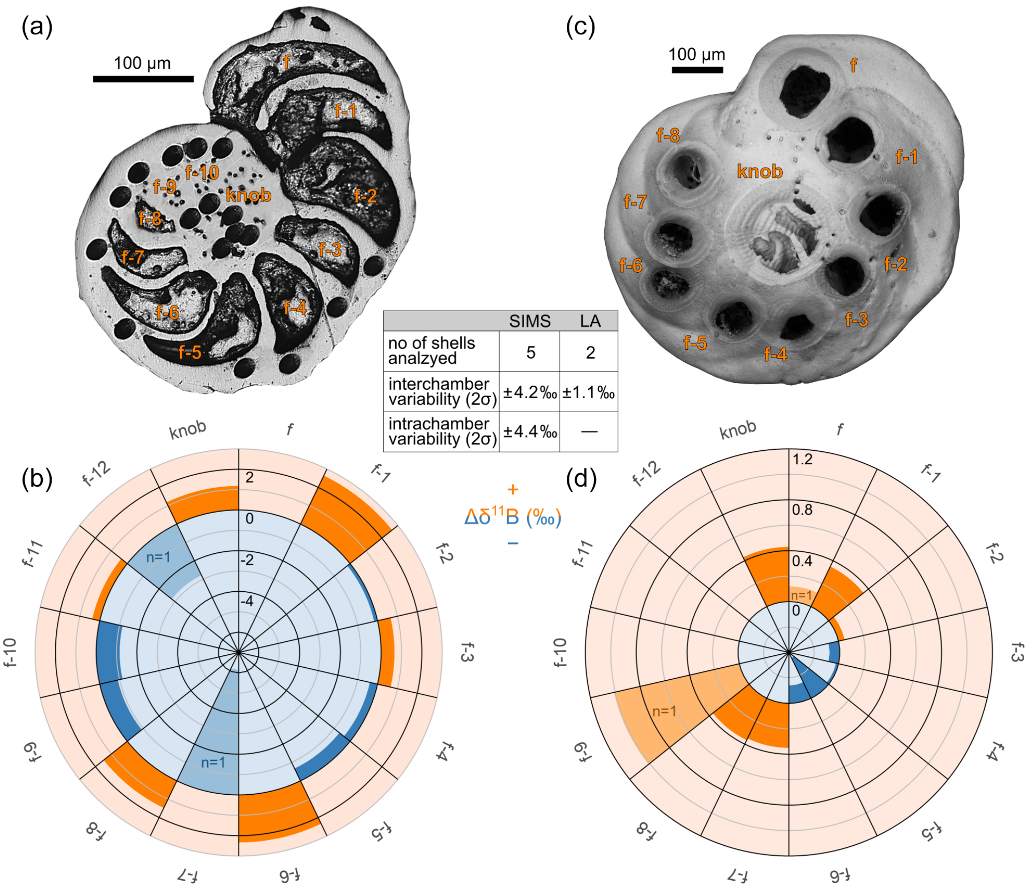

	SIMS	LA
no of shells analzyed	5	2
interchamber variability (2σ)	±4.2‰	±1.1‰
intrachamber variability (2σ)	±4.4‰	—

Figure 4. Intra-shell variability of δ^{11}B using SIMS **(a)** and LA-MC-ICPMS **(b)** on selected large individuals of *C. wuellerstorfi*. The residual $\Delta\delta^{11}$B (difference between single-spot and mean δ^{11}B, Eq. 2) averaged from all analyzed specimens is shown for each chamber (f is the final chamber, $f-1$ the penultimate one, and so on). Orange color stands for higher-than-mean and blue for lower-than-mean values. Lighter colors indicate data that are based on only one measurement. The inset table summarizes the measured intra-shell variability derived from the two techniques.

from the larger ablated area (see inset picture in Fig. 7), although this behavior is not systematic and was observed in only two thirds of the cases.

3.2 Inter-shell δ^{11}B variability

Apart from the seven specimens used for inspecting the chamber-to-chamber variability, 16 individuals of *C. wuellerstorfi* were laser-ablated using a large area of at least 300 µm in diameter to cover a major part of the spiral side, and in 14 specimens subsequently analyzed for the composition of the thicker umbilical knob using a smaller crater (inset picture in Fig. 7). This way, we approached quasi-bulk δ^{11}B values for single shells. Together with the δ^{11}B medians from the two specimens described in the previous section, a total of 18 shells were used for determining the inter-shell δ^{11}B variability using LA-MC-ICPMS (Fig. 5). It should be noted that we usually report the average as median, since it is less sensitive to outliers than the mean and also reflects the average of a non-uniform distribution. For SIMS analyses, the medians of single-spot analyses were calculated for each of the five shells.

The SIMS data reveal a huge spread of single-spot δ^{11}B across the five specimens (Sect. 3.1), but the δ^{11}B values averaged for each shell exhibit a narrower range between tests, with a median δ^{11}B of 16.08 ‰ ± 2.70 ‰ (2σ) (Fig. 5). In contrast, the single-site LA data across all 18 individuals show a smaller variation in δ^{11}B than the SIMS data, where the values averaged for each shell yield a median of 15.90 ‰ ± 1.62 ‰ (2σ). Both the average δ^{11}B measurement uncertainty for LA of ±0.9 ‰ (2σ) and the variation difference between foraminiferal shells and WP22 of ∼ 0.4 ‰ suggest a residual inter-shell variability on the order of 0.4 ‰

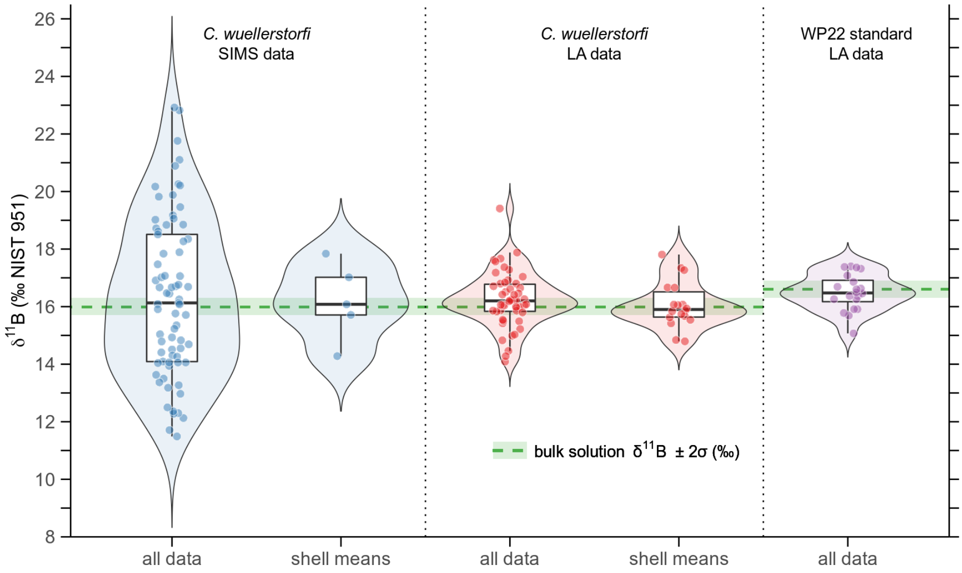

Figure 5. Violin, box and jitter plots showing the distribution of all single-site δ^{11}B values and single-shell means, both for the SIMS and laser ablation techniques. For comparison, the distribution of δ^{11}B values measured on the in-house reference material WP22 is displayed as well. The green dashed lines and bars represent the bulk solution $\delta^{11}\text{B} \pm 2\sigma$ values.

to 0.7 ‰. Similarly, if an uncertainty of ±2.50 ‰ (2σ) for SIMS measurements is taken into account, the remaining inter-shell variability is only ∼ 0.2 ‰. Therefore, we estimate the "true" variability between shells of a population to be ∼ 0.4 ‰, which is the same as the variation estimated for the intra-shell variability (Sect. 3.1).

For shells where both large areas and knobs were measured ($n = 14$), it is interesting to note that if only the large LA craters are considered, the mean δ^{11}B is 15.87 ‰ ± 1.78 ‰ (2σ), while it is 16.27 ‰ ± 2.75 ‰ (2σ), if solely the small LA craters are taken into account (see Fig. 7, inset picture). As the volume of the large LA craters is ∼ 3 times larger than the smaller ones, the resulting variability among means of three resampled small-crater values is $1.59 (= 2.75/\sqrt{3})$ ‰ (2σ), which is quite close to the 1.78 ‰ derived from large craters, and confirms our conclusion that the δ^{11}B variability is dependent on the scale at which it is measured.

3.3 Bulk solution δ^{11}B

Both the SIMS and LA results reveal median values that match the bulk δ^{11}B of 15.99 ‰ ± 0.30 ‰ (2σ) measured in solution to within analytical uncertainties (Fig. 5). It should be noted again that the same specimens measured in solution had been measured before by LA, ensuring that we compare different techniques based on the same set of samples. Similarly, the average δ^{11}B of 16.48 ‰ ± 1.26 ‰ (2σ) in the reference material WP22 determined with LA-MC-ICPMS is not distinguishable from the bulk solution value of 16.60 ‰ ± 0.30 ‰ (2σ), which confirms the robustness of the LA technique, and also the SIMS results, as the median foraminifera values are identical for LA and SIMS techniques.

The δ^{11}B values obtained from all three methods fit in with the calibration data set for *C. wuellerstorfi* from the study by Rae et al. (2011) (Fig. 6) and confirm that the boron isotopic composition in this species closely matches that of borate of ambient seawater. Further, it proves that LA-MC-ICPMS and SIMS yield accurate results for δ^{11}B, if the data set is large enough to overcome the issues of intra- and inter-shell variability (∼ 0.4 ‰), and analytical uncertainty of microanalytical techniques (∼ ±0.9 ‰ and ±2.5 ‰ for LA and SIMS, respectively).

3.4 Implications for paleoreconstruction studies

The large intra- and inter-shell variations in δ^{11}B described in Sects. 3.1 and 3.2 raise the question whether microanalytical techniques such as SIMS or LA-MC-ICPMS can be used for analyzing δ^{11}B in *C. wuellerstorfi* to reconstruct past deep-water pH. The SIMS method requires careful embedding of foraminifer shells in epoxy and polishing down to a planar surface, which precludes further processing for bulk solution analyses, for example. However, because the size of the beam spot is small (20 µm or less), it is still possible to measure some other elemental and isotopic ratios at the same location on the sample; e.g., the same foraminifera specimens were used to measure δ^{18}O (Rollion-Bard et al., 2008), δ^{11}B (Rollion-Bard and Erez, 2010) and δ^{7}Li (Vigier

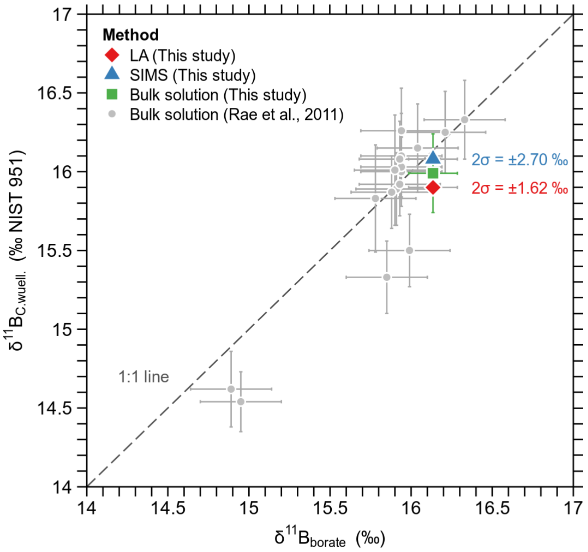

Figure 6. Median δ^{11}B of Holocene (5.6 ka) *C. wuellerstorfi* from GeoB core 1032 (Walvis Ridge, South Atlantic) measured with different techniques, shown along with the core-top calibration from (Rae et al., 2011). Note that the bulk solution analysis of this study was carried out on the same population measured before with laser ablation. Pooled δ^{11}B uncertainties for SIMS ($n = 5$ shells) and LA-MC-ICPMS ($n = 18$ shells) are shown as numbers, as error bars exceed the y axis scale.

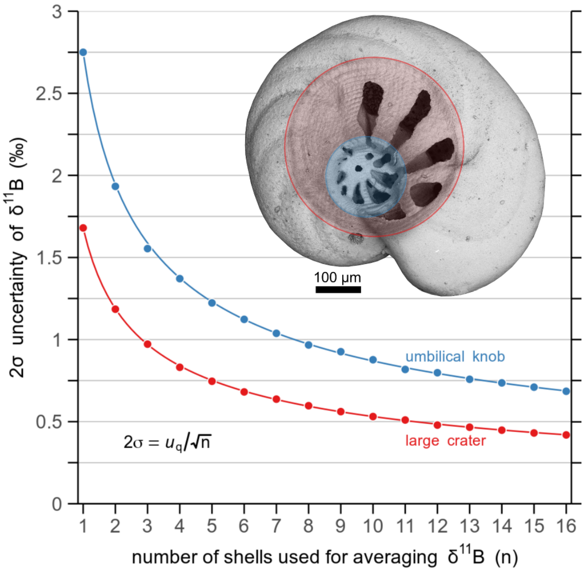

Figure 7. Results from Monte Carlo simulations of 2σ uncertainty for δ^{11}B using LA-MC-ICPMS in relation to the number of analyzed *C. wuellerstorfi* shells (n). In red is the estimated uncertainty based on "large crater", and in blue on "umbilical knob" measurements (see inset scanning electron microscope picture for different areas). The estimated 2σ uncertainty can be described by a function of the quoted uncertainty (u_q) and n (Eq. 3).

et al., 2015). The SIMS technique is very useful for biomineralization studies (e.g., Rollion-Bard and Erez, 2010), but for paleoreconstruction of deep-sea pH, where high precision is necessary, it may not be the most appropriate technique for routine downcore δ^{11}B analysis. However, here we will inspect LA-MC-ICPMS as a potential tool for paleo-pH studies.

To attain information on the number of shells required for accurate LA analysis of δ^{11}B to within a target uncertainty, we applied a Monte Carlo approach to generate two data sets with 10 000 δ^{11}B data each, within a quoted uncertainty of ±1.68 ‰ and ±2.75 ‰ (2σ) for "large crater" and "knob" measurements, respectively, as given by the original data set ($n = 16$ and $n = 14$, resp.). The average δ^{11}B values are considered identical between large craters and umbilical knobs, as in the original data they agree to within analytical uncertainty. Then we applied the "combn()" function of the R package "utils v3.4.4" (R Core Team, 2018) on each of the simulated data sets. With this function, we can calculate the uncertainty by generating all possible combinations of n shells taken from the simulated populations. For instance, if we would randomly pick five shells from this sediment sample, the analyzed δ^{11}B would be accurate to within ±0.75 ‰ with a probability of 95 %, if large areas, and ±1.22 ‰, if only the knob areas were analyzed. If we targeted a standard uncertainty of ±0.50 ‰, which is equivalent to a pH uncertainty of roughly ±0.1, we would need to measure ∼ 12 specimens with LA, if large areas, and ∼ 14 specimens, if only the knob areas were analyzed (Fig. 7). The relationship between number of analyzed shells (n) and the estimated 2σ uncertainty is given by the quoted variability u_q, i.e. the measured δ^{11}B variation across a population (as 2σ), and n:

$$2\sigma = \frac{u_q}{\sqrt{n}}. \qquad (3)$$

Given that the analysis uncertainty of the same amount measured in solution is about ±0.3 ‰, bulk solution analysis appears to be the more convenient technique for reconstructing paleo-pH. In contrast, the LA technique may be useful for generating high-resolution records, where sharp pH trends would partly compensate for the larger standard uncertainty or when only a few foraminifera specimens are available. Further, LA, like SIMS, has the potential to provide insight into ontogenetic δ^{11}B variations, helping to better understand the biological uptake of boron during chamber formation.

4 Conclusions

Microanalytical methods such as SIMS or LA-MC-ICPMS are potentially powerful tools for studying biomineralization processes or possible alternatives to conventional bulk solution analysis of δ^{11}B in benthic foraminifera, if sample material is limited. For this study, we measured a population of 23 *C. wuellerstorfi* in total using SIMS and femtosecond LA-MC-ICPMS and compared the results with the bulk-solution δ^{11}B, revealing consistent average values among the different techniques. While the medians agree to within $\pm 0.1\,‰$, a large intra-shell variability was observed, with up to $6.8\,‰$ and $4.5\,‰$ (2σ) derived from the SIMS and LA methods, respectively. We propose that the larger spread for SIMS, compared to LA, can be attributed to the much smaller volume $(\sim 200^{-1})$ of calcite being analyzed in each run and hence supposedly reflects a larger heterogeneity of δ^{11}B in the foraminiferal test on a smaller scale. When analytical uncertainties and scale-dependent differences in δ^{11}B variations are taken into account, the intra-shell variability is likely on the order of $\pm 0.4‰$ and $3\,‰$ (2σ) on a 100 and 20 µm scale, respectively.

The δ^{11}B variability between shells exhibits total ranges of $\sim 3\,‰$ for both techniques, suggesting that a number of shells needs to be analyzed for accurate mean δ^{11}B values. We applied a simple resampling method and conclude that about 12 shells of *C. wuellerstorfi* must be analyzed using LA-MC-ICPMS to obtain an accurate average value to within $\pm 0.5\,‰$ (2σ). Hence, we suggest that, based on this high number of required individuals, the bulk solution MC-ICPMS method remains the first choice for analysis of δ^{11}B in routine paleo-pH studies.

Data availability. The boron isotope data collected for this study are available from Table S1 in the Supplement.

Supplement. The supplement related to this article is available online at: https://doi.org/10.5194/bg-17-5365-2020-supplement.

Author contributions. MR, CRB, IH, and JB conceived the study. MR, CRB, and PL carried out measurements, analyzed the data, and performed data statistics. AB, KUR, and GS maintained and provided access to analytical instruments at AWI. JB, CRB, and IH raised funding for the French-German project "B2SeaCarb". MR produced the figures for the paper. MR and CRB wrote the first draft of the paper, and all authors interpreted, edited, and reviewed the paper.

Competing interests. The authors declare that they have no conflict of interest.

Acknowledgements. This research was carried out in the framework of the joint French/German project "B2SeaCarb" and was supported by the Deutsche Forschungsgemeinschaft (DFG) grant number BI 432/10-1 to Jelle Bijma and DFG grant number HO 3257/5-1 to Ingo Horn. On the French side, the project was supported by the French National Research Agency (ANR) grant number ANR-16-CE92-0010 to Claire Rollion-Bard. Claire Rollion-Bard thanks Nordine Bouden (CRPG) for his technical help, and the MARUM GeoB core repository is acknowledged for providing sediment samples. Kaoru Kubota as well as the referees Dennis Mayk and Lubos Polerecky are thanked for their help in improving the paper.

Financial support. This research has been supported by the Deutsche Forschungsgemeinschaft (grant nos. BI 432/10-1 and HO 3257/5-1) and the Agence Nationale de la Recherche (grant no. ANR-16-CE92-0010).

The article processing charges for this open-access publication were covered by the University of Bremen.

Review statement. This paper was edited by Jack Middelburg and reviewed by Dennis Mayk and Lubos Polerecky.

References

Blamart, D., Rollion-Bard, C., Meibom, A., Cuif, J.-P., Juillet-Leclerc, A., and Dauphin, Y.: Correlation of boron isotopic composition with ultrastructure in the deep-sea coral *Lophelia pertusa*: Implications for biomineralization and paleo-pH, Geochem. Geophy. Geosy., 8, Q12001, https://doi.org/10.1029/2007GC001686, 2007.

Branson, O., Kaczmarek, K., Redfern, S. A. T., Misra, S., Langer, G., Tyliszczak, T., Bijma, J., and Elderfield, H.: The coordination and distribution of B in foraminiferal calcite, Earth Planet. Sc. Lett., 416, 67–72, https://doi.org/10.1016/j.epsl.2015.02.006, 2015.

Fietzke, J., Heinemann, A., Taubner, I., Böhm, F., Erez, J., and Eisenhauer, A.: Boron isotope ratio determination in carbonates via LA-MC-ICP-MS using soda-lime glass standards as reference material, J. Anal. At. Spectrom., 25, 1953, https://doi.org/10.1039/c0ja00036a, 2010.

Fietzke, J., Ragazzola, F., Halfar, J., Dietze, H., Foster, L. C., Hansteen, T. H., Eisenhauer, A., and Steneck, R. S.: Century-scale trends and seasonality in pH and temperature for shallow zones of the Bering Sea, P. Natl. Acad. Sci. USA, 112, 2960–2965, https://doi.org/10.1073/pnas.1419216112, 2015.

Gaillardet, J., Lemarchand, D., Göpel, C., and Manhès, G.: Evaporation and Sublimation of Boric Acid: Application for Boron Purification from Organic Rich Solutions, Geostand. Newsl., 25, 67–75, https://doi.org/10.1111/j.1751-908X.2001.tb00788.x, 2001.

Hemming, N. G. and Hanson, G. N.: Boron isotopic composition and concentration in modern marine carbonates, Geochim. Cosmochim. Ac., 56, 537–543, https://doi.org/10.1016/0016-7037(92)90151-8, 1992.

Hönisch, B., Bickert, T., and Hemming, N. G.: Modern and Pleistocene boron isotope composition of the benthic foraminifer *Cibicidoides wuellerstorfi*, Earth Planet. Sci. Lett., 272, 309–318, https://doi.org/10.1016/j.epsl.2008.04.047, 2008.

Horn, I. and von Blanckenburg, F.: Investigation on elemental and isotopic fractionation during 196 nm femtosecond laser ablation multiple collector inductively coupled plasma mass spectrometry, Spectrochim. Acta B-At. Spectrosc., 62, 410–422, https://doi.org/10.1016/j.sab.2007.03.034, 2007.

Howes, E. L., Kaczmarek, K., Raitzsch, M., Mewes, A., Bijma, N., Horn, I., Misra, S., Gattuso, J.-P., and Bijma, J.: Decoupled carbonate chemistry controls on the incorporation of boron into Orbulina universa, Biogeosciences, 14, 415–430, https://doi.org/10.5194/bg-14-415-2017, 2017.

Inoue, M., Nohara, M., Okai, T., Suzuki, A., and Kawahata, H.: Concentrations of Trace Elements in Carbonate Reference Materials Coral JCp-1 and Giant Clam JCt-1 by Inductively Plasma-Mass Spectrometry, Geostand. Geoanal. Res., 28, 411–416, 2004.

Kaczmarek, K., Horn, I., Nehrke, G., and Bijma, J.: Simultaneous determination of δ^{11}B and B / Ca ratio in marine biogenic carbonates at nanogram level, Chem. Geol., 392, 32–42, https://doi.org/10.1016/j.chemgeo.2014.11.011, 2015a.

Kaczmarek, K., Langer, G., Nehrke, G., Horn, I., Misra, S., Janse, M., and Bijma, J.: Boron incorporation in the foraminifer Amphistegina lessonii under a decoupled carbonate chemistry, Biogeosciences, 12, 1753–1763, https://doi.org/10.5194/bg-12-1753-2015, 2015b.

Kasemann, S. A., Schmidt, D. N., Bijma, J., and Foster, G. L.: In situ boron isotope analysis in marine carbonates and its application for foraminifera and palaeo-pH, Chem. Geol., 260, 138–147, https://doi.org/10.1016/j.chemgeo.2008.12.015, 2009.

Klochko, K., Kaufman, A. J., Yao, W., Byrne, R. H., and Tossell, J. A.: Experimental measurement of boron isotope fractionation in seawater, Earth Planet. Sci. Lett., 248, 276–285, https://doi.org/10.1016/j.epsl.2006.05.034, 2006.

Louvat, P., Moureau, J., Paris, G., Bouchez, J., Noireaux, J., and Gaillardet, J.: A fully automated direct injection nebulizer (d-DIHEN) for MC-ICP-MS isotope analysis: application to boron isotope ratio measurements, J. Anal. At. Spectrom., 29, 1698–1707, https://doi.org/10.1039/C4JA00098F, 2014.

Malherbe, J., Penen, F., Isaure, M.-P., Frank, J., Hause, G., Dobritzsch, D., Gontier, E., Horréard, F., Hillion, F., and Schaumlöffel, D.: A New Radio Frequency Plasma Oxygen Primary Ion Source on Nano Secondary Ion Mass Spectrometry for Improved Lateral Resolution and Detection of Electropositive Elements at Single Cell Level, Anal. Chem., 88, 7130–7136, https://doi.org/10.1021/acs.analchem.6b01153, 2016.

Mayk, D., Fietzke, J., Anagnostou, E., and Paytan, A.: LA-MC-ICP-MS study of boron isotopes in individual planktonic foraminifera: A novel approach to obtain seasonal variability patterns, Chem. Geol., 531, 119351, https://doi.org/10.1016/j.chemgeo.2019.119351, 2020.

Misra, S., Owen, R., Kerr, J., Greaves, M., and Elderfield, H.: Determination of δ^{11}B by HR-ICP-MS from mass limited samples: Application to natural carbonates and water samples, Geochim. Cosmochim. Ac., 140, 531–552, https://doi.org/10.1016/j.gca.2014.05.047, 2014.

Okai, T., Suzuki, A., Terashima, S., Inoue, M., Nohara, M., Kawahata, H., and Imai, N.: Collaborative Analysis of GSJ/AIST Geochemical Reference Materials JCp-1 (Coral) and JCt-1 (Giant Clam), Chikyu Kagaku, 38, 281–286, 2004.

Rae, J. W. B., Foster, G. L., Schmidt, D. N., and Elliott, T.: Boron isotopes and B / Ca in benthic foraminifera: Proxies for the deep ocean carbonate system, Earth Planet. Sc. Lett., 302, 403–413, https://doi.org/10.1016/j.epsl.2010.12.034, 2011.

Raitzsch, M. and Hönisch, B.: Cenozoic boron isotope variations in benthic foraminifers, Geology, 41, 591–594, https://doi.org/10.1130/G34031.1, 2013.

Raitzsch, M., Hathorne, E. C., Kuhnert, H., Groeneveld, J., and Bickert, T.: Modern and late Pleistocene B / Ca ratios of the benthic foraminifer *Planulina wuellerstorfi* determined with laser ablation ICP-MS, Geology, 39, 1039–1042, https://doi.org/10.1130/G32009.1, 2011.

Raitzsch, M., Bijma, J., Benthien, A., Richter, K.-U., Steinhoefel, G., and Kučera, M.: Boron isotope-based seasonal paleo-pH reconstruction for the Southeast Atlantic – A multispecies approach using habitat preference of planktonic foraminifera, Earth Planet. Sc. Lett., 487, 138–150, https://doi.org/10.1016/j.epsl.2018.02.002, 2018.

Raitzsch, M., Bijma, J., Bickert, T., Schulz, M., Holbourn, A., and Kučera, M.: Eccentricity-paced atmospheric carbon-dioxide variations across the middle Miocene climate transition, Clim. Past Discuss., https://doi.org/10.5194/cp-2020-96, in review, 2020.

R Core Team: A Language and Environment for Statistical Computing, R Foundation for Statistical Computing, Vienna, available at: https://www.R-project.org (last access: 29 February 2020), 2018.

Rollion-Bard, C. and Blamart, D.: In: Biomineralization Sourcebook: Characterization of Biominerals and Biomimetic Materials, pp. 249–261, CRC Press, Taylor & Francis Group, Boca Raton, FL, 2014.

Rollion-Bard, C., Erez, J., and Zilberman, T.: Intra-shell oxygen isotope ratios in the benthic foraminifera genus Amphistegina and the influence of seawater carbonate chemistry and temperature on this ratio, Geochim. Cosmochim. Ac., 72, 6006–6014, https://doi.org/10.1016/j.gca.2008.09.013, 2008.

Rollion-Bard, C. and Erez, J.: Intra-shell boron isotope ratios in the symbiont-bearing benthic foraminiferan *Amphistegina lobifera*: Implications for δ^{11}B vital effects and paleo-pH reconstructions, Geochim. Cosmochim. Ac., 74, 1530–1536, https://doi.org/10.1016/j.gca.2009.11.017, 2010.

Rollion-Bard, C., Chaussidon, M., and France-Lanord, C.: pH control on oxygen isotopic composition of symbiotic corals, Earth Planet. Sc. Lett., 215, 275–288, https://doi.org/10.1016/S0012-821X(03)00391-1, 2003.

Sadekov, A., Lloyd, N. S., Misra, S., Trotter, J., D'Olivo, J., and McCulloch, M.: Accurate and precise microscale measurements of boron isotope ratios in calcium carbonates using laser ablation multicollector-ICPMS, J. Anal. At. Spectrom., 34, 550–560, https://doi.org/10.1039/C8JA00444G, 2019.

Standish, C. D., Chalk, T. B., Babila, T. L., Milton, J. A., Palmer, M. R. and Foster, G. L.: The effect of matrix interferences on in situ boron isotope analysis by laser ablation multi-collector inductively coupled plasma mass spectrometry, Rapid Commun. Mass Sp., 33, 959–968, https://doi.org/10.1002/rcm.8432, 2019.

Steinhoefel, G., Horn, I., and von Blanckenburg, F.: Matrix-independent Fe isotope ratio determination in silicates using UV femtosecond laser ablation, Chem. Geol., 268, 67–73, https://doi.org/10.1016/j.chemgeo.2009.07.010, 2009.

Thil, F., Blamart, D., Assailly, C., Lazareth, C. E., Leblanc, T., Butsher, J., and Douville, E.: Development of laser ablation multi-collector inductively coupled plasma mass spectrometry for boron isotopic measurement in marine biocarbonates: new improvements and application to a modern *Porites* coral, Rapid Commun. Mass Sp., 30, 359–371, https://doi.org/10.1002/rcm.7448, 2016.

Vigier, N., Rollion-Bard, C., Levenson, Y., and Erez, J.: Lithium isotopes in foraminifera shells as a novel proxy for the ocean dissolved inorganic carbon (DIC), C.R. Geosci., 347, 43–51, https://doi.org/10.1016/j.crte.2014.12.001, 2015.

Wang, B.-S., You, C.-F., Huang, K.-F., Wu, S.-F., Aggarwal, S. K., Chung, C.-H., and Lin, P.-Y.: Direct separation of boron from Na- and Ca-rich matrices by sublimation for stable isotope measurement by MC-ICP-MS, Talanta, 82, 1378–1384, https://doi.org/10.1016/j.talanta.2010.07.010, 2010.

Yu, J. and Elderfield, H.: Benthic foraminiferal B / Ca ratios reflect deep water carbonate saturation state, Earth Planet. Sc. Lett., 258, 73–86, https://doi.org/10.1016/j.epsl.2007.03.025, 2007.

Yu, J., Foster, G. L., Elderfield, H., Broecker, W. S., and Clark, E.: An evaluation of benthic foraminiferal B / Ca and δ^{11}B for deep ocean carbonate ion and pH reconstructions, Earth Planet. Sc. Lett., 293, 114–120, https://doi.org/10.1016/j.epsl.2010.02.029, 2010.

BIBLIOGRAPHIE

Acon, B., McLean, J., Montaser, A., 2000. A Large Bore-Direct Injection High Efficiency Nebulizer for Inductively Coupled Plasma Spectrometry. *Anal Chem*, Vol. **72**(8), p. 1885–1893. (Cité en pages 95 et 102)

Aggarwal, J., Sheppard, D., Mezger, K., Pernicka, E., 2003. Precise and Accurate Determination of Boron Isotope Ratios by Multiple Collector ICP-MS: Origin of Boron in the Ngawha Geothermal System, New Zealand. *Chem. Geol.*, Vol. **199**(3-4), p. 331–342. (Cité en page 114)

Aggarwal, S. K., You, C.-F., 2016. A Review on the Determination of Isotope Ratios of Boron with Mass Spectrometry. *Mass Spectrom. Rev.*, Vol. **36**(4), p. 499–519. (Cité en pages 114 et 145)

Aigner, T., Bachmann, G. H., 1992. Sequence-Stratigraphic Framework of the German Triassic. *Sediment. Geol.*, Vol. **80**(1-2), p. 115–135. (Cité en page 69)

Al-Ammar, A. S., Gupta, R. K., Barnes, R. M., 2000. Elimination of Boron Memory Effect in Inductively Coupled Plasma-Mass Spectrometry by Ammonia Gas Injection into the Spray Chamber during Analysis. *Spectrochim. Acta Part B At. Spectrosc.*, Vol. **55**(6), p. 629–635. (Cité en pages 114 et 115)

Allègre, C. J., Louvat, P., Gaillardet, J., Meynadier, L., Rad, S., Capmas, F., 2010. The Fundamental Role of Island Arc Weathering in the Oceanic Sr Isotope Budget. *Earth and Planetary Science Letters*, Vol. **292**(1), p. 51–56. (Cité en page 61)

Allen, K. A., Hönisch, B., Eggins, S. M., Haynes, L. L., Rosenthal, Y., Yu, J., 2016. Trace Element Proxies for Surface Ocean Conditions: A Synthesis of Culture Calibrations with Planktic Foraminifera. *Geochimica et Cosmochimica Acta*, Vol. **193**, p. 197–221. (Cité en page 175)

Allen, K. A., Hönisch, B., Eggins, S. M., Rosenthal, Y., 2012. Environmental Controls on B/Ca in Calcite Tests of the Tropical Planktic Foraminifer Species Globigerinoides Ruber and Globigerinoides Sacculifer. *Earth Planet. Sci. Lett.*, Vol. **351–352**, p. 270–280. (Cité en pages 11 et 144)

Allen, P. A., 2007. The Huqf Supergroup of Oman: Basin Development and Context for Neoproterozoic Glaciation. *Earth-Sci. Rev.*, Vol. **84**(3-4), p. 139–185. (Cité en pages xxvii, 73 et 74)

Alves, A., 2020. *Impact de La Super-Éruption Du Volcan Toba (74ka) Sur La Température et Le pH de l'océan*. Rapport de stage Master 2 - Climat, Environnemen, Application et Recherche (CLEAR) - Interactions Climat Environnement et télédétection (ICE), Université Paris-Saclay. (Cité en pages xxxii, 169, 172, 173, 174, 176 et 177)

Ambrose, S. H., 1998. Late Pleistocene Human Population Bottlenecks, Volcanic Winter, and Differentiation of Modern Humans. *Journal of Human Evolution*, Vol. **34**(6), p. 623–651. (Cité en page 166)

Anagnostou, E., John, E. H., Edgar, K. M., Foster, G. L., Ridgwell, A., Inglis, G. N., Pancost, R. D., Lunt, D. J., Pearson, P. N., 2016. Changing Atmospheric CO2 Concentration Was the Primary Driver of Early Cenozoic Climate. *Nature*, Vol. **533**(7603), p. 380–384. (Cité en pages xxv, xxvii, 2, 9, 28, 29, 30, 44, 50, 80, 81 et 114)

Anand, P., Elderfield, H., Conte, M. H., 2003. Calibration of Mg/Ca Thermometry in Planktonic Foraminifera from a Sediment Trap Time Series. *Paleoceanography*, Vol. **18**(2). (Cité en pages 144 et 175)

Arrhenius, S., Holden, E. S., 1897. ON THE INFLUENCE OF CARBONIC ACID IN THE AIR UPON THE TEMPERATURE OF THE EARTH. *Publ. Astron. Soc. Pac.*, Vol. **9**(54), p. 14–24. (Cité en page 2)

Bąbel, M., Schreiber, B., 2014. Geochemistry of Evaporites and Evolution of Seawater. *Dans : Treatise on Geochemistry (Second Edition)*. Vol. 9. Elsevier, p. 483–560. (Cité en pages xxvi, xxvii, 67, 75 et 76)

Babila, T. L., 2014. Evaluation of the Biogeochemical Controls on B/Ca of Globigerinoides Ruber White from the Oceanic Flux Program, Bermuda. *Earth Planet. Sci. Lett.*, p. 10. (Cité en pages 144 et 158)

Balan, E., Pietrucci, F., Gervais, C., Blanchard, M., Schott, J., Gaillardet, J., 2016. First-Principles Study of Boron Speciation in Calcite and Aragonite. *Geochim. Cosmochim. Acta*, Vol. **193**, p. 119–131. (Cité en page 144)

Barclay, R. S., Wing, S. L., 2016. Improving the Ginkgo CO2 Barometer: Implications for the Early Cenozoic Atmosphere. *Earth and Planetary Science Letters*, Vol. **439**, p. 158–171. (Cité en page 6)

Barker, S., Greaves, M., Elderfield, H., 2003. A Study of Cleaning Procedures Used for Foraminiferal Mg/Ca Paleothermometry: MG/CA PALEOTHERMOMETRY. *Geochem. Geophys. Geosystems*, Vol. **4**(9), p. n/a–n/a. (Cité en pages 117, 118, 137, 144, 147 et 169)

Barnosky, A. D., Matzke, N., Tomiya, S., Wogan, G. O. U., Swartz, B., Quental, T. B., Marshall, C., McGuire, J. L., Lindsey, E. L., Maguire, K. C., Mersey, B., Ferrer, E. A., 2011. Has the Earth's Sixth Mass Extinction Already Arrived? *Nature*, Vol. **471**(7336), p. 51–57. (Cité en page 5)

Baroni, M., Thiemens, M. H., Delmas, R. J., Savarino, J., 2007. Mass-Independent Sulfur Isotopic Compositions in Stratospheric Volcanic Eruptions. *Science*, Vol. **315**(5808), p. 84–87. (Cité en page 166)

Bartdorff, O., Wallmann, K., Latif, M., Semenov, V., 2008. Phanerozoic Evolution of Atmospheric Methane: PHANEROZOIC EVOLUTION OF ATMOSPHERIC CH $_4$. *Global Biogeochem. Cycles*, Vol. **22**(1), p. n/a–n/a. (Cité en page 2)

Barth, S., 1993. Boron Isotope Variations in Nature: A Synthesis. *Geol Rundsch*, Vol. **82**(4). (Cité en page 17)

Bassinot, F. C., Labeyrie, L. D., Vincent, E., Quidelleur, X., Shackleton, N. J., Lancelot, Y., 1994. The Astronomical Theory of Climate and the Age of the Brunhes-Matuyama Magnetic Reversal. *Earth and Planetary Science Letters*, Vol. **126**(1), p. 91–108. (Cité en page 173)

Bazzano, A., Latruwe, K., Grotti, M., Vanhaecke, F., 2017. Determination of the Isotopic Composition of Sub-Ng Amounts of Sr in Antarctic Snow by Multi-Collector ICP-Mass Spectrometry. *J. Anal. At. Spectrom.*, Vol. **32**(5), p. 1004–1008. (Cité en page 127)

Becker, J. S., Dietze, H. J., McLean, J. A., Montaser, A., 1999. Ultratrace and Isotope Analysis of Long-Lived Radionuclides by Inductively Coupled Plasma Quadrupole Mass Spectrometry Using a Direct Injection High Efficiency Nebulizer. *Anal Chem*, Vol. **71**(15), p. 3077–3084. (Cité en page 95)

Beerling, D. J., Fox, A., Stevenson, D. S., Valdes, P. J., 2011. Enhanced Chemistry-Climate Feedbacks in Past Greenhouse Worlds. *PNAS*, Vol. **108**(24), p. 9770–9775. (Cité en page 2)

Belmaker, R., Lazar, B., Beer, J., Christl, M., Tepelyakov, N., Stein, M., 2013. 10Be Dating of Neogene Halite. *Geochim. Cosmochim. Acta*, Vol. **122**, p. 418–429. (Cité en pages 67 et 68)

Bendahl, L., Gammelgaard, B., Jøns, O., Farver, O., Honorè Hansen, S., 2001. Interfacing Capillary Electrophoresis with Inductively Coupled Plasma Mass Spectrometry by Direct Injection Nebulization for Selenium Speciation. *J. Anal. At. Spectrom.*, Vol. **16**(1), p. 38–42. (Cité en page 95)

Bentov, S., Erez, J., 2005. Novel Observations on Biomineralization Processes in Foraminifera and Implications for Mg/Ca Ratio in the Shells. *Geology*, Vol. **33**(11), p. 841. (Cité en page 144)

Bereiter, B., Lüthi, D., Siegrist, M., Schüpbach, S., Stocker, T. F., Fischer, H., 2012. Mode Change of Millennial CO2 Variability during the Last Glacial Cycle Associated with a Bipolar Marine Carbon Seesaw. *PNAS*, Vol. **109**(25), p. 9755–9760. (Cité en pages xxxii, 176 et 177)

Bernardin, M., Bessueille-Barbier, F., Le Masle, A., Lienemann, C.-P., Heinisch, S., 2018. Suitable Interface for Coupling Liquid Chromatography to Inductively Coupled Plasma-Mass Spectrometry for the Analysis of Organic Matrices. 1 Theoretical and Experimental Considerations on Solute Dispersion. *Journal of Chromatography A*, Vol. **1565**, p. 68–80. (Cité en page 95)

Berner, R. A., 1991. A Model for Atmospheric CO 2 over Phanerozoic Time. *Am. J. Sci.*, Vol. **291**(4), p. 339–376. (Cité en page 57)

Berner, R. A., 1992. Weathering, Plants, and the Long-Term Carbon Cycle. *Geochimica et Cosmochimica Acta*, Vol. **56**, p. 3225–3231. (Cité en page 3)

Berner, R. A., 2004. *The Phanerozoic Carbon Cycle: CO_2 and O_2*. Oxford University Press, Oxford ; New York. (Cité en pages 8, 37 et 54)

Berner, R. A., 2006. GEOCARBSULF: A Combined Model for Phanerozoic Atmospheric O2 and CO2. *Geochimica et Cosmochimica Acta*, Vol. **70**(23), p. 5653–5664. (Cité en pages 2, 8 et 37)

Berner, R. A., Lasaga, A. C., Garrels, R. M., 1983. The Carbonate-Silicate Geochemical Cycle and Its Effect on Atmospheric Carbon Dioxide over the Past 100 Million Years. *Am. J. Sci.*, Vol. **283**(7), p. 641–683. (Cité en pages 8, 59 et 61)

Berner, R. A., Mackenzie, F. T., 2011. Burial and Preservation of Carbonate Rocks Over Phanerozoic Time. *Aquat. Geochem.*, Vol. **17**(4-5), p. 727–733. (Cité en pages xxiv, 37, 38 et 53)

Bijma, J., Pörtner, H.-O., Yesson, C., Rogers, A. D., 2013. Climate Change and the Oceans – What Does the Future Hold? *Mar. Pollut. Bull.*, Vol. **74**(2), p. 495–505. (Cité en page 15)

Black, B. A., Neely, R. R., Lamarque, J.-F., Elkins-Tanton, L. T., Kiehl, J. T., Shields, C. A., Mills, M. J., Bardeen, C., 2018. Systemic Swings in End-Permian Climate from Siberian Traps Carbon and Sulfur Outgassing. *Nat. Geosci.*, Vol. **11**(12), p. 949–954. (Cité en page 163)

Bourquin, S., Poli, E., Durand, M., Courel, L., 1995. Stratigraphie Des Evaporites Du Trias Francais; Exemple de Sequences de Depot Des Series Carniennes et Leur Cadre Morpho-Structural. *Bulletin de la Société Géologique de France*, Vol. **166**(5), p. 493–505. (Cité en page 69)

Bowring, S. A., Grotzinger, J. P., Condon, D. J., Ramezani, J., Newall, M. J., Allen, P. A., 2007. Geochronologic Constraints on the Chronostratigraphic Framework of the Neoproterozoic Huqf Supergroup, Sultanate of Oman. *Am. J. Sci.*, Vol. **307**(10), p. 1097–1145. (Cité en pages 73 et 74)

Brand, U., Veizer, J., 1980. Chemical Diagenesis of a Multicomponent Carbonate System - 1. Trace Elements. *Journal of Sedimentary Petrology*, Vol. **50**, p. 1219–1236. (Cité en page 82)

Brand, U., Veizer, J., 1981. Chemical Diagenesis of a Multicomponent Carbonate System; 2, Stable Isotopes. *Journal of sedimentary petrology*, Vol. **51**, p. 987–997. (Cité en page 82)

Branson, O., Kaczmarek, K., Redfern, S. A., Misra, S., Langer, G., Tyliszczak, T., Bijma, J., Elderfield, H., 2015. The Coordination and Distribution of B in Foraminiferal Calcite. *Earth Planet. Sci. Lett.*, Vol. **416**, p. 67–72. (Cité en pages 21 et 144)

Breecker, D. O., Sharp, Z. D., McFadden, L. D., 2010. Atmospheric CO2 Concentrations during Ancient Greenhouse Climates Were Similar to Those Predicted for A.D. 2100. *PNAS*, Vol. **107**(2), p. 576–580. (Cité en page 7)

Brennan, S. T., Lowenstein, T. K., 2002. The Major-Ion Composition of Silurian Seawater. *Geochim. Cosmochim. Acta*, Vol. **66**(15), p. 2683–2700. (Cité en pages xxvi, 61, 75, 77 et 78)

Brennan, S. T., Lowenstein, T. K., Cendon, D. I., 2013. The Major-Ion Composition of Cenozoic Seawater: The Past 36 Million Years from Fluid Inclusions in Marine Halite. *Am. J. Sci.*, Vol. **313**(8), p. 713–775. (Cité en pages xxvi, 31, 47, 61, 74, 75, 77 et 78)

Brennan, S. T., Lowenstein, T. K., Horita, J., 2004. Seawater Chemistry and the Advent of Biocalcification. *Geology*, Vol. **32**(6), p. 473. (Cité en pages xxvi, 31, 61 et 75)

Broughton, P. L., 2018. Orogeny and the Collapse of the Devonian Prairie Evaporite Karst in Western Canada: Impact on the Overlying Cretaceous Athabasca Oil Sands. *Geol. Soc. Lond. Spec. Publ.*, Vol. **466**(1), p. 25–78. (Cité en pages xxvii, 70 et 71)

Burgess, S. D., Bowring, S. A., 2015. High-Precision Geochronology Confirms Voluminous Magmatism before, during, and after Earth's Most Severe Extinction. *Am. Assoc. Adv. Sci. AAAS*. (Cité en pages 59 et 163)

Caldeira, K., Wickett, M. E., 2003. Anthropogenic Carbon and Ocean pH: Oceanography. *Nature*, Vol. **425**(6956), p. 365–365. (Cité en page 114)

Caminade, C., McIntyre, K. M., Jones, A. E., 2019. Impact of Recent and Future Climate Change on Vector-Borne Diseases: Climate Change and Vector-Borne Diseases. *Ann. N. Y. Acad. Sci.*, Vol. **1436**(1), p. 157–173. (Cité en page 5)

Carlson, S. J., 2016. The Evolution of Brachiopoda. *Annu. Rev. Earth Planet. Sci.*, Vol. **44**(1), p. 409–438. (Cité en page 82)

Caron, B., del Manzo, G., Villemant, B., Bartolini, A., Moreno, E., Le Friant, A., Bassinot, F., Baudin, F., submitted. The Young Toba Tuff: A Multiple or a Single Cataclysmic Eruption Story? *Nat. Commun.* (Cité en pages xxxii, 166, 167, 168, 171, 172, 173, 174, 176 et 177)

Catanzaro, E. J., Champion, C. E., Garner, E. L., Marinenko, G., Sappenfield, K. M., Shields, W. R., 1970. Standard Reference Materials : Boric Acid; Isotopic, and Assay Standard Reference Materials. *US Natl. Bur. Stand. Spec. Publ.*, Vol. **260**, p. 17–70. (Cité en pages xxx, 30, 33, 37, 100, 117, 126 et 149)

Cathro, D. L., Warren, J. K., Williams, G. E., 1992. Halite Saltern in the Canning Basin, Western Australia: A Sedimentological Analysis of Drill Core from the Ordovician-Silurian Mallowa Salt. *Sedimentology*, Vol. **39**(6), p. 983–1002. (Cité en page 71)

Caves Rugenstein, J. K., Ibarra, D. E., von Blanckenburg, F., 2019. Neogene Cooling Driven by Land Surface Reactivity Rather than Increased Weathering Fluxes. *Nature*, Vol. **571**(7763), p. 99–102. (Cité en page 51)

Cerling, T. E., 1991. Carbon Dioxide in the Atmosphere; Evidence from Cenozoic and Mesozoic Paleosols. *Am. J. Sci.*, Vol. **291**(4), p. 377–400. (Cité en page 7)

Cerling, T. E., 1992. Use of Carbon Isotopes in Paleosols as an Indicator of the P(CO2) of the Paleoatmosphere. *Global Biogeochemical Cycles*, Vol. **6**, p. 307–314. (Cité en page 7)

Chalk, T., Foster, G., Wilson, P., 2019. Dynamic Storage of Glacial CO2 in the Atlantic Ocean Revealed by Boron [CO 3 2 -] and pH Records. *Earth Planet. Sci. Lett.*, Vol. **510**, p. 1–11. (Cité en page 10)

Chalk, T. B., Hain, M. P., Foster, G. L., Rohling, E. J., Sexton, P. F., Badger, M. P. S., Cherry, S. G., Hasenfratz, A. P., Haug, G. H., Jaccard, S. L., Martínez-García, A., Pälike, H., Pancost, R. D., Wilson, P. A., 2017. Causes of Ice Age Intensification across the Mid-Pleistocene Transition. *Proc. Natl. Acad. Sci.*, Vol. **114**(50), p. 13114–13119. (Cité en pages 29 et 114)

Chesner, C. A., 2012. The Toba Caldera Complex. *Quaternary International*, Vol. **258**, p. 5–18. (Cité en pages xxxii, 164 et 165)

Chetelat, B., Gaillardet, J., Freydier, R., Negrel, P., 2005. Boron Isotopes in Precipitation: Experimental Constraints and Field Evidence from French Guiana. *Earth Planet. Sci. Lett.*, Vol. **235**(1-2), p. 16–30. (Cité en page 133)

Chetelat, B., Liu, C.-Q., Gaillardet, J., Wang, Q., Zhao, Z., Liang, C., Xiao, Y., 2009. Boron Isotopes Geochemistry of the Changjiang Basin Rivers. *Geochim. Cosmochim. Acta*, Vol. **73**(20), p. 6084–6097. (Cité en pages xxiv, 35 et 36)

Cheung, W. W. L., Watson, R., Pauly, D., 2013. Signature of Ocean Warming in Global Fisheries Catch. *Nature*, Vol. **497**(7449), p. 365–368. (Cité en page 15)

Clarkson, M. O., Kasemann, S. A., Wood, R. A., Lenton, T. M., Daines, S. J., Richoz, S., Ohnemueller, F., Meixner, A., Poulton, S. W., Tipper, E. T., 2015. Ocean Acidification and the Permo-Triassic Mass Extinction. *Science*, Vol. **348**(6231), p. 229–232. (Cité en pages xxv, xxviii, 28, 31, 46, 51, 58, 82, 83, 114 et 145)

Cobb, K. M., Orland, I. J., Carolin, S., Adkins, J. F., Valley, J. W., Jersild, A., LeGrande, A. N., Colose, C., 2017. Borneo Stalagmites Reveal Climatic Excursions Associated with Toba Ash Layers Prior to Greenland Stadial 20. *AGU Fall Meeting Abstracts*, Vol. **21**. (Cité en page 167)

Cocks, L. R. M., Torsvik, T. H., 2007. Siberia, the Wandering Northern Terrane, and Its Changing Geography through the Palaeozoic. *Earth-Sci. Rev.*, Vol. **82**(1-2), p. 29–74. (Cité en pages xxvii, 72 et 73)

Cogné, J.-P., Humler, E., 2004. Temporal Variation of Oceanic Spreading and Crustal Production Rates during the Last 180 My. *Earth Planet. Sci. Lett.*, Vol. **227**(3-4), p. 427–439. (Cité en pages xxvi, 54 et 57)

Cogné, J.-P., Humler, E., 2006. Trends and Rhythms in Global Seafloor Generation Rate: SEAFLOOR GENERATION RATE. *Geochem. Geophys. Geosystems*, Vol. **7**(3), p. n/a–n/a. (Cité en pages xxvi, 54 et 57)

Coltice, N., Seton, M., Rolf, T., Müller, R., Tackley, P., 2013. Convergence of Tectonic Reconstructions and Mantle Convection Models for Significant Fluctuations in Seafloor Spreading. *Earth Planet. Sci. Lett.*, Vol. **383**, p. 92–100. (Cité en pages xxvi et 54)

Costa, A., Smith, V. C., Macedonio, G., Matthews, N. E., 2014. The Magnitude and Impact of the Youngest Toba Tuff Super-Eruption. *Front. Earth Sci.*, Vol. **2**, p. 16. (Cité en pages 164 et 166)

Courtillot, V. E., Renne, P. R., 2003. On the Ages of Flood Basalt Events. *Comptes Rendus Geoscience*, Vol. **335**(1), p. 113–140. (Cité en page 163)

Crick, L., Burke, A., Hutchison, W., Kohno, M., Moore, K. A., Savarino, J., Doyle, E. A., Mahony, S., Kipfstuhl, S., Rae, J. W. B., Steele, R. C. J., Sparks, R. S. J., Wolff, E. W., 2021. New Insights into the ~74 Ka Toba Eruption from Sulfur Isotopes of Polar Ice Cores. *Clim. Past Discuss.*, p. 1–28. (Cité en page 166)

Crutzen, P. J., 2002. Geology of Mankind. *Nature*, Vol. **415**(6867), p. 23–23. (Cité en page 3)

Dang, H., Jian, Z., Wu, J., Bassinot, F., Wang, T., Kissel, C., 2018. The Calcification Depth and Mg/Ca Thermometry of Pulleniatina Obliquiloculata in the Tropical Indo-Pacific: A Core-Top Study. *Mar. Micropaleontol.*, Vol. **145**, p. 28–40. (Cité en pages 168 et 175)

Dansgaard, W., Johnsen, S. J., Clausen, H. B., Dahl-Jensen, D., Gundestrup, N. S., Hammer, C. U., Hvidberg, C. S., Steffensen, J. P., Sveinbjörnsdottir, A. E., Jouzel, J., Bond, G., 1993. Evidence for General Instability of Past Climate from a 250-Kyr Ice-Core Record. *Nature*, Vol. **364**(6434), p. 218. (Cité en pages 2, 6 et 10)

Davis, C. V., Rivest, E. B., Hill, T. M., Gaylord, B., Russell, A. D., Sanford, E., 2017. Ocean Acidification Compromises a Planktic Calcifier with Implications for Global Carbon Cycling. *Sci. Rep.*, Vol. **7**(1), p. 2225. (Cité en pages 168 et 178)

Day, J., Uyeno, T., Norris, W., Witzke, B. J., Bunker, B. J., 1996. Middle-Upper Devonian Relative Sea-Level Histories of Central and Western North American Interior Basins. *Dans : Special Paper 306: Paleozoic Sequence Stratigraphy; Views from the North American Craton*. Vol. 306. Geological Society of America, p. 259–275. (Cité en page 70)

De Hoog, J. C. M., Savov, I. P., 2018. Boron Isotopes as a Tracer of Subduction Zone Processes. *Dans : Marschall, H., Foster, G. (Eds.), Boron Isotopes*. Springer International Publishing, Cham, p. 217–247. (Cité en page 114)

de la Vega, E., Chalk, T. B., Wilson, P. A., Bysani, R. P., Foster, G. L., 2020. Atmospheric CO2 during the Mid-Piacenzian Warm Period and the M2 Glaciation. *Sci. Rep.*, Vol. **10**(1). (Cité en page 29)

de Moel, H., Ganssen, G. M., Peeters, F. J. C., Jung, S. J. A., Kroon, D., Brummer, G. J. A., Zeebe, R. E., 2009. Planktic Foraminiferal Shell Thinning in the Arabian Sea Due to Anthropogenic Ocean Acidification? *Biogeosciences*, Vol. **6**(9), p. 1917–1925. (Cité en page 178)

de Nooijer, L., Spero, H., Erez, J., Bijma, J., Reichart, G., 2014. Biomineralization in Perforate Foraminifera. *Earth-Sci. Rev.*, Vol. **135**, p. 48–58. (Cité en pages 24 et 144)

De'ath, G., Lough, J. M., Fabricius, K. E., 2009. Declining Coral Calcification on the Great Barrier Reef. *Science*, Vol. **323**(5910), p. 116–119. (Cité en page 15)

Degueldre, C., Favarger, P. Y., Wold, S., 2006. Gold Colloid Analysis by Inductively Coupled Plasma-Mass Spectrometry in a Single Particle Mode. *Analytica Chimica Acta*, Vol. **555**(2), p. 263–268. (Cité en page 107)

del Manzo, G., 2018. *Reconstruction de l'histoire Éruptive de La Dernière Éruption de Toba, Sumatra (YTT, 74 Kyr) Par Étude Téphrochrono-Stratigraphique*. Rapport de stage Master 2 en Géochimie, Géobiologie, Géomatériaux et Environnement (3GE), Université de Paris, Institut de physique du globe de Paris. (Cité en pages xxxii, 167, 171, 172, 173, 174, 176 et 177)

Delaney, M. L., W.H.Bé, A., Boyle, E. A., 1985. Li, Sr, Mg, and Na in Foraminiferal Calcite Shells from Laboratory Culture, Sediment Traps, and Sediment Cores. *Geochimica et Cosmochimica Acta*, Vol. **49**(6), p. 1327–1341. (Cité en page 144)

Dellinger, M., Hilton, R. G., Nowell, G. M., 2020. Measurements of Rhenium Isotopic Composition in Low-Abundance Samples. *J. Anal. At. Spectrom.*, Vol. **35**(2), p. 377–387. (Cité en pages xxx, 127 et 128)

Demicco, R. V., Lowenstein, T. K., Hardie, L. A., Spencer, R. J., 2005. Model of Seawater Composition for the Phanerozoic. *Geology*, Vol. **33**(11), p. 877. (Cité en pages xxvi et 61)

Dickson, A. G., 1990. Thermodynamics of the Dissociation of Boric Acid in Synthetic Seawater from 273.15 to 318.15 K. *Deep Sea Res. Part Oceanogr. Res. Pap.*, Vol. **37**(5), p. 755–766. (Cité en pages 30, 144 et 156)

Domeier, M., Torsvik, T. H., 2014. Plate Tectonics in the Late Paleozoic. *Geosci. Front.*, Vol. **5**(3), p. 303–350. (Cité en pages xxvii et 71)

Doney, S. C., Fabry, V. J., Feely, R. A., Kleypas, J. A., 2009. Ocean Acidification: The Other CO $_2$ Problem. *Annu. Rev. Mar. Sci.*, Vol. **1**(1), p. 169–192. (Cité en pages 15 et 29)

Doney, S. C., Mahowald, N., Lima, I., Feely, R. A., Mackenzie, F. T., Lamarque, J.-F., Rasch, P. J., 2007. Impact of Anthropogenic Atmospheric Nitrogen and Sulfur Deposition on Ocean Acidification and the Inorganic Carbon System. *PNAS*, Vol. **104**(37), p. 14580–14585. (Cité en pages 163, 164 et 168)

d'Orbigny, A., 1826. *Tableau Méthodique de La Classe Des Céphalopodes*. Vol. 7 de Annales Des Sciences Naturelles, p. 96–169 & 245–314. (Cité en page 146) d'Orbigny, A., 1839. Foraminifères. *Dans : Histoire Physique, Politique et Naturelle de l'Ile de Cuba*. Arthus Bertrand, Paris, p. 1–51. (Cité en page 171)

East, M., Müller, R. D., Williams, S., Zahirovic, S., Heine, C., 2020. Subduction History Reveals Cretaceous Slab Superflux as a Possible Cause for the Mid-Cretaceous Plume Pulse and Superswell Events. *Gondwana Res.*, Vol. **79**, p. 125–139. (Cité en pages xxvi, 54 et 55)

Eastoe, C., Long, A., Land, L. S., Kyle, J., 2001. Stable Chlorine Isotopes in Halite and Brine from the Gulf Coast Basin: Brine Genesis and Evolution. *Chem. Geol.*, Vol. **176**(1-4), p. 343–360. (Cité en page 75)

Eastoe, C., Peryt, T., Petrychenko, O. Y., Geisler-Cussey, D., 2007. Stable Chlorine Isotopes in Phanerozoic Evaporites. *Appl. Geochem.*, Vol. **22**(3), p. 575–588. (Cité en page 75)

Eggenkamp, H., Bonifacie, M., Ader, M., Agrinier, P., 2016. Experimental Determination of Stable Chlorine and Bromine Isotope Fractionation during Precipitation of Salt from a Saturated Solution. *Chemical Geology*, Vol. **433**, p. 46–56. (Cité en page 185)

Eggenkamp, H., Kreulen, R., Koster Van Groos, A., 1995. Chlorine Stable Isotope Fractionation in Evaporites. *Geochim. Cosmochim. Acta*, Vol. **59**(24), p. 5169–5175. (Cité en page 75)

Eggenkamp, H., Louvat, P., Agrinier, P., Bonifacie, M., Bekker, A., Krupenik, V., Griffioen, J., Horita, J., Brocks, J., Bagheri, R., 2019a. The Bromine and Chlorine Isotope Composition of Primary Halite Deposits and Their Significance for the Secular Isotope Composition of Seawater. *Geochim. Cosmochim. Acta*, Vol. **264**, p. 13–29. (Cité en pages 43, 45, 48 et 75)

Eggenkamp, H., Louvat, P., Griffioen, J., Agrinier, P., 2019b. Chlorine and Bromine Isotope Evolution within a Fully Developed Upper Permian Natural Salt Sequence. *Geochim. Cosmochim. Acta*, Vol. **245**, p. 316–326. (Cité en page 49)

Ekart, D. D., Cerling, T. E., Montanez, I. P., Tabor, N. J., 1999. A 400 Million Year Carbon Isotope Record of Pedogenic Carbonate: Implications for Paleoatmospheric Carbon Dioxide. *Am. J. Sci.*, Vol. **299**(10). (Cité en page 7)

Elderfield, H., 1996. A Biomineralization Model for the Incorporation of Trace Elements into Foraminiferal Calcium Carbonate. *Earth Planet. Sci. Lett.*, Vol. **142**(3-4), p. 409–423. (Cité en page 144)

Elderfield, H., Ganssen, G., 2000. Past Temperature and δ 18 O of Surface Ocean Waters Inferred from Foraminiferal Mg/Ca Ratios. *Nature*, Vol. **405**(6785), p. 442–445. (Cité en page 175)

Emiliani, C., 1955. Pleistocene Temperatures. *J. Geol.*, Vol. **63**(6), p. 538–578. (Cité en page 143)

Engebretson, D. C., Kelley, K. P., Cashman, H. J., Richards, M. A., 1992. 180 Million Years of Subduction. *GSA Today Geol Soc Am*, Vol. **2**(5), p. 93–100. (Cité en pages xxvi, 54 et 55)

Epov, V. N., Berail, S., Jimenez-Moreno, M., Perrot, V., Pecheyran, C., Amouroux, D., Donard, O. F. X., 2010. Approach to Measure Isotopic Ratios in Species Using Multicollector-ICPMS Coupled with Chromatography. *Anal. Chem.*, Vol. **82**(13), p. 5652–5662. (Cité en pages 106 et 151)

Epstein, S., Buchsbaum, R., Lowenstam, H. A., Urey, H. C., 1953. REVISED CARBONATE-WATER ISOTOPIC TEMPERATURE SCALE. *GSA Bulletin*, Vol. **64**(11), p. 1315–1326. (Cité en page 143)

Erez, J., 2003. The Source of Ions for Biomineralization in Foraminifera and Their Implications for Paleoceanographic Proxies. *Reviews in Mineralogy and Geochemistry*, Vol. **54**, p. 115–149. (Cité en pages 24, 144 et 175)

Evans, D., Müller, W., Erez, J., 2018. Assessing Foraminifera Biomineralisation Models through Trace Element Data of Cultures under Variable Seawater Chemistry. *Geochim. Cosmochim. Acta*, Vol. **236**, p. 198–217. (Cité en page 144)

Evans, D., Wade, B. S., Henehan, M., Erez, J., Müller, W., 2016. Revisiting Carbonate Chemistry Controls on Planktic Foraminifera Mg / Ca: Implications for Sea Surface Temperature and Hydrology Shifts over the Paleocene–Eocene Thermal Maximum and Eocene–Oligocene Transition. *Clim. Past*, Vol. **12**(4), p. 819–835. (Cité en page 175)

Fan, Q., Ma, Y., Cheng, H., Wei, H., Yuan, Q., Qin, Z., Shan, F., 2015. Boron Occurrence in Halite and Boron Isotope Geochemistry of Halite in the Qarhan Salt Lake, Western China. *Sediment. Geol.*, Vol. **322**, p. 34–42. (Cité en pages 31, 32, 45 et 48)

Fanlo, I., Ayora, C., 1998. The Evolution of the Lorraine Evaporite Basin: Implications for the Chemical and Isotope Composition of the Triassic Ocean. *Chem. Geol.*, Vol. **146**(3-4), p. 135–154. (Cité en page 69)

Farmer, J. R., Hönisch, B., Uchikawa, J., 2016. Single Laboratory Comparison of MC-ICP-MS and N-TIMS Boron Isotope Analyses in Marine Carbonates. *Chem. Geol.*, Vol. **447**, p. 173–182. (Cité en pages 115 et 145)

Feely, R. A., 2004. Impact of Anthropogenic CO2 on the CaCO3 System in the Oceans. *Science*, Vol. **305**(5682), p. 362–366. (Cité en page 178)

Feng, C., Gao, C., Yin, Q.-Z., Jacobsen, B., Renne, P. R., Wang, J., Chang, S.-C., 2018. Tracking Physicochemical Conditions of Evaporite Deposition by Stable Magnesium Isotopes: A Case Study of Late Permian Langbeinites. *Geochem. Geophys. Geosystems*, Vol. **19**(8), p. 2615–2630. (Cité en pages xxvii et 70)

Feulner, G., 2012. The Faint Young Sun Problem. *Rev. Geophys.*, Vol. **50**(2). (Cité en page 2)

Fietzke, J., Liebetrau, V., Günther, D., Gürs, K., Hametner, K., Zumholz, K., Hansteen, T. H., Eisenhauer, A., 2008. An Alternative Data Acquisition and Evaluation Strategy for Improved Isotope Ratio Precision Using LA-MC-ICP-MS Applied to Stable and Radiogenic Strontium Isotopes in Carbonates. *J. Anal. At. Spectrom.*, Vol. **23**(7), p. 955. (Cité en page 151)

Fietzke, J., Ragazzola, F., Halfar, J., Dietze, H., Foster, L. C., Hansteen, T. H., Eisenhauer, A., Steneck, R. S., 2015. Century-Scale Trends and Seasonality in pH and Temperature for Shallow Zones of the Bering Sea. *Proc Natl Acad Sci USA*, Vol. **112**(10), p. 2960–2965. (Cité en page 114)

Fischer, L., Zipfel, B., Koellensperger, G., Kovac, J., Bilz, S., Kunkel, A., Venzago, C., Hann, S., 2014. Flow Injection Combined with ICP-MS for Accurate High Throughput Analysis of Elemental Impurities in Pharmaceutical Products According to USP <232>/<233>. *Journal of Pharmaceutical and Biomedical Analysis*, Vol. **95**, p. 121–129. (Cité en page 96)

Foster, G., 2008. Seawater pH, pCO2 and [CO2-3] Variations in the Caribbean Sea over the Last 130 Kyr: A Boron Isotope and B/Ca Study of Planktic Foraminifera. *Earth Planet. Sci. Lett.*, Vol. **271**(1-4), p. 254–266. (Cité en pages xxx, 10, 11, 22, 24, 29, 93, 114, 115, 123, 132, 137, 144, 145 et 157)

Foster, G. L., Hönisch, B., Paris, G., Dwyer, G. S., Rae, J. W., Elliott, T., Gaillardet, J., Hemming, N. G., Louvat, P., Vengosh, A., 2013. Interlaboratory Comparison of Boron Isotope Analyses of Boric Acid, Seawater and Marine CaCO3 by MC-ICPMS and NTIMS. *Chem. Geol.*, Vol. **358**, p. 1–14. (Cité en pages 33, 133 et 145)

Foster, G. L., Lear, C. H., Rae, J. W., 2012. The Evolution of pCO2, Ice Volume and Climate during the Middle Miocene. *Earth Planet. Sci. Lett.*, Vol. **341–344**, p. 243–254. (Cité en pages xxv, xxvii, 29, 30, 44, 79, 80 et 81)

Foster, G. L., Marschall, H. R., Palmer, M. R., 2018. Boron Isotope Analysis of Geological Materials. *Dans : Marschall, H., Foster, G. (Eds.), Boron Isotopes*. Springer International Publishing, Cham, p. 13–31. (Cité en pages 114 et 145)

Foster, G. L., Ni, Y., Haley, B., Elliott, T., 2006. Accurate and Precise Isotopic Measurement of Sub-Nanogram Sized Samples of Foraminiferal Hosted Boron by Total Evaporation NTIMS. *Chem. Geol.*, Vol. **230**(1-2), p. 161–174. (Cité en pages 114 et 145)

Foster, G. L., Pogge von Strandmann, P. A. E., Rae, J. W. B., 2010. Boron and Magnesium Isotopic Composition of Seawater: DATA BRIEF. *Geochem. Geophys. Geosystems*, Vol. **11**(8), p. n/a–n/a. (Cité en pages xxiv, 19, 28, 30, 33, 35, 36 et 156)

Foster, G. L., Rae, J. W., 2016. Reconstructing Ocean pH with Boron Isotopes in Foraminifera. *Annu. Rev. Earth Planet. Sci.*, Vol. **44**(1), p. 207–237. (Cité en pages xxiv, 18, 19 et 21)

Foster, G. L., Royer, D. L., Lunt, D. J., 2017. Future Climate Forcing Potentially without Precedent in the Last 420 Million Years. *Nat. Commun.*, Vol. **8**, p. 14845. (Cité en pages xxiii, 3, 9 et 10)

Fox, L., Stukins, S., Hill, T., Miller, C. G., 2020. Quantifying the Effect of Anthropogenic Climate Change on Calcifying Plankton. *Sci Rep*, Vol. **10**(1), p. 1620. (Cité en page 15)

François, L., Goddéris, Y., 1998. Isotopic Constraints on the Cenozoic Evolution of the Carbon Cycle. *Chem. Geol.*, Vol. **145**(3-4), p. 177–212. (Cité en page 54)

Freeman, K. H., Hayes, J. M., 1992. Fractionation of Carbon Isotopes by Phytoplankton and Estimates of Ancient CO2 Levels. *Glob. Biogeochem. Cycles*, Vol. **6**(2), p. 185–198. (Cité en page 8)

Freund, R., Garfunkel, Z., Zak, I., Goldberg, M., Weissbrod, T., Derin, B., Bender, F., Wellings, F. E., Girdler, R. W., 1970. The Shear along the Dead Sea Rift [and Discussion]. *Philos. Trans. R. Soc. Lond. Ser. Math. Phys. Sci.*, Vol. **267**(1181), p. 107–130. (Cité en page 68)

Gaffin, S., 1987. Ridge Volume Dependence on Seafloor Generation Rate and Inversion Using Long Term Sealevel Change. *Am. J. Sci.*, Vol. **287**(6), p. 596–611. (Cité en pages xxvi, 55 et 56)

Gaillardet, J., Allègre, C. J., C. J., 1995. Boron Isotopic Compositions of Corals: Seawater or Diagenesis Record? *Earth Planet. Sci. Lett.*, Vol. **136**(3-4), p. 665–676. (Cité en page 145)

Gaillardet, J., Dupré, B., Louvat, P., Allègre, C. J., 1999. Global Silicate Weathering and CO2 Consumption Rates Deduced from the Chemistry of Large Rivers. *Chemical Geology*, Vol. **159**(1), p. 3–30. (Cité en page 59)

Gaillardet, J., Lemarchand, D., 2018. Boron in the Weathering Environment. *Dans : Marschall, H., Foster, G. (Eds.), Boron Isotopes*. Springer International Publishing, Cham, p. 163–188. (Cité en pages 30, 36, 37, 49, 50, 78 et 114)

Gaillardet, J., Lemarchand, D., Göpel, C., Manhès, G., 2001. Evaporation and Sublimation of Boric Acid: Application for Boron Purification from Organic Rich Solutions. *Geostand. Geoanalytical Res.*, Vol. **25**(1), p. 67–75. (Cité en pages xxix, 115, 116, 118, 131, 133, 146 et 148)

Galy, A., Belshaw, N. S., Halicz, L., O'Nions, R. K., 2001. High-Precision Measurement of Magnesium Isotopes by Multiple-Collector Inductively Coupled Plasma Mass Spectrometry. *Int. J. Mass Spectrom.*, Vol. **208**(1), p. 89–98. (Cité en page 122)

García-Veigas, J., Rosell, L., Zak, I., Playà, E., Ayora, C., Starinsky, A., 2009. Evidence of Potash Salt Formation in the Pliocene Sedom Lagoon (Dead Sea Rift, Israel). *Chem. Geol.*, Vol. **265**(3-4), p. 499–511. (Cité en pages xxvi et 68)

Gazeau, F., Parker, L. M., Comeau, S., Gattuso, J.-P., O'Connor, W. A., Martin, S., Pörtner, H.-O., Ross, P. M., 2013. Impacts of Ocean Acidification on Marine Shelled Molluscs. *Mar. Biol.*, Vol. **160**(8), p. 2207–2245. (Cité en page 15)

Gibbs, M. T., 1999. Global Chemical Erosion over the Last 250 My; Variations Due to Changes in Paleogeography, Paleoclimate, and Paleogeology. *Am. J. Sci.*, Vol. **299**(7-9), p. 611–651. (Cité en pages xxvi, xxviii, 39, 56, 57, 86 et 87)

Goddéris, Y., Donnadieu, Y., Carretier, S., Aretz, M., Dera, G., Macouin, M., Regard, V., 2017. Onset and Ending of the Late Palaeozoic Ice Age Triggered by Tectonically Paced Rock Weathering. *Nat. Geosci.*, Vol. **10**(5), p. 382–386. (Cité en pages 61 et 62)

Goddéris, Y., Donnadieu, Y., Le Hir, G., Lefebvre, V., Nardin, E., 2014. The Role of Palaeogeography in the Phanerozoic History of Atmospheric CO2 and Climate. *Earth-Sci. Rev.*, Vol. **128**, p. 122–138. (Cité en pages xxiv, xxvi, xxviii, 8, 38, 39, 53, 56, 57, 62, 86 et 87)

Golonka, J., 2007. Late Triassic and Early Jurassic Palaeogeography of the World. *Palaeogeogr. Palaeoclimatol. Palaeoecol.*, Vol. **244**(1-4), p. 297–307. (Cité en page 69)

Gonzalez, C., 2014. *Quantification de l'acidification de l'océan par l'analyse géochimique des coraux profonds*. Thèse de doctorat, Paris-Sud, Laboratoire des Sciences du Climat et de l'Environnement (LSCE). (Cité en page 30)

Gordienko, I., 2006. Geodynamic Evolution of Late Baikalides and Paleozoides on the Folded Periphery of the Siberian Craton. *Geologiya i Geofizika*, Vol. **47**, p. 53–70. (Cité en page 72)

Gorin, G., Racz, L., Walter, M., 1982. Late Precambrian–Cambrian Sediments of Huqf Group, Sultanate of Oman. *American Association of Petroleum Geologists Bulletin*, Vol. **66**. (Cité en page 73)

Gou, L.-F., Jin, Z., Galy, A., Sun, H., Deng, L., Xu, Y., 2019. Effects of Cone Combinations on Accurate and Precise Mg-Isotopic Determination Using Multi-Collector Inductively Coupled Plasma Mass Spectrometry. *Rapid Commun. Mass Spectrom.*, Vol. **33**(4), p. 351–360. (Cité en pages 123 et 126)

Gou, L.-F., Jin, Z.-D., Deng, L., He, M.-Y., Liu, C.-Y., 2018. Effects of Different Cone Combinations on Accurate and Precise Determination of Li Isotopic Composition by MC-ICP-MS. *Spectrochim. Acta Part B At. Spectrosc.*, Vol. **146**, p. 1–8. (Cité en pages 123 et 126)

Gourgiotis, A., Manhès, G., Louvat, P., Moureau, J., Gaillardet, J., 2015. Transient Signal Isotope Analysis: Validation of the Method for Isotope Signal Synchronization with the Determination of Amplifier First-Order Time Constants. *Rapid Commun. Mass Spectrom.*, Vol. **29**(18), p. 1617–1622. (Cité en page 127)

Goyet, C., Healy, R., Ryan, J., Kozyr, A., 2000. *Global Distribution of Total Inorganic Carbon and Total Alkalinity below the Deepest Winter Mixed Layer Depths*. Rap. Tech. ORNL/CDIAC-127; NDP-076, Oak Ridge National Lab., TN (US). (Cité en page 156)

Gray, W. R., Evans, D., 2019. Nonthermal Influences on Mg/Ca in Planktonic Foraminifera: A Review of Culture Studies and Application to the Last Glacial Maximum. *Paleoceanogr. Paleoclimatology*, Vol. **34**(3), p. 306–315. (Cité en page 184)

Gray, W. R., Rae, J. W. B., Wills, R. C. J., Shevenell, A. E., Taylor, B., Burke, A., Foster, G. L., Lear, C. H., 2018. Deglacial Upwelling, Productivity and CO2 Outgassing in the North Pacific Ocean. *Nat. Geosci.*, Vol. **11**(5), p. 340–344. (Cité en pages 144, 175 et 179)

Greenop, R., Hain, M. P., Sosdian, S. M., Oliver, K. I. C., Goodwin, P., Chalk, T. B., Lear, C. H., Wilson, P. A., Foster, G. L., 2017. A Record of Neogene Seawater Δ^{11}B Reconstructed from Paired Δ^{11}B Analyses on Benthic and Planktic Foraminifera. *Clim. Past*, Vol. **13**(2), p. 149–170. (Cité en pages xxv, xxvii, xxviii, 30, 31, 44, 46, 80, 81, 83 et 127)

Greenop, R., Sosdian, S. M., Henehan, M. J., Wilson, P. A., Lear, C. H., Foster, G. L., 2019. Orbital Forcing, Ice Volume, and CO $_2$ Across the Oligocene-Miocene Transition. *Paleoceanogr. Paleoclimatology*, Vol. **34**(3), p. 316–328. (Cité en page 29)

Grishina, S., Dubessy, J., Kontorovich, A., Pironon, J., 1992. Inclusions in Salt Beds Resulting from Thermal Metamorphism by Dolerite Sills (Eastern Siberia, Russia). *Eur. J. Mineral.*, Vol. **4**(5), p. 1187–1202. (Cité en pages 49 et 72)

Grotti, M., Terol, A., Todolí, J. L., 2014. Speciation Analysis by Small-Bore HPLC Coupled to ICP-MS. *TrAC Trends in Analytical Chemistry*, Vol. **61**, p. 92–106. (Cité en page 95)

Gruber, N., Clement, D., Carter, B. R., Feely, R. A., van Heuven, S., Hoppema, M., Ishii, M., Key, R. M., Kozyr, A., Lauvset, S. K., Lo Monaco, C., Mathis, J. T., Murata, A., Olsen, A., Perez, F. F., Sabine, C. L., Tanhua, T., Wanninkhof, R., 2019. The Oceanic Sink for Anthropogenic CO $_2$ from 1994 to 2007. *Science*, Vol. **363**(6432), p. 1193–1199. (Cité en page 15)

Guex, J., Pilet, S., Müntener, O., Bartolini, A., Spangenberg, J., Schoene, B., Sell, B., Schaltegger, U., 2016. Thermal Erosion of Cratonic Lithosphere as a Potential Trigger for Mass-Extinction. *Sci. Rep.*, Vol. **6**(1), p. 23168. (Cité en page 163)

Guillermic, M., Misra, S., Eagle, R., Villa, A., Chang, F., Tripati, A., 2020. Seawater pH Reconstruction Using Boron Isotopes in Multiple Planktonic Foraminifera Species with Different Depth Habitats and Their Potential to Constrain pH and <I>P</I>CO<Sub>2</Sub> Gradients. *Biogeosciences*, Vol. **17**(13), p. 3487–3510. (Cité en pages 22, 144, 174 et 184)

Gutjahr, M., Bordier, L., Douville, E., Farmer, J., Foster, G. L., Hathorne, E. C., Hönisch, B., Lemarchand, D., Louvat, P., McCulloch, M., Noireaux, J., Pallavicini, N., Rae, J. W. B., Rodushkin, I., Roux, P., Stewart, J. A., Thil, F., You, C.-F., 2020. Sub-Permil Interlaboratory Consistency for Solution-Based Boron Isotope Analyses on Marine Carbonates. *Geostand. Geoanalytical Res.* (Cité en pages 33, 117, 133 et 138)

Gutjahr, M., Ridgwell, A., Sexton, P. F., Anagnostou, E., Pearson, P. N., Pälike, H., Norris, R. D., Thomas, E., Foster, G. L., 2017. Very Large Release of Mostly Volcanic Carbon during the Palaeocene–Eocene Thermal Maximum. *Nature*, Vol. **548**(7669), p. 573–577. (Cité en pages xxv, xxvii, 9, 29, 30, 44, 50, 80, 81, 145, 151 et 170)

Haines, P., Wingate, M., 2005. Contrasting Depositional Histories, Detrital Zircon Provenance and Hydrocarbon Systems: Did the Larapintine Seaway Link the Canning and Amadeus Basins during the Ordovician? *Dans : Northern Territory Geological Survey, Special Publication*. Vol. 2. (Cité en page 71)

Haines, P. W., Hand, M., Sandiford, M., 2001. Palaeozoic Synorogenic Sedimentation in Central and Northern Australia: A Review of Distribution and Timing with Implications for the Evolution of Intracontinental Orogens. *Aust. J. Earth Sci.*, Vol. **48**(6), p. 911–928. (Cité en page 71)

Hajj, F., Poszwa, A., Bouchez, J., Guérold, F., 2017. Radiogenic and "Stable" Strontium Isotopes in Provenance Studies: A Review and First Results on Archaeological Wood from Shipwrecks. *J. Archaeol. Sci.*, Vol. **86**, p. 24–49. (Cité en page 34)

Halevy, I., Bachan, A., 2017. The Geologic History of Seawater pH. *Science*, Vol. **355**(6329), p. 1069–1071. (Cité en page 47)

Halverson, G. P., Dudás, F. Ö., Maloof, A. C., Bowring, S. A., 2007. Evolution of the 87Sr/86Sr Composition of Neoproterozoic Seawater. *Palaeogeogr. Palaeoclimatol. Palaeoecol.*, Vol. **256**(3-4), p. 103–129. (Cité en pages xxv, xxvi, 41 et 61)

Haq, B. U., Schutter, S. R., 2008. A Chronology of Paleozoic Sea-Level Changes. *Science*, Vol. **322**(5898), p. 64–68. (Cité en pages 71 et 72)

Hardie, L. A., 1984. Evaporites; Marine or Non-Marine? *Am. J. Sci.*, Vol. **284**(3), p. 193–240. (Cité en page 74)

Hardie, L. A., 1996. Secular Variation in Seawater Chemistry: An Explanation for the Coupled Secular Variation in the Mineralogies of Marine Limestones and Potash Evaporites over the Past 600 m.y. *Geology*, Vol. **24**(3), p. 279. (Cité en pages xxvi, 31 et 61)

Harvie, C. E., Møller, N., Weare, J. H., 1984. The Prediction of Mineral Solubilities in Natural Waters: The Na-K-Mg-Ca-H-Cl-SO 4-OH-HCO 3-CO 3-CO 2-H 2O System to High Ionic Strengths at 25°C. *Geochimica et Cosmochimica Acta*, Vol. **48**, p. 723–751. (Cité en pages xxvii, 76 et 78)

Hathorne, E. C., Gagnon, A., Felis, T., Adkins, J., Asami, R., Boer, W., Caillon, N., Case, D., Cobb, K. M., Douville, E., deMenocal, P., Eisenhauer, A., Garbe-Schönberg, D., Geibert, W., Goldstein, S., Hughen, K., Inoue, M., Kawahata, H., Kölling, M., Cornec, F. L., Linsley, B. K., McGregor, H. V., Montagna, P., Nurhati, I. S., Quinn, T. M., Raddatz, J., Rebaubier, H., Robinson, L., Sadekov, A., Sherrell, R., Sinclair, D., Tudhope, A. W., Wei, G., Wong, H., Wu, H. C., You, C.-F., 2013. Interlaboratory Study for Coral Sr/Ca and Other Element/Ca Ratio Measurements: INTERLABORATORY STUDY FOR CORAL SR/CA. *Geochem. Geophys. Geosystems*, Vol. **14**(9), p. 3730–3750. (Cité en page 170)

Hay, W., Soeding, E., DeConto, R., Wold, C., 2002. The Late Cenozoic Uplift - Climate Change Paradox. *Int. J. Earth Sci.*, Vol. **91**(5), p. 746–774. (Cité en pages 37 et 54)

Hay, W. W., Migdisov, A., Balukhovsky, A. N., Wold, C. N., Flögel, S., Söding, E., 2006. Evaporites and the Salinity of the Ocean during the Phanerozoic: Implications for Climate, Ocean Circulation and Life. *Palaeogeogr. Palaeoclimatol. Palaeoecol.*, Vol. **240**(1-2), p. 3–46. (Cité en pages xxiv, 31, 37, 38, 54, 67 et 77)

Haynes, L. L., Hönisch, B., Dyez, K. A., Holland, K., Rosenthal, Y., Fish, C. R., Subhas, A. V., Rae, J. W. B., 2017. Calibration of the B/Ca Proxy in the Planktic Foraminifer *Orbulina Universa* to Paleocene Seawater Conditions: Paleocene B/Ca in Cultured *Orbulina Universa*. *Paleoceanography*, Vol. **32**(6), p. 580–599. (Cité en pages 11 et 144)

Hays, J. D., Imbrie, J., Shackleton, N. J., 1976. Variations in the Earth's Orbit: Pacemaker of the Ice Ages. *Science*, Vol. **194**(4270), p. 1121–1132. (Cité en page 3)

Haywood, A. M., Ridgwell, A., Lunt, D. J., Hill, D. J., Pound, M. J., Dowsett, H. J., Dolan, A. M., Francis, J. E., Williams, M., 2011. Are There Pre-Quaternary Geological Analogues for a Future Greenhouse Warming? *Proc. R. Soc. A*, Vol. **369**(1938), p. 933–956. (Cité en pages 5 et 9)

He, M., Jin, Z., Lu, H., Deng, L., Luo, C., 2016. The Different Cones Combination Enhanced Sensitivity on MC-ICP-MS: The Results from Boron Isotope Analysis. *Int. J. Mass Spectrom.*, Vol. **408**, p. 33–37. (Cité en pages 115, 122 et 123)

He, M.-Y., Deng, L., Lu, H., Jin, Z.-D., 2019. Elimination of the Boron Memory Effect for Rapid and Accurate Boron Isotope Analysis by MC-ICP-MS Using NaF. *J. Anal. At. Spectrom.*, Vol. **34**(5), p. 1026–1032. (Cité en page 115)

Heinemann, A., Fietzke, J., Melzner, F., Böhm, F., Thomsen, J., Garbe-Schönberg, D., Eisenhauer, A., 2012. Conditions of *Mytilus Edulis* Extracellular Body Fluids and Shell Composition in a pH-Treatment Experiment: Acid-Base Status, Trace Elements and δ ^{11} B: BORON ISOTOPES IN *MYTILUS EDULIS*. *Geochem. Geophys. Geosystems*, Vol. **13**(1), p. n/a–n/a. (Cité en page 137)

Hemming, N., Hanson, G., 1992. Boron Isotopic Composition and Concentration in Modern Marine Carbonates. *Geochim. Cosmochim. Acta*, Vol. **56**(1), p. 537–543. (Cité en pages 10, 18, 21, 29, 30, 114, 115, 137, 144 et 145)

Hemming, N., Hanson, G., 1994. A Procedure for the Isotopic Analysis of Boron by Negative Thermal Ionization Mass Spectrometry. *Chem. Geol.*, Vol. **114**(1-2), p. 147–156. (Cité en pages 115 et 145)

Hemming, N., Reeder, R., Hanson, G., 1995. Mineral-Fluid Partitioning and Isotopic Fractionation of Boron in Synthetic Calcium Carbonate. *Geochim. Cosmochim. Acta*, Vol. **59**(2), p. 371–379. (Cité en page 21)

Hemming, N. G., Guilderson, T. P., Fairbanks, R. G., 1998. Seasonal Variations in the Boron Isotopic Composition of Coral: A Productivity Signal? *Glob. Biogeochem. Cycles*, Vol. **12**(4), p. 581–586. (Cité en page 21)

Henehan, M. J., Edgar, K. M., Foster, G. L., Penman, D. E., Hull, P. M., Greenop, R., Anagnostou, E., Pearson, P. N., 2020. Revisiting the Middle Eocene Climatic Optimum "Carbon Cycle Conundrum" With New Estimates of Atmospheric pCO $_2$ From Boron Isotopes. *Paleoceanogr. Paleoclimatology*, Vol. **35**(6). (Cité en page 29)

Henehan, M. J., Foster, G. L., Bostock, H. C., Greenop, R., Marshall, B. J., Wilson, P. A., 2016. A New Boron Isotope-pH Calibration for Orbulina Universa , with Implications for Understanding and Accounting for 'Vital Effects'. *Earth Planet. Sci. Lett.*, Vol. **454**, p. 282–292. (Cité en pages xxiv, 22, 23, 24, 127, 142, 144, 157, 158, 174 et 184)

Henehan, M. J., Foster, G. L., Rae, J. W. B., Prentice, K. C., Erez, J., Bostock, H. C., Marshall, B. J., Wilson, P. A., 2015. Evaluating the Utility of B / C a Ratios in Planktic Foraminifera as a Proxy for the Carbonate System: A Case Study of *G Lobigerinoides Ruber* . *Geochem. Geophys. Geosyst.*, Vol. **16**(4), p. 1052–1069. (Cité en pages 11 et 144)

Henehan, M. J., Rae, J. W., Foster, G. L., Erez, J., Prentice, K. C., Kucera, M., Bostock, H. C., Martínez-Botí, M. A., Milton, J. A., Wilson, P. A., Marshall, B. J., Elliott, T., 2013. Calibration of the Boron Isotope Proxy in the Planktonic Foraminifera Globigerinoides Ruber for Use in Palaeo-CO2 Reconstruction. *Earth Planet. Sci. Lett.*, Vol. **364**, p. 111–122. (Cité en pages xxx, 22, 132, 144 et 179)

Henehan, M. J., Ridgwell, A., Thomas, E., Zhang, S., Alegret, L., Schmidt, D. N., Rae, J. W. B., Witts, J. D., Landman, N. H., Greene, S. E., Huber, B. T., Super, J. R., Planavsky, N. J., Hull, P. M., 2019. Rapid Ocean Acidification and Protracted Earth System Recovery Followed the End-Cretaceous Chicxulub Impact. *Proc. Natl. Acad. Sci.*, p. 201905989. (Cité en pages xxv, xxvii, 9, 15, 29, 30, 44, 50, 81, 114 et 145)

Hill, C. A., 1999. Reevaluation of the Hovey Channel in the Delaware Basin, West Texas. *AAPG Bull.*, Vol. **83**(2), p. 277–294. (Cité en page 70)

Hills, J. M., 1984. Sedimentation, Tectonism, and Hydrocarbon Generation in Delaware Basin, West Texas and Southeastern New Mexico. *AAPG Bull.*, Vol. **68**(3), p. 250–267. (Cité en page 70)

Hoffman, P. F., Kaufman, A. J., Halverson, G. P., Schrag, D. P., 1998. A Neoproterozoic Snowball Earth. *Science*, Vol. **281**(5381), p. 1342–1346. (Cité en page 59)

Hogan, J. F., Blum, J. D., 2003. Boron and Lithium Isotopes as Groundwater Tracers: A Study at the Fresh Kills Landfill, Staten Island, New York, USA. *Applied Geochemistry*, Vol. **18**(4), p. 615–627. (Cité en pages 17 et 30)

Holcomb, M., Rankenburg, K., McCulloch, M., 2014. CHAPTER 8. High-Precision MC-ICP-MS Measurements of δ ^{11} B: Matrix Effects in Direct Injection and Spray Chamber Sample Introduction Systems. *Dans : Grice, K. (Ed.), Detection Science*. Royal Society of Chemistry, Cambridge, p. 251–270. (Cité en page 75)

Holland, H. D., Horita, J., Seyfried, W. E., 1996. On the Secular Variations in the Composition of Phanerozoic Marine Potash Evaporites. *Geology*, Vol. **24**(11), p. 993. (Cité en page 31)

Holt, N. M., García-Veigas, J., Lowenstein, T. K., Giles, P. S., Williams-Stroud, S., 2014. The Major-Ion Composition of Carboniferous Seawater. *Geochim. Cosmochim. Acta*, Vol. **134**, p. 317–334. (Cité en pages xxvi, 31, 61, 74, 77 et 78)

Hönisch, B., Bijma, J., Russell, A. D., Spero, H. J., Palmer, M. R., Zeebe, R. E., Eisenhauer, A., 2003. The Influence of Symbiont Photosynthesis on the Boron Isotopic Composition of Foraminifera Shells. *Mar. Micropaleontol.*, Vol. **49**(1-2), p. 87–96. (Cité en page 157)

Hönisch, B., Eggins, S., Haynes, L. L., Allen, K. A., Holland, K. D., Lorbacher, K., 2019. *Boron Proxies in Paleoceanography and Paleoclimatology*. New Analytical Methods in Earth and Environmental Science Series. John Wiley & Sons, Hoboken, NJ. (Cité en pages xxiii, xxiv, 6, 16, 25, 43 et 47)

Hönisch, B., Hemming, N., Grottoli, A., Amat, A., Hanson, G., Bijma, J., 2004. Assessing Scleractinian Corals as Recorders for Paleo-pH: Empirical Calibration and Vital Effects. *Geochim. Cosmochim. Acta*, Vol. **68**(18), p. 3675–3685. (Cité en pages 29 et 145)

Hönisch, B., Hemming, N. G., 2005. Surface Ocean pH Response to Variations in pCO2 through Two Full Glacial Cycles. *Earth Planet. Sci. Lett.*, Vol. **236**(1-2), p. 305–314. (Cité en page 29)

Hönisch, B., Hemming, N. G., Archer, D., Siddall, M., McManus, J. F., 2009. Atmospheric Carbon Dioxide Concentration Across the Mid-Pleistocene Transition. *Science*, Vol. **324**(5934), p. 1551–1554. (Cité en pages 29, 78 et 114)

Hönisch, B., Ridgwell, A., Schmidt, D. N., Thomas, E., Gibbs, S. J., Sluijs, A., Zeebe, R., Kump, L., Martindale, R. C., Greene, S. E., Kiessling, W., Ries, J., Zachos, J. C., Royer, D. L., Barker, S., Marchitto, T. M., Moyer, R., Pelejero, C., Ziveri, P., Foster, G. L., Williams, B., 2012. The Geological Record of Ocean Acidification. *Science*, Vol. **335**(6072), p. 1058–1063. (Cité en pages 15, 29, 47 et 114)

Horita, J., 1990. Stable Isotope Paleoclimatology of Brine Inclusions in Halite: Modeling and Application to Searles Lake, California. *Geochim. Cosmochim. Acta*, Vol. **54**(7), p. 2059–2073. (Cité en page 75)

Horita, J., Friedman, T. J., Lazar, B., Holland, H. D., 1991. The Composition of Permian Seawater. *Geochim. Cosmochim. Acta*, Vol. **55**(2), p. 417–432. (Cité en pages 48 et 61)

Horita, J., Weinberg, A., Das, N., Holland, H. D., 1996. Brine Inclusions in Halite and the Origin of the Middle Devonian Prairie Evaporites of Western Canada. *Journal of Sedimentary Research*, Vol. **66**(5), p. 956–964. (Cité en pages 47, 48, 74, 75 et 78)

Horita, J., Zimmermann, H., Holland, H. D., 2002. Chemical Evolution of Seawater during the Phanerozoic: Implications from the Record of Marine Evaporites. *Geochimica et Cosmochimica Acta*, Vol. **66**(21), p. 3733–3756. (Cité en pages xxiv, xxvi, 31, 32, 43, 47, 48, 61, 74, 75, 76, 77, 78 et 185)

Horwitz, E. P., Dietz, M. L., Fisher, D. E., 1991. Separation and Preconcentration of Strontium from Biological, Environmental, and Nuclear Waste Samples by Extraction Chromatography Using a Crown Ether. *Anal. Chem.*, Vol. **63**(5), p. 522–525. (Cité en page 34)

Hounslow, M. W., Domeier, M., Biggin, A. J., 2018. Subduction Flux Modulates the Geomagnetic Polarity Reversal Rate. *Tectonophysics*, Vol. **742–743**, p. 34–49. (Cité en pages xxvi et 55)

Hovland, M., Rueslåtten, H., Johnsen, H. K., 2018. Large Salt Accumulations as a Consequence of Hydrothermal Processes Associated with 'Wilson Cycles': A Review Part 1: Towards a New Understanding. *Mar. Pet. Geol.*, Vol. **92**, p. 987–1009. (Cité en pages 50 et 185)

Huang, C.-Y., Zhao, M., Wang, C.-C., Wei, G., 2001. Cooling of the South China Sea by the Toba Eruption and Correlation with Other Climate Proxies ~71,000 Years Ago. *Geophys. Res. Lett.*, Vol. **28**(20), p. 3915–3918. (Cité en page 165)

Hudec, M. R., Jackson, M. P. A., 2007. Terra Infirma: Understanding Salt Tectonics. *Earth-Science Reviews*, Vol. **82**(1), p. 1–28. (Cité en page 49)

Ishikawa, T., Nagaishi, K., 2011. High-Precision Isotopic Analysis of Boron by Positive Thermal Ionization Mass Spectrometry with Sample Preheating. *J Anal Spectrom*, Vol. **26**(2), p. 359–365. (Cité en page 145)

Ishikawa, T., Nakamura, E., 1993. Boron Isotope Systematics of Marine Sediments. *Earth Planet. Sci. Lett.*, Vol. **117**(3-4), p. 567–580. (Cité en page 78)

Isson, T. T., Planavsky, N. J., 2018. Reverse Weathering as a Long-Term Stabilizer of Marine pH and Planetary Climate. *Nature*, Vol. **560**(7719), p. 471–475. (Cité en page 61)

Jensen, B. P., Gammelgaard, B., Hansen, S. H., Andersen, J. V., 2003. Comparison of Direct Injection Nebulizer and Desolvating Microconcentric Nebulizer for Analysis of Chlorine-, Bromine- and Iodine-Containing Compounds by Reversed Phase HPLC with ICP-MS Detection. *J. Anal. At. Spectrom.*, Vol. **18**(8), p. 891–896. (Cité en page 95)

Jin, J., Bergman, K. M., 1999. Sequence Stratigraphy of the Middle Devonian Winnipegosis Carbonate-Prairie Evaporite Transition, Southern Elk Point Basin. *Carbonates Evaporites*, Vol. **14**(1), p. 64–83. (Cité en page 70)

Joachimski, M. M., Simon, L., van Geldern, R., Lécuyer, C., 2005. Boron Isotope Geochemistry of Paleozoic Brachiopod Calcite: Implications for a Secular Change in the Boron Isotope Geochemistry of Seawater over the Phanerozoic. *Geochim. Cosmochim. Acta*, Vol. **69**(16), p. 4035–4044. (Cité en pages xxv, xxviii, 28, 31, 44, 45, 46, 47, 48, 51, 56, 57, 82 et 83)

John, S. G., Adkins, J. F., 2010. Analysis of Dissolved Iron Isotopes in Seawater. *Mar. Chem.*, Vol. **119**(1-4), p. 65–76. (Cité en pages xxx, 127 et 128)

Jones, G. S., Gregory, J. M., Stott, P. A., Tett, S. F. B., Thorpe, R. B., 2005. An AOGCM Simulation of the Climate Response to a Volcanic Super-Eruption. *Clim Dyn*, Vol. **25**(7), p. 725–738. (Cité en pages 166 et 167)

Jorabchi, K., Kahen, K., Gray, C., Montaser, A., 2005. In Situ Visualization and Characterization of Aerosol Droplets in an Inductively Coupled Plasma. *Anal. Chem.*, Vol. **77**(5), p. 1253–1260. (Cité en page 95)

Jurikova, H., Gutjahr, M., Wallmann, K., Flögel, S., Liebetrau, V., Posenato, R., Angiolini, L., Garbelli, C., Brand, U., Wiedenbeck, M., Eisenhauer, A., 2020. Permian–Triassic Mass Extinction Pulses Driven by Major Marine Carbon Cycle Perturbations. *Nat. Geosci.* (Cité en pages 9, 15, 28, 29, 31, 51, 58, 59, 82, 114 et 163)

Jurikova, H., Liebetrau, V., Gutjahr, M., Rollion-Bard, C., Hu, M. Y., Krause, S., Henkel, D., Hiebenthal, C., Schmidt, M., Laudien, J., Eisenhauer, A., 2019. Boron Isotope Systematics of Cultured Brachiopods: Response to Acidification, Vital Effects and Implications for Palaeo-pH Reconstruction. *Geochim. Cosmochim. Acta*, Vol. **248**, p. 370–386. (Cité en pages xxx, 82, 116, 117, 131, 133, 134, 135, 137, 139, 150, 169 et 170)

Kakihana, H., Kotaka, M., Satoh, S., Nomura, M., Okamoto, M., 1977. Fundamental Studies on the Ion-Exchange Separation of Boron Isotopes. *BCSJ*, Vol. **50**(1), p. 158–163. (Cité en pages 19 et 21)

Kasemann, S. A., Pogge von Strandmann, P. A., Prave, A. R., Fallick, A. E., Elliott, T., Hoffmann, K.-H., 2014. Continental Weathering Following a Cryogenian Glaciation: Evidence from Calcium and Magnesium Isotopes. *Earth and Planetary Science Letters*, Vol. **396**, p. 66–77. (Cité en page 59)

Kasemann, S. A., Prave, A. R., Fallick, A. E., Hawkesworth, C. J., Hoffmann, K.-H., 2010. Neoproterozoic Ice Ages, Boron Isotopes, and Ocean Acidification: Implications for a Snowball Earth. *Geology*, Vol. **38**(9), p. 775–778. (Cité en pages xxv, xxviii, 10, 31, 45, 46, 48, 51, 59, 82 et 83)

Katz, M. E., Cramer, B. S., Franzese, A., Honisch, B., Miller, K. G., Rosenthal, Y., Wright, J. D., 2010. TRADITIONAL AND EMERGING GEOCHEMICAL PROXIES IN FORAMINIFERA. *J. Foraminifer. Res.*, Vol. **40**(2), p. 165–192. (Cité en page 144)

Khodri, M., Izumo, T., Vialard, J., Janicot, S., Cassou, C., Lengaigne, M., Mignot, J., Gastineau, G., Guilyardi, E., Lebas, N., Robock, A., McPhaden, M. J., 2017. Tropical Explosive Volcanic Eruptions Can Trigger El Niño by Cooling Tropical Africa. *Nat. Commun.*, Vol. **8**(1), p. 778. (Cité en page 163)

Khodri, M., Leclainche, Y., Ramstein, G., Braconnot, P., Marti, O., Cortijo, E., 2001. Simulating the Amplification of Orbital Forcing by Ocean Feedbacks in the Last Glaciation. *Nature*, Vol. **410**(6828), p. 570–574. (Cité en page 165)

Kısakürek, B., Eisenhauer, A., Böhm, F., Garbe-Schönberg, D., Erez, J., 2008. Controls on Shell Mg/Ca and Sr/Ca in Cultured Planktonic Foraminiferan, Globigerinoides Ruber (White). *Earth and Planetary Science Letters*, Vol. **273**(3), p. 260–269. (Cité en page 175)

Kiss, E., 1988. Ion-Exchange Separation and Spectrophotometric Determination of Boron in Geological Materials. *Anal. Chim. Acta*, Vol. **211**, p. 243–256. (Cité en page 115)

Klochko, K., Cody, G. D., Tossell, J. A., Dera, P., Kaufman, A. J., 2009. Re-Evaluating Boron Speciation in Biogenic Calcite and Aragonite Using 11B MAS NMR. *Geochim. Cosmochim. Acta*, Vol. **73**(7), p. 1890–1900. (Cité en page 23)

Klochko, K., Kaufman, A. J., Yao, W., Byrne, R. H., Tossell, J. A., 2006. Experimental Measurement of Boron Isotope Fractionation in Seawater. *Earth Planet. Sci. Lett.*, Vol. **248**(1-2), p. 276–285. (Cité en pages xxiv, 19, 21, 30, 114, 144 et 156)

Kloppmann, W., Négrel, P., Casanova, J., Klinge, H., Schelkes, K., Guerrot, C., 2001. Halite Dissolution Derived Brines in the Vicinity of a Permian Salt Dome (N German Basin). Evidence from Boron, Strontium, Oxygen, and Hydrogen Isotopes. *Geochim. Cosmochim. Acta*, Vol. **65**(22), p. 4087–4101. (Cité en pages 74 et 75)

Knauth, L., Beeunas, M. A., 1986. Isotope Geochemistry of Fluid Inclusions in Permian Halite with Implications for the Isotopic History of Ocean Water and the Origin of Saline Formation Waters. *Geochim. Cosmochim. Acta*, Vol. **50**(3), p. 419–433. (Cité en page 75)

Konrad, W., Royer, D. L., Franks, P. J., Roth-Nebelsick, A., 2020. Quantitative Critique of Leaf-based Paleo-CO $_2$ Proxies: Consequences for Their Reliability and Applicability. *Geological Journal*, p. gj.3807. (Cité en pages 6 et 7)

Koornneef, J., Bouman, C., Schwieters, J., Davies, G., 2014. Measurement of Small Ion Beams by Thermal Ionisation Mass Spectrometry Using New 1013Ohm Resistors. *Anal. Chim. Acta*, Vol. **819**, p. 49–55. (Cité en page 127)

Kucera, M., 2007. Chapter Six Planktonic Foraminifera as Tracers of Past Oceanic Environments. *Dans : Hillaire–Marcel, C., De Vernal, A. (Eds.), Developments in Marine Geology*. Vol. 1 de Proxies in Late Cenozoic Paleoceanography. Elsevier, p. 213–262. (Cité en page 22)

Lacis, A. A., Schmidt, G. A., Rind, D., Ruedy, R. A., 2010. Atmospheric CO2: Principal Control Knob Governing Earth's Temperature. *Science*, Vol. **330**(6002), p. 356–359. (Cité en page 2)

Lamy, F., 2016. The Expedition PS97 of the Research Vessel POLARSTERN to the Drake Passage in 2016. https://epic.awi.de/id/eprint/41674/. (Cité en page 146)

Lane, C. S., Chorn, B. T., Johnson, T. C., 2013. Ash from the Toba Supereruption in Lake Malawi Shows No Volcanic Winter in East Africa at 75 Ka. *PNAS*, Vol. **110**(20), p. 8025–8029. (Cité en pages xxxii, 165 et 166)

Larson, R. L., 1991. Latest Pulse of Earth: Evidence for a Mid-Cretaceous Superplume. *Geology*, Vol. **19**(6), p. 547. (Cité en pages xxvi, 54 et 56)

Lavigne, F., Degeai, J.-P., Komorowski, J.-C., Guillet, S., Robert, V., Lahitte, P., Oppenheimer, C., Stoffel, M., Vidal, C. M., Surono, Pratomo, I., Wassmer, P., Hajdas, I., Hadmoko, D. S., de Belizal, E., 2013. Source of the Great A.D. 1257 Mystery Eruption Unveiled, Samalas Volcano, Rinjani Volcanic Complex, Indonesia. *PNAS*, Vol. **110**(42), p. 16742–16747. (Cité en page 163)

Lawrence, K. E., Rice, G. W., Fassel, V. A., 1984. Direct Liquid Sample Introduction for Flow Injection Analysis and Liquid Chromatography with Inductively Coupled, Argon Plasma Spectrometric Detection. *Anal. Chem.*, Vol. **56**(2), p. 289–292. (Cité en page 95)

Lazar, B., Holland, H. D., 1988. The Analysis of Fluid Inclusions in Halite. *Geochim. Cosmochim. Acta*, Vol. **52**(2), p. 485–490. (Cité en page 185)

Le Quéré, C., Andrew, R. M., Friedlingstein, P., Sitch, S., Pongratz, J., Manning, A. C., Korsbakken, J. I., Peters, G. P., Canadell, J. G., Jackson, R. B., Boden, T. A., Tans, P. P., Andrews, O. D., Arora, V. K., Bakker, D. C. E., Barbero, L., Becker, M., Betts, R. A., Bopp, L., Chevallier, F., Chini, L. P., Ciais, P., Cosca, C. E., Cross, J., Currie, K., Gasser, T., Harris, I., Hauck, J., Haverd, V., Houghton, R. A., Hunt, C. W., Hurtt, G., Ilyina, T., Jain, A. K., Kato, E., Kautz, M., Keeling, R. F., Klein Goldewijk, K., Körtzinger, A., Landschützer, P., Lefèvre, N., Lenton, A., Lienert, S., Lima, I., Lombardozzi, D., Metzl, N., Millero, F., Monteiro, P. M. S., Munro, D. R., Nabel, J. E. M. S., Nakaoka, S.-i., Nojiri, Y., Padin, X. A., Peregon, A., Pfeil, B., Pierrot, D., Poulter, B., Rehder, G., Reimer, J., Rödenbeck, C., Schwinger, J., Séférian, R., Skjelvan, I., Stocker, B. D., Tian, H., Tilbrook, B., Tubiello, F. N., van der Laan-Luijkx, I. T., van der Werf, G. R., van Heuven, S., Viovy, N., Vuichard, N., Walker, A. P., Watson, A. J., Wiltshire, A. J., Zaehle, S., Zhu, D., 2018. Global Carbon Budget 2017. *Earth Syst. Sci. Data*, Vol. **10**(1), p. 405–448. (Cité en page 5)

Lea, D. W., 2003. Trace Elements in Foraminiferal Calcite. *Dans : Sen Gupta, B. K. (Ed.), Modern Foraminifera*. Springer Netherlands, Dordrecht, p. 259–277. (Cité en page 144)

Lea, D. W., Mashiotta, T. A., Spero, H. J., 1999. Controls on Magnesium and Strontium Uptake in Planktonic Foraminifera Determined by Live Culturing. *Geochimica et Cosmochimica Acta*, Vol. **63**(16), p. 2369–2379. (Cité en pages 144 et 175)

Leclercq, A., Nonell, A., Todolí Torró, J. L., Bresson, C., Vio, L., Vercouter, T., Chartier, F., 2015. Introduction of Organic/Hydro-Organic Matrices in Inductively Coupled Plasma Optical Emission Spectrometry and Mass Spectrometry: A Tutorial Review. Part II. Practical Considerations. *Analytica Chimica Acta*, Vol. **885**, p. 57–91. (Cité en page 95)

Lécuyer, C., Grandjean, P., Reynard, B., Albarède, F., Telouk, P., 2002. 11B/10B Analysis of Geological Materials by ICP–MS Plasma 54: Application to the Boron Fractionation between Brachiopod Calcite and Seawater. *Chem. Geol.*, Vol. **186**(1-2), p. 45–55. (Cité en pages xxv, xxviii, 29, 31, 46, 50, 51, 82, 83, 137 et 145)

Lee, K., Kim, T.-W., Byrne, R. H., Millero, F. J., Feely, R. A., Liu, Y.-M., 2010. The Universal Ratio of Boron to Chlorinity for the North Pacific and North Atlantic Oceans. *Geochim. Cosmochim. Acta*, Vol. **74**(6), p. 1801–1811. (Cité en pages xxiv, 19, 30 et 156)

Leeman, W. P., Sisson, V., 1996. Leeman et al 1996.Pdf. *Dans : Boron: Mineralogy, Petrology and Geochemistry in the Earth's Crust*, Reviews in Mineralogy #33 Édition. Mineralogical Society of America, E.S. Grew, L.M. Anovitz, p. 645–708. (Cité en pages xxiv, 17 et 35)

Lemarchand, D., Gaillardet, J., Göpel, C., Manhès, G., 2002a. An Optimized Procedure for Boron Separation and Mass Spectrometry Analysis for River Samples. *Chem. Geol.*, Vol. **182**(2-4), p. 323–334. (Cité en pages xxxiii, 33, 100, 115, 116, 135, 136 et 138)

Lemarchand, D., Gaillardet, J., Lewin, É., Allègre, C., 2002b. Boron Isotope Systematics in Large Rivers: Implications for the Marine Boron Budget and Paleo-pH Reconstruction over the Cenozoic. *Chem. Geol.*, Vol. **190**(1-4), p. 123–140. (Cité en pages xxiv, xxv, xxvii, xxviii, 19, 28, 30, 31, 35, 36, 37, 39, 43, 44, 46, 48, 49, 50, 51, 56, 59, 61, 62, 78, 79, 80, 81, 82 et 83)

Lemarchand, D., Gaillardet, J., Lewin, É., Allègre, C. J., 2000. The Influence of Rivers on Marine Boron Isotopes and Implications for Reconstructing Past Ocean pH. *Nature*, Vol. **408**(6815), p. 951. (Cité en pages 30, 78 et 80)

Lemarchand, E., Schott, J., Gaillardet, J., 2007. How Surface Complexes Impact Boron Isotope Fractionation: Evidence from Fe and Mn Oxides Sorption Experiments. *Earth Planet. Sci. Lett.*, Vol. **260**(1-2), p. 277–296. (Cité en pages 49 et 171)

Lemelle, L., Bartolini, A., Simionovici, A., Tucoulou, R., De Nolf, W., Bassinot, F., de Garidel-Thoron, T., 2020. Nanoscale Trace Metal Imprinting of Biocalcification of Planktic Foraminifers by Toba's Super-Eruption. *Sci. Rep.*, Vol. **10**(1), p. 10974. (Cité en page 170)

Lenton, T. M., Daines, S. J., Mills, B. J., 2018. COPSE Reloaded: An Improved Model of Biogeochemical Cycling over Phanerozoic Time. *Earth-Sci. Rev.*, Vol. **178**, p. 1–28. (Cité en pages 8 et 37)

Lewis, S. L., Maslin, M. A., 2015. Defining the Anthropocene. *Nature*, Vol. **519**(7542), p. 171–180. (Cité en pages xxiii, 4 et 5)

Li, G., Elderfield, H., 2013. Evolution of Carbon Cycle over the Past 100 Million Years. *Geochim. Cosmochim. Acta*, Vol. **103**, p. 11–25. (Cité en page 54)

Li, Z., Bogdanova, S., Collins, A., Davidson, A., De Waele, B., Ernst, R., Fitzsimons, I., Fuck, R., Gladkochub, D., Jacobs, J., Karlstrom, K., Lu, S., Natapov, L., Pease, V., Pisarevsky, S., Thrane, K., Vernikovsky, V., 2008. Assembly, Configuration, and Break-up History of Rodinia: A Synthesis. *Precambrian Res.*, Vol. **160**(1-2), p. 179–210. (Cité en pages xxvii et 73)

Lin, J., Liu, Y., Hu, Z., Chen, W., Zhang, L., Chen, H., 2019. Accurate Measurement of Lithium Isotopes in Eleven Carbonate Reference Materials by MC - ICP - MS with Soft Extraction Mode and 10 ^{12} Ω Resistor High-Gain Faraday Amplifiers. *Geostand. Geoanalytical Res.*, Vol. **43**(2), p. 277–289. (Cité en page 127)

Liu, F., Chai, J., Wang, B., Liu, J., Zhang, X., Wang, Z., 2016. Global Monsoon Precipitation Responses to Large Volcanic Eruptions. *Sci. Rep.*, Vol. **6**(1), p. 24331. (Cité en page 163)

Liu, W., Xiao, Y., Peng, Z., An, Z., He, X., 2000. Boron Concentration and Isotopic Composition of Halite from Experiments and Salt Lakes in the Qaidam Basin. *Geochim. Cosmochim. Acta*, Vol. **64**(13), p. 2177–2183. (Cité en pages 31, 32, 43, 45, 47, 48 et 75)

Liu, Y., Peng, Z., Zhou, R., Song, S., Liu, W., You, C.-F., Lin, Y.-P., Yu, K., Wu, C.-C., Wei, G., Xie, L., Burr, G. S., Shen, C.-C., 2014. Acceleration of Modern Acidification in the South China Sea Driven by Anthropogenic CO2. *Sci. Rep.*, Vol. **4**(1). (Cité en pages 29 et 116)

Liu, Y.-W., Aciego, S. M., Wanamaker, A. D., Sell, B. K., 2013. A High-Throughput System for Boron Microsublimation and Isotope Analysis by Total Evaporation Thermal Ionization Mass Spectrometry: New Boron Microsublimation Technique and Isotope Analysis by TE-TIMS. *Rapid Commun. Mass Spectrom.*, Vol. **27**(15), p. 1705–1714. (Cité en page 145)

Liu, Y.-W., Sutton, J. N., Ries, J. B., Eagle, R. A., 2020. Regulation of Calcification Site pH Is a Polyphyletic but Not Always Governing Response to Ocean Acidification. *Sci. Adv.*, Vol. **6**(5), p. eaax1314. (Cité en page 137)

Lloyd, N. S., Sadekov, A. Y., Misra, S., 2018. Application of 10 ^{13} Ohm Faraday Cup Current Amplifiers for Boron Isotopic Analyses by Solution Mode and Laser Ablation Multicollector Inductively Coupled Plasma Mass Spectrometry. *Rapid Commun. Mass Spectrom.*, Vol. **32**(1), p. 9–18. (Cité en pages 115, 123, 127, 129 et 145)

Louvat, P., Bouchez, J., Paris, G., 2011a. MC-ICP-MS Isotope Measurements with Direct Injection Nebulisation (d-DIHEN): Optimisation and Application to Boron in Seawater and Carbonate Samples. *Geostand. Geoanalytical Res.*, Vol. **35**(1), p. 75–88. (Cité en pages xxviii, xxx, 33, 92, 95, 98, 100, 114, 115, 117, 119, 120, 132, 145 et 148)

Louvat, P., Gaillardet, J., Paris, G., Dessert, C., 2011b. Boron Isotope Ratios of Surface Waters in Guadeloupe, Lesser Antilles. *Appl. Geochem.*, Vol. **26**, p. S76–S79. (Cité en pages 49 et 185)

Louvat, P., Gayer, E., Gaillardet, J., 2014a. Boron Behavior in the Rivers of Réunion Island, Inferred from Boron Isotope Ratios and Concentrations of Major and Trace Elements. *Procedia Earth Planet. Sci.*, Vol. **10**, p. 231–237. (Cité en pages xxx, 49, 132 et 185)

Louvat, P., Moureau, J., Paris, G., Bouchez, J., Noireaux, J., Gaillardet, J., 2014b. A Fully Automated Direct Injection Nebulizer (d-DIHEN) for MC-ICP-MS Isotope Analysis: Application to Boron Isotope Ratio Measurements. *J Anal Spectrom*, Vol. **29**(9), p. 1698–1707. (Cité en pages xxix, 33, 95, 96, 100, 103, 106, 115, 119, 120, 121, 122, 123, 129, 145, 148, 151, 152 et 157)

Louvat, P., Tharaud, M., Buisson, M., Rollion-Bard, C., Benedetti, M. F., 2019. μ-dDIHEN: A New Micro-Flow Liquid Sample Introduction System for Direct Injection Nebulization in ICP-MS. *J. Anal. At. Spectrom.*, Vol. **34**(8), p. 1553–1563. (Cité en pages xxix, xxxi, 93, 115, 116, 119, 120, 121, 122, 123, 125, 128, 129, 131, 145, 148, 149, 150, 151 et 169)

Lowenstein, T., Kendall, B., Anbar, A., 2014. The Geologic History of Seawater. *Dans : Treatise on Geochemistry*. Elsevier, p. 569–622. (Cité en pages xxvi, 47, 61 et 74)

Lowenstein, T. K., 1988. Origin of Depositional Cycles in a Permian "Saline Giant": The Salado (McNutt Zone) Evaporites of New Mexico and Texas. *Geol. Soc. Am. Bull.*, Vol. **100**(4), p. 592–608. (Cité en page 70)

Lowenstein, T. K., 2001. Oscillations in Phanerozoic Seawater Chemistry: Evidence from Fluid Inclusions. *Science*, Vol. **294**(5544), p. 1086–1088. (Cité en pages xxvii, 31, 74, 75 et 76)

Lowenstein, T. K., Timofeeff, M. N., Kovalevych, V. M., Horita, J., 2005. The Major-Ion Composition of Permian Seawater. *Geochim. Cosmochim. Acta*, Vol. **69**(7), p. 1701–1719. (Cité en pages xxvi, 61, 75, 77 et 78)

Lucas, S., Anderson, O., 1993. Stratigraphy of the Permian–Triassic Boundary in Southeastern New Mexico and West Texas. *NM Geol. Soc. Guidebook*, Vol. **44**. (Cité en page 70)

Lueker, T. J., Dickson, A. G., Keeling, C. D., 2000. Ocean pCO2 Calculated from Dissolved Inorganic Carbon, Alkalinity, and Equations for K1 and K2: Validation Based on Laboratory Measurements of CO2 in Gas and Seawater at Equilibrium. *Marine Chemistry*, Vol. **70**(1), p. 105–119. (Cité en page 156)

Luterbacher, J., Pfister, C., 2015. The Year without a Summer. *Nat. Geosci.*, Vol. **8**(4), p. 246–248. (Cité en page 163)

Lüthi, D., Le Floch, M., Bereiter, B., Blunier, T., Barnola, J.-M., Siegenthaler, U., Raynaud, D., Jouzel, J., Fischer, H., Kawamura, K., Stocker, T. F., 2008. High-Resolution Carbon Dioxide Concentration Record 650,000–800,000 Years before Present. *Nature*, Vol. **453**(7193), p. 379–382. (Cité en pages 2, 6 et 10)

M. DeConto, R., Pollard, D., 2016. Contribution of Antarctica to Past and Future Sea-Level Rise. *Nature*, Vol. **531**, p. 591–597. (Cité en page 5)

Mackenzie, F. T., Morse, J. W., 1992. Sedimentary Carbonates through Phanerozoic Time. *Geochim. Cosmochim. Acta*, Vol. **56**(8), p. 3281–3295. (Cité en page 54)

Makishima, A., Nakamura, E., 2012. High-Resolution MC-ICPMS Employing Amplifiers with a 1012 Ohm Resistor for Bulk Sulfur Determination in Biological and Geological Samples. *J. Anal. At. Spectrom.*, Vol. **27**(5), p. 891. (Cité en page 127)

Manuella, F. C., Scribano, V., Carbone, S., 2018. Abyssal Serpentinites as Gigantic Factories of Marine Salts and Oil. *Mar. Pet. Geol.*, Vol. **92**, p. 1041–1055. (Cité en page 50)

Mao, H.-R., Liu, C.-Q., Zhao, Z.-Q., 2019. Source and Evolution of Dissolved Boron in Rivers: Insights from Boron Isotope Signatures of End-Members and Model of Boron Isotopes during Weathering Processes. *Earth-Sci. Rev.*, Vol. **190**, p. 439–459. (Cité en page 45)

Mark, D. F., Petraglia, M., Smith, V. C., Morgan, L. E., Barfod, D. N., Ellis, B. S., Pearce, N. J., Pal, J. N., Korisettar, R., 2014. A High-Precision 40Ar/39Ar Age for the Young Toba Tuff and Dating of Ultra-Distal Tephra: Forcing of Quaternary Climate and Implications for Hominin Occupation of India. *Quaternary Geochronology*, Vol. **21**, p. 90–103. (Cité en page 165)

Marschall, H. R., 2018. Boron Isotopes in the Ocean Floor Realm and the Mantle. *Dans : Marschall, H., Foster, G. (Eds.), Boron Isotopes*. Springer International Publishing, Cham, p. 189–215. (Cité en pages xxiv, 30, 35, 37, 61 et 114)

Marschall, H. R., Wanless, V. D., Shimizu, N., Pogge von Strandmann, P. A., Elliott, T., Monteleone, B. D., 2017. The Boron and Lithium Isotopic Composition of Mid-Ocean Ridge Basalts and the Mantle. *Geochim. Cosmochim. Acta*, Vol. **207**, p. 102–138. (Cité en pages xxiv, 35, 37, 59 et 61)

Martin, P. A., Lea, D. W., 2002. A Simple Evaluation of Cleaning Procedures on Fossil Benthic Foraminiferal Mg/Ca: CLEANING PROCEDURES. *Geochem. Geophys. Geosystems*, Vol. **3**(10), p. 1–8. (Cité en pages 151 et 170)

Martínez-Botí, M. A., Foster, G. L., Chalk, T. B., Rohling, E. J., Sexton, P. F., Lunt, D. J., Pancost, R. D., Badger, M. P. S., Schmidt, D. N., 2015a. Plio-Pleistocene Climate Sensitivity Evaluated Using High-Resolution CO2 Records. *Nature*, Vol. **518**(7537), p. 49–54. (Cité en pages xxv, xxvii, 10, 43, 44, 48, 80, 81 et 145)

Martínez-Botí, M. A., Marino, G., Foster, G. L., Ziveri, P., Henehan, M. J., Rae, J. W. B., Mortyn, P. G., Vance, D., 2015b. Boron Isotope Evidence for Oceanic Carbon Dioxide Leakage during the Last Deglaciation. *Nature*, Vol. **518**(7538), p. 219–222. (Cité en pages xxxi, 22, 24, 29, 152, 156 et 157)

Massey, F. J., 1951. The Kolmogorov-Smirnov Test for Goodness of Fit. *J. Am. Stat. Assoc.*, Vol. **46**(253), p. 68–78. (Cité en page 108)

Mathien-Blard, E., Bassinot, F., 2009. Salinity Bias on the Foraminifera Mg/Ca Thermometry: Correction Procedure and Implications for Past Ocean Hydrographic Reconstructions. *Geochem. Geophys. Geosystems*, Vol. **10**(12). (Cité en page 175)

Mattes, B. W., Conway Morris, S., 1990. Carbonate/Evaporite Deposition in the Late Precambrian — Early Cambrian Ara Formation of Southern Oman. *Geol. Soc. Lond. Spec. Publ.*, Vol. **49**(1), p. 617–636. (Cité en page 73)

Mavromatis, V., Montouillout, V., Noireaux, J., Gaillardet, J., Schott, J., 2015. Characterization of Boron Incorporation and Speciation in Calcite and Aragonite from Co-Precipitation Experiments under Controlled pH, Temperature and Precipitation Rate. *Geochimica et Cosmochimica Acta*, Vol. **150**, p. 299–313. (Cité en page 51)

McCaffrey, M. A., Lazar, B., Holland, H. D., 1987. The Evaporation Path of Seawater and the Coprecipitation of Br (Super -) and K (Super +) with Halite. *Journal of Sedimentary Research*, Vol. **57**(5), p. 928–937. (Cité en pages xxvi, xxvii, 67 et 76)

McCulloch, M. T., Holcomb, M., Rankenburg, K., Trotter, J. A., 2014. Rapid, High-Precision Measurements of Boron Isotopic Compositions in Marine Carbonates: Boron Isotopic Measurements in Marine Carbonates. *Rapid Commun. Mass Spectrom.*, Vol. **28**(24), p. 2704–2712. (Cité en pages 115 et 145)

McDonough, W., Sun, S., 1995. The Composition of the Earth. *Chem. Geol.*, Vol. **67**, p. 1050–1056. (Cité en page 17)

McKie, T., 2017. Paleogeographic Evolution of Latest Permian and Triassic Salt Basins in Northwest Europe. *Dans : Permo-Triassic Salt Provinces of Europe, North Africa and the Atlantic Margins*. Elsevier, p. 159–173. (Cité en pages xxvii et 69)

Mclean, J. A., Minnich, M. G., Iacone, L. A., Liu, H., Montaser, A., 1998. Nebulizer Diagnostics: Fundamental Parameters, Challenges, and Techniques on the Horizon. *J. Anal. At. Spectrom.*, Vol. **13**(9), p. 829–842. (Cité en page 103)

McLean, J. A., Zhang, H., Montaser, A., 1998. A Direct Injection High-Efficiency Nebulizer for Inductively Coupled Plasma Mass Spectrometry. *Anal Chem*, Vol. **70**(5), p. 1012–1020. (Cité en pages 96 et 102)

Merdith, A. S., Collins, A. S., Williams, S. E., Pisarevsky, S., Foden, J. D., Archibald, D. B., Blades, M. L., Alessio, B. L., Armistead, S., Plavsa, D., Clark, C., Müller, R. D., 2017. A Full-Plate Global Reconstruction of the Neoproterozoic. *Gondwana Res.*, Vol. **50**, p. 84–134. (Cité en pages xxvi et 55)

Metelkin, D., Vernikovsky, V., Kazansky, A., 2012. Tectonic Evolution of the Siberian Paleocontinent from the Neoproterozoic to the Late Mesozoic: Paleomagnetic Record and Reconstructions. *Russ. Geol. Geophys.*, Vol. **53**(7), p. 675–688. (Cité en page 72)

Mills, B. J., Krause, A. J., Scotese, C. R., Hill, D. J., Shields, G. A., Lenton, T. M., 2019. Modelling the Long-Term Carbon Cycle, Atmospheric CO2, and Earth Surface Temperature from Late Neoproterozoic to Present Day. *Gondwana Res.*, Vol. **67**, p. 172–186. (Cité en pages xxiii, xxiv, xxvi, 7, 8, 9, 31, 37, 38, 53, 59 et 61)

Mills, B. J. W., Scotese, C. R., Walding, N. G., Shields, G. A., Lenton, T. M., 2017. Elevated CO2 Degassing Rates Prevented the Return of Snowball Earth during the Phanerozoic. *Nat. Commun.*, Vol. **8**(1). (Cité en pages xxiv, xxvi, 8, 37, 38, 53, 55 et 56)

Millson, J. A., Mercadier, C. G. L., Livera, S. E., Peters, J. M., 1996. The Lower Palaeozoic of Oman and Its Context in the Evolution of a Gondwanan Continental Margin. *J. Geol. Soc.*, Vol. **153**(2), p. 213–230. (Cité en pages xxvii et 73)

Minnich, M. G., McLean, J. A., Montaser, A., 2001. Spatial Aerosol Characteristics of a Direct Injection High Efficiency Nebulizer via Optical Patternation. *Spectrochimica Acta Part B: Atomic Spectroscopy*, Vol. **56**(7), p. 1113–1126. (Cité en page 103)

Misra, S., Froelich, P. N., 2012. Lithium Isotope History of Cenozoic Seawater: Changes in Silicate Weathering and Reverse Weathering. *Science*, Vol. **335**(6070), p. 818–823. (Cité en page 62)

Misra, S., Greaves, M., Owen, R., Kerr, J., Elmore, A. C., Elderfield, H., 2014a. Determination of B/Ca of Natural Carbonates by HR-ICP-MS. *Geochem. Geophys. Geosystems*, Vol. **15**(4), p. 1617–1628. (Cité en page 147)

Misra, S., Owen, R., Kerr, J., Greaves, M., Elderfield, H., 2014b. Determination of δ11B by HR-ICP-MS from Mass Limited Samples: Application to Natural Carbonates and Water Samples. *Geochim. Cosmochim. Acta*, Vol. **140**, p. 531–552. (Cité en pages xxx, 93, 114, 115, 116, 118, 123, 129, 131, 132, 133, 145, 146, 147 et 148)

Monnin, E., 2001. Atmospheric CO2 Concentrations over the Last Glacial Termination. *Science*, Vol. **291**(5501), p. 112–114. (Cité en page 5)

Mora, C., Dousset, B., Caldwell, I. R., Powell, F. E., Geronimo, R. C., Bielecki, C. R., Counsell, C. W. W., Dietrich, B. S., Johnston, E. T., Louis, L. V., Lucas, M. P., McKenzie, M. M., Shea, A. G., Tseng, H., Giambelluca, T. W., Leon, L. R., Hawkins, E., Trauernicht, C., 2017. Global Risk of Deadly Heat. *Nat. Clim. Change*, Vol. **7**(7), p. 501–506. (Cité en page 5)

Mora, C., Spirandelli, D., Franklin, E. C., Lynham, J., Kantar, M. B., Miles, W., Smith, C. Z., Freel, K., Moy, J., Louis, L. V., Barba, E. W., Bettinger, K., Frazier, A. G., Colburn IX, J. F., Hanasaki, N., Hawkins, E., Hirabayashi, Y., Knorr, W., Little, C. M., Emanuel, K., Sheffield, J., Patz, J. A., Hunter, C. L., 2018. Broad Threat to Humanity from Cumulative Climate Hazards Intensified by Greenhouse Gas Emissions. *Nat. Clim. Change*, Vol. **8**(12), p. 1062–1071. (Cité en page 5)

Mucek, A. E., Danišík, M., de Silva, S. L., Schmitt, A. K., Pratomo, I., Coble, M. A., 2017. Post-Supereruption Recovery at Toba Caldera. *Nat. Commun.*, Vol. **8**(1), p. 15248. (Cité en page 167)

Muller, R. D., Sdrolias, M., Gaina, C., Steinberger, B., Heine, C., 2008. Long-Term Sea-Level Fluctuations Driven by Ocean Basin Dynamics. *Science*, Vol. **319**(5868), p. 1357–1362. (Cité en pages xxvi et 54)

Müller, R. D., Seton, M., Zahirovic, S., Williams, S. E., Matthews, K. J., Wright, N. M., Shephard, G. E., Maloney, K. T., Barnett-Moore, N., Hosseinpour, M., Bower, D. J., Cannon, J., 2016. Ocean Basin Evolution and Global-Scale Plate Reorganization Events Since Pangea Breakup. *Annu. Rev. Earth Planet. Sci.*, Vol. **44**(1), p. 107–138. (Cité en pages 54 et 55)

Müller, T., Jurikova, H., Gutjahr, M., Tomašových, A., Schlögl, J., Liebetrau, V., v. Duarte, L., Milovský, R., Suan, G., Mattioli, E., Pittet, B., Eisenhauer, A., 2020. Ocean Acidification during the Early Toarcian Extinction Event: Evidence from Boron Isotopes in Brachiopods. *Geology*. (Cité en pages xxv, xxviii, 29, 31, 46, 50, 82, 83 et 163)

Nam, S.-H., Lim, J.-S., Montaser, A., 1994. High-Efficiency Nebulizer for Argon Inductively Coupled Plasma Mass Spectrometry. *J. Anal. At. Spectrom.*, Vol. **9**(12), p. 1357–1362. (Cité en page 95)

Nehrke, G., Keul, N., Langer, G., de Nooijer, L. J., Bijma, J., Meibom, A., 2013. A New Model for Biomineralization and Trace-Element Signatures of Foraminifera Tests. *Biogeosciences*, Vol. **10**(10), p. 6759–6767. (Cité en pages 24 et 144)

Newman, K., 2012. Effects of the Sampling Interface in MC-ICP-MS: Relative Elemental Sensitivities and Non-Linear Mass Dependent Fractionation of Nd Isotopes. *J Anal Spectrom*, Vol. **27**(1), p. 63–70. (Cité en page 123)

Ni, Y., Foster, G. L., Bailey, T., Elliott, T., Schmidt, D. N., Pearson, P., Haley, B., Coath, C., 2007. A Core Top Assessment of Proxies for the Ocean Carbonate System in Surface-Dwelling Foraminifers: PROXIES FOR THE OCEAN CARBONATE SYSTEM. *Paleoceanography*, Vol. **22**(3), p. n/a–n/a. (Cité en page 144)

Ni, Y., Foster, G. L., Elliott, T., 2010. The Accuracy of δ11B Measurements of Foraminifers. *Chem. Geol.*, Vol. **274**(3-4), p. 187–195. (Cité en page 145)

Ninkovich, D., Sparks, R. S. J., Ledbetter, M. T., 1978. The Exceptional Magnitude and Intensity of the Toba Eruption, Sumatra: An Example of the Use of Deep-Sea Tephra Layers as a Geological Tool. *Bull Volcanol*, Vol. **41**(3), p. 286. (Cité en pages 164, 165, 167 et 176)

Nir, O., Vengosh, A., Harkness, J. S., Dwyer, G. S., Lahav, O., 2015. Direct Measurement of the Boron Isotope Fractionation Factor: Reducing the Uncertainty in Reconstructing Ocean Paleo-pH. *Earth Planet. Sci. Lett.*, Vol. **414**, p. 1–5. (Cité en page 21)

Niu, H., Houk, R., 1996. Fundamental Aspects of Ion Extraction in Inductively Coupled Plasma Mass Spectrometry. *Spectrochim. Acta Part B At. Spectrosc.*, Vol. **51**(8), p. 779–815. (Cité en page 126)

Noireaux, J., Mavromatis, V., Gaillardet, J., Schott, J., Montouillout, V., Louvat, P., Rollion-Bard, C., Neuville, D., 2015. Crystallographic Control on the Boron Isotope Paleo-pH Proxy. *Earth Planet. Sci. Lett.*, Vol. **430**, p. 398–407. (Cité en pages 23 et 51)

Ohnemueller, F., Prave, A. R., Fallick, A. E., Kasemann, S. A., 2014. Ocean Acidification in the Aftermath of the Marinoan Glaciation. *Geology*, Vol. **42**(12), p. 1103–1106. (Cité en pages xxv, xxviii, 10, 31, 45, 46, 48, 51, 59, 82 et 83)

Oi, T., Nomura, M., Musashi, M., Ossaka, T., Okamoto, M., Kakihana, H., 1989. Boron Isotopic Compositions of Some Boron Minerals. *Geochim. Cosmochim. Acta*, Vol. **53**(12), p. 3189–3195. (Cité en page 45)

Opdyke, B. N., Wilkinson, B. H., 1988. Surface Area Control of Shallow Cratonic to Deep Marine Carbonate Accumulation. *Paleoceanography*, Vol. **3**(6), p. 685–703. (Cité en page 54)

Oppenheimer, C., 2002. Limited Global Change Due to the Largest Known Quaternary Eruption, Toba ≈74kyr BP? *Quaternary Science Reviews*, Vol. **21**(14), p. 1593–1609. (Cité en pages 165 et 166)

Orr, J. C., Fabry, V. J., Aumont, O., Bopp, L., Doney, S. C., Feely, R. A., Gnanadesikan, A., Gruber, N., Ishida, A., Joos, F., Key, R. M., Lindsay, K., Maier-Reimer, E., Matear, R., Monfray, P., Mouchet, A., Najjar, R. G., Plattner, G.-K., Rodgers, K. B., Sabine, C. L., Sarmiento, J. L., Schlitzer, R., Slater, R. D., Totterdell, I. J., Weirig, M.-F., Yamanaka, Y., Yool, A., 2005. Anthropogenic Ocean Acidification over the Twenty-First Century and Its Impact on Calcifying Organisms. *Nature*, Vol. **437**(7059), p. 681–686. (Cité en pages 78 et 114)

Osborne, E. B., Thunell, R. C., Gruber, N., Feely, R. A., Benitez-Nelson, C. R., 2020. Decadal Variability in Twentieth-Century Ocean Acidification in the California Current Ecosystem. *Nat. Geosci.*, Vol. **13**(1), p. 43–49. (Cité en page 158)

Otto-Bliesner, B. L., 1995. Continental Drift, Runoff, and Weathering Feedbacks: Implications from Climate Model Experiments. *J. Geophys. Res.*, Vol. **100**(D6), p. 11537. (Cité en pages xxvi, xxviii, 39, 56, 57, 86 et 87)

Pace, H. E., Rogers, N. J., Jarolimek, C., Coleman, V. A., Higgins, C. P., Ranville, J. F., 2011. Determining Transport Efficiency for the Purpose of Counting and Sizing Nanoparticles via Single Particle Inductively Coupled Plasma Mass Spectrometry. *Anal Chem*, Vol. **83**(24), p. 9361–9369. (Cité en pages 100 et 107)

Pagani, M., 2002. The Alkenone-CO2 Proxy and Ancient Atmospheric Carbon Dioxide. *Philos Trans A Math Phys Eng Sci*, Vol. **360**(1793), p. 609–632. (Cité en page 8)

Pagani, M., Lemarchand, D., Spivack, A., Gaillardet, J., 2005. A Critical Evaluation of the Boron Isotope-pH Proxy: The Accuracy of Ancient Ocean pH Estimates. *Geochim. Cosmochim. Acta*, Vol. **69**(4), p. 953–961. (Cité en pages 11, 21, 23, 30 et 59)

Palmer, M., Spivack, A., Edmond, J., 1987. Temperature and pH Controls over Isotopic Fractionation during Adsorption of Boron on Marine Clay. *Geochim. Cosmochim. Acta*, Vol. **51**(9), p. 2319–2323. (Cité en pages xxiv, 35, 36 et 79)

Palmer, M. R., Pearson, P. N., Cobb, S. J., 1998. Reconstructing Past Ocean pH-Depth Profiles. *Science*, Vol. **282**(5393), p. 1468–1471. (Cité en pages xxv, xxvii, 30, 44, 79 et 81)

Pang, X., Bassinot, F., Sepulcre, S., 2020. Cleaning Method Impact on the Mg/Ca of Three Planktonic Foraminifer Species: A Downcore Study along a Depth Transect. *Chem. Geol.*, Vol. **549**, p. 119690. (Cité en pages 144, 147 et 169)

Paredes, E., Asfaha, D. G., Ponzevera, E., Brach-Papa, C., Bocxstaele, M. V., Todolí, J. L., Quétel, C. R., 2011. MC-ICPMS Isotope Ratio Measurements Using an Ultra-Low Flow Sample Introduction System. *J. Anal. At. Spectrom.*, Vol. **26**(7), p. 1372–1379. (Cité en page 96)

Paredes, E., Asfaha, D. G., Quétel, C. R., 2013. Isotope Ratio Measurements by MC-ICPMS below 10 μL Min-1 under Continuous Sample Flow Conditions. Exploring the Limits with Strontium. *J. Anal. At. Spectrom.*, Vol. **28**(3), p. 320–326. (Cité en page 96)

Paredes, E., Grotti, M., Mermet, J. M., Todolí, J. L., 2009. Heated-Spray Chamber-Based Low Sample Consumption System for Inductively Coupled Plasma Spectrometry. *J. Anal. At. Spectrom.*, Vol. **24**(7), p. 903–910. (Cité en page 96)

Paris, G., Bartolini, A., Donnadieu, Y., Beaumont, V., Gaillardet, J., 2010a. Investigating Boron Isotopes in a Middle Jurassic Micritic Sequence: Primary vs. Diagenetic Signal. *Chem. Geol.*, Vol. **275**(3-4), p. 117–126. (Cité en pages xxxiii, 33, 135 et 136)

Paris, G., Gaillardet, J., Louvat, P., 2010b. Geological Evolution of Seawater Boron Isotopic Composition Recorded in Evaporites. *Geology*, Vol. **38**(11), p. 1035–1038. (Cité en pages xxv, xxvii, xxviii, 28, 31, 33, 34, 40, 41, 43, 44, 45, 46, 47, 48, 57, 58, 62, 63, 75, 81 et 83)

Parker, D. E., Wilson, H., Jones, P. D., Christy, J. R., Folland, C. K., 1996. The Impact of Mount Pinatubo on World-Wide Temperatures. *Int. J. Climatol.*, Vol. **16**(5), p. 487–497. (Cité en page 163)

Parker, W. K., Jones, T. R., 1865. On Some Foraminifera from the North Atlantic and Arctic Oceans, Including Davis Straits and Baffin's Bay. *Dans : On Some Foraminifera from the North Atlantic and Arctic Oceans, Including Davis Straits and Baffin's Bay*. Vol. 155. Philosophical Transactions of the Royal Society of London, p. 325–441. (Cité en page 168)

Pattan, J. N., Shane, P., Banakar, V. K., 1999. New Occurrence of Youngest Toba Tuff in Abyssal Sediments of the Central Indian Basin. *Marine Geology*, Vol. **155**(3), p. 243–248. (Cité en page 165)

Payne, J. L., Clapham, M. E., 2012. End-Permian Mass Extinction in the Oceans: An Ancient Analog for the Twenty-First Century? *Annu. Rev. Earth Planet. Sci.*, Vol. **40**(1), p. 89–111. (Cité en page 9)

Pearson, P. N., Foster, G. L., Wade, B. S., 2009. Atmospheric Carbon Dioxide through the Eocene–Oligocene Climate Transition. *Nature*, Vol. **461**(7267), p. 1110–1113. (Cité en pages xxv, xxvii, 10, 43, 44, 80 et 81)

Pearson, P. N., Palmer, M. R., 1999. Middle Eocene Seawater pH and Atmospheric Carbon Dioxide Concentrations. *Science*, Vol. **284**(5421), p. 1824–1826. (Cité en pages xxv, xxvii, 10, 29, 30, 44, 79 et 81)

Pearson, P. N., Palmer, M. R., 2000. Atmospheric Carbon Dioxide Concentrations over the Past 60 Million Years. *Nature*, Vol. **406**(6797), p. 695–699. (Cité en pages xxv, xxvii, 9, 10, 28, 29, 30, 43, 44, 48, 50, 79, 81, 114 et 144)

Pelejero, C., Calvo, E., Hoegh-Guldberg, O., 2010. Paleo-Perspectives on Ocean Acidification. *Trends Ecol. Evol.*, Vol. **25**(6), p. 332–344. (Cité en page 15)

Pelejero, C., Calvo, E., McCulloch, M. T., Marshall, J. F., Gagan, M. K., Lough, J. M., Opdyke, B. N., 2005. Preindustrial to Modern Interdecadal Variability in Coral Reef pH. *Science*, Vol. **309**(5744), p. 2204–2207. (Cité en page 29)

Penman, D. E., Hönisch, B., Rasbury, E. T., Hemming, N. G., Spero, H. J., 2013. Boron, Carbon, and Oxygen Isotopic Composition of Brachiopod Shells: Intra-Shell Variability, Controls, and Potential as a Paleo-pH Recorder. *Chem. Geol.*, Vol. **340**, p. 32–39. (Cité en pages 82 et 137)

Pergantis, S. A., Heithmar, E. M., Hinners, T. A., 1995. Microscale Flow Injection and Microbore High-Performance Liquid Chromatography Coupled with Inductively Coupled Plasma Mass Spectrometry via a High-Efficiency Nebulizer. *Anal. Chem.*, Vol. **67**(24), p. 4530–4535. (Cité en page 96)

Peters, S. T., Münker, C., Wombacher, F., Elfers, B.-M., 2015. Precise Determination of Low Abundance Isotopes (174Hf, 180W and 190Pt) in Terrestrial Materials and Meteorites Using Multiple Collector ICP-MS Equipped with 1012Ω Faraday Amplifiers. *Chem. Geol.*, Vol. **413**, p. 132–145. (Cité en page 127)

Petit, J. R., Jouzel, J., Raynaud, D., Barkov, N. I., Barnola, J.-M., Basile, I., Bender, M., Chappellaz, J., Davis, M., Delaygue, G., Delmotte, M., Kotlyakov, V. M., Legrand, M., Lipenkov, V. Y., Lorius, C., PÉpin, L., Ritz, C., Saltzman, E., Stievenard, M., 1999. Climate and Atmospheric History of the Past 420,000 Years from the Vostok Ice Core, Antarctica. *Nature*, Vol. **399**(6735), p. 429–436. (Cité en pages 2, 6 et 10)

Petrychenko, O. Y., Peryt, T. M., Chechel, E. I., 2005. Early Cambrian Seawater Chemistry from Fluid Inclusions in Halite from Siberian Evaporites. *Chem. Geol.*, Vol. **219**(1-4), p. 149–161. (Cité en page 72)

Pfeifer, M., Lloyd, N. S., Peters, S. T. M., Wombacher, F., Elfers, B.-M., Schulz, T., Münker, C., 2017. Tantalum Isotope Ratio Measurements and Isotope Abundances Determined by MC-ICP-MS Using Amplifiers Equipped with 10^{10}, 10^{12} and 10^{13} Ohm Resistors. *J. Anal. At. Spectrom.*, Vol. **32**(1), p. 130–143. (Cité en page 127)

Pierrot, Wallace, Lewis, 2011. MS Excel Program Developed for CO2 System Calculations. . (Cité en page 156)

Pin, C., Bassin, C., 1992. Evaluation of a Strontium-Specific Extraction Chromatographic Method for Isotopic Analysis in Geological Materials. *Anal. Chim. Acta*, Vol. **269**(2), p. 249–255. (Cité en page 34)

Pinto, V. H. G., Manatschal, G., Karpoff, A. M., Ulrich, M., Viana, A. R., 2017. Seawater Storage and Element Transfer Associated with Mantle Serpentinization in Magma-Poor Rifted Margins: A Quantitative Approach. *Earth Planet. Sci. Lett.*, Vol. **459**, p. 227–237. (Cité en page 50)

Prokoph, A., Shields, G., Veizer, J., 2008. Compilation and Time-Series Analysis of a Marine Carbonate δ18O, δ13C, 87Sr/86Sr and δ34S Database through Earth History. *Earth-Sci. Rev.*, Vol. **87**(3-4), p. 113–133. (Cité en pages xxv, xxvi, 41 et 61)

Raab, M., Friedman, G. M., Spiro, B., Starinsky, A., Zak, I., 2000. The Geological History of Pliocene-Pleistocene Evaporites in Mount Sedom (Israel) and How Strontium and Sulfur Isotopes Relate to Their Origin. *Carbonates Evaporites*, Vol. **15**(2), p. 93–114. (Cité en page 43)

Rae, J. W., Foster, G. L., Schmidt, D. N., Elliott, T., 2011. Boron Isotopes and B/Ca in Benthic Foraminifera: Proxies for the Deep Ocean Carbonate System. *Earth Planet. Sci. Lett.*, Vol. **302**(3-4), p. 403–413. (Cité en pages xxx, xxxi, xxxii, 22, 24, 114, 132, 137, 144, 145, 147, 151, 152, 170 et 171)

Rae, J. W. B., 2018. Boron Isotopes in Foraminifera: Systematics, Biomineralisation, and CO2 Reconstruction. *Dans : Marschall, H., Foster, G. (Eds.), Boron Isotopes: The Fifth Element*. Advances in Isotope Geochemistry. Springer International Publishing, Cham, p. 107–143. (Cité en page 144)

Rae, J. W. B., Burke, A., Robinson, L. F., Adkins, J. F., Chen, T., Cole, C., Greenop, R., Li, T., Littley, E. F. M., Nita, D. C., Stewart, J. A., Taylor, B. J., 2018. CO2 Storage and Release in the Deep Southern Ocean on Millennial to Centennial Timescales. *Nature*, Vol. **562**(7728), p. 569–573. (Cité en pages 10 et 114)

Raitzsch, M., Bijma, J., Benthien, A., Richter, K.-U., Steinhoefel, G., Kučera, M., 2018. Boron Isotope-Based Seasonal Paleo-pH Reconstruction for the Southeast Atlantic – A Multispecies Approach Using Habitat Preference of Planktonic Foraminifera. *Earth Planet. Sci. Lett.*, Vol. **487**, p. 138–150. (Cité en pages xxx, xxxi, 22, 24, 116, 118, 127, 131, 132, 144, 145, 146, 148, 155, 156, 157, 170 et 179)

Raitzsch, M., Hathorne, E. C., Kuhnert, H., Groeneveld, J., Bickert, T., 2011. Modern and Late Pleistocene B/Ca Ratios of the Benthic Foraminifer Planulina Wuellerstorfi Determined with Laser Ablation ICP-MS. *Geology*, Vol. **39**(11), p. 1039–1042. (Cité en page 144)

Raitzsch, M., Hönisch, B., 2013. Cenozoic Boron Isotope Variations in Benthic Foraminifers. *Geology*, Vol. **41**(5), p. 591–594. (Cité en pages xxv, xxvii, xxviii, 28, 30, 31, 43, 44, 46, 48, 50, 80, 81 et 83)

Raitzsch, M., Rollion-Bard, C., Horn, I., Steinhoefel, G., Benthien, A., Richter, K.-U., Buisson, M., Louvat, P., Bijma, J., 2020. Technical Note: Single-Shell Δ^{11}B Analysis of *Cibicidoides Wuellerstorfi* Using Femtosecond Laser Ablation MC-ICPMS and Secondary Ion Mass Spectrometry. *Biogeosciences*, Vol. **17**(21), p. 5365–5375. (Cité en page 144)

Rampino, M. R., Self, S., 1992. Volcanic Winter and Accelerated Glaciation Following the Toba Super-Eruption. *Nature*, Vol. **359**(6390), p. 50–52. (Cité en pages 165 et 166)

Renne, P. R., Sharp, W. D., Montañez, I. P., Becker, T. A., Zierenberg, R. A., 2001. 40Ar/39Ar Dating of Late Permian Evaporites, Southeastern New Mexico, USA. *Earth Planet. Sci. Lett.*, Vol. **193**(3-4), p. 539–547. (Cité en page 67)

Ridgwell, A., 2005. A Mid Mesozoic Revolution in the Regulation of Ocean Chemistry. *Mar. Geol.*, Vol. **217**(3-4), p. 339–357. (Cité en page 82)

Riebesell, U., Zondervan, I., Rost, B., Tortell, P. D., Zeebe, R. E., Morel, F. M. M., 2000. Reduced Calcification of Marine Plankton in Response to Increased Atmospheric CO2. *Nature*, Vol. **407**(6802), p. 364–367. (Cité en page 15)

Rigaudier, T., Lécuyer, C., Gardien, V., Suc, J.-P., Martineau, F., 2011. The Record of Temperature, Wind Velocity and Air Humidity in the δD and δ18O of Water Inclusions in Synthetic and Messinian Halites. *Geochim. Cosmochim. Acta*, Vol. **75**(16), p. 4637–4652. (Cité en page 75)

Rino, S., Kon, Y., Sato, W., Maruyama, S., Santosh, M., Zhao, D., 2008. The Grenvillian and Pan-African Orogens: World's Largest Orogenies through Geologic Time, and Their Implications on the Origin of Superplume. *Gondwana Res.*, Vol. **14**(1-2), p. 51–72. (Cité en page 59)

Risacher, F., Clement, A., 2001. A Computer Program for the Simulation of Evaporation of Natural Waters to High Concentration. *Computers & Geosciences*, Vol. **27**(2), p. 191–201. (Cité en page 78)

Roberts, E. A., Houseman, G. A., 2001. Geodynamics of Central Australia during the Intraplate Alice Springs Orogeny: Thin Viscous Sheet Models. *Geol. Soc. Lond. Spec. Publ.*, Vol. **184**(1), p. 139–164. (Cité en page 71)

Robock, A., Ammann, C. M., Oman, L., Shindell, D., Levis, S., Stenchikov, G., 2009. Did the Toba Volcanic Eruption of ~74 Ka B.P. Produce Widespread Glaciation? *J. Geophys. Res. Atmospheres*, Vol. **114**(D10). (Cité en pages 163 et 166)

Rogers, M. B., Pratt, B., 2017. Stratigraphy of the Middle Devonian Keg River and Prairie Evaporite Formations, Northeast Alberta, Canada. *Bull. Can. Pet. Geol.*, Vol. **65**(1), p. 5–63. (Cité en page 70)

Rollion-Bard, C., Blamart, D., Trebosc, J., Tricot, G., Mussi, A., Cuif, J.-P., 2011. Boron Isotopes as pH Proxy: A New Look at Boron Speciation in Deep-Sea Corals Using 11B MAS NMR and EELS. *Geochim. Cosmochim. Acta*, Vol. **75**(4), p. 1003–1012. (Cité en page 23)

Rowley, D. B., 2002. Rate of Plate Creation and Destruction: 180 Ma to Present. *Geol. Soc. Am. Bull.*, Vol. **114**(8), p. 927–933. (Cité en pages xxvi et 54)

Roy, R. N., Roy, L. N., Vogel, K. M., Porter-Moore, C., Pearson, T., Good, C. E., Millero, F. J., Campbell, D. M., 1993. The Dissociation Constants of Carbonic Acid in Seawater at Salinities 5 to 45 and Temperatures 0 to 45°C. *Mar. Chem.*, Vol. **44**(2-4), p. 249–267. (Cité en page 144)

Royer, D., 2014. Atmospheric CO2 and O2 During the Phanerozoic: Tools, Patterns, and Impacts. *Dans : Treatise on Geochemistry*. Elsevier, p. 251–267. (Cité en pages 8 et 37)

Royer, D. L., 2016. Climate Sensitivity in the Geologic Past. *Annu. Rev. Earth Planet. Sci.*, Vol. **44**(1), p. 277–293. (Cité en pages xxiii et 3)

Royer, D. L., Wing, S. L., Beerling, D. J., Jolley, D. W., Koch, P. L., Hickey, L. J., Berner, R. A., 2001. Paleobotanical Evidence for Near Present-Day Levels of Atmospheric CO2 During Part of the Tertiary. *Science*, Vol. **292**(5525), p. 2310–2313. (Cité en pages 6 et 7)

Russell, A. D., Hönisch, B., Spero, H. J., Lea, D. W., 2004. Effects of Seawater Carbonate Ion Concentration and Temperature on Shell U, Mg, and Sr in Cultured Planktonic Foraminifera. *Geochimica et Cosmochimica Acta*, Vol. **68**(21), p. 4347–4361. (Cité en pages 144 et 175)

Russell, W. A., Papanastassiou, D. A., 1978. Calcium Isotope Fractionation in Ion-Exchange Chromatography. *Anal. Chem.*, Vol. **50**(8), p. 1151–1154. (Cité en page 34)

Rustad, J. R., Bylaska, E. J., Jackson, V. E., Dixon, D. A., 2010. Calculation of Boron-Isotope Fractionation between B(OH)3(Aq) And. *Geochim. Cosmochim. Acta*, Vol. **74**(10), p. 2843–2850. (Cité en page 21)

Sabine, C. L., Feely, R. A., Gruber, N., Key, R. M., Lee, K., Bullister, J. L., Wanninkhof, R., Wong, C. S., Wallace, D. W. R., Tilbrook, B., Millero, F. J., Peng, T.-H., Kozyr, A., Ono, T., Rios, A. F., 2004. The Oceanic Sink for Anthropogenic CO2. *Science*, Vol. **305**(5682), p. 367–371. (Cité en page 15)

Sadekov, A., Lloyd, N. S., Misra, S., Trotter, J., D'Olivo, J., McCulloch, M., 2019. Accurate and Precise Microscale Measurements of Boron Isotope Ratios in Calcium Carbonates Using Laser Ablation Multicollector-ICPMS. *J. Anal. At. Spectrom.*, Vol. **34**(3), p. 550–560. (Cité en page 115)

Saldi, G. D., Noireaux, J., Louvat, P., Faure, L., Balan, E., Schott, J., Gaillardet, J., 2018. Boron Isotopic Fractionation during Adsorption by Calcite – Implication for the Seawater pH Proxy. *Geochim. Cosmochim. Acta*, Vol. **240**, p. 255–273. (Cité en pages 51, 100 et 106)

Sánchez, R., Todolí, J. L., Lienemann, C.-P., Mermet, J.-M., 2013. Determination of Trace Elements in Petroleum Products by Inductively Coupled Plasma Techniques: A Critical Review. *Spectrochimica Acta Part B: Atomic Spectroscopy*, Vol. **88**, p. 104–126. (Cité en page 95)

Sanchez-Valle, C., Reynard, B., Daniel, I., Lecuyer, C., Martinez, I., Chervin, J.-C., 2005. Boron Isotopic Fractionation between Minerals and Fluids: New Insights from in Situ High Pressure-High Temperature Vibrational Spectroscopic Data. *Geochim. Cosmochim. Acta*, Vol. **69**(17), p. 4301–4313. (Cité en page 21)

Sandberg, P. A., 1983. An Oscillating Trend in Phanerozoic Non-Skeletal Carbonate Mineralogy. *Nature*, Vol. **305**(5929), p. 19–22. (Cité en pages xxvi et 61)

Sanyal, A., Bijma, J., 1999. A Comparative Study of the Northwest Africa and Eastern Equatorial Pacific Upwelling Zones as Sources of CO $_2$ during Glacial Periods Based on Boron Isotope Paleo-pH Estimation. *Paleoceanography*, Vol. **14**(6), p. 753–759. (Cité en page 29)

Sanyal, A., Bijma, J., Spero, H., Lea, D. W., 2001. Empirical Relationship between pH and the Boron Isotopic Composition of *Globigerinoides Sacculifer* : Implications for the Boron Isotope Paleo-pH Proxy. *Paleoceanography*, Vol. **16**(5), p. 515–519. (Cité en pages 22, 24 et 144)

Sanyal, A., Hemming, N. G., Broecker, W. S., Lea, D. W., Spero, H. J., Hanson, G. N., 1996. Oceanic *p* H Control on the Boron Isotopic Composition of Foraminifera: Evidence from Culture Experiments. *Paleoceanography*, Vol. **11**(5), p. 513–517. (Cité en pages 29 et 144)

Sanyal, A., Hemming, N. G., Hanson, G. N., Broecker, W. S., 1995. Evidence for a Higher pH in the Glacial Ocean from Boron Isotopes in Foraminifera. *Nature*, Vol. **373**(6511), p. 234–236. (Cité en page 144)

Scher, H. D., Griffith, E. M., Buckley, W. P., 2014. Accuracy and Precision of ^{88}Sr/^{86}Sr and ^{87}Sr/^{86}Sr Measurements by MC-ICPMS Compromised by High Barium Concentrations: Sr ISOTOPES FROM Ba-RICH MATRICES. *Geochem. Geophys. Geosystems*, Vol. **15**(2), p. 499–508. (Cité en page 34)

Schiebel, R., 2002. Planktic Foraminiferal Sedimentation and the Marine Calcite Budget: MARINE CALCITE BUDGET. *Glob. Biogeochem. Cycles*, Vol. **16**(4), p. 3–1–3–21. (Cité en page 168)

Schiebel, R., Hemleben, C., 2017. *Planktic Foraminifers in the Modern Ocean*. Springer Berlin Heidelberg, Berlin, Heidelberg. (Cité en pages 22, 82, 146 et 168)

Schiebel, R., Smart, S. M., Jentzen, A., Jonkers, L., Morard, R., Meilland, J., Michel, E., Coxall, H. K., Hull, P. M., de Garidel-Thoron, T., Aze, T., Quillévéré, F., Ren, H., Sigman, D. M., Vonhof, H. B., Martínez-García, A., Kučera, M., Bijma, J., Spero, H. J., Haug, G. H., 2018. Advances in Planktonic Foraminifer Research: New Perspectives for Paleoceanography. *Rev. Micropaléontologie*, Vol. **61**(3-4), p. 113–138. (Cité en page 144)

Schlitzer, R., 2015. Data Analysis and Visualization with Ocean Data View. *CMOS Bull. SCMO*, Vol. **43**(1), p. 9–13. (Cité en page 156)

Scholle, P. A., Ulmer, D. S., Melim, L. A., 1992. Late-Stage Calcites in the Permian Capitan Formation and Its Equivalents, Delaware Basin Margin, West Texas and New Mexico: Evidence for Replacement of Precursor Evaporites. *Sedimentology*, Vol. **39**(2), p. 207–234. (Cité en page 69)

Schröder, S., Schreiber, B. C., Amthor, J. E., Matter, A., 2003. A Depositional Model for the Terminal Neoproterozoic-Early Cambrian Ara Group Evaporites in South Oman: *Deposition of Terminal Neoproterozoic-Early Cambrian Evaporites in Oman*. *Sedimentology*, Vol. **50**(5), p. 879–898. (Cité en page 74)

Schulz, H., Emeis, K.-C., Erlenkeuser, H., von Rad, U., Rolf, C., 2002. The Toba Volcanic Event and Interstadial/Stadial Climates at the Marine Isotopic Stage 5 to 4 Transition in the Northern Indian Ocean. *Quaternary Research*, Vol. **57**(1), p. 22–31. (Cité en page 165)

Schwartzman, D. W., Volk, T., 1989. Biotic enhancement of weathering and the habitability of Earth. *NATURE*, Vol. **340**(6233), p. 457–460. (Cité en page 3)

Scribano, V., Carbone, S., Manuella, F. C., Hovland, M., Rueslåtten, H., Johnsen, H.-K., 2017. Origin of Salt Giants in Abyssal Serpentinite Systems. *Int. J. Earth Sci.*, Vol. **106**(7), p. 2595–2608. (Cité en pages 50 et 185)

Seki, O., Foster, G. L., Schmidt, D. N., Mackensen, A., Kawamura, K., Pancost, R. D., 2010. Alkenone and Boron-Based Pliocene pCO2 Records. *Earth Planet. Sci. Lett.*, Vol. **292**(1-2), p. 201–211. (Cité en page 8)

Self, S., Blake, S., 2008. Consequences of Explosive Supereruptions. *Elements*, Vol. **4**(1), p. 41–46. (Cité en page 163)

Sen, S., Stebbins, J. F., Hemming, N. G., Ghosh, B., 1994. Coordination Environments of B Impurities in Calcite and Aragonite Polymorphs: A 11B MAS NMR Study. *American Mineralogist*, Vol. **79**(9-10), p. 819–825. (Cité en page 144)

Seton, M., Gaina, C., Muller, R., Heine, C., 2009. Mid-Cretaceous Seafloor Spreading Pulse: Fact or Fiction? *Geology*, Vol. **37**(8), p. 687–690. (Cité en pages xxvi et 54)

Seton, M., Müller, R., Zahirovic, S., Gaina, C., Torsvik, T., Shephard, G., Talsma, A., Gurnis, M., Turner, M., Maus, S., Chandler, M., 2012. Global Continental and Ocean Basin Reconstructions since 200Ma. *Earth-Sci. Rev.*, Vol. **113**(3-4), p. 212–270. (Cité en page 55)

Shalev, N., Lazar, B., Köbberich, M., Halicz, L., Gavrieli, I., 2018. The Chemical Evolution of Brine and Mg-K-Salts along the Course of Extreme Evaporation of Seawater – An Experimental Study. *Geochim. Cosmochim. Acta*, Vol. **241**, p. 164–179. (Cité en pages xxvi, 67 et 185)

Short, E. E., Caminade, C., Thomas, B. N., 2017. Climate Change Contribution to the Emergence or Re-Emergence of Parasitic Diseases. *Infect. Dis. Res. Treat.*, Vol. **10**, p. 117863361773229. (Cité en page 5)

Shuttleworth, R., Bostock, H., Chalk, T., Calvo, E., Jaccard, S., Pelejero, C., Martínez-García, A., Foster, G., 2020. Early Deglacial CO2 Release from the Sub-Antarctic Atlantic and Pacific Oceans. *Earth Planet. Sci. Lett.*, p. 116649. (Cité en pages 10 et 29)

Sicre, M.-A., Khodri, M., Mignot, J., Allard, P., Balkanski, Y., Bard, É., 2017. 5. Effet Des Éruptions Volcaniques Sur Le Climat. *Dans : Jeandel, C., Mosseri, R. (Eds.), Le Climat à Découvert*. À Découvert. CNRS Éditions, Paris, p. 201–203. (Cité en page 178)

Siemann, M. G., 2003. Extensive and Rapid Changes in Seawater Chemistry during the Phanerozoic: Evidence from Br Contents in Basal Halite: Changes in Seawater Chemistry during the Phanerozoic. *Terra Nova*, Vol. **15**(4), p. 243–248. (Cité en page 74)

Sigman, D. M., Boyle, E. A., 2000. Glacial/Interglacial Variations in Atmospheric Carbon Dioxide. *Nature*, Vol. **407**(6806), p. 859–869. (Cité en page 2)

Sigman, D. M., Hain, M. P., Haug, G. H., 2010. The Polar Ocean and Glacial Cycles in Atmospheric CO2 Concentration. *Nature*, Vol. **466**(7302), p. 47–55. (Cité en page 2)

Silva, D., Piazolo, S., Daczko, N. R., Houseman, G., Raimondo, T., Evans, L., 2018. Intracontinental Orogeny Enhanced by Far-Field Extension and Local Weak Crust. *Tectonics*, Vol. **37**(12), p. 4421–4443. (Cité en page 71)

Simon, L., Lécuyer, C., Maréchal, C., Coltice, N., 2006. Modelling the Geochemical Cycle of Boron: Implications for the Long-Term δ11B Evolution of Seawater and Oceanic Crust. *Chem. Geol.*, Vol. **225**(1-2), p. 61–76. (Cité en pages xxv, xxviii, 30, 31, 46, 79, 82, 83 et 84)

Smith, E. I., Jacobs, Z., Johnsen, R., Ren, M., Fisher, E. C., Oestmo, S., Wilkins, J., Harris, J. A., Karkanas, P., Fitch, S., Ciravolo, A., Keenan, D., Cleghorn, N., Lane, C. S., Matthews, T., Marean, C. W., 2018. Humans Thrived in South Africa through the Toba Eruption about 74,000 Years Ago. *Nature*, Vol. **555**(7697), p. 511–515. (Cité en page 165)

Smith, H., Spivack, A. J., Staudigel, H., Hart, S. R., 1995. The Boron Isotopic Composition of Altered Oceanic Crust. *Chem. Geol.*, Vol. **126**(2), p. 119–135. (Cité en pages xxiv, 35 et 36)

Spaak, G., Edwards, D. S., Foster, C. B., Pagès, A., Summons, R. E., Sherwood, N., Grice, K., 2017. Environmental Conditions and Microbial Community Structure during the Great Ordovician Biodiversification Event; a Multi-Disciplinary Study from the Canning Basin, Western Australia. *Glob. Planet. Change*, Vol. **159**, p. 93–112. (Cité en pages xxvii et 72)

Spear, N., Holland, H., Garcia-Veígas, J., Lowenstein, T., Giegengack, R., Peters, H., 2014. Analyses of Fluid Inclusions in Neoproterozoic Marine Halite Provide Oldest Measurement of Seawater Chemistry. *Geology*, Vol. **42**(2), p. 103–106. (Cité en pages 31 et 75)

Spivack, A., Palmer, M., Edmond, J., 1987. The Sedimentary Cycle of the Boron Isotopes. *Geochim. Cosmochim. Acta*, Vol. **51**(7), p. 1939–1949. (Cité en pages 36 et 78)

Spivack, A. J., Edmond, J. M., 1987. Boron Isotope Exchange between Seawater and the Oceanic Crust. *Geochimica et Cosmochimica Acta*, Vol. **51**(5), p. 1033–1043. (Cité en pages xxiv, 30, 35, 36 et 78)

Spivack, A. J., You, C.-F., Smith, H. J., 1993. Foraminiferal Boron Isotope Ratios as a Proxy for Surface Ocean pH over the Past 21 Myr. *Nature*, Vol. **363**(6425), p. 149. (Cité en pages 30 et 78)

Stefánka, Z., Koellensperger, G., Stingeder, G., Hann, S., 2006. Down-Scaling Narrowbore LC-ICP-MS to Capillary LC-ICP-MS: A Comparative Study of Different Introduction Systems. *J. Anal. At. Spectrom.*, Vol. **21**(1), p. 86–89. (Cité en page 95)

Steffen, W., Richardson, K., Rockstrom, J., Cornell, S. E., Fetzer, I., Bennett, E. M., Biggs, R., Carpenter, S. R., de Vries, W., de Wit, C. A., Folke, C., Gerten, D., Heinke, J., Mace, G. M., Persson, L. M., Ramanathan, V., Reyers, B., Sorlin, S., 2015. Planetary Boundaries: Guiding Human Development on a Changing Planet. *Science*, Vol. **347**(6223), p. 1259855–1259855. (Cité en page 5)

Steffen, W., Rockström, J., Richardson, K., Lenton, T. M., Folke, C., Liverman, D., Summerhayes, C. P., Barnosky, A. D., Cornell, S. E., Crucifix, M., Donges, J. F., Fetzer, I., Lade, S. J., Scheffer, M., Winkelmann, R., Schellnhuber, H. J., 2018. Trajectories of the Earth System in the Anthropocene. *Proc. Natl. Acad. Sci.*, Vol. **115**(33), p. 8252–8259. (Cité en page 5)

Stein, M., 2001. The Sedimentary and Geochemical Record of Neogene-Quaternary Water Bodies in the Dead Sea Basin - Inferences for the Regional Paleoclimatic History. *Journal of Paleolimnology*, Vol. **26**(3), p. 271–282. (Cité en page 68)

Stein, M., Starinsky, A., Agnon, A., Katz, A., Raab, M., Spiro, B., Zak, I., 2000. The Impact of Brine-Rock Interaction during Marine Evaporite Formation on the Isotopic Sr Record in the Oceans: Evidence from Mt. Sedom, Israel. *Geochim. Cosmochim. Acta*, Vol. **64**(12), p. 2039–2053. (Cité en pages 43, 68, 74 et 75)

Steinthorsdottir, M., Vajda, V., 2015. Early Jurassic (Late Pliensbachian) CO2 Concentrations Based on Stomatal Analysis of Fossil Conifer Leaves from Eastern Australia. *Gondwana Research*, Vol. **27**(3), p. 932–939. (Cité en page 6)

Stewart, J. A., Christopher, S. J., Kucklick, J. R., Bordier, L., Chalk, T. B., Dapoigny, A., Douville, E., Foster, G. L., Gray, W. R., Greenop, R., Gutjahr, M., Hemsing, F., Henehan, M. J., Holdship, P., Hsieh, Y.-T., Kolevica, A., Lin, Y.-P., Mawbey, E. M., Rae, J. W. B., Robinson, L. F., Shuttleworth, R., You, C.-F., Zhang, S., Day, R. D., 2021. NIST RM 8301 Boron Isotopes in Marine Carbonate (Simulated Coral and Foraminifera Solutions): Inter-Laboratory δ11B and Trace Element Ratio Value Assignment. *Geostand. Geoanalytical Res.*, Vol. **45**(1), p. 77–96. (Cité en pages xxx, 117, 134, 135 et 139)

Storey, M., Roberts, R. G., Saidin, M., 2012. Astronomically Calibrated 40Ar/39Ar Age for the Toba Supereruption and Global Synchronization of Late Quaternary Records. *PNAS*, Vol. **109**(46), p. 18684–18688. (Cité en page 165)

Sundquist, E., Ackerman, K. V., 2014. The Geologic History of the Carbon Cycle. Dans : *Treatise on Geochemistry*. Elsevier, p. 361–398. (Cité en pages 7, 8 et 59)

Sutton, J. N., Liu, Y.-W., Ries, J. B., Guillermic, M., Ponzevera, E., Eagle, R. A., 2018. δ11B as Monitor of Calcification Site pH in Divergent Marine Calcifying Organisms. *Biogeosciences*, Vol. **15**(5), p. 1447–1467. (Cité en page 137)

Svensson, A., Bigler, M., Blunier, T., Clausen, H. B., Dahl-Jensen, D., Fischer, H., Fujita, S., Goto-Azuma, K., Johnsen, S. J., Kawamura, K., Kipfstuhl, S., Kohno, M., Parrenin, F., Popp, T., Rasmussen, S. O., Schwander, J., Seierstad, I., Severi, M., Steffensen, J. P., Udisti, R., Uemura, R., Vallelonga, P., Vinther, B. M., Wegner, A., Wilhelms, F., Winstrup, M., 2013. Direct Linking of Greenland and Antarctic Ice Cores at the Toba Eruption (74 Ka BP). *Clim. Past*, Vol. **9**(2), p. 749–766. (Cité en pages 166 et 167)

Swihart, G. H., Moore, P. B., Callis, E. L., 1986. Boron Isotopic Composition of Marine and Nonmarine Evaporite Borates. *Geochim. Cosmochim. Acta*, Vol. **50**(6), p. 1297–1301. (Cité en page 45)

Swingedouw, D., Ortega, P., Mignot, J., Guilyardi, E., Masson-Delmotte, V., Butler, P. G., Khodri, M., Séférian, R., 2015. Bidecadal North Atlantic Ocean Circulation Variability Controlled by Timing of Volcanic Eruptions. *Nat. Commun.*, Vol. **6**(1), p. 6545. (Cité en page 166)

Taberner, C., CendoÂn, D. I., Pueyo, J. J., Ayora, C., 2000. The Use of Environmental Markers to Distinguish Marine vs. Continental Deposition and to Quantify the Signi®cance of Recycling in Evaporite Basins. *Sediment. Geol.*, p. 28. (Cité en page 74)

Takasaki, Y., Inagaki, K., Sabarudin, A., Fujii, S.-I., Iwahata, D., Takatsu, A., Chiba, K., Umemura, T., 2011. Multielement Analysis of Micro-Volume Biological Samples by ICP-MS with Highly Efficient Sample Introduction System. *Talanta*, Vol. **87**, p. 24–29. (Cité en page 96)

Tharaud, M., Gondikas, A. P., Benedetti, M. F., von der Kammer, F., Hofmann, T., Cornelis, G., 2017. TiO2 Nanomaterial Detection in Calcium Rich Matrices by spICPMS. A Matter of Resolution and Treatment. *J. Anal. At. Spectrom.*, Vol. **32**(7), p. 1400–1411. (Cité en page 107)

Tierney, J. E., Poulsen, C. J., Montañez, I. P., Bhattacharya, T., Feng, R., Ford, H. L., Hönisch, B., Inglis, G. N., Petersen, S. V., Sagoo, N., Tabor, C. R., Thirumalai, K., Zhu, J., Burls, N. J., Foster, G. L., Goddéris, Y., Huber, B. T., Ivany, L. C., Turner, S. K., Lunt, D. J., McElwain, J. C., Mills, B. J. W., Otto-Bliesner, B. L., Ridgwell, A., Zhang, Y. G., 2020. Past Climates Inform Our Future. *Science*, Vol. **370**(6517). (Cité en pages 5, 9 et 29)

Timmreck, C., 2012. Modeling the Climatic Effects of Large Explosive Volcanic Eruptions. *WIREs Clim. Change*, Vol. **3**(6), p. 545–564. (Cité en pages xxxi, 164, 168 et 178)

Timofeeff, M., Lowenstein, T., Brennan, S., Demicco, R., Zimmermann, H., Horita, J., von Borstel, L., 2001. Evaluating Seawater Chemistry from Fluid Inclusions in Halite: Examples from Modern Marine and Nonmarine Environments. *Geochim. Cosmochim. Acta*, Vol. **65**(14), p. 2293–2300. (Cité en pages 31, 74 et 75)

Timofeeff, M. N., Lowenstein, T. K., da Silva, M. A. M., Harris, N. B., 2006. Secular Variation in the Major-Ion Chemistry of Seawater: Evidence from Fluid Inclusions in Cretaceous Halites. *Geochim. Cosmochim. Acta*, Vol. **70**(8), p. 1977–1994. (Cité en pages 74, 75, 77 et 78)

Toyofuku, T., Matsuo, M. Y., de Nooijer, L. J., Nagai, Y., Kawada, S., Fujita, K., Reichart, G.-J., Nomaki, H., Tsuchiya, M., Sakaguchi, H., Kitazato, H., 2017. Proton Pumping Accompanies Calcification in Foraminifera. *Nat. Commun.*, Vol. **8**, p. 14145. (Cité en page 144)

Tripati, A. K., Roberts, C. D., Eagle, R. A., 2009. Coupling of CO2 and Ice Sheet Stability Over Major Climate Transitions of the Last 20 Million Years. *Science*, Vol. **326**(5958), p. 1394–1397. (Cité en pages 10 et 144)

Trumbull, R. B., Slack, J. F., 2018. Boron Isotopes in the Continental Crust: Granites, Pegmatites, Felsic Volcanic Rocks, and Related Ore Deposits. *Dans : Marschall, H., Foster, G. (Eds.), Boron Isotopes*. Springer International Publishing, Cham, p. 249–272. (Cité en page 114)

Turchyn, A. V., DePaolo, D. J., 2019. Seawater Chemistry Through Phanerozoic Time. *Annu. Rev. Earth Planet. Sci.*, Vol. **47**(1), p. 197–224. (Cité en pages 59 et 61)

Uchikawa, J., Penman, D. E., Zachos, J. C., Zeebe, R. E., 2015. Experimental Evidence for Kinetic Effects on B/Ca in Synthetic Calcite: Implications for Potential B(OH)4- and B(OH)3 Incorporation. *Geochim. Cosmochim. Acta*, Vol. **150**, p. 171–191. (Cité en page 23)

Ulmishek, G. F., 2001. *Petroleum Geology and Resources of the Nepa-Botuoba High, Angara-Lena Terrace, and Cis-Patom Foredeep, Southeastern Siberian Craton, Russia*. Report 2201C. (Cité en page 72)

Urey, H. C., Lowenstam, H. A., Epstein, S., McKINNEY, C. R., 1951. MEASUREMENT OF PALEOTEMPERATURES AND TEMPERATURES OF THE UPPER CRETACEOUS OF ENGLAND, DENMARK, AND THE SOUTHEASTERN UNITED STATES. *GSA Bulletin*, Vol. **62**(4), p. 399–416. (Cité en pages 6, 14, 22, 144 et 175)

van der Kaars, S., Williams, M. A. J., Bassinot, F., Guichard, F., Moreno, E., Dewilde, F., Cook, E. J., 2012. The Influence of the ∼73 Ka Toba Super-Eruption on the Ecosystems of Northern Sumatra as Recorded in Marine Core BAR94-25. *Quaternary International*, Vol. **258**, p. 45–53. (Cité en pages xxxii, 167, 171, 172 et 173)

van der Meer, D., van den Berg van Saparoea, A., van Hinsbergen, D., van de Weg, R., Godderis, Y., Le Hir, G., Donnadieu, Y., 2017. Reconstructing First-Order Changes in Sea Level during the Phanerozoic and Neoproterozoic Using Strontium Isotopes. *Gondwana Res.*, Vol. **44**, p. 22–34. (Cité en pages xxvi, 55 et 61)

Van Der Meer, D. G., Zeebe, R. E., van Hinsbergen, D. J. J., Sluijs, A., Spakman, W., Torsvik, T. H., 2014. Plate Tectonic Controls on Atmospheric CO2 Levels since the Triassic. *Proc. Natl. Acad. Sci.*, Vol. **111**(12), p. 4380–4385. (Cité en pages xxvi, 8, 37, 54, 55, 56 et 61)

Vega, E., Foster, G. L., Martínez-Botí, M. A., Anagnostou, E., Field, M. P., Kim, M. H., Watson, P., Wilson, P. A., 2020. Automation of Boron Chromatographic Purification for δ^{11} B Analysis of Coral Aragonite. *Rapid Commun. Mass Spectrom.*, Vol. **34**(11). (Cité en pages xxx, 116, 127, 132 et 137)

Veizer, J., Ala, D., Azmy, K., Bruckschen, P., Buhl, D., Bruhn, F., Carden, G. A. F., Diener, A., Ebneth, S., Godderis, Y., Jasper, T., Korte, C., Pawellek, F., Podlaha, O. G., Strauss, H., 1999. 87Sr/86Sr, δ13C and δ18O Evolution of Phanerozoic Seawater. *Chemical Geology*, Vol. **161**(1), p. 59–88. (Cité en pages xxv, xxvi, 33, 34, 41, 61 et 82)

Vengosh, A., Chivas, A. R., McCulloch, M. T., 1989. Direct Determination of Boron and Chlorine Isotopic Compositions in Geological Materials by Negative Thermal-Ionization Mass Spectrometry. *Chem. Geol. Isot. Geosci. Sect.*, Vol. **79**(4), p. 333–343. (Cité en page 145)

Vengosh, A., Chivas, A. R., McCulloch, M. T., Starinsky, A., Kolodny, Y., 1991a. Boron Isotope Geochemistry of Australian Salt Lakes. *Geochimica et Cosmochimica Acta*, Vol. **55**(9), p. 2591–2606. (Cité en pages 45, 49 et 50)

Vengosh, A., Chivas, A. R., Starinsky, A., Kolodny, Y., Baozhen, Z., Pengxi, Z., 1995. Chemical and Boron Isotope Compositions of Non-Marine Brines from the Qaidam Basin, Qinghai, China. *Chemical Geology*, Vol. **120**(1), p. 135–154. (Cité en page 45)

Vengosh, A., Kolodny, Y., Starinsky, A., Chivas, A. R., McCulloch, M. T., 1991b. Coprecipitation and Isotopic Fractionation of Boron in Modern Biogenic Carbonates. *Geochim. Cosmochim. Acta*, Vol. **55**(10), p. 2901–2910. (Cité en pages xxiv, 10, 18, 21, 29, 30, 35, 36, 114, 115 et 144)

Vengosh, A., Starinsky, A., Kolodny, Y., Chivas, A. R., Raab, M., 1992. Boron Isotope Variations during Fractional Evaporation of Sea Water: New Constraints on the Marine vs. Nonmarine Debate. *Geology*, Vol. **20**(9), p. 799. (Cité en pages 45, 47, 48, 49 et 75)

Vérard, C., Hochard, C., Baumgartner, P. O., Stampfli, G. M., Liu, M., 2015. Geodynamic Evolution of the Earth over the Phanerozoic: Plate Tectonic Activity and Palaeoclimatic Indicators. *J. Palaeogeogr.*, Vol. **4**(2), p. 167–188. (Cité en pages xxvi, 55 et 61)

Vérard, C., Veizer, J., 2019. On Plate Tectonics and Ocean Temperatures. *Geology*, Vol. **47**(9), p. 881–885. (Cité en page 2)

Vogl, J., Rosner, M., 2011. Production and Certification of a Unique Set of Isotope and Delta Reference Materials for Boron Isotope Determination in Geochemical, Environmental and Industrial Materials. *Geostand. Geoanalytical Res.*, Vol. **36**(2), p. 161–175. (Cité en pages xxix, xxx, xxxi, 33, 100, 103, 104, 117, 125, 129, 130, 149 et 169)

Vollstaedt, H., Eisenhauer, A., Wallmann, K., Böhm, F., Fietzke, J., Liebetrau, V., Krabbenhöft, A., Farkaš, J., Tomašových, A., Raddatz, J., Veizer, J., 2014. The Phanerozoic $\Delta 88/86$Sr Record of Seawater: New Constraints on Past Changes in Oceanic Carbonate Fluxes. *Geochim. Cosmochim. Acta*, Vol. **128**, p. 249–265. (Cité en page 82)

Walker, J. C. G., Hays, P. B., Kasting, J. F., 1981. A Negative Feedback Mechanism for the Long-Term Stabilization of Earth's Surface Temperature. *J. Geophys. Res. Oceans*, Vol. **86**(C10), p. 9776–9782. (Cité en pages 2, 59, 61 et 163)

Walker, M., Johnsen, S., Rasmussen, S. O., Popp, T., Steffensen, J.-P., Gibbard, P., Hoek, W., Lowe, J., Andrews, J., Björck, S., Cwynar, L. C., Hughen, K., Kershaw, P., Kromer, B., Litt, T., Lowe, D. J., Nakagawa, T., Newnham, R., Schwander, J., 2009. Formal Definition and Dating of the GSSP (Global Stratotype Section and Point) for the Base of the Holocene Using the Greenland NGRIP Ice Core, and Selected Auxiliary Records. *J. Quat. Sci.*, Vol. **24**(1), p. 3–17. (Cité en page 5)

Wang, B.-S., You, C.-F., Huang, K.-F., Wu, S.-F., Aggarwal, S. K., Chung, C.-H., Lin, P.-Y., 2010. Direct Separation of Boron from Na- and Ca-Rich Matrices by Sublimation for Stable Isotope Measurement by MC-ICP-MS. *Talanta*, Vol. **82**(4), p. 1378–1384. (Cité en pages xxx, 115, 116, 131, 132, 133, 146 et 148)

Wang, J., Hansen, E. H., 2003. On-Line Sample-Pre-Treatment Schemes for Trace-Level Determinations of Metals by Coupling Flow Injection or Sequential Injection with ICP-MS. *TrAC Trends in Analytical Chemistry*, Vol. **22**(11), p. 836–846. (Cité en page 96)

Ward, R. F., Kendall, C. G. S. C., Harris, P. M., 1986. Upper Permian (Guadalupian) Facies and Their Association with Hydrocarbons - Permian Basin, West Texas and New Mexico. *Am Assoc Pet Geol Bull U. S.*, Vol. **70:3**. (Cité en page 69)

Warren, J. K., 2010. Evaporites through Time: Tectonic, Climatic and Eustatic Controls in Marine and Nonmarine Deposits. *Earth-Sci. Rev.*, Vol. **98**(3-4), p. 217–268. (Cité en pages xxiv, 32 et 67)

Webby, B. D., 1978. History of the Ordovician Continental Platform Shelf Margin of Australia. *J. Geol. Soc. Aust.*, Vol. **25**(1-2), p. 41–63. (Cité en page 71)

Wei, G., McCulloch, M. T., Mortimer, G., Deng, W., Xie, L., 2009. Evidence for Ocean Acidification in the Great Barrier Reef of Australia. *Geochimica et Cosmochimica Acta*, Vol. **73**(8), p. 2332–2346. (Cité en pages 29, 114 et 145)

Wei, H.-Z., Jiang, S.-Y., Tan, H.-B., Zhang, W.-J., Li, B.-K., Yang, T.-L., 2014. Boron Isotope Geochemistry of Salt Sediments from the Dongtai Salt Lake in Qaidam Basin: Boron Budget and Sources. *Chem. Geol.*, Vol. **380**, p. 74–83. (Cité en page 45)

Westphal, C. S., Kahen, K., Rutkowski, W. F., Acon, B. W., Montaser, A., 2004. Demountable Direct Injection High Efficiency Nebulizer for Inductively Coupled Plasma Mass Spectrometry. *Spectrochim. Acta Part B At. Spectrosc.*, Vol. **59**(3), p. 353–368. (Cité en pages 95, 115 et 119)

Westphal, C. S., McLean, J. A., Acon, B. W., Allen, L. A., Montaser, A., 2002. Axial Inductively Coupled Plasma Time-of-Flight Mass Spectrometry Using Direct Liquid Sample Introduction. *J. Anal. At. Spectrom.*, Vol. **17**(7), p. 669–675. (Cité en page 96)

Wiederin, D. R., Smith, F. G., Houk, R. S., 1991. Direct Injection Nebulization for Inductively Coupled Plasma Mass Spectrometry. *Anal. Chem.*, Vol. **63**(3), p. 219–225. (Cité en page 95)

Wielandt, D., Bizzarro, M., 2011. A TIMS-Based Method for the High Precision Measurements of the Three-Isotope Potassium Composition of Small Samples. *J Anal Spectrom*, Vol. **26**(2), p. 366–377. (Cité en pages 126 et 128)

Wieser, M. E., Schwieters, J. B., 2005. The Development of Multiple Collector Mass Spectrometry for Isotope Ratio Measurements. *Int. J. Mass Spectrom.*, Vol. **242**(2-3), p. 97–115. (Cité en pages 126 et 127)

Williams, G. E., 1991. Milankovitch-Band Cyclicity in Bedded Halite Deposits Contemporaneous with Late Ordovician-Early Silurian Glaciation, Canning Basin, Western Australia. *Earth Planet. Sci. Lett.*, Vol. **103**(1-4), p. 143–155. (Cité en page 71)

Williams, L. B., Hervig, R. L., 2004. Boron Isotope Composition of Coals: A Potential Tracer of Organic Contaminated Fluids. *Applied Geochemistry*, Vol. **19**(10), p. 1625–1636. (Cité en pages 17 et 30)

Wind, M., Eisenmenger, A., D. Lehmann, W., 2002. Modified Direct Injection High Efficiency Nebulizer with Minimized Dead Volume for the Analysis of Biological Samples by Micro- and Nano-LC-ICP-MS. *J. Anal. At. Spectrom.*, Vol. **17**(1), p. 21–26. (Cité en page 95)

Winkelmann, R., Levermann, A., Ridgwell, A., Caldeira, K., 2015. Combustion of Available Fossil Fuel Resources Sufficient to Eliminate the Antarctic Ice Sheet. *Sci. Adv.*, Vol. **1**(8), p. e1500589. (Cité en pages xxiii, 5 et 10)

Woodward, F. I., 1987. Stomatal Numbers Are Sensitive to Increases in CO 2 from Pre-Industrial Levels. *Nature*, Vol. **327**(6123), p. 617–618. (Cité en page 6)

Wu, H. C., Dissard, D., Douville, E., Blamart, D., Bordier, L., Tribollet, A., Le Cornec, F., Pons-Branchu, E., Dapoigny, A., Lazareth, C. E., 2018. Surface Ocean pH Variations since 1689 CE and Recent Ocean Acidification in the Tropical South Pacific. *Nat. Commun.*, Vol. **9**(1). (Cité en pages 29 et 114)

Xia, Z., Horita, J., Reuning, L., Bialik, O. M., Hu, Z., Waldmann, N. D., Liu, C., Li, W., 2020. Extracting Mg Isotope Signatures of Ancient Seawater from Marine Halite: A Reconnaissance. *Chemical Geology*, Vol. **552**, p. 119768. (Cité en pages 48 et 49)

Yan, Y., Bender, M. L., Brook, E. J., Clifford, H. M., Kemeny, P. C., Kurbatov, A. V., Mackay, S., Mayewski, P. A., Ng, J., Severinghaus, J. P., Higgins, J. A., 2019. Two-Million-Year-Old Snapshots of Atmospheric Gases from Antarctic Ice. *Nature*, Vol. **574**(7780), p. 663–666. (Cité en pages 2 et 6)

Yang, W., Spencer, R. J., Krouse, H., Lowenstein, T. K., Casas, E., 1995. Stable Isotopes of Lake and Fluid Inclusion Brines, Dabusun Lake, Qaidam Basin, Western China: Hydrology and Paleoclimatology in Arid Environments. *Palaeogeogr. Palaeoclimatol. Palaeoecol.*, Vol. **117**(3-4), p. 279–290. (Cité en page 75)

You, C.-F., Chan, L. H., Spivack, A. J., Gieskes, J. M., 1995. Lithium, Boron, and Their Isotopes in Sediments and Pore Waters of Ocean Drilling Program Site 808, Nankai Trough: Implications for Fluid Expulsion in Accretionary Prisms. *Geology*, Vol. **23**(1), p. 37. (Cité en page 36)

You, C.-F., Spivack, A. J., Smith, J. H., Gieskes, J. M., 1993. Mobilization of Boron in Convergent Margins: Implications for the Boron Geochemical Cycle. *Geology*, Vol. **21**(3), p. 207. (Cité en pages xxiv, 35 et 36)

Yu, J., Day, J., Greaves, M., Elderfield, H., 2005. Determination of Multiple Element/Calcium Ratios in Foraminiferal Calcite by Quadrupole ICP-MS: FORAMINIFERAL CALCITE. *Geochem. Geophys. Geosystems*, Vol. **6**(8), p. n/a–n/a. (Cité en pages 148 et 170)

Yu, J., Elderfield, H., Greaves, M., Day, J., 2007a. Preferential Dissolution of Benthic Foraminiferal Calcite during Laboratory Reductive Cleaning: BENTHIC FORAMINIFERAL CALCITE. *Geochem. Geophys. Geosystems*, Vol. **8**(6), p. n/a–n/a. (Cité en pages 144, 147 et 169)

Yu, J., Elderfield, H., Hönisch, B., 2007b. B/Ca in Planktonic Foraminifera as a Proxy for Surface Seawater pH: B/Ca IN PLANKTIC FORAM AS A PROXY FOR pH. *Paleoceanography*, Vol. **22**(2). (Cité en pages 10, 144 et 147)

Zalasiewicz, J., Waters, C. N., Williams, M., Barnosky, A. D., Cearreta, A., Crutzen, P., Ellis, E., Ellis, M. A., Fairchild, I. J., Grinevald, J., Haff, P. K., Hajdas, I., Leinfelder, R., McNeill, J., Odada, E. O., Poirier, C., Richter, D., Steffen, W., Summerhayes, C., Syvitski, J. P., Vidas, D., Wagreich, M., Wing, S. L., Wolfe, A. P., An, Z., Oreskes, N., 2015. When Did the Anthropocene Begin? A Mid-Twentieth Century Boundary Level Is Stratigraphically Optimal. *Quat. Int.*, Vol. **383**, p. 196–203. (Cité en page 5)

Zeebe, R. E., 2012. LOSCAR: Long-Term Ocean-Atmosphere-Sediment CArbon Cycle Reservoir Model v2.0.4. *Geosci. Model Dev.*, Vol. **5**(1), p. 149–166. (Cité en pages 15 et 61)

Zeebe, R. E., Ridgwell, A., Zachos, J. C., 2016. Anthropogenic Carbon Release Rate Unprecedented during the Past 66 Million Years. *Nat. Geosci.*, Vol. **9**(4), p. 325–329. (Cité en page 9)

Zeebe, R. E., Sanyal, A., Ortiz, J. D., Wolf-Gladrow, D. A., 2001. A Theoretical Study of the Kinetics of the Boric Acid–Borate Equilibrium in Seawater. *Mar. Chem.*, Vol. **73**(2), p. 113–124. (Cité en pages 10, 23 et 30)

Zeebe, R. E., Wolf-Gladrow, D., 2001. *CO2 in Seawater: Equilibrium, Kinetics, Isotopes*. No. 65 dans Elsevier Oceanography Book Series. (Cité en pages 21 et 155)

Zeebe, R. E., Wolf-Gladrow, D. A., Bijma, J., Hönisch, B., 2003. Vital Effects in Foraminifera Do Not Compromise the Use of δ ^{11} B as a Paleo- p H Indicator: Evidence from Modeling: CRETACEOUS MARINE TEMPERATURE EVOLUTION. *Paleoceanography*, Vol. **18**(2), p. n/a–n/a. (Cité en pages 24 et 157)

Zhang, Q., T. Snow, J., Holdship, P., Price, D., Watson, P., M. Rickaby, R. E., 2018. Direct Measurement of Multi-Elements in High Matrix Samples with a Flow Injection ICP-MS: Application to the Extended Emiliania Huxleyi Redfield Ratio. *J. Anal. At. Spectrom.*, Vol. **33**(7), p. 1196–1208. (Cité en page 96)

Zhang, S., Henehan, M. J., Hull, P. M., Reid, R. P., Hardisty, D. S., v.S. Hood, A., Planavsky, N. J., 2017. Investigating Controls on Boron Isotope Ratios in Shallow Marine Carbonates. *Earth Planet. Sci. Lett.*, Vol. **458**, p. 380–393. (Cité en pages 51 et 137)

Zhao, Y., Wei, H.-Z., Liu, X., Wang, Y.-J., Jiang, S.-Y., Eastoe, C. J., Peryt, T. M., 2020. Isotope Evidence for Multiple Sources of B and Cl in Middle Miocene (Badenian) Evaporites, Carpathian Mountains. *Applied Geochemistry*, p. 104819. (Cité en pages 45, 47 et 49)

Zielinski, G. A., 2000. Use of Paleo-Records in Determining Variability within the Volcanism–Climate System. *Quaternary Science Reviews*, Vol. **19**(1), p. 417–438. (Cité en page 167)

Zimmermann, H., 2001. On the Origin of Fluids Included in Phanerozoic Marine Halite—Basic Interpretation Strategies. *Geochim. Cosmochim. Acta*, Vol. **65**(1), p. 35–45. (Cité en pages 74 et 75)

Zoorob, G., Tomlinson, M., Wang, J., Caruso, J., 1995. Evaluation of the Direct Injection Nebulizer in the Coupling of High-Performance Liquid Chromatography to Inductively Coupled Plasma Mass Spectrometry. *J. Anal. At. Spectrom.*, Vol. **10**(10), p. 853–858. (Cité en page 95)